Vol. 15 • No. 2 • October 2021

ISSN: 0976 - 1330

Journal of GEOMATICS

INDIAN SOCIETY OF GEOMATICS

Journal of Geomatics

(A Publication of the Indian Society of Geomatics)

Vol. 15. No. 2 Research articles October 2021

Vol. 15. No. 2 Research articles October 2021

Special Section: Flood Assessment and Modeling

Adaptive nonlinear image denoising techniques with application to satellite imagery

Bhaskar Dubey*[1], Sweety Sindhav [2] and B. Kartikeyan[1]
[1]Image Analysis and Quality Evaluation Division, Space Applications Centre, ISRO, Ahmedabad, Gujarat, India,
[2]L.D. College of Engineering, Ahmedabad, Gujarat, India,
*Email: bhaskard@sac.isro.gov.in,

(Received: Mar 23, 2021; in final form July 12, 2021)

Abstract: In this paper, we have developed GLCM based technique to adapt the radiometric parameter estimation in the bilateral and trilateral filters. Bilateral and trilateral filters are the one amongst the widely used filters for noise removal in images. Filter performance heavily depends on the parameters selected and accurate estimation of parameters from noisy images is a challenging task. We have developed an efficient technique that adaptively estimate several noise-parameters involved in the denoising process, for instance, radiometric variance, SNR, and impulse variance. Detailed and complete algorithms are provided for noise parameters estimation. A comparative study of the performance of various nonlinear filters using our adaptive method of noise parameters estimation and with other methods known in the literature is carried out on Lena image corrupted with different levels of Gaussian and impulse noise. It is shown with several examples that the quality of denoised images using our approach is significantly better than the existing approaches in the literature. The results are also demonstrated on several high-resolution satellite images.

Keywords: Impulsive-noise, Gaussian-noise, NLM-filter, Trilateral-filter, SNR

1. Introduction

Noise is an unwanted by-product that occurs in images during various stages such as acquisition, transmission, and pre-processing. The principal sources of noise in digital images, especially in remote sensing images acquired by a satellite, are atmospheric and environmental conditions, sensor-temperature, and statistical nature of photon collection process by detectors (photon noise), electronic port biases between detecting elements, electromagnetic interference in the transmission channel, demodulation decompression and derandomization etc. Image noise can be random or may exhibits fixed patterns, which are undesired variation of intensity in images acquired by a sensor. Several types of noises are usually present in the images, for example, electronic and pattern noise, Gaussian noise, Gamma noise (Boyat and Joshi 2015), Photon noise (Deledalle et al., 2010), Speckle noise (Maity et al., 2015), Impulse noise (Al-amri and Kalyankar 2010). Each type of noise possesses certain characteristic, which makes them different from each other

It is difficult to estimate precisely the amount of noise present in the images. Also, important details such as edges and textures should not be obscured while removing noise and also no other details should get added. The problem with most of the image denoising techniques is that while removing the unwanted noise some of the image information is also lost. The aim of any denoising technique is to minimize the loss of original image information.

Several denoising techniques have been proposed in the literature. For instance, mean, median based filters in spatial domain (Kaur 2015), filtering high frequency component via FFT in frequency domain, TV (Total variation) norm minimisation based method (Rudin et al., 1992), bilateral (Tomasi and Manduchi 1998), trilateral (Garnett et al. 2005) filters and NLM filter (Wang et al. 2018) etc. Mean filter is a basic linear filter used for smoothening of the images. Although, it reduces noise from the image, it fails at preserving edges and other artefacts. To overcome this drawback a Gaussian filter was designed, which weighs nearby pixels more heavily compared to far away pixels. Yet another enhancement to the Gaussian filter is a bilateral filter that uses product of two kernels, one in spatial direction and other in radiometric direction with two different parameters for each direction. The two parameters are spatial weight and radiometric weight. The pixels closer to the centre pixel are weighted more by the spatial kernel and the pixels similar in intensity to the centre pixel are weighted more by the radiometric kernel. Similarly, in trilateral filter yet another kernel that corresponds to impulse is introduced in addition to spatial and radiometric kernels.

Several authors in the literature have investigated upon the bilateral and trilateral filters; however, selection of parameters has always remained a challenge. In (Veerakumar et al. 2019), empirical mode decomposition method is employed to identify impulse pixel and employed bilateral filter for noise removal. In their experiment, they state both the parameters spatial weight and radiometric weight were set on trial and error basis. Authors have tested for different values of spatial weight from 0 to 10 and for radiometric weight from 0 to 100 in order to get the optimal results. Similarly, in (Garnett R. et al. 2005) authors do not provide much detail on the parameters selection.

In this paper, we develop bi/trilateral filtering based techniques in which noise parameters are efficiently estimated using a novel adaptive technique. Thus, the objective of the paper is two folded: (1) It provides a novel adaptive technique for estimation of noise parameters involved in nonlinear filtering based on bilateral and trilateral filters. (2) A comparative study of the performance of bilateral, trilateral and NLM filters over different images, with different types and different levels of noise, is carried out. It is established through several comparison that the trilateral filter using our adaptive method of noise parameters estimation, (which we term as

Adaptive Bilateral/Trilateral filters (ABF/ATF)), performs significantly better than the standard bilateral/trilateral filters (BFH/TFH) which uses homogeneous area based method for noise parameters estimation. Further, ATF is shown to perform better than other established nonlinear filter like Non-local means (NLM).

The organisation of the paper is as follows. Section 2, briefly discuss few basic image noise models and related work. Section 3 discusses the methodology for adaptive estimation of noise parameters along with implementation of bilateral and trilateral filters. Complete description is provided on selection of parameters involved in the filters. Section 4 discusses the denoising results on several test images derived from Lena image and provides a detailed comparison of the performance of various filters. We have also applied our results on Indian cartographic satellite images and other high-resolution satellite images in order to show the efficacy of proposed approach in removing noises that occur in practical satellite based image acquisition. These results dealing with satellite images are presented in section 5. Finally, we conclude the paper in section 6 along with future scope of the work.

2. Basic background and related work

In this section, we briefly review the related work in the literature and present some of the known nonlinear image denoising techniques. We mainly deal with Gaussian and impulse noise.

2.1. Noise models

2.1.1. Impulse noise

Impulse noise is introduced in the image due to bit error in transmission while analog-to-digital conversion, faults in sensor hardware, hot or cold pixels in the detectors. Impulse noise is substitutive noise, which replaces some of the pixels in an image with some different pixels value. In an image, mathematically it is expressed by Eq. (1).

$$U_{ij} = \begin{cases} n_{ij,} & p \\ U^0 ij, & (1-p) \end{cases} \quad (1)$$

where, n_{ij} is taken from a uniform or discrete distribution and it replaces the pixels in the image with probability p. $U^0 ij$ is the original values of non-impulsive pixels in the image, that is, these pixels are not affected by impulse noise.

2.1.2. Gaussian noise

Gaussian noise is introduced mainly during the image acquisition. The sensor tends to have its own electronic circuit noise. Gaussian noise is an additive noise. That is when the images are corrupted by Gaussian noise; a noisy value is added to the original pixel value.

$$U_{ij} = U^0_{ij} + n_{ij} \quad (2)$$

Where U^0_{ij} represents the original pixel value at (i, j) in the uncorrupted image, when the noise n_{ij} is added at pixel (i, j) leads to the corrupted image U_{ij}. The noise value n_{ij} is derived from a normal distribution.

2.2. Bilateral filter

The bilateral filter is a nonlinear filter that is a modification to the Gaussian filter and is shown to be effective in edge preservation. The early reference to the idea of bilateral filter can be traced back to (Overton and Weymouth 1979), which is further studied and extended by (Tomasi and Manduchi 1998). The Bilateral filter has two weighting functions namely spatial weight and radiometric weight. For every pixel in the image, a (2N+1) × (2N+1) window is considered around the pixel and the centre pixel is replaced by the weighted average using spatial weight and radiometric weight. The spatial weight determines the spatial proximity of the pixel in the given window with respect to the centre pixel and the radiometric weight determines the radiometric similarity the pixels in the window compared to the centre pixel.

In an image let p be the current pixel and K be a kernel of size (2N+1) × (2N+1) around p. Let q be any pixel belonging to the kernel K. The spatial weight $w_S(p,q)$ is modelled using a Gaussian distribution function, which gives high weights to the spatially closer pixels to p in kernel K. The spatial weight$w_S(p,q)$ is expressed as:

$$w_S(p,q) = \exp^{-\frac{|p-q|^2}{2\sigma_S^2}}. \quad (3)$$

The radiometric weight $w_R(p,q)$ is a function used to weight more on pixels having similar intensity to the centre pixel p and less otherwise.. The radiometric weight is obtained by taking the Gaussian distance between absolute difference of the grey levels of central pixel p $(with\ greylevel\ u_p)$ and the pixel q in the kernel $(with\ greylevel\ u_q)$ around pixel p and is expressed as:

$$w_R(p,q) = \exp^{-\frac{|u_p-u_q|}{2\sigma_R^2}}. \quad (4)$$

Thus, the total weight assigned for the pixel p is given by:

$$w(p,q) = w_S(p,q) w_R(p,q). \quad (5)$$

The filter performance heavily depends on the parameter σ_s and σ_R. These parameters need to be estimated efficiently for optimal performance of the bilateral filter.

2.3. Trilateral filter

In images corrupted by impulse noise, the impulse pixel value is replaced by some arbitrary value coming from a uniform or discrete distribution. Therefore, it becomes very important to identify an impulse pixel. The bilateral filter efficiently removes the Gaussian noise efficiently but fails to remove impulse noise. This led to development of trilateral filter which works well both, with the Gaussian noise and the impulse noise and the mixture of both. Trilateral filter finds enormous application in denoising the high contrast images (Choudhury and Tumblin 2003), medical images (Wong et al. 2004) and in satellite imagery.

Mostly the filtering algorithm consists of two steps: Noisy pixel identification and noisy pixel correction. Garnet et al., 2005 introduces a trilateral filter that uses a statistical parameter ROAD (Rank Order Absolute Difference) statistic, which automatically identifies the impulse pixel very efficiently.

ROAD Statistic Calculation Steps

(1) For a given pixel select a window around the pixel of size (2N+1)*(2N+1) where N is a natural number.

(2) Take the absolute difference of every pixel in the window with respect to the centre pixel.

(3) Select the m smallest value from the above step where m is any number less than or equal to half the total number of pixels in the window.

(4) The sum of the m values in step 3 gives us the ROAD value of the pixel.

ROAD statistic is used to measure how similar are the pixels to the centre pixel in the given kernel. The ROAD statistic of the entire image is calculated using a kernel of 3 by 3 matrix, 5 by 5 window can also be considered however computational cost will increase. *ROAD* statistic efficiently captures impulse pixels in the given window. It uses the fact that in a given natural image the intensity among the neighbouring pixels does not vary much including the edge pixels. Therefore, a *ROAD* value will be high only if the impulse is present and the *ROAD* value of a non-impulse pixel stays relatively lower.

The trilateral filter is designed by incorporating the ROAD statistic into the bilateral filter to efficiently detect the impulse pixel. In the Trilateral filter, a new impulsive weighting function is added apart from the spatial weight and radiometric weight function. Impulsive weighting function uses the *ROAD* statistic to identify impulse pixels. The spatial weight and radiometric weight efficiently remove Gaussian noise and impulse noise is removed by the impulsive weight once the impulse pixel is identified by the *ROAD* statistic. The following equation (6) defines the impulsive weight

$$w_I(p) = exp^{-\frac{R(p)^2}{2\sigma_I^2}}, \tag{6}$$

Where $w_I(p)$is the impulsive weight and $R(p)$denotes the ROAD value of pixel p. σ_I acts as a threshold (a measure of impulsive variance) above which the pixel is considered to be impulse pixel.

A trilateral filter is designed to remove impulse noise, Gaussian noise, and a mixture of impulse and Gaussian noise. So firstly, there should be a mechanism to identify whether the pixel considered is an impulse pixel or not. In the following expression (7), *J(p,q)* defines the degree of impulsiveness of a pixel q with respect to pixel p

$$J(p,q) = 1 - \exp^{-\left(\frac{R(p)+R(q)}{2}\right)^2 / 2\sigma_J^2}. \tag{7}$$

Eq. (7) results in a value between 0 and 1. It results in 0 if neither of the p or q is impulse pixel. If any of p or q is impulse then its ROAD value will be significantly higher and thus it will give value 1. We need to be careful that the impulsive weight needs to be applied only when an impulsive pixel is present. If there is no impulse then only radiometric weight be applied instead of impulsive weight. σ_j is the parameter that controls the shape of the function *J(p,q)*.

Thus, for the trilateral filter, the total weight applied to a pixel is expressed by:

$$w(x,y) = w_s(x,y) w_R(x,y)^{1-J(x,y)} w(y)_I^{J(x,y)}. \tag{8}$$

From equation (8), it can be observed that if the value of joint impulsivity $J(p,q)$ is 0 the radiometric weight is applied and the impulsive weight does not add any significance similarly, when $J(p,q)$ is 1, the impulsive weight is applied and the radiometric weight does not add any significance.

The restored pixel $\tilde{p}$ is the result of normalizing the weights given by

$$\tilde{p} = \frac{\sum_{q\in k} w(x,y) U_y}{\sum_{q\in k} w(x,y)}. \tag{9}$$

When there are no impulses the trilateral filter turns into a bilateral filter and thus efficiently removes the Gaussian noise. If there are impulse pixels present, the impulsive weight gets activated and thus impulse pixels are treated detected and removed efficiently.

2.4. Non-Local Mean (NLM) filter

NLM filter utilises the redundancy in real world images. It is based on the principle that there exists plenty of non-neighbouring pixels in real-world images that contain near similar information or self-similarity in the neighbourhood. NLM filtering techniques is also one of the widely used technique in the literature for noise removal from images (Buades et al. 2005; Karnati et al., 2009), Wang et al. 2018). Essentially, NLM filter considers two windows while denoising the search window and the target window (or the patch). The algorithm looks for patches similar to target window in the search window. While searching for similar patterns as that of target in the search window, a similarity measure, radiometric Gaussian distance between target and a patch in the search window is assigned to every patch in the search window. The pixel under consideration is replaced by the weighted sum of the means of all patches in the search window.

3. Noise parameters estimation and implementation

The parameter needs to be identified efficiently to get the best performance of the filters. Specifically, the study extends the work of (Garnett et. al, 2005) by providing an adaptive method, to estimate the parameters in bilateral/trilateral filters. In this section we provide our adaptive method for efficient estimation of noise parameters in the bilateral and trilateral filters. In subsequent sections, rigorous comparative analysis is carried out to establish that the parameters estimated using the proposed adaptive approach denoises the image better than existing techniques.

3.1. Spatial-weight parameter (σ_S)

For the spatial weight the parameter, σ_S needs to be selected properly. By taking a very low $\sigma_S$value, the filter tends to over smoothen the image.

As, $\sigma_S$is proportional to size of the moving-window because as the window size increases more pixels are taken into consideration and thus the threshold σ_S should also be increased. In this experiment for the Lena and the satellite images a window of 5x5 is taken and the value of$\sigma_S$is considered as 2. Usually σ_S value is dependent on system/optics PSF, usually in many high-resolution satellite missions more than 95 percent of the energy is within +/- 2 pixels around the peak. However, it may be significantly different than 2 and also it need not have bell-shaped structure. In that case, it has to be first fitted to optimal Gaussian function and then σ_S is estimated.

3.2. Radiometric-weight parameter (σ_R)

The parameter σ_R acts as a threshold up to which the pixels in the given window can be used in convolution. The lower value of σ_R means considering a lesser number of pixels similar to the centre pixel and large value of σ_R indicates more number of pixels to be considered similar and the filter starts accepting the pixels with high absolute difference with that of centre pixel. Selectingσ_R becomes a difficult task as it does not depend on any fixed parameter. There are several methods suggested in the literature for estimation noise and SNR parameters, for instance, (Gao 1993, Fu P. et el. 2012, Ren H. et el. 2014, Wang X. et al. 2009,), which uses uniform area from the image for SNR estimation. In this study, we have developed an adaptive method to estimate the value of σ_R.

The adaptive method for σ_R estimation

Often the noise levels in an image is signal-dependent, thus it is required to estimate noise levels corresponding to various intensity levels in an automatic manner. Essentially, our aim is to estimate different σ_R values based on the pixel intensity. As the pixel intensity varies, different standard deviations (σ_R) is obtained.

The proposed method automatically determines the homogeneity level based on the Grey level co-occurrence matrix(GLCM) (Reulke and Weichelt 2012). It identifies nearly homogeneous image patches in the image. Let $\mathrm{C_d}$ be the square matrix of size N, where N represents the grey levels in the image. $\mathrm{C_d}(\mathrm{k},\mathrm{l})$ represents the number of pairs of pixels which are apart by a displacement vector d and having the grey-levels k and l, respectively. Here displacement vector d is considered as (1,1).Effectively the matrix $\mathrm{C_d}$ gives some kind of similarity measure on the image; if the image patch is homogeneous, that is the range of grey level is small and the $\mathrm{C_d}$ is clustered near the main diagonal. Finally, homogeneity level matrix $\mathrm{h}(i,j)$is obtained by suppressing the heterogeneous pixel pairs by dividing the entries in $\mathrm{C_d}$ by$1+(k-l)^2$, thus,

$$\mathrm{h}(i,j) = \sum_{k}^{N}\sum_{l}^{N}\frac{C_d(k,l)}{1+(k-l)^2}. \quad (10)$$

A high value of $\mathrm{h}(i,j)$indicates high homogeneity level at the pixel neighbourhood. Further, $\mathrm{h}(i,j)$is segmented with appropriate threshold in order to get the reasonably homogeneous areas in the image for automatic noise and SNR estimation. The algorithm steps to find different noise values and SNR are as follows:

(1) Calculate the GLCM matrix, which is used to identify the homogeneous region in the image automatically.
(2) Threshold to select the pixel is set to 0.99. The threshold value is selected based on size of images, their dynamic ranges, and knowledge of system noise using lab-based experiment or by some other method, e.g., using homogeneous area method. Setting a high threshold will miss many nearly homogeneous patches and similarly a too low value will overestimate the homogeneous patches.
(3) From the non-zero region, obtain the local mean and local standard deviation of the image.
(4) Divide local mean values ranging from the minimum to maximum of the local mean evenly with the class size 5. Class size should be kept as low as possible for better results; however computational load will increase for very low values. It is found with experimentation that the class size ranging from 5 to 10 gives optimal results.
(5) The mean local standard deviation of each class acts as the standard deviation of that particular class.
(6) Finally, a lookup table of different classes consisting of mean value and its corresponding local standard deviation is constructed.

For each pixel, σ_R is adaptively selected from the lookup table, depending on the pixel value a different standard deviation is obtained. Figure 1 shows Lena image (left) with its GLCM matrix (right).

Figure 1. Lena (left) and its GLCM (Grey Level Co-occurrence) matrix (right)

3.3. Impulsive-weight parameter (σ_I)

It is necessary to distinguish impulse pixels from the rest of the uncorrupted pixels. An impulse pixel exhibits higher ROAD value. σ_I should be set to such a value above which the pixel is considered to be affected by impulse noise. A higher value of σ_I needs to be selected as the pixel corrupted by impulse noise has higher ROAD value. In this study, the threshold $\sigma_I$is approximately set to the mean of ROAD values. In this study, the threshold is set to 100 for the simulated Lena images. The threshold has to be carefully selected, as it is a measure of how much the center pixel is differing from its neighbours to be qualified as an impulse pixel. The threshold may vary from image to image, more precisely; it is depending on the typical imaging system characteristic, for e.g., radiance to count conversion, dynamic ranges etc.

4. Comparative study of proposed technique with existing de-noising techniques

In this section, we conduct an experiment on Lena images corrupted with various noise levels. We then compare the denoising results in terms of PSNR and RMSE using our method and other standard method suggested in the literature.

The Lena image is incorporated with various types and different levels of noise to establish the efficiency of the filter. We have used Lena images corrupted with high to moderate levels of (10dB, 15dB, 20dB, and 30dBPSNR) Gaussian noise and applied various denoising techniques to compare the results. We have also added the mixed noise, (i.e., combination of impulsive and Gaussian noise) to the Lena image in order to compare the performance of trilateral filter with other filters. In Figure 2, we have shown the denoising results for the case high noise (10dB PSNR) Lena image. Similarly, in Figure 3, the denoising results are shown on Lena image corrupted with 30 dB PSNR and 10 percent uniform impulsive noise. Visual images are not shown for the 15, 20 dB PSNR case, however Table 1 presents the comparative summary of SNR improvement in all the cases.

Figure 2. Lena image with (a) 10dB PSNR (Gaussian noise) has denoising results (b) Bilateral Filter, (c) Adaptive Bilateral Filter, (d) Trilateral Filter, (e) Adaptive Trilateral Filter and (f) NLM filter

4.1 Quantitative comparative analysis

In this subsection, we have compared the performance of various denoising methods that are applied on Lena images in Figure 2 and Figure 3. First, we show the performance of Bilateral filter using standard method (based on uniform area (Gao 1993)) and with our method, that is, adaptive Bilateral method. We further show the comparative results using standard trilateral filter and adaptive trilateral filter. Subsequently, we also compare the performance of adaptive bilateral, trilateral and NLM filters.

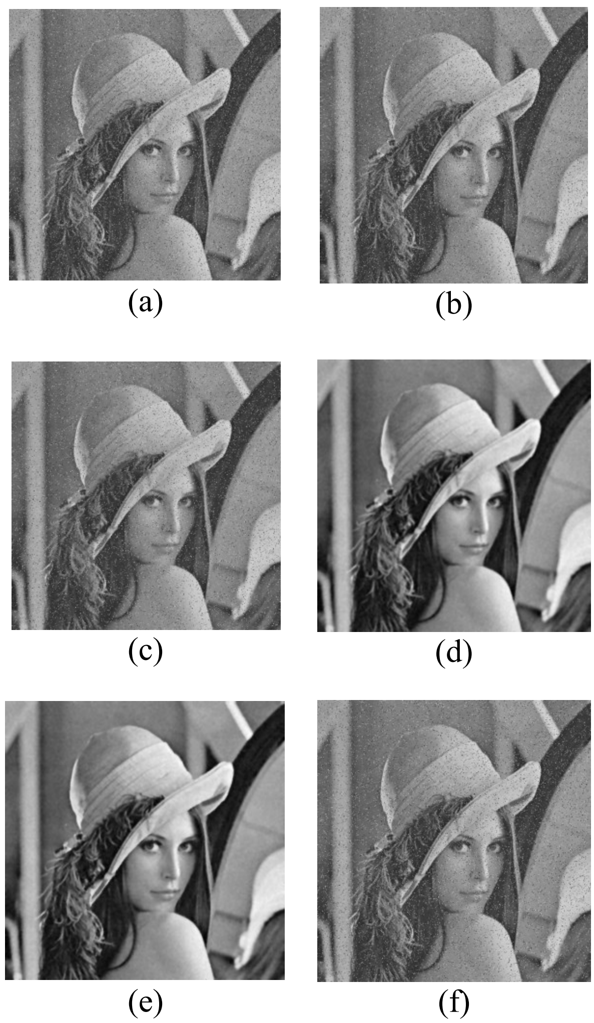

Figure 3. Lena image with (a) 30dB PSNR (Gaussian noise) + 10% Impulse noise has denoising results (b) Bilateral filter, (c) Adaptive bilateral filter (ABF) (d) Trilateral filter, (e) Adaptive trilateral filter (ATF) and (f) NLM filter

4.1.1. Comparison of standard bilateral and adaptive bilateral filters

In this experiment, three different cases of Lena image corrupted noise levels equivalent to 10 dB PSNR, 20dB PSNR and 30 dB PSNR with 10 percent uniform impulsive noise. In each case SNR of noisy image, image filtered with standard bilateral filter with parameters estimated using homogeneous area (BFH) and adaptive bilateral filter (ABF), and the original uncorrupted image are recorded. It is clear from the plots in Figure 4 that the SNR of the image filtered with adaptive bilateral filter is significantly higher than other methods.

4.1.2. Comparison of standard trilateral and adaptive trilateral filters

In this case, we again consider the same experiment as in the case 4.1.1 of bilateral filter. In each case SNR of noisy image, image filtered with standard trilateral filter (TFH) and adaptive trilateral filter (ATF) and also the original uncorrupted image are recorded. In Figure 5 (a), 5(b) SNR comparison is presented for 10 dB PSNR case and 20 dB PSNR case, respectively. In Figure 5(c), the SNR plots are shown for 30 dB PSNR case with 10 percent uniform impulsive noise. It is clearly observed from Figure 5 that SNR of the image filtered with adaptive trilateral filter is significantly higher than the standard method (TFH). In all the cases, it is concluded that ATF denoises the images better than standard trilateral filter (TFH).

4.1.3. Comparison of adaptive bilateral, adaptive trilateral and NLM filters

We now compare the relative performances of ABF, ATF and NLM filters under the same experiment as in above two cases.

The SNR results of denoised images using different techniques are shown in Figure 6. It is clear from Figure 6 that the adaptive trilateral-filter performs better than the bilateral and NLM filters in all cases. The Non-Local Mean Filter gives competing result to ATF visually and in terms of SNR in few cases, especially in moderate to low levels of noise, for example in 20dB SNR case. However, for very high levels of noise as shown in Figure 6(a), ATF supremely dominates the NLM filters. Further, even in low levels of Gaussian noise (30 dB PSNR case) if impulsive noise is present, then also NLM performance is significantly deteriorated compared to ATF. Thus, quantitative analysis results clearly suggests that the ATF performs significantly better than the bilateral and the NLM filters.

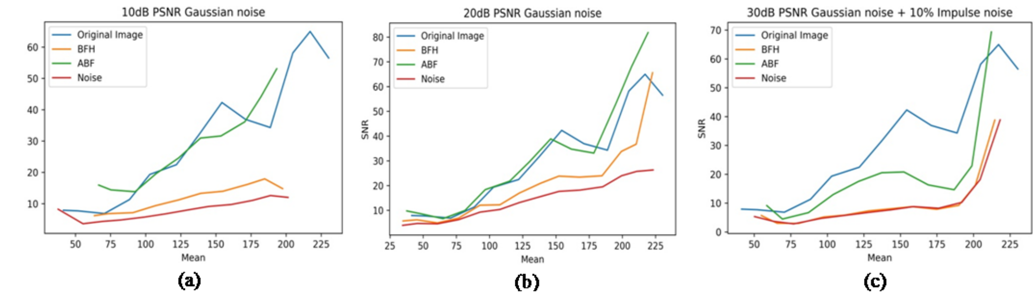

Figure 4. **Bilateral Filter SNR evaluation on Lena image (a) 10dB PSNR (σ = 80.6) Gaussian noise,(b) 20dB PSNR (σ = 25.5) Gaussian noise, (c) 30dB PSNR (σ = 8.06)Gaussian noise + 10% Impulse noise**

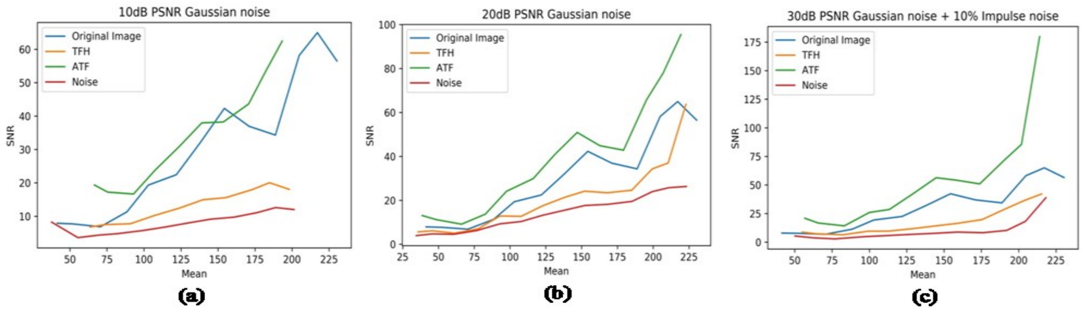

Figure 5. **Trilateral Filter SNR evaluation on Lena image (a) 10dB PSNR (σ = 80.6) Gaussian noise, (b) 20dB PSNR (σ = 25.5) Gaussian noise, (c) 30dB PSNR (σ = 8.06) Gaussian noise + 10% Impulse noise**

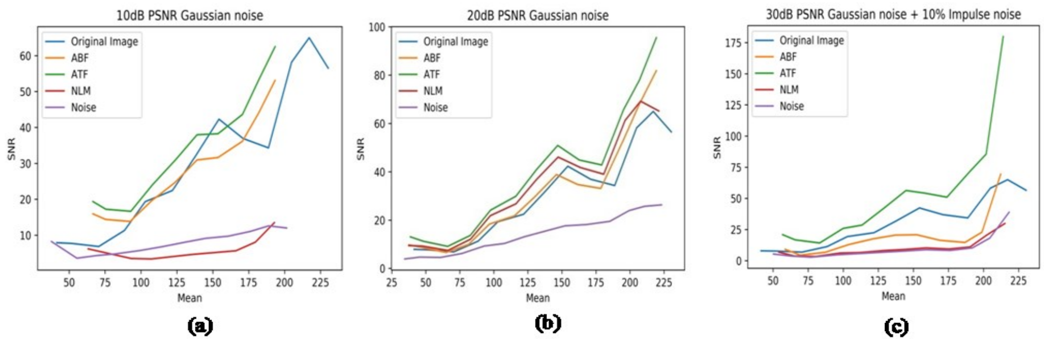

Figure 6. **SNR evaluation on Lena image (a) 10dB PSNR (σ = 80.6) Gaussian noise, (b) 20dB PSNR (σ = 25.5) Gaussian noise, (c) 30dB PSNR (σ = 8.06) Gaussian noise + 10% Impulse noise**

The detailed SNR results including the other cases 15 and 30 dB PSNR in addition to cases considered above are shown in Table 1.

Table 1 shows the PSNR and relative PSNR comparison of ABF, ATF, and NLM filters in five different cases having low to high levels of noise. In Table 2, RMSE caparison of ABF, ATF and NLM filters are shown.

From the results in Table 1 and Table 2, it can be concluded that ATF performs significantly better than ABF and NLM for moderate to high noise (15, 10 dB PSNR cases) conditions and with impulse noise (30 dB PSNR + 10 percent impulse). Although, for low to moderate SNR cases (30 dB and 20 dB PSNR cases) NLM filter performs slightly better than ATF.

5. Application of nonlinear de-noising techniques on satellite images

In this section, we have applied the different nonlinear denoising techniques on several high-resolution satellite images. Few sample satellite images from (Abramov, Sergey et al., 2019) and some Indian high resolution satellite images are used for simulation and quantitative evaluation was carried out on these images. Figure 7(a) shows a high-resolution Indian satellite image, which is obtained through a rigorous ground, based experiment that uses spatially designed cloth targets of different grey-shades for radiometric characterization. The image is panchromatic (PAN), a single band image, with spatial resolution .65m. The white dot on the black cloth is the sun-image obtained via a convex mirror target deployed on the ground. The adaptive bilateral and trilateral filters are applied on this image and SNR of the denoised image is estimated using each method. Figure 7(b) and 7(c), shows the de-noising results of Figure 7(a) using ABF and ATF, respectively. Figure 8(a), shows the uniform targets identified from the image which are labelled as B (Black), DG (Dark Grey), MG (Mid Grey), LG (Light Grey) and W (White).

Figure 8(b) shows the SNR results estimated using these identified targets. It is clear from the Figure 8(b), post-denoising SNR is significantly improved. Further ABF and ATF performances are nearly same due to the fact that image does not have much impulsive contents. Nevertheless, the white dot appeared on target “B” is treated as impulse and is removed while denoising with ATF as desired (see Figure 7c).

We have also compared the MTF before and after the denoising process using our filters. In Figure 9, edge image chips are extracted from the CARTOSAT experiment image for MTF estimation. Figure (9a), 9(b) ,9(c) show the four times zoomed edge targets taken from Figure (7a), 7(b), 7(c), respectively.

Table 1. PSNR comparison of Adaptive BF, Adaptive TF, and NLM on Lena image

Types of Filters	30 dB PSNR Gaussian noise		20 dB PSNR Gaussian Noise		15 dB PSNR Gaussian Noise		10 dB PSNR Gaussian Noise		30 dB PSNR Gaussian + 10% impulse noise	
	Absolute PSNR	Relative PSNR	Absolute PSNR	Relative PSNR	Absolute PSNR	Relative PSNR	Absolute PSNR	Relative PSNR	Absolute PSNR	Relative PSNR
Noisy image	28.33 dB	1.0	20.21 dB	1.0	17.38 dB	1.0	15.78 dB	1.0	18.50 dB	1.0
Adaptive BF	32.14 dB	1.55	22.13 dB	1.24	18.78 dB	1.17	17.00 dB	1.15	18.65 dB	1.02
Adaptive TF	33.26 dB	1.76	22.88 dB	1.36	19.02 dB	1.20	17.18 dB	1.17	28.33 dB	3.40
NLM	35.12 dB	2.18	22.96 dB	1.37	18.47 dB	1.13	16.37 dB	1.07	18.72 dB	1.03

Table 2. RMSE comparison of Adaptive BF, Adaptive TF, and NLM on Lena image

Types of Filters	30 dB PSNR Gaussian noise	20 dB PSNR Gaussian noise	15 dB PSNR Gaussian noise	10 dB PSNR Gaussian noise	30 dB PSNR Gaussian + 10% impulse noise
Noisy image	10.06	23.28	34.46	41.44	26.22
Adaptive BF	8.78	19.81	29.34	35.98	25.06
Adaptive TF	8.70	17.90	28.80	35.24	10.03
NLM	7.82	19.97	30.40	38.69	25.30

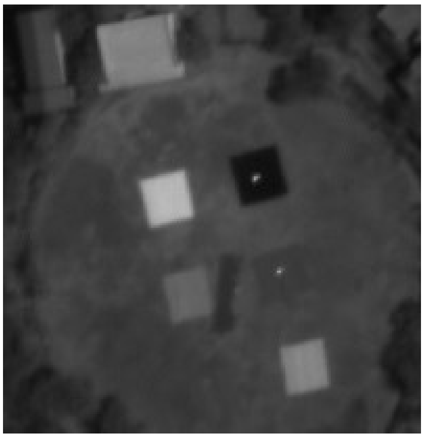

(a)

(b)

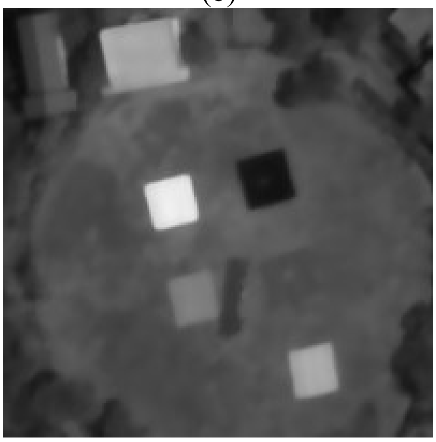

(c)

Figure 7. Denoising (a) Satellite Image with (b) Adaptive Bilateral filter and (c) Adaptive Trilateral filter

The MTF comparison results are shown in Figure 10. Original image MTF at Nyquist frequency is .88 and the MTF after applying ABF is 1.6. Further, the MTF value at Nyquist frequency after applying the ATF is 4.6. This shows that after filtering with ATF, MTF of the image is significantly improved. It is also observed that filtering with ABF slightly attenuates the MTF at mid frequencies as shown in Figure 10

We have taken few more images as shown in Figure 11 from different high-resolution satellites. The proposed adaptive nonlinear filtering methods are demonstrated on these satellite images and the results are also compared with NLM method.

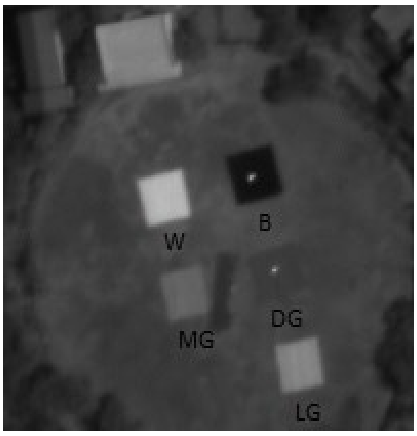

(a)

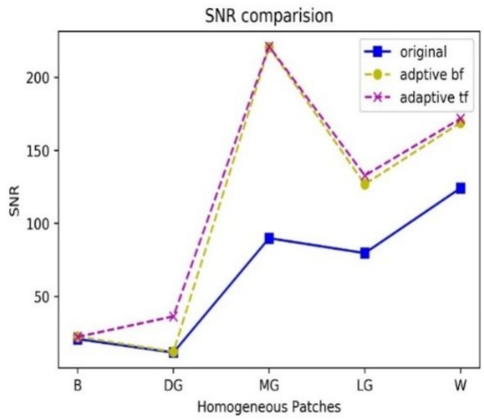

(b)

Figure 8. (a) Different grey levels homogeneous patches in Satellite image and (b) SNR Comparison of Homogeneous Patches

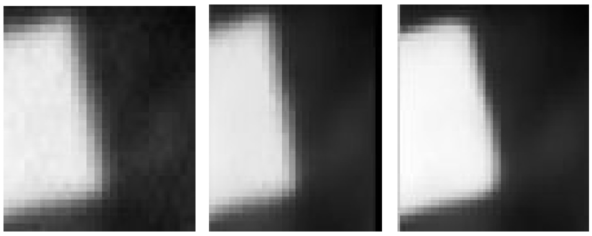

(a)Original chip (b) Filtered with ABF (c) Filtered with ATF

Figure 9. Edge targets image chips for MTF comparison

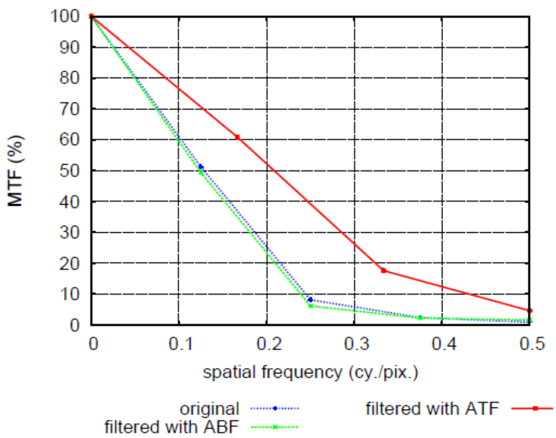

Figure 10. MTF comparison result

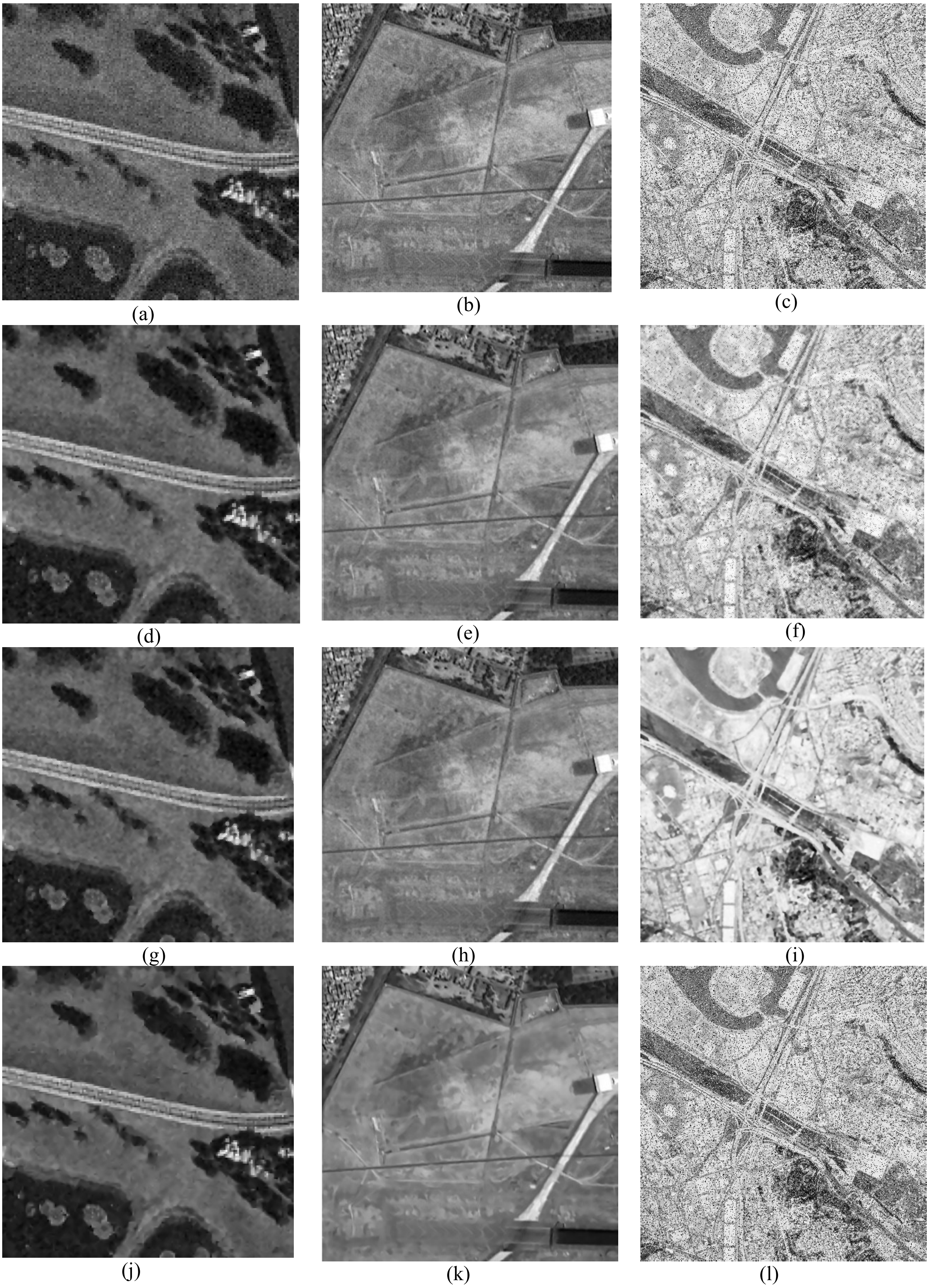

Figure 11. **Satellite Images 1st row (a) Image 1 (b) Image 2 (c) Image 3. 2nd row (d), (e), (f) restored with ABF. 3rd row (g), (h), (i) restored with ATF.4th row (j), (k), (l) restored with NLM filter.**

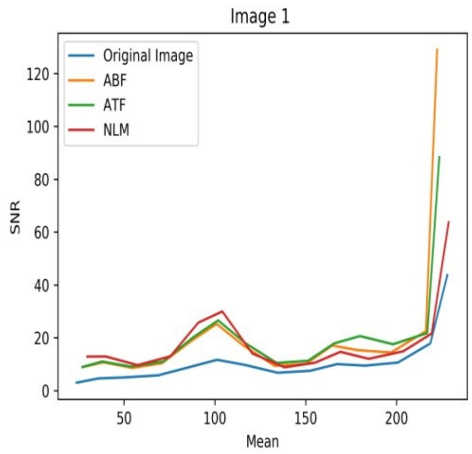

(a)

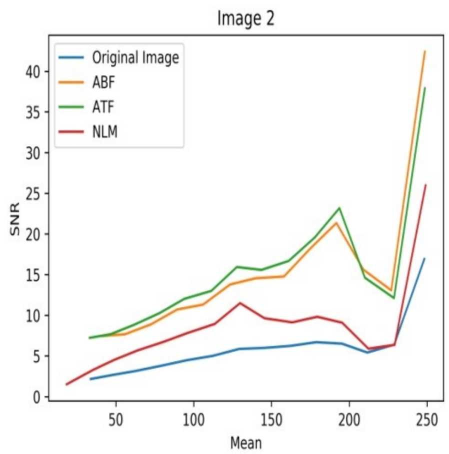

(b)

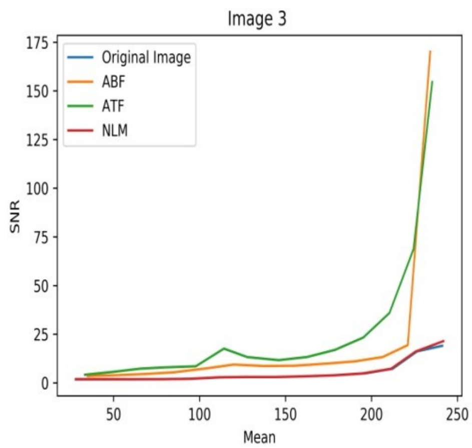

(c)

Figure 12. SNR evaluation on original and denoised satellite images in Figure 11 (a) Image 1 (b) Image 2 (c) Image3

In Figure 11 (a), (b), (c), three different original satellite images are shown. These images contain noises that are possibly introduced during image acquisition and transmission stages. Figure 11(c) contains sufficient impulsive noise content. In Figure 11, row 2-4, shows the denoising results using ABF, ATF and NLM filters applied on the images shown in Figure 11 row 1, respectively. Visually row 3 in Figure 11, that is, denoised images using ATF, seems better than the other rows. Further, in Figure 12 the performance of different denoising results are estimated in terms of SNR. It is clear from Figure 12 that images in row 3 (filtered with ATF) have higher SNR compared to ABF and NLM filter. Thus, similar to test images of previous section (Lena images) in case of general remote sensing images as well, ATF performs superior than the other two methods.

6. Conclusions

In this paper, we have developed a novel adaptive technique that estimates the noise parameters required in nonlinear bilateral/trilateral denoising process. Detailed algorithms are provided to estimate the parameters used in different methods. Adaptive method uses the concept of GLCM in order to automatically demarcate nearly homogeneous area in the image. Further, by appropriate thresholding on GLCM, we estimate noise and SNR levels for various intensities in an automatic manner. This method is capable to estimate low to moderate levels of noise very efficiently. The paper also discusses the performance of various denoising methods on standard test image (the Lena image) as well as on high-resolution satellite images. A rigorous comparative study is carried out to demonstrate that the present approach gives significantly better denoising results compared to other approaches in the literature. Present adaptive bilateral (ABF) and adaptive trilateral (ATF) filters give at least 50 percent improvement in SNR in almost all the cases compared to standard bilateral and trilateral filters.

Furthermore, the adaptive trilateral filter performs better than the adaptive bilateral and NLM filters. SNR improvement using ATF is at least 30 percent more than the ABF in almost all cases. Further, when impulse noise is present in images, SNR improvement using ATF is at least twice in comparison to NLM.

Thus, we conclude that our adaptive approach of parameters estimation for trilateral filter gives better results compared to other methods suggested in the literature. Moreover, the presented approach is shown to work efficiently in different noise conditions and noise levels when compared to other nonlinear denoising methods, for instance, NLM. Cleary, the present investigation not only establishes the superiority of proposed adaptive nonlinear image denoising techniques, that is, ATF and ABF, over existing techniques but also enriches our knowledge about their comparative performances. Further, for the future work, we feel that the denoising techniques presented in the paper can be applied in conjunction with some image-restoration framework, for instance FTVD framework (Wang Y. et al. 2008), for optimum restoration result.

Acknowledgements
The authors thank Director, SAC, Shri. N. M. Desai for continued support and encouragement towards this work. The authors further thank Group Director, SIPG, Shri. Debajyoti Dhar for keen interest and support for this work.

References

Al-amri S.S. and N.V. Kalyankar (2010). A comparative study of noise removal from remote sensing image. International Journal of Computer Science Issues (IJCSI), 7(1), 32-36.

Buades A., B. Coll and J.-M. Morel (2005). A non-local algorithm for image denoising, In Proc. IEEE Compu. Soc. Conf. Computer Vis. and Pattern Recog., 2, 60-65.

Boyat A.K. and B. K. Joshi (2015). A review paper: Noise models in digital image processing. Signal & Image Processing: An International Journal (SIPIJ), 6 (2), 63-75

Choudhury P. and J. Tumblin (2003). The trilateral filter for high contrast images and meshes, In ACM SIGGRAPH (Eurographics Symp. on Rendering), 1-11, doi:10.1145/1198555.1198565.

Deledalle C., F. Tupin and L. Denis (2010). Poisson NL means: Unsupervised non local means for Poisson noise, Proc. of IEEE 17thInt. Conf. on Image Processing, 801-804, doi: 10.1109/ICIP.2010.5653394

Fu P., Q. Sun, Z. Ji and Q. Chen (2012). A new method for noise estimation in single-band remote sensing images" Proc. of IEEE Int. Conf. on Fuzzy Systems and Knowledge Discovery (FSKD 2012), 1664-1668, doi:10.1109/FSKD.2012.6234225.

Gao B-C. (1993). An operational method for estimating signal to noise ratios from data acquired with imaging spectrometers, Remote Sensing of Environment, 43(1), 23-33.

Garnett R., H. Timothy, C. Charles and H. Wenjie (2005). A universal noise removal algorithm with an impulse detector. IEEE Transactions on image processing, 14(11), 1747-1754.

Karnati V., M. Uliyar and S. Dey. (2009). Fast non-local algorithm for image denoising", 16th IEEE Int. Conf. on Image Processing, Cairo, 3873-3876.

Kaur S. (2015). Noise types and various removal techniques." International Journal of Advanced Research in Electronics and Communication Engineering (IJARECE), 4 (2), 226-230

Maity A., A. Pattanaik, S. Sagnika and S. Pani (2015). A comparative study on approaches to speckle noise reduction in images, Proc. of IEEE Int. Conf. on Computational Intell. and Networks, 148-155, doi: 10.1109/CINE.2015.36.

Overton K. J. and T. E. Weymouth (1979). A noise reducing preprocessing algorithm, in Proc. IEEE Computer Science Conf. Pattern Recognition and Image Processing, Chicago, IL, 498–507.

Ren H., C. Du, R. Liu, Q. Qin, G. Yan, Z.-L. Li and J. Meng (2014). Noise evaluation of early images for Landsat-8 operational land imager, Optics Express, 22(22), doi: 10.1364/OE.22.027270.

Reulke R. and H. Weichelt (2012). SNR Evaluation of the RapidEye Space-borne Cameras, Photogrammetrie, Fernerkundung, Geoinformation, 1, 29-38.

Rudin L.I., S. Osher and E. Fatemi (1992). Nonlinear total variation based noise removal algorithms, Physica D, 60, 259-268.

Sergey, A., Uss, Mykhail, Lukin Vladimir, Vozel Benoit, Chehdi, Kacem, Egiazarian Karen. (2019). Enhancement of component images of multispectral data by denoising with reference. Remote Sensing. DOI:11. 611. 10.3390/rs11060611.

Tomasi C. and R. Manduchi (1998). Bilateral filtering for gray and color images. Proc. of IEEE Int. Conf. Computer Vision, 839–846.

Veerakumar T., B. N. Subudhi and S. Esakkirajan (2019). Empirical mode decomposition and adaptive bilateral filter approach for impulse noise removal. Expert Systems with Applications, (Elsevier), 121, 18-27.

Wang G., Y. Liu, W. Xiong and Y. Li. (2018). An improved non-local means filter for color image denoising". Optik, 173, 157–173, doi: 10.1016/j.ijleo.2018.08.013

Wang X., L. Tang, C. Li, B. Yuan and B. Zhu (2009). A practical SNR estimation scheme for remotely sensed optical imagery, Proc. SPIE 7384, Int. Symp. On Photoelectronic Detection and Imaging: Advances in Imaging Detectors and Appl., 738434, doi: 10.1117/12.848049.

WangY., J. Yang, W. Yin and Y. Zhang (2008). A new alternating minimization algorithm for total variation image reconstruction, SIAM J. on Imaging Sciences, 1(3), 248-272.

Wong W.C.K, A.C.S Chung and S.C.H. Yu (2004). "Trilateral filtering for biomedical images, 2nd IEEE Int. Symp. on Biomedical imaging: Nano to Macro, 820-823.

Spatio-temporal variability assessment of pre-monsoon temperature to deduce their impact on Forest Fire events in relation to relief across Himalayan region

Rahul Kashyap* and A. C. Pandey
Department of Geoinformatics, Central University of Jharkhand, Ranchi, India
*Email: rahulkashyaprsm@gmail.com

(Received: Oct 22, 2020; in final form: Aug 19, 2021)

Abstract: In recent times a great deal of climatic variability including temperature trends have been recorded in the Himalaya. In the past two decades Forest fires have been one of the most common hazards in the Himalaya. This study attempt spatio-temporal as well as relief-based analysis and variability of temperature and its relation with Forest Fire events over the various parts of the Himalayan region in pre-monsoon-March, April and May (MAM) over the years 2000-2018 using MERRA-2 daily Air temperature data, MODIS C6 fire points and ASTER DEM for elevation. The seasonal mean temperature of each year as well as seasonal mean over the entire time span and Forest Fire events distribution are related with relief. Western Himalaya is by far the coolest, followed by the Central Himalaya, while the Eastern Himalaya is the warmest. Over the years 2001- 2018 on an average the maximum forest fire events are seen in the Western Himalaya at 706 followed by the Central Himalaya at 257 and the least in the Eastern Himalaya at 177. The spatial distribution of forest fire events shows a good coherence with the high mean temperature distribution all over the Himalaya. 74.61% of the forest fire events in the Himalaya takes place at mean temperature of more than 15°C. The Western Himalaya leads with 96.55 % followed by Central Himalaya at 83.2% and Eastern Himalaya at 44.18%. The pre-monsoon mean temperatures above 15°C are the primary cause for the majority of the forest fire events in the Himalaya at the elevation range below 2600m.

Keywords: Forest Fires, Temperature, Elevation, Pre-monsoon, Himalaya

1. Introduction

Climate change is one of the most debated topics in recent decades. The global warming trends are being associated with the higher concentration of greenhouse gases and aerosols along with the changes in land use and land cover patterns (Bhutiyani et al. 2010; Stocker et al. 2013). Temperature projections for the 21st century suggest an acceleration in the warming trends as compared to observed in the 20th century (Ruosteenoja et al. 2003). It is predicted that most of the Asian landmass will be showing a significant warming trend by the end of this decade. The trends of warming in Southeast Asia is least rapid and very much similar to the global mean warming, stronger over South Asia and Eastern Asia, and greatest in the continental interior of Asia (Central, Western, and Northern Asia). Significant warming is expected in arid regions of Asia and the Himalayan highlands, including the Tibetan Plateau (Gao et al. 2003; Yao et al. 2006). The sinks and reservoirs of heat and moisture are influenced by the diverse land surface characteristics of the Himalaya. The land surface-atmosphere momentum, water, and energy exchanges are greatly affected by varying topography and heterogeneity of land surface. An important component of any regional and global climate modelling system is the evaluation of such influences in land–atmosphere system (Xue et al. 1996; Pan et al. 1999; Zeng et al. 1999).

The most important factor for the climatic studies of a region is its temperature variability (Dimri et al. 2014). Based on regional climate models, it is predicted that the temperatures in the Indian sub-continent is expected to rise by 3.5-5.5ºC by 2100, and on the Tibetan Plateau by 2.5ºC by 2050 and 5ºC by 2100 as per the regional climate models (RCMs) (Kumar et al. 2006). Reliable projections of climate change in the Himalaya are rather difficult to achieve and even high resolution climatic models could not achieve it owing to extreme topography and complex reactions to the greenhouse effect. The warming in the Himalaya has been much greater than the global average of 0.74°C for the last 100 years as per various studies (Solomon et al. 2007; Du et al. 2004). The effects of climate change are highly variable in the Himalaya due to variable warming, cooling added by its complex topography (Shekhar et al. 2010).

Globally as well as in South east Asia, a considerably trending extreme event produced due to natural as well as anthropogenic events is wild fires (Bar et al. 2019). Mountainous ecosystems such as Himalaya are ecologically fragile owing to frequent extreme events and fires is a major one among them (Bar et al. 2021). The major cause of frequent fires in the mountainous regions is the presence of high fire fuel materials such as dry Chirpine needles, and dry litter materials (Dobriyal et al. 2017. Pre-monsoon is the most crucial season for fires in the Himalayan region (Bar et al. 2020a).

Most parts of Himalaya, especially Western Himalaya is facing severe fires in pre-monsoon season leading to reduced LAI and browning trends in vegetation (Bar et al. 2020b). Fires cause a great deal of loss to the terrestrial ecosystem by reducing the productivity and biodiversity which can be quantified using remote sensing techniques (Sannigrahi et al. 2020). India usually has a fire season in January to May which coincides with summers (Bahuguna et al. 2002). Wide ranging adverse ecological, social as well as economic impacts are caused due to forest fires (Upadhyay 2016). Several remote sensing based spectral indices have been explored to assess the impact of fire on forest ecosystem at local, regional and global scales in the recent decades (Milne et al. 1986; White et al. 1996; Lentile et al. 2006; Chen et al. 2015). Frequent wild fires have been recorded along the foothills of the Himalaya and in the deciduous forests all around the globe generally. In recent years a significant increase in wild fire size, frequency has been attributed to extended droughts (prolonged dry weather), together with rapidly expanding exploitation of tropical forest (Roy et al. 2004). The global increase in fire frequency is related to climate warming as per some studies (Overpeck et al. 1990).

Remote sensing has served as an efficient method of gathering data about complex inaccessible regions such as the Himalaya (Kashyap et al. 2021). Owing to their synoptic view, repetitive coverage and up to-datedness, remote sensing materials are an unprecedentedly powerful and efficient tool to study the temperature trends, regional, seasonal variation where stations are usually challenging to establish that are usually located in remote, inaccessible and inhospitable environments. This study attempt spatio-temporal as well as relief-based analysis and variability of mean temperature and its relation with Forest Fire events over the various parts of the Himalayan region in pre-monsoon (MAM) over the years 2000-2018 using MERRA-2 daily Air temperature data, MODIS C6 fire points and ASTER DEM for elevation.

2. Study area

Orography of Himalaya governs the regional weather system and monsoon of Indian sub-continent (Kashyap et al. 2021). The highest mountain range/landmass of the world is the mighty Himalaya. The complex topography and varied land-cover/land-use patterns are basically typical characteristics of this region. The weather and climatic patterns over the south Asian region is greatly affected and dominated by the Himalaya (Kumar et al. 1999; Dey et al. 1982). A characteristic feature of mountainous regions is heterogeneous topography and a great deal of climatic variability (Bhutiyani et al. 2007). Large scale variations of temperature and precipitation trends are common in such regions (Jhajharia et al. 2011). These regions basically act as indicators of change with focus on trends and consequences as they are most vulnerable to climate change. (Solomon et al. 2007; UNEP 2009).

The study area comprises of Western Himalaya combining the Indian states of Jammu -Kashmir, Ladakh, Himachal Pradesh and Uttarakhand having an area of 3,31,392 sq. km; the Central Himalaya comprising the Nepal Himalaya having an area of 1,47,516 sq. km and the Eastern Himalaya combining the Bhutan Himalaya and Indian Eastern Himalaya in the state of Arunachal Pradesh having an area of 1,22,137sq. km as in Figure 1.

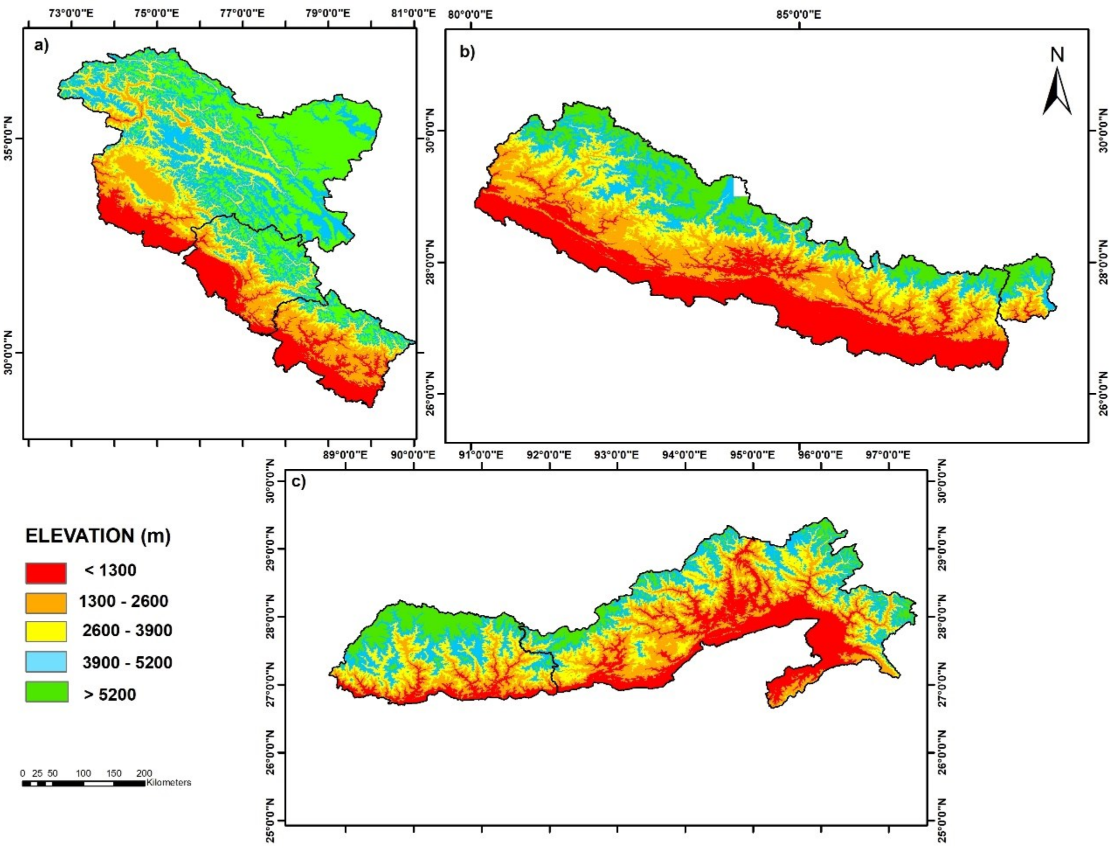

Figure 1. Study area map showing the elevation of: a) Western Himalaya, b) Central Himalaya and c) Eastern Himalaya

Table 1. Showing the data used, resolution, purpose and source

Data Used	Resolution	Purpose	Source
MERRA-2 Air temperature	Spatial- 31.25 km Temporal-Daily	Mean Temperature Standard Anomaly Temperature	(https://giovanni.gsfc.nasa.gov/giovanni/)
MODIS C6 FIRE POINTS	Spatial- 1 km	FIRE POINTS	(https://firms.modaps.eosdis.nasa.gov/)
ASTER DEM	Spatial- 30 km	Elevation	(https://earthexplorer.usgs.gov/)

(Temperature data is for pre-monsoon (MAM) season for years 2000-18 and Fire points for 2001-18, MAM)

3. Data and methodology

3.1 Data used

Various satellite data products were used in the recent study for the computation of spatial temperature variability, forest fire points and relief variation across the entire length of Himalaya. The details of data sets incorporated during the course of the study are given in Table 1 and described below.

3.1.1 MERRA-2 Air temperature

The temperature data used in the study is "M2SDNXSLV_T2MMEAN", MERRA-2 Air temperature data with resolution of 0.5° x 0.625°. The Modern-Era Retrospective analysis for Research and Applications version 2 (MERRA-2) is a NASA atmospheric reanalysis for the satellite era using the Goddard Earth Observing System Model, Version 5 (GEOS-5) with its Atmospheric Data Assimilation System (ADAS), version 5.12.4. The MERRA project focuses on historical climate analyses for a broad range of weather and climate time scales and places the NASA EOS suite of observations in a climate context. MERRA-2 was initiated as an intermediate project between the ageing MERRA data and the next generation of Earth system analysis envisioned for the future coupled reanalysis.

3.1.2 MODIS C6 Fire Points

Forest Fire locations are obtained Near real-time (NRT) Moderate Resolution Imaging Spectroradiometer (MODIS) Thermal Anomalies / Fire locations - Collection 6 processed by NASA's Land, Atmosphere Near real-time Capability for EOS (LANCE) Fire Information for Resource Management System (FIRMS).

3.1.3 DEM

The elevation data used in this study is the Advanced Spaceborne Thermal Emission and Reflection Radiometer (ASTER) Global Digital Elevation Model Version 3 (GDEM 003) developed by the Ministry of Economy, Trade, and Industry (METI) of Japan and the United States National Aeronautics and Space Administration (NASA) jointly. The first version of the ASTER GDEM released in June 2009 that was generated using stereo-pair images collected by the ASTER instrument onboard Terra. ASTER GDEM coverage spans from 83° north latitude to 83° south, encompassing 99 percent of Earth's landmass.

3.2. Methodology

The daily temperature data for each month is stacked together and mean is calculated to obtain the monthly stack data. The monthly stacked data for all three months i.e., March, April and May (MAM) are stacked together to obtain the yearly stack data. The yearly stacked data sets for all years from 2000- 2018 are stacked together and the overall seasonal mean is calculated. From the yearly accumulated data, the overall seasonal mean is calculated. The forest fire locations obtained by MODIS C6 Fire points is related to both the seasonal mean over the years and the overall mean temperature by taking the intersection of the mean temperature for the entire period (converted to vector) and the elevation ranges (converted to vector) by tabulating the cross-class to class matrix of ranges of precipitation and elevation. The same logic was applied for the overall forest fire distribution and the elevation ranges (converted to vector) to obtain the percentage of landslides with the elevation ranges. DEM data is used to relate both temperature as well as forest fires with relief in the various parts of the Himalaya. An inter-relationship was established between temperature, elevation and forest fires showing the working methodology incorporated during the course of the study as depicted in Figure 2.

4. Results and discussion

4.1. Spatio-temporal variability of pre -monsoon mean temperature (2000-2018)

4.1.1. Western Himalaya:

The yearly mean temperature of March-May season in the Western Himalaya over the years 2000-2018 varies from -14.2°C to 34.5°C. Usually, the north eastern corner of the Western Himalaya in the state of Jammu and Kashmir and some eastern parts records the minimum or temperature ranging from below 0°C while the low temperature is in between 0°C and 7.5°C is seen in the eastern and the central parts of the state of Jammu and Kashmir. The moderate temperature of 7.5°C to 15°C is observed in the north western corner in some patches and in the central part from Jammu and Kashmir in the proceeding in the southwest direction in the central and then moving towards the eastern part of the state of Himachal Pradesh and Uttarakhand, the high temperatures of 15°C to 25°C is seen in the westernmost part of the state of Jammu and Kashmir, the central part of the state of Uttarakhand and the eastern part of the state of Himachal Pradesh .The maximum temperature of more than 25°C is seen in the western corner of the state of Jammu and Kashmir , the south eastern part, the eastern part of the state of Himachal Pradesh and the south eastern part of the state of Uttarakhand as shown in Figure 3

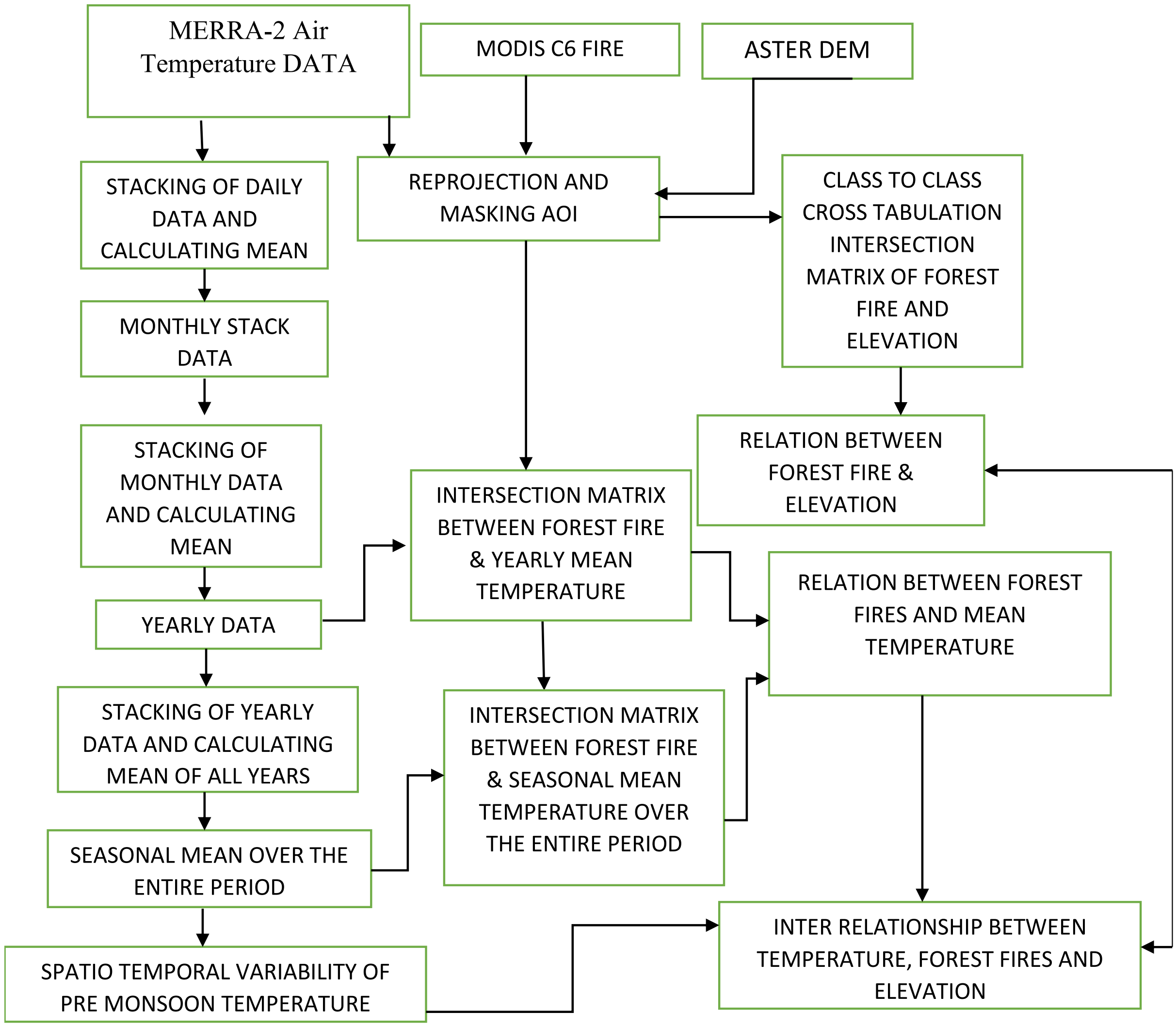

Figure 2. Methodology flowchart

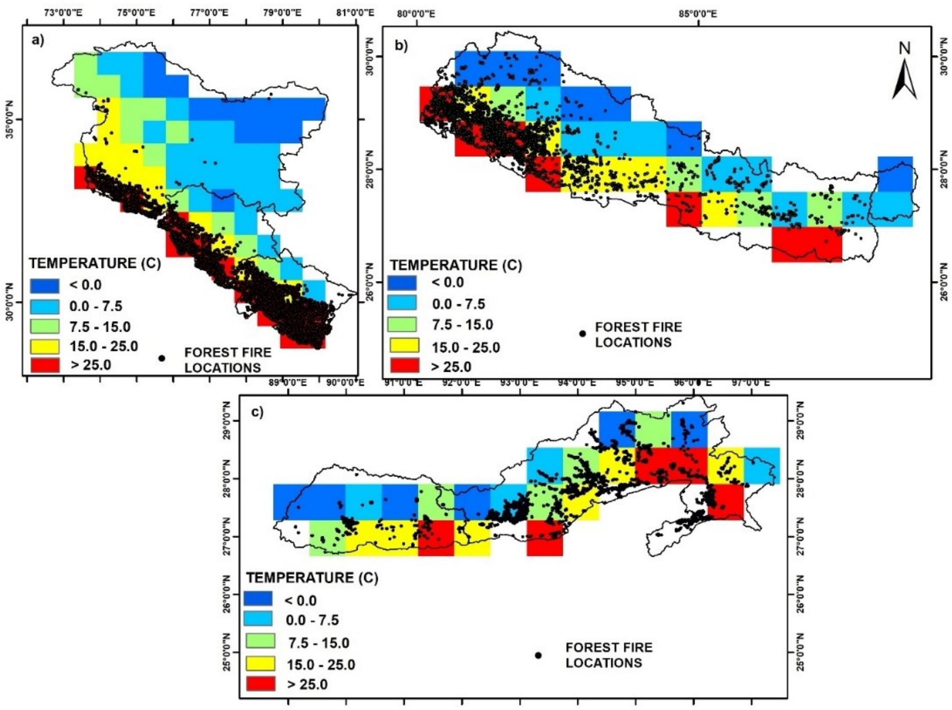

Figure 3. Mean Temperature during pre-monsoon (MAM) in different parts of Himalaya: a) Western Himalaya; b) Central Himalaya; c) Eastern Himalaya over the period 2000-2018

4.1.2. Central Himalaya

The yearly mean temperature of March-May season of the Central Himalaya over the year 2000 to 2018 varies between -7.2°C to 34°C. The Central i.e. Nepal Himalaya in a small northern patch especially in the north western side has recorded a minimum temperature of below 0°C ; area of low temperature between 0°C to 7.5°C is seen in areas such as the north-central part and in some small patches in the eastern and the easternmost corner over the years areas having a moderate temperature of 7.5°C to 15°C is in very small patches in the central and western part , the high temperatures between 15°C to 25°C is seen in the westernmost corner and then moving towards the central part then moving towards the south eastern part. The maximum temperature of more than 25°C is seen in the western to the south western corner moving towards from the western side towards the southern side as it can say like a ladder step in the southern and the south eastern part moving from the western to the southern and to the south eastern part there are is not many variations over the years as it is mostly constant as shown in Figure 3.

4.1.3. Eastern Himalaya

The yearly mean temperature of the March-May season in the Eastern Himalaya varies from -3.6°C to 25.6°C. The area having a minimum temperature of below 0°C is seen in the northwest corner of Bhutan Himalaya over the years. The area having the low temperature that is 0°C to 7.5 °C is seen in the areas such as the western part of the Bhutan Himalaya , small patches in the northern part moving from the east to the moving from the western to the eastern part of the Arunachal Pradesh , area having a moderate temperature of 7.5 °C to 15 °C is seen in small patches in the central and western part of Bhutan Himalaya and most of the Arunachal Pradesh, areas having higher temperature is between 15°C to 25°C in seen in the southern part of the Bhutan Himalaya, the central , southern and the south eastern part of the state of Arunachal Pradesh area receiving maximum temperature of above 25°C is seen in the south Eastern corner of the Bhutan Himalaya and the south eastern corner of Arunachal Pradesh as shown in Figure 3.

4.2. Pre-Monsoon temperature variability in various parts of the Himalaya

A great deal of spatio-temporal variability in temperature trends is very observable in the various parts of the Himalaya over the last two decades. An inconsistent and random trend of increase and decrease is evident in the maximum as well as the minimum mean temperature.

The trend of the maximum mean temperature of the Western and the Central Himalaya is almost in synchronization over the years following almost similar trend of ascend and descend which is slightly different from Eastern Himalaya.

One can see that at the highest minimum mean temperature is seen by the Western Himalaya over the years followed by the Central Himalaya and the highest by Eastern Himalaya. The Western Himalaya get around mostly around -12°C, the Central Himalaya is mostly around -5°C Eastern is at highest it is mostly around -3°C. So, it can be said that the Western Himalaya is by far the coolest followed by the Central Himalaya, while the Eastern Himalaya is the warmest as shown in Figure 4.

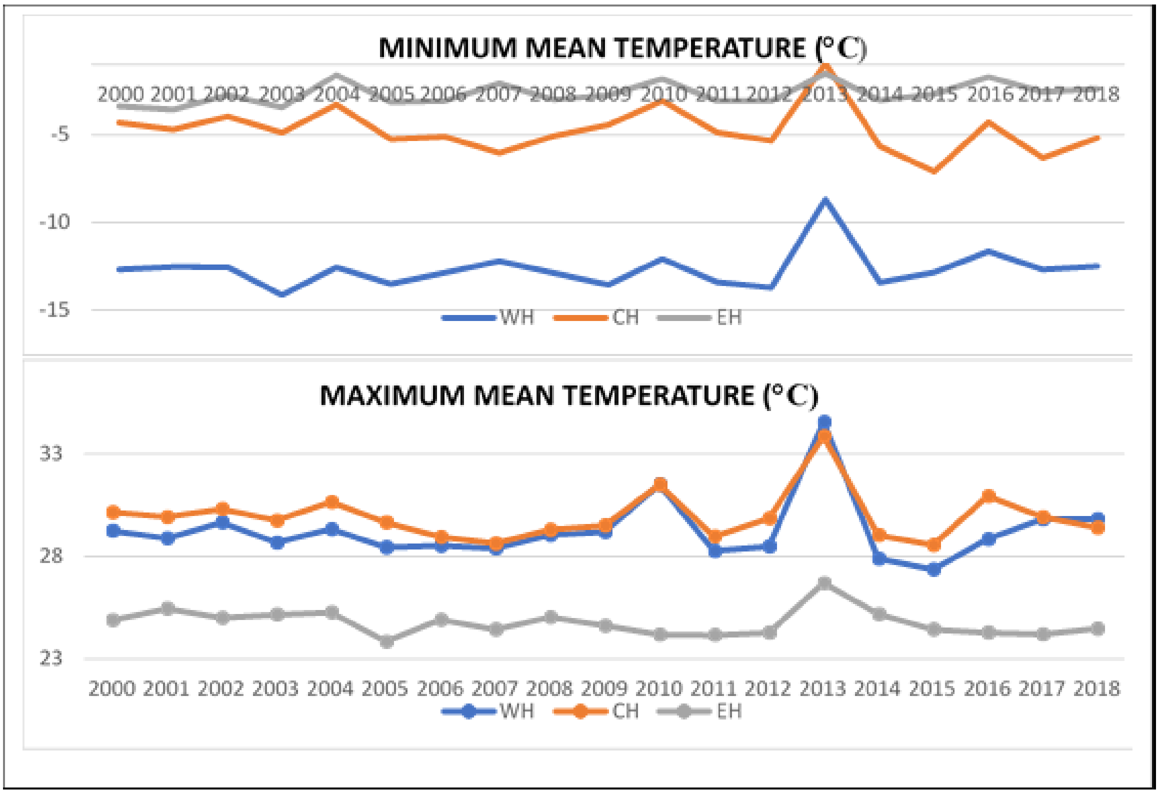

Figure 4. Maximum and Minimum Mean Temperature in various parts of Himalaya in MAM (2000-2018)

.

4.3. Forest Fire Events in various parts of the Himalaya in pre-monsoon season

The spatial as well as temporal distribution of forest fire events in the Himalaya it not uniform with respect to elevation.There is significant variability in the disribution of forest fire events in various elevation levels . Mostly the fire events are seen in lower elevation areas of below 1300m. Some fire activities are also recorded in elevation range upto 2600m. Fire events above 2600 m are very rare in various parts of Himalaya as shown in Figure 5.

4.3.1. Frequency of Forest Fire events across the Himalaya

It can be said that over the years 2001- 2018 on an average the maximum forest fire events are seen in the Western Himalaya at 706 followed by the Central Himalaya at 257 and the least in the Eastern Himalaya at 177. There are many years viz., 2003, 2005, 2008, 2009, 2012, 2016, and 2018 exhibits higher number of forest fire events while rest of the years recorded lower number of forest fire events as shown in Figure 6.

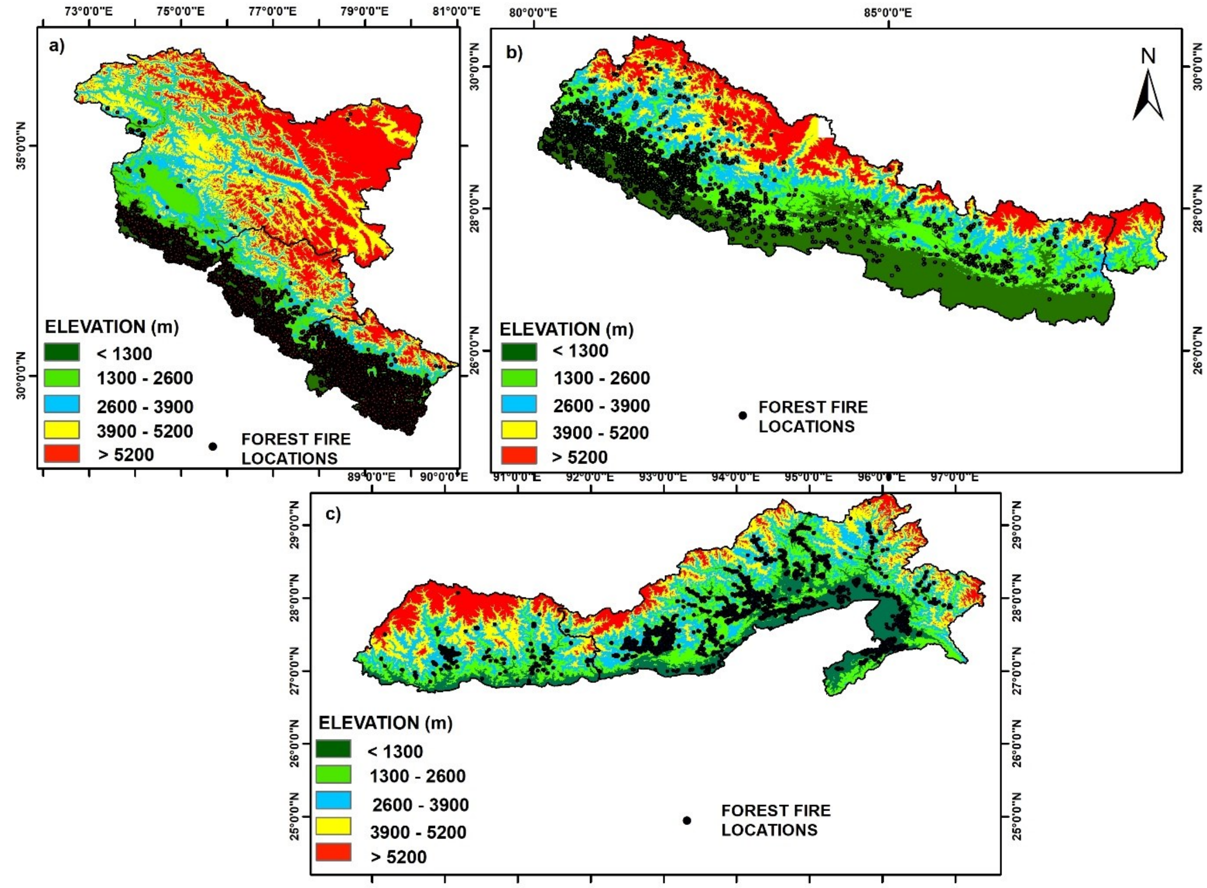

Figure 5. Forest Fire locations with elevation in different parts Himalaya: a) Western Himalaya; b) Central Himalaya; c) Eastern Himalaya in MAM (2000-2018)

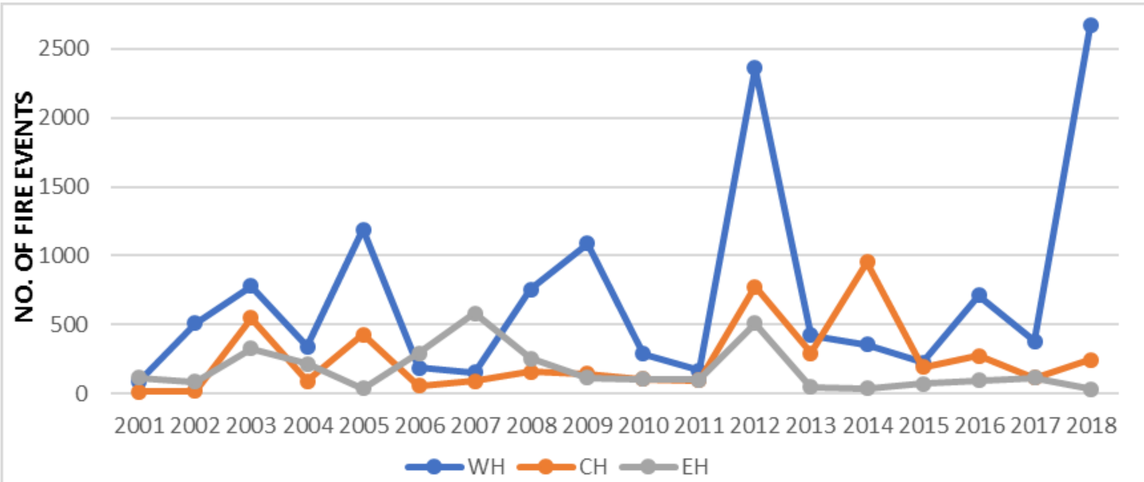

Figure 6. Frequency of Forest Fire Events in various parts of Himalaya during MAM (2000-2018)

4.3.2. Variation in Forest Fire events with elevation

It is very much evident that the forest fire events in Himalayan region are mostly seen in the areas of relatively lower elevation while higher elevation records almost negligible forest fire events. A vast majority of 96.51 % of the forest fire events in Himalaya took place at elevation below 2600m. The Western Himalaya leads with 99.3% followed by Central Himalaya at 95.61% and Eastern Himalaya at 94.62%. For elevation below 1300 m Eastern Himalaya leads with 65.46% followed by Western Himalaya at 64.72% and Central Himalaya at 41.67%. While for elevation in the range of 1300 to 2600 m, Central Himalaya leads with 53.94 % followed by Western Himalaya at 34.59 % and least in the Eastern Himalaya at 29.16 % as in Figure 7.

4.4. Relation of Forest Fire events with temperature

The forest fire events show a great deal of correlation with moderate to high mean temperature distribution all over the Himalaya. Over all it can be said that a vast majority of 85.68% of forest fire events in the Himalaya takes place in areas of high or very high mean temperatures. The maximum agreement between the forest fire events and high or very high mean temperature is seen in the Western Himalaya with a maximum of 100% in 2014, a minimum of 96.34% in 2006 and the overall average being a whopping 98.87% ; followed by the Central Himalaya with a maximum of 98.42% in 2014, a minimum of 60% in 2001and the overall average being a very high 81.52%, while the Eastern Himalaya has relatively lower values with a maximum of 88.09% in 2005, a minimum of 43.49% in 2001 and the overall average being 76.65% as in Figure 8.

The forest fire events are mostly seen in the areas of higher mean temperature while areas of lower mean temperature records almost negligible forest fire events except for Eastern Himalaya which has forest fire events almost at all temperatures. A vast majority of 74.61% of the forest fire events in Himalaya takes place at mean temperature of more than 15℃. The Western Himalaya leads with 96.55 % followed by Central Himalaya at 83.2% and Eastern Himalaya at 44.18%. For mean temperature between 15 to 25℃ Central Himalaya leads with 38.4% followed by Western Himalaya at 31.41 % and least in the Eastern Himalaya at 25.87%. While for mean temperature above 25 ℃, Western Himalaya leads with 65.14% followed by Central Himalaya at 44.19% and least in the Eastern Himalaya at 18.3%.

Also, it can be very evidently seen that the forest fire events are most frequent in the lowest elevation levels and least frequent in the highest elevation. It can said that there is an inverse relationship between the frequency of forest fire events and elevation. This can be obviously attributed to the higher mean temperatures in lower elevations and vice versa as in Figure 9.

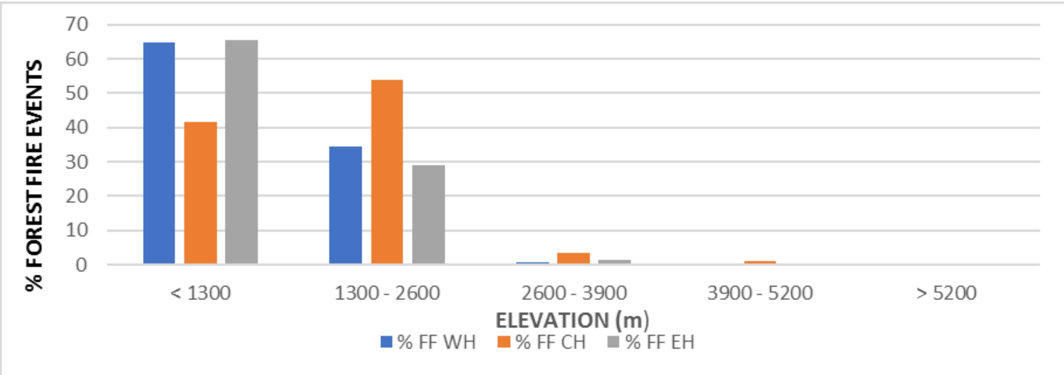

Figure 7. Percentage (%) of Forest Fire Events with elevation in various parts of Himalaya in MAM (2000-2018)

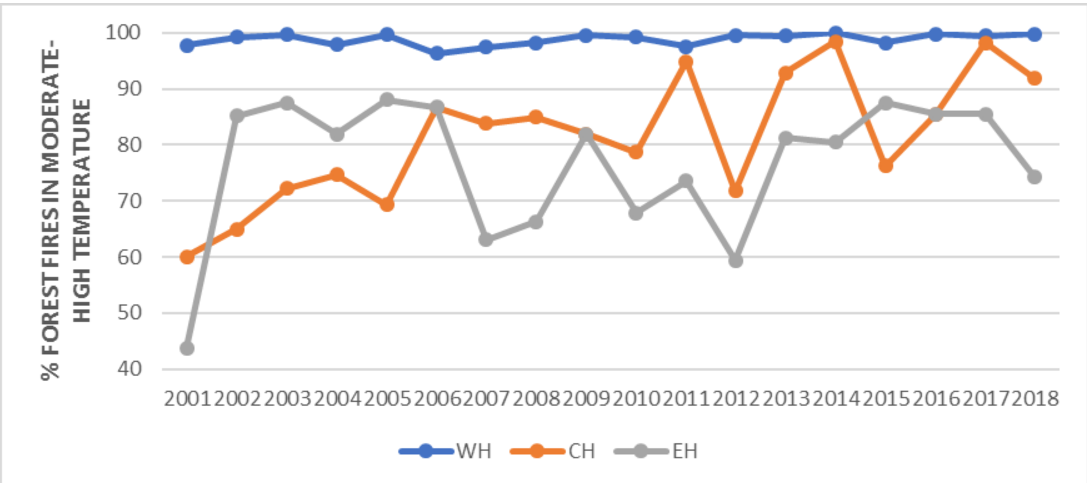

Figure 8. The percentage (%) of Forest Fire Events in moderate - high mean temperature in various parts of Himalaya in MAM (2000-2018)

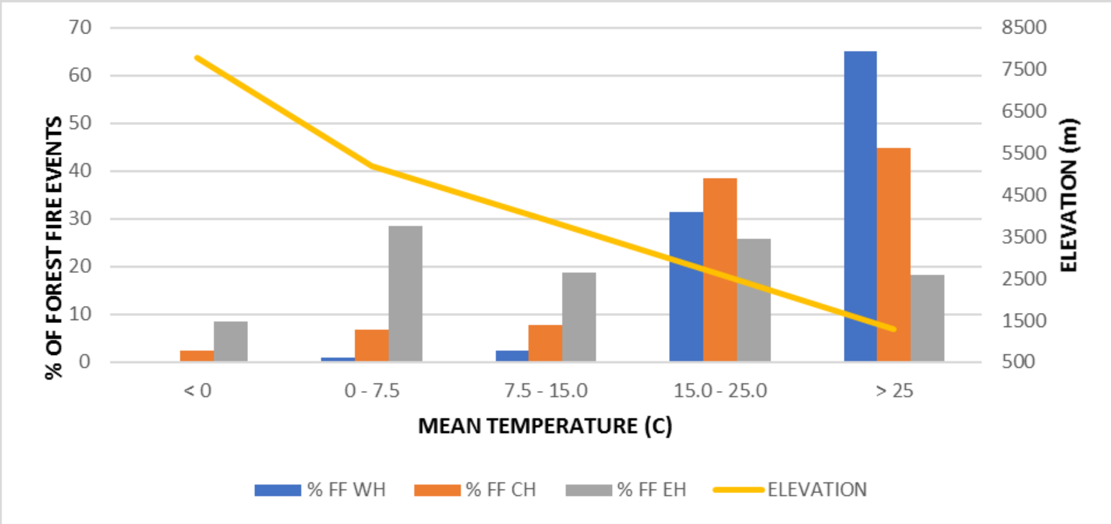

Figure 9. Graph showing percentage (%) of Forest Fire Events with Mean Temperature in various parts of Himalaya MAM along with elevations (2000-2018)

5. Conclusions

The trend of the maximum mean temperature of the Western and the Central Himalaya is almost in synchronization over the years following almost similar trend of ascend and descend which is slightly different from Eastern Himalaya.

It can be seen that at the highest minimum mean temperature is seen by the Western Himalaya over the years followed by the Central Himalaya and the highest by Eastern Himalaya. The Western Himalaya get around mostly around -12°C, the Central Himalaya is mostly around -5°C Eastern is at highest it is mostly around -3°C. Thus, it can be said that Western Himalaya is by far the coolest followed by the Central Himalaya, while the Eastern Himalaya is the warmest.

It can be said that over the years 2001- 2018 on an average the maximum forest fire events are seen in the Western Himalaya at 706 followed by the Central Himalaya at 257 and the least in the Eastern Himalaya at 177. A vast majority of 96.51 % of the forest fire events in the Himalaya takes place at an elevation below 2600m. The Western Himalaya leads with 99.3% followed by Central Himalaya at 95.61% and Eastern Himalaya at 94.62%. For elevation below 1300 m Eastern Himalaya leads with 65.46% followed by Western Himalaya at 64.72% and Central Himalaya at 41.67%.

A vast majority of 74.61 % of the forest fire events in the Himalaya takes place at a mean temperature of more than 15 °C. The Western Himalaya leads with 96.55 % followed by Central Himalaya at 83.2 % and Eastern Himalaya at 44.18 %. The pre -monsoon mean temperatures above 15°C are the primary cause for most of the Forest Fire events in the Himalaya at the elevation range of below 2600m.

The study provides insights on the variability trends of pre-monsoon temperatures and forest fire events with elevation in various parts of the Himalaya. The incorporation of some other climatic drivers such as precipitation, relative humidity, wind velocity and vegetation dynamics would provide a more robust result. Also, taking into account the global climatic oscillations such as ENSO would provide insights in the role of oceanic warming in inducing fires.

Acknowledgements

The authors would like to acknowledge all the data providing sources such as NASA's Giovanni and Fire Information for Resource Management System (FIRMS) and USGS for allowing free data access of all the required data sets incorporated during the course of this study.

References

Bahuguna V.K. and S. Singh (2002). Fire Situation in India. International Forest Fire Journal of Applied Earth Observation and Geoinformation, 40, 91-99. doi: 10.1016/j.jag.2015.04.005

Bar S. and B.R. Parida (2019). A combined Approach of unsupervised and supervised Robust classification for forest fire patches identification using Sentinel 2A on Google earth engine cloud platform. In AGU Fall Meeting 2019. AGU

Bar S., B.R. Parida and A.C. Pandey (2020a). Landsat-8 and Sentinel-2 based Forest fire burn area mapping using machine learning algorithms on GEE cloud platform over Uttarakhand, Western Himalaya. Remote Sensing Applications: Society and Environment, 18, 100324.

Bar S., and B.R. Parida (2020b). Synergetic relation of Forest fire, vegetation proportion and Leaf area index over Western Himalaya. In AGU Fall Meeting 2020. AGU.

Bar S., B.R. Parida, G. Roberts, A.C. Pandey, P. Acharya and J. Dash (2021). Spatio-temporal characterization of landscape fire in relation to anthropogenic activity and climatic variability over the Western Himalaya, India. GIScience and Remote Sensing, 58(2), 281-299.

Bhutiyani M., V.S. Kale and N.J. Pawar (2007). Long-term trends in maximum, minimum and mean annual air temperatures across the Northwestern Himalaya during the twentieth century. Climate Chang, 85(1-2), 159-177.

Bhutiyani M., V.S. Kale and N.J. Pawar (2010). Climate change and the precipitation variations in the northwestern Himalaya:1866–2006. International Journal of Climatology: A Journal of the Royal Meteorological Society, 30(4), 535-548.

Chen G., M.R. Metz, D.M. Rizzo, W.W. Dillon and R.J. Meentemeyer (2015). Object-based assessment of burn severity in diseased forests using high-spatial and high-spectral resolution MASTER airborne imagery. ISPRS Journal of Photogrammetry and Remote Sensing, 102, 38-47.

Dey B.K., and O.S.R.U. Bhanu Kumar (1982). An apparent relationship between Eurasian spring snow cover and the advance period of the Indian summer monsoon. Journal of Applied Meteorology, 21(12), 1929-1932.

Dimri, A. P., and A. Chevuturi (2014). Model sensitivity analysis study for western disturbances over the Himalaya. Meteorology and Atmospheric Physics, 123(3-4), 155-180.

Dobriyal M. and A. Bijalwan (2017). Forest fire in western Himalaya of India: a review. New York Science Journal, 10(6), 39-46

Du M., S. Kawashima, S. Yonemura, X.Z. Zhang and S.B. Chen (2004). Mutual influence between human activities and climate change in the tibetan plateau during recent years. Global and Planetary Change, 41, 241-249

Gao Li D.L, Z.C. Zhao and F. Giorgi (2003). Climate change due to greenhouse effects in Qinghai-Xizang Plateau and along the Qianghai-Tibet Railway. Plateau Meteorol. 22(5), 458–463

Jhajharia D., V.P. Singh (2011). Trends in temperature, diurnal temperature range and sunshine duration in Northeast India. International Journal of Climatology, 31, 1353–1367. doi: 10.1002/joc.2164

Kashyap R, A.C. Pandey, and B.R. Parida (2021). Spatio-temporal variability of monsoon precipitation and their effect on precipitation triggered landslides in relation to relief in Himalayas. Spatial Information Research, 1-13.

Kumar J., R.J. Nelson and R.S. Zeigler (1999). Population structure and dynamics of Magnaporthe grisea in the Indian Himalaya. Genetics, 152(3), 971-984.

Kumar R. K, A.K. Sahai, K. Krishna Kumar, S.K. Patwardhan, P.K. Mishra, J.V. Revadkar, K. Kamala, G.B. Pant (2006). High resolution climate change scenario for India for the 21st century. Current Science, 90, 334-345

Lentile L., Z.A. Holden, A.M. Smith, M.J. Falkowski, A.T. Hudak, P. Morgan, ... and N.C. Benson (2006). Remote sensing techniques to assess active fire characteristics and post-fire effects. International Journal of Wildland Fire, 15(3), 319-345.

Milne A. (1986). The use of remote sensing in mapping and monitoring vegetational change associated with bushfire events in Eastern Australia. Geocarto Int. 1, 25–32.

Overpeck J., D. Rind and R. Golberg (1990). Climate-induced changes in forest disturbances and vegetation. Nature; 343, 51-53.

Pan Z., E. Takle, M. Segal and R. Arritt (1999). Simulation of potential impacts of man-made land cover change on US summer climate under various synoptic regimes. Journal of Geophysical Research: Atmospheres. 104 6515 6528

Roy P.S. (2004). Forest Fire and Degradation Assessment using Satellite Remote Sensing and Geographic Information System. Satellite Remote Sensing and GIS Applications in Agricultural Meteorology, 362-363.

Ruosteenoja K., T.R. Carter, K. Jylhä and H. Tuomenvirta (2003). Future climate in world regions: an intercomparison of model-based projections for the new IPCC emissions scenarios.

Sannigrahi S., F. Pilla, B. Basu, A.S. Basu, K. Sarkar, S. Chakraborti and P.S. Roy (2020). Examining the effects of forest fire on terrestrial carbon emission and ecosystem production in India using remote sensing approaches. Science of the Total Environment, 725, 138331

Shekhar MS, H. Chand, S. Kumar, K. Srinivasan and A. Ganju (2010). Climate-change studies in the western Himalaya. Ann Glaciol, 51(54), 105-112.

Solomon S. (2007). IPCC (2007): Climate change the physical science basis. AGUFM, 2007, U43D-01.

Stocker T.F., D. Qin, G.K. Plattner, M. Tignor, S.K. Allen, J. Boschung, and P.M. Midgley (2013). Climate change 2013: The physical science basis. Contribution of working group I to the fifth assessment report of the intergovernmental panel on climate change, 1535.

UNEP (2009). Mountains as Early Indicators of Climate Change. Proceedings of the International Conference, 17-18 April 2008, Padova, ItalyXaiojing

Upadhyay K. (2016). Uttarakhand battles fire crisis, The Hindu. Dehradun. 30 April 2016.

White S., K.C. Ryan, C. Key and S.W. Running (1996). Remote Sensing of Forest Fire Severity and Vegetation Recovery. Int. J. Wildland Fire, 6(3), 125–136. doi:10.1071/WF9960125

Xue Y., M.J. Fennessy and P.J.Sellers (1996). Impact of vegetation properties on US summer weather prediction. Journal of Geophysical Research: Atmospheres. 7419–7430.

Yao T, X.J. Guo, T. Lonnie, K.Q. Duan, N.L. Wang, J.C. Pu, B.Q. Xu, X.X. Yang and W.Z. Sun (2006). Record and Temperature Change over the Past 100 years in Ice Cores on the Tibetan Plateau. Science in China: Series D Earth Science, 49(1), 1-9.

Zeng N., J.D. Neelin, K.M. Lau and C.J. Tucker (1999). Enhancement of interdecadal climate variability in the Sahel by vegetation interaction. Science, 286, 1537–154.

An assessment of SRTM, ASTER and LiDAR digital elevation models in the western part of South Africa

Mihlali Malindi and Patroba Achola Odera*
Division of Geomatics, School of Architecture, Planning and Geomatics, University of Cape Town, Rondebosch 7701, South Africa
*Email: patroba.odera@uct.ac.za

(Received: Oct 12, 2020; in final form: Sept 1, 2021)

Abstract: A digital elevation model (DEM) is one of the most essential datasets in earth's surface process analysis. Accuracy values of DEMs are necessary for objective selection of appropriate DEM and estimation of DEM related errors in spatial modelling and analysis. In this study, the performance of 1 arc-second Shuttle Radar Topography Mission (SRTM) and Advanced Space-borne Thermal Emission and Reflection Radiometer (ASTER) digital elevation models are evaluated in the western part of South Africa and the City of Cape Town (CCT) using ground-based levelling data. Airborne Light Detection and Ranging (LiDAR) DEM is also assessed, but only within the CCT due to unavailability of LiDAR data in other parts of South Africa. A total of 4,442 and 246 levelling data points (Trigonometric heights) are used to assess the vertical accuracies of the DEMs in western part of South Africa and CCT, respectively. Results show that SRTM DEM performs better than ASTER DEM in the western part of South Africa. The standard deviations of the differences between DEMs implied and ground observed levelling data at 4,442 points are ±8.0 and ±10.5 m for SRTM and ASTER DEMs, respectively. Assessment results within CCT show that LiDAR performs better than SRTM and ASTER in the City of Cape Town. The standard deviations of the differences between DEMs implied and ground observed levelling data at 246 points over CCT are ±4.1, ±9.3, and ±10.9 m for LiDAR, SRTM and ASTER DEMs, respectively, confirming superiority of LiDAR DEM over SRTM and ASTER DEMs. These results are applicable in enabling an objective selection of DEMs for various applications in the area of study.

Keywords: SRTM, ASTER, LiDAR, DEMs, vertical accuracy

1. Introduction

A digital elevation model (DEM) is one of the most essential spatial datasets in many geospatial and related studies. It can be defined as a raster layer or a 3D representation of the earth surface, where each cell of a raster has a value corresponding to its elevation. According to Hilton et al. (2003), a DEM represents heights of the earth from a reference surface (usually a mean sea level or its approximation by appropriate geopotential model). DEMs have a variety of applications such as 3D visualization, view-shed visibility analysis, landscaping, hydrology and water modelling, geological modelling, marine and land observation (Singh, 2019), among many other geo-processes. A DEM can be generated from a variety of data sources, these include data from aerial platforms (aerial photographs, LiDAR etc.) and satellite images, data collected physically from the ground using ground surveying techniques (e.g. traversing and spirit levelling) and data from digitized topographic maps (Singh, 2019).

Aerial photographs, Airborne Light Detection and Ranging, and satellite-based imagery are more frequently used data sources compared to ground surveys and topographic maps (Gómez et al, 2012). The aerial photographs and satellite-based imagery provide data at a relatively lower cost compared to Airborne Light Detection and Ranging. They also produce data that are broadly consistent with the required spatial, spectral and temporal resolution to interpolate new DEMs (Gómez et al, 2012). Airborne Light Detection and Ranging (LiDAR) technology generates high precision topographic products (DEMs). However, LiDAR technology includes high costs that rely on the infrastructure and the distances covered, resulting in its limited use especially in developing countries (Gómez et al, 2012).

According to Singh (2019), DEM users decide on a data source to use based on price, accuracy, sampling density and pre-processing requirements. While price, sampling density and pre-processing requirements are readily available from DEM developers, accurate information about vertical accuracy of a DEM is never known nationally or locally, until a local assessment is carried out. The evidence of this fact is available in different DEMs vertical accuracies obtained in various parts of the world (e.g. Mandla and Kamal, 2008; Zhao et al., 2011; Gómez et al, 2012; Jing et al, 2013; Ioannidis et al., 2014; Kolecka and Kozak, 2014; Varga and Bašić, 2015; Gesch et al., 2016; Morais et al., 2017; Njimu and Odera, 2017; Elkhrachy, 2018).

Although DEMs validation studies have been conducted in various parts of the world, the vertical accuracy of satellite and airborne-based DEMs covering South Africa has not been rigorously assessed and there is a need for such an assessment to facilitate informed decision on the choice of appropriate DEM for various applications. Therefore, this paper carries out a vertical accuracy assessment of airborne-based DEM (LiDAR) and freely available satellite-based DEMs [Shuttle Radar Topography Mission (SRTM: van Zyl, 2001; Farr et al., 2007), and Advanced Space-borne Thermal Emission and Reflection Radiometer (ASTER: Tachikawa et al., 2011)] over the City of Cape Town and a larger region covering western part of South Africa using ground levelling data points (Trigonometric heights), as the reference data. This paper also assesses the influence of elevation and slope on the vertical accuracy of SRTM, ASTER and LiDAR DEMs.

2 Materials and Methods

2.1 Study area

The study area is the western part of South Africa and City of Cape Town (Figure 1). Western part of South Africa (longitudes 16° 45′ ~ 22° 2′ E and latitudes 34° 8′ ~ 24° 8′ S) has a total area of approximately 318,626 km^2. The City of Cape Town (CCT) is chosen as a subset within the study area due to the availability of LiDAR data. It has a total area of approximately 2,455 km^2.

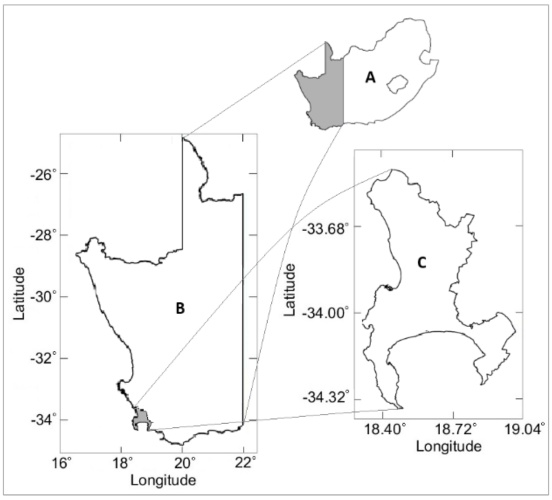

Figure 1: Study area - South Africa (A), western part of South Africa (B) and City of Cape Town (C).

2.2 Datasets

There are 4,442 levelling data points (Trigonometric heights) in the western part of South Africa, including 246 points in CCT. A spatial representation of these data points is shown in Figure 2. The levelling data cover the portion from 22° 2′ E to the western boundary of South Africa. The levelling data, with a general height accuracy of about ±0.1 m is treated as the reference data on which the DEMs are assessed in this study. The levelling data was provided by the South African's National Geospatial Information (NGI). The South African vertical datum (land levelling datum) is based on spheroidal orthometric height system, hence the trigonometric heights are very close to normal orthometric heights. The study area (including CCT) has a large range of elevation variations from 0 to 2,300 m above mean sea level (Figure 2), with a high slope range variations from 0 to 78° (Figure 3).

Shuttle Radar Topography Mission (SRTM), and Advanced Space-borne Thermal Emission and Reflection Radiometer (ASTER) digital elevation models have a spatial resolution of 30 m, offering worldwide coverage and freely available on the USGS website (http://earthexplorer.usgs.gov/). The datasets were downloaded as GeoTIFF (Georeferenced Tagged Image File Format), in geographic coordinates (latitude, longitude). The horizontal datum is the World Geodetic System of 1984 (WGS84), and the vertical datum is the Earth Gravitational Model of 1996 (EGM96). Light Detection and Ranging (LiDAR) data was provided by the City of Cape Town. It was captured in the years 2011 to 2015. The point cloud has a density of 2 to 3 points/m^2. The LiDAR data was processed and referenced onto the current South African geodetic datum (Hart94 datum) and land levelling datum, for horizontal and vertical positioning, respectively. Hart94 datum is based on WGS84 reference system (Wonnacott, 1999), hence all datasets (LiDAR, ASTER and SRTM) are based on the same horizontal geodetic datum. The heights obtained from ground levelling, LiDAR, ASTER and SRTM are also compatible because spheroidal orthometric height system used in South Africa is close to normal height system as applied in practice. The graphical representation of elevations and slopes for all the DEMs are similar to Figures 2 and 3, respectively, due to a small plotting scale, hence not repeated here.

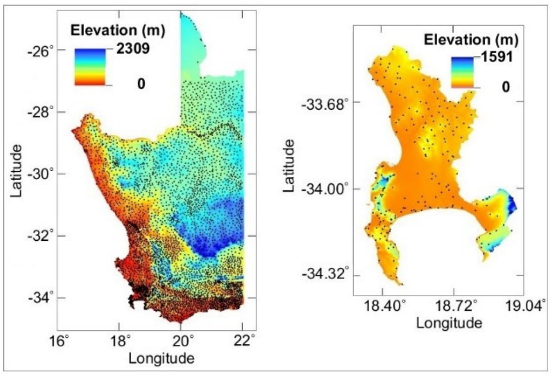

Figure 2: Spatial distribution of 4,442 levelling points in the western part of South Africa on SRTM DEM (left) and 246 levelling points in the City of Cape Town on LiDAR DEM (right). Black dots represent levelling data points.

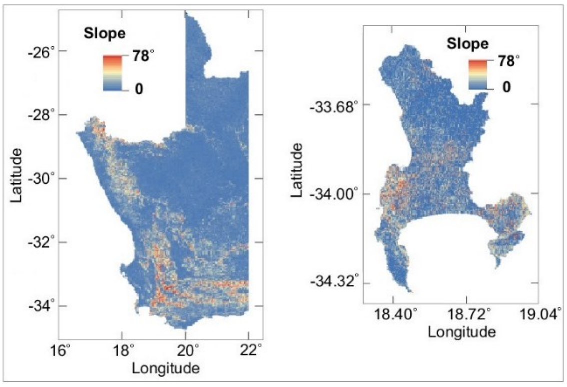

Figure 3: Slope variation in the area of study, western part of South Africa on SRTM DEM (left) and City of Cape Town on LiDAR DEM (right). Units for slope are in angular degrees.

2.3 Numerical evaluation

Assessment of the vertical accuracy of DEMs is achieved by comparing SRTM, ASTER and LiDAR DEMs heights with the ground levelling (trigonometric) data in western part of South Africa and the City of Cape Town (basically a subset of the entire study area). The DEMs heights are retrieved using the coordinates of 4,442 levelling points in the western part of South Africa and 246 levelling points in the City of Cape Town (Figure 2). Differences between the levelling and DEMs implied heights are computed as,

$$\Delta H = H_{Trig} - H_{DEM} \quad (1)$$

where ΔH is the difference in height between trigonometric height (H_{Trig}) and DEM height (H_{DEM}).

In carrying out the evaluation of the influences that changes in elevation and slope have on the performance of the DEMs, the levelling heights data points are sorted in ascending order with respect to the elevation and slope ranges. For the western part of South Africa, the elevation ranges are 0 – 500, 500 – 1000, 1000 – 1500, and > 1500 m, while slope ranges are 0 – 0.5, 0.5 – 10, 10 – 14, 14 – 21, 21 – 28, 28 – 35, and 35 – 78°. For the City of Cape Town, the elevation ranges are 0 – 300, 300 – 600, 600 – 900, and >900 m, while slope ranges are the same as the ones for the western part of South Africa. The height ranges are not equal in western part of South Africa and the City of Cape Town due to the need to have at least 10 points per range (of course 30 points should ideally be the minimum). A careful balancing of ground levelling data numbers and elevation/slope ranges is done to get reasonable representative analysis from the available data. Admittedly, an ideal number of points in each elevation and slope ranges was not possible in the City of Cape Town, especially in high elevation and high slope areas.

3. Results and Discussion

The statistics of the differences between ground control and DEMs heights in the western part of South Africa and the City of Cape Town are given in Table 1. The standard deviations for SRTM and ASTER DEMs are ±8.0 and ±10.5 m respectively, with a proximate ranges of 65.9 and 89.2 m for SRTM and ASTER DEMs, respectively (Figure 4), indicating a better performance for SRTM than ASTER over the western part of South Africa. SRTM has a smaller offset/mean (6.2 m) than ASTEER (10.2 m) from the levelling network. The offset is positive in both cases, indicating a general underestimation of orthometric height by both SRTM and ASTER DEMs in the western part of South Africa.

Similar comparisons in the City of Cape Town show superiority of LiDAR DEM followed by SRTM and ASTER DEMs, with standard deviations of the differences between ground control and DEMs heights at ±4.1, ±9.3 and ±10.9 m, respectively, with a proximate ranges of 27.0, 53.5 and 77.2 m for LiDAR, SRTM and ASTER, respectively (Figure 5). LiDAR has the smallest offset (0.7 m) followed by SRTM (6.3 m) and ASTER (8.9 m) from the levelling network in the City of Cape Town. Again, a positive offset is observed for all the three DEMs, indicating a general underestimation of orthometric height by LiDAR, SRTM and ASTER DEMs in the City of Cape Town. However, the LiDAR offset is significantly smaller relative to SRTM and ASTER offsets in the City of Cape Town.

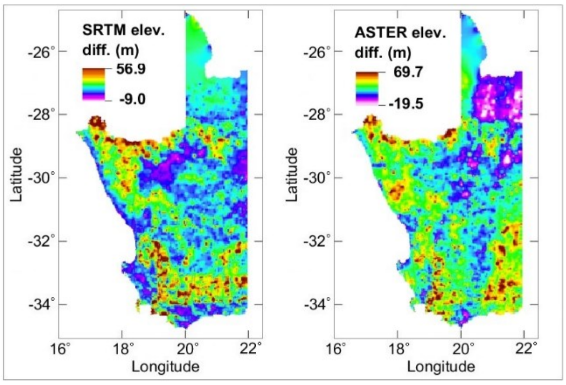

Figure 4: Spatial distribution of the differences between ground levelling and DEMs heights in western part of South Africa, SRTM (left) and ASTER (right).

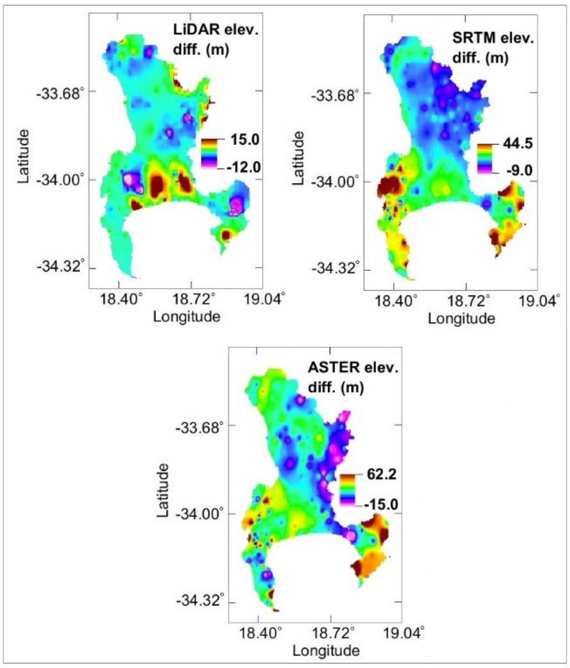

Figure 5: Spatial distribution of the differences between ground levelling and DEMs heights in the City of Cape Town, LiDAR (left), SRTM (right) and ASTER (center).

The variations between ground levelling and DEMs data with elevation and slope over the western part of South Africa are given in Figures 6 and 7, respectively. In general, the vertical accuracy of SRTM and ASTER DEMs decrease with increase in elevation and slope in the study area. However, it is worth noting that the differences between levelling and DEMs data are more correlated with slope (Figure 7) than elevation (Figure 6) in the western part of South Africa. SRTM performs better than ASTER DEM in all elevation and slope ranges in the area of study. These results in western part of South Africa are considered statically more reliable, given higher numbers of data points at each range than the City of Cape Town. A closer look at Figures 6 and 7 reveal a negative trend in the vertical accuracy of DEMs with respect to the number of test points. This is a difficult problem to deal with, unless ground control points are designed to allow for equal number of points per height range and slope range. Another problem is the distribution of the control points used; ideally, equal distribution should be maintained for unbiased results. As it is today, most studies including this study are limited to the existing control points (normally not designed for DEM evaluation), hence presence of biased results in the absolute sense. A well designed baseline for testing DEMs is therefore necessary for unbiased results.

Table 1: Overall statistics of the differences between ground levelling and DEMs implied elevations over the western part of South Africa and the City of Cape Town (units are in m).

	western part of South Africa		City of Cape Town		
	SRTM	ASTER	LiDAR	SRTM	ASTER
Points	4,442	4,442	246	246	246
Mean	6.2	10.2	0.7	6.3	8.9
SD	±8.0	±10.5	±4.1	±9.3	±10.9

The mentioned deficiencies in the test data do not in any way render the current results irrelevant, as a relative comparison of DEMs is still achievable with the existing control points, due to the fact that all DEMs are subjected to the same points (even if not well distributed in a rigorous sense). The relativity and biasness in the results are clearly demonstrated in the current study. Figures 8 and 9 show similar comparisons (in a smaller area with fewer control points) as in Figures 6 and 7 (in a larger area with many control points). LiDAR DEM performs better than SRTM and ASTER DEMs in all elevation and slope ranges in the City of Cape Town, with SRTM performing better than ASTER DEM. Although the general trends are maintained, there is a weaker correlations of vertical accuracies with respect to elevation and slope in Figures 8 and 9 compared to Figures 6 and 7.

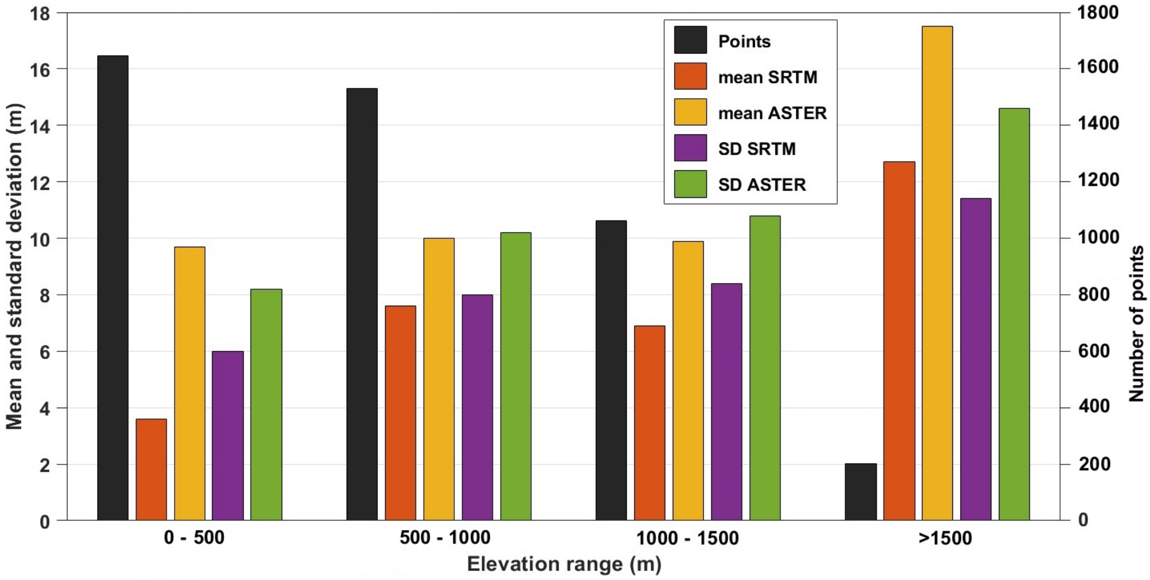

Figure 6: Variation of mean and standard deviation of the differences between ground levelling and DEMs heights with elevation in the western part of South Africa.

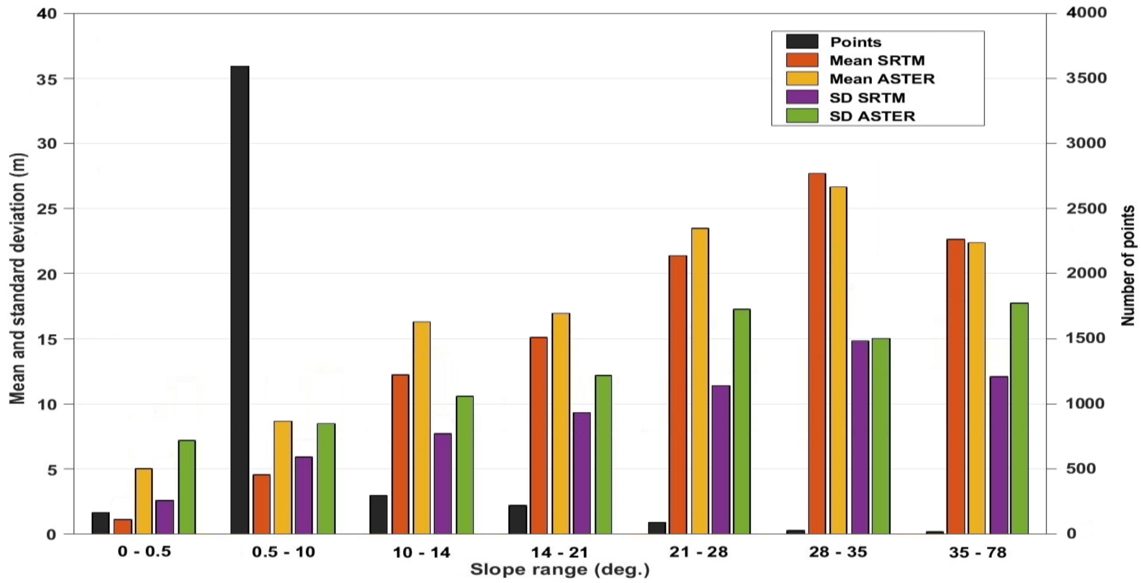

Figure 7: Variation of mean and standard deviation of the differences between ground levelling and DEMs heights with slope in the western part of South Africa.

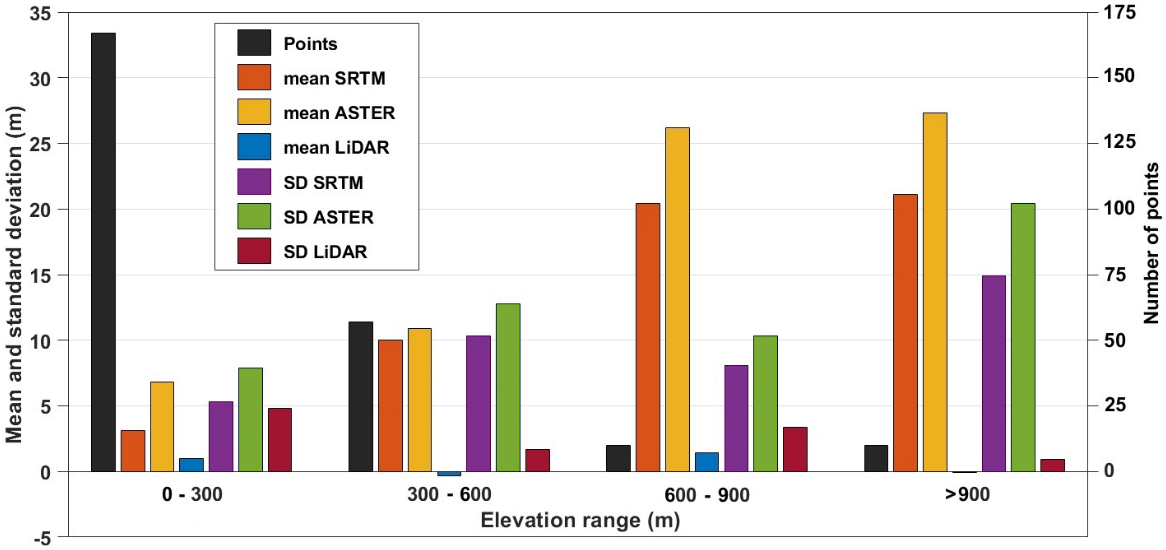

Figure 8: Variation of mean and standard deviation of the differences between ground levelling and DEMs heights with elevation in the City of Cape Town.

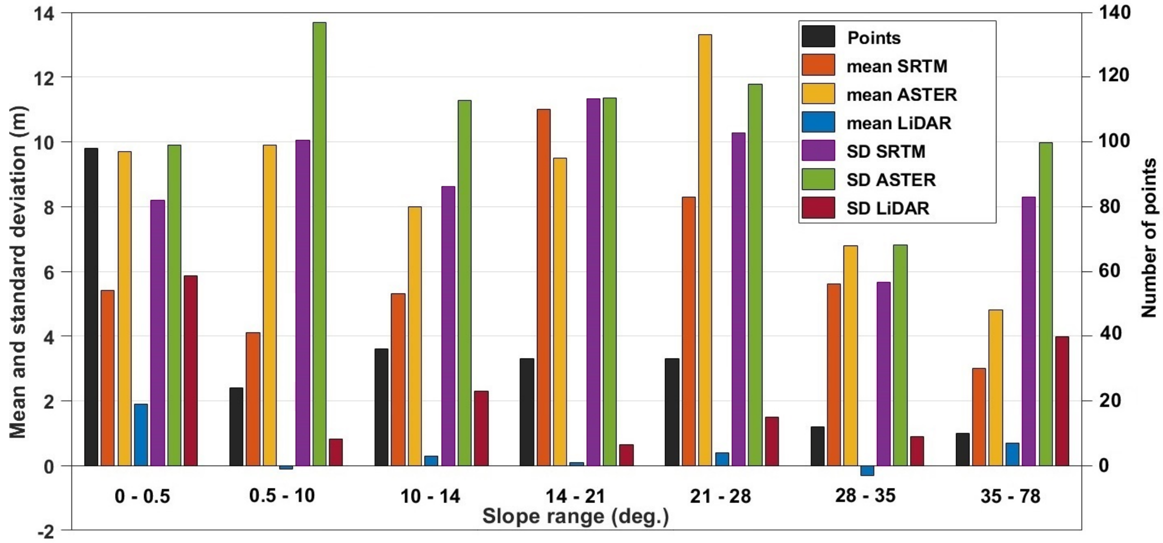

Figure 9: Variation of mean and standard deviation of the differences between ground levelling and DEMs heights with slope in the City of Cape Town.

4. Conclusions

We have carried out an assessment of vertical accuracy of LiDAR, SRTM and ASTER DEMs over the western part of South Africa. LiDAR DEM is only available within the City of Cape Town, hence only SRTM and ASTER DEMs are considered in the western part of South Africa while all the three DEMs (LiDAR, SRTM and ASTER) are assessed together in the City of Cape Town. The vertical accuracy assessment of the DEMs is achieved by comparing levelled heights (obtained through trigonometric levelling) with DEMs implied heights in the whole study area and at varying elevations and slopes.

Results indicate/confirm superiority of LiDAR with a standard deviation of ±4.1 m, over SRTM (±9.3 m) and ASTER (±10.9 m) over the City of Cape Town. Vertical accuracies of SRTM and ASTER DEMs in western part of South Africa are ±8.0 and ±10.5 m respectively. Both SRTM and ASTER DEMs perform better in low and flat areas than high and steep areas, while the vertical accuracy of LiDAR DEM is not significantly affected by elevation and slope. Admittedly, the few ground control points in the high areas in the City of Cape Town could not guarantee statistically stable results for elevation and slope ranges, hence strictly no clear trends were observed. The DEMs vertical accuracy parameters obtained in this study can be used in selecting appropriate DEM(s) for various applications over the study area.

Acknowledgements

We would like to thank the South African National Geospatial Information and the City of Cape Town for providing levelling and LiDAR data, respectively. SRTM and ASTER DEMs were freely made available by United States Geological Survey. We are grateful to the two anonymous reviewers, for their comments and suggestions that have been used to improve the quality of the paper.

References

Elkhrachy, I. (2018). Vertical accuracy assessment for SRTM and ASTER Digital Elevation Models: A case study of Najran city, Saudi Arabia. Ain Shams Engineering Journal, 9(4), 1807–1817. https://doi.org/10.1016/j.asej.2017.01.007

Farr, T.G., P.A. Rosen, E. Caro, R. Crippen, R. Duren, S. Hensley, M. Kobrick, M. Paller, E. Rodriguez, L. Roth, D. Seal, S. Shaffer, J. Shimada, J. Umland, M. Werner, M. Oskin, D. Burbank and D. Alsdorf (2007). The Shuttle Radar Topography Mission. Review of Geophysics, 45, RG2004. https://doi.org/10.1029/2005RG000183

Gesch, D., M. Oimoen, J. Danielson and D. Meyer (2016). Validation of the aster global digital elevation model version 3 over the conterminous United States. ISPRS - International Archives of the Photogrammetry, Remote Sensing and Spatial Information Sciences, XLI-B4, 143–148. https://doi.org/10.5194/isprs-archives-XLI-B4-143-2016

Gómez, M., J. Lencinas, A. Siebert and G. Díaz (2012). Accuracy Assessment of ASTER and SRTM DEMs: A Case Study in Andean Patagonia. GIScience and Remote Sensing, 49(1), 71–91. https://doi.org/10.2747/1548-1603.49.1.71

Hilton, R., W. Featherstone, P. Berry, C. Johnson and J. Kirby (2003). Comparison of digital elevation models over Australia and external validation using ERS-1 satellite radar altimetry. Australian Journal of Earth Sciences, 50(2), 157–168. https://doi.org/10.1046/j.1440-0952.2003.00982.x

Ioannidis, C., E. Xinogalas and S. Soile (2014). Assessment of the global digital elevation models ASTER and SRTM in Greece. Survey Review, 46, 342–354. https://doi.org/10.1179/1752270614Y.0000000114

Jing, C., A. Shortridge, S. Lin and J. Wu (2013). Comparison and validation of SRTM and ASTER GDEM for a subtropical landscape in Southeastern China. International Journal of Digital Earth, 7(12), 969–992. https://doi.org/10.1080/17538947.2013.807307

Kolecka N. and J. Kozak (2014). Assessment of the Accuracy of SRTM C- and X-Band High Mountain Elevation Data: a Case Study of the Polish Tatra Mountains. Pure and Applied Geophysics, 171(6), 897–912. https://doi.org/10.1007/s00024-013-0695-5

Mandla, V. and J. Kamal (2008). Digital Elevation Model Accuracy Aspects. Journal of Applied Sciences. 8(1), 134–139. https://doi.org/10.3923/jas.2008.134.139

Morais, J.D., T.S. Faria, M.A.T. Elmiro, M.A. Nero, A.de.A. Silva and R.A.de.A. Nobrega (2017). Altimetry assessment of ASTER GDEM v2 and SRTM v3 digital elevation models: a case study in urban area of Belo Horizonte, Mg, Brazil. Boletim de Ciências Geodésicas, 23(4), 654–668. http://dx.doi.org/10.1590/S1982-21702017000400043

Njimu, S.K. and P.A Odera (2017). Assessment of Classical, ASTER and SRTM DEMs in Nairobi Region, Kenya. Journal of Agriculture, Science and Technology, 18(2), 109–119. http://ojs.jkuat.ac.ke/index.php/JAGST/article/view/22

Singh, S. (2019). Difference between DEM/DTM and DSM. GIS Resources. http://www.gisresources.com/confused-dem-dtm-dsm

Tachikawa, T., M. Hato, M. Kaku and A. Iwasaki (2011). Characteristics of ASTER GDEM version 2. International Geoscience and Remote Sensing Symposium (IGARSS), 3657–3660. https://www.int-arch-photogramm-remote-sens-spatial-inf-sci.net/XLI-B4/143/2016/isprs-archives-XLI-B4-143-2016.pdf

Van Zyl, J.J. (2001). The Shuttle Radar Topographic Mission (SRTM): A breakthrough in remote sensing of topography. Acta Astronautica, 48(5), 559–565.https://doi.org/10.1016/S0094-5765(01)00020-0

Varga, M. and T. Bašić (2015). Accuracy Validation and Comparison of Global Digital Elevation Models over Croatia. International Journal of Remote Sensing, 36, 70–189. https://doi.org/10.1080/01431161.2014.994720

Wonnacott, R.T. (1999). The implementation of the Hartebeesthoek94 co-ordinate system in South Africa. Survey Review, 35(274), 243–250. https://doi.org/10.1179/sre.1999.35.274.243

Zhao S., W. Cheng, C. Zhou, Xi. Chen, S. Zhang, Z. Zhou, H. Liu and H. Chai (2011). Accuracy assessment of the ASTER GDEM and SRTM3 DEM: an example in the Loess Plateau and North China Plain of China. International Journal of Remote Sensing, 32(23), 8081–8093. https://doi.org/10.1080/01431161.2010.532176

Spatial Distribution Analysis of Soil Erosion, Sediment Yield and Transport Capacity in the Ankobra River Basin – A Case Study

B. Kumi-Boateng*, M. S. Peprah and E.K. Larbi
Faculty of Mineral Resources Technology, Department of Geomatic Engineering, University of Mines and Technology, Tarkwa, Ghana West Africa
*Email: kumi@umat.edu.gh

(Received: Oct 12, 2020; in final form: Sept 4, 2021)

Abstract: Soil erosion is one of the natural geomorphic processes that may have economic and environmental impacts. Its acceleration due to human activities may constitute serious hazards. Identification of the impacts of soil erosion can be the foremost step in controlling the dynamic step of soil degradation in agricultural and mining areas. This will assist decision makers to develop strategies to help mitigate this menace**.** This study demonstrates the application of Revised Universal Soil Loss Equation (RUSLE) and Sediment Distributed Delivery (SEDD) models integrated with Geographic Information System (GIS) to estimate annual soil loss and the sediment delivery of the Ankobra River Basin in Ghana. Digital Elevation Model, land use map, rainfall data and soil map were input to the model to display the spatial distribution of soil erosion and sediment yield in the basin. The model estimated an annual soil erosion ranges maximum up to 4650 tons/ha/yr with a mean and standard deviation of 24.64 tons/ha/yr and 14.07 tons/ha/yr respectively. The sediment yield rage up to 448.936 tons/ha/year with a mean and standard deviation of 2.13 tons/ha/yr and 11.8 tons/ha/yr respectively. The estimated transport capacity value ranges from 0 to 601kg/m^2/yr with a mean of 3.6 kg/m^2/yr and a standard deviation of 11.5 kg/m^2/yr. Conversely, the results revealed about 15.41 % of the basin is susceptible to severe erosion. The modelled results showed that soil erosion rate varied with land use types. Additionally, the South Western part of the basin has the highest erosion rate. The study demonstrates that the RUSLE and SEDD models integrated with GIS provides relatively easy, cost-effective and fast approach in the estimation of spatially distributed soil erosion and sediment yield of river basins. The results will help in the planning and management of natural resources to ensure sustainable development of the Ankobra River Basin.

Keywords: Ankobra River Basin, Revised Universal Soil Loss Equation, Soil Erosion Modelling, Sediment Yield Modelling, Susceptibility Mapping, Transport Capacity

1. Introduction

Soil erosion is a natural process of removal of soil material and transporting through the action of erosive agents such as water, wind, snow avalanches, gravity, and human disturbance (Yariyan et al., 2020; Panitharathine et al., 2019). Soil erosion has remained a serious environmental problem when combined with climate-induced high intensity rainfall or snow avalanches (Yariyan et al., 2020; Panitharathine et al., 2019; Kumi-Boateng et al., 2020). Soil erosion and its associated sediments transported to river basins and sea bodies are considered as one of the main natural occurring hazard processes and water pollution in ecosystems found in developing countries including Ghana (Prieto-Amparam et al., 2019; Kusimi et al., 2015; Kusimi, 2008). This has become an ongoing research focuses and is receiving much attention by numerous researchers due to its socio-economic and environmental impacts (Kusimi et al., 2015; Akrasi and Ansa-Asare, 2008). This naturally occurring event has been accelerated as a result of global increase of climate change (Amisigo et al., 2018; Lee et al., 2013) and human anthropogenic activities (Lee et al., 2013; Aduah et al., 2015; Aduah et al., 2017; Ayivor and Gordon, 2012; Boye et al., 2019; Samlafo and Ofoe, 2017, Kusi-Ampofo and Boachie-Yiadom, 2012). The soil resources are limited and its usage is of utmost importance; since it sustains the biogeochemical processes and home for a great diversity of microorganisms (Panitharathine et al., 2019). Sustained soil development, conservation, and restoration is one of today's main challenges for humankind (Lee et al., 2013). Understanding the causative factors and processes controlling catchment sediment yield is crucial and fundamental for water resources management and sediment (Boakye et al., 2018). Hence, a quantitative estimate of the amount of sediments from the catchment area is a very important factor for soil and soil water conservation, planning and management (Lee et al., 2013). Early warnings and emergency responses to this natural occurring hazard are needed so that governmental agencies and planners can prevent as much damage as possible (Kumi-Boateng et al., 2020). Therefore, it is essential to identify soil erosion prone zones and its associated sediment yield to prevent or mitigate adverse effects of soil erosion in spatial contest.

Several well-known studies have been in existence and utilize for soil erosion susceptibility mapping. These approaches are primarily of two types thus; physical models and experiential models (Hategekimana et al., 2020). Notably among them are; The Water Erosion Prediction Project (WEPP) developed by the United States Department of Agriculture (Reitsma et al., 2015; Defersha et al., 2012), WATEM/SEDEM (Alatorre et al., 2012), EROSION 3D (Defersha et al., 2012), the Limburg Soil Erosion Model (LISEM) (Perez-Molina et al., 2017) and The European Soil Erosion Model EUROSEM (Ganasri and Ramesh, 2016) are broadly used physical models. Though these approaches are grounded on real procedures, they understand large numbers of input parameters with rigorous computation (Hategekimana et al., 2020). Furthermore, simulation of these models for a specific area requires observed sediment loss data, which are not available for ungauged watersheds (Pelacani et al., 2008;

Jiang et al., 2007). Conversely, some qualitative analysis based on statistical indices have also been deployed to prioritize areas with adverse soil erosion hazards. Some of the examples of these well-known qualitative analysis include; Analytical Hierarchy Process (Boufeldja et al., 2020; Sadhasivam et al., 2020; Vijith and Dodge-Wan, 2019; Tairi et al., 2019), Enzyme-induced Carbonate Precipitation assisted by a sodium alginate (Almajed et al., 2020), Compound factor (Sadhasivam et al., 2020), Frequency ratio (Senanayake et al., 2020; Zabihi et al., 2018), Principal Component Analysis (Prieto-Amparan et al., 2019), Group analysis (Prieto-Amparan, et al., 2019), Ordinary Kriging (Samanta et al., 2016; Lee et al., 2012), Logistic regression (Arabameri et al., 2020b; Yariyan et al., 2020; Aduah et al., 2018b), Belief function (Yariyan et al., 2020), Probability density (Yariyan et al., 2020), Cs Techniques (An et al., 2014; Orkhonselenge et al., 2008), Kinematic runoff and Erosion (Goodrich et al., 2012), Compound parameter (Prieto-Amparan et al., 2019), Weight of Evidence (Zabihi et al., 2018), Index of entropy (Zabihi et al., 2018), Thiessen polygon (Lee et al., 2012), Inverse Distance Weighting (Lee et al., 2012), K-Nearest Neigbour (Avand et al., 2019), rainfall-runoff-sediment yield simulation (Lee et al., 2013), Sediment Delivery ratio (Rajbanshi and Bhattacharya, 2020; Boakye et al., 2020), and Regression analysis (Akrasi and Ansa-Asare, 2008; Vassilakis et al., 2016; Boye et al., 2019).

These classical methods are woefully inadequate, because there are always new areas that periodically experience splash of running waters (Kumi-Boateng et al., 2020). Therefore, there was a need to explore novel techniques in identifying and mapping soil erosion zones that will help in planning and managing the problem in spatial context. In recent years, the utilization of soft computing techniques has been successfully applied and duly investigated in prioritizing soil erosion prone areas (Arabameri et al., 2020a; Yariyan et al., 2020). Notably among these novel ensemble models are; Multivariate partial Least Square regression variable importance projection statistics (Rajbanshi and Bhattacharya, 2020), Random forest (Pourghasemi et al., 2020; Avand et al., 2019), Random Subspace algorithms (Nhu et al., 2020), ANN-Bagging (Nhu et al., 2020; Arabameri et al., 2020c), AdaBoost (Nhu et al., 2020), Reduced Pruning Error Tree (Nhu et al., 2020), Fractal rainfall disaggregation (Sihem, 2009), Boruta algorithm (Pourghasemi et al., 2020), Naïve Bayes trees (Arabameri et al., 2020b), Fisher's Linear Discriminant Analysis (Arabameri et al., 2020b), and Technique for order preference by similarity to ideal solution AHP (Sadhasivam et al., 2020). However, other techniques such as contour banking, backfilling methods, phytoremediation techniques, Siberia model, geofluv natural regrade design, shuffled frog leaping algorithm, particle swarm optimization, brain inspired emotional neural network, group method of data handling, support vector machine, multivariate adaptive regression splines, extreme learning machine, discrete wavelet transform, radial basis functions artificial neural network, Vise Kriterijumska Optimizacija I Kompromisno Resenje, biogography Optimized, CHAID tree ensemble, Harris hawks optimization, ANN-Dagging, histogram equalization, adaptive thresholding techniques, multivariate geomorphometric approach, Dempster Shafer theory, and many others that were not considered in this study can be used in the future research.

Soil erosion is an ongoing occurring event, and as a natural hazard, it cannot be completely eradicated in the world (Kumi-Boateng et al., 2020). However, the evaluation of its effect on the environment is problematic, due to its spatial configuration, intricate biophysical developments, measurement methods, and the degree of its existence (Boakye et al., 2020; Kusimi, 2008) leading to inadequate or sometimes unavailability of reliable data, especially in developing countries for planning and project implementation purposes (Boakye et al., 2020). Moreover, its effect can be minimized by undertaking the integrated management and developmental approach that can promote the coordinated management and development of water, land and related resources (Kumi-Boateng et al., 2020). In addition to land degradation, additional difficulties caused by soil erosion comprise loss of soil nutrients, deteriorating crop yields, reduction in soil productivity, and pollution of surface and groundwater resources by sediment, fertilizer nutrients and insecticide residues (Kusimi et al., 2015). In order to improve water quality and restore impaired watersheds, managers need to make decisions using data that they are able to prioritize its impacts (Kusimi, 2008). Data collection can be expensive, tedious and time consuming, so in such situations using modelling approach makes sense (Boakye et al., 2020; Kusimi, 2008), particularly in the developing countries where institutions and organizations charged with the monitoring and collection of data are ill-equipped in terms of personnel, equipment and funding (Boakye et al., 2020). Models for sediment yield, when applied to those areas lacking data, provide invaluable information for predicting future impacts of agricultural activities, land use, stream stabilization and sediment storage in reservoirs (Kusimi, 2008). To minimize the cost of field measurements of soil erosion and sediment yield, many data mining models have been developed and used to effectively estimate soil erosion, which aid in developing soil erosion management plans in many river basins (Kusimi et al., 2015). Sediment yield and surface erosion at a watershed or regional scale are at present modelled using empirical models such as the universal soil loss equation (USLE) (Hategekimana et al., 2020).

The revised universal soil loss equation (RUSLE) is an updated version of the Universal Model of the Soil Loss Equation (USLE) (Hategekimana et al., 2020; Kusimi et al., 2015). The USLE was developed by the United States Department of Agriculture (USDA) in 1978 (Smith, 1999). It can predict water under various influences (for example, land use, relief, soil and climate) and guide the development of protective erosion control plans (Nam et al., 2003). RUSLE model contains a computer program that is easy to calculate and contains analysis of research data that is not available for USLE (Alexandridis et al., 2015). Although USLE has been retained in RUSLE, factor evaluation technology has been modified and new data has been introduced to evaluate terms under specific conditions (Hategekimana et al., 2020). In the RUSLE model, the potential risk of soil erosion includes only the product of three natural factors (rainfall erosion, soil erodibility, and the length and slope of the slope) to indicate areas of high vulnerability (Panagos et al., 2015a; Panagos et al., 2015b; Panagos et al., 2015c; Panagos et al., 2017). In addition to, the estimated soil erosion risk is caused by natural and human factors (rainfall erosion, soil erodibility, slope length, slope coverage management and supporting practice factors) (Panagos et al., 2015c). It has been widely used yielding very promising results. Its application in a GIS environment can provide a spatial distribution of erosion and soil loss, which requires a small and simple input data set; and is relatively easy to use (Hategekimana et al., 2020). Conversely, its data requirements are not too complex, and literature has shown that it has been successfully used to estimate soil erosion of catchments and farmlands as revealed in the following literatures (Hategekimana et al., 2020; Senanayake et al., 2020; Ayalew, 2014; Kalambuka and Kumar, 2017; Kusimi et al., 2015; Saavedra, 2005; Sihem, 2009; Panitharathine et al., 2019; Tesfaye et al., 2018; Basri et al., 2019; Shoman, 2017; Tundu et al., 2018; Samanta et al., 2016; Mesfin and Taddese, 2019; Boakye et al., 2020; Koirala et al., 2019; Maqsoom et al., 2020; Rizalihadi et al., 2013; Amah et al., 2020; Boufeldja et al., 2020; Chalise and Kumar, 2020; Rajbanshi and Bhattacharya, 2020).

Even though the RUSLE and its integration with Geospatial technologies have gotten acknowledgment among hydrologist and erosion researchers, its application in Ghana is exceptionally low (Boakye et al., 2020). Considering the unavailability of soil loss and sediment yield data, and the need to monitor soil erosion, there is the need to adopt appropriate models to demonstrate the spatial distribution of soil erosion and sediment yield, especially in basins experiencing drastic land use and cover changes (Boakye et al., 2020; Boakye et al., 2018; Abroampah et al., 2014; Woldemariam and Harka, 2020; Adjei et al., 2014; Ayivor and Gordon, 2012; Mensah, 2009). One of such important basins is the Ankobra River basin in Ghana (Aduah et al., 2015; Aduah et al., 2017). The climatic environment makes the basin susceptible to rainfall erosion (Aduah et al., 2018a; Aduah et al., 2018b). Previous studies concerning the study area revealed that, the Ankobra River which serves as the main source of potable drinking water for the residents at Tarkwa Nsuaem municipality and also as a source of water for production at the intake points of the Ghana Water Company Limited (Kusi-Ampofo and Boachie-Yiadom, 2012) have become unsuitable for drinking (Samlafo and Ofoe, 2017). This is as the result of the presence of heavy metals such as Arsenic which makes it fell within the poor drinking water quality (Samlafo and Ofoe, 2017). Hence, the water needs to be treated to reduce the arsenic quantity before drinking, since these heavy metals can have serious health issues on humans (Bam et al., 2020; Mirchooli et al., 2019; Joe-Asare et al., 2018; Seidu and Ewusi, 2018). These heavy metals distributed into the Ankobra River is by means of anthropogenic activities such as illegal mining, unsafe farming practice, illegal fishing, and improper waste management resulting in increased cost of production and gradually drying up of the water body (Asante-Annor et al., 2018; Samlafo and Ofoe, 2017; Kusi-Ampofo and Boachie-Yiadom, 2012; Mensah, 2009). This results in the irregular supply of potable water from the Bonsa Treatment plant to the residents of Tarkwa and its environs (Seidu and Ewusi, 2018), and many of the residents rely on unwholesome source of water for drinking and domestic activities (Joe-Asare et al., 2018). However, the increase in climate change (Raneesh et al., 2011), rampant increasing of the activities and operations of illegal miners known as artisanal miners in the basin and alluvial mining within the river bed (Aduah et al., 2015), and the increasing urbanization (Mensah, 2009), can significantly alter the erosion regime of the basin. It is therefore likely that the estimates might not be reflecting the current situation, but can be precise used as knowledge of which is important for basin management to ensure sustainability of the ecosystem. In view of this, the study applies the RUSLE model to display the spatial distribution of soil erosion and the sediment yield of Ankobra River Basin. The study integrated the RUSLE and Sediment Delivery Distributed (SEDD) model with GIS and Remote Sensing techniques to identify the sediment generating areas for prioritized attention. This is important for effective catchment management to reduce the soil loss rate and the amount of sediment yield in the Ankobra River Basin, thereby ensuring the sustainability of the ecosystem, longevity of reservoirs/dams, treatment plants and an improved agricultural and mining productivity. Moreover, RUSLE was used to model soil erosion and sediment yield in the Ankobra Basin with regards to previous works which assessed sediment yield, sediment sources and bank erosion in order to determine the spatial patterns/trends in surface soil erosion and sediment yield of the basin. Therefore, the current study is devoted to prioritize soil erosion hazard areas of Ankobra based on the geo-environmental parameters. The modeling procedure is established using the aforementioned soft computing methods. Additionally, the present study provides a reliable methodology for erosion prioritization within Ankobra Basin, contributing to multiple flood occurrences, hazard risks, and water resource engineering disciplines. This is highly essential for such a region where the reliable flooding management and sustainability is very much needed.

2. Study area

The Ankobra River basin is located between latitude 005° 00′ N and 6° 30′ N and longitudes 001° 45′ and 002° 30′ W. It belongs to the Western River system and cover an area of about 3953 km^2. The river takes its source from the hills north of basin dare (near Bibiani) and flows for about 260 km mostly due south before it enters the Gulf of Guinea at Asanta a few kilometers west of Axim (Mensah et al., 2015). Ankobra River and its surrounding tributaries including Buri, Anoni, Sumin, and Ayiasu, drain the area depicting a dendritic pattern (Samlafo and Ofoe, 2017). The Ankobra River is the source of potable drinking water for residents at Western district and also provides many local communities within Tarkwa Nsuaem municipality with water for domestic as well as industrial purposes (Aduah et al., 2018a; Seidu and Ewusi, 2018, Samlafo and Ofoe, 2017). Geographically, the area is generally low relief, with the elevations varying between 30 m to 340 m above the mean sea level (MSL). The study area experiences one of the highest rainfalls in Ghana. The rainfall season of the area is bimodal, with the highest season found between February and July and the minor season between August and November with high relative humidity of 70 to 80% throughout the year (Aduah et al., 2017; Peprah and Mensah, 2017). The rainfall ranges between 900 mm and 1700 mm per annum and the annual average minimum and maximum temperatures of 22 ºC and 32 ºC, respectively (Aduah et al., 2018a; Peprah et al., 2017). The land use and land cover of the area consists of thick evergreen and secondary forests, with scattered shrubs and farms (Aduah et al., 2015). The forest is full of climbers and lianas, which are able to reach into the upper tree layer (Samlafo and Ofoe, 2017). Economic trees include mahogany, wawa, odum, sapele among others (Samlafo and Ofoe, 2017. Tarkwa Nsuaem municipality can boast of large forest reserves like the Bonsa reserve, Ekumfi reserve, Neung south reserve and Neung north reserve (Samlafo and Ofoe, 2017). The basin's geology is characterized by Birimian and Tarkwaian rock systems geological information, while the soil is composed mostly of Ferric Acrisols, according to the Food and Agricultural Organisations'(FAO) soil classification system and forest oxysols, according to the Ghana soil classification system (Aduah et al., 2015). Economically, the Birimian rocks are regarded as the most important formations due to its mineral potentials (Samlafo and Ofoe, 2017). These geological formations are the reasons for the existence of high mineral deposits in the Municipality (Joe-Asare et al., 2018). Conversely, many gold and manganese mining companies are located in the Municipality which contributes significantly to the national development of Ghana (Boye et al., 2018; Joe-Asare et al., 2018). A detailed information about the Birimian and Tarkwaian supergroup can be found in (Kwesi et al., 2020; Asante-Annor et al., 2018; Kuma and Ewusi, 2009). Major economic activities in the catchment area include open-pit gold mining, small scale mining, rubber cultivation, cocoa harvesting, oil palm harvesting, cola harvesting and food crop production (Aduah et al., 2020; Larbi et al., 2018). Figure 1a and Figures 1b represents the location and digital elevation map of the study area (African map; Ghana map; Ankobra Basin; DEM of Ankobra basin).

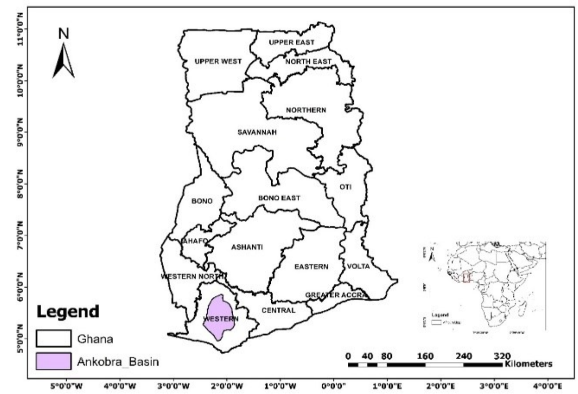

Figure 1a. Regional map of Ghana showing the study area

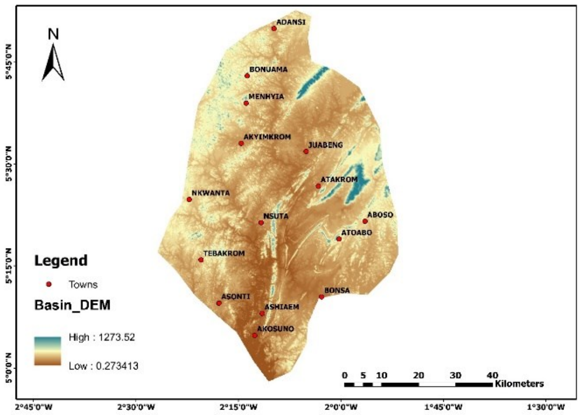

Figure 1b. Digital Elevation of the study area

3. Resources and methods used

3.1. Resources

The Cost factors used for the estimation of the long term average annual soil loss are; Precipitation data downloaded from the world climate website (https://www.worldclim.org/data/index.html), Digital Elevation Model (DEM) downloaded from (https://lpdaac.usgs.gov/products/astgtmv003/), soil data obtained from (https://data.isric.org) and the Land Use and Land Cover data downloaded from the Earth explorer website (https://earthexplorer.usgs.gov).

3.2. Methods used

3.2.1. Revised Universal Soil Loss Equation (RUSLE)

The Revised Universal Soil Loss Equation (RUSLE) is an empirically based model used for the estimation of the average annual soil erosion of an area of interest, based on a number of conditions such as cropping systems and management techniques (Kouli et al., 2008). The aim is to prioritize erosion control and management practices at the area of interest. RUSLE is an improved version of the Universal Soil Loss Equation (USLE) (Wischmeier and Smith., 1978). Five major factors (rainfall pattern, soil type, topography, land cover and management practices) are used in the computation of the average annual soil loss according to Equation (1):

$$A = R \times K \times LS \times C \times P \tag{1}$$

where; A is the computed spatial average soil loss per unit area (t/ha/year); R is the rainfall-runoff erosivity factor (MJ mm ha/h/year); K is the soil erodibility factor (t ha MJ^{-1}mm^{-1}); LS is slope length and steepness factor (dimensionless); C is the cover management factor (dimensionless); P is the conservation support practice factor (dimensionless). All cost surface maps were generated in the ArcGIS environment according to the methodology shown in Figure 2.

3.2.2. Rainfall Erosivity Factor (R)

Rainfall factor (R), an index unit, is a measure of the erosive force of a specific rainfall. This is determined as a function of the volume, intensity, velocity, distribution, frequency and duration of the rainfall (Prasannakumar *et* *al*., 2011). This implies higher rainfall intensity and duration results in higher erosion potential. Thus, high R value indicates high soil detachment and transport (Boakye et al., 2020). The annual R factor is determined from the summation of every rainstorm, the result of aggregate vitality and the greatest 30 min force I_{30} (Morgan, 2005). Long term normal R values are related with accessible precipitation information, annual precipitation and Modified Fournier Index (MFI) (Mbugua, 2009). The Modified Fournier Index (MF) is very important as it measures precipitation forcefulness, useful in estimation of rainfall over long periods and changes between different periods and years. The R factor is as computed in Equation (2) developed for West Africa (Boakye et al., 2020);

$$R = 5.444MFI - 416 \quad (2)$$

MF, which is the modified Fournier Index is expressed in Equation (3) as:

$$MFI = \sum_{i=1}^{12} \frac{P_i^2}{P} \quad (3)$$

.

where; P_i is the monthly average amount of precipitation for month, i (mm) and P is the average annual quantity of precipitation (mm).

In this study, the monthly rainfall data for the years (2012 to 2018) were downloaded from the world climate website (https://www.worldclim.org/data/index.html), and used for calculating the mean annual rainfall. The rainfall map (Figure 3a) was generated in the ArcGIS environment through mask extraction using the study area as a boundary file from the world rainfall data. Figure 3b represents the R factor map generated using the annual mean rainfall data in the ArcGIS environment. The monthly rainfall data range from 2012 to 2018 is tabulated in Table 1. The rainfall erosivity factor R for the years 2012 to 2018 was found to be in the range of 230 to 373 MJ mm ha/h/year with a mean of 297 MJ mm ha/h/year. The annual mean rainfall recorded was between 836.12 mm to 1614.61 mm with a mean of 1200 mm.

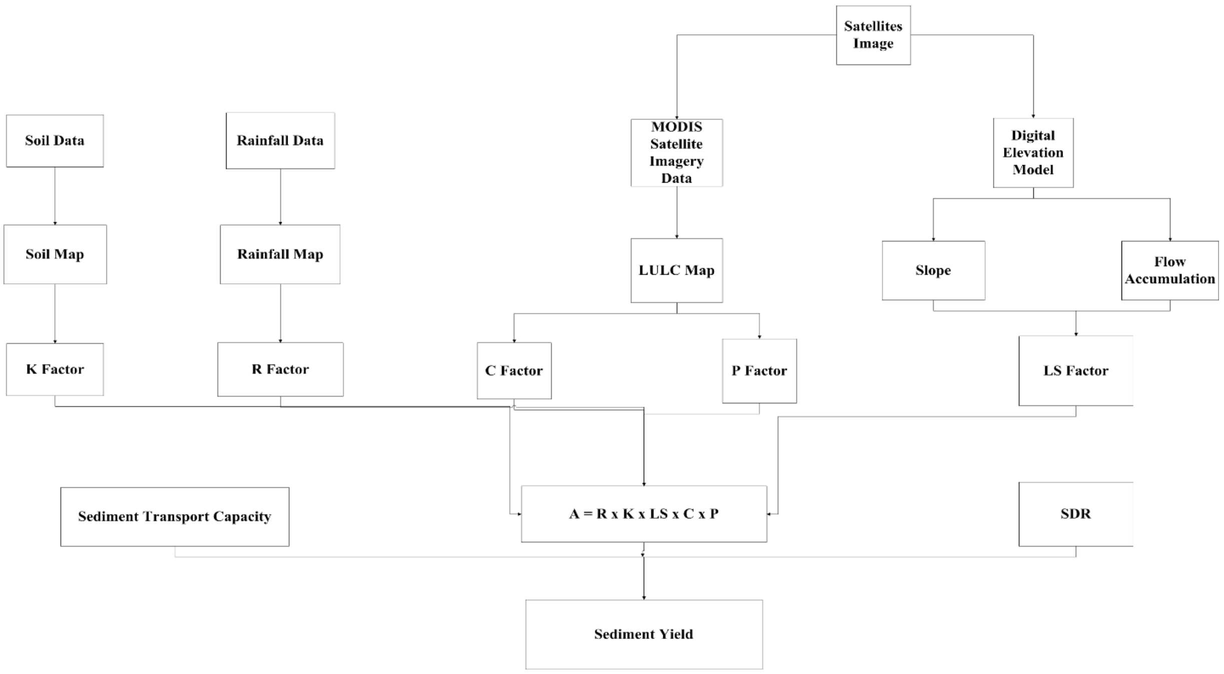

Figure 2. Flowchart of Project Methodology

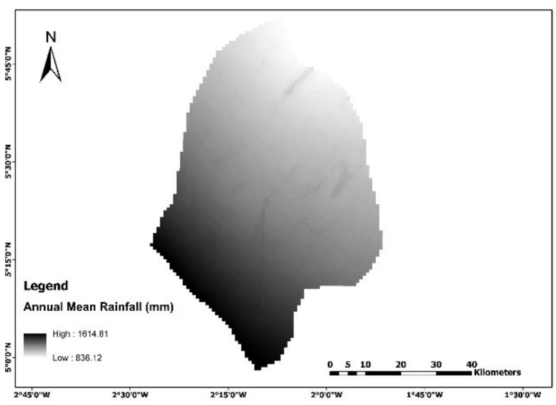

Figure 3a. Annual Mean Rainfall Map

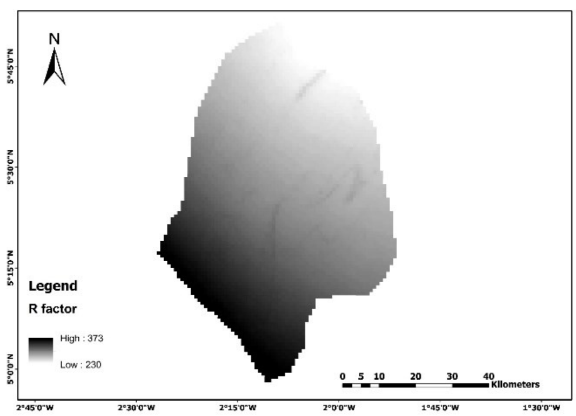

Figure 3b. R factor Map

Table 1. Monthly Rainfall data Range (2012-2018)

Monthly	Rainfall (mm)
January	24-45
February	55-82
March	108-154
April	141-174
May	188-277
June	204-371
July	105-147
August	58-78
September	95-156
October	176-235
November	108-157
December	51-82
Average R (MJ mm ha/h/year)	373 - 230

3.2.3. Soil Erodibility factors (K)

Soil Erodibility (K) is the measure of the soil's resistance to detachment and transport. Different soil types have varying resistance and susceptibility to erosion. These are expressed as a function of their particle size, drainage potential, structural integrity, organic content, cohesiveness and structural integrity (Prasannakumar et al., 2011; Boakye et al., 2020). The soil data used was downloaded from (https://data.isric.org) website. With regard to the soil codes and soil types available in the study area, the soil has been classified into five major categories. Fine textured soils with high clay content are resistant to detachment, thereby a low K factors ranging from 0.05 to 0.15. Coarse textured soils such as sandy soils also have K values from 0.05 to 0.2 because of high infiltration resulting in low run off even though these particles are easily detached. Medium textured soils, such as silt loam have moderate K values (about 0.25) because they are moderately susceptible to particle detachment and they produce run off at moderate rates. Soils with high silt content have a high susceptibility to erosion and hence it's associated high K values, ranging from 0.25 to 0.4; thus, an average value of 0.325 is considered. Soils experiencing extreme detachment were assigned a K value of 0.4 (Khare et al., 2016; Kouli et al., 2008). Also, the different soil layers were aggregated over the standard depth interval of 0 to 30 cm depth by taking a weighted average using trapezoidal rule represented by Equation (4) (Yang et al., 2018). The trapezoidal rule considers an experimented pH values at different mosaic soil depths. Soil depths of 0 to 30 cm with soil pH values at the first four standard depths equal to 4.5, 5.0, 5.3 and 5.0. The soil map was prepared in the ArcGIS environment using the soil codes and its associated characteristics represented by Figure 4a and tabulated in Table 2 (Khare et al., 2016) respectively. The Final K factor map considering 0 to 30 cm depth using the trapezoidal rule was also generated in the ArcGIS environment as shown by Figure 4b.

$$\frac{1}{b-a}\int_a^b f(x)dx \approx \frac{1}{(b-a)}\frac{1}{2}\sum_{k=1}^{N-1}(x_{k+1}-x_k)(f(x_k))+f((x_{k+1})) \qquad (4)$$

where; N is the number of depths; x_k is the k-th depth; $f(x_k)$ is the value of target variable (that is, soil property at depth, x_k ; a,b refers to the standard depth intervals

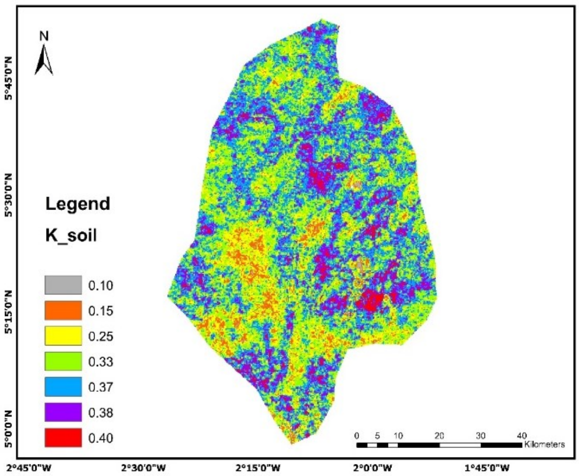

Figure 4a. K Soil Map Classification

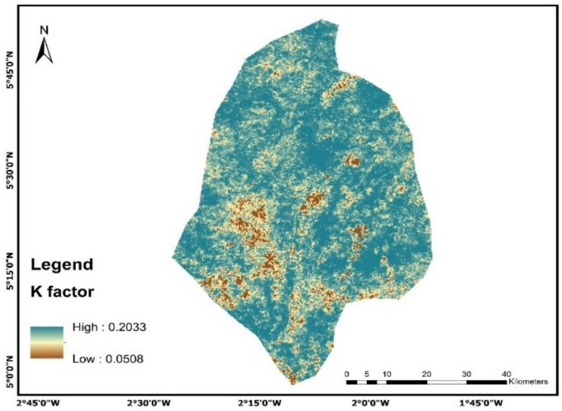

Figure 4b. K factor Map

.

Table 2. Soil erodibility factor for different types of soil at Ankobra Basin

Soil codes	Soil types	K_K	Erosion rate
1,2,38,39,43,44,47	Fine textured soils (high clay content)	0.05 - 0.15	Slight erosion
8,12,14,15,18,19,20,27,28,29,30,32, 33,35,36,37,40,41,42,45,46	Coarse textured soils (sandy soils)	0.05 - 0.2	Moderate erosion
7,10,11,13,21,23,24,25,26,34	Medium textured soils (silt loam)	0.25	Severe erosion
3,4,5,6,16,17,22,31	Soils with high silt content	0.25 - 0.4	Very severe erosion
9,48,49	Soils with severe soil erosion	0.4	Extremely severe erosion

3.2.4. Slope Length and Steepness factor (LS)

The L and S factors used in RUSLE portrays the effects of topography on soil erosion. It has been found that higher overland flow velocities and erosion results from increasing slope length and slope steepness (Kouli et al., 2008). Slope steepness has a higher influence in gross soil loss than changes in slope length (McCool et al., 1987). Slope length has been described as the distance from the point of origin of overland flow to the point where either the slope gradient decreases enough where deposition begins or the flow is concentrated in a defined channel (Wischmeier and Smith, 1978). The influence of topography on soil erosion are known by the LS factor which is a product of the slope length (L) and slope steepness (S) converging onto a required point such as a cell on a GIS raster surface (Kouli et al., 2008). The Digital Elevation Model (DEM) of the study area was used as input data for the LS computation using the ArcGIS Spatial Analyst tool and Arc hydro extension according to Equation (5) as proposed by Moore and Burch (1986). The DEM was downloaded from the usgs website (https://lpdaac.usgs.gov/products/astgtmv003/).

$$LS = (Flow\ accumulation\ \times cell\ size/22.13)^{0.4} \times (\sin slope/0.0896)^{1.3} \quad (5)$$

where; Flow accumulation denotes the accumulated upslope contributing area for a given cell; LS is the combined slope length and slope steepness factor; cell size is the size of the grid cell (30m was used for this studies) and sin slope is the slope degree value in sin. The LS factor map is represented by Figure 5, which value ranges from 2685.58 to 0, with a mean and standard deviation of 12.777 and 81.178 respectively.

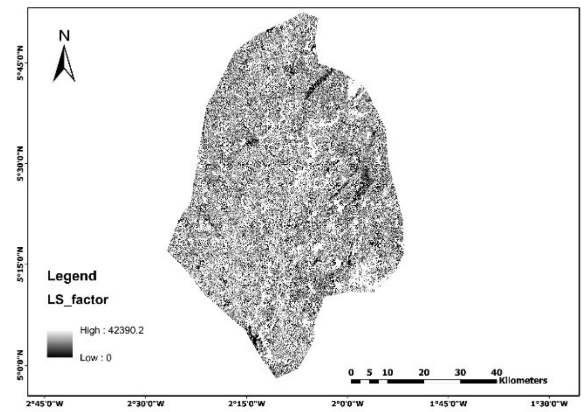

Figure 5. LS factor map

3.2.5. Cover management (C)

The C factor represents the effect of soil disturbing activities, plants, crop sequence and productivity level, soil cover and subsurface bio-mass on soil erosion. It is defined as the ratio of soil loss from land cropped under specific conditions to the corresponding loss from clean-tilled, continuous fallow (Prasannakumar et al., 2011; Boakye et al., 2020). The C factor map was generated from the Land use and Land cover (LULC) map represented by Figure 6a. The LULC data was obtained from MODIS satellite imagery data (https://earthexplorer.usgs.gov) and classified using the IGBP classification scheme (https://yceo.yale.edu/modis-land-cover-product-mcd12q/). The LULC comprises of six classes namely; Grassland, Dense Forest, Urban and Built up area, Barren/Sparsely vegetated, Cropland and water. The Normalized Difference Vegetation Index (NDVI) indicates the vegetation vigor and health used to generate the C factor value map of the study area represented by Equation (6) (Kouli et al., 2008).

$$C = \exp\left[-\alpha \frac{NDVI}{(\beta - NDVI)}\right] \quad (6)$$

where; α and β are unitless parameters that determine the shape of the curve relating to NDVI and the C factor map. The scaling approach represented in Equation (6) gives better outcomes rather than assuming a linear relationship (Van der Knijff et al., 2000). The parameters α and β were assigned values 2 and 1 respectively. The C factor was then generated from Equation (6) in the ArcGIS environment. The C factor value varies from 0.5460 to 0.074 as shown by Figure 6b.

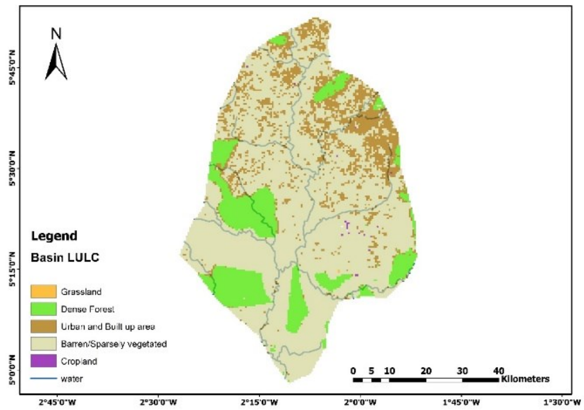

Figure 6a. Land Use Land Cover Map

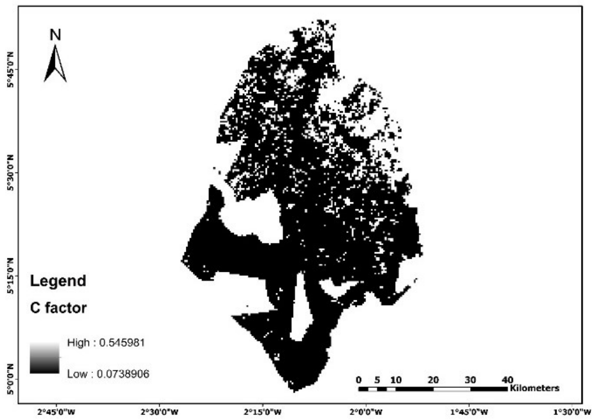

Figure 6b. Cover Management Factor

3.2.6. Conservation Practice factor (P)

The support practice factor (P factor) is the soil loss ratio with a specific support practice such as terraces, contouring, strip-cropping and contour furrows to the corresponding soil loss with up and down slope tillage (Boakye et al., 2020). In the present study, the P factor map was generated from the LULC data. The values of P factor range from 0 to 1, in which the highest value is assigned to areas with no conservation practices (dense forest) (Prasannakumar et al., 2011). The minimum value corresponds to built-up land and plantation area with strip and contour cropping. The lower the P value, the more effective the conservation practices.

3.2.7. Sediment Yield and Sediment Delivery Ratio

Considering L_i to be the measure of the soil loss created inside the i_{th} cell of the basin, then the sediment yield of the cell can be expressed according to Equation 7 (Jain et al., 2000):

$$SE = L_i * SDR_i \tag{7}$$

where; SE is the sediment yield; SDR_i is the sediment delivery ratio. SDR_i enables us to determine the gross soil loss from the i_{th} cell that really reaches a stream system, given as a component of movement time (Boakye et al., 2020; Ferro et al., 1995).

$$SDR_i = \exp(-\delta t_i) \tag{8}$$

where t_i is travel time (h) for cell i and δ is basin specific parameter. The movement time, t_i for every cell along a stream path can be expressed as (Jain et al., 2000);

$$t_i = \sum_{i=1}^{y} \frac{l_i}{v_i} \tag{9}$$

l_i is the length of fragment (flow length) in the stream way and is equivalent to the length of the side or askew relying upon the stream heading in the cell, and v_i is the stream speed for the cell (m/s). The flow length, l_i was formed from the DEM of the basin. The flow velocity, v_i depicts the land surface slope and the land cover characteristics (Mbugua, 2009).

$$v_i = c_i \sqrt{s_i} \tag{10}$$

where; s_i is the slope of the i cell and c_i is the coefficient dependent on the LULC. Substituting (10) and (9) into (8) gives;

$$SDR_i = \exp\left(-\delta \sum_{i=1}^{y} \frac{l_i}{c_i\sqrt{s_i}}\right) \tag{11}$$

The LULC coefficients can be found in Table 3, the basin specific parameter, δ describes the morphology of the basin. The basin specific parameter δ, was assigned a value of 1 due to the insensitivity of the sediment yield to the basin (Kusimi et al., 2015).

3.2.8. Sediment Transport Capacity (Grid Basis)

The Sediment Transport Capacity solves the problem of deposition of huge amount of sediment at the flow convergent point which frequently occurred in the hilly catchment (Verstraeten et al., 2007). It is compared to the sediment load to determine whether detachment or deposition is occurring (Finkner et al., 1989). It can be expressed according to Equation 12 as:

$$T_{ci} = K_{TCi} \times R \times K_i \times A_{si}^{1.44} \times S_i^{1.44} \tag{12}$$

where; T_{ci} is the sediment transport capacity (kg/m^2/year); K_{TCi} is the transport capacity coefficient in cell i, which reflects the vegetative coefficient within the transport capacity; K_i is the soil erodibility factor in cell i (t ha MJ^{-1}mm^{-1}); A_{si} is the upstream contributing area; S_i is the slope of the i_{th} cell. The calibration range for K_{TCi} as given by Verstraeten et al., 2007 is (0.00001 to 0.0002). A_{si} which is the specific area at cell i is expressed in Equation (13) given by Moore and Wilson, 1992;

$$A_{si} = \left(\frac{A_{up}}{W_n}\right) \tag{13}$$

where; A_{up} is the upslope contributing area for overland grid; W_n is the unit width normal to flow direction.

4. Results and discussion

The paper aims at using the grid base method of RUSLE to study and prepare the annual soil erosion maps, sediment yield and the sediment transport capacity of the Ankobra river basin. The annual mean rainfall map (2012 to 2018) ranges from 1614.61mm to 836.12mm represented in Figure 3a. It has a mean of 1200 mm and a standard deviation of 197.653 mm. The R factor map in Figure 3b was generated from the annual mean rainfall using the modified Fournier Index (MFI) expressed in Equation (2). The Rainfall erosivity factor (R) ranges from 373 MJ mm ha/h/year to 230 MJ mm ha/h/year with a mean and standard deviation of 297 MJ mm ha/h/year and 36.307 MJ mm ha/h/year respectively. The MFI also ranges from 85.432 to 134.052, which implies the basin is prone to severe downpour (Boakye et al., 2020). The soil map was prepared based on the standard soil codes as reported in the work of Khare et al., (2016). The Kk values of the soil map of the basin ranges from 0.10 to 0.40 according to Figure 4a. The respective soil codes, soil types, Kk values and erosion rates are as tabulated in Table 2. Kk values ranging from 0.05 to 0.15 recorded slight erosion rates whereas those from 0.25 to 0.4 were noted for severe erosion rates. From Figure 4a, the level of severity of the rate of soil erosion falls in the range of 0.15 to 0.4 but higher Kk values were skewed to the eastern side of the basin. From Figure 4b, the final soil erodibility (K) factor map was generated considering the trapezoidal formula using depths ranging from 0 to 30 cm as expressed in Equation (4). The trapezoidal rule also considers the pH values at various depths of the soil for a more accurate result. The K factor ranges from 0.2033 t ha MJ^{-1}mm^{-1} to 0.0508 t ha MJ^{-1}mm^{-1} with a mean and standard deviation of 0.168 t ha MJ^{-1}mm^{-1} and 0.030 t ha MJ^{-1}mm^{-1} respectively. The K factor range implies the general rate of soil erosion in the basin lies in the moderate zone. The slope length and steepness (LS) factor is represented in Figure 5. The LS factor was prepared from the basin DEM using ArcGIS spatial analyst extension where both flow length and flow accumulation was computed and inserted into Equation (5). The range of the LS factor was from 0 to 2685.58 with a mean of 12.777 and a standard deviation of 81.178. High elevation areas such as Beposo, Eshrieso, Wassa Bekwai, Hiawa and Juabeng showed recorded higher LS values, where as plain areas such as Teberebe, Bogoso, Nsuta and Tarkwa recorded lower LS values. The Land use and Land cover map were grouped into six (6) major classes as represented in Figure 6a namely; Grassland, Dense forest, Urban and Built-up areas, Barren/Sparsely vegetated, Cropland and water having percentage area coverages of 0.016%, 14.74%, 16.0%, 69.28%, 0.11% and 0.32% respectively. The LULC was used in the generation of the NDVI map in the ArcGIS environment and was factored in Equation (6) for the preparation of the Cover Management factor (C). The *C* factor ranges from 0.075 to 0.545 according to Figure 6b. It has a mean of 0.07 and a standard deviation of 0.018. High C factor values was recorded for the dense forest, grasslands and water whereas Low *C* values were associated with urban and built up areas, barren/sparsely vegetated and croplands. This was so because high cover management (C factor) are associated with places with low vegetative cover because of the high rate of detachment or deposition by rainfall compared to areas with good vegetative cover with a higher degree of resistance to soil deposition. The tabulation of the various classes of the land use and land cover, their area coverages and coefficients, C_i are represented in Table 3. The coefficients of the LULC were given by Kusimi *et al*., (2015). From Figure 7, The Support practice (P) factor ranges from 0 to 1 with a mean of 0.155 and a standard deviation of 0.363 respectively. It describes practices that enhances or minimizes soil loss in the basin (Boakye *et al*., 2020). High *P* values are mostly assigned to areas with no conservation practices (strip cropping, terraces, contouring) such as water urban and built up areas and Forest covers whiles low *P* values.

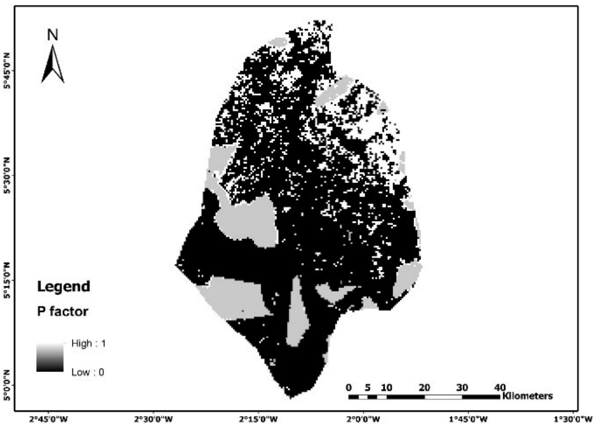

Figure 7. Support Practice Factor

The potential yearly soil loss is estimated from the product of factors (R, K, LS, C and P) representing the geo-environmental scenario of the basin in a spatial context. From Figure 8, the estimated annual soil loss ranges from 0 to 4650 tons/ha/yr with a mean of 24.64 tons/ha/yr and a standard deviation of 14.07 tons/ha/yr. The results were correlated and compared with similar studies, area having similar geo-environmental and rainfall characteristics (Boakye *et al*., 2020; Kusimi *et al*.,2015; Mensah *et al*.,2015; Mbugua, 2009) for validation purpose of proposed method in the study area. They were found to be comparable with an annual average soil erosion rate of 0 to 9000 tons/ha/yr. The grouping of the different soil erosion severity zones was carried out considering field conditions. The soil erosion prone zones were classified into four (4) types namely; low, moderate, severe and very severe erosion zones as tabulated in Table 4. The range implies 69 % of the basin experiences low erosion, 30.86 % constitutes moderate to severe erosion rates whereas very severe zones form 0.02 % of the total area of the basin. The spatial pattern of classified soil erosion risk zones indicates areas with low to moderate erosion risks are uniformly distributed in the basin whereas those with severe to very severe erosion risks are dominant at the south and west areas of the basin. Towns found at the low to moderate erosion risk zones comprises of Aboso, Fureso, Bopieso, Ashiaem, Nsuta, Beposo, Eshireso and Menhyia. Most towns located in the severe to very severe erosion risk zones were noted for illegal gold mining, alluvial mining and sand winning. They include Bogoso, Prestea, Tarkwa, Kwasikrom, Akyempim, Asonti, Bonsa, Techiman and Hiawa. The Sediment delivery ratio (SDR) ranges from 0 to 1. It describes the fraction of eroded sediments delivered to the point of question (Boakye *et al*., 2020). The SDR values were low except those at the high elevation zones where the rivers take their source. The rivers exhibited relatively higher SDR values. This implies erosion occurring in the urban and built up areas, grassland, barren and sparsely vegetated areas are entrained into the river channels and transported downstream.

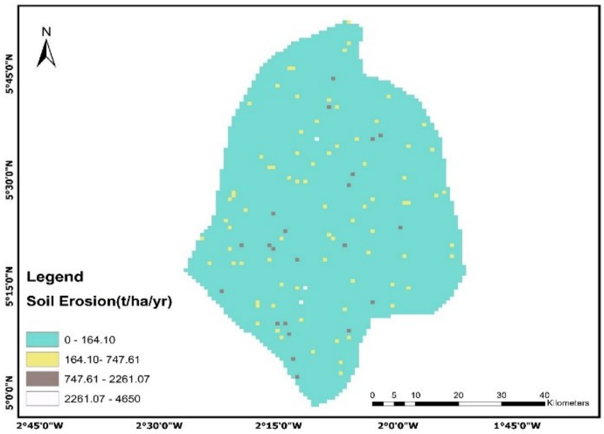

Figure 8. Annual Soil Erosion

Table 3. LULC classes, Area Coverage and coefficients

LULC classes	Area(hectares)	Percentage (%)	Coefficient, c_i
Grassland	63.9	0.016	0.4572
Dense forest	58300.7	14.74	0.7600
Urban and Built up areas	61407.9	16.0	6.3398

Barren and Sparsely vegetated	273920	69.28	0.4572
Cropland	426	0.11	0.4572
Water	1280.6	0.32	0.1250

Table 4. Annual Soil Erosion Severity zones

Erosion risk range (t/ha/yr)	Severity Class	Area (%)
0-164.10	Low	69%
164.10-747.61	Moderate	15.47%
747.61-2261.07	Severe	15.39%
2261.07-4650	Very Severe	0.02%

The Sediment Yield of the basin ranges from 0 to 448.936 tons/ha/yr as represented in Figure 9b. The mean and standard deviation was 2.13 tons/ha/yr and 11.8 tons/ha/yr respectively. Even though, the mean was relatively lower than that of the African catchment of 4.93 tons/ha/yr (Vanmaercke *et al.*, 2014), the situation continues to worsen year after year due to excessive illegal mining, alluvial mining and sand winning in the Ankobra basin. From Figure 10, The Transport capacity ranges from 0 to 601.38 kg/m^2/yr with a mean of 3.6 kg/m^2/yr and a standard deviation of 11.5 kg/m^2/yr. It was observed that the transport capacity values was even higher for areas with low slope gradient as observed in areas with low LS factors that carry sediment from steep slopes due to the incorporation of the upslope contributing area (A_{up}). The Transport capacity map was overlaid with the sediment delivery map to study areas where deposition and detachment is occurring. It was observed that sediments were transported from high elevation areas to plain areas which recorded high mean sediment yield values. Some plain areas also recorded an appreciable amount of soil loss due to the excessive illegal mining activities occurring in such areas such as Tarkwa, Bogoso, Prestea, Akyempim and Bonsa. Also, in order to assess the role of human intervention at the basin, the Land use land cover (LULC) map was overlaid with the annual soil loss and sediment yield map to study the situation of soil loss and sediment yield at the different land cover types. It was found that the annual soil loss in the basin occurred in the following decreasing order based on the respective means of the classes of the annual soil erosion; Barren/sparsely vegetated, urban and built up areas, cropland, forest and water. The sediment yield was also classified into six (6) groups, their respective means was used as a basis for the generation of the highest to lowest order of land cover types with respect to high sediment deposits; water, grassland, urban and built up areas, cropland, forest and barren/sparsely vegetated. It was observed that areas experiencing high detachment or soil loss recorded low sediment deposition or yield. Barren/sparsely vegetated areas recorded the highest annual soil loss with a mean of 9.7 whiles water recorded the highest sediment yield with a mean of 10.7. This offered a good knowledge for the right support practice management to be delivered. The results of the annual soil loss, sediment yield, support practice factor (P), mean and area are represented in Table 5.

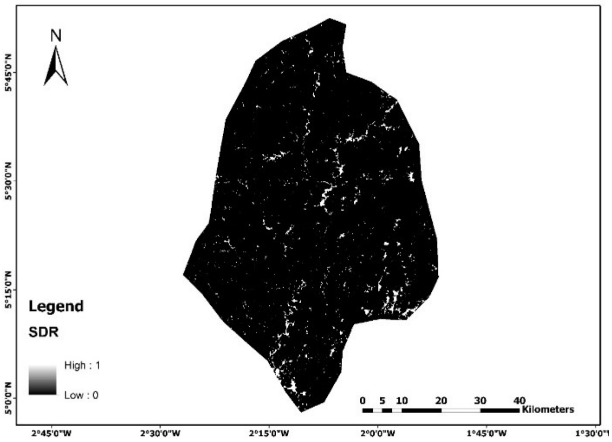

Figure 9a. Sediment Delivery ratio

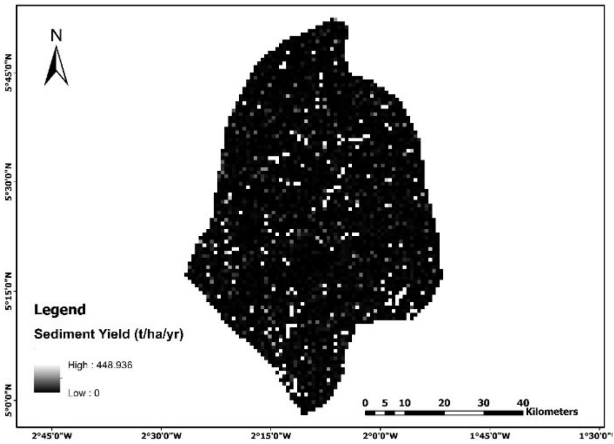

Figure 9b. Sediment Yield

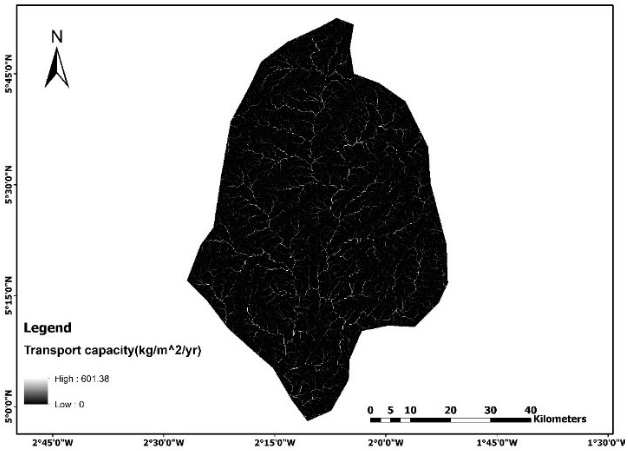

Figure 10. Transport capacity

Table 5. The results of the annual loss, sediment yield, support practice factor (P), mean and area

LULC	Erosion(t/ha/yr)	Mean(t/ha/yr)	Area (%)	Sediment Yield(t/ha/yr)	Mean(t/ha/yr)	Area (%)	P values
Barren	0 - 72.93	9.7	69	0 - 3.52	2.5	69.84	0.33
Water	72.93 - 328.22	1.7	15.47	3.52 - 19.40	10.7	15.22	0
Cropland	328.22 - 747.61	5.3	14.89	19.40 -54.57	4.6	14.47	0.5
Grassland	747.61-1258.17	6.4	0.4	54.57 - 107.40	8.5	0.18	0.7
Urban	1258.17 -2261.07	7.5	0.1	107.40 - 227.11	6.3	0.17	0.8
Forest	2261.07 - 4650	4.8	0.02	227.11-448.94	3.6	0.10	1

5. Conclusions and recommendations

Soil erosion is a major problem in lower basin of Rivers found in Ghana for several decades. Existing studies reveal several methodologies for gathering representative data required for the RUSLE and determines its expediency for envisaging soil loss and soil management planning. The fore told extent of soil loss and its geographical allocation can deliver a basis for wide spread conservation and ecological land use for the basin. The areas with severe soil erosion permit distinctive precedence for the execution of control. Methodology followed in this study would aid enrich fragmentation of erosion patches, and finally lessening or resolve the soil erosion problem. Conversely, a more precise on ground data could be prerequisite in comprehensive studies directing at the assessment of dissimilar extenuation measures and assessment of various management circumstances under concrete and upcoming land use and predictable climate change. The present study aimed to quantitatively distribute soil erosion and sediment in Ankobra River Basin utilizing (RUSLE and SDD) models in a GIS environment considering various causative geo-environmental variables such as Precipitation data, Digital Elevation Models, Soil data, Land use and Land cover by simulating the available data with remote sensing images in a GIS environment. Approximately 15.41 % of the river basin was observed to be under severe and very severe erosion rates, while about 69 % of the basin is very low to low prone to erosion risk. The lower basin is relatively big and characterized by spatial heterogeneity of erosion factors. In regards to the achieved results in this study, the capabilities of RUSLE and SDD models together with geospatial technology is of highly significance for a primary mapping of soil erosion rate. The study revealed that nearly, the area is having steep slope and high intensity rainfall patterns, which have a positive impact on erosion rates. The model estimated annual soil loss of 4650 tons/ha/year in the basin. High soil erosion occurs mostly in the farmlands, mining and settlement areas. An average of 448.936 tons/ha/year of sediment yield was also predicted by the model. Most of the sediments eroded from the catchment area entrained into the rivers and streams causing siltation and pollution. Areas characterized with severe to very severe soil loss should be given special and immediate conservation priority to reduce or control the rate of soil erosion whilst low to moderate prone areas should be protected from further erosion. The predicted amount of soil loss and sediment yield could facilitate comprehensive and sustainable land management through conservation planning for the watershed. Areas characterized by high to very high soil loss should be given special priority to reduce or control the rate of soil erosion by means of conservation planning. The study demonstrates that the RUSLE together with GIS and RS provides great advantage to estimate soil loss rate over areas though the input parameter values need to be calibrated to the specific area.

However, other models such as generalized regression neural network, fuzzy logics, adaptive neuro-fuzzy inference system, Gaussian process regression, decision trees, population-based evolutionary algorithms, invasive weed optimization, differential evolution, firefly, bees algorithms, elephant herding, optimization evolutionary techniques, least squares support vector machine, kernel ridge regression, simple addictive weighting, bivariate statistics, statistical index, weighted linear combinations, certainty factor, multivariate regression, discriminant analysis, genetic algorithm, generalized addictive model, Bayesian logistic regression, evidential belief functions, alternating decision trees, functional trees, kernel logistic regression, quadratic discriminate analysis, generalized linear model, gradient boosting machine, flexible discriminant analysis, generalized logistics models, boosted regression trees, probability density-index of entropy, frequency ratio-index of entropy, binary logistic regression, multivariate logistic model, stochastic gradient descent, Bayes network, functional algorithm, ABSGD model, decision trees, sequential minimal optimization, cascade generalization optimization, ant colony optimization, differential evolution algorithm, flexible discriminant analysis, and league championship optimization, that were not considered are recommended for future studies within the study area

Acknowledgements
Our sincere appreciation goes to the Survey and Mapping Division of Lands Commission and Geological Survey Department of Ghana for providing us with the necessary data used in the investigation of the research findings.

References

Abroampah P. M., E. Boakye and P.P.K.Yalley (2014). The Impact of Sofokrom Quarry on River Anankwari, International Journal of Science and Research (IJSR), 4(11), 1057-1062.

Adjei P. O. W., D. Buor and P. Addrah (2014). Geo-Spatial Analysis of Land Use and Land Cover Changes in the Lake Bosomtwe Basin of Ghana, Ghana Journal of Geography, 6, 1-23.

Aduah M.S, G.P.W. Jewitt and M.L.W. Toucher (2020). Estimating Scenario-Based Impacts of Climate and Land Use Changes on Potential River Ecology of a Rainforest Catchment in Ghana, West Africa, Ghana Journal of Technology, 4(2), 43 - 56.

Aduah M.S, G.P.W. Jewitt and M.L.W. Toucher. (2017). Assessing Suitability of the ACRU Hydrological Model in a Rainforest Catchment in Ghana, West Africa Water Science, 31, 198-214.

Aduah M.S, G.P.W. Jewitt and M.L.W. Toucher (2018a). Assessing Impacts of Land Use Changes on the Hydrology of a Lowland Rainforest Catchment in Ghana, West Africa, Water, 10(9), 1-15.

Aduah M. S., M.L.W. Toucher and G.P.W. Jewitt (2018b). Estimating Potential Future (2030 and 2040) Land Use in the Bonsa Catchment, Ghana, West Africa, South African Journal of Geomatics, 7(3), 279-291.

Aduah M. S., M.L. Warburton and G.P.W. Jewitt (2015). Analysis of Land Cover Changes in the Bonsa Catchment, Ankobra Basin, Ghana, Applied Ecology and Environmental Research, 13 (4), 935-955.

Akrasi S. A., and O.D. Ansa-Asare (2008). Assessing Sediment and Nutrient Transport in the Pra Basin of Ghana, West African Journal of Applied Ecology, 13(1), 45-54.

Alatorre L. C., S. Begueria, N. Lana-Renault, A. Navas, and J.M. Garcia-Ruiz (2012). Soil Erosion and Sediment Delivery in a Mountain Catchment Under Scenarios of Land Use Change Using a Spatial Distributed Numerical Model, Hydrology and Earth System Sciences, 16, 1321-1334.

Alexandridis T.K., A.M. Sotiropoulou, G. Bilas, N. Karapetsas and N.G. Silleos (2015). The Effects of Seasonality in Estimating the C-Factor of Soil Erosion Studies. L. Degrad. Dev. 2015, 26, 596–603.

Almajed A., K. Lemboye, M.G. Arab and A. Alnuaim (2020). Mitigating Wind Erosion of Sand Using Biopolymer-Assisted EICP Technique, Soils and Foundation, (Article in Press), xxx(xxxx)xxx, 1-16.

Amah J. I., O.P. Aghamelu, O.V. Omonona and I.M. Onwe (2020). A Study of the Dynamics of Soil Erosion Using RUSLE2 Modelling and Geospatial Tool in Edda-Afikpo Mesas, South Eastern Nigeria, Pakistan Journal of Geology (PJG), 4(2), 56-71.

Amisigo B. A., F.Y. Logah, E. Obuobie and K. Kankam-Yeboah (2018). Impacts of Climate Change on Stream Inflows into the Volta Lake, Ghana Journal of Science, 58, 23-33.

An J., F. Zheng and B. Wang (2014). Using Cs Technique to Investigative the Spatial Distribution of Erosion and Deposition Regimes for a Small Catchment in the Black Soil Region, Northeast China, Catena, 123, 243-251.

Arabameri A., W. Chen, L. Lombardo, T. Blaschke and D.T. Bui (2020b). Hybrid Computational Intelligence Models for Improvement of Gully Erosion Assessment, Remote Sensing, 12(140), 1-25.

Arabameri A., O.A. Nalivan, S. Saha, J. Roy, B. Pradhan, J.P. Tiefenbacher and P.T.T. Ngo (2020a). Novel Ensemble Approaches of Machine Learning Techniques in Modelling the Gully Erosion Susceptibility, Remote Sensing, 12(1890), 1-30.

Arabameri A., S. Saha, J. Roy, J.P. Tiefenbacher, A. Cerda, T. Biggs, P. Biswajeet, P.T.T. Ngo and A.L. Collins (2020c). A Novel Ensemble Computational Intelligence Approach for the Spatial Prediction of Land Subsidence Susceptibility, Science of the Environment, 726(138595), 1-18.

Asante-Annor A., S.A. Konadu, and E. Ansah (2018). Determination of Potential Landfill Site in Tarkwa Area Using Multi-Criteria GIS, Geophysical and Geotechnical Evaluation, Journal of Geoscience and Environment Protection, 6, 1-27.

Avand M., S. Janizadeh, S.A. Naghibi, H.R. Pourghasemi, S.K. Bozchaloei and T. Blaschke (2019). A Comparative Assessment of Random Forest and K-Nearest Neighbor Classifiers for Gully Erosion Susceptibility Mapping, Water, 11(2076), 1-19.

Ayalew G. (2014). A Geographic Information System Based Soil Loss and Sediment Estimation in Gerli Watershed, Highlands of Ethiopia, Journal of Environment and Earth Science, 4(9), 62-74.

Ayivor J. S. and C. Gordon (2012). Impact of Land Use on River Systems in Ghana, West African Journal of Applied Ecology, 20(3), 83-95.

Bam E. K. P., A.M. Akumah and S. Bansah (2020). Geochemical and Chemometric Analysis of Soils from a Data Scare River Catchment in West Africa, Environmental Research Communications, 2(035001), 1-19.

Basri E. M., O.M. Adam, S.Y. The and W.O.W. Maznah (2019). Identification of Critical Erosion Prone Areas in Temengor Reservoir Basin Using Universal Soil Loss Equation (USLE) and Geographic Information System

(GIS), Conference Series: Earth and Environmental Science, 380(012011), 1-14.

Boakye, E., G.K. Anornu, J.A. Quaye-Ballard and E.A. Donkor (2018). Land Use Change and Sediment Yield Studies in Ghana: Review, Journal of Geography and Regional Planning, 11(9), 122-133.

Boakye E., F.O.K. Anyemedu, E.A. Donkor and J.A. Quaye-Ballard (2020). Spatial Distribution of Soil Erosion and Sediment Yield in the Pra River Basin, Springer Nature Applied Sciences, 2(320), 1-12.

Boufeldja S., K.B. Hamid, A. Bouanani and A. Belkendil (2020). Identification of Zones at Risk of Erosion by the Combination of a Digital Model and the Method of Multi-Criteria Analysis in the Arid Regions: Case of the Bechar Wadi Watershed, Applied Water Science, 10(121), 1-18.

Boye C. B., I. Boateng, A.K. Appeaning and G. Wiafe (2019). An Assessment of the Contribution of Fluvial Sediment Discharge to Coastal Stability: A Case Study of Western Region of Ghana, African Journal of Environmental Science and Technology, 13(5), 191-200.

Boye C. B., M.S. Peprah, and N.K. Kodie (2018). Geographic Assessment of Telecommunication Signals in a Mining Community: A Case Study of Tarkwa and Its Environs, Ghana Journal of Technology, 2 (2), 41-49.

Chalise D., and L. Kumar (2020). Land Use Change Affects Water Erosion in the Nepal Himalayas, PLOS ONE, 15(4), 1-19.

Defersha M. B., A.M. Melesse and M.E. McClain (2012). Watershed Scale Application of WEPP and EROSION 3D Models for Assessment of Potential Sediment Source Areas and Runoff Flux in the Mara River Basin, Kenya, Catena, 95, 63-72.

Ferro V. and M. Minacapilli (1995). Sediment delivery processes at basin scale, Hydrology Science Journal 40:703-717, https://doi.org.110.1080/02626669509491460.

Finkner S.C., M.A. Nearing, G.R. Foster and J.E. Gilley (1989). A Simplified Equation for Modelling Sediment Transport Capacity, Biological Systems Engineering, Papers and Publications, 120, https://digitalcommons.un/.edu/biosysengfacpub//20.

Ganasri B.P., and H. Ramesh (2016) H. Assessment of soil erosion by RUSLE model using remote sensing and GIS – A case study of Nethravathi Basin. Geoscience Frontiers, 7, 953–961.

Goodrich D. C., I.S. Burns, C.L. Unkrich, D.J. Semmens, D.P. Guertin, M. Hernandez, S. Yatheendradas, J.R. Kennedy and L.R. Levick (2012). KINEROS2/AGWA: Model Use, Calibration, and Validation, American Society of Agricultural and Biological Engineers, 55(4), 1561-1574.

Hategekimana Y., M. Allan, Q. Meng, Y. Nie and M. Elhag (2020). Quantification of Soil Losses along the Coastal Protected Areas in Kenya. Land, 9(137), 1-17.

Jain M.K., U.C. Kothyari (2000). Estimation of soil erosion and sediment yield using GIS, Hydrology Science Journal, 45(5):771-786, https://doi.org/10.1080/02626660009492376.

Jiang T., Y. D. Chen, C. Xu, X. Chen, X. Chen, and V.P. Singh (2007). Comparison of hydrological impacts of climate change simulated by six hydrological models in the Dongjiang Basin, South China. Journal of Hydrology, 336, 316–333.

Joe-Asare T., M.S. Peprah and M.M. Opoku (2018). Assessment of the Potability of Underground Water from a Small-Scale Underground Mine: A Case Study, Ghana Mining Journal, 18 (2), 61-67.

Kalambukattu J. G. S. Kumar (2017). Modelling Soil Erosion Risk in a Mountainous Watershed of Mid-Himalaya by Integrating RUSLE Model with GIS, Eurasian Journal of Science, 6(2), 92-105.

Khare D., A. Mondal, S. Kundu and P.K. Mishra (2016). Climate change Impact on soil erosion in the Mandakini River Basin, North India, Applied Water Science, doi:10.1007/313201-016-0419-y.

Koirala P., S. Thakuri, S. Joshi and R. Chauhan (2019). Estimation of Soil Erosion in Nepal Using a RUSLE Modelling and Geospatial Tool, Geosciences, 9(147), 1-19.

Kouli M., P. Soupios and F. Vallianatos (2008). Soil Erosion prediction using the Revised Universal Soil Loss Equation (RUSLE) in a GIS framework, Chania, Northwestern crete, Greece, Environmental Geology, doi: 10.1007/s00254-008-1318-9.

Kuma J. S. and A. Ewusi (2009). Water Resources Issues in Tarkwa Municipality, Southwest Ghana, Ghana Mining Journal, 11, 37 - 46.

Kumi-Boateng B., M.S. Peprah and E.K. Larbi (2020). The Integration of Analytical Hierarchy Process (AHP), Fuzzy Analytical Hierarchy Process (FAHP), and Bayesian Belief Network (BBN) for Flood Prone Areas Identification – A Case Study of the Greater Accra Region, Ghana. Journal of Geomatics, 14(2), 100-122.

Kusi-Ampofo S., and T. Boachie-Yiadom (2012). Assessing the social and environmental impacts of illegal mining operations in River Bonsa, A research Report Commissioned by Pure Fm, Tarkwa and funded by the Business Sector Advocacy Challenge (BUSAC) fund, 1-48.

Kusimi J. M. (2008). Analysis of Sedimentation Rates in the Densu River Channel: The Result of Ersion and Anthropogenic Activities in the Densu Basin, West African Journal of Applied Ecology, 14, 1-14.

Kusimi J. M., G.A.B. Yiran, E.M. Attua (2015). Soil Erosion and Sediment Yield Modelling in the Pra Basin River Basin of Ghana Using the Revised Universal Soil Loss Equation, Ghana Journal of Geography, 7(2), 38-57.

Kwesi E. A. A, K.N. Asamoah, F.A. Arthur and J.A. Kwofie (2020). Mapping of Ground Water Vulnerability for Landfill Site Selection Assessment at the District Level – A Case Study at the Tarkwa Nsuaem Municipality of Ghana, Ghana Journal of Technology, 4 (2), 57 - 65.

Larbi E. K., C.B. Boye and M.S. Peprah (2018). A GIS Approach in Optimal Route Selection in the Mining Communities Using the Analytical Hierarchy Process and the Least Cost Path Analysis, 5th UMaT Biennial International Mining and Mineral Conference, Tarkwa, Ghana, GLM 50-62.

Lee G. H., K.H. Lee, K.S. Jung and C.L. Jang (2012). Analysis on the Effect of Spatial Distribution of Rainfall on Soil Erosion and Deposition, Journal of Korea Water Resources Association, 45(7), 657-674.

Lee G., W. Yu and K. Jung APIP (2013). Catchment-Scale Soil Erosion and Sediment Yield Simulation Using a Spatially Distributed Erosion Model, Environmental Earth Science, 70(1), 33-47.

Maqsoom A., B. Aslam, U. Hassan, Z.A. Kazmi, M. Sodangi, R.F. Tufail and D. Farooq (2020). Geospatial Assessment of Soil Erosion Intensity and Sediment Yield Using the Revised Universal Soil Loss Equation (RUSLE) Model, International Journal of Geo-Information, 9(356), 1-16.

Mbugua W. E. (2009). Using GIS techniques to determine RUSLE "R" and "LS" factors for Kapingazi River Catchment. Master of Science Research Project Report submitted to the Department of Geomatic Engineering and Geospatial Information Systems, Jomo Kenyatta University of Agriculture and Technology, pp 9-11.

McCool D. K., L.C. Brown and G.R. Foster, G.R. (1987). Revised Slope steepness factor for the Universal Soil Loss Equation, Trans Am Soc Agric Eng. 30:1387-1396.

Mensah A. M. (2009). The Influence of Land-Use Activities on Nutrients Inputs into Upland Catchment Streams, Ghana, Unpublished Dissertation, ULB Bonn, Bonn, Germany, 1-271.

Mensah J., O.A. Amoako and S. Kankam (2015). Ankobra River Estuarine Community climate Vulnerability Assessment, The USAID/Ghana sustainable Fisheries Management Project (SFMP). Narranganse tt, RI: Coastal Resources Center, Graduate school of oceanography, University of Rhode Island and Hen Mpoano. GH2014_ACT023_HM 70pp.

Mesfin Y. and S. Taddese (2019). Assessment of Soil Erosion and Land Use and Land Cover Change Using RUSLE Model, GIS, and Remote Sensing: A Case Study of Wombeya Watershed, Awash Basin, Ethiopia, International Journal of Current Research, 11 (07), 5730-5738.

Mirchooli F., A. Motevalli, H.R. Pourghasemi, M. Mohammadi, P. Bhattacharya, F.F. Maghsood and J.P. Tiefenbacher (2019). How do Data -Mining Models Consider Arsenic Contamination in Sediments and Variables Importance? Environmental Monitoring Assessment, 191(77), 1-19.

Moore I. and J.P. Wilson (1992). Length Slope Factor for the Revised Universal Soil Loss Equation: Simplified Method of Solution, Journal of Soil and Water Conservation, Vol.47, No.4, pp.423-428.

Moore I.D. and G.J. Burch (1986) Physical basis of the Length Slope factor in the Universal Soil Loss Equation, Soil Science Society of America, 50(5), 1294-1298.

Morgan R.P.C. (2005). Soil Erosion and Conservation, National Soil Resources Institute, Cransfield University, Oxford, https://doi.org/10.1002/9781118351475.ch22.

Nam P., D. Yang, S. Kanae, T. OKI and K. Musiake (2003). Global Soil Loss Estimate Using RUSLE Model: The Use of Global Spatial Datasets on Estimating Erosive Parameters. Geoinformatics, 14, 49–53.

Nhu V. H., S. Janizadeh, M. Avand, W. Chen, M. Farzin, E. Omidvar, A. Shirzadi, H. Shahabi, J.J. Clague, A. Jaafari, F. Mansoorypoor, B.T. Pham, B.B. Ahmad and S. Lee (2020). GIS-Based Gully Erosion Susceptibility Mapping: A Comparison of Computational Ensemble Data Mining Models, Applied Sciences, 10(2039), 1-29.

Orkhonselenge A., K. Kashiwaga and Y.K. Kim (2008). Intensity of Soil Erosion and Sedimentation Inferred from Spatial Distribution of Radionuclide ^{137}Cs in Hillslope Catchments, Soil Korea, Sediment Dynamics in Changing Environemnts, (Proceedings of a Symposium Held in Christ Church, New Zealand, December 2008), IAHS Publishing 325, 2008, 130-134.

Panagos P., C. Ballabio, P. Borrelli, K. Meusburger, A. Klik, S. Rousseva, M.P. Tadić, S. Michaelides, M. Hrabalíková and P. Olsen (2015a). Rainfall erosivity in Europe. Science of the Total Environment, 511, 801–814.

Panagos P.; P. Borrelli and K.A. Meusburger (2015b). New European Slope Length and Steepness Factor (LS-Factor) for Modeling Soil Erosion by Water. Geosciences, 5, 117–126.

Panagos P., P. Borrelli, K. Meusburger, C. Alewell, E. Lugato and L. Montanarella (2015c). Estimating the soil erosion cover-management factor at the European scale. Land use policy, 48, 38–50.

Panagos P., P. Borrelli, K. Meusburger, B. Yu, A. Klik, K.J. Lim, J.E. Yang, J. Ni, C. Miao, N. Chattopadhyay, S.H. Sadeghi, Z. Hazbavi, M. Zabihi, G.A. Larionov, S.F. Krasnov, A.V. Gorobets, Y. Levi, G. Erpul, C. Birkel, N. Hoyos, V. Naipal, P.T.S. Oliveira, C.A. Bonilla, M. Meddi, W. Nel, H. Al Dashti, M. Boni, N. Diodato, K. Van Oost, M. Nearing and C. Ballabio (2017). Global rainfall erosivity assessment based on high-temporal resolution rainfall records. Scientific Reports 7(4175), 1-12.

Panitharathine D. L. D., N.S. Abeysingha, K.G.S Nirmanee and A. Mallawatantri (2019). Application of Revised Universal Soil Loss Equation (RUSLE) Model to Assess Soil Erosion in "Kalu Ganga" River Basin in Sri Lanka, Applied and Environmental Soil Science, 2019, 1-15.

Pelacani S., M. Märker and G. Rodolfi (2008). Simulation of soil erosion and deposition in a changing land use: A modelling approach to implement the support practice factor. Geomorphology, 99, 329–340.

Peprah M. S. and I.O. Mensah (2017). Performance Evaluation of the Ordinary Least Square (OLS) and Total Least Square (TLS) in Adjusting Field Data: An Empirical

Study on a DGPS Data, South African Journal of Geomatics, 6 (1), 73-89.

Peprah M. S., Y.Y. Ziggah and I. Yakubu (2017), "Performance Evaluation of the Earth Gravitational Model (EGM2008) – A Case Study", South African Journal of Geomatics, 6(1), 47-72.

Pérez-Molina E., R. Sliuzas, J. Flacke and V. Jetten (2017). Developing a cellular automata model of urban growth to inform spatial policy for flood mitigation: A case study in Kampala, Uganda. Computers, Environment and Urban Systems, 65, 53–65.

Pourghasemi H. R., N. Kariminejad, M. Amiri, M. Edalat, M. Zarafshar, T. Blaschke and A. Cerda (2020). Assessing and Mapping Multi-Hazard Risk Susceptibility Using a Machine Learning Technique, Scientific Reports, 10(3203), 1-11.

Prasannakumar V., H. Vijith, S. Abinod and N. Geetha (2011). Estimation of soil erosion risk within a small mountainous sub-watershed in Kerala, India, using Revised Universal Soil Loss Equation (RUSLE) and geo-information technology, China University of Geosciences (Beijing), doi:10.1016/j.gsf.2011.11.003.

Prieto-Amparan J. A., A. Pinedo-Alvarez, G. Vazquez-Quintero, M.C. Valles-Aragon, A.E. Rascon-Ramos, M. Martinez-Salvador and F. Villarreal-Guerrero (2019). A Multivariate Geomorphometric Approach to Prioritize Erosion-Prone Watersheds, Sustainability, 11(540), 1-21.

Rajbanshi J. and S. Bhattacharya (2020). Assessment of Soil Erosion, Sediment Yield and Basin Specific Controlling Factors Using RUSLE-SDR and PLSR Approach in Konar River Basin, India, Journal of Hydrology, 587(124935), 1-17.

Raneesh K. Y., and G. Thampi (2011). A Study on the Impact of Climate Change on Streamflow at the Watershed Scale in the Humid Tropics, Hydrological Science Journal, 56(6), 946-965.

Reitsma K. D., B.H. Dunn, U. Mishra, S.A. T. DeSutter and D.E. Clay (2015). Land-use change impact on soil sustainability in a climate and vegetation transition zone. Agronomy Journal, 107, 2363–2372.

Rizalihadi A. M., B.E. Fatimah and C.L. Nazia (2013). The Influence of Rill Density on Soil Erosion against USLE-Soil Method, *Proceedings of the 7th International Conference on Asian and Pacific Coasts (ASPAC 2013),* Bali, Indonesia, September 24-26, 2013, 101-106.

Saavedra C. (2005). Estimating Spatial Patterns of Soil Erosion and Deposition in the Andean Region Using Geo-Information Techniques, A Case Study in Cochabamba, Bolivia, Unpublished PhD Dissertation, International Institute for Geo-Informational Science and Earth Observation, ITC, Enschede, The Netherlands, 1-265.

Sadhasivam N., A. Bhardwaj, H.R. Pourghasemi and N.P. Kamaraj (2020). Morphometric Attributes-Based Soil Erosion Susceptibility Mapping in Dnyanganga Watershed of India Using Individual and Ensemble Models, Environmental Earth Sciences, 79(360), 360-388.

Samanta R. K., G.S. Bhunia and P.K. Shit (2016). Spatial Modelling of Soil Erosion Susceptibility Mapping in Lower Basin of Subarnarekha River (India) Based on Geospatial Techniques, 2(99), 1-13.

Samlafo V. B. and E.O. Ofoe (2017). Water Quality Assessment of River Bonsa in Tarkwa, a Mining-Impacted Area of Ghana, Chemical Science International Journal, 20(4), 1-8.

Seidu J. and A. Ewusi (2018). Assessment of Groundwater Quality Using Hydrogeochemical Indices and Statistical Analysis in the Tarkwa Mining Area of Ghana, Journal of Environmental Hydrology, 26, 1-15.

Senanayake S., B. Pradhan, A. Huete and J. Brennan (2020). Assessing Soil Erosion Hazards Using Land-Use Change and Landslide Frequency Ratio Method: A Case Study of Sabaragamuwa Province, Sri Lanka, Remote Sensing, 12 (1483), 1-18.

Shoman M. M. (2019). Estimation of Soil Erosion in Some Wadis of the North Western Coast -Egypt Using RUSLE Model and GIS, International Journal of Advanced Research (IJAR), 7(5), 290-302.

Sihem J. (2009). Water Erosin Modelling Using Fractal Rainfall Disaggregation, A Study in Semiarid Tunisia, Unpublished PhD Dissertation, Department of Water Resources Engineering, Lund Institute of Technology, Lund University, Lund, Sweden, 1-147.

Smith H. J. (1999). Application of empirical soil loss models in southern Africa: A review. South African Journal Plant Soil, 16, 158–163.

Tairi A., A. Elmouden and M. Aboulouafa (2019). Soil Erosion Risk Mapping Using the Analytical Hierarchy Process (AHP) and Geographic Information System in the Tifnout-Askaoun Watershed, Southern Morocco, European Scientific Journal, 15(30), 338-356.

Tesfaye G., Y. Debebe and K. Fikirie (2018). Soil Erosion Risk Assessment Using GIS Based USLE Model for Soil and Water Conservation Planning in Somodo Watershed, South West Ethiopia, International Journal of Environmental & Agricultural Research (IJOEAR), 4(5), 35-43.

Tundu C., M.J. Tumbare and J.M.K. Onema (2018). Sedimentation and Its Impacts/Effects on River System and Reservoir Water Quality: Case Study of Mazowe Catchment, Zimbabwe, Proceedings of the International Association of Hydrological Sciences, 377, 57-66.

Van der Knijff J.M., R.J.A. Jones and L. Montanarella (2000). Soil Erosion Risk Assessment in Europe, EUR 19044 EN. Office for official Publications of the European Communities, Luxembourg, pp 34.

Vassilakis E., A. Tsokos and E. Kotsi (2016). Shoreline Change Detection and Coastal Erosion Monitoring Using Digital Processing of a Time Series of High Spatial Resolution Remote Sensing Data, Bulletin of the Geological Society of Greece, 50 (3), 1747-1755.

Verstraeten G., J. Poesen, J. De Vente and X. Koninckx (2003), Sediment Yield Variability in Spain: A quantitative and semi-qualitative analysis using reservoir rates, Geomorpholoy, 50, 327-348.

Vijith H. and D. Dodge-Wan (2019). Modelling Terrain Erosion Susceptibility of Logged and Regenerated Forested Region in Northern Borneo through the Analytical Hierarchy Process (AHP) and GIS Techniques, Geoenvironmental Disasters, 6 (8), 1-18.

Wischmeier W.H. and D.D. Smith (1978). Predicting rainfall erosion losses- A Guidance to conservation planning, Agriculture Handbook, No.537, US Department of Agriculture Science and Education Administration, Washington, DC, USA, 163pp.

Woldemariam G. W. and A.E. Harka (2020). Effect of Land Use and Land Cover Change on Soil Erosion in Erer Sub-Basin, Northeast Wabi Shebelle Basin, Ethiopia, Land, 9(111), 1-25.

Yang L., R. Zhao Z. Shi, A. Raphael, V. Rossel, D. Wan and Z. Liang (2018). Integrating multi-source data to improve water erosion mapping in Tibet, China, catena 169 (2018), 31-45, doi: https://doi.org/10.1016/j.catena.2018.05.021.

Yariyan P., M. Avand, R.A. Abbaspour, M. Karami and J.P. Tiefenbacher (2020). GIS-Based Spatial Modelling of Snow Avalanches Using Four Novel Ensemble Models, Science of the Total Environment, 745(141008), 1-51.

Zabihi M., F. Mirchooli, A. Motevalli, A. K. Darvishan, H.R. Pourghasemi, M. A. Zakeri and F. Sadighi (2018). Spatially Modelling of Gully Erosion in Mazandaran Province, Northen Iran, Catena, 168, 1-13.

An assessment of spatiotemporal changes in the command area of Krishnarajasagar project

M. Sushma, P. Srikanth,, P.P. Nageswara Rao* and D.K. Prabhuraj
Karnataka State Remote Sensing Applications Centre, Doora Samvedi Bhavana, Bengaluru-560097, India.
*Email: ppn1953@gmail.com

(Received: May 28, 2021; in final form: Sept 9, 2021)

Abstract: Irrigated croplands are the bread baskets of our country, but the mismanagement of the scarce water resources and wrong cropping patterns have threatened their sustainability. The present study demonstrates the role of remote sensing (RS) and geographic information system (GIS) in assessing the cropland under irrigation and rainfed condition including the changes in the cropping pattern in the command areas of the Krishnarajsagar (KRS) project. The study area covers a larger part of Mandya and a small part of Mysuru districts. RS data from satellite sensors namely, Thematic Mapper (TM) of Landsat-5, Operational Land Imager (OLI) of Landsat-8 and Linear Imaging Self-scanning System (LISS)-III onboard the RESOURCESAT-2 covering *Kharif, Rabi* and summer seasons of different years (1992-93, 1998-99, 2004-05, 2011-12 and 2019-20) were analyzed. The ground truth collected with global positioning system (GPS) during summer months 2015 and November 2019 and statistical reports of the Karnataka State Directorate of Economics and Statistics (DES) were used for training the algorithm and accuracy assessment. The ArcGIS version 10.1 and QGIS version 2.4 software have been used for spatial data preparation, processing, and generation of maps. Supervised classification of digital data was carried out using ERDAS Imagine. It was found that over the period of nearly 20 years (between 1992-2012); there was 8.64% increase in the irrigated cropland and 28.74% reduction in the rainfed crop area. The area under sugarcane crop has increased by 45.51% while that of paddy (rice) has reduced by 40.4%. However, during the period between 2011-12 and 2019-20, the study showed reduction in the area under both paddy (rice) and sugarcane crops making way for other crops.

Keywords: Irrigated cropland inventory, RESOURCESAT-2, LISS-III, OLI, NDVI, Cropping pattern changes.

1. Introduction

Irrigation is a major input for growing agricultural crops and ensures food security in most Asian countries. Irrigated agriculture continues to be the major contributor for increasing the food production to meet the calorie needs of the expanding population. In many large irrigated projects in India, there is huge scope for increasing the area under protective irrigation if appropriate crop rotation and water management practices are adopted. Irrigation induces changes in cropping patterns across space and time that may have implications on the economic returns to the farmers and environmental impact. Several command areas are experiencing waterlogging, salinity and alkalinity problems. The water use efficiency of canal irrigation systems is not as expected due to conveyance losses, lack of proper operation and maintenance, violation of approved cropping patterns, diversion of irrigated cropland to other purposes, etc. The concerned authorities are implementing several new programmes to improve the water use efficiency like the Accelerated Irrigation Benefits Programme (AIBP), Pradhan Mantri Krishi Sinchayi Yojana's 'Har Khet Ko Pani' etc. for improving the canal infrastructure, repair of feeder channels and rejuvenation of village tanks. Successful implementation of these programmes need more reliable and accurate system of assessment of the irrigation potential, created and utilized.

Several studies have been reported on the use of satellite RS technology for irrigated cropland inventory (Thiruvengadachari, 1981, Nageswara Rao and Mohan kumar, 1994) and system performance evaluation (Thiruvengadachari et al 1994, Thiruvengadachari and Sakthivadivel, 1997, Raju et al., 1997, Murthy et al., 1998, Saindranath et al., 2000, Ray et al., 2002, Panigrahy et al., 2005). Murthy et al. (2003) have used advanced algorithms for classifying irrigated crops. Multi-temporal optical and microwave data were used to identify multiple crops in irrigated agricultural system (Raju et al., 2008). Panigrahy et al. (2010) reported that the RS and GIS could be used for assessing the cropping patterns. The use of artificial neural networks for the classification of the Moderate-resolution Imaging Spectroradiometer (MODIS) gave an overall classification accuracy of 80.3% and kappa coefficient of 0.76. Dhumal et al. (2013) reported that RS is good source of information for decision making related to crop monitoring. Gumma et al. (2014) demonstrated that IRS-P6 LISS-III sensor having 23.6 metre (m) spatial resolution one-time data fusion with MODIS 250-m time series data is very useful for identifying crop type, the source of irrigation water and the way in which it is applied. Neetu et al. (2014) demonstrated the use of multi-date C-band synthetic aperture radar (SAR) data of RISAT-1 for rice crop classification, assessment of its growth pattern and spatial mapping of different cropping patterns.

An assessment of the dynamics of cropping patterns of Mandya district was reported by Ashwini and Kiresur (2017). They reported that "given the availability of irrigation water, the current cropping pattern with greater emphasis on paddy and sugarcane for commercial reasons and ragi for domestic consumption purposes, would be likely to continue in the near future". They recommended that the famers need to drift away from paddy so as to improve the soil health and economic returns. For this to happen, alternative profitable cropping systems need to be popularized in the area.

The objectives of the present study are i) to use the RS and GIS technologies to assess the spatial extent of irrigated and rainfed crop areas, ii) to identify the major crops within the irrigated cropland and iii) study the change in cropping patterns (proportion of area under different crops at different points of time) in the command area of KRS project.

2. Materials and methods

2.1. Study Area

The study area covers large parts of the KRS Command area (Figure 1), that includes substantial irrigated area in Mandya district and a fraction of irrigated area in Mysuru district. It is located between 12º13' and 13º04'N latitude and 76º19' and 77º20'E longitude. The main soil types are red loamy soils and red sandy soils. Major crops in Mandya district are sugarcane, paddy, ragi, mulberry and others. In the *taluks* of Mandya, Malavalli, Maddur and Nagamangala the soils are generally shallow and gravelly. These soils which are highly leached and poor in bases have a very low water-holding capacity. On the other hand, the soils under the old channel areas of Malavalli, Pandavapura and Srirangapattana are rich in clay, more fertile and suitable for raising irrigated crops. Some of the low lying areas have saline or alkaline patches that developed in the recent past, especially in T.Narasipura *taluk*. The soils are by and large deficient in nitrogen and phosphorous content and rich in iron content. The area is endowed with favourable climate all through the year. Temperature usually ranges from 15 to 35°C. Average annual rainfall in the area is around 695 millimetres distributed in about 45 rainy days, spread over a period of about 7 months from the second half of April to October.

The sowing period of major crops during *Kharif* season begins in 2nd week of July and ends by 2nd week of August. During *Rabi* season, the sowing period starts in the 3rd week of October and ends by 2nd week of November. Harvesting periods of the crops vary depending on their crop growth duration. Agro-climatological length of growing period in the study area is 120-150 days. Paddy and sugarcane are the important crops grown under irrigation during *Kharif* as well as *Rabi* / summer seasons. Ragi, Maize, Cowpea and Groundnut are grown as rain-fed crops during *Kharif* and to a small extent during *Rabi* season. However, Pigeon pea is grown during *Kharif* season only. Mandya district has sizable area under horticulture crops and a variety of fruits, vegetables and commercial flowers are grown. The district has 1,26,121 ha net irrigated area which accounts for 67 per cent of the net sown area., almost 51 percent canal irrigated and the remaining by minor-irrigation tanks, open and bore wells, etc.

2.2 Satellite data used

Satellite data acquired by LISS-III sensor onboard RESOURCESAT (RS)-2, (23.5 metre spatial resolution), covering *Kharif, Rabi* and summer season and TM and OLI sensors onboard Landsat-7 and Landsat-8 satellites (30 metre spatial resolution) were used for analysis. The digital numbers (DN) from each of these sensors were converted to top of atmosphere (TOA) reflectance using rescaling factors and parameters found in metadata file supplied with data. It is a two-step process: DN to radiance and radiance to TOA, the details of which are given in the user manuals. In addition, NDVI products of Moderate Resolution Imaging Spectroradiometer (MODIS) sensor onboard Terra satellite was used, which are atmospherically corrected, bi-directional surface reflectance, gridded 16-day composited 1-kilometre spatial resolution data. The sources and dates of RS data used in the study are given in table 1. In all 21 scenes of medium spatial resolution data were analysed.

Figure 1. Location of the study area

2.3 Ground truth

Ground truth was collected during September 2014 (Kharif) and February 2015 (Rabi), May 2015 (Summer) and November 2019 at several ground control points (GCPs). A smart phone camera with in-built global positioning system was used to take photographs mainly at the intersections of road, rail, canal and at many selected crop specific locations. These photographs were geo-tagged., indicating the latitude, longitude and time of photography. Ground truth of the past years (1993 to 2013) was collected through personal interviews of the farmers from many villages such as Budanoor, Chikkamandya, Pandavapura, Hanne Koppalu, Hosahalli etc. In addition, we consulted the land records maintained at Gram Panchayat level by the revenue collection agencies. This information was used for selecting training sets (samples) to classify the data and for accuracy assessment of the output generated.

2.4 Supervised classification

Supervised classification was carried out for all the three seasons' data to determine the cropping pattern changes and to estimate the area under irrigated and rainfed croplands in the study area. ERDAS IMAGINE and ArcGIS software were used for analysis and visualization, respectively. The classification was carried out by giving sufficient training sets (sample points collected during ground truth) so that the maximum likelihood algorithm gets trained properly before performing the classification. As provided by the software ERDAS IMAGINE, signature separability assessment was carried out by plotting cospectral ellipses, descriptive statistics and error matrix.

More details on separability and accuracy are given in section 2.7. All the non-agricultural layers are masked on each image before carrying out the supervised classification to make the classification easier and to get better classified results. Spectral signatures were generated for each of the major crop types and associated land cover types. After recoding the classified image using GIS analyst tool, the area of the major classes such as irrigated and rainfed cropland, and within the cropland major crops like sugarcane, paddy, and rainfed / fallow-lands were mapped.

Table 1. Remotely sensed data used in the study

Cropping Season	Satellite Data / No. of Scenes	Dates	Source
Kharif	RS-2 LISS III 4 scenes	16-11-2011 22-12-2011	Bhuvan portal / NRSC, Hyderabad
	Landsat-5 TM 9 scenes	14-01-1992 05-03-1993 16-11-1993 06-05-1998 07-04-1999 18-02-1999 16-12-2004 18-02-2005 25-05-2005	USGS Web site
	Landsat-8 OLI 2 scenes	13-11-2013 11-01-2020	USGS Web site
Rabi	RS-2 LISS III 6 scenes	15-01-2012 08-02-2012	Bhuvan Portal / NRSC, Hyderabad
Summer		20-04-2012	
Through-out year	Terra-MODIS 12 scenes	2012-13	USGS Web site
Other shape files	KRS Project Command Area boundary	Karnataka State Remote Sensing Applications Centre (KSRSAC)	
All three seasons	Historical Crop area Statistics (1993-2013)	Directorate of Economics and Statistics, Karnataka, GP-level Revenue Records	

2.5 Cropping pattern analysis

Cropping pattern refers to the proportion of land under cultivation of different crops at different points of time. Cropping pattern analysis was done using LISS-III, TM and OLI data for the years 1992-93, 1998-99, 2004-2005, 2011-12 and 2019-20. The image classification was carried out based on the spectral reflectance of the cover types and ground truth collected during the field visit. A time series study of the change in cropping patterns was carried out from the year 1992-93 to 2011-12 and for the crop year 2019-20. The sequence of overall methodology followed in the study is illustrated in Figure 2.

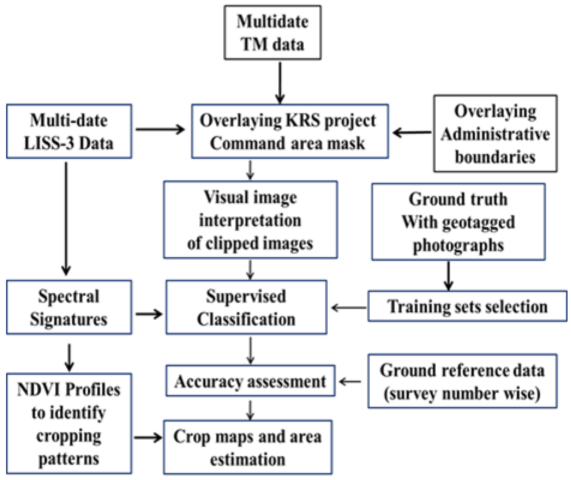

Figure 2. Sequence of steps followed in identification of irrigated areas and cropping pattern analysis.

2.6 Change analysis

Multi-date image analysis for change detection as described by Jensen (2016) was adopted in the present study. Digital image data of each date was subjected to supervised classification taking the best spectral bands and the areas estimated each time under the major land cover / crop types were compared with the area estimates made in 1992-93 (first base reference year) and 2011-12 (the second reference year). The change in area under each cover type was expressed in percent.

2.7 Separability analysis and accuracy assessment

Separability analysis of the classes was carried out at the training stage by running Transformed Divergence (TD) using spectral bands green, red, NIR, SWIR1 and SWIR2 of Landsat-8 OLI sensor (Jensen, 2016). The TD values were as following: Average 1997, minimum 1666 and maximum 2000. The TD values of paddy (rice) and sugarcane, the two major crops in our study area, ranged from 1837 to 1931.

Accuracy of estimates of area under major crops was carried out with the help of ground truth samples collected during the growth cycle of crops grown in the study area. These samples were divided into training and test samples. An error matrix was created between the digital classified output and ground reference data (test samples). The diagonal of the matrix gave the number of pixels that were assigned to the correct class. The sub-routines available in ERDAS IMAGINE were used to know how well the image was classified, to characterize errors, and the accuracy of estimates derived from it. Overall classification accuracy (OCA), producer's accuracy and user's accuracy were calculated. OCA expressed in percentage and Kappa coefficient was generated as per Congalton and Green (1999). The Kappa coefficient is measure of agreement between the two sources of data.

3. Results and discussion

3.1 Spectral signatures of major crops

Spectral signatures of land cover types including major crops along with deciduous forest (D. Forest), fallow lands and water in the month of November 2013 are shown in Figure 3. The separability of signatures in the blue band (483 nm) and green band (561nm) is not impressive., whereas it is fairly good in pigment absorption red band (656 nm) and near infrared (NIR, 865 nm). The signature of water is very distinct in NIR and shortwave infrared (SWIR)-1 (1609 nm) and SWIR-2 (2201 nm). The NIR reflectance from sugarcane crop is higher than all other crops because of its greater green biomass per unit area. The NIR reflectance from sugarcane is higher than that of paddy (rice), mulberry, coconut and deciduous forest in that order. Fallow lands, both dry and wet showed much less reflectance in the NIR region than green crop covered areas. The spectral separability of sugarcane, paddy (rice) and coconut crops were not very distinct in the SWIR-1 and SWIR-2 spectral bands compared to that between mulberry, deciduous forest and fallow lands. The spectral response from plants in the SWIR-1 and SWIR-2 is affected by soil moisture during early stages and leaf-water content in the later stages of crop growth. That could be one of the reasons for more reflectance from fallow lands, deciduous forest and mulberry than that of paddy (rice) and sugarcane.

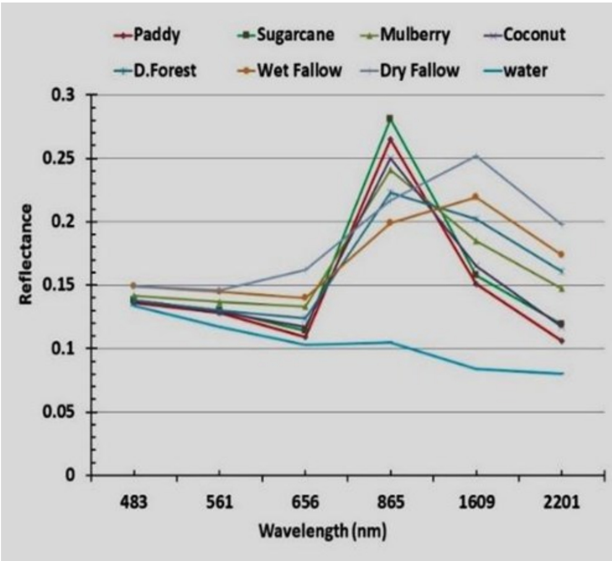

Figure 3. Spectral reflectance of major cover types in the study area during November 2013 using Landsat-8 OLI data.

3.2 Temporal profiles of NDVI of major crops

The changes in NDVI over the crop growing period, called NDVI profiles, of mulberry, *Kharif* paddy (rice) (labelled as K.Rice), summer paddy (rice) (labelled as S. Rice), ragi and sugarcane crops are shown in Figure 4.

It is clear that the *Kharif* season paddy (rice) reached its NDVI maximum (0.63) in the month of September and that of summer paddy (rice) crop attained its maximum NDVI (0.65) in May month. The NDVI profile of ragi crop started in May and gradually reached its maximum in September followed by reduction then onwards. The NDVI profile of mulberry is responding very nicely to leaf picking and green-up phases. The profile of sugarcane crop has increased continuously from January and reached its maximum by next December. It was inferred from the NDVI-temporal profiles that it is difficult to distinguish the *Kharif* rice crop from mulberry during August month and Sugarcane and *Kharif* Rice crops during September month because their profiles are very close. The study of the NDVI profiles gave us an insight into the duration of crops, "crop windows" that permit maximum separability and in choosing appropriate period of data acquisition. The NDVI profiles also gave clue about the number of major crops grown in each season.

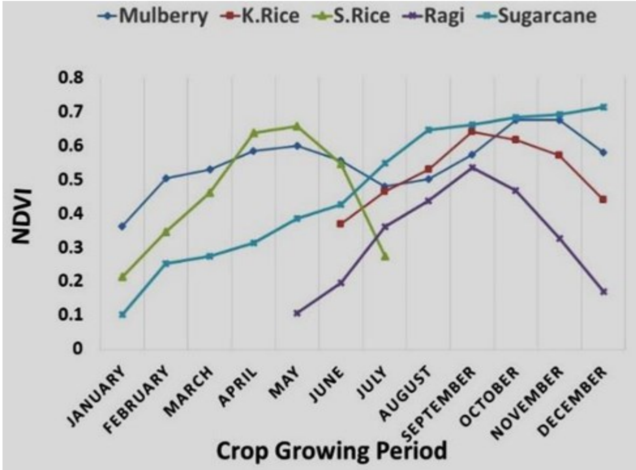

Figure 4. Spectral-temporal profiles of major crops grown in the KRS project command Area.

3.3 Change in area under irrigated and rainfed croplands

Identification of irrigated crop lands and rainfed / fallow lands was possible because of the variation in spectral response observed in the NIR and SWIR bands (see Figure 3). The change in the total irrigated and rainfed areas in the KRS project command from 1992-1993 to 2011-2012 is shown in table 2 and their spatial distribution in Figure 5. It was found that there was an increase in the irrigated cropland by 8.64 % and decrease in the area under rainfed cropland (includes dryland and tail-end irrigated fallow fields) by 28.74%. This may be due to the improved water supply due to canal lining leading to favourable hydrological soil condition and microclimate in the area and also due to better price for the irrigated food crops.

Table 2. Areas (ha) under irrigated and rainfed crop land and change over time

Cover type	1992-93 (a)	Mean of 1998-99 2004-05 2011-12 (b)	Change (%)
Rainfed cropland	29982	21363	28.74 (-)
Irrigated cropland	109815	119307	8.64 (+)

% change = {[(b) - (a)] ÷ (a)} ×100

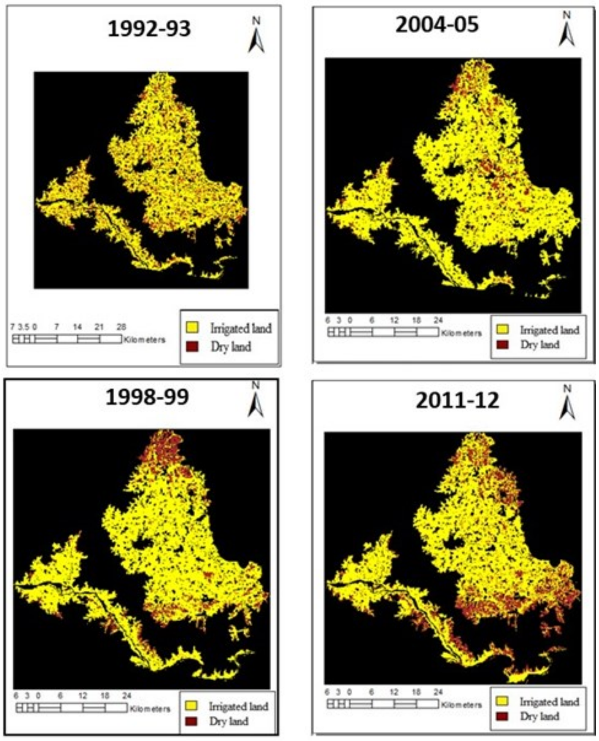

Figure 5. Spatial and temporal variation in the irrigated cropland (Yellow colour) and rain-fed cropland (Brick red colour) in the KRS project command.

3.4 Change in the area under major crops during 1992-93 and 2011-12

Supervised classification of LISS-III data acquired on 16-11-2011 gave an overall classification accuracy of 91.04% (kappa 0.91) with acceptable accuracy of producers' and users' accuracy (table 3). The classification accuracy of OLI sensor data acquired on 11-01-2020 is given in table 4. It may be noted that the overall classification accuracy was better with 23.5 m spatial resolution data than with 30 m spatial resolution data. These results are in tune with the findings of Singh et al. (2001) who studied the effect of spatial resolution on crop classification using several types of sensors and found that accuracy of wheat classification increased considerably from coarse resolution (188 m) to moderate resolution (100 m) and remained relatively flat over a range of higher spatial resolution data till it increased at 23 m spatial resolution. Similar observations were made by Velpuri et al. (2009) who concluded that finer spatial resolution data gave better accuracy of irrigated area because the small fragmented areas are detected better.

Table 3: Classification accuracy of major crop covers in the command area of KRS project during 2011-12 using LISS-III sensor data acquired on (16-11-2011).

Land cover / Crop Type	Producers Accuracy (%)	Users Accuracy (%)
Sugarcane	82.33	83.32
Paddy (Rice)	84.21	91.12
Fallow land	94.44	89.47
Rain-fed cropland	100	94.74
Overall classification accuracy = 91.04 %, Kappa = 0.91		

Table 4. Classification accuracy of major crop covers in the command area of KRS project during 2019-20 using Landsat-8 OLI Sensor data acquired on (11-01-2020).

Crop Type	Producers Accuracy (%)	Users Accuracy (%)
Sugarcane	71	71
Paddy (Rice)	87	70
Coconut	91	100
Mulberry	75	75
Rainfed cropland	86	100
Fallow land	100	100
Built-up	100	80
Water	71	100
Overall classification accuracy = 84.31 %, Kappa = 0.84		

Changes in major crop areas between 1992-93 and 2011-12 are shown table 5. Spatial distribution of major crops (paddy (rice) and sugarcane) and associated cover types is shown in Figure 6. The analysis indicated that the area under sugarcane crop has increased 45.51% between 1992-93 and 2011-12 while the area under paddy (rice) has decreased by 40.40 %. Also note that there has been an increase in area under rainfed crops including fallow lands by 1.92%. The shift from paddy (rice) cultivation to sugarcane may be due to better benefit to cost ratio of sugarcane cultivation, less labour requirement and fairly good yield of sugarcane (50 tonnes per hectare) with high demand and good price at that time.

Table 5. Major crop area changes estimated (ha) and their change over time

Land cover / Crop Type	1992-93 (a)	Mean of three times estimates (b)	Change (%)
Paddy (Rice)	75411	44939	(-) 40.40
Sugarcane	28571	41573	(+) 45.51
Rainfed + fallow land	77420	78913	(+) 1.92

% change = {[(b) - (a)] ÷ (a)} ×100

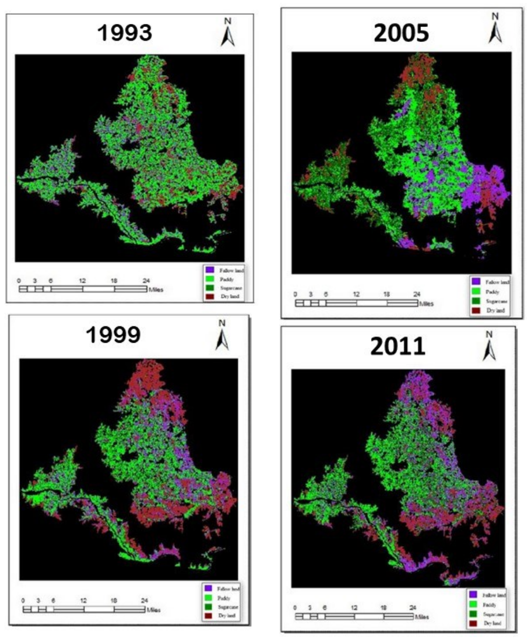

Figure 6. Spatial and temporal variation in the cropping pattern in the KRS project command. Green colour: paddy, Dark green: sugarcane, brick red: rain-fed cropland, Violet: fallow land.

3.5 Change in area under major crops during 2011-12 and 2019-20

Area estimates of major crops and rainfed / fallow lands and their change between 2011-12 and 2019-20 and comparison of changes estimated using DES data and that made with RS data are in table 6. Using RS data, we found that there was 5.11% reduction in the area under paddy (rice) and 26.45% reduction under sugarcane crop. While the DES-based estimates showed a 3.63 % reduction in area under paddy (rice) and 28.83% reduction in sugarcane crop area. One positive change noticed during this period is reduction in the area under rainfed / fallow lands (49.11% as per DES estimates and 42.36% as per RS estimates). These changes may be due to improvements in the water conveyance systems, reducing losses due to the leakages, seepages, etc and changing cropping patterns. Another reason for reduction in the area under paddy and sugarcane may be due to reduced rainfall, water table going down, or reservoir drying up due to droughts, etc as reported by Nageswara Rao and Mohankumar, (1994). Based on the analysis of observed rainfall patterns, trends and variability observed in the past 30 years (1989-2018), Guhathakurta et al. (2020) have found the rainfall variation especially in the July month, the rice transplanting period, is very high in Mandya district. This interior district also experienced a smaller number of rainy days during that period.

We tried to answer the question why the cropping pattern was changing in the command area of KRS project? It is not difficult to answer this question because farmers chose their crops depending on climatic factors and economics. Farmers of the KRS command area are no exception. They moved from paddy (rice) cultivation to sugarcane because the cost of labour is less and income from the sugarcane is more than from paddy (rice) with less cost of investment but not realizing that the per unit area water demand of sugarcane is much more than that of paddy (rice). Another reason for change in the cropping pattern may be the incentives given to farmers to diversify their cropping systems so as to increase their sources of income all through the year.

Table 6. Comparison of changes in area under land cover / crop types estimated by DES and RS between 2011-12 and 2019-20.

Land cover / Crop Type	Area (Ha) 2011-12 (a)	Area (Ha) 2019-20 (b)	% Change
Paddy (rice)	DES 58947	DES 56805	(-) 3.63
	RS 39115	RS 36969	(-) 5.11
Sugarcane	DES 39903	DES 30973	(-) 28.83
	RS 54607	RS 40159	(-) 26.45
Rainfed+ Fallow land	DES 83495	DES 42484	(-) 49.11
	RS 71455	RS 41177	(-) 42.36

% change = {[(b) - (a)] ÷ (a)} ×100

4. Conclusions

Image classification techniques applied on RS data from LISS-III, TM and OLI sensors have been found to provide valuable information on the changing scenario of area under irrigated and rainfed croplands in the command areas of KRS project. It also helped us in identifying which cropping pattern changes are dominating the project command so that appropriate decisions could be taken to improve the efficiency of irrigation projects. We hope that better-spatial-resolution and cloud-free data may further improve the accuracy of information generated on the spatiotemporal changes in the study area.

Acknowledgements

The authors sincerely thank Director, KSRSAC for providing the satellite data, laboratory facilities for data processing and for sparing the shape files of the administrative boundaries. We acknowledge that we have used several open-source data from USGS web site and ISRO’s Bhuvan portal and data procured from NRSC, Hyderabad by KSRSAC, Bengaluru. We are grateful to the Karnataka State DES for allowing us to refer their “District at a Glance” publications of Mandya and Mysuru districts. Thanks, are also due to two anonymous reviewers for their valuable comments and suggestions.

References

Ashwini B.C. and V. R. Kiresur, (2017). Dynamics of cropping pattern in Mandya district of Karnataka, J. Farm Sci., 30 (2), 220-225.

Congalton R.G. and K. Green (1999). Assessing the Accuracy of Remotely Sensed Data: Principles and Practices. Lewis Publishers, Boca Raton, London and New York.

Dhumal R.K., Y.D. Rajendra, K.V. Kale, and S.C. Mehrotra (2013). Classification of Crops from remotely sensed Images: An Overview, Int. J. Engineering Research and Applications, 3 (3), 758-761.

Guhathakurta P., S. Sanap, P. Menon, A. K. Prasad, S.T. Sable and S. C. Advani (2020). Observed Rainfall Variability and Changes Over Karnataka State. Met Monograph No.: ESSO / IMD /HS / Rainfall Variability / 13(2020) / 37 IMD, Pune- 411005.

Gumma M.K., P. Kesava Rao, P. S. Thenkabail, V.M. Reddi, G. Naresh, I. A. Mohammed and I.M. D. Rafi (2014). Crop Dominance Mapping with IRS-P6 and MODIS 250-m Time Series Data. Agriculture, 4, 113-131.

Jensen J. R. (2016). Introductory Digital image Processing: A Remote Sensing Perspective, Pearson Education Inc.

Murthy C.S., P.V. Raju, S. Jonna, K.A. Hakeem, and S. Thiruvengadachari (1998). Satellite derived crop calendar for canal operation schedule in Bhadra project command area, India, International Journal of Remote Sensing, 19 (15), 2865–2876.

Murthy C.S., S. Thiruvengadachari, P.V. Raju, and K.V.S. Badrinath (2003). Classification of wheat crop with multi-temporal images: performance of maximum likelihood and artificial neural networks. International Journal of Remote Sensing, 24 (23), 4871–4890.

Nageswara Rao P.P. and A. Mohankumar (1994). Cropland Inventory in the command area of Krishnarajasagar project using satellite data. International Journal of Remote Sensing, 15 (6), 1295-1305.

Neetu M. Prashnani, D. K. Singh, R. Joshi., and S.S. Ray (2014). Understanding crop growing pattern in Bardhman district of West Bengal using multi-date RISAT 1MRS data, Volume XL-8.

Panigrahy S., K.R. Manjunath, and S.S. Ray, (2005). Deriving cropping system performance indices using remote sensing and GIS. International Journal of Remote Sensing, 26 (12), 2595-2606.

Panigrahy S., G. Upadhyay., S. S. Ray., J.S. Parihar (2010). Mapping of cropping system for the Indo-Gangetic Plain using multi-date SPOT NDVI-VGT data. Journal of Indian Society of Remote Sensing, 38 (4), 627– 632.

Raju P.V., S. Jonna, C.S. Murthy, K. Abdul Hakeem, and S.T. Chari, (1997). Performance evaluation of a canal delivery system using satellite and field data, Proc. of workshop on Remote Sensing and GIS Applications in Water Resources Engineering, Bangalore, India, II, 11-20.

Raju P.V., M.V.R. Sesha Sai and P.S. Roy (2008). In-season time series analysis of Resourcesat-1 AWiFS data for estimating irrigation water requirement, International Journal of Applied Earth Observation and Geoinformation, 10, 220–228.

Ray S.S., V.K. Dadhwal, and R.R. Navalgund (2002). Performance evaluation of an irrigation command area using remote sensing: A Case Study of Mahi Command, Gujarat, India, Agricultural Water Management, 56 (2), 81-91.

Saindranath J., P.V. Narasimha Rao, and S. Thiruvengadachari (2000). Radarsat data analysis for monitoring and evaluation of irrigation projects in the monsoon, International Journal of Remote Sensing, 21 (17), 3219–3226.

Singh R.P. V.K. Dadhwal, K.P. Singh and R.R. Navalgund (2001). Study on sensor's spatial, radiometric and temporal resolution requirements for crop monitoring: Proceedings of symposium on Advances in Electronics (ELECTRO2001). Jan. 4-6. B.H.U, Varanasi, India, 213-218.

Thiruvengadachari S. (1981). Satellite sensing of irrigation pattern in semiarid areas: An Indian study. Photogrammetric Engineering and Remote Sensing, 47:1493–1499.

Thiruvengadachari S., S. Jonna, P. V. Raju, C.S. Murthy and K.A. Hakeem (1994). System performance evaluation and diagnostic analysis of canal irrigation projects. Asian Conference on Remote Sensing, Bangalore, India: B2-1 to B-2-6.

Thiruvengadachari S., and R. Sakthivadivel (1997). Satellite remote sensing for assessment of irrigation system performance: A case study in India. Research Report 9. International Irrigation Management Institute. Colombo, Sri Lanka.

Velpuri N.M., P.S. Thenkabail, M.K. Gumma, C.B. Biradar, P.Noojipady, V. Dheeravath, and L.Yuanjie, (2009). Influence of resolution in irrigated area mapping and area estimations. Photogrammetric Engineering and Remote Sensing, 75, 1383–1395.

Assessment of wildlife habitat and natural resources with special reference to water management in dry deciduous forest ecosystem of Gujarat state, India

Aditya Dharaiya[1*], Vaidehi Shah[2], Dhaval Gadhavi[3] and Nishith Dharaiya[2]
[1]Geology Department, M. G. Science Institute, Ahmedabad, Gujarat, India
[2]Wildlife & Conservation Biology Research Lab, Hemchandracharya North Gujarat University, Patan, Gujarat, India
[3]Chhota Udepur Forest division, Chhota Udepur, Gujarat, India
*Email: adiradhu@gmail.com

(Received: July 22, 2021; in final form: Sept 13, 2021)

Abstract: Remote Sensing and GIS has a tremendous impact in the research and on the natural resource management and conservation. It has a wide range of applications in various fields of research and it has proved to be useful as a decision-making tool. In conservation science also the geospatial techniques have proved its applicability. The present study has been carried out to address the issue of human-wildlife conflict due to water scarcity especially during the dry season. To prepare the NDVI and hydrology maps of the Ratanmahal Wildlife Sanctuary the high-resolution Sentinel 2B satellite and Cartosat 1 DEM are used. The field data are superimposed on the drainage map and some critical locations are identified as the recommendations to build water containment structures like wildlife guzzlers, dams, reservoirs, etc. for longer period of time as well as to improve the habitat. We suggested seven such locations of land use sites in order to restrict the human-wildlife interaction. The study will help in advancing the habitat management, water conservation and formulate effective wildlife management strategies in the dry deciduous ecosystem.

Keywords: Ratanmahal wildlife sanctuary, Sloth bear, hydrological analysis, NDVI, GIS

1. Introduction

Food and water are the major resources which drives the movement of wildlife especially the large mammals such as lion (*Panthera leo*), tiger (*P. tigris*), leopard (*P. pardus*), sloth bear (*Melursus ursinus*) and many others towards the human dominated area (Athreya & Belsare, 2007; Bhattacharjee & Parthasarathy, 2013; du Toit, 2002; Gore et al., 2008; Manral et al., 2016). Water is considered to be one of the most essential and significant resource for all the living organisms for their survival. Mostly, in the dry season or during the drought conditions it becomes difficult for the wildlife to find water in the natural habitats; though food can be easily available for many of the large mammals (Epaphras et al., 2008). Movement of the large mammals outside their natural habitats often creates the conflict situations due to which either the animal or the human is at risk. Such movements were often reported in fragmented landscapes with large mammals like, tiger, elephant and sloth bear (Banerjee et al., 2020; Kinnaird et al., 2003; Linkie et al., 2006; Wikramanayake et al., 2004). Deforestation and urbanisation (say, road development) are the primary causes of habitat and forest fragmentation, which causes a tremendous loss to the forests ecosystems and also a major threat to the viability of wildlife populations (Ferreras, 2001). Ecological corridors have proven as a better solution in such areas, where the corridor was designed using multitemporal fragmentation and corridor analysis through GIS (Banerjee et al., 2010; Sethy et al., 2021; Yadav et al., 2012). It is very important to conquer this situation in order to mitigate the human-wildlife conflicts and to enhance the opportunity of coexistence (Bhattacharjee & Parthasarathy, 2013; Maheshwari et al., 2014). This study focuses on wildlife habitat management through hydrological aspects and may help in water conservation for the longer period of time in the dry season.

Cattle and domestic dogs are easily available prey for the large cats such as tiger, lion and leopard. Lakes and water reservoirs near settlements often used for the irrigation which also acts as a source of water for wild animals in dry seasons. In the forests of Central Gujarat-India, the sloth bear is the flagship species and one of the wild animals that is accountable for attacks on humans (Garcia et al., 2016; Pérez et al., 2017; Singh et al., 2018). Sloth bear is often reported wandering in human dominated areas for water as its primary food i.e., fruits and insects are available in the forest. However; during summer, the paucity of natural water within the forest push other wild animals like sloth bear and leopards towards the human settlements in search of water that is available at ease (Malik et al., 2018). The sharing of resources may increase the interactions and conflicts between human and wildlife.

According to the forest record, in the past five years, more than 500 cases of conflicts of leopard and sloth bear with humans have been recorded in the Central Gujarat of which most of were recorded during summer (Personal communication with Deputy Conservator of Forest). The increase of conflicts not only disturbs the well-being of locals but also raises a feeling of retribution towards the animals. To overcome this situation use of remote sensing and geospatial technology plays an important role (Dharaiya & Ratnayeke, 2009). Moreover, the ground survey technique has limitations for difficulty of sampling in limited time. Remote sensing and Geographical Information System (GIS) have proven extremely useful in this study, especially for analysing the hydrology and understanding the natural drainage pattern and location of water retaining areas. The results of RS and GIS analysis provide a synoptic view and the real-time information of a large area. Satellite imageries, Digital Elevation Model (DEM) are used to establish the Forest Cover classification of the study area using optical Multispectral Remote sensing, along with some vector datasets.

The study aims to support the forest management in establishing and maintaining areas for water management in Ratanmahal Wildlife Sanctuary. To begin with our work, available water holes (natural and man-made) such as, small reservoirs, puddles, etc., were surveyed and tagged with their geo locations through field surveys during the study period (2019-20). In the present study, we have attempted to identify the areas for water conservation and management using hydrological analysis on the GIS platform and made recommendations to the forest management. This might retain the water for the longer period of time for wildlife and also improve the habitat as a whole.

2. Materials and methods

2.1. Study area

The present study has been carried out in the Ratanmahal Wildlife Sanctuary (RWLS), which is one of the important sloth bear sanctuaries of Gujarat. RWLS is a hilly isle known to be the habitat of the sloth bears which falls in the southernmost part of Dahod district of Gujarat and bordering Madhya Pradesh state of India. It has the total area of 55.65km^2 and located between 74º4′ - 74º10′ E longitude and 22º32′ - 22º34′N latitude (Figure 1). Geologically, it is located at the convergence of the Vindhya Range and Malwa plateau harboured by dry teak forests at the foothills and mixed deciduous forests with dry bamboo brakes on the periphery (Trivedi, 2003). The mean annual precipitation is recorded as 1115mm which mostly occurs during June to October whereas, July and August are the rainiest days. The sanctuary has dry and subtropical climate with the mean temperature ranging from 20.7 ºC in winter and 33.6 ºC in summer season and the average annual temperature is around 20.7 ºC. The hilly and jagged terrain of this sanctuary has the highest elevation of 670m with undulating landscape. The high concentration of mahua (*Madhuca longifolia*) trees provides food to sloth bears. The forests of Ratanmahal form the catchment of river Panam, a major river of Central Gujarat that originates at the foothills of this sanctuary. It drains through the districts of Dahod and Panchmahals. The sanctuary is rich in flora and also possesses within-habitat heterogeneity (Trivedi, 2003, 2001); and it is the home of hundreds of identified plant species (including trees, shrubs, grasses and climbers). Apart from the Sloth bear (*Melursus ursinus*) as a flagship species, the other large mammals include leopard (*Panthera pardus*), hyena (*Hyena hyena*), small Indian civet (*Viverricula indica*), four-horned antelope (*Tetracerus quadricornis*), and Hanuman langur (*Semnopithecus vetulus*). The sanctuary also has a rich avian diversity and several species of amphibian and reptiles.

2.2 Data acquisition and analysis

The field surveys were carried out from March, 2019 to February 2020 to locate the existing water holes and the drainage pattern within the sanctuary. The water holes were geotagged using the GPS (Garmin eTrax30) and were further classified into natural and man-made ones. The flow diagram in Figure 2 illustrates the general methodology employed for the entire study. The dataset of Sentinel 2B Satellite Sensor with 10m resolution was acquired from the European Space Agency (ESA) (https://scihub.copernicus.eu/dhus/#/home) of May, 2020 in order to determine the forest cover of the study area. The Sentinel 2 is a multi-spectral imaging mission, which has a high resolution, wide swath, high revisit frequency of five days and orbit phased at 180º. It carries an optical instrument payload which samples 13 bands, where four bands at 10m, six bands at 20m and remaining three bands at 60m spatial resolutions, respectively. Further, the study area was clipped from the imagery and the forest cover classification was performed through reclassification method followed by Normalized Difference Vegetation Index (NDVI) spectral index (Hess et al., 1996) on the ArcGIS® platform.

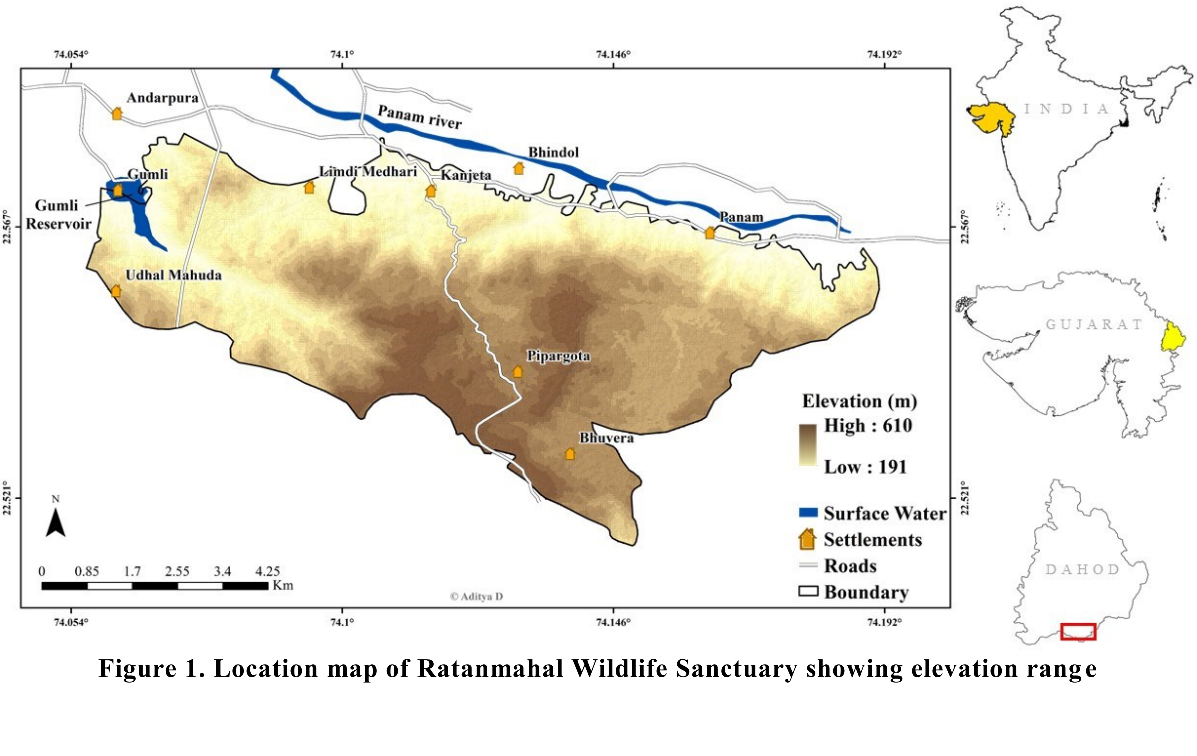

Figure 1. Location map of Ratanmahal Wildlife Sanctuary showing elevation range

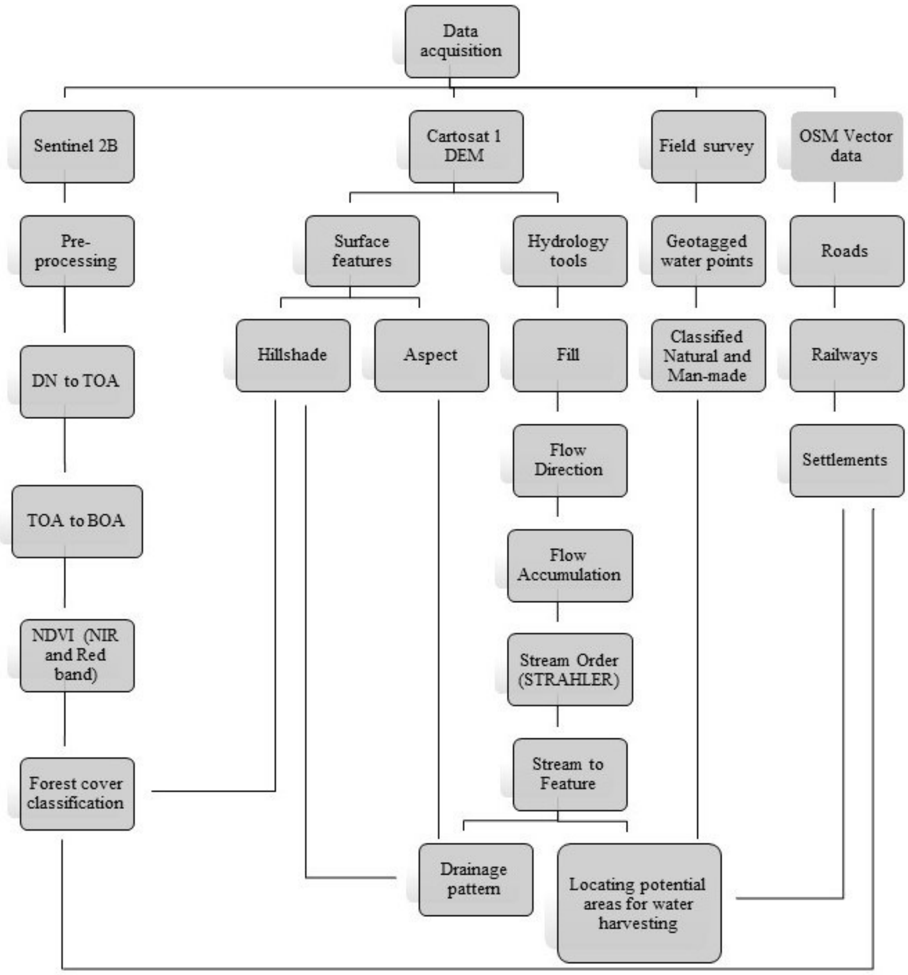

Figure 2. Flowchart illustrating the brief methodology

2.2.1 Forest cover classification

The forest covered was classified based on the NDVI algorithm followed by reclassifying the spectral values of the output and the classes were determined. The NDVI ratio can be determined from the contribution of wavelengths of RED and near-infrared (NIR) bands. Strong and well-nourished vegetation will absorb most of the RED wavelengths that it receives and will reflect back a large proportion of the near-infrared light, whereas poor condition vegetation or thin areas, will reflect more of the red wavelength light and less NIR light (Alexander, 2020). It is significant to determine the surface reflectance of the required bands to obtain accuracy in the outcome. Thus, the imagery was pre-processed and using the raster calculator the Digital Number (DN) values were converted to Top of Atmosphere (TOA) reflectance by multiplying the DN values to 10000. Further, the TOA reflectance values were divided by 10000 to convert the TOA reflectance to the surface reflectance or Bottom of Atmosphere (BOA) reflectance of RED (ρ = 0.062) and NIR (ρ = 0.337) bands (Rulinda et al., 2012). The NDVI values have been calculated using the following formula using raster calculator:

$$\mathrm{NDVI} = \rho\mathrm{NIR} - \rho\mathrm{RED} \,/\, \rho\mathrm{NIR} + \rho\mathrm{RED} \qquad (1)$$

Where NIR = (band 8 of Sentinel 2B), RED = (band 4 of Sentinel 2B), and ρ stands for reflectance of each band. Basically, the NDVI ranges from -1 to +1, for example, the negative values indicate the water body and on the other hand, if the value is close to +1, there is a high possibility of dense green leaves. But when NDVI is close to 0, there could not be any green leaves and corresponds to barren areas of rock, sand, snow. Low positive values represent Scrub or Grasslands (~ 0.2 to 0.4), while high positive values represent temperate and dense forests (values approaching 1). The accuracy assessment of the classified image was done using 105 random training points. After generating the random points, the error matrix and KAPPA statistics were calculated for accuracy assessment.

2.2.2. Hydrology

All the surveyed water holes were further classified as natural and man-made according to the information collected from the office of the forest department. The Cartosat 1 Digital Elevation Model (DEM) of spatial resolution 2.5m was obtained from Bhuvan, a geoportal of ISRO (Indian Space Research Organization) (https://bhuvan-app3.nrsc.gov.in/). It was used as an input raster and five main features were generated (i.e. Fill sinks, Flow Direction, Flow Accumulation, Stream Order and Stream to feature) on ArcGIS® platform (Malik et al., 2018). The Cartosat-1 satellite is placed in the polar Sun synchronous orbit at 618km from the Earth and has a recording swath of about 30km with a spatial resolution of 2.5m (Murthy et al., 2008). Alongside, several land use vector layers viz., roads, railways, and, settlements, along with the state and country boundaries were directly digitised in the software using the Open Street Map (OSM) server (https://www.openstreetmap.org/#map=15/24.4803/72.7920&layers=N). It is an open-source collaborative project to create a free editable map of the world. Following steps were carried out to study the habitat and generating the drainage pattern.

(a). Fill Sinks
Basically, this function fills all the sinks in the DEM to generate a depression less surface raster layer. This tool helps to remove imperfection by "filling" sinks to identify the flow direction, which helps in preventing water from being virtually trapped in higher elevation cells. On the contrary, it might result in an erroneous flow-direction grid (Teng et al., 2020). Thus, the sinks should be filled to ensure proper delineation of basins and streams in order to prevent discontinuation of the derived drainage network.

(b). Flow Directions
Flow direction is used to calculate the flow weight and assigns the respective value to each grid cell based on the steepest slope on a triangular facet (Tarboton, 1997). It identifies all the sinks in the DEM and raises their elevation to the lowest level of pour point around their edge by using the eight directions pour point model. While running the flow direction algorithm, the resulting values ranges from 1, 2, 4, 8, 16, 32, 64, and 128 which describes all the adjacent eight directions at a given point (Khezri et al., 2013). It thus, shows the overall flow paths of water, provided each cell with a unique value which determines the flow from higher to lower elevation such that, each grid cell flows only to one of the eight neighbouring cells with respect to the steepest descent or max drop. The expression processes in the GIS environment and is calculated as follows:

$$\text{Max drop} = \text{change in z-value} / \text{distance} * 100 \qquad (2)$$

(c). Flow Accumulation
To run this algorithm, the output of previous algorithm flow direction was given as an input raster. The algorithm of Flow accumulation calculates the accumulated flow as the accumulated weight of all the cells flowing into each downslope cell in the output raster. By default, a weight of 1 was applied to each cell, and the value of cells in the output raster would be the number of cells that flow into each cell. Cells with a high flow accumulation are considered as the areas of concentrated flow and may be used to identify stream channels. It is used to calculate the total number of grid cells contributing to each grid cell in the catchment and assigns the ranged value to the cell. The linear expression of Flow accumulation > 200 was used as a threshold in the raster calculator, in order to simplify the number of streams in order to specify stream ordering further.

(d). Stream order
Using flow accumulation and flow direction as input raster, the Stream order tool was executed. It is a method of assigning a numeric order to link in a stream network. This order is a method for identifying and classifying types of streams based on their numbers of tributaries. In this study, the order method used was "STRAHLER". Here, all the links without any tributaries are assigned as an order of 1 and are referred to as first order. The stream order increases when streams of the same order intersect. Therefore, the intersection of two first-order links will create a second-order link, the intersection of two second-order links will create a third-order link, and similarly to fourth-order.

(e). Stream to feature
After determining the STRAHLER order, Stream to feature function was executed to convert the output raster into the polyline feature, which would be depicted as Streams in the vector form. The streams were then classified based on three STRAHLER orders. All the above outputs were finalized and overlaid on the existing water points in the study area.

2.2.3. Water harvesting structures
By observing the streams, with respect to the water holes and forest cover, some of the artificial water containment structures such as wildlife guzzlers, dams, reservoirs, etc. were highlighted as the potential areas where water can be accumulated or harvested. The high amount of accumulation was considered at the junction, where the stream gets the third order. It was corroborated that the proposed water points should not be close to any land use such as settlements, roads and existing water points. Hence, the areas were focused on, where there would be suitable vegetation such as closed and open type of forests, even scrublands, and habitat for sloth bears and other wildlife.

2.2.4 Surface feature
Along with hydrology, one of the surface features Hillshade and Aspect was also processed to depict the tone and texture of hilly terrain area of the sanctuary. The Hillshade tool creates a shaded relief raster from a surface raster considering the illuminating source angle at infinity. The Aspect tool identifies the downslope direction of the maximum rate of change in value from each cell to its neighbours and it can be thus, considered as the slope direction based on the compass direction. Those were, further overlaid on the Forest cover and hydrology map for correlating the direction of drainage pattern and water structures with respect to forest cover, land use sites and elevation.

3. Results and discussion

During the field survey, total 28 water points of different categories (12 natural, 4 man-made and 12 unidentified) were located. Human settlements were observed near 14 of these water points (6 Man-made + 8 Natural). These water points were found either close to the tribal towns or any other land use which may create the situations of sudden encounter of human and wildlife (Syombua, 2013). This may happen more frequently when there is no water in dry season and the wild animals such as sloth bear and leopard may create the conflicting situations. Although the small area of about 55km^2, Ratanmahal sanctuary have a varied land cover with rich floral diversity. During reclassification, the classes were defined with respect to the obtained spectral values of the NDVI like, the values ranging from -0.42 to 0.016 are shown as water body, similarly 0.016 to 0.250 as Bare soil, 0.249 to 0.342 as Scrub land, 0.342 to 0.434 as Grasslands, 0.434 to 0.546 as Open Deciduous Forest and 0.546 to 0.826 as Closed Deciduous Forest. The statistics of forest cover classification reveals that 22.36% (12.26 Sq. km) of the area is covered by Grasslands, 21.43% (11.75 Sq. km) by the Open deciduous forest, 21.03% (11.53 Sq. km) by Closed deciduous forest, 16.16% (8.86 Sq. km) by Scrublands, 10.05% (5.51 Sq. km) by Bare soil, 8.88% (4.87 Sq. km) by the human settlements and other land use sites (say, roads, agriculture) and 0.054% (0.03 Sq. km) by the surface water bodies (Figure 3). Thus, it can be inferred that, there is very scarce amount of water present in the sanctuary and here comes the need to conserve the water in the sanctuary. The elevation map shows the highest elevation is 670m and the downward slope faces towards North and West of the sanctuary (Figure 1). Majority of the human settlements were relocated from the forest area; however, two of the tribal villages are still located within the sanctuary where the forest cover is dense. Using random sampling strategy 105 training points were specified and the error matrix was generated for calculating KAPPA coefficient and overall accuracy of the classified image which resulted in 0.821 and 85.6%, respectively.

The hydrological analysis of the sanctuary depicts that several water channels or streams runs from the higher to lower elevation to fill the respective basins. In present study, the catchments are higher at the lower elevation towards North direction as the slope is facing towards North and West. The water channels drain and meet at the foothills to the River Panam to the North and at Gumli reservoir to the West (Figure 4). The STRAHLER order analysis of the streams depicts that there are more than 500 small and big streams drain through the study area, out of which 5 streams are of third order and the total flow length of all the streams are around 15km, hence they should be said as major streams. Higher the order a streams gets, higher will be the accumulation at the catchment in the respective junctions. Therefore, according to Figure 5, the junctions of such streams with higher flow accumulation and with more distance from the land use sites were further surveyed and located to highlight as the potential areas for water harvesting where water containment structures can be made. Forest areas can act as sponges, ensuring stable base-flows in downstream drainage systems and increasing water infiltration into the soil, depending on local conditions (Kumar et al., 2015). This, combined with the amount of precipitation that occurs in the sanctuary, can aid in retaining and harvesting water at the highlighted potential areas. These water structures might help to reduce the human and wildlife encounters and can provide water within the sanctuary for longer period of time. It is thus, meant to be built at the lower elevation and away from the existing land use locations, which will help reduce the risk of human-wildlife conflicts.

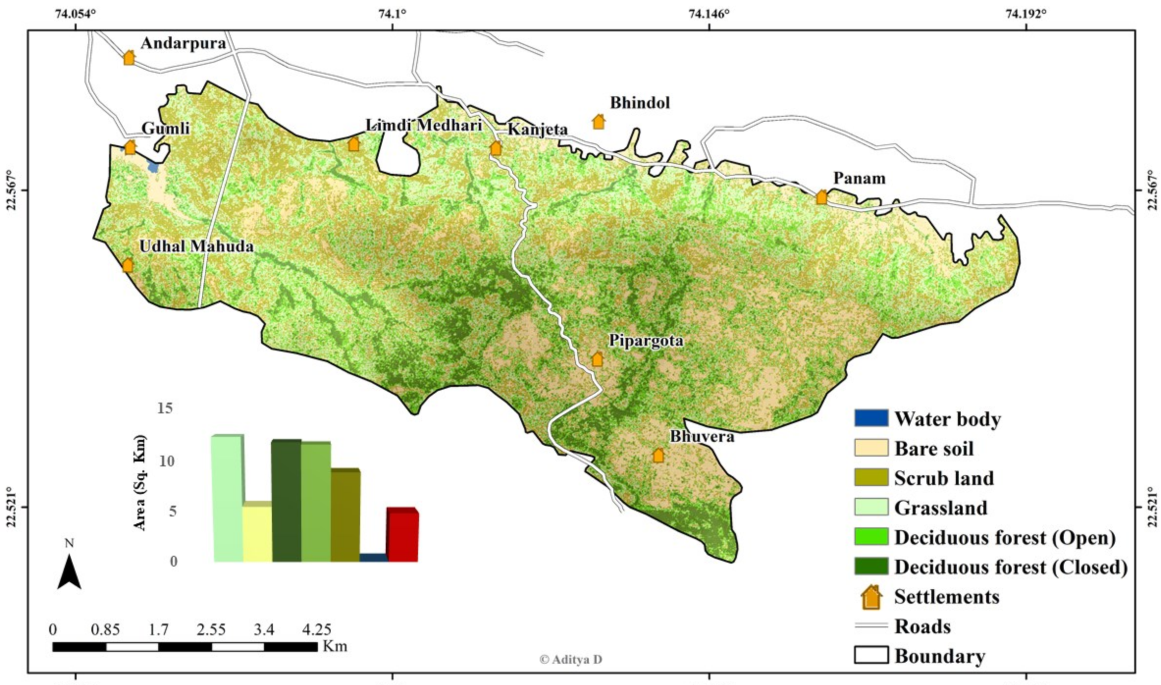

Figure 3. Map and statistics of forest cover classification in Ratanmahal wildlife sanctuary

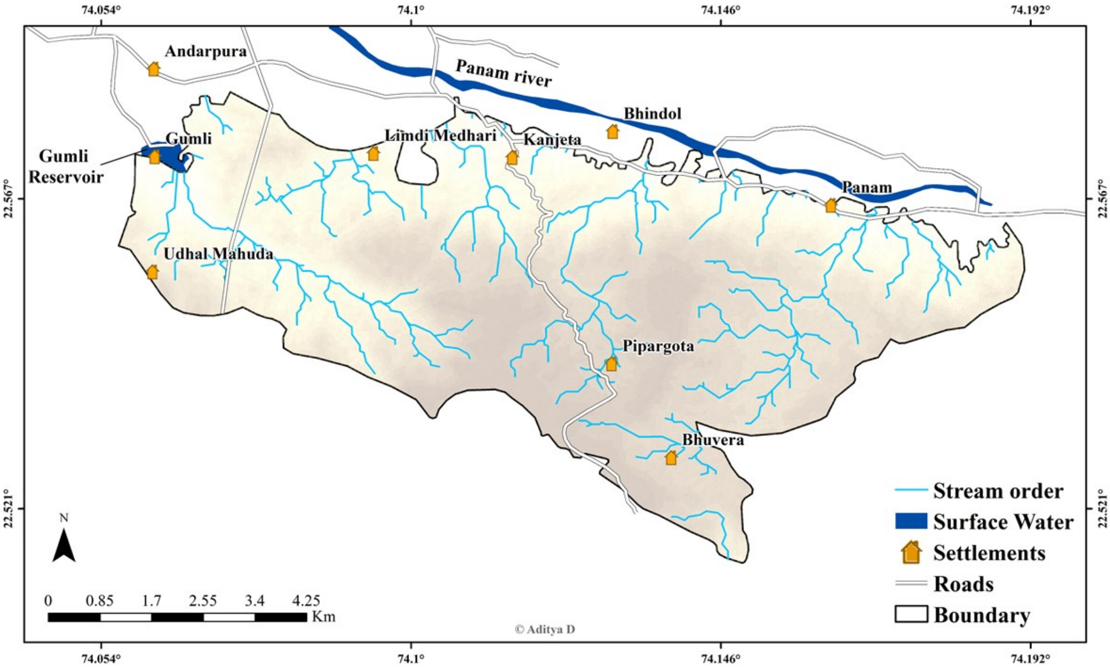

Figure 4. Drainage pattern within the sanctuary

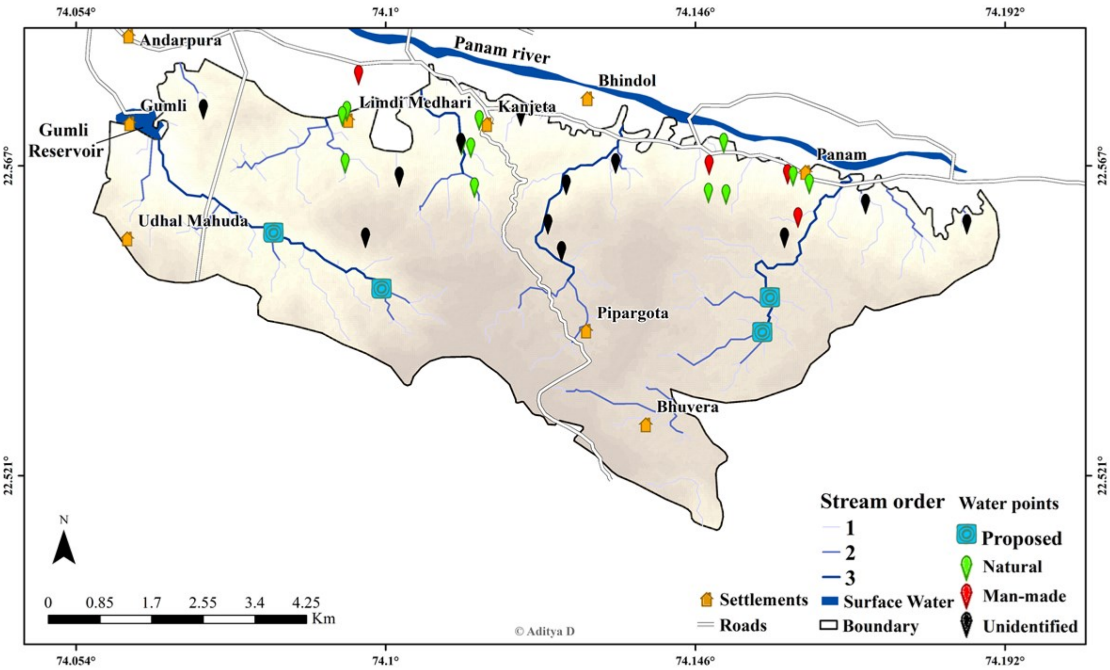

Figure 5. Map showing stream classification based on STRAHLER method and highlighted areas for water containment structures

Wildlife conservation is a challenging task and fairly depends on the quality and availability of natural resources. Conservation not only means to preserve and to protect, but also, it is meant to be sustainable use of the natural resources, which might remain suitable for all organisms including humans. The hydrological analysis illustrated in this study (Figure 4) depicts the drainage pattern in Ratanmahal wildlife sanctuary, central Gujarat. An Attempt was made to create the hydrological maps as simplified and self-understandable so that it can be appreciated by the forest managers. The integrated GIS and remote sensing technology approach used in this study has allowed to interpret, process and analyse with high accuracy in construction and simulation of this model. It has also provided a reliable as well as effective means to map the locations of water containment structures which will help the forest department in making precise decisions about the wildlife habitat improvement, that might in future also help in reducing the movements of wildlife in the villages around the sanctuary and conserving and managing the water resource. The entire methodology may increase the efficiency of data collection targeting the natural resources. Geospatial technology will also act very convenient for providing information, quite useful in the identification and analysis of factors that affect the types and quality of different micro habitats that can help to manage in an effective and efficient manner. Hence, for ensuring the sustainable use of natural resources, competent and useful decisions could be taken that meet the needs and demands of the current as well as future ecosystem conditions. Another aspect of the benefits of GIS-based approaches in hydrological analysis is that one can combine different layers of geographic data and create new integrated information through which one could have better understanding and a straight forward perception to the reality. Thus, GIS-based hydrological analysed outcomes can be proved as a great help in providing a spatial element that is being lacked by other hydrological models, and will come very handy in future for wildlife conservation and management in a sustainable mode.

4. Conclusions

The findings of this study conclude some important habitat management actions in Ratanmahal wildlife sanctuary such as, the water points proposed are away from human settlements and within the forest area, which restrict the wild animal movements in villages and help to reduce the human-wildlife conflicts. The water points are within the convenient and safe hydrological zones that enable the wildlife to access. The proposed water accumulation structures will enhance the potentiality of water resource management for the wildlife manager and can be a model for other wildlife sanctuaries for habitat and water resource management.

Acknowledgements
The authors sincerely acknowledge chief conservator of forest Vadodara circle for permitting to carry out field surveys, the Principal, M.G. Science Institute, Ahmedabad, for providing laboratory facilities. We are also thankful to Dr. C.P. Singh, Scientist, SAC ISRO, Ahmedabad, for critical comments and suggestions during the study and for improving this manuscript. The forest field staff of Ratanmahal WLS are also acknowledged for assistance during the field work.

References

Alexander C. (2020). Normalised difference spectral indices and urban land cover as indicators of land surface temperature (LST). International Journal of Applied Earth Observation and Geoinformation, 86(July 2020), 102013, 1-11. https://doi.org/10.1016/j.jag.2019.102013

Athreya V. and A. Belsare. (2007). Vidya Athreya & Aniruddha Belsare Human-Leopard Conflict Management Guidelines.

Banerjee K., V. Jhala and B. Pathak. (2010). Demographic structure and abundance of Asiatic lions Panthera leo persica in Girnar Wildlife Sanctuary, Gujarat, India. Oryx, 44(2), 248–251. https://doi.org/10.1017/S0030605309990949

Banerjee S., T. Kauranne and M. Mikkila. (2020). Land use change and wildlife conservation-case analysis of LULC change of pench-satpudawildlife corridor in Madhya Pradesh, India. Sustainability (Switzerland), 12(12), 1-17. https://doi.org/10.3390/SU12124902

Bhattacharjee A. and N. Parthasarathy. (2013). Coexisting With Large Carnivores: A Case Study From Western Duars, India. Human Dimensions of Wildlife, 18(1), 20–31. https://doi.org/10.1080/10871209.2012.698403

Dharaiya N. and S. Ratnayeke. (2009). Escalating Human-Sloth Bear Conflicts in North Gujarat: a tough time to encourage support for bear conservation. International Bear News, 18(3), 12–14.

du Toit T. (2002). Making parks work: Strategies for Preserving Tropical Nature. Trends in Ecology & Evolution, 17(11), 538. https://doi.org/10.1016/s0169-5347(02)02622-8

Epaphras M., E. Gereta., A. Lejora., E. Ole Meing'ataki., G. Ng'umbi., Y. Kiwango., E. Mwangomo., F. Semanini, L. Vitalis., J. Balozi and G. Mtahiko. (2008). Wildlife water utilization and importance of artificial waterholes during dry season at Ruaha National Park, Tanzania. Wetlands Ecology and Management, 16(3), 183–188. https://doi.org/10.1007/s11273-007-9065-3

Ferreras P. (2001). Landscape structure and asymmetrical inter-patch connectivity in a metapopulation of the endangered Iberian lynx. Biological Conservation, 100(1), 125–136. https://doi.org/10.1016/S0006-3207(00)00213-5

Garcia C., M. Joshi and Dharaiya, N. (2016). Assessment of human-sloth bear conflicts in North Gujarat, India. Ursus, 27(1), 5–10. https://doi.org/10.2192/URSUS-D-15-00012.1

Gore L., A. Knuth., W. Scherer and D. Curtis. (2008). Evaluating a conservation investment designed to reduce human-wildlife conflict. Conservation Letters, 1(3), 136–145. https://doi.org/10.1111/j.1755-263x.2008.00017.x

Hess T., W. Stephens and G. Thomas. (1996). Modelling NDVI from decadal rainfall data in the North East Arid Zone of Nigeria. Journal of Environmental Management, 48(3), 249–261. https://doi.org/10.1006/jema.1996.0076

Khezri S., H. Shahabi and B. Ahmad. (2013). Application of GIS and Remote sensing Techniques in Assessment of Natural Hazards in the Central Zab Basin , Northwest of Iran. 3(March 2013), 765–773.

Kinnaird F., W. Sanderson., G. O'Brien., T. Wibisono and G. Woolmer. (2003). Deforestation trends in a tropical landscape and implications for endangered large mammals. Conservation Biology, 17(1), 245–257. https://doi.org/10.1046/j.1523-1739.2003.02040.x

Kumar, N., S. Yamaç and A. Velmurugan. (2015). Applications of Remote Sensing and GIS in Natural Resource Management. Journal of the Andaman Science Association, 20(1), 1–6.

Linkie M., G. Chapron., J. Martyr., J. Holden and N. Leader-Williams. (2006). Assessing the viability of tiger subpopulations in a fragmented landscape. Journal of Applied Ecology, 43(3), 576–586. https://doi.org/10.1111/j.1365-2664.2006.01153.x

Maheshwari A., N. Midha and A. Cherukupalli. (2014). Participatory Rural Appraisal and Compensation Intervention: Challenges and Protocols While Managing Large Carnivore-Human Conflict. Human Dimensions of Wildlife, 19(1), 62–71. https://doi.org/10.1080/10871209.2013.828247

Malik A., M. Proctor and N. Dharaiya. (2018). Use of Geospatial Techniques to Target Water Sources for Sloth Bears, Aimed at Alleviating Conflicts with People. International Bear News, 18(3), 12–14.

Manral U., S. Sengupta., A. Hussain., S. Rana and N. Badola. (2016). Human Wildlife Conflict in India: a Review of Economic Implication of Loss. Indian Forester, 142(10), 928–940. http://www.indianforester.co.in/index.php/indianforester/article/view/93647

Murthy K., S. Rao., P. Rao and V. Jayaraman. (2008). Analysis of DEM generated using Cartosat-1 stereo data over Mausanne Les Alpiles–Cartosat scientific appraisal programme (CSAP TS–5). The International Archives of the Photogrammetry, Remote Sensing and Spatial Information Sciences, 37(1), 1–6.

Pérez A., K. Santamaria., D. Operario., E. Tarkang., B. Zotor., R. Cardoso., N. de., U. Autor., I. De., A. Dos., E. Vendas., S. Empresas., O. Atividades., N. Artigo., E. Gest., F. Para., R. Miranda., A. Ferreira., J. Oliver., M. Dario and E. Volk. (2017). An Unusual Attractant Spurs Sloth Bear Break-ins in Maharashtra, India. BMC Public Health, 26(1), 1–8. http://dx.doi.org/10.1016/j.jana.2015.10.005%0Ahttp://www.biomedcentral.com/1471-2458/12/58%0A

Rulinda M., A. Dilo., W. Bijker and A. Stein. (2012). Characterising and quantifying vegetative drought in East Africa using fuzzy modelling and NDVI data. Journal of Arid Environments, 78, 169–178. https://doi.org/10.1016/j.jaridenv.2011.11.016

Sethy J., S. Gouda and S. Chauhan. (2021). Study on the impacts of LULC change on the wildlife habitat and the livelihood of people in and around Dampa Tiger Reserve , Mizoram , India. 13(May), 1–7.

Singh N., S. Sonone and N. Dharaiya. (2018). Sloth bear attacks on humans in central India: Implications for species conservation. Human-Wildlife Interactions, 12(3), 338–347. https://doi.org/10.26077/2mgq-fs29

Syombua J. (2013). Land use and land cover changes and their implications for human-wildlife conflicts in the semi-arid rangelands of southern Kenya. Journal of Geography and Regional Planning, 6(5), 193–199. https://doi.org/10.5897/jgrp2013.0365

Tarboton G. (1997). A new method for the determination of flow directions and upslope areas in grid digital elevation models. Water Resources Research, 33(2), 309–319. https://doi.org/10.1029/96WR03137

Teng J., J. Vaze., K. Tuteja and J. Gallant. (2020). Class spatial analyst: A GIS based tool for distributed hydrological modelling. MODSIM 2005 - International Congress on Modelling and Simulation: Advances and Applications for Management and Decision Making, Proceedings, 1485–1491.

Trivedi P. (2001) Biodiversity study: Ratanmahal Wildlife Sanctuary. Bird study interim report II. Unpublished report. Gandhinagar, India: GEER Foundation.

Trivedi P. (2003) Bird study of Purna Wildlife Sanctuary, Dangs under biodiversity study of Purna Wildlife Sanctuary. Unpublished final report. Gandhinagar, India: GEER Foundation.

Wikramanayake E., M. McKnight., E. Dinerstein., A. Joshi., B. Gurung and D. Smith. (2004). Designing a conservation landscape for tigers in human-dominated environments. Conservation Biology, 18(3), 839–844. https://doi.org/10.1111/j.1523-1739.2004.00145.x

Yadav K., M. Kapoor and K. Sarma. (2012). Land Use Land Cover Mapping, Change Detection and Conflict Analysis of Nagzira-Navegaon Corridor, Central India Using Geospatial Technology. International Journal of Remote Sensing and GIS, 1(2), 90–98. www.rpublishing.org

https://forests.gujarat.gov.in/ratanmahal-sanctuary.htm, [accessed on August 20, 2020].

Geospatial Information Extraction from Big Satellite Data using CUDA-enabled GPU Parallel Computing Technique

Sivakumar V*, Ankit G and Biju C
Centre for Development of Advanced Computing (C-DAC), Pune, Maharashtra, India
*Email: vsivakumar@cdac.in

(Received: Jul 16, 2021; in final form: Sept 16, 2021)

Abstract: Earth observational satellite images can provide massive quantities of data that in principle could be processed rapidly and provide valuable information to several domain specific applications. The Graphics Processing Unit (GPU) based parallel computation approach plays an important role in processing and analysing a large volume of satellite imageries and speed-up the computations. In the present paper, we implemented the indices computation algorithms i.e., Modified Normalized Difference Water Index (MNDWI) and Soil-Adjusted Vegetation Index (SAVI) for extracting useful information from satellite imagery using NVIDIA CUDA-enabled GPU's. We performed both parallel and serial approaches and compared the execution time and performances. Water and vegetation features were successfully delineated from multispectral LANDSAT – 8 satellite images. Performance result was compared with the conventional and GPU parallel computing approaches and achieved a speed up to ~6X on NVIDIA M2090 GPU. This experimental result shows that outputs can be achieved at high speed with the best utilization of GPU resources and an efficient parallelization approach. Result highlights that big data (larger area, resolution, size, etc) can be handled much easily with GPU parallel computing approach. This technique would be useful for the applications like natural resource monitoring, urban development, disaster management and agriculture.

Keywords: Geospatial, indices computation, parallel computing, NVIDIA-CUDA, GPU, MNDWI, SAVI

1. Introduction

Since the launch of Sputnik-1 (the world's first satellite in 1957), advancements in satellite and sensor technologies are growing at exponential pace. Satellite remote sensing is increasingly becoming an important tool for real-time monitoring of global vegetation cover, surface water bodies, volcanic activity, tsunamis, landslides, droughts and floods (Bilotta et al., 2013). Satellite images are important sources for extracting geographic information (Mancino, 2013) and analysing it using various methods such as NDVI, MNDWI, SAVI, classification, etc. to extract landscape elements. Earth observational satellite data size and volume are rapidly increasing due to enhancement of the spatial, spectral, temporal and radiometric resolution of the satellite sensors (Plaza et al., 2011a; Plaza et al., 2011b; Bilotta et al., 2013; Lee et al., 2011). Remote sensing data are big data due to their volume, variety and velocity (Li Y. et al. 2020). These big data emerged as a new paradigm to provide unprecedented data content and value for Digital Earth. However, data processing technology poses main challenges, especially related to computing speed and efficiency in handling the large volume of satellite data in real time (Bhojne et al., 2013; Yang et al., 2015; Pektürk and Unal, 2018; Li Y. et al. 2020). Relatively low-cost high-end processors are conventionally used for satellite data analysis, though these systems are not sufficient to process very large images (Jones et al., 2003; Rumanek et al., 2011). Therefore, it is agreed that conventional approaches are inadequate for these new generation sensors (Plaza et al, 2009a).

Parallel computing techniques and methods in the field of computer science is evolving to meet the increasing demands for processing speed and handling a big data (Brightwell et al., 2000, Dorband et al., 2003; Pektürk and Unal, 2018). For instance, many current and future applications of remote sensing in Earth science, space science, and soon in exploration science require real-time or near real-time processing capabilities (Plaza, 2009b). GPU based parallelization approach unlocks a new avenue for boosting computing power (Jeong et al., 2012; Liu & Hu, 2011) and for the advancement of research field. It provides a remarkable improvement in handling a large volume of data and performance (Tejaswai et al., 2013). GPU's architectures are massively used for resource-intensive computation. Over the past few years, the performance of GPUs has been improving at a much faster rate than the performance of CPUs (Yang et al, 2008; Jeong et al., 2012; Nickolls and Dally, 2010). Initially, this technique was applied for imaging, vision and graphics; nowadays these architectures serve in a wide range of multi-purpose applications. However, the GPU architecture does not suit all applications, this can lead to performance shortage (Fresse et al., 2011). NVIDIA-CUDA uses C programming tools and C compiler, which make programs to have more compatibility and portability (Yang et al., 2008). The exploding GPU capability has attracted more and more scientists and engineers to use it as a cost-effective high-performance computing platform, including scientists in remote sensing areas (Bernabe et al., 2013; Lee et al., 2011). With many applications, the objective of this study is to i). Compute the MNDWI and SAVI indices from satellite imageries, ii). Implement and perform both parallel and serial approaches and, iii). Compare execution times and quality of performances using NVIDIA CUDA-enabled GPUs.

1.1. Related Work

Various indices computation from satellite images has been well explored and used in many applications for a long time. Limited number of attempts have been made in recent times to increase the processing speed and performance using high performance computing (Alvarez-Cedillo et al., 2014). NITA Iulian and Olga ALDEA, implemented NDVI and NDWI index computing algorithm on a CUDA-enabled Graphics Card and an Intel Q6600 (Niţă, et al., 2012). However, the speed up was not that significant. To increase the processing speed, they developed a MATLAB based framework to accelerate the speedup of multispectral data processing and they achieved 10.94X. Wang-Juan & Sun-Jianchao computed NDVI from satellite images using NVIDIA CUDA (Wang & Sun, 2013), and achieved up to an 8X acceleration ratio compared with the serial CPU program.

1.2. CUDA hardware architecture

CUDA (Compute Unified Device Architecture) is a parallel programming model released in 2007 by NVIDIA. It is the most commonly used programming language for GPUs. CUDA parallel programming platform controls NVIDIA GPUs for processing (for technical details refer: Cook, 2013). It is used for developing a range of general-purpose applications for GPUs that are highly parallel in nature and run-on hundreds of GPU's processor cores. NVIDIA's graphics card is a new technology that is based on multithreaded computing architecture. It consists of a set of streaming multi-processors (SM) (Figure 1). Each SM has three types of memories, such as constant memory, texture memory and global memory (CUDA, 2013; Cook, 2013).

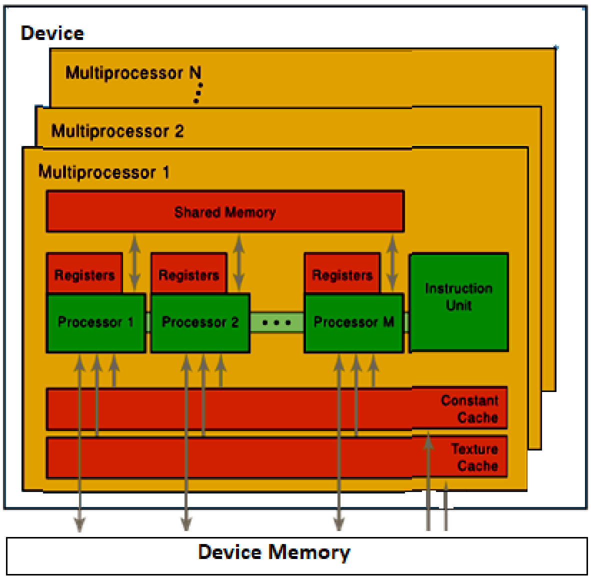

Figure 1. Hardware architecture of CUDA (Modified after CUDA, 2013)

1.3. Indices computing algorithms

In this section, proposed two algorithms to implement the framework for Indices computing from satellite imagery. (1) Modified Normalized Difference Water Index (MNDWI) and Soil-Adjusted Vegetation Index (SAVI).

1.3.1. MNDWI computing algorithm

Satellite remote sensing techniques have the ability to map surface water features and monitor the dynamics of surface water. Several techniques are used for the extraction of water information from satellite imagery. One of the important technique is the spectral water index method. MNDWI is one of the spectral water index method for computing water index from satellite imagery. MNDWI is modified NDWI which will enhance open water features while efficiently suppressing and even removing built-up land noise as well as vegetation and soil noise. The MNDWI is expressed as follows (Xu, 2006)

$$MNDWI = \frac{Green - MIR}{Green + MIR}$$

where MIR is a middle infrared band such as band 6 of Landsat satellite.

1.3.2. SAVI computing algorithm

Vegetation indices (VIs) derived from satellite data are one of the primary sources of information for operational monitoring of the Earth's vegetative cover (Gilabert et al., 2002). It is currently an increasing interest in vegetation characterizations with remote sensing techniques (Qi et al., 1994). The Normalized Difference Vegetation Index (NDVI) is a standard algorithm designed to estimate the amount of above-ground green vegetation cover from the measurements of red and near-infrared reflectance bands of the satellite image (Rouse et al., 1974). The disadvantage of this is that it will not be considered external factor effects, such as soil background variations (Huete et al., 1985; Huete, 1989). To enhance and identify the vegetation features more clearly, Huete in 1988 developed a soil-adjusted vegetation index (SAVI) for reducing the soil background effects. The SAVI is expressed as follows (Huete, 1988):

$$SAVI = \frac{NIR - R}{NIR + R + L} 1 + L$$

where NIR is the reflectance in a near-infrared band, R is a red band and L = 0.5 which is a constant to reduce soil noise.

1.4. Spectral signature

Response of electromagnetic energy at the various spectral regions of the material is known as spectral signature (Lillesand & Kiefer, 2005). Spectral signature (spectral reflectance pattern) is an important key to identify and discriminate the various kind of objects on the earth surface. Figure 2 show the spectral reflectance patterns of water, vegetation, urban and open land from the test area. The reflectance of water bodies was generally low, shown in a decreasing order: blue> green> red> near-infrared> mid-infrared (band 6: 1.57 - 1.65 µm) (Wang et al., 2013). There was strong absorption caused by water in near-infrared and mid-infrared regions of the spectrum. Similarly, for the vegetation sample, strong absorption was existing in red band (band 4: 0.64 - 0.67 µm) and high reflectance in the near-infrared (band 5: 0.85 - 0.88µm). Thus, we can clearly distinguish water/vegetation and background features such as shadow, soil, buildings, open land, etc. (Xu, 2006; Wang et al., 2013).

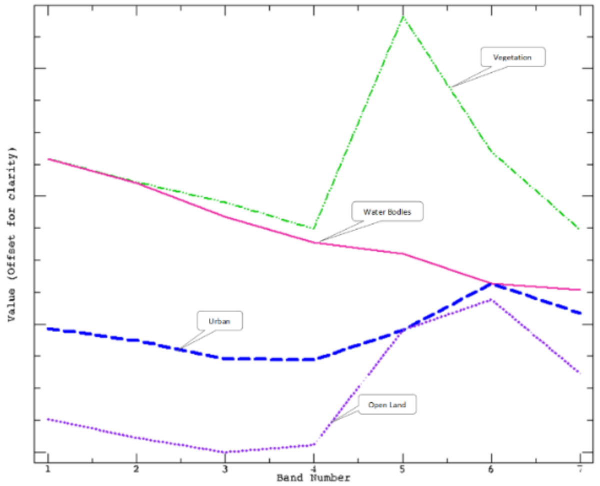

Figure 2. Spectral signature of selected features / object on Landsat image

2. Materials and methods

2.1 Pre-Processing

Landsat-8 Operational Land Imager (OLI) image was downloaded from the USGS data archive database for demonstrating the present study (Figure 8). The test image area covers the North Mumbai area. April month (12 April, 2014) data (cloud free) have been downloaded for the experiment. Table 1 shows the specification of the Landsat - 8 OLI satellite imagery. This image contains eleven spectral bands and all the bands were stacked (layer-stacked) together using image processing software (ERDAS 2010) in a single workstation environment.

Table 1. Shows the specification of the Landsat - 8 OLI satellite imagery

Spectral Band	Wavelength (µm)	Resolution
Band 1 - Coastal / Aerosol	0.433 - 0.453	30 m
Band 2 – Blue	0.450 - 0.515	30 m
Band 3 – Green	0.525 - 0.600	30 m
Band 4 - Red	0.630 - 0.680	30 m
Band 5 – NIR	0.845 - 0.885	30 m
Band 6 – SWIR	1.560 - 1.660	30 m
Band 7 – SWIR	2.100 - 2.300	30 m
Band 8 – PAN	0.500 - 0.680	15 m
Band 9 – Cirrus	1.360 - 1.390	30 m
Band 9 - LWIR-1	10.30–11.30	100 m
Band 11 - LWIR-2	11.50–12.50	100 m

2.2 Algorithm implementation

Figure 3 show a detailed processing flow adopted in this study. Algorithms were implemented in C using CUDA due to its advantages over other GPU APIs (NVIDIA, 2012). CUDA is a general-purpose parallel architecture, with a programming model and software environment that allows developers to use CUDA, a high-level programming language, in applications with fine-grained parallelism and execute them in massive parallel threads (NVIDIA, 2010). Stacked satellite imagery was uploaded to the file system and desired bands (b3, b4, b5 & b6) were read and transferred to DRAM (Dynamic random-access memory) of NVIDIA M2090 GPU using GDAL open-source library. The execution was parallelized using C-DAC's PARAM Yuva-II supercomputer, by assigning one thread per pixel (Figure 4). The computation of output for one pixel in the target image is independent of computing other pixels. We enable one thread to compute one pixel of the original image with CUDA. In the procedure, the grid is divided into blocks and each block is composed of threads. Then each thread can be executed independently to compute the relevant pixel of the target image. We also executed the MNDWI and SAVI algorithms over serial computation approach. Many studies were computed and derived result based on resizing of big satellite imagery into small subsets (e.g., Liu at al., 2014; Gulo at al., 2013; Plaza at al., 2009c; Valero-Lara, 2012) This method computes, pixel by pixel, rows and columns.

1.1.1. PseudoCode of MNDWI parallel Computing

```
void function calculateMNDWI
For(int pixel=0; pixel<no_of_pixels; pixel++) {
    difference = green(pixel) – mir/band-6(pixel)
    sum = green(pixel) + mir/band-6(pixel)
    mndwi(pixel) = difference / sum}
```

1.1.2. PseudoCode of SAVI parallel Computing

```
void function calculateSAVI
For(int pixel =0; pixel<no_of_pixels; pixel++) {
    numerator = nir(pixel) – red(pixel)
    denominator = nir(pixel) + red(pixel) + L
    savi(pixel)= (numerator / denominator) * (1+L)
```

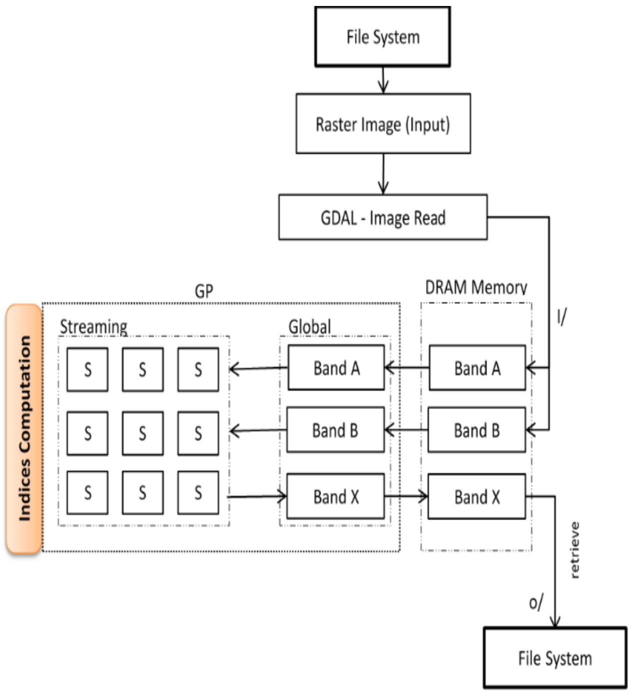

Figure 3. Algorithm implementation and satellite data processing flow

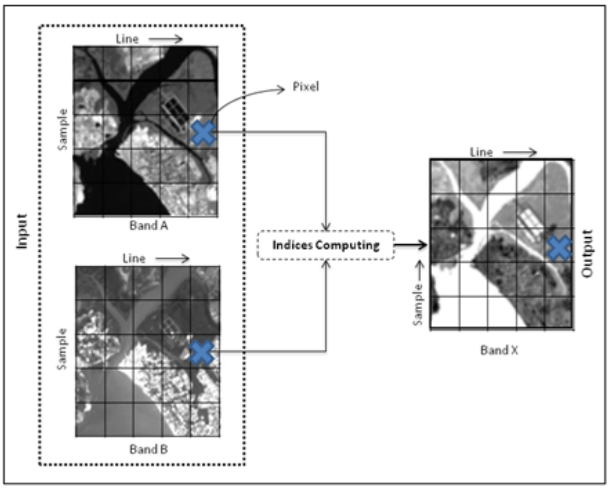

Figure 4. Parallelization methods for indices computation from satellite imagery

3. Experimental results

In this section, the test results are discussed and evaluated. The proposed two different types of indices computations have been tested on NVIDIA CUDA-enabled GPU which is embedded with C-DAC's PARAM Yuva-II supercomputer. A GPU is used for these experiments and it is the NVIDIA™ Tesla M2090, it features 512 processor cores operating at 1.3 GHz, with peak double precision floating point performance of 665 GFlops, Peak single precision floating point performance of 1331 GFlops, total dedicated memory of 6 GB, 1.85 GHz memory (with 384-bit GDDR5 interface) and memory bandwidth of 177GB/s. We implemented MNDWI and SAVI algorithms on GPU parallel and serial approaches for 3 sets of satellite data. The MNDWI and SAVI indices are computed from Landsat 8 OLI satellite imagery. We implemented the spatial distribution of MNDWI and SAVI are shown in Figure 8. The minimum MNDWI and SAVI values of the ground surface are around 0.17, 0.46 and maximum values are around 0.325, 0.81 respectively. The execution time with the total number of pixels in an image is compared to validate the performance (Table 6 & 7). Remote sensing–based spectral indices provide an efficient method in the automated identification of land use and cover classes. In the obtained results it is evident that indices calculation over satellite imagery gave promising results with rapid speed. The results show that big data can be handled much easier with GPU parallel computing model. This technique would be more relevant in handling big satellite data with very large aerial coverage in applications like natural resource monitoring andestimation, urban development, disaster management and agriculture. This result indicates that the execution time depends on the algorithm. Figure 4 show that execution time is rapidly increase with increasing image size (total number of pixels) (Figure 6). Data transfer time i.e., DRAM to GPU memory is considered for calculating the execution time. We can achieve average throughput of 5.67GB/s during memory transfer. The Execution Dependency stall reason occurs if an input dependency is not yet available due to bandwidth constraints. (Figure 7). The number of threads, grid size and block size used in the experiment are given in Table 2, 3 and 4. Table 5 shows results of achieved efficiency on GPU. Statistics of achieved Efficiency on GPU is given in Table 7. We obtained approximately 6x speedup in this test and performance efficiency on GPU is given in Table 2 and 3 and Figure 5.

Table 2. MNDWI computation performance of various test images

Data Set	Total Pixels	Parallel execution time (ms)	Data copy to GPU band1+band2(ms)	Data copy back from GPU (ms)	Total time for parallel execution (ms)	Time for serial execution (ms)	Speed up
Test Image 1	187853031	23	123+123	114	382	2253	6
Test Image 2	377862551	45	249+249	230	772	4669	6
Test Image 3	425061081	52	279+279	258	868	4912	6

Table 3. SAVI computation performance of various test images

Data Set	Total Pixels	Parallel execution time (ms)	Data copy to GPU band1+band2(ms)	Data copy back from GPU (ms)	Total time for parallel execution (ms)	Time for serial execution (ms)	Speed up
Test Image 1	187853031	22	123+123	114	381	1302	3
Test Image 2	377862551	43	249_249	230	770	3221	4
Test Image 3	425061081	49	279+279	258	865	5749	6

Table 4. Parallel execution MNDWI and SAVI

	Test Image 1	Test Image 2	Test Image 3
No of Pixels (Sample*Line)	14241 * 13191	20681*18271	14841*28641
Total Pixels	187853031	377862551	425061081
Execution Time (MNDWI) (ms)	23	45	52
Execution Time (SAVI) (ms)	21	43	49

Table 5. Serial execution MNDWI and SAVI

	Test Image 1	Test Image 2	Test Image 3
No of Pixels (Sample*Line)	14241 * 13191	20681*18271	14841*28641
Total Pixels	187853031	377862551	425061081
Execution Time (MNDWI) (ms)	2253	4669	4912
Execution Time (SAVI) (ms)	1302	3221	5749

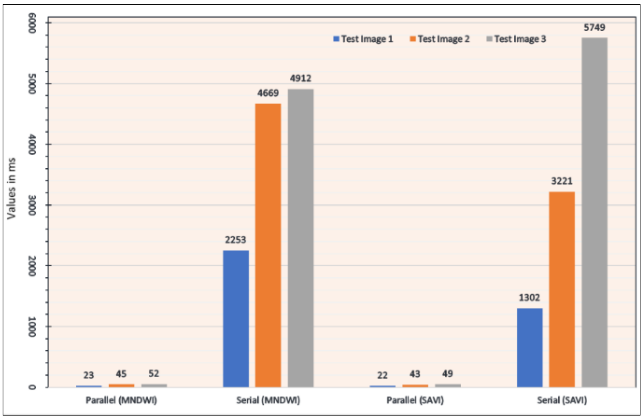

Figure 5. GPU parallel and serial computation performance of various test images

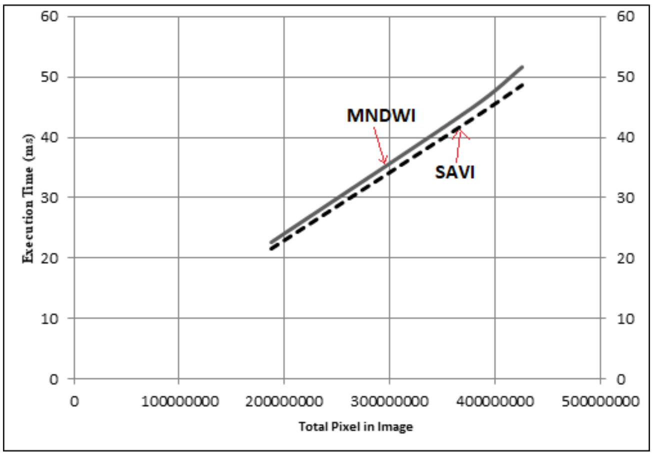

Figure 6. Comparison of execution time with number of pixels

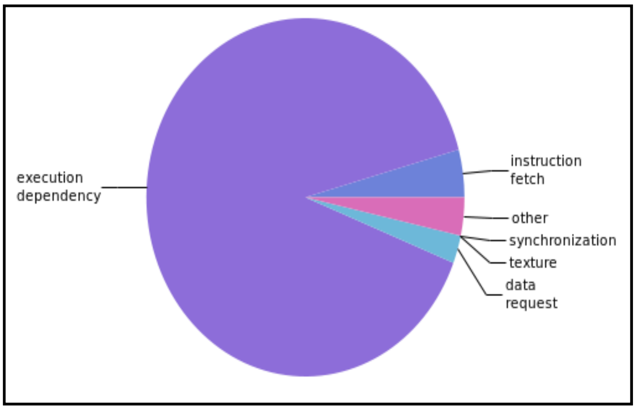

Figure 7. Stall reasons pie chart show high execution dependency, it is because of bandwidth constraints. These long dependencies are typically caused by dependencies on global memory. Pie chart was derived using NVIDIA Visual Profiler.

Table 6. Details of Computational timing

Parameter	Value (MNDWI Computing)	Value (SAVI Computing)
Total no. of threads	187853031 (14241*13191)	187853031 (14241*13191)
Threads that run concurrently	24576 (48 warps each of 32 threads * 16 SM)	24576 (48 warps each of 32 threads * 16 SM)

Table 7. Statistics of achieved efficiency on GPU

Attribute	Details
Achieved Performance	563.559093 GFlops
Achieved occupancy	81.4 %
Warp Execution Efficiency	100 %
Global memory Store Efficiency	100 %
Global memory Load Efficiency	100 %
Branch Efficiency	100 %
Multiprocessor activity	99.9 %

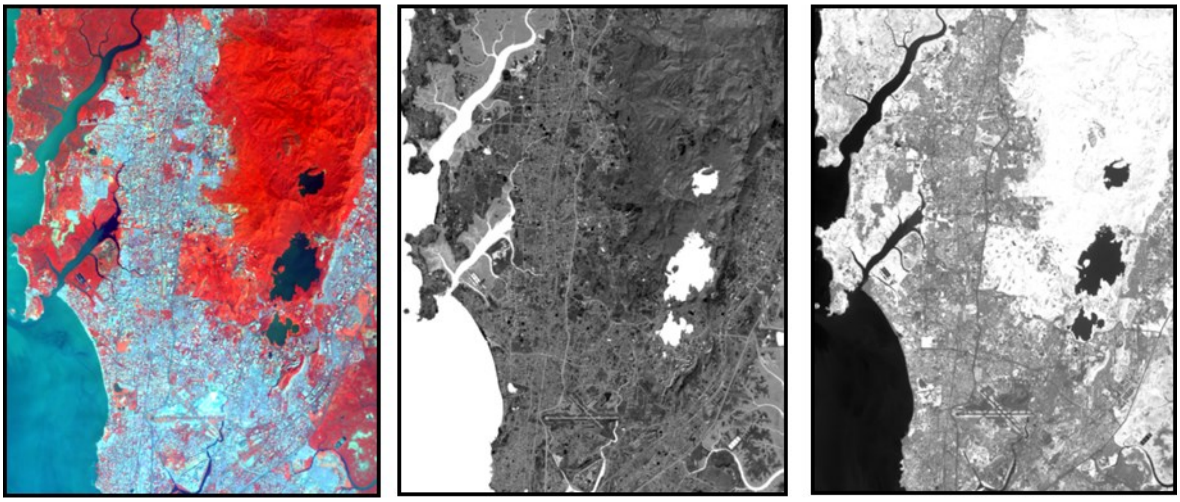

Figure 8. Sample screenshot of input and output image of test area. Left image - FCC (Band: 5, 3, 1) of input Landsat- 8 OLI image; middle image - MNDWI output image, brighter pixels show water features (indices values range 0.17 to 0.325); right image - SAVI output image, brighter pixels show vegetation features (indices values range 0.46 to 0.81)

4. Conclusions

GPUs based parallel computation approach is suitable for rapidly getting useful information from satellite imagery and converting real world information. The implemented MNDWI and SAVI algorithms have been successfully delineated water and vegetation features from multispectral LANDSAT–8 satellite imagery. Based on the random ground validation, it was anticipated that results are in acceptable level. A sufficient speedup of ~ 6X was achieved in this experiment. The achieved performance was 564 GFlops with NVIDIA™ Tesla M2090 GPU. This method can be further extended to computing various indices from different types of optical satellite imageries at high speed. While there are still some essential challenges in this method, the data transfer from DRAM to GPU and vice-versa. Our experimental results are expected to present new insights into implementation of various indices calculation algorithms from satellite imageries at a largescale using parallel computational techniques. The further scope of the study would be experimenting image subset-based computation approach, optimization of performance and utilization of multiple GPUs.

Acknowledgments
The authors acknowledge the C-DAC HPC infrastructure and support provided for this research. The authors thank the manuscript handling editor and anonymous reviewers for their insightful suggestions/comments and careful reading that improved the manuscript.

References

Alvarez-Cedillo J., Herrera-Lozada J. and Rivera-Zarate I. (2014). Implementation Strategy of NDVI Algorithm with Nvidia Thrust. In Image and Video Technology, Springer Berlin Heidelberg, 184-193.

Bernabe S., S. Sanchez, A. Plaza, S. Lopez, J.A. Benediktsson and R. Sarmiento (2013). Hyperspectral Unmixing on GPUs and Multi-Core Processors: A Comparison, Selected Topics in Applied Earth Observations and Remote Sensing, IEEE Journal, 6(3), 1386-1398.

Bhojne M., A. Chakravarti, A. Pallav, and V. Sivakumar (2013). High performance computing for satellite image processing and analyzing–a review. International Journal of Computer applications Technology and research, 2(4), 424-430.

Bilotta G., R.Z. Sanchez and G. Ganci (2013). Optimizing Satellite Monitoring of Volcanic Areas Through GPUs and Multi-Core CPUs Image Processing: An OpenCL Case Study, Selected Topics in Applied Earth Observations and Remote Sensing, IEEE Journal, 6(6), 2445-2452.

Brightwell R., L. Fisk, D. Greenberg, T. Hudson, M. Levenhagen, A. Maccabe, R. Riesen, E. Christophe, J. Michel and J. Inglada (2011). Remote Sensing Processing: From Multicore to GPU, IEEE Selected Topics in Applied Earth Observations and Remote Sensing, 4(3), 643-652.

Cook S. (2013). CUDA Programming: A Developer's Guide to Parallel Computing with GPUs, Morgan Kaufmann Publishers Inc., San Francisco, CA, USA, 1st edition, 1-84.

CUDA. (2013). Toolkit documentation,. Available: https://developer.nvidia.com, 1-38.

Dorband J., J. Palencia and U. Ranawake, (2003). Commodity computing clusters at goddard space flight center, J. Space Commun, 3, 1-1.

Fresse V., D. Houzet and C. Gravier (2011). Evaluation of CPU and GPU architectures for spectral image analysis algorithms. In IS&T/SPIE Electronic Imaging, pp. 78720M-78720M. International Society for Optics and Photonics, 7-128.

Gilabert M. A., J. González-Piqueras, F. J. Garcıa-Haro and J. Meliá, (2002). A generalized soil-adjusted vegetation index. Remote Sensing of Environment, 82, 303-3102.

Gulo C. A., de Arruda, H. F., Sementille, A. C., de Araujo, A. F., Tavares, J. M. R., (2013). Parallelization in GPGPU of an image smoothing method based on a variational model. In ICCEBS2013-International Conference on Computational and Experimental Biomedical Sciences, 1-4.

Huete A. R., (1988). A soil-adjusted vegetation index (SAVI). Remote Sensing of Environment, 25, 295 – 309.

Huete A. R., (1989). Soil influences in remotely sensed vegetation-canopy spectra, in Theory and Applications of Optical Remote Sensing (G. Asrar, Ed.), 107-141.

Huete A. R., R.D. Jackson and D.F. Post (1985). Spectral response of a plant canopy with different soil backgrounds, Remote Sens. Environ,17:37-53.

Jeong I. K., M.G. Hong, K.S. Hahn, J. Choi and C. Kim (2012). Performance Study of Satellite Image Processing on Graphics Processors Unit Using CUDA. Korean Journal of Remote Sensing, 28(6), 6-9.

Jones D.R., R. Elizabeth, B.D.M. Jurrus and A.P. Kenneth (2003). Gigapixel-size real-time interactive image processing with parallel computers, In Parallel and Distributed Processing Symposium, 2003. IEEE Proceedings, 7.

Lee C.A., S.D. Gasster, A. Plaza, C. Chein-I and Bormin Huang (2011). Recent Developments in High Performance Computing for Remote Sensing: A Review, IEEE Selected Topics in Applied Earth Observations and Remote Sensing, 4(3), 508,527.

Li Y. et al., (2020). Big Data and Cloud Computing. In: Guo H., Goodchild M., Annoni A. (eds) Manual of Digital Earth. Springer, Singapore, 1-231.

Lillesand T. M. and R.W. Kiefer (2005). Remote Sensing and Image Interpretation. John Wiley & Sons, Inc. New Jersey, 1-245.

Liu Y., J. Hu (2011). GPU-based parallelization for fast circuit optimization, ACM Trans. Design Automation of Electronic Systems, 16(3), 24:1-14.

Liu P., Yuan, T., Ma, Y., Wang, L., Liu, D.,Yue, S. (2014). Parallel processing of massive remote sensing images in a GPU architecture, computing and informatics, 33(1), 197-217.

Mancino G., A. Nolè, F. Ripullone and A. Ferrara (2013). Landsat TM imagery and NDVI differencing to detect vegetation change: assessing natural forest expansion in Basilicata, southern Italy, iForest-Biogeosciences and Forestry, 76.

NASA. (2013). Landsat Data Continuity Mission Brochure,1-1. Available: http://landsat.gsfc.nasa.gov

Nickolls J. and W.J. Dally (2010). The GPU computing era, IEEE Micro., 30, 56–69.

Niţă I. and A. Olga (2012). Using Multiprocessor Systems for Multispectral Data Processing. U.P.B. Sci. Bull., Series C, 74(4), 1-7.

NVIDIA. (2010). CUDA Programming Guide 3.2. NVIDIA, pp.1-153. Available from: http://developer.down-load.nvidia.com/compute/-cuda/3_2_prod/toolkit/docs/CUDA_C_Programming_Guide.pdf.

NVIDIA®. (2012). Nsight™ Development Platform, Visual Studio Edition 2.2 User Guide 2012, 1-71. [accessed from https://developer.nvidia.com]

Pektürk M. K. and M. Ünal (2018). Performance-Aware High-Performance Computing for Remote Sensing Big Data Analytics, In Data Mining, 69.

Plaza A., (2009 b). Special issue on architectures and techniques for real-time processing of remotely sensed images, J. Real-Time Image Process., 4, 191–193.

Plaza A., J. A. Benediktsson, J. Boardman, J. Brazile, L. Bruzzone, G. Camps-Valls, J. Chanussot, M. Fauvel, P. Gamba, J. Gualtieri, M. Marconcini, J. C. Tilton and G. Trianni, (2009a). Recent advances in techniques for hyperspectral image processing, Remote Sens. Environ., 113, 110–122.

Plaza A., J. Plaza and S. Sánchez (2009c). Parallel implementation of endmember extraction algorithms using NVidia graphical processing units, IEEE International Geoscience and Remote Sensing Symposium, 5, V-208.

Plaza A., D. Qian, C. Yang-Lang and R.L. King (2011b). High Performance Computing for Hyperspectral Remote Sensing, Selected Topics in Applied Earth Observations and Remote Sensing, IEEE Journal, 4(3), 528,544.

Plaza A., J. Plaza, A. Paz and S. Sánchez (2011a). Parallel Hyperspectral Image and Signal Processing (Applications

Corner), Signal Processing Magazine, IEEE, 28(3), 119,126.

Qi J., Al Chehbouni, A. R. Huete, Y. H. Kerr and S1 Sorooshian (1994). A modified soil adjusted vegetation index. Remote sensing of environment, 48(2), 119-126.

Rouse J. W., R.H. Haas, J.A. Schell, D.W. Deering and J.C. Harlan (1974). Monitoring the vernal advancement of retrogradation of natural vegetation (p. 371). Greenbelt, MD: NASA/GSFC (Type III, Final report), 1-43.

Rumanek M., T. Danek and A. Lesniak (2011). High performance image processing of satellite images using graphics processing units, Geoscience and Remote Sensing Symposium (IGARSS), 2011 IEEE International, 559 (561), 24-29.

Tejaswai K.P., D. R. Shanmukha, T. Nair and A. V. V. Prasad, (2013). GPU Accelerated Automated Feature Yang C, M. Sun, K. and Liu et al., (2015). Contemporary computing technologies for processing big spatiotemporal data. In: Kwan M-P, Richardson D, Wang D et al (eds) Space-time integration in geography and GI-Science: research frontiers in the US and China. Springer Netherlands, Dordrecht, 327–351.

Yang Z., Y. Zhu and P. Yong (2008). Parallel image processing based on CUDA. In Computer Science and Software Engineering, 2008 International Conference, 3, 198-201.

Extraction from Satellite Images. International Journal of Distributed & Parallel Systems 4(2), 1-3.

Valero-Lara P. (2012). MRF satellite image classification on GPU, In 2012 41st International Conference on Parallel Processing Workshops, 149-156.

Wang J. and J. Sun (2013). A New Type of NDVI Algorithm Based on GPU Dividing, 1-94.

Wang Y., F. Huang and W. Yuchun (2013). Water body extraction from LANDSAT ETM+ image using MNDWI and KT transformation. In. Geoinformatics, 1-5.

Xu H, (2006). Modification of normalised difference water index (NDWI) to enhance open water features in remotely sensed imagery. International Journal of Remote Sensing, 27(14), 3025-3033.

Static-PPP Behaviour using GPS, GLONASS and Mixed GPS/GLONASS Single/Dual Observations under Different Satellites Geometry Processed by CSRS-PPP Version-3 Service (Riyadh, KSA)

Ashraf Farah[1, 2,*]
[1] College of Engineering, King Saud University, Riyadh, KSA
[2] College of Engineering, Aswan University, Aswan, Egypt
*Email: afarah@ksu.edu.sa

(Received: April 20, 2021; in final form: Sept 24, 2021)

Abstract: Precise Point Positioning (PPP) is GNSS positioning technique that saves cost with acceptable accuracy for enormous applications. PPP proves its efficiency through two decades comparing with traditional Differential positioning technique. PPP uses one receiver collecting observations at unknown station without the need for reference station with known coordinates. PPP-collected observations must undergone extensive mitigation of different GNSS errors. Static-PPP accuracy depends mainly on observations type (dual or single frequency), used systems (GPS or GLONASS or mixed GPS/GLONASS), satellites geometry and observations duration. Since end 2012, PPP users could depend on GLONASS system as an alternative for GPS system or make use of mixed observations from both systems. CSRS-PPP service is used to process PPP observations by millions of users over a decade. CSRS-PPP service updated its software to version 3 end of 2020. This research investigates static-PPP accuracy variation on Riyadh, KSA based on different factors; observations type, used system, satellites geometry and observations duration.

Keywords: Static-PPP, GPS, GLONASS, mixed GPS/GLONASS, CSRS-PPP

1. Introduction

PPP is a standalone Precise Point Positioning approach that uses un-differenced, dual-frequency pseudo range and carrier-phase observations along with precise satellite orbit and clock products to produce decimetre to sub-centimetre positioning in real-time and post-processing (Bisnath and Gao, 2008: Cai, 2009).

Differential Positioning considers for many decades the most accurate positioning technique. The limitations for DGPS are; the need for a reference station, the distance limitation between the rover and reference station, and the need for simultaneous observations between the reference and rover stations, which increases the cost of DGPS over autonomous positioning (Hofmann-Wellenhof and Lichtenegger, 2008). PPP, as a cost-effective technique, requires a single user GNSS receiver, to achieve sub-centimetre horizontal and few centimetres vertical positioning accuracy. Static and kinematic data processing can be done using the PPP technique either in post-processing or real-time mode (Chen and Gao, 2005; Leandro, 2009).

PPP accuracy depends on many factors but mainly on used systems (single or mixed), observations type (single or dual frequency), length of observations, satellites geometry and processing software capabilities. The advancement and modernization of various satellite constellations results in more visible satellites and more observations. A combined use of various satellite systems in PPP is expected to improve the positioning accuracy, reliability and solution convergence period (Soycan, 2012). GLONASS is a global radio-based satellite navigation system operated for the Russian government by the Russian Aerospace Defence Force. It is the only alternative to GPS, which is fully-operational alternative navigation system with global coverage and similar precision. Since 2013, GLONASS had achieved 100% global coverage with a full orbital constellation of 24 satellites. The GLONASS satellites' designs have undergone several upgrades, with the latest version being GLONASS-K (Aggrey, 2014).

PPP- processing software has great impact on resulted PPP-accuracy for different types of observations and different GNSS systems. Processing softwares have different capabilities and different processing scenarios that affect output PPP accuracies. PPP user could use four online PPP services (CSRS-PPP, GAPS, APPS and magicGNSS) (UNB-PPP, 2015). Also, Bernese, processing software could be used for processing PPP observations (Soycan, 2012; Bernese, 2021).

2. CSRS-PPP service

The CSRS-PPP service provides precise post-processed position estimates from GPS/GLONASS observation files. Resulted position estimates are referred to the International Terrestrial Reference Frame (ITRF14). Position estimates are computed for users operating in static or kinematic modes using precise GPS & GLONASS orbits and clocks (CSRS-PPP (a), 2021). Past studies proved efficiency and accuracy of CSRS-PPP service such as (Farah, 2013, 2014, 2016). CSRS-PPP launched its version (3) software on 16 August 2018. CSRS-PPP modernization plan includes PPP-ambiguity resolution, faster convergence using external ionospheric information and processing of multi-GNSS observations (CSRS-PPP (b), 2021).

PPP-Ambiguity resolution processing provides centimetre-level accuracies more rapidly by transforming ambiguous carrier- phase observations into precise ranges. It involves that epochs are first processed in a chronological order to ensure that all information is available prior to resolving ambiguities. Then, starting with the last epoch successfully processed, ambiguity resolution is attempted. This process is repeated for all epochs in reverse order (CSRS-PPP (b), 2021). PPP-ambiguity resolution technique used by CSRS-PPP service has limitations such as; minimum observation duration of 5 minutes is required to resolve ambiguities, resolving GLONASS ambiguities is not applicable, not all ambiguities need to be resolved and successful ambiguity validation needs at least 4 satellites that their ambiguities have been resolved simultaneously (CSRS-PPP (b), 2021).

3. Test study scope

The study investigated effects of different parameters on precision of static-PPP. Those parameters are; used system (GPS or GLONASS or mixed GPS/GLONASS), observations type (single or dual frequency), satellite Geometry (poor DOP or good DOP) and different lengths of observation duration. Two observation sets of 3.5 hrs (GPS day 21233) (16/9/2020) and 5.0 hrs (GPS day 21240) (20/9/2020) was collected with (Sokkia GRX1) (Sokkia, 2021) dual frequency receiver in a station (24° 43' 26.77720" N Lat., 46° 36' 56.53429" E Long., 643.713m height) (2735362.695 m (N), 663416.587 m (E) UTM (North) Zone 38) within King Saud University KSU-campus, Riyadh, KSA, using 1 sec observation interval and 10^{o} cut-off elevation angle. The two observation sets were divided into different lengths of observation duration using TEQC software (TEQC, 2021). The good quality of the collected observations was checked using TEQC software. The different sets of observations were processed and the PPP solutions (WGS-84 datum) were estimated through CSRS-PPP service.

Mission planning process was investigated for the two sets of observations during collecting observations-two days. Graphs of number of visible satellites and DOP values (HDOP, VDOP and PDOP) were plotted for different systems (GLONASS, GPS and mixed GPS/GLONASS). Figure (1) present no. of visible satellites from used constellations for two observed days (GPS day 21233& 21240). Figures 2 and 3 present DOP values (HDOP& VDOP& PDOP) from used constellations for two observed day (GPS day 21233& 21240)

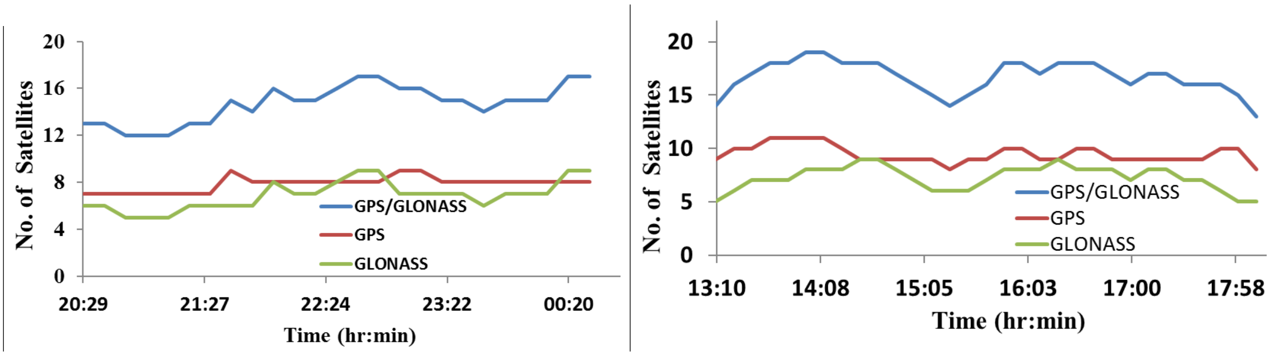

Figure 1. Number of Visible Satellites from (GPS & GLONASS & GPS/GLONASS) During Static Test Observations Collection Period a) GPS day 21233 b) GPS day 21240

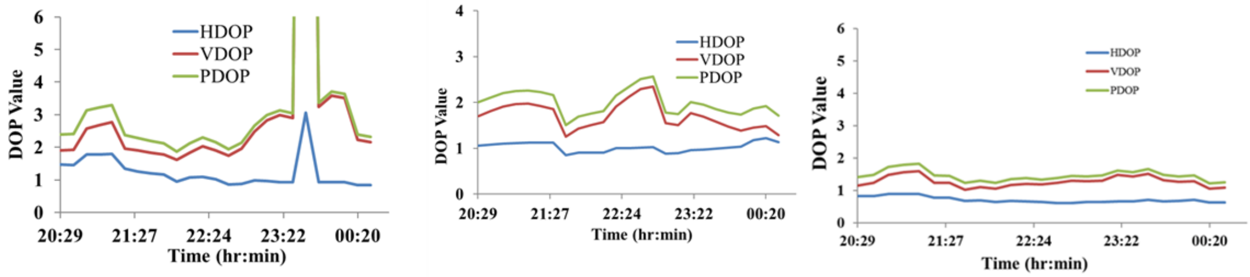

Figure 2. Variation of DOP values (HDOP & VDOP & PDOP) During Static Test Observations Collection Period (GPS day 21233) a) GLONASS b) GPS c) GPS/GLONASS

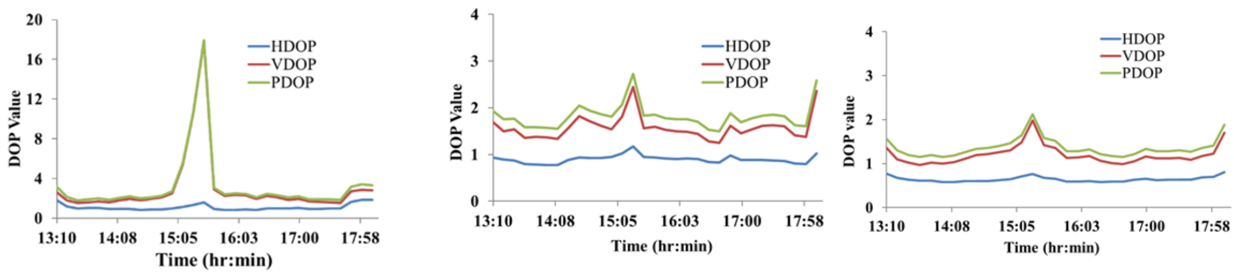

Figure 3. Variation of DOP values (HDOP & VDOP & PDOP) During Static Test Observations Collection Period (GPS day 21240) a) GLONASS b) GPS c) GPS+GLONASS

4. Results

4.1 Dual frequency observations (GPS DAY 21233)

Variation of Static-PPP precision with respect to different duration for dual frequency observations for GPS day 21233 were observed.

The observation in different modes (GLONASS, GPS and mixed GPS/GLONASS) are shown as in Figure 4.

4.2. Single frequency observations (GPS DAY 21233)

Variation of Static-PPP precision with observation duration for different single frequency observations from (GLONASS, GPS and mixed GPS/GLONASS) for GPS day 21233 resulting from this study are presented graphically in Figure 5.

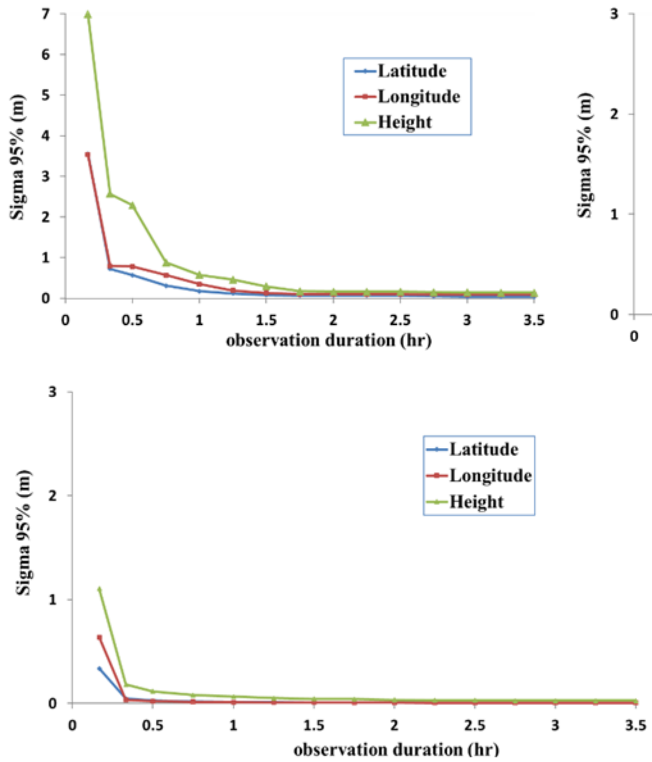

Figure 4. Static-PPP Positioning Precision as a function of observation duration for dual frequency observations (GPS day 21233) a) GLONASS b) GPS c) GPS+GLONASS

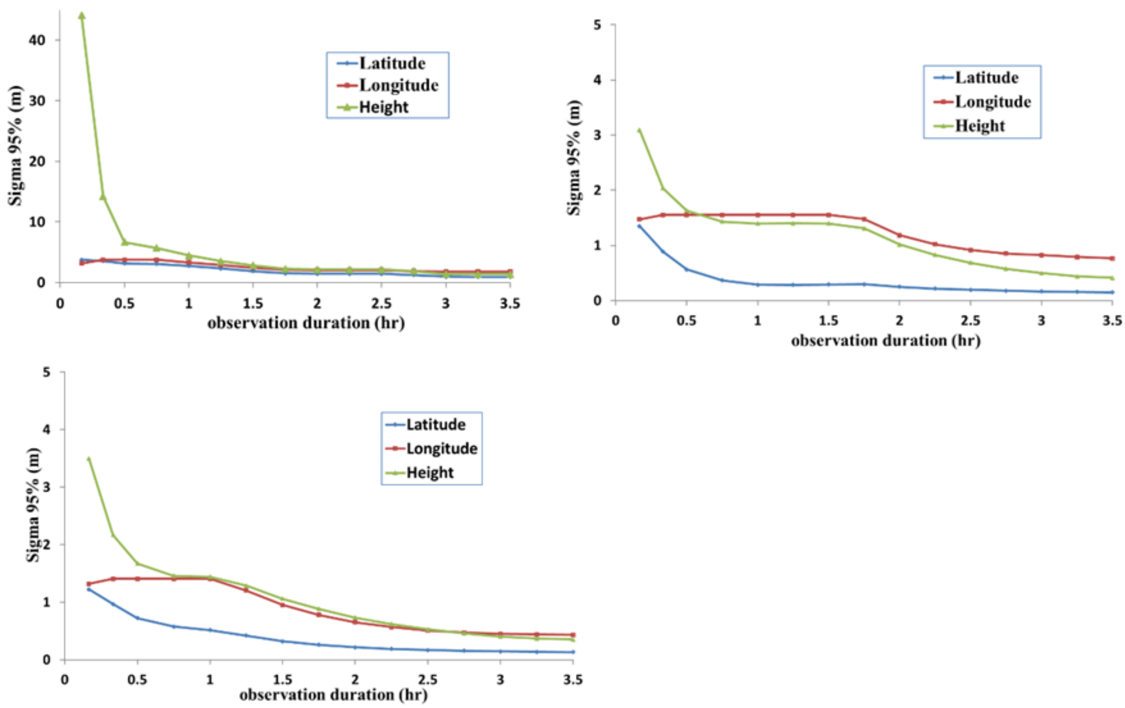

Figure 5. Static-PPP Positioning Precision as a function of observation duration for single frequency observations (GPS day 21233) a) GLONASS b) GPS c) GPS+GLONASS

4.3. Dual frequency observations (GPS DAY 21240)
Variation of Static-PPP precision with observation duration for different dual frequency observations from (GLONASS, GPS and mixed GPS/GLONASS) for GPS day 21240 resulting from this study are presented graphically in Figure 6.

4.4. Single frequency observations (GPS DAY 21240)
Variation of Static-PPP precision & observation duration for different single frequency observations (GPS day 21240) are observed. The observation from (GLONASS, GPS and mixed GPS/GLONASS) are shown in Figure 7

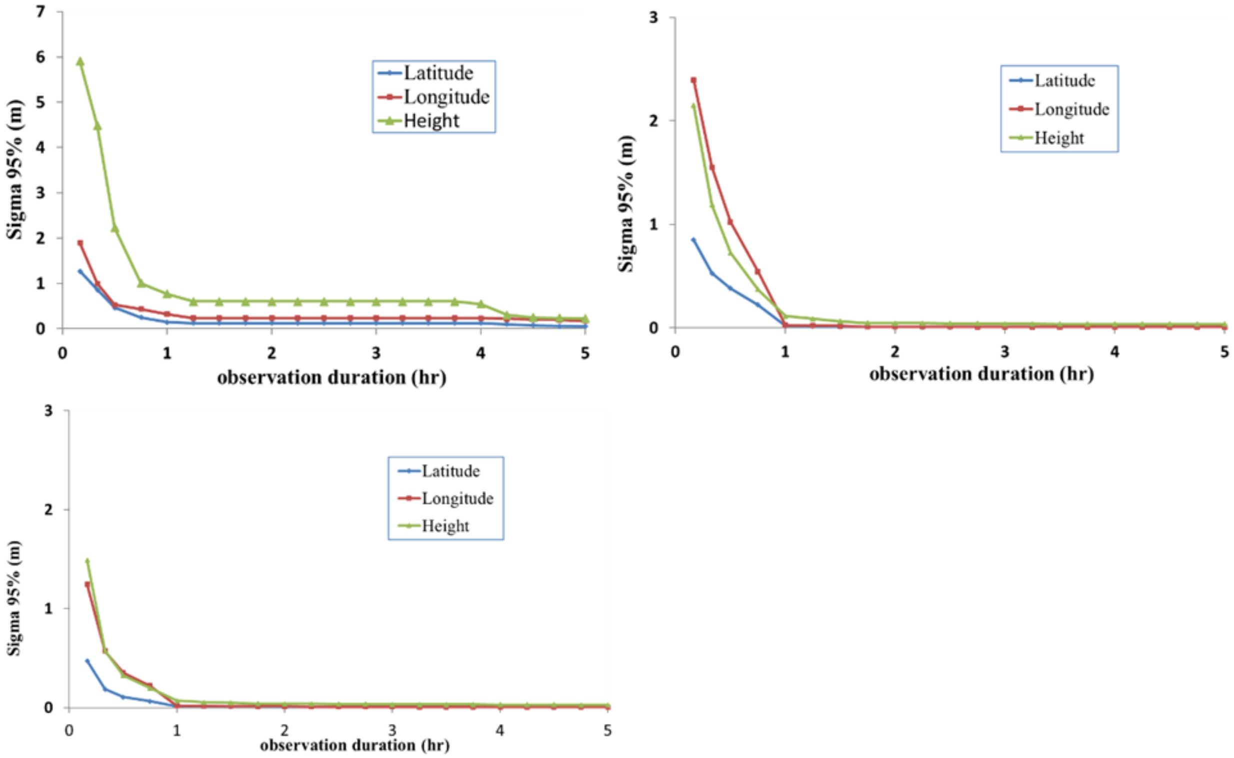

Figure 6. Static-PPP Positioning Precision as a function of observation duration for dual frequency observations (GPS day 21240), a) GLONASS b) GPS c) GPS+GLONASS

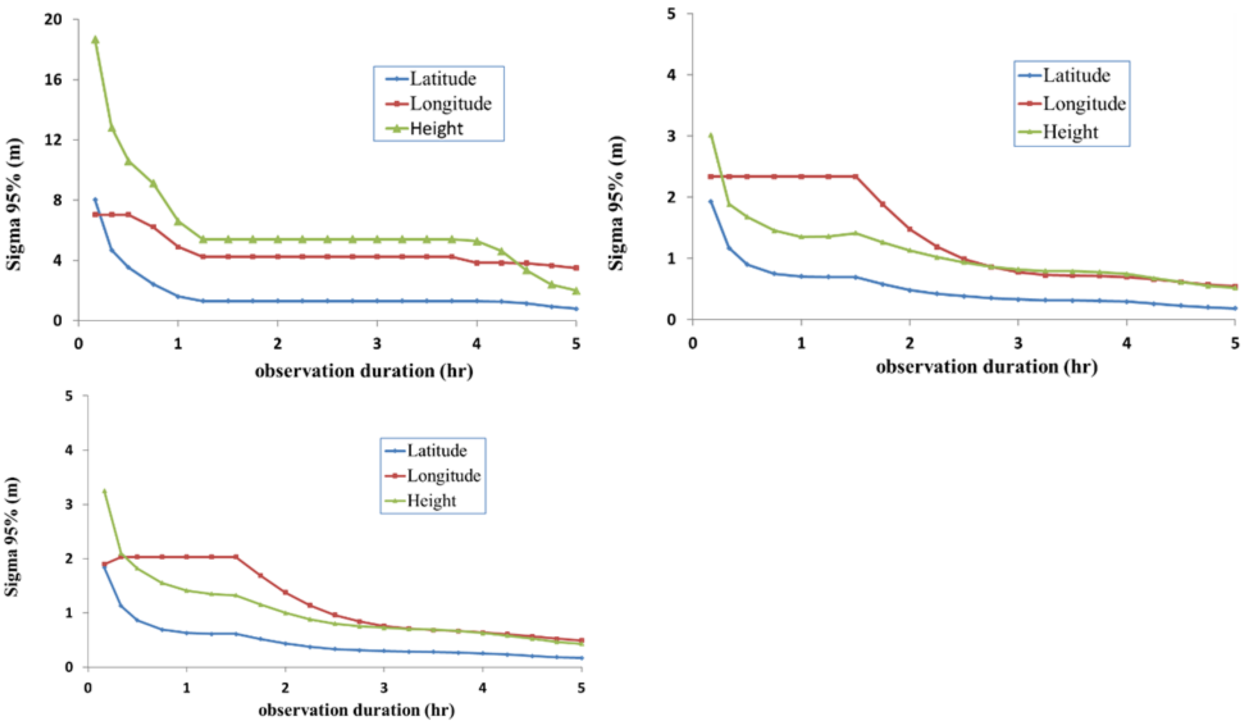

Figure 7. Static-PPP Positioning Precision as a function of observation duration for single frequency observations (GPS day 21240) a) GLONASS b) GPS c) GPS+GLONASS

5. Discussion

Static–PPP accuracy depends basically on satellite geometry, used systems, observations type and observation durations. Those are the parameters that have been studied in this research. Two observation sets were collected on the tested station in two different days (21233& 21240 GPS Day) to reflect different satellite geometry (Figures 1 and 3). The collected observations from GLONASS, GPS and mixed GPS/GLONASS were processed separately to reflect used system effect on static-PPP accuracy. The observations from each system were processed twice as; dual frequency and single frequency observations. The processed observations were varying in observation duration starting from 10 min. to 3.50 hrs (21233 GPS Day) and from 10 min. to 5.0 hrs (21240 GPS Day). The solutions were fixed for (GPS & mixed GPS/GLONASS) observations while they were float for GLONASS observations.

Satellite geometry (number of visible satellites & DOP values) has great effect on resulted static-PPP accuracy (Table 1). Under good satellite geometry, static-PPP accuracy could be improved with more observation duration however this is not the case where satellite geometry is poor as the accuracy could not improve even with more observation duration. This behaviour is shown in (GPS Day 21233) for GLONASS system where the accuracy stands still for dual/single frequency observations for observation duration (2hrs, 2.25 hrs and 2.50 hrs). This behaviour is repeated also in (GPS Day 21240) for GLONASS system where the accuracy stands still for dual/single frequency observations for observation duration (1.25 hrs, 1.5 hrs, 1.75 hrs, 2 hrs, 2.25 hrs, 2.5 hrs, 2.75 hrs, 3.0 hrs, 3.25 hrs, 3.5 hrs and 3.75 hrs). However, GPS system and mixed GPS/GLONASS system behaviour is proving that static-PPP accuracy is directly proportional with observation duration. Total number of GPS satellites and GLONASS satellites for the two test days are 31 and 24 satellites which declare why average number of GPS visible satellites is 7 while average number of GLONASS visible satellites is 6, however average no. of visible satellites for combined GPS/GLONASS system is 14 satellites (GPS Day 21233). For (GPS Day 21240) average number of GPS visible satellites is 9 while average number of GLONASS visible satellites is 7, however average no. of visible satellites for combined GPS/GLONASS system is 16 satellites. It can be concluded also that using a certain system with the same observation type for the same observation duration in two different days does not guarantee the same static-PPP accuracy, which reflects the effect of satellite geometry on resulted accuracy.

GLONASS dual-frequency observation could provide static-PPP horizontal accuracy in the centimetre level and vertical accuracy in the decimetre level by using two hours observation duration. GPS dual-frequency observation could provide static-PPP horizontal and vertical accuracy in the centimetre level by using one-hour observation duration. Mixed GPS/GLONASS dual-frequency observation could provide static-PPP horizontal and vertical accuracy in the centimetre level by using 30 minutes observation duration.

Table 1. Average no. of visible satellites & Average (PDOP & GDOP) values for tested station at tested GPS Days (21233&21240)

GPS Day	System	Avg. no. visible satellites	Avg. PDOP	Avg. GDOP
21233	GPS	7	1.996	2.280
	GLONASS	6	3.958	4.523
	GPS/GLONASS	14	1.459	1.877
21240	GPS	9	1.817	2.075
	GLONASS	7	3.200	3.625
	GPS/GLONASS	16	1.361	1.734

GLONAS single-frequency observation could provide static-PPP accuracy in the sub-meter level for latitude coordinate and sub-two meter level for longitude and height coordinates by using three hours observation duration. GPS single-frequency observation could provide static-PPP horizontal and vertical accuracy in the half-meter level by using four to five hours observation duration. Mixed GPS/GLONASS single-frequency observation could provide static-PPP horizontal and vertical accuracy in the half-meter level by using 2.5 hours observation duration. GPS system provides better behaviour than GLONASS system for both observations types (single & dual frequency). GPS provide saving in observation duration by 50 % to have the same accuracy provided by GLONASS system.
Mixed GPS/GLONASS constellation provides better satellite geometry than depending on single system; GPS or GLONASS. More number of visible satellites and better DOP values are guaranteed. Mixed observations provide saving in observation duration by 50 % to have the same accuracy provided by GPS system. Mixed observations provide much better accuracy than GLONASS system with more than 100% saving in observation duration.

6. Conclusions

This research presents detailed study for main factors affecting static-PPP accuracy; used system (GPS or GLONASS or mixed GPS/GLONASS), observations type (single or dual frequency), satellites geometry (good or poor DOP). It can be concluded that satellites geometry has great impact on output accuracy, so mission planning process is essential.

GPS (31 satellites constellation) is the most reliable system for PPP-users comparing with GLONASS (24 satellites constellation). However, GLONSS current constellation provides strong alternative for PPP users. GLONASS provides similar accuracy to GPS using longer periods of observations duration under favourite satellites geometry conditions. The ideal performance for static-PPP results from using mixed GPS/GLONASS observations, which remedies any poor satellites geometry from any individual system.

Static-PPP accuracy in the centimetre level for horizontal and vertical coordinates could be obtained using dual frequency observations for two hours (GLONASS only) or one hour (GPS only) or 30 minutes (mixed GPS/GLONASS). While, Static-PPP accuracy in the centimetre level for horizontal and vertical coordinates could be obtained using dual frequency observations for two hours (GLONASS only) or one hour (GPS only) or 30 minutes (mixed GPS/GLONASS).

Static-PPP accuracy in the 50 centimetres level for horizontal and vertical coordinates could be obtained using single frequency observations for 2.75 hours (mixed GPS/GLONASS observations) or 5 hours (GPS only). While, Static-PPP accuracy in the 50 centimetres level for horizontal and vertical coordinates could be obtained using GLONASS single frequency observations for more than five hours.

References

Aggrey J. (2014). Multi-GNSS Precise Point Positioning Software Architecture and Analysis of GLONASS Pseudo-range Biases. Master thesis. York University, Canada.

Bernese (2021). Bernese 5.2 user manual. http://www.bernese.unibe.ch/docs/DOCU52.pdf. [Accessed on 3/2/2021].

Bisnath S. and Y. Gao. (2008). Current State of Precise Point Positioning and Future Prospects and Limitations. International Association of Geodesy Symposia, 133, 615-623.

Cai C. (2009). Precise Point Positioning Using Dual-Frequency GPS and GLONASS Measurements. Calgary: UCGE Reports No. 20291, 40-52.

Chen K. and Y. Gao. (2005). Real-Time Precise Point Positioning Using Single Frequency Data, Proceedings of the 18th International Technical Meeting of the Satellite Division of The Institute of Navigation (ION GNSS 2005), Long Beach, CA, September 2005, 1514-1523.

CSRS-PPP (2021a). CSRS-PPP: Canadian Spatial Reference System (CSRS) Precise Point Positioning (PPP) service. http://www.geod.nrcan.gc.ca/products-produits/ppp_e.php (2013). [Accessed on 3/2/2021]

CSRS-PPP (2021b). CSRS-PPP version 3 tutorial. https://webapp.geod.nrcan.gc.ca/geod/tools-outils/sample_doc_filesV3/NRCan%20CSRS-PPP-v3_Tutorial%20EN.pdf. [Accessed on 3/2/2021]

Farah A. (2013). Effect analysis of GPS observation type and duration on convergence behaviour of static PPP". Journal of Geomatics, 7(2).

Farah A. (2014). Assessment study of static-PPP convergence behaviour using GPS, GLONASS and mixed GPS/GLONASS observations. Artificial Satellites Journal of Planetary Geodesy, 49(1), DOI: 10.2478/arsa- 2014-0005

Farah A. (2016). Accuracy evaluation for online Precise Point Positioning Services". Journal of Geomatics, 10(1).

Hofmann-Wellenhof B. and H. Lichtenegger (2008). "Global Navigation Satellite Systems. New York: Springer Wien, 33-58.

Leandro R. F. (2009). Precise point positioning a new approach for positioning, atmospheric studies, and signal analysis." Fredericton, New Brunswick, Canada, Technical Report No. 267,

Sokkia (2021). Sokkia-GRX1 operator's manual. https://eu.sokkia.com/sites/default/files/sc_files/downloads/7010-0965- rvc_grx1_om_secured .pdf. [Accessed on 3/2/2021]

Soycan M. (2012). A quality evaluation of precise point positioning within the Bernese GPS Software Version 5.0. Arabian Journal for Science and Engineering, 37(1), 147–162.

TEQC (2021). TEQC-UNAVCO tutorial.http://facility.unavco.org/software/teqc/doc/UNAVCO_Teqc_ Tutorial.pdf. [Accessed on 4/2/2021]

UNB-PPP (2021). The precise point positioning service. University of New Brunswick (UNB) http://www2.unb.ca/gge/Resources/PPP/OnlinePPPs.html . [Accessed on 10/2/2021]

Land Cover classification of Punjab state using Sentinel-2 data and Machine Learning within the Google Earth Engine Cloud Platform

Harpinder Singh*, Aarti Kochhar, P.K. Litoria and Brijendra Pateriya
Punjab Remote Sensing Centre, Punjab Agricultural University Campus, Ludhiana, Punjab, India
*Email: harpinder13@gmail.com

(Received: August 13, 2021; in final form: Oct 7, 2021)

Abstract: Change of land use and land cover over the past few years has severely affected the environment and has led to land degradation. The need for mapping and classification of land cover has become fundamental for monitoring, supporting and decision making for the environment and ecosystem related issues. Classification of land cover on a large scale, like for a complete state or country, is an extensive task and requires a lot of resources (computing power, storage, time). This paper explores the computing capabilities of Google Earth Engine (GEE) for producing a land cover classification of Punjab state in India. Random Forest (RF) machine learning algorithm has been used to classify the Sentinel-2 satellite data. In addition to the satellite imagery, four spectral indices (NDVI, NDBI, MNDWI and BSI) were generated from the Sentinel-2, and the slope and elevation layers were generated from the ALOS (Advanced Land Observing Satellite) data. These datasets have been used to improve classification accuracy. Punjab has been classified into five classes: built-up, bare soil, water, vegetation and sand. The overall accuracy of 94.98% was achieved with a kappa index of 0.93. Collaboration of Sentinel-2 dataset, Google's high-resolution imagery and local knowledge to create training and validation points is another key strength of this research work.

Keywords: Machine Learning, Random Forest, GEE Cloud Computing, Land Cover, Sentinel-2, ALOS

1. Introduction

Land use helps understand the arrangement for which humans are using land, and land cover helps identify the physical features present on the earth's surface. Many factors like growing population, deforestation, loss of biodiversity, industrialization etc., are associated with the change of land use and land cover. The study of land use, land cover and its change can help us understand the environment and the ecosystem (Gillespie et al., 2008). Such data is an essential prerequisite for analyzing an area's environment processes and problems (Anderson, 1976).

Satellite remote sensing has provided a new paradigm in land use and land cover studies and monitoring of other environmental factors (Wulder et al., 2018). The potential of satellite remote sensing can be further enhanced by combining it with Artificial Intelligence (AI) for future applications. Machine learning (ML), a subset of artificial intelligence technology, gets a computer to work on a perception basis like human beings. Machine learning uses statistical techniques to allow the computer to "learn" with data without being explicitly programmed. Triggered from an abundance of free data from remote sensing, its collaboration with ML has helped dig out the depths of satellite imagery that are difficult to follow with human visual interpretation.

Primary use cases of remote sensing and AI collaboration are image classification, object detection, semantic segmentation and instance segmentation. In image classification, a label is assigned to a complete image (of a patch of the earth). In object detection, an algorithm finds an object within the image, for example, finding houses with swimming pools using aerial imagery. Each image pixel is separately classified in semantic segmentation, and instance segmentation is for precise 3D object detection.

Although satellite remote sensing is extremely useful, downloading, storing, and analyzing such BIG datasets require specialized hardware and software. Chi et al. (2016) discuss various problems related to the BIG geospatial data processing systems. It is not possible to run complex machine learning algorithms on satellite imagery using simple desktop resources. Ma et al. (2015) reviews techniques like parallel processing, clusters and cloud computing as solutions to the BIG geospatial analytics problems discussed above. There are many cloud computing platforms available for geospatial big data analytics, to name a few include Earth on Amazon Web Services (AWS), Azure-AI for Earth and Google Earth Engine (GEE). GEE, the most popular, provides a ready to use platform with high computational capabilities for planetary-scale geospatial big data analytics (Gorelick et al., 2017). It is provided free of cost for research purposes. GEE hosts capabilities for simple and complex mathematical algorithms, image processing techniques and machine learning operations. In addition to the analytical algorithms, it also contains a petabyte catalogue of freely available satellite imagery and other geospatial datasets. It helps perform various spectral and spatial analyses on a single satellite image and a batch of images. GEE library includes both supervised and unsupervised machine learning algorithms (Amani et al., 2020). For efficient image processing, GEE uses Java Just-In-Time (JIT) compiler to optimize pixel-based operations.

GEE has spread across a wide range of remote sensing applications. The most widely studied application areas include land use, land cover and crop mapping, agriculture, climate change and disaster management (Tamiminia et al., 2020; Mutanga and Kumar, 2019). Other applications include studies involving water bodies (including rivers, lakes, oceans etc.), natural disasters, wetlands, forests, climate change, urban, soil, archaeology, habitat mapping and nuclear non-proliferation. GEE has a variety of applications in data processing, like radiometric correction, cloud detection, and mosaic image generation (Tamiminia et al., 2020).

Ghorbanian et al. (2020) used the Sentinel-1 and Sentinel-2 satellite datasets in the GEE platform to generate a land cover map with 13 classes of the entire country of Iran. Iran was covered using 67 satellite scenes in ascending mode and 63 scenes in descending mode. A pixel-based RF algorithm was implemented for developing the land cover maps. Simple Non-Iterative Clustering (SNIC) was incorporated for post-classification segmentation. Handling 11,994 and 2,889 scenes of Sentinel-1 and Sentinel-2, respectively, was possible only with the high computation capacity of GEE. In a similar study, Sun et al. (2019) produced an urban-land map for China using Sentinel-1A SAR (Synthetic Aperture Radar) and Sentinel-2 optical imagery. Mountain pixels were masked using slope images from SRTM (Shuttle Radar Topography Mission) DEM data. The final output was a binary classified land cover map with two classes: urban and non-urban. The overall accuracy of 88.03% was achieved in this research over the GEE cloud platform. The capabilities of GEE are such that the land cover classification map for the entire globe, continent or country can be prepared using a simple desktop computer. A 10m resolution land cover map of the entire Africa has been prepared by Li et al. (2020) using Sentinel-2 satellite data.

Parente et al. (2018) developed 17 temporal series maps for land use of pastureland in Brazil using Random Forest (RF) algorithm and MODIS (Moderate Resolution Imaging Spectroradiometer) data. Tsai et al. (2018) classified the area of Fanjingshan National Nature Reserve using decision tree and RF algorithms. Since the area is mountainous and prone to clouds, CFmask products were used for the analysis. Landsat 5 TM and Landsat 8 OLI products were used within the GEE platform. NDVI, Normalized Difference Green and Red (NDGR), Normalized Difference Shortwave Infrared and Near Infrared (NDII), MSAVI (Modified SAVI), and Spectral Variability Vegetation Index (SVVI) were calculated and further used for the classification work. The initial mapping of seven classes was further categorized into four classes: built-up, agriculture, forest, and bamboo/conifer vegetation, to avoid discretion issues.

Besides focusing on urbanization, land use and land cover modelling have also been used to map coastal wetland areas. Farda (2017) studied the area of Segara Anakan Lagoon, Indonesia using Landsat 3 MSS, Landsat 5 TM, Landsat 7 ETM and Landsat 8 OLI. ASTER GDEM (Advanced Space borne Thermal Emission and Reflection Radiometer Global Digital Elevation Model) was additionally incorporated for elevation data. After comparing various machine learning algorithms on GEE, it was concluded that the highest accuracy for land use mapping of the coastal wetland is with the CART (Classification and Regression Tree) algorithm.

2. Research gaps and objectives

Based on a broader review of GEE based studies, only 12% focused on Land cover applications. The total contribution of India in GEE based studies, including all applications, were only 5%. While the contributions for land cover studies of Indian regions using GEE is negligible.

1) The proposed framework provides a reliable land cover map of the complete Punjab state of India.
2) Most of the studies in the literature have analyzed Landsat based satellite products. The proposed framework provides land cover at 10m resolution using the Sentinel-2 earth observation data. The latest images of January-February (2020) were retrieved for the study.
3) Classification of land cover on a large scale, like for a complete state or country, is an extensive task and requires a lot of resources (computing power, storage, time). GEE can be very useful for such studies, but only a few papers have focused on utilizing its benefits. According to the literature review, there are very few studies in India involving GEE based land cover classification over large areas, e.g. states in India.

3. Study area and datasets

In this section, the study area is first introduced and subsequently, the information about the satellite datasets is provided.

3.1. Study area

The study area is Punjab State, part of the Indus plain, which covers a geographical area of 50,362 sq. km. It lies between 29^0 33’ & 32^0 31’ N latitude and 73^0 53’ & 76^0 55' E longitude. The state experiences three distinct seasons, the hot season from April to June, the rainy season from July to September and the winter season extending from October to March. The Punjab state is intensively cultivated. The cropping pattern of Punjab shows a predominance of wheat, rice and cotton. For this research, based on Punjab's dominant land cover classes, we generalized the classes as built-up, vegetation, water, bare soil, and sand.

3.2. Datasets

Sentinel-2 is a wide-swath, high-resolution and multi-spectral imaging mission by the European Space Agency (ESA). It is popular, free and open satellite imagery. This earth observation dataset with a swath of 290Kms consists of 13 spectral bands (443–2190 nm). The spatial resolution of four visible and near-infrared bands of Sentinel-2 satellite is 10m, 20m for the six red edge and shortwave infrared bands and 60m for the three atmospheric correction bands. Sentinel-2 revisits after ten days, but since it is a constellation of two satellites phased out at 180 degrees, the cycle remains for only five days. The images of January-February 2020 were retrieved from the GEE image library for image processing and analysis.

ALOS (Advanced Land Observing Satellite) World 3D is a global digital surface model (DSM) dataset by Japan Aerospace Exploration Agency (JAXA) (ALOS). It has a horizontal resolution of approximately 30 meters. It is based on the DSM dataset of the World 3D Topographic Data (5-meter mesh version).

4. Methods

GEE has been used for image processing and analysis for this research. The methods include filtering the images based on the cloud cover, creation of the composite image, generating various indices and adding them to the satellite image to create an image stack, generation of the training and validation datasets, applying machine learning classifier, generating classification maps, and assessing accuracies of the classified map. The methodology of the research is as shown in Figure1.

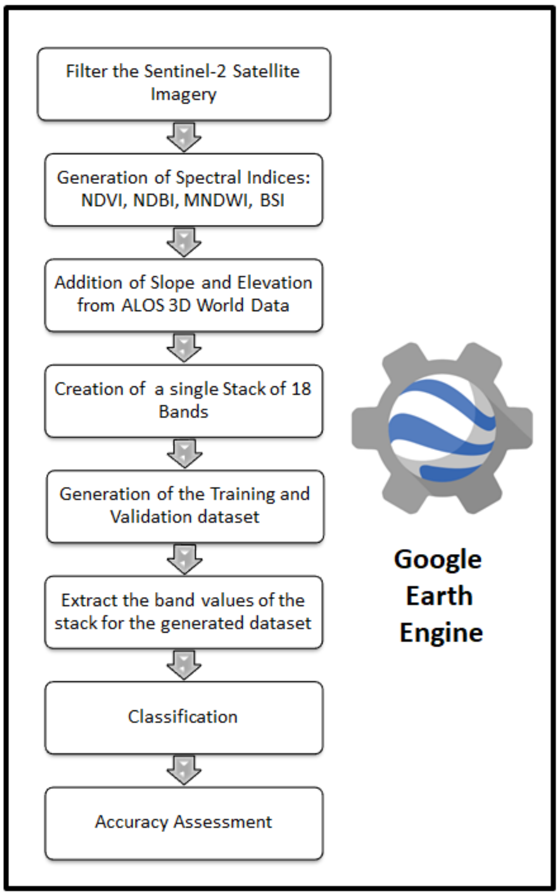

Figure 1. Research Methodology

4.1. Multi-Sensor image stack

The Sentinel-2 images were filtered based on three parameters cloud cover, study area boundary and acquisition date. The images acquired between 01-Jan-2020 and 29-Feb-2020were selected. The Sentinel-2 metadata MSK_CLDPRB (Cloud Probability Map), MSK_SNWPRB (Snow Probability Map) and CLOUDY_PIXEL_PERCENTAGE were used to filter out images with clouds and snow. Images with a cloud probability of less than 10% were considered. The Sentinel2 cloud masking function "maskS2clouds" provided in the GEE, has been used to mask individual cloud pixels. A median composite image was generated with all the filtered images. This composite had all the twelve spectral bands which are available in a Sentinel-2 image.

The slope and elevation layers were generated from the ALOS dataset. The band AVE_DSM (Height above sea level) was used for this purpose. Finally, these two bands were also added to the stack of twelve images taking the count to fourteen.

4.2. Spectral indices

Spectral indices are extensively used in the existing literature for land cover mapping. As these indices are based on expert knowledge, they enhance and help identify the land cover classes, such as vegetation, urban, water and bare soil. Thus, for this research, we adopt four popular spectral indices: Normalized Difference Vegetation Index (NDVI) (Rouse et al., 1974), Normalized Difference Built-up Index (NDBI) (Zha et al., 2003), Modified Normalized Difference Water Index (MNDWI) (Xu, 2006) and the Bare Soil Index (BSI) (Roy, 1997). These four spectral indices are closely associated with the land cover classes defined in our study; their formulas are summarized in Table1.

These four indices were generated from the Sentinel-2 composite and were added to the previous stack of images. The final stack to be used for the classification consisted of eighteen bands.

4.3. Training and validation set generation

The training and validation set were generated in the GEE environment. This dataset was generated very carefully for built-up, vegetation, water, bare soil and sand classes, based on the local knowledge, Sentinel-2 and Google's high-resolution imagery. In this dataset, 388 points represented urban, 157 as bare, 205 as water, 230 as vegetation and 217 as sand. The distribution of all the points is as shown in Figure2. This figure also shows the Sentinel-2 composite of Punjab in the background. These points were used to sample and extract the pixel values of all the eighteen bands from the previous steps. Seventy per cent of points were selected for the training and thirty per cent for the validation of the classification.

4.4. Classification

GEE provides many supervised classification algorithms like RF, SVM and Maximum Likelihood Classification (MLC) for image classification. For this study, an RF classifier is chosen as the supervised classification method for land cover mapping.

RF is an ensemble classifier that consists of many classification trees. During classification, a pixel is assigned a class label by each decision tree, and the class which gets the maximum votes is assigned to the pixel. The overfitting issue can be controlled as only a subset of the training data is used to train each decision tree. RF is flexible and fast while dealing with large, multi-dimensional datasets. It is a popular choice in the remote sensing community for the classification of earth observation datasets. For this research, 50 trees have been selected which meet the computation time and accuracy requirements. The scale of analysis is determined by the argument provided to the scale parameter in sampling and reduction steps i.e. 10 m for this research. Therefore, the resolution of the classified output raster is 10m.

Table 1. Spectral indices used in this research

S. No	Index	Details	General Formula	Application	Reference
1	NDVI	Normalized Difference Vegetation Index	(NIR - RED) / (NIR + RED)	Vegetation's photosynthetic activity (greenness)	(Rouse *et al.*, 1974)
2	NDBI	Normalized Difference Built-up Index	(SWIR - NIR) / (SWIR + NIR)	Automatically mapping urban areas	(Zha *et al.*, 2003)
3	MNDWI	Modified Normalized Difference Water Index	(Green - SWIR) / (Green + SWIR)	Enhancing water bodies	(Xu, 2006)
4	BSI	Bare Soil Index	((SWIR+R)−(NIR+B))/((SWIR+R)+(NIR+B))	Enhancing bare soil areas, fallow lands	(Roy *et al.*, 1997)

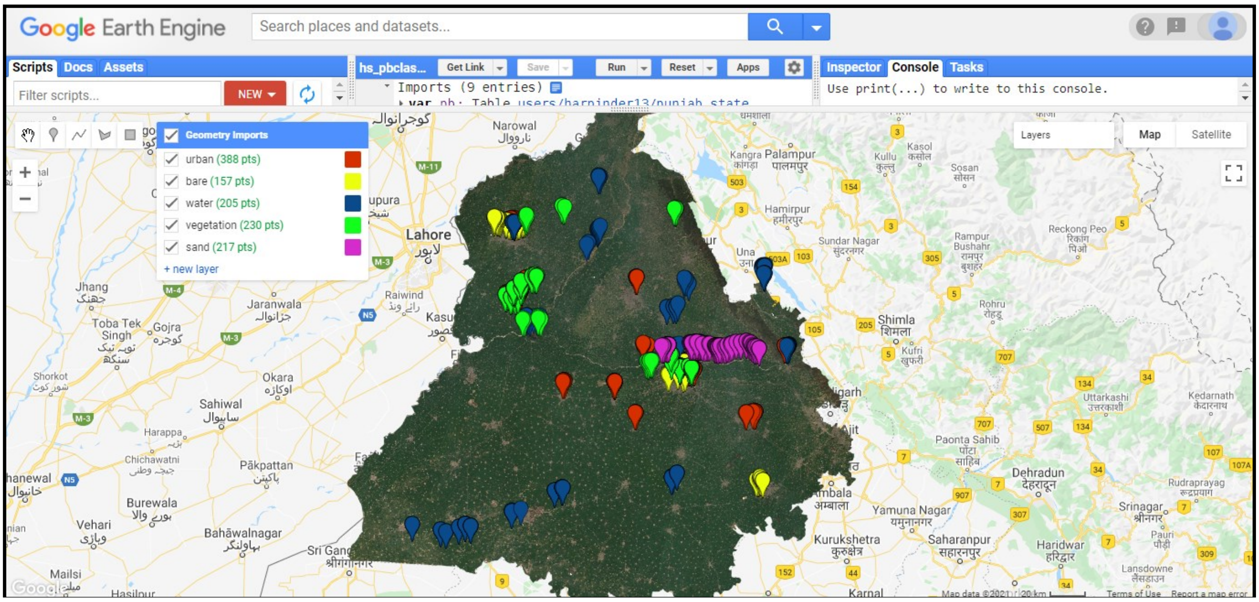

Figure 2. Training and Validation Dataset

4.5. Accuracy Assessment

A confusion error matrix was generated with the process chain to understand the overall user and producer accuracies. Overall accuracy was calculated to an agreement between the map and the reference information with the kappa index.

5. Results and Discussion

The accuracy assessment results using the RF classifier for land cover classifications are shown in a confusion matrix in Table2. The results showed that the RF classifier produces the potential agreement for overall classification with 94.98% accuracy. According to the user classification accuracies, water has the maximum (100%), and the bare class has the least values (87.75%). The Kappa statistic, a metric that compares an observed accuracy with an expected accuracy (random chance), is satisfactory with a value of 0.93.

Whole of Punjab state has been classified for land cover (Figure 3). Figure4 shows the classification results of a zoomed part of the Ludhiana district.

The Sentinel-2 dataset has been used for this research because it has the best spectral and spatial resolution among all the freely available Earth Observation (EO) datasets. This dataset has been filtered to January and February as the wheat crop, which covers a large area of Punjab, is greenest during this time, and there is less mixing of spectral signatures of various land cover classes. the start of the research, only four land cover classes were selected, but during the classification, it was found that there was a lot of mixing between the river sand and urban class. The sandy areas were not being classified as bare soil but as urban areas. Therefore, a new land cover class (sand) was created. Also, the forests, orchards and plantations are included in the vegetation class.

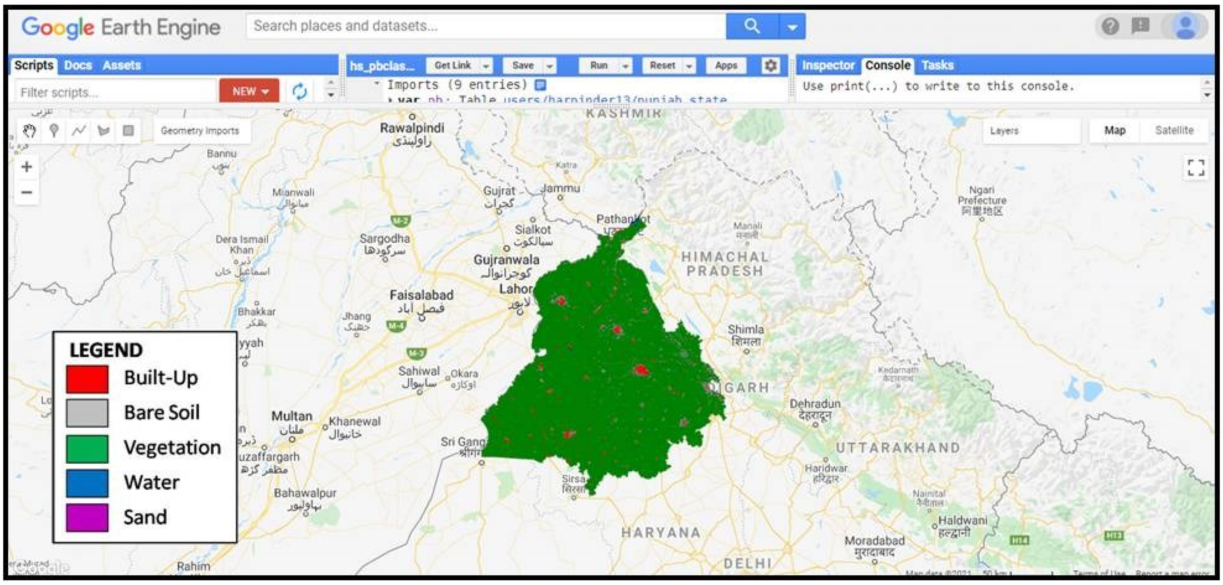

Figure 3. Classified land cover of Punjab State

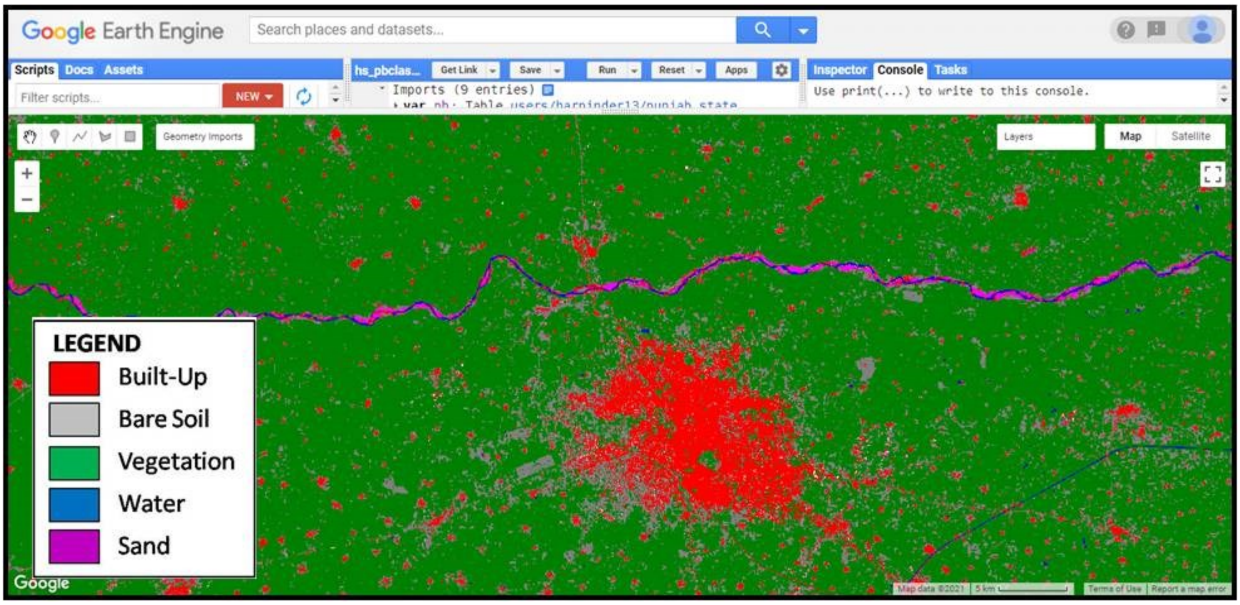

Figure 4. Classified land cover of part of Ludhiana district

Table 2. Classification Accuracy Assessment (Confusion Matrix)

	Truth Data							
Classifier Results	**Class**	**Urban**	**Bare**	**Water**	**Vegetation**	**Sand**	**Classification Overall**	**User's Accuracy (Precision)**
	Urban	120	3	0	1	4	128	93.75%
	Bare	5	43	0	1	0	49	87.75%
	Water	0	0	98	0	0	98	100%
	Vegetation	2	5	0	93	0	100	93%
	Sand	2	0	0	0	82	84	97.61%
	Truth Overall	129	51	98	95	86	459	
	Producer's Accuracy (Recall)	93.02%	84.31%	100%	97.89%	95.34%		
	Overall Accuracy (OA)	94.98%						
	Kappa	0.93						

The spectral responses for each band(Sentinel-2) for each class is represented as a spectral signature plot. The average spectral signature plot for the training data is shown in Figure5. Figure6 shows the average spectral signatures (Indices) for the five classes of Training dataset. These charts helps in visually determining the separability of classes and the quality of the training dataset. According to the two figures we can see that the classes have very different signatures. Therefore, the RF classifier is able to separate them well.

The random forest(RF) variable importance plot has been shown in Figure7. According to the plot, the top five important parameters for the classification are elevation, B1 (Ultra Blue/Coastal aerosol), NDVI, B11 (Short Wave Infra Red) and B2(Blue). Slope is the least important parameter. NDVI and BSI are more important than MNDWI and NDBI.

The classification accuracy is measured and analyzed using the confusion matrix, but visual inspection of the results and local land cover knowledge plays an important role. Therefore, the training and validation datasets were created in a phased manner; few data points were generated, and the classification was attempted. The results were visually inspected, the misclassified areas were identified and based on local knowledge, and the Google satellite imagery, more training data points were generated. This process was continued until the results were visually correct and the overall classification accuracy was satisfactory.

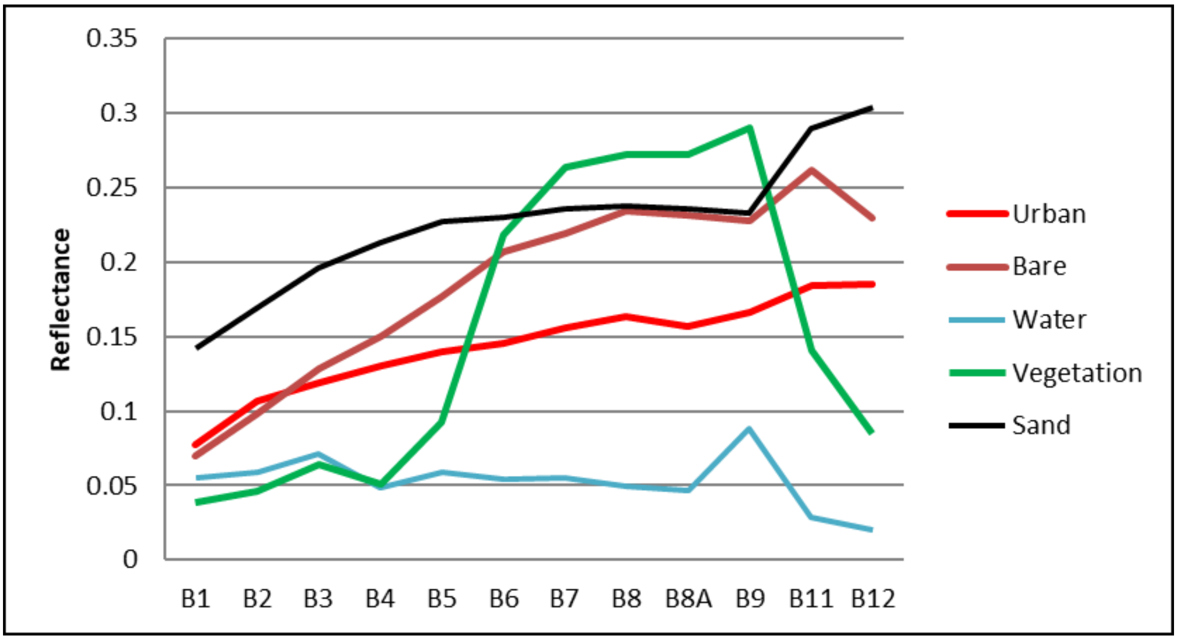

Figure 5. Average spectral signatures (Sentinel-2 bands) for the five classes of the training dataset

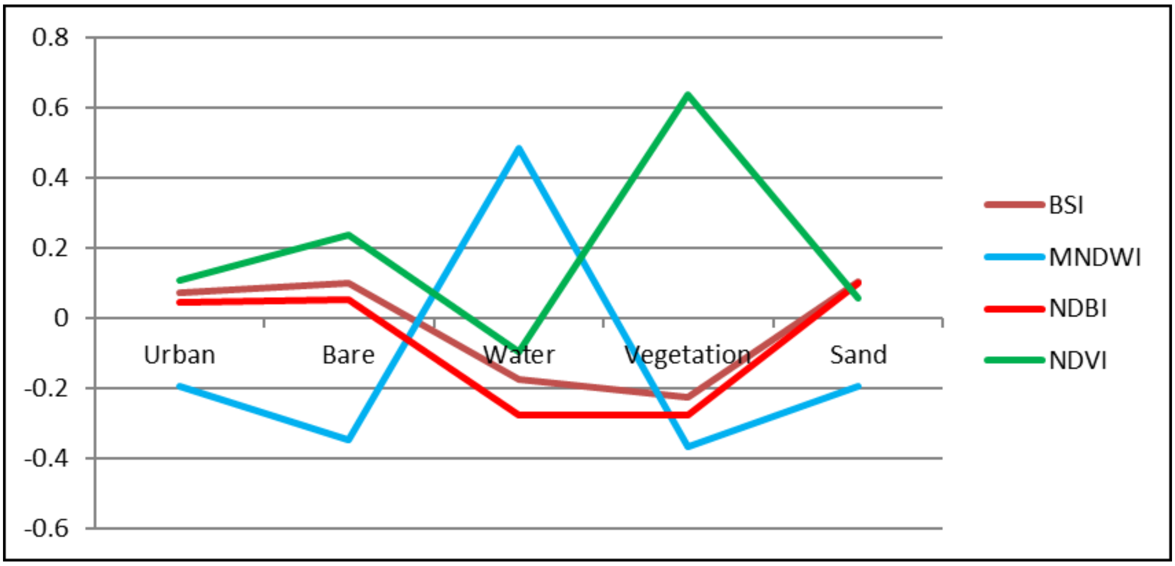

Figure 6. Average spectral signatures (Indices) for the five classes of the training dataset

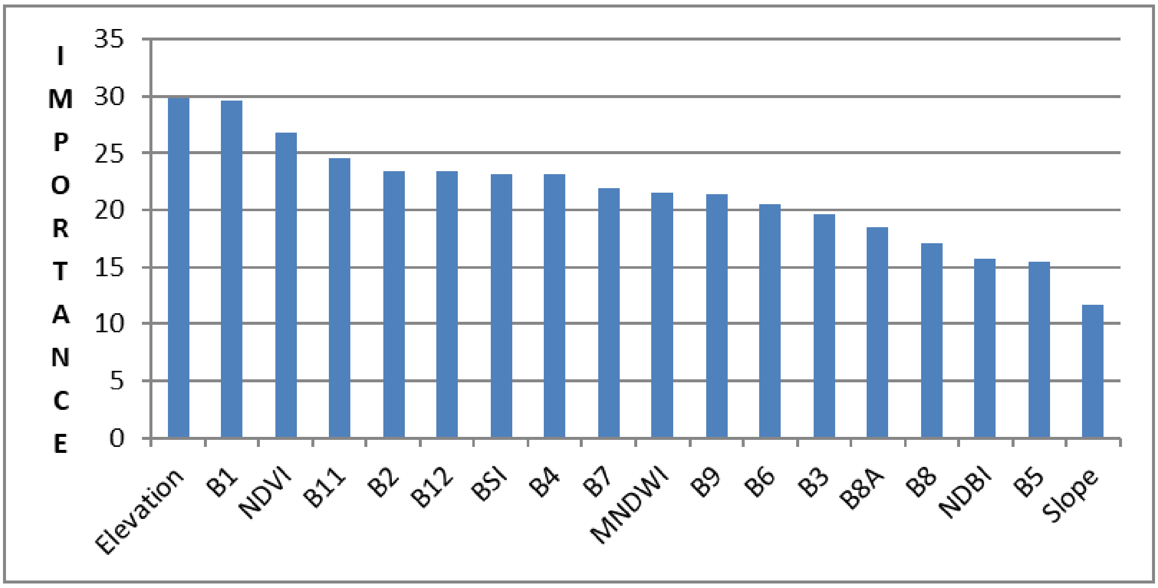

Figure 7. Random forest variable importance plot (B1: Ultra Blue/Coastal aerosol; B2: Blue; B3: Green; B4: Red; B5, B6, B7, B8A: Vegetation Red Edge; B8: Near Infra Red; B9: Water vapour; B10: Short Wave Infra Red-Cirrus; B11, B12: Short Wave Infra Red)

6. Conclusions and future work

Traditionally, ground surveying data is used to prepare land use maps for a large state. Therefore, it is essential to develop an efficient method for automatic land cover classification. This study demonstrates an effective way of utilizing a cloud-based earth observation tool for producing a land cover classification map of Punjab. Usage of the freely available Sentinel-2 dataset and openly available tool ensures the extension of work by other researchers. A land cover map of Punjab state was produced with five classes: built-up, bare soil, water, vegetation and sand. Pre-filtration of the dataset based on cloud cover, study area boundary and acquisition date helps achieve an overall accuracy of 94.98% with a precision of 93.75% for built-up, 87.75% for bare soil, 100% for water, 93% for vegetation and 97.61% for sand. The study is confined to the defined classes to analyze the land cover variability, and it can be extended by adding more land-use classes. Future enhancement in the study can be done with the integration and comparison with other machine learning classification techniques and the variety of remotely sensed datasets. Such BIG data analysis involving the processing of enormous EO datasets on local computers requires many resources (computation, storage, specialized software and time). This study amply demonstrates the use of GEE for big geospatial data analytics on the cloud using only a simple computer and network connectivity.

References

ALOS Global Digital Surface Model ALOS World 3D - 30m (AW3D30). Retrieved January 25, 2021, from https://www.eorc.jaxa.jp/ALOS/en/aw3d30/index.htm

Amani M., A. Ghorbanian, S.A. Ahmadi, M. Kakooei, A. Moghimi, S.M. Mirmazloumi, and B. Brisco (2020). Google earth engine cloud computing platform for remote sensing big data applications: A comprehensive review, IEEE Journal of Selected Topics in Applied Earth Observations and Remote Sensing, 13, 5326-5350.

Anderson J. R. (1976). A land use and land cover classification system for use with remote sensor data, US Government Printing Office, 964.

Chi M., A. Plaza, J.A. Benediktsson, Z. Sun, J. Shen and Y. Zhu (2016). Big data for remote sensing: Challenges and opportunities, Proceedings of the IEEE, 104(11), 2207-2219.

Sentinel-2 Missions. https://sentinel.esa.int/web/sentinel/missions/sentinel-2 [accessed on January 25, 2021].

Farda N. M. (2017). Multi-temporal land use mapping of coastal wetlands area using machine learning in Google earth engine, In IOP Conference Series: Earth and Environmental Science, 98(1), 12042.

Ghorbanian A., M. Kakooei, M. Amani, S. Mahdavi, A. Mohammadzadeh and M. Hasanlou (2020). Improved land cover map of Iran using Sentinel imagery within Google Earth Engine and a novel automatic workflow for land cover classification using migrated training samples, ISPRS Journal of Photogrammetry and Remote Sensing, 167, 276-288.

Gillespie T. W., G.M. Foody, D. Rocchini, A.P. Giorgi and S. Saatchi (2008). Measuring and modelling biodiversity from space, Progress in physical geography, 32(2), 203-221.

Gorelick N., M. Hancher, M. Dixon, S. Ilyushchenko, D. Thau and R. Moore (2017). Google Earth Engine: Planetary-scale geospatial analysis for everyone, Remote sensing of environment, 202, 18-27.

Li Q., C. Qiu, L. Ma, M. Schmitt and X.X. Zhu (2020). Mapping the land cover of Africa at 10 m resolution from multi-source remote sensing data with Google Earth Engine, Remote Sensing, 12(4), 602.

Ma Y., H. Wu, L. Wang, B. Huang, R. Ranjan, A. Zomaya and W. Jie (2015). Remote sensing big data computing: Challenges and opportunities, Future Generation Computer Systems, 51, 47-60.

Mutanga O. and L. Kumar (2019). Google earth engine applications, MDPI.

Parente L. and L. Ferreira (2018). Assessing the spatial and occupation dynamics of the Brazilian pasturelands based on the automated classification of MODIS images from 2000 to 2016, Remote Sensing, 10(4), 606.

Rouse J. W., R.H. Haas, J.A. Schell and D.W. Deering (1974). Monitoring vegetation systems in the Great Plains with ERTS, NASA special publication, 351, 309.

Roy P. S., S. Miyatake and A. Rikimaru (1997). Biophysical spectral response modeling approach for forest density stratification, In Proc. The 18th Asian Conference on Remote Sensing.

Sun Z., R. Xu, W. Du, L. Wang and D. Lu (2019). High-resolution urban land mapping in China from sentinel 1A/2 imagery based on Google Earth Engine, Remote Sensing, 11(7), 752.

Tamiminia H., B. Salehi, M. Mahdianpari, L. Quackenbush, S. Adeli and B. Brisco (2020). Google Earth Engine for geo-big data applications: A meta-analysis and systematic review, ISPRS Journal of Photogrammetry and Remote Sensing, 164, 152-170.

Tsai Y. H., D. Stow, H.L. Chen, R. Lewison, L. An and L. Shi (2018). Mapping vegetation and land use types in Fanjingshan National Nature Reserve using google earth engine, Remote Sensing, 10(6), 927.

Wulder M. A., N.C. Coops, D.P. Roy, J.C. White and T. Hermosilla (2018). Land cover 2.0, International Journal of Remote Sensing, 39(12), 4254-4284.

Xu H. (2006). Modification of normalized difference water index (NDWI) to enhance open water features in remotely sensed imagery, International Journal of Remote Sensing,27(14), 3025-3033.

Zha Y., J. Gao and S. Ni (2003). Use of normalized difference built-up index in automatically mapping urban areas from TM imagery, International Journal of Remote Sensing, 24(3), 583-594.

Morphometric, Hypsometric and Hydrogeomorphic Investigation in the Region of Painganga River Basin in Buldhana District, Maharashtra, India, Using Remote Sensing & GIS Techniques.

Mohan A. Sonar[1], Sandip K. Sirsat[1]*, Vishranti B. Kadam[2] and Rushikesh B. Golekar [3]
[1]Department of Geology, Government Institute of Science, Aurangabad, Maharashtra, India
[2]Department of Geology, Deogiri College, Aurangabad, Maharashtra, India
[3]Department of Geology, G. B. Tatha Tatyasaheb Khare Commerce, Parvatibai Gurupad Dhere Arts and Shri. Mahesh Janardan Bhosale Science College, Ratnagiri, Maharashtra, India
*Email: sksirsat@gmail.com

(Received: July 22, 2021; in final form: Oct 12, 2021)

Abstract: We present a hydro-geomorphological study to demarcate the groundwater potential zones in the water scarcity prone Painganga river basin, which is a sub-basin of Godavari River and located in the Buldhana district of Maharashtra, India. In this, we measured the linear, aerial and relief aspects of this drainage basin along with the slope contribution. Furthermore, a geographic information system (GIS) technique has been utilized to measure the order and length of the streams of the Painganga River. We find that the hydrogeological condition in the studied area is largely controlled by topographic features such as rivers, slopes and hills. The river basin has seven orders with a dendritic and sub dendritic type of drainage pattern without any structural or tectonic control. The drainage pattern is dominated by the first order streams and there is a decreasing trend in stream frequency and order with an increase in the stream order. The basin has an intermediate textural ration (7.549) with a nearly elongated shape. The pervasive nature of the relatively weathering resistant Deccan basalt in the basin pushed the ruggedness number to a minimum level (1.172). Digital elevation model and relief ratio of Painganga River basin suggests a moderate relief. The hypsometric integral value of the basin is in equilibrium stage and river appears to be in a mature phase of development.

Keywords: GIS, Geomorphology, Morphometry, Hypsometry, Painganga River.

1. Introduction

Morphometric analysis includes, the size and mathematical study of the outline of Earth forms, including its landforms (Clarke, 1996; Agarwal, 1998; Obi Reddy et al., 2002; Rai et al., 2017) and it is an important indicator of landform structure and hydrogeologic processes (Horton, 1932; Miller, 1953; Soni, 2017; Gizachew & Berhan, 2018), losses of materials from a watershed, soil physical properties, erosional features and land processes (Khare et al., 2014). It is also important for determining an empirical relation for hydrological activities in arid regions (Tahan et al., 2016). Morphometric study of a basin delivers vital information about the drainage characteristics of a basin (Aparna et al., 2015; Dubey et al., 2015; Strahler, 1964). Morphometric analysis was introduced by Horton (1932, 1945), to study the origin of river networks. Further works were made by Strahler (1952, 1964). Morphometric study was carried out effectively through the measurement of linear aspect, areal aspect and relief aspect of a river basin is computed to derive the general parameter of the basin (Melton, 1958; Miller, 1953; Strahler, 1964; Malik & Shukla, 2018). In drainage basin analysis, the morphometric study plays an important role in order to recognize the hydrogeological behaviour of drainage basin and expresses the prevailing climate, geology, geomorphology and structure etc. The association between the drainage characteristics and aforementioned features are well known by Horton (1945), Strahler (1957), Melton (1958), Pakhmode et. al., (2013) and Gangalakunta et. al. (2004). Various hydrological phenomena can be associated with the physiographic appearances of a drainage basin such as size, shape, slope of the drainage area, drainage density, size and length of the contributories, etc. (Magesh et al. 2012a).
Recently the use of remote sensing and GIS techniques in morphometric study has been increased and delivers an important tool in the assessment of morphometric parameters/characteristics (Asfaw and Workineh, 2019) and also provide effective tool for extraction of river basin and its drainage network (Gebre et al., 2015). Biswajit (2016) noted that remote sensing and GIS help to describe terrain parameters such as nature of bedrock, soil erosion, infiltration and surface runoff. A number of researchers who have conducted morphometric analysis by applying geospatial methods confirmed that, detailed and updated information of drainage basin can be generated in a systematic way (Aparna et al., 2015; Ayele et al. 2017; Farhan et al., 2017; Gizachew & Berhan, 2018; Gutema et al., 2017; Javed et al., 2009; Kulkarni, 2013; Magesh et al. 2012b; Pande & Moharir, 2017; Prakash et al., 2016; Singh et al., 2014; Singh, et al., 2008).

In this study, to evaluate the current situation of the groundwater in the Godavari River basin, we selected the Painganga river basin from Buldhana District of Maharashtra. This study stems with the fact that the Painganga river basin is declared as one of the water scarcities zones of the Maharashtra State due to a continuous declining trend of rainfall and groundwater level since last decade (CGWB report 2019). The river has a seasonal flow with mostly dry during the summer season. In year 2010, Buldhana district received an approximate rainfall 1039.8 mm, whereas in year 2019 it decreased to 842.02 mm. This had a great impact on the groundwater level, which declined drastically. The main objective of this study is to understand the hydrogeological and geomorphological characteristics of the Painganga basin in order to locate the groundwater potential zones that can be utilized by the local peoples.

Hypsometry has been employed to erosion rates of a landscape and resolve spatially variable uplift and whether the landform is characteristic of fluvial or glacial processes (e.g., Strahler, 1952; Montgomery et al., 2001; Brocklehurst and Whipple, 2004; Walcott and Summerfield, 2008; Pedersen, 2010). In the hypsometric study, which is the association of parallel cross sectional drainage basin area for the elevation, one can identify the physical stage of watershed (natural hydrological entities that cover an area from which rainwater flows to a particular stream/river) and erosion susceptibility of the drainage basin. Here we perform a morphometric and hypsometric analysis of the Painganga river basin using Remote Sensing and Geographical Information System (GIS) techniques in order to understand the local hydrogeological and geomorphological characteristics to demarcate the groundwater potential zones.

1.1 Study area

The study area for this work falls in survey of India Toposheet 55-D3, 55-D7, 55-D8 and 55-D12 and lies between 76°08'10" E to 76°38'30" E and 19°59'40" N to 20°17'00" N. The Painganga River originates at an altitude of ~686 m from above the mean sea level (MSL) in the Buldhana ranges of Maharashtra State, India (Figure 1). It flows through east-south-east direction from Buldhana and Washim districts. Khadakpurna, Dhamana, Koradi, Jamvani Peth rivers are the tributaries that meet Painganga river in Buldhana district. The Buldhana district is bordered by Madhya Pradesh State in the north, on the east by Akola district, on the south by Parbhani district, in the west by Aurangabad and Jalgaon district and in the northeast by Amravati district.

1.2 Geology of study area

Geologically, the most of the area of the Painganga river basin is covered by deccan trap of the upper Cretaceous to lower Eocene age (Deshpande, 2012) show in Figure 2. The Deccan lava succession in this area is grouped under the Sahyadri group. The vesicular and massive basaltic lava flows in the studied area have provided with a multi-layered aquifer system (CGWB Report Buldhana, 2013). The water bearing capacity of vesicular basalts largely depend upon the density and degree of inter connectivity of among the vesicles, whereas water bearing capacity of massive basalt depends on the presence of joints and depth of weathering. In the studied area, road cut section on Chikhli-Mehkar highway near the Barai Phata (Lat: 20° 12'59" and Long: 76° 25' 84") the multiple fractures and jointing patterns can be seen in massive basalt (Figure 3A). Similarly, blocks of joints were observed in Kanchani Mahal hill section (Lat: 20° 07' 76" and Long: 76°35'74") in massive basalt (Figure 3B). Redboles, which are formed by alteration of the basalt, are also commonly observed with a dimension of up to 2m width in different places such as Kanchani Mahal, Sultanpur, Pardi and Shara villages (Figure 3C). The basalts in the basin area also lead to the spheroidal weathering along the top of the lava flow (Figure 3D). There appears to be several lineaments in the study area, which are one of the structural features that control the groundwater movement.

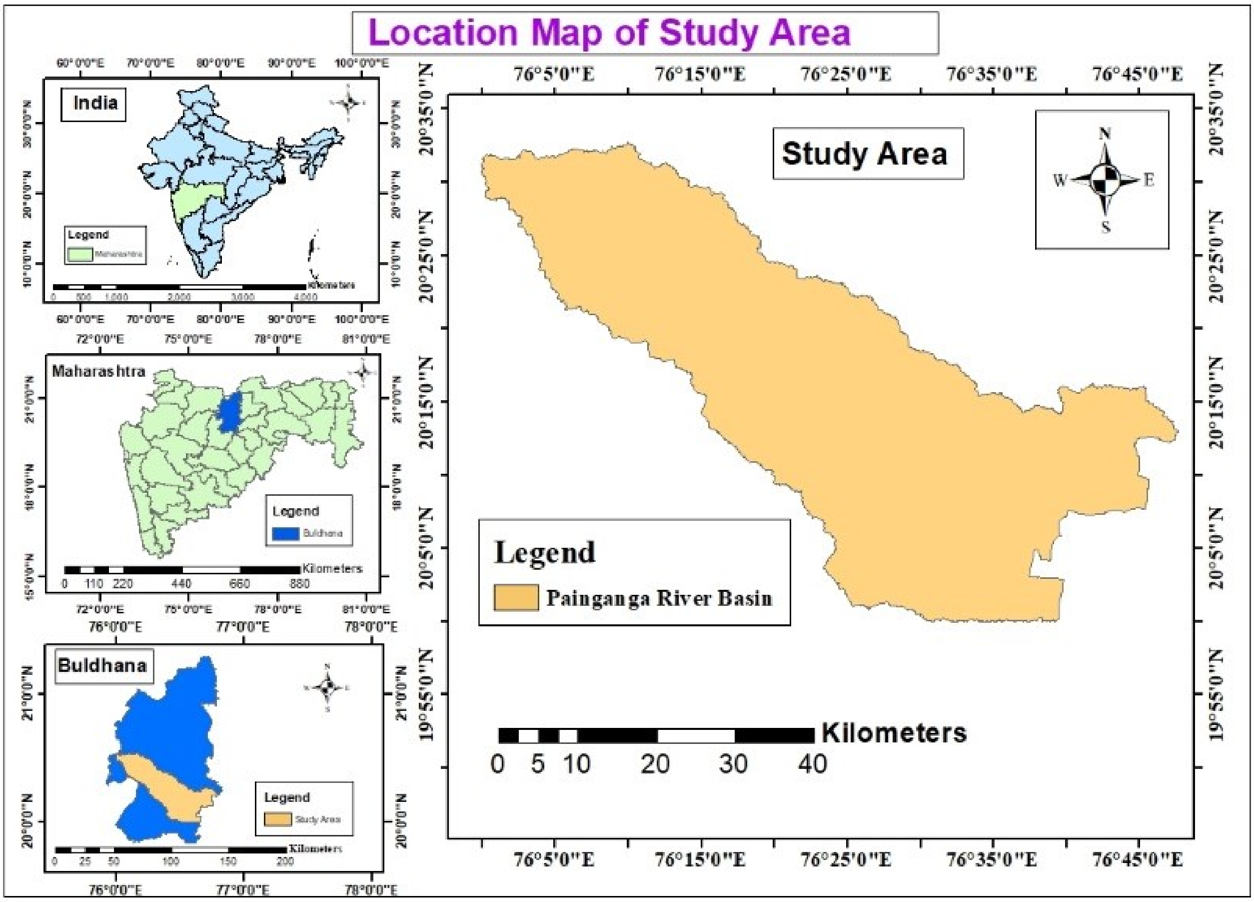

Figure 1. Location map of study area

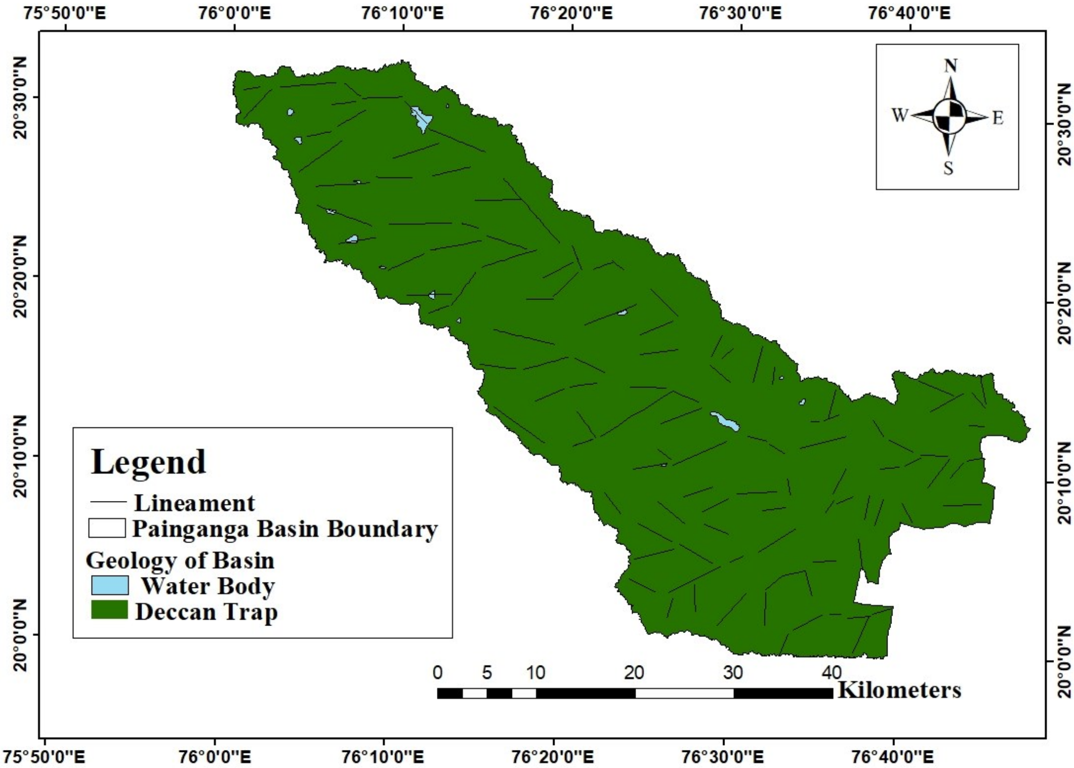

Figure 2. Geological map of Painganga Basin in Buldhana District (Source: G. G. Deshpande, 2012; GSDA Buldhana and Bhukosh, GSI).

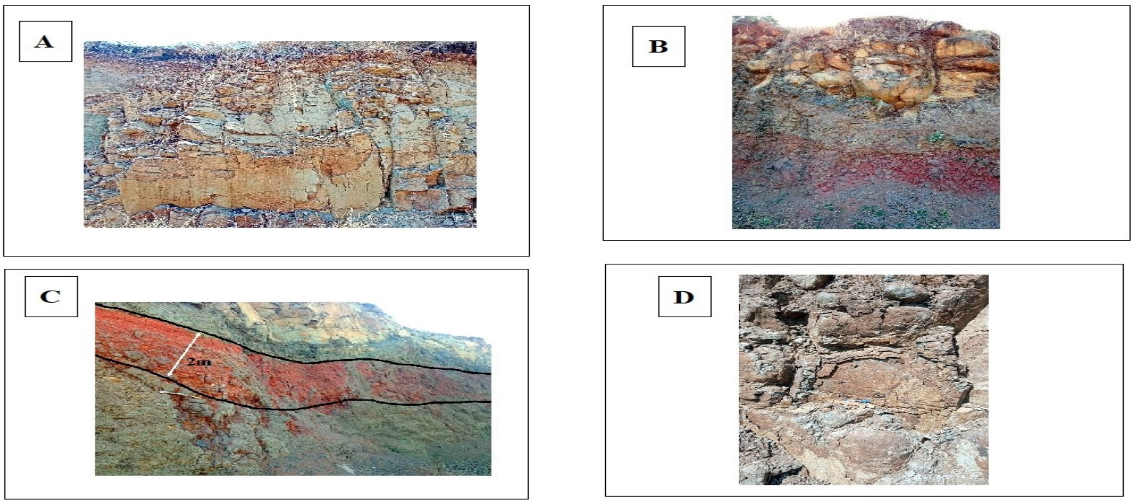

Figure 3. Field photo (A) Jointing pattern in massive basalt of road cutting section (B) Jointing pattern near to kanchani mahal (C) Redbole (D) Spheroidal weathering.

2. Analytical methods

Hydro-geomorphological map of the watershed is prepared using remote sensing and GIS techniques. The survey of India Toposheet number 55-D3, 55-D7, 55-D8 and 55-D12 with the scale of 1:50000 were used for preparation of the base map. The scanned toposheet number 55D/3, 55D/7, 55D/8 and 55D/12 geo-referenced in Arc GIS 10.3 and stream systems were digitized using the Arc digitizing tool and Strahler (1964) stream ordering method. Quantitative morphometric analysis of Painganga river basin is carried out and calculated the various aspect ratios (linear, areal and relief) using standard techniques. Morphometric parameters related to stream including the order, length, length ratio and bifurcation ratio along with the aerial features like drainage density, stream frequency, form factor, circulatory ratio and elongated ratio has been calculated. Percentage hypsometric curve (Strahler, 1952), which involves a ratio of relative height expressed in percentage (cumulative (hx100)/H) is plotted on the relative height and relative area expressed in percentage (cumulative (ax100)/A). In this calculation, 'a' and 'h' respectively denote the area and height between the successive contours, and 'A' and 'H' respectively denote the total area and total height of the basin. The areas between successive contours measured by digital planimeter and their respective heights obtained from the topographic maps are the basic data required for the study of area-height relationship. After plotting these values on a simple arithmetic graph paper and joining all the points, a smooth line percentage hypsometric curve was prepared. The hypsometric integral (HI) was calculated mathematically from the graph. Longitudinal profile of the Painganga River is drawn from the contour map. Drainage basin analysis was carried out by using SRTM-DEM data with a 90 m resolution map collected from USGS database (https://earthexplorer.usgs.gov). DEM map created by sing software Arc GIS 10.3 (Figure 4). The extractions of stream network were prepared using hydrology tool in Arc GIS 10.3 software and the methodology is shown in flow chart diagram (Figure 5) and other additional processes in Figure 6. Basin boundary was collected from GSDA office, Buldhana, Maharashtra and Geomorphological map data was downloaded from Bhukosh, Geological Survey of India. Groundwater potential zone map was created with the help of groundwater capability of geomorphic unit observed in basin area.

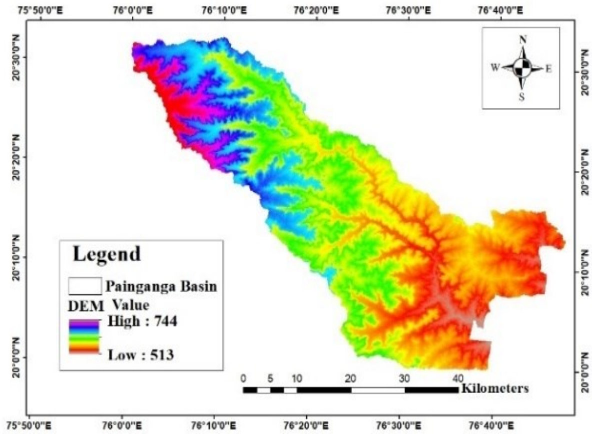

Figure 4. DEM of study area

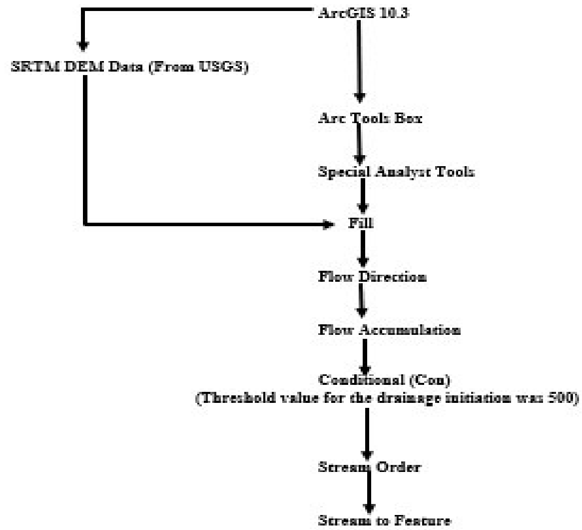

Figure 5. Flowchart for stream order extraction

3. Results

The drainage characteristics of Painganga River basin has been examined with reference to linear, aerial and relief aspects. The digital elevation model (DEM), drainage map, contour map and geomorphological map of the Painganga river basin shown in Figure 4, Figure 7, Figure 8 and Figure 11, respectively. Detailed morphometric data are enclosed in Table 2 and geomorphic unit in Table 3. Where, B-Butte, ES- Escarpment slope, M-Mesa, PLH - plateau highly dissected, PLM- Plateau moderately dissected, PLS-plateau slightly dissected, PLW- plateau weathered and PLWS- plateau weathered shallow.

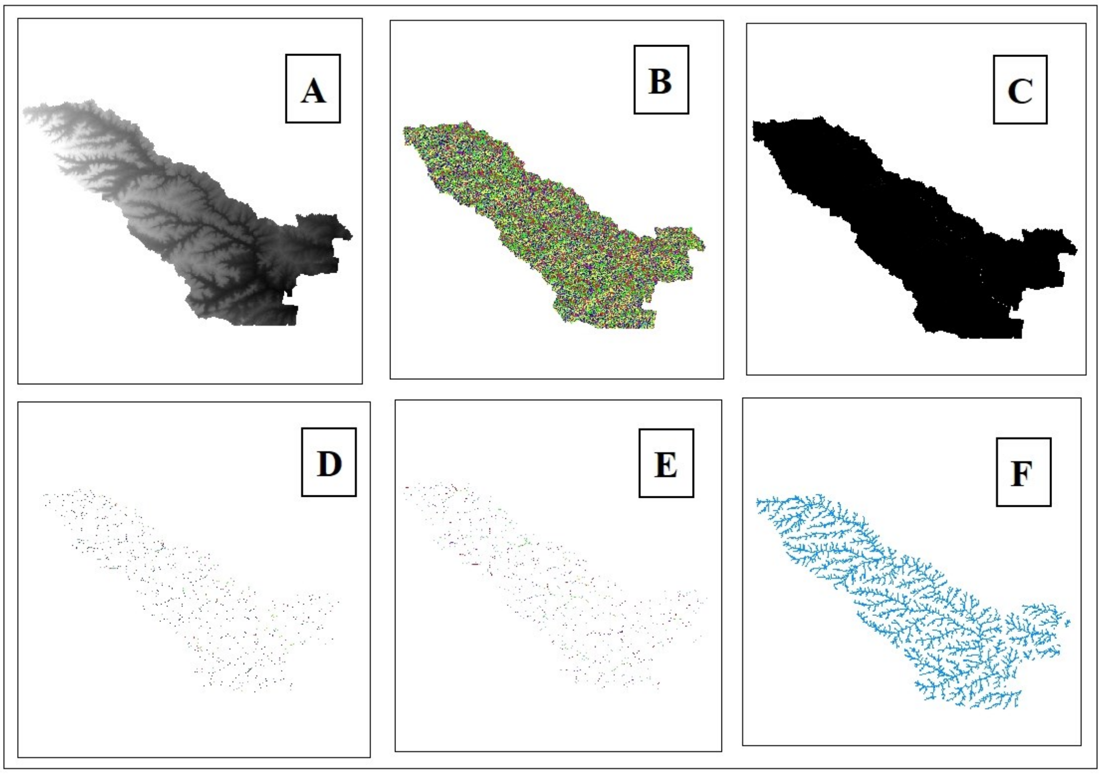

Figure 6. Stream network extraction using DEM data: (A) Fill (B) Flow direction (C) Flow accumulation (D) Conditional (Con) (E) Stream Order (F) Stream to Feature.

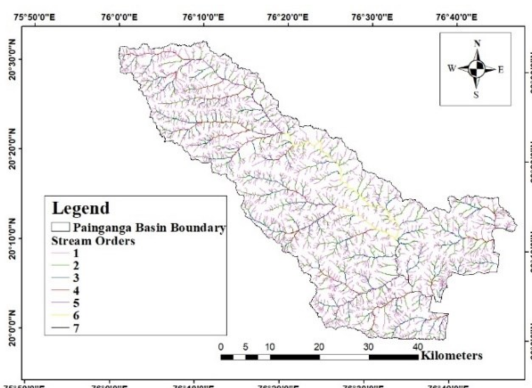

Figure 7. Drainage Map of Painganga River Basin

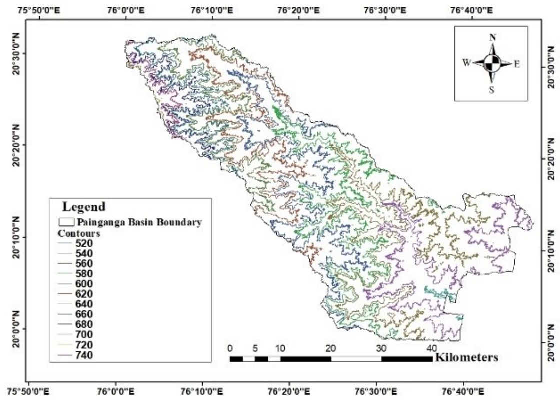

Figure 8. Contour Map of Painganga River Basin

3.1 Linear morphometric aspects

a) Stream order (U): The main step in any drainage basin is investigation of order designation, stream orders and is based on ranking of streams. The results revealed that the first order streams have maximum frequency and there is a decrease in stream frequency as the stream order increases.

b) Stream Number (Nu): The number of streams decrease as the order increases and higher the stream order lower the permeability and infiltration. Stream of each order is counted to get the number of streams of the given order (u). Stream lengths of the different stream orders were calculated. In the study area, the total no of streams is 3208, out of which first order streams have 2438. The second order streams are 598, third order are 133, fourth order are 31, fifth order are 5, sixth order are 02and seventh order are 1 (Table 1).

c) Stream Length (Lu): Stream length is one of the most significant geomorphological parameters of any basin, as it reflects the surface run-off actions. Total length of first order streams are ~1709.94 km, which is highest among all the stream orders. This length decreases as the stream order increases with second order at ~647.39 km, third order at ~310.15 km, fourth order at ~159.73 km, fifth order at ~72.10 km, sixth order at ~59.17 km and seventh order at ~19.71 km.

d) Bifurcation Ratio (Rb): Bifurcation ratio is a ratio of number of streams for a given order to the number of streams of the next higher order (Ziaur et al., 2012). Bifurcation ratio is a factor that affects the discharge rate of a river mainly after the precipitation. According to Strahler (1964), the bifurcation ratio (Rb) larger than 5 is an indication of structural control of the drainage and vice versa for the low bifurcation ratio. Higher bifurcation ratio (Rb) also indicates some sort of geological control, for example mean bifurcation ratio values for a flat and rolling surfaces is up to 2.0 and for mountains and highly dissected basins it is 3 and 4. Within a basin, bifurcation ratio tends to decrease with increasing order. Mean bifurcation ratio of the studied area is ~3.927, which indicates that there is no geological and structure control on the drainage pattern

e) Stream Length Ratio: The ratio of mean stream length of a given order to mean stream length of the next lower order (Horton, 1945). It is the ratio of the total length of streams to the total no of streams and particular ordered stream (Singh et al., 2020). Change in the stream length ratio from one order to another order indicates the development of youth stage of streams. The stream length ratio in the study area varies from 1.218 to 3.002given in Table 1.

f) Rho Coefficient: Horton (1945) defined the Rho coefficient as the ratio between stream length ratio and the bifurcation ratio. Rho coefficient determines the relationship between drainage density and physiographic development of the basin, and allow the evaluation of storage capacity of drainage network (Horton, 1945). Rho coefficient of the study area is 0.556 and this value indicates moderate hydrological storage during the flood. It is influenced by climatic, geological, geomorphological and anthropogenic factors (Prabu and Baskaran, 2013).

Table 1. Stream length Bifurcation Ration of Painganga river basin.

Stream Order	No. of Stream	Minimum Length of Stream in km	Maximum Length of Stream in km	Mean Length of Stream in km	Total Length of Stream in km	Stream Length Ratio	Bifurcation Ratio
I	2438	0.00043	3.602	0.701	1709.94	2.641	-
II	598	0.017	6.089	1.082	647.39	2.087	4.077
III	133	0.021	10.135	2.332	310.15	1.942	4.496
IV	31	0.042	17.508	5.152	159.73	2.215	4.290
V	05	6.532	32.244	14.420	72.10	1.218	6.2
VI	02	15.387	43.787	29.587	59.17	3.002	2.5
VII	01	19.716	19.716	19.716	19.71	-	2.0
Total	3208	-	-	-	2978.19	13.105	23.563
Mean	-	-	-	-	496.365	2.184	3.927

3.2 Basin geometry

a) Basin Perimeter (P): Basin perimeter is an external boundary of the watershed that enclosed its area. It is considered as a divide between the watersheds and may be used as an indicator of watershed size and shape. We have computed the basin perimeter by using ArcGIS-10.3 software, which is ~322.961 km (Table 2).

b) Basin Area (A): Area of the Painganga river basin is one most important parameter, which is similar to the length of the stream drainage to established a stimulating relation between the total basin areas and the total stream lengths, which are supported by the contributing areas (Schumm, 1956). In our study of the Painganga river basin, the basin area is ~1891.144 sq. km (Table 2).

c) Basin Length (Lb): Schumm (1956) defined the basin length as the highest dimension of the basin parallel to the main drainage line. The length of the Painganga river basin in accordance with this definition is ~107.934 km (Table 2).

d) Length Area Relation (Lar): Hack (1957), establish that for a large number of basins, stream length and basin area is related by a simple power function. The length area relation of the Painganga river basin is ~1588.561 (Table 2).

e) Lemniscates (k): Lemniscate's value is used to measure the slope of the basin. Lemniscates (K) value for the Painganga river basin is ~1.540, which shows that the watershed occupies the maximum area in its regions of inception with large number of streams of higher order.

f) Form Factor (Ff): Form factor is the ratio of basin area to the square of basin length (Zaidi, 2011). It correlates between catchment area and catchment length (Fryirs and Brierley 2013). A basin with higher form factor is usually circular and have high peak flows for shorter time period, whereas elongated basin with lower value of form factor has low peak flows for longer time period (Akram et al., 2011). In our study area, the value of form factor is 0.057 (Table 2) indicating that the basin represents elongated shape with lower peak flows for longer time period.

g) Elongation Ratio (Re): Schumm (1956) described elongation ratio as the ratio of diameter of a circle of the same area as the drainage basin and the maximum length of the basin. Re values close to unity correspond to regions of low relief, the Re values in the range 0.6-0.8 are usually associated with high relief and steep ground slope. These values can be divided into three categories namely (a) circular (>0.9), (b) oval (0.8-0.9), (c)less elongated (0.7-0.8) (d) elongated (<0.7). The Re values of the Painganga river basin is 0.455 indicating an elongated shape (Table 2).

h) Texture Ratio (T): Texture ratio (T) is a ratio of total number of streams of any order and perimeter of the area in which it lays. It is an important factor in the drainage morphometric analysis which is depending on the underline lithology, infiltration capacity and relief aspect of the terrain. Texture ratio is depending on a number of natural factors such as climate, rainfall, vegetation, rock and soil type, infiltration ability, relief and stage of development. Based on the values of T it is classified as 0 to 4 Coarse; 4 to 10 Intermediate; 10 to 15 Fine; 15< very fine (bad l and topography). In the present study area texture ratio (7.549) of the basin is categorize as intermediate in the nature (Table 2).

i) Circulatory Ratio (Rc): The circularity ratio (Rc) is the ratio of basin area (Au) to the area of a circle (Ac) having same perimeter as the basin (Strahler, 1964). It is affected by the lithological character of the basin and generally relates with length and frequency of the streams, geological structures, land use/land cover, climate, relief and slope of the basin (Rudraiah et al., 2008). The watershed values are less than 0.5 indicate basin elongation whereas the enduring watersheds have values greater than 0.5, values suggesting that they are more or less circular in shape, characterized by moderate to high relief. In the study area, Rc value is 0.228 and this value indicates basin is elongated (Table 2).

j) Compactness coefficient (Cc): Compactness coefficient is expressed as the ratio of the length of drainage basin boundary and the perimeter of a circle with same area (Prabu and Baskaran, 2013). It is the relationship between the shape of drainage basin and circle. The compactness coefficient of study area is 2.110 (Table 2).

3.3 Drainage texture analysis

a) Stream Frequency (Fs): The stream frequency introduced by Horton (1932 and 1945), it is calculated by the total number of streams of all orders and basin per unit area. It exhibits positive relationship with drainage density in the watershed representing an increase in stream population with respect to increase in drainage density. In the present study, the stream frequency of the watershed is 1.696. This value indicates that the rocks of valley are solid in nature (Table 2).

b) Drainage Density (Dd): Drainage density is the stream length per unit area of watershed is another element of drainage analysis (Horton 1945; Strahler 1952 and Melton 1958). Drainage density indicates the closeness of spacing of channels and provides a numerical measurement of the landscape dissection and surface runoff potential (Horton, 1945). In general, high drainage density value is outcome of impermeable sub-surface material, thin vegetation and mountainous relief whereas area having more resistant rock or more permeable subsoil materials, broad vegetative covers. Low drainage density leads to coarse drainage texture suggesting the area having permeable sub-soil material while high drainage density leads to fine drainage texture thereby implying relatively impermeable rock structure. The drainage density is described as low when < 2 km, moderate when it is between 2 to 5 km and high when it is > 5 km. The drainage density has calculated by ArcGIS-10.3 using Spatial Analyst Tool. The drainage density for this watershed is 1.575 km indicating low drainage density (Table 2).

c) Drainage Texture: Drainage texture (T) is one of the significant concepts of geomorphology, which means relative spacing of drainage lines. It is the total number of streams of all orders per perimeter of basin area (Horton 1945). Smith (1950) have classified drainage texture into five different textures i. e. very coarse (<2), coarse (2 to 4), moderate (4 to 6), fine (6 to 8) and very fine (>8). The low drainage density leads to coarse drainage and high drainage density shows fine drainage texture (Arulbalaji and Padmalal, 2020). The value of drainage texture in study area is 2.671 (Table 2) which indicate that the texture is coarse and coarse drainage texture represent to a presence of massive and resistive rocks (Ziaur et. al. 2012).

d) Drainage Pattern (Dp): Drainage pattern is the universal arrangement of channels in a drainage basin. Two types of drainage patterns namely dendritic to sub-dendritic are recorded in the studied basin. In a drainage basin generally, dendritic pattern is common pattern and composed of fairly non heterogeneous rock without control by the fundamental geological structures. Dendritic pattern is formed when the longer time of formation of a drainage basin.

e) Length of overland flow (Lf): Length of overland flow (Lf) is the length of water over the ground surface before it gets concentrated into definite stream channel (Horton, 1945). Lf is one of the most important independent variables affecting hydrological and physiographic development of drainage basins (Akram et al. 2011). The Lf is nearly equal to the half of the reciprocal of drainage density. The Lf value of study area is 0.787 (Table 2).

f) Constant channel maintenance (C): Schumm (1956) used the termed constant of stream maintenance C inverse of drainage density. This constant, is expressed in units of square feet per foot, has the measurement of length and therefore increase in magnitude as the scale of the landform unit increases. The value C of basin is 0.635 (Table 2). It means that on an average 0.635 surface is needed in basin for creation of one linear foot of the stream channel.

.

Table 2. Detailed drainage basin parameters, acronyms, formula and results of Painganga river basin.

Sr. No.	Parameters	Acronym	Formula	Results
Linear Morphometry				
1	Stream order	U	-	1-7
2	Stream Number	Nu	Nu = N1+N2+...Nn	3208
3	Stream Length	Lu	-	2978.19 km
4	Stream Length Ratio	Lur	Lur = Lu / Lu-1	1.218 - 3.002
5	Bifurcation Ratio	Rb	Rb = Nu / N(u+1)	2.0 - 6.2
6	Mean Bifurcation Ratio	-	-	3.927
7	Rho Coefficient	ρ	Lur / Rb	0.556
Basin Geometry				
8	Basin Perimeter	P	-	322.961km
9	Basin Area	A	-	1891.144 km^2
10	Basin Length	Lb	-	107.934 km
11	Length Area Relation	Lar	Lar = 1.4 * A0.6	1588.561
12	Lemniscates	K	$k = Lb^2 / 4* A$	1.540
13	Form Factor	Ff	$Ff = A / Lb^2$	0.162
14	Elongation Ratio	Re	$Re = 2\sqrt{(A/\pi)} / Lb$	0.455
15	Texture Ratio	T	$T = N_1 / P$	7.549
16	Circulatory Ratio	Rc	$Rc = 4\pi A / P^2$	0.228
17	Compactness Coefficient	Cc	$Cc = 0.2841\times P / A^{0.5}$	2.110
Drainage Texture Analysis				
18	Stream Frequency	Fs	Fs = Nu /A	1.696
19	Drainage Density	Dd	Dd = Lu / A	1.575 km
20	Drainage Texture	T	T = Dd × Fs	2.671
21	Drainage Pattern	Dp	-	Dendritic to Sub-dendritic
22	Length of Overland Flow	Lf	Lf = ½ Dd	0.787 km
23	Constant Channel Maintenance	C	C = 1 / Dd	0.635
24	Ruggedness Number	Rn	Rn = Dd × (H/1000)	1.172
25	Maximum Height of Basin	Z	-	744 m
26	Minimum Height of Basin	z	-	513m
27	Total Basin Relief	H	H= Z-z	231 m
28	Relief Ratio	Rh	Rh = H/ Lb	6.893
29	Absolute Relief	Ra	-	744 m
30	Dissection Index	Dis	Dis = Rh / Ra	0.009

g) Ruggedness Number (Rn): Ruggedness Number (Rn) is the product of basin relief and the drainage density which indicates the structural complexity of the terrain (Schumm, 1956). The low ruggedness value of basin implies that region is less flat to soil erosion and have basic structural complexity in relationship with relief and drainage density. The high ruggedness value activates the change of erosion and affects the water potential of the basin. The Rn value of the Painganga river basin is 1.172 (Table 2).

h) Relief Ratio (Rh): The relative relief of basin is a difference in the elevation between the highest point and the lowest point on the basin. The relief ratio is dimensionless number which provides a measured in elevation per unit length of river (Fryirs and Brierley, 2013). The relief ratio of study area is 6.893 (Table 2). This value indicates that study area with moderate relief ratio.

i) Absolute Relief (Ra): The difference in elevation between a given location and sea level. Ra is the maximum height of a known location in a river basin. The absolute relief of the area is 744m (Table 2).

j) Dissection Index (Dis): The ratio between relative reliefs to its absolute relief is called dissection index (Mahala 2020). The value of dissection index ranges between 0 (absence of vertical dissection) to 1 (vertical areas) and dissection value near to 0 indicates maximum denudation stages of evaluation and near to 1 indicate minimum denudation of geomorphic evolution (Mahala, 2020). Dissection index of the basin is 0.009 which indicate that the basin is moderately dissected (Table 2)

3.4 Hypsometric analysis

Hypsometry is the measurement of height of land from sea level. It also represents the association between elevation and area of basin in any watershed or catchment (Strahler 1952 and Golekar et al. 2015). Hypsometric curve (HC) and hypsometric integral (HI) are very important to calculate basin flood response and erosional stage. The Hypsometric curve of Painganga basin suggests that the larger part of the area is moderate to gentle slope (Figure 9). The curve can be characterized as mature/equilibrium stage of landscape development. The curve shows 54 % of area comes under the elevation between 500m -560m and curve shows 36 % of the area between 560m -620m elevation. Whereas curve shows 8 % area between 620m-680m elevation and curve shows 1 % area between 680m-740m elevation. From the present study of contour map, we have calculated two ratios as follows: 1) Area of a given contour inside the basin boundary. 2) Contour height of the over the stream mouth. A graph of relative area verses relative height plotted for Painganga basin.

3.5 Profile analysis

Longitudinal profile is drawn from the topographic map which is an image observation of the real environment of the landscape. The longitudinal section of the valley is called longitudinal profile. The entire distance from source to the mouth of a particular river is considered. The graph drawn reveals the relief impact of the river course (Singh, 1997). The longitudinal profile provides breaks in the longitudinal course of the river flow. These breaks may indicate nick points, and helps in examining the nature and control of landform development (Singh, 1997). Longitudinal profile gives geomorphologists an insight of relief and topographical impact on river flow (Babar, 2005).

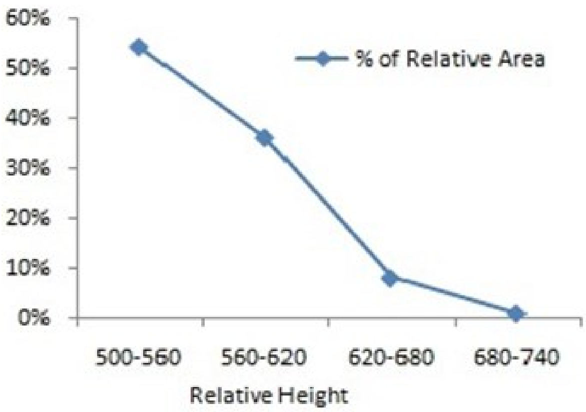

Figure 9. Hypsometric curve of Painganga river basin

3.5.1 Longitudinal profile of the Painganga river basin

The Painganga River originates near village Madh at 681 m and flows almost straight towards east (Figure 10). The slope is gentle with a drop in elevation from 681m to 609m, spreading over 20 km (Figure10). From the south of village Sagwan, Painganga River turns toward south east. After that slope of river Painganga shows moderately gentle with a drop in elevation from 609m to 577m, spreading over 20 km (Figure10). After 40 km of river course, longitudinal profile seen that the river channel is near to the flat with a drop in elevation from 577m to 565m (Figure 10). Once more Painganga river channel showed that moderately gentle slope with a drop in elevation from 609m to 577m, spreading over 20 km (Figure 10). Afterward the 80 km from origin the river channel is near to the flat with a drop in elevation from 533m to 516m (Figure10)

3.5.2 Hypsometric Integral (HI)

Hypsometric investigation can be carried out to conclude stages of river development. The relative area and relative height data are calculated using contour map of 20 m contour interval in ArcGIS-10.3 software. Strahler (1952) classed values of HI and HC into three important classes. Pike and Wilson (1971) proved mathematically that the elevation-relief ratio E which is defined as integration of the hypsometric curve gives the hypsometric integral (I) and given in equation below;

$$E \approx Hsi = \frac{\text{Elev mean} - \text{Elev min}}{\text{Elev max} - \text{Elev min}}$$

Where, E is the elevation-relief ratio equivalent to the hypsometric integral HI; Elevation mean is the weighted mean elevation of the basin estimated from the identifiable contours of the delineated basin; Elevation minimum and Elevation maximum are the minimum and maximum elevations within the basin, the hypsometric integral is expressed in percentage units. If HI values >0.60 is youth stage (Convex Curve), 0.30 to 0.60 for mature stage (Sigmoidal Curve) and HI <0.30 for old stage (Concave Curve).

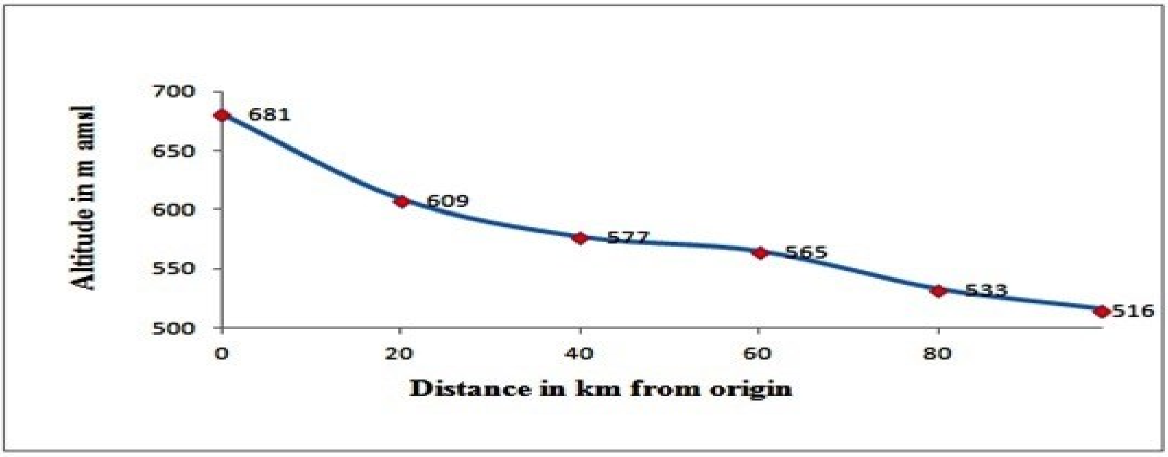

Figure 10. Longitudinal profile of the Painganga river basin.

3.6 Hydrogeomorphology

Geomorphological unit in the studied area were given in map (Figure 11 and Table 3). Hydrogeomorphology is a developing interdisciplinary scientific field, which studies the relationships between geomorphology and hydrology (surface water/groundwater). In a general sense, it links together several fields related with geosciences, hydrology and physical geography, such as geology, hydrogeology, geomorphology, remote sensing, applied geophysics, soil and rock geotechnics, climatology and natural hazards (Babar, 2005). Hydrogeomorphology operates in an interdisciplinary framework focused on the relationship between hydrologic processes with Earth materials and the interaction of geomorphic processes relating surface water/groundwater flow regime (Babar, 2005). Alluvial plain represents the runoff zone while valley belongs to discharge zone, and the denudational hills constitute the infiltration area. It is classified into three zones on the basis of their groundwater potential zone as a) Very favorable zones b) Good to moderate zones and c) Poor zone. The groundwater potential zones are identified with the help of geomorphological units.

3.6.1 Mesa and Buttes: Mesas and buttes are generally found in fairly dry areas. The ground water prospect is very poor in these areas due to fast runoffs over steep slopes so they fall under the category of very poor groundwater potential zone (Figure 11). The area covered by mesa and buttes are 2.64sqkm and 2.20sqkm respectively.

3.6.2 Escarpments: Escarpments are observed in top of the hills and normally seen as step-like surfaces (Singh et al., 2013). It is classified as poor groundwater accumulation zones (Singh et al., 2013) and its cover128.51sqkm area.

3.6. 3 Dissected Plateau (DPT): An extensive flat top and steep slopes formed over horizontally layered Deccan basalts that may be crossed by fractures, joints and lineaments are called as plateaus (Babar, 2005). These units can be expressed regarding the slope of the area, runoff characteristics, drainage density, stream frequency and relief ratio of the area (Babar, 2005). In the present study area, six plateaus were observed, i.e., highly dissected plateau, moderately dissected plateau, slightly dissected plateau, un-dissected plateau, weathered plateau and shallow weathered plateau.

a) Plateau Highly Dissected: This unit geomorphic represents a plateau more often dissected by deep valleys separating individual mesa and buttes and shallow aquifers completely drain away into deep valleys (Sharma and Shukla, 2015). This geomorphic unit is secondary in the studied river basin. The land of this unit is dissected by the streams of the watershed giving rise to a terrain consisting of flat-topped ridges and steep scarps. This unit in the study area covers about 0.04 % of the total area of the basin (0.69 km^2).

b) Plateau moderately dissected: The soils covering in this plateau are moderately thick and well drained. High moisture capacity suggests that the irrigation requirement is moderate in the moderately dissected plateau area. The groundwater potential in these units is moderate to high. In this geomorphic unit shallow aquifer partially drains out into deep valleys (Sharma and Shukla, 2015). Moderately dissected plateau is demarcated as PLM in geomorphological map of the study area which showed in light pink colored (Figure 11). The area covers by this unit is about 1.26 % of the total area of the basin (24.71 km^2).

c) Plateau slightly dissected: This unit covered by 979.81 sqkm area in middle portion of the Painganga river basin. This unit is inferred to recharge and storage zone for groundwater. PLS is good potential zones for groundwater resources or groundwater exploration.

d) Plateau un-dissected: The land of this unit is dissected by the streams of giving rise to un-dissected terrain consisting of flat-topped hills and steep scarps. The groundwater potential in these units is very poor (Babar, 2005). This unit is observed between moderately dissected plateau and eroded lad by stream. The runoff from these areas can be arrested through the construction of check dams and other strategies. Plateau un-dissected is demarcated as PLU in geomorphological map of the study area which showed in sky blue colored (Figure 11). The area covers by this unit is about 6.98 % of the total area of the basin (136.55 km^2).

e) Plateau weathered: Plateau weathered are found in the basin along the major stream in lower reaches. These units have good potential for agriculture. The area covers from this unit is about 14.89 % of the total area of the basin (291.55 km^2). Plateau weathered is demarcated as PLW in geomorphological map of the study area which showed in light green colored (Figure 11). The Plateau weathered is consisting of weathered product of the surrounding basaltic rocks, mostly comprise moderately thick gravel beds along with sand and silt layers. The groundwater potential ranges from good to moderate.

f) Plateau weathered shallow: Plateau weathered shallow are found in the watershed along the stream in middle reaches. These units have moderate potential for groundwater. The area covers from this unit is about 19.97 % of the total area of the basin (390.93 km^2). Plateau weathered shallow is demarcated as PLWS in geomorphological map of the study area which showed in dark purple colored (Figure 11). The Plateau weathered shallow is consisting of moderately weathered product of the surrounding basaltic rocks, mostly comprise moderately thick gravel beds along with sand and silt layers. This area shows groundwater availability only in the winter season, while during summer season most of the wells in going to dry.

Table 3. Area covers by different Geomorphological units in the Painganga river basin, Buldhana district.

Sr. No.	Name of the Geomorphological Unit	Area (km^2)	Percentage of the area
01	Butte	2.20	0.11 %
02	Escarpment slope	128.51	6.56 %
03	Mesa	2.64	0.13 %
04	PLH - Plateau highly dissected	0.69	0.04 %
05	PLM - Plateau moderately dissected	24.71	1.26 %
06	PLS - Plateau slightly dissected	979.81	50.05 %
07	PLU - Plateau un-dissected	136.55	6.98 %
08	PLW - Plateau weathered	291.55	14.89 %
09	PLWS - Plateau weathered shallow	390.93	19.97 %
Total Area		1957.59	100.00 %

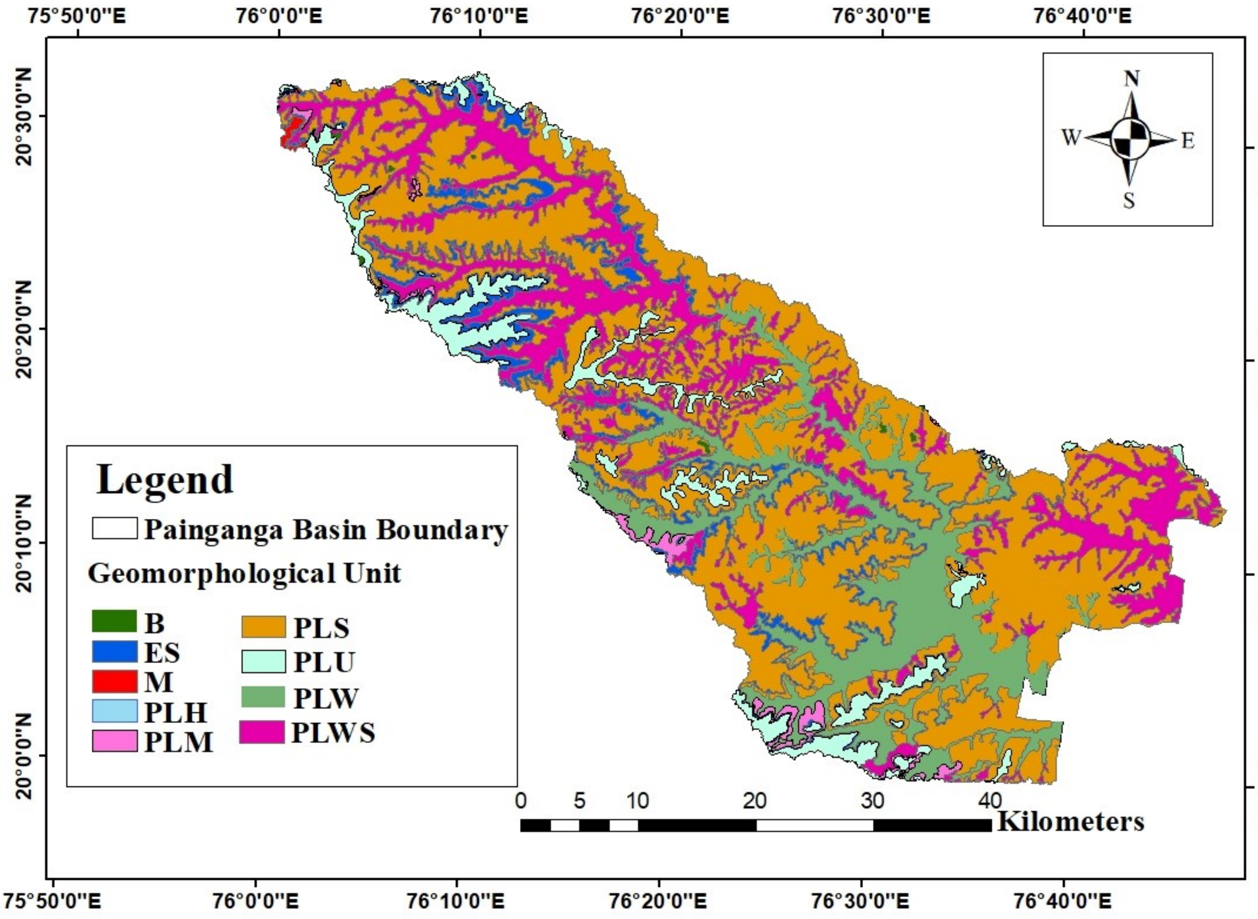

Figure 11. Geomorphological Map of Painganga River Basin (Source: Bhukosh, Geological Survey of India).

4. Discussion

The number of total streams in current study area is 3208 which covers Ist order 76.00%, IInd order 18.64%, IIIrd order 4.14%, IVth order 0.97%, Vth order 0.15%, VIth order 0.06% and VIIth order streams 0.03%. Due to high numbers of the Ist and IInd orders in the high elevated areas, runoff is higher in these parts of the basin. The first order streams present in larger number indicates a uniform lithology and a gentle slope (Kale and Gupta, 2001, Singh and Awasthi, 2011), which suggests that the major portion of precipitation goes to the surface runoff. Morphometry of basin is characterized by a linear and an aerial relief aspect. There is a linear relationship with small deviation of the stream numbers and stream length against stream order. This is an implication of trend line that conform a linear relationship of the stream number and stream length. Stream length ratio is showing variation between streams of different orders, which may be due to the variation in topography. The difference between one order to another order of stream length ratios indicates a mature stage of geomorphic development, further suggesting an important correlation with runoff and erosional status of the basin. The value of bifurcation ratio ranges from 3 to 5 that indicates the basin may have any geological structures but do not distort drainage pattern (Nag, 1998). However, bifurcation ratio value >5 revels that basin is lithological and structurally controlled (Strahler, 1964) and the value of bifurcation ratio <3 it means the basin has any flat region. This bifurcation ratio value (3.927) calculated for the studied area indicates that the geological composition and structure of the area do not control the drainage pattern and flat basin region. Rho coefficient value of the studied basin is 0.556 indicating basin belongs to a moderate hydrological storage during the flood. Elongated nature of the river basin has an implication on both hydrologic and geomorphic processes (Singh et al., 2020). The flow of water of this basin distributed over a longer period of time for distribution, susceptible to erosion and sediment load (Angilliri, 2008). Stream frequency values of the Painganga river basin indicate that the rocks of valley are solid in nature. Ruggedness value of the basin is relatively high, which suggests that there is a chance of high erosion and low water potentiality. This relief ratio values indicates that study area has a moderate relief ratio. From the drainage texture ratio of the studied area, it is observed that the basin can be categorize into an intermediate stage in the nature. Drainage density of the Painganga rivers basin show low values that indicates high infiltration rates (Babar, 2005). This suggest that the study area is most feasible for constructions of new soil and water conservation structure for further development of groundwater. The length of overland flow values of the Painganga basin indicates gentle slopes and longer flow paths. The Re values usually ranges between 0.6 to 1.0 over a wide variety of climate and geologic types. The Re values near to 1.0 are the features of the area of very low relief zone; while, the values in a range of 0.6 to 0.8 generally occur in areas of high relief and steep ground slope (Strahler, 1964). The elongation ratio (Re = 0.455) of given basin shows that the basin is elongated and dendritic drainage pattern which is indicate that less structural control and homogeneous lithology (Shimpi et. al., 2014). Dendritic drainage pattern is relation with areas having homogeneous lithology and very gentle or flat, rolling topographic (Shimpi et. al., 2014). Study area, the streams or rivers, some of which appear fracture-controlled in their flow path give rise to dendritic drainage pattern. Groundwater tables affect the position and shape by the topography and physiography (Shimpi et. al., 2014). The flow of water in elongated basin takes more time for susceptible to erosion and sediment load (Angilliri, 2008). The low circulatory ratio value ratio (Rc= 0.228) of the basin is consistent with the elongated in shaped, low discharge of runoff and highly permeable conditions of subsurface soil. The hypsometric integral (HI) value of the Painganga river basin is 0.50 and this value indicates that the basin is mature stage of river development (Figure 9). In the mature stage, river has more water flow in the stream channel, i.e., the river has a greater discharge than the youthful river channel. This mean the river is capable to carrying more a greater volume of sediments. A study of longitudinal profile reveals the character of Painganga River. The difference in elevation suggests that the river has developed "rapids". It is formed due to different erosion, relief and presence of lineament and or joints (Golekar et al., 2015). In the present study area plateau highly dissected, plateau moderately dissected, plateau un-dissected, plateau weathered shallow and plateau weathered units were observed as hydro-geomorphological units. Based on hydrogeological characteristics of the hydro-geomorphological units following recharging structure is recommended for the development of groundwater. Plateau Highly Dissected - in this area, recharge shafts like recharging structures are feasible for the further groundwater development. Plateau moderately dissected - in this area, recharge trenches, Nala bunds, contour bunds, percolation tanks and ground water dams recharging structures are recommended for the further groundwater development. Plateau weathered - These areas were developed along the fractures and such places can be exploited for groundwater through deep bore. Hypsometric integral value of Painganga river basin is 0.50, indicated that 50 percent of the original rock masses still exit in Painganga river basin. It was observed from the H_{si} value that the given basin is in mature/equilibrium stage of landscape development and it show Sigmoidal Curve. This revealed that the soil erosion from this basin was derived primarily from the incision of channel beds, down slop movement of top soil and bed rock material, cutting of stream banks and washout of the soil mass. The hydrological response of the basin attaining mature stage will have slow rate of erosion unless there are very high intense storms leading to high runoff peaks (Ritter et al., 2002). The good and very good groundwater potential zones (Figure 12) are confined generally to high rainfall regions which in turn have high infiltration potential. The moderate groundwater potential zones (Figure 12) occur mostly in the valleys and areas of high drainage density. The poor and very poor groundwater potential zones (Figure 12) occur in the steep slope and high drainage density.

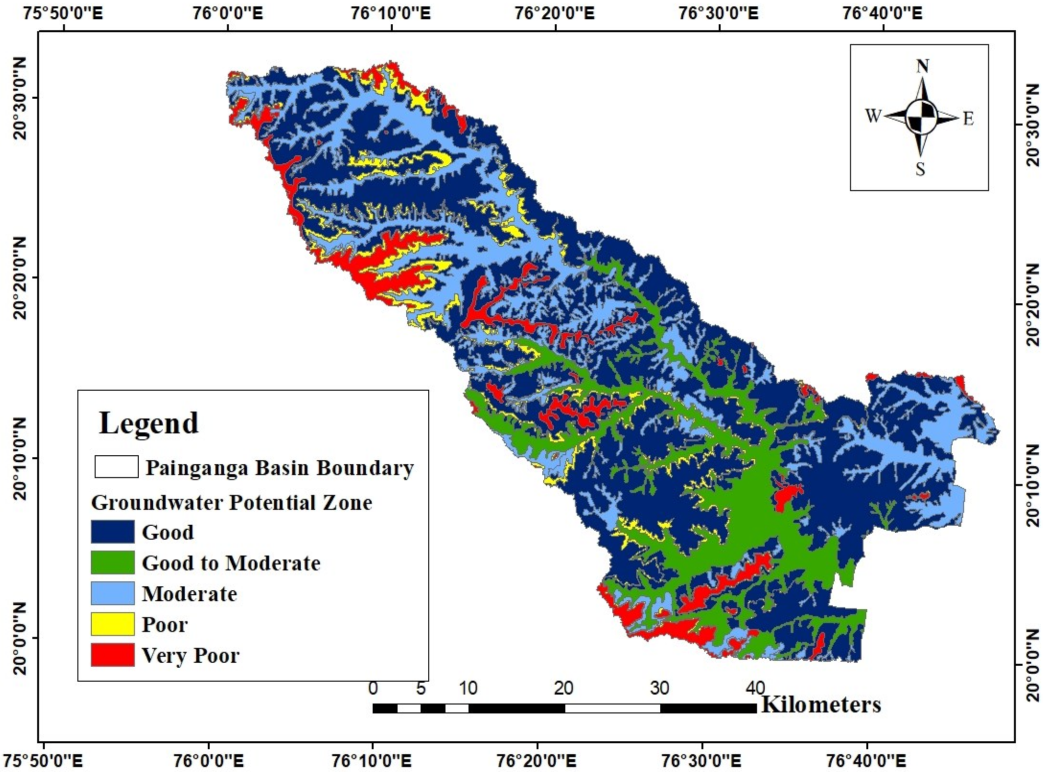

Figure 12. Groundwater potential zones map of Painganga River Basin.

5. Conclusions

The hydrogeological conditions are controlled by topographic features like rivers, slopes, mountains, hills etc. because the geomorphological setup of the area greatly influences the occurrence and movement of groundwater. Considering this fact attempt has been made to undertake detailed morphometric analysis of the Painganga river basin which will be helpful for knowing the relationship of morphometric parameters with groundwater potential and development. GIS techniques have proved that it is correct and a capable tool in drainage description. Three main morphometric features are used i.e., drainage network, basin geometry and drainage texture ratio. The basin under studied is seven orders and its stream order, length ratio and bifurcation ratio indicate that the basin is dendritic and sub dendritic type of drainage pattern. There is no structural or tectonic control. Drainage morphometry data of the present study area indicates that the first order stream present is maximum number of streams. It is also observed that the stream frequency is reduced as the stream order is increases. The total lengths of streams are seen to be decreasing as the stream order increases. Texture ratio of basin is intermediate in nature and elongation ratio and circulatory ratio indicates that shape of basin approximately elongated shape. The ruggedness number of this basin show low value (1.172) due to the occurrence of hard resistant basalts. Digital elevation model and relief ratio of Painganga River basin show moderately relief. The hypsometric integral value the basin is in the equilibrium stage and that the basin is in a mature phase of river development. The hydrogeomorphic units like PLM and PLW have good to moderate for groundwater potential, PLWS have moderately for groundwater potential. The hydro-geomorphic units like PLH, and escarpment (ES) are poor groundwater potential zone and PLU, Mesa and Butte are very poor for groundwater potential zone.

Acknowledgments

Financial assistance, in the form of Junior Research Fellowship is awarded to one of the author (Sandip K. Sirsat) by the Chhatrapati Shahu Maharaj Research, Training and Human Development Institute (SARTHI), Pune. (An Autonomous Institute of Government of Maharashtra) is gratefully acknowledged. Authors are also thankful to Director and Head, Department of Geology, Government Institute of Science, Aurangabad, for providing research facility to carry out this work.

References

Agarwal C.S. (1998). Study of drainage pattern through aerial data in Naugarh area of Varanasi district, U.P. Journal of Indian Society of Remote Sensing, 26, 169-175.

Akram J., Y.K. Mohd and R. Subah, (2011). Watershed prioritization using morphometric and land use land cover parameters: A remote sensing and GIS based approach. Journal of Geological Society of India, 78, 63-75.

Angilliri Y. E. (2008). Morphometric Analysis of Colanguil river basin and flash flood hazard, San Jaun, Argentina. Environ. Geol., 55, 107-111.

Aparna P., K. Nigee, P. Shimna and T. K. Drissia (2015). Quantitative Analysis of Geomorphology and Flow Pattern Analysis of Muvattupuzha River Basin Using Geographic Information System. Journal Aquatic Procedia, 4, 609-616.

Arulbalaji P. and D. Padmalal (2020). Sub-watershed Prioritization Based on Drainage Morphometric Analysis:

A Case Study of Cauvery River Basin in South India. Journal of Geological Society of India, 95, pp.25-35.

Asfaw D. and G. Workineh (2019). Quantitative analysis of morphometry on Ribb and Gumara watersheds: Implications for soil and water conservation. International Soil and Water Conservation Research, 7, pp.150–157.

Ayele A., H. Yasuda, K. Shimizu, H. Nigussie, and W. Kifle (2017). Quantitative analysis and implications of drainage morphometry of the Agula watershed in the semi-arid northern Ethiopia. Applied Water Science, 7, 3825–3840.

Babar Md. (2005). A Text book Hydrogeomorphology Fundamentals application and techniques: New India Publishing Agency, Pitam Pura, New Delhi, 137.

Biswajit M. (2016). Analysis of Hydrological Inferences through Morphometric Analysis: A Remote Sensing-GIS Based Study of Gandheswari River Basin in Bankura District, West Bengal Int. Jour. of Humanities & Social Science Studies, 2(4), 68-80.

Brocklehurst S., and K. X. Whipple (2004). Hypsometry of glaciated landscapes, Earth Surf. Processes Landforms, 29(7), 907-926.

Central Ground Water Board Report of Buldhana District, Central Region Nagpur, (2013).

Central Ground Water Board Report of Buldhana District, Central Region Nagpur, (2019).

Clarke J.I. (1996). Morphometry from Maps. Essays in geomorphology. Elsevier publication, Co., New York, 235-274.

Deshpande G.G. (2012). Geology of Maharashtra, published by the Geological Society of India, Bangalore, 156-157.

Dubey S.K., D. Sharma and N. Mundetia (2015). Morphometric analysis of the Banas River Basin using the geographical information system, Rajasthan, India. Journal of Hydrology, 3(5), 47-54.

Tahan E.I., A.H.M.H. and H.E.M. Elhanafy (2016). Statistical analysis of morphometric and hydrologic parameters in arid regions, a case study of Wadi Hadramaut. Arabian J. Geosci., 9(2), 1-10.

Farhan Y., A. Anbar and N.R. Al-Shaikh (2017). Prioritization of semi-arid agricultural watershed using morphometric and principal component analysis, remote sensing, and GIS techniques, the Zerqa River Watershed, Northern Jordan. Agricultural Sciences, 8, 113–148.

Fryirs K.A. and G.J. Brierley (2013). Geomorphic analysis if river systems: An approach to reading the landscape. West Sussex: Wiley Blackwell Publication, 29-62.

Gangalakunta, P., O. Reddy, A.K. Maji and K.S. Gajbhiye (2004). Drainage morphometry and its influence on landform characteristics in a basaltic terrain, Central India-A remote sensing and GIS approach. Internat. Jour. Appl. Earth and Geoinformation, 6, 1-16.

Gebre T., T. Kibru, S. Tesfaye, and G. Taye (2015). Analysis of Watershed Attributes for Water Resources Management Using GIS: The Case of Chelekot Micro-Watershed, Tigray, Ethiopia. Journal of Geographic Information System, 7, 177-190.

Gizachew K., and G. Berhan (2018). Hydro-geomorphological characterization of Dhidhessa River Basin, Ethiopia. International Soil and Water Conservation Re-search, 6, 175-183.

Golekar R.B., M.V. Baride, S.N. Patil and S.H. Adil (2015). Altimetric and hypsometric Analysis for soil and water conservation: A case study of Anjani and Jhiri river basin, Northern Maharashtra, India. Earth Science Research Journal, 19(1), 51 – 58.

Gutema D., T. Kassa and A.K. Sifan (2017). Morphometric analysis to identify erosion prone areas on the upper Blue Nile using GIS: case study of Didessa and Jema sub- basin, Ethiopia. International Research Journal of Engineering and Technology, 4(8), 1773-1784.

Hack J.T. (1957). Studies of longitudinal profiles in Virginia and Maryland. US Geological Survey professional paper, 294(b), 45-97.

Horton R.E. (1932). Drainage basin characteristics, Trans. Amer. Geophy. Union, 13, 350-361.

Horton R.E. (1945). Erosional development of streams and their drainage basins. Hydrophysical approach of quantitative morphology. Bulletin of Geological society of America, 56(3), 275-370.

Javed A., M.Y. Khanday and R. Ahmed (2009). Prioritization of sub-watershed based on morphometric and land use analysis using remote sensing and GIS techniques. Journal of Indian Society Remote Sensing, 37, 261-274.

Kale V.S. and A. Gupta (2001). Introduction to geomorphology. New Delhi: Academic (India) Publisher (Chapter 3).

Khare D., A. Mondal, P.K. Mishra, S. Kundu and P.K. Meena (2014). Morphometric analysis for prioritization using remote sensing and GIS techniques in a Hilly catchment in the state of Uttarakhand, India. Indian Journal of Science and Technology, 7(10), 1650–1662.

Kulkarni M. D. (2013). The basic concept to study morphometric analysis of river drainage basin: A review. International Journal of Science and Research, 4(7), 2277-2280.

Mahala A. (2020). The significance of morphometric analysis to understand the hydrogeological and morphological characteristics in two different morpho-climatic settings. Applied Water Science, v.10, pp.33.

Magesh N. S., N. Chandrasekar and S. Kaliraj (2012a) A GIS based automated extraction tool for the analysis of basin morphometry. Bonfring Int. Jour. Ind. Eng. Manag. Sci., 2(1), 32–35.

Magesh N.S., N. Chandrasekar and J.P. Soundranayagam (2012b). Delineation of groundwater potential zones in Theni district Tamil Nadu using remote sensing GIS and MIF techniques. Geoscience Frontiers, 3, 189–196.

Malik M. S. and J.P. Shukla (2018). A GIS-based morphometric analysis of Kandaihimmat watershed, Hoshangabad district, M.P. India. Indian Journal of Geo Marine Sciences, 47(10), 1980-1985.

Melton M.A. (1958). Correlation structure of morphometric properties of drainage system and their controlling agents, Journal Geol, 66, 442-460.

Miller V. C. (1953). A quantitative geomorphic study of drainage basin characteristics in the Clinch Mountain area Virginia and Tennessee. Department Geology Columbia University (ONR Project Tech–Report NT 389-042, No. 3), 189-200.

Montgomery D. B., G. Balco and S.D. Willett (2001). Climate, tectonics and the morphology of the Andes, Geology, 29, 579–582.

Nag S. K. (1998). Morphometric analysis using remote sensing techniques in the Chaka sub-basin purulia distrct, West Bengal. Journal of Indian Society of Remote Sensing, 26, 69-76.

Obi Reddy G.E., A.K. Maji and K.S. Gajbhiye (2002). GIS for morphometric analysis of drainage basins. GIS lndia, 4(11), 9-14.

Pakhmode V., H. Kulkarni and S.B. Deolankar (2013). Hydrological drainage analysis in watershed programme planning: A case study from the Deccan basalt, India. Hydrogeology Jour., Springer Veerlang, 11, 595-604.

Pande C. B. and K. Moharir (2017). GIS based quantitative morphometric analysis and its consequences: A case study from Shanur River Basin, Maharashtra India. Applied Water Science, 7, 861–871.

Pedersen V. K. (2010). Alpine glacial topography and the rate of rock column uplift, Geomorphology, 122(1–2), pp.129–139.

Pike R.J. and S.E. Wilson (1971). Elevation-Relief Ratio, Hypsometric Integral, and Geo morphic Area- Altitude Analysis. Geological Siciety of America Bullettin, 82, 1079-1084.

Prabu P. and R. Baskaran (2013). Drainage Morphometry of Upper Vaigai River Sub-basin, Western Ghats, South India Using Remote Sensing and GIS. Journal of Geological Society of India, 82, 519-528.

Prakash K., S. Singh and U.K. Shukla (2016). Morphometric changes of the Varuna river basin, Varanasi district, Uttar Pradesh. Journal of Geomatics, 10(1), 48-54.

Rai P.K., K. Mohan, S. Mishra, A. Ahmad and V.N. Mishra (2017). A GIS-based approach in drainage morphometric analysis of Kanhar River Basin, India. Applied Water Science, 7(1), pp.217-232.

Ritter D. F., R.C. Kochel and J.R. Miller (2002). Process Geomorphology. McGraw Hill, Boston.

Rudraiah M, S. Govindaiah and S.S. Vittal (2008) Morphometry using Remote Sensing and GIS techniques in the sub-basins of Kagna river basin, Gulbarga district, Karnataka, India. J of Indian Soc of Rem Sensing., 36, 351-60.

Schumm S.A. (1956) Evolution of drainage systems and slopes in badlands at Perth Ambos, New Jersey. Geological of Society of America, 67, 597-646.

Sharma A.K. and J.P. Shukla (2015). A Remote Sensing and GIS Based Approach to Evaluate the Ground Water Prospects of Baghain Watershed, Panna and Satna Districts of M.P., India: A Case Study. Journal of Geological Society of India, 86, 733-741.

Shimpi S., C. Mahajan and V.M. Rokade (2014). Drainage morphometric approach for evaluation of water conservation potential and artificial recharge structures site suitability. Gondwana Geological Magazine, 14, 57-64.

Singh A. P., A.K. Arya and D.S. Singh (2020). Morphometric Analysis of Ghaghara River Basin, India, Using SRTM Data and GIS. Journal of Geological Society of India, 95, 169- 178.

Singh D. S. and A. Awasthi (2011). Implication of Drainage Basin Parameterss of Chhoti Gandak River, Ganga Plain, India. Journal of Geological Society of India, 78, 370-378.

Singh P., J.K. Thakur and S. Kumar (2013). Delineating groundwater potential zones in a hard-rock terrain using geospatial tools. Hydrological Sciences Journal, 58(1), 213–223.

Singh O., A. Sarangi and M. Sharma (2008). Hypsometric integral estimation methods and its relevance on erosion status of North-Western Lesser Himalayan Watersheds. Water Resource Manage, 22, 1545–1560.

Singh P., A. Gupta and M. Singh (2014). Hydrological inferences from watershed analysis for water resource management using remote sensing and GIS techniques. Egypt Journal Remote Sensing Space Science, 17, 111–121.

Singh S. (1997). Geomorphology, Prayag Pustak Bhawan, Allahabad, 18- 107.

Smith K. G. (1950). Standards for grading texture of erosional topography. Amer. Jour. Sci., 248, 655-668.

Soni S. (2017). Assessment of morphometric characteristics of Chakrar watershedin Madhya Pradesh India using geospatial technique. Applied Water Science, 7, 2089–2102.

Strahler A.N. (1952). Hypsometric (area-altitude) analysis of erosional topography. Geological Society of America, 63, 1117-1142.

Strahler A. N. (1957). Quantitative analysis of watershed geomorphology. Trans. Amer. Geophys. Union, 38, 913-920.

Strahler A.N. (1964). Quantitative geomorphology of drainage basins and channel networks, In: V. T. Chow (Ed.), Handbook of Applied Hydrology, McGraw Hill Book Company, New York, Section 4-11.

Walcott R. C. and M.A. Summerfield (2008). Scale dependence of hypsometric integral: An analysis of southeast African basins, Geomorphology, 96(1–2), 174–186.

Zaidi F.K. (2011). Drainage basin morphometry for identifying zones for artificial recharge: A case study from the Gangas river basin, India. Journal of Geological Society of India, 77, 160-166.

Ziaur R.A., L.A.K. Rao and Y. Alia (2012). GIS morphometric analysis of Yamuna drainage network in parts of Fatehbad area of Agra district, Uttar Pradesh. Journal of Geological Society of India, 79, 505-514.

Impact of effect of meteorological parameters on fog formation using satellite data over the Indo-Gangetic Plains region

Arun S H[1,2]*, Sasmita Chaurasia[1], Atul Kumar Varma[1] and Raj Kumar[3]
[1]EPSA, Space Applications Centre, ISRO, Jodhpur Tekra, Ahmedabad- 380 015, Gujarat, India
[2]Department of Physics, Gujarat University, Navrangpura, Ahmedabad- 380 009, Gujarat, India
[3] National Remote Sensing Centre, ISRO, Hyderabad- 500 037, Telangana, India
*Email: arunshphysics05@gmail.com

(Received: Aug 19, 2021; in final form: Oct 15, 2021)

Abstract: The effect of different meteorological parameters such as soil moisture and surface temperature on the evolution of fog over the Indo-Gangetic Plains (IGP) has been investigated. The study has been carried out for the winter seasons (November to February) during the years 2015-16, 2016-17 and 2017-18 over six locations in the IGP using the Soil Moisture Active Passive (SMAP) satellite soil moisture and surface temperature product. Indian National Satellite (INSAT-3D) derived fog product has been used to identify the occurrence of fog over the same location in study period. An increase in soil moisture and decrease in surface temperature before the onset of fog has been clearly identified for 77% of cases. Moreover, a positive relation between the maximum soil moisture in monsoon and number of fog days in winter has also been observed. In addition, a positive relation has also been identified between the number of days having soil moisture more than 20% in monsoon season and the number of fog days in winter season. The results of these analysis can give better insights to development and nature of fog over the IGP. These findings can also be used to better predict its occurrence in future nowcasting/forecasting applications.

Keywords: Fog, Soil moisture, Surface temperature, Monsoon, INSAT-3D, SMAP

Introduction

Indo Gangetic Plains (IGP) is severely affected by fog during every winter (November-February). The low visibility condition due to fog is a major obstacle to flight operations, shipping and land transportations. Fog formation is related to thermodynamical, radiative and microphysical processes as well as surface conditions (Gultepe et al., 2007). Radiation and advection fog are the most common types of fog over the IGP in which former one is a night time phenomenon formed under clear sky and high relative humidity conditions whereas the later one formed due to the advection of warm air over cold surface. Radiational cooling produces temperature inversion which results a stable layer of air associated with a light breeze (< 5 m s^{-1}) for the convective circulation of the air. Western disturbance is considered to be one of the major cause for the dense fog conditions over the IGP (Dimri et al., 2006). The terrestrial structure of the IGP of low elevation and the Himalayan ranges on the northern side act as a medium for trapping fog for longer period. A large moisture content produced by the river Ganga and its tributaries as well as the irrigated wheat field over this region in the beginning of the winter season adds moisture to the atmosphere which becomes a favourable condition for the formation of radiation fog over the IGP. In addition, agricultural crop burning before the winter is also a major reason for the dense fog conditions over the IGP (Badarinath et al., 2009). The impact of crop residue burning over northern India and the long range transport of aerosols during the post monsoon season of 2012 has been examined using the satellite and ground based measurements (Kaskaoutis et al., 2014). The impact of crop residue burning on the air quality over the IGP has been studied. The study observed an increased risk in the ambient air quality over the IGP due to crop residue burning. The dominance of anthropogenic urban industrial aerosols during the winter season over Kanpur has been studied in detail by Singh et al. (2004). A large number of thermal power plants situated in the IGP provide cloud condensation nuclei which are favorable for fog formation (Prasad et al., 2006).

Satellite based fog monitoring is highly effective due to its improved spatial, spectral and temporal resolution. Use of satellite remote sensing for fog studies has been discussed in many earlier studies (Eyre et al., 1984; Kudoh and Noguchi, 1991; Anthis and cracknell et al., 1999; Bendix et al., 2005; Cermak and Bendix, 2011; Gautam, 2014; Yi L et al., 2015; Chaurasia and Jenamani, 2017; Arun et al., 2018; Dey 2018; Arun et al., 2021). Brightness temperature difference technique has been used for the detection of fog at night time (Ellrod.1995; Lee et al., 1997; Chaurasia et al., 2011a) whereas temporal differencing technique and spatial homogeneity test has been performed for the identification of fog during day time over the IGP (Chaurasia and Gohil, 2015). A collective method has been implemented for the detection of fog over the Delhi Earth Station (DES) using ground based Ceilometer (Arun et al., 2018a). Fog Stability Index (FSI) technique based on temperature and humidity profiles of sounder observations has the potential to detect fog even in the presence of high clouds (Song and Yum, 2013; Wantuch 2001; Arun et al., 2018b). The same algorithm is effective for both day and night time analysis. A long term assessment of general trends of fog over the IGP has been performed (Kutty et al., 2020) and the study shown that an increase in fog frequency is highly related to changes in meteorological parameters. In spite of notable improvements in fog detection, fog forecasting still remains a challenging task. Accurate estimation of meteorological parameters is the crucial factors in fog forecasting system.

Meteorological parameters such as surface temperature, soil moisture, wind speed etc., play a crucial role on the evolution of fog over the IGP. Jenamani (2007) used the hourly fog data and daily maximum and minimum temperature during the major winter months (December and January) to estimate the monthly average temperature and relate their trends. Their study was carried out for the period of 1960 to 2005 and it has shown a fall in average maximum temperature by 2-3 K since 1989 and increase in average fog hours per day by 8 hours. Sathiyamoorthy et al., (2016) analyzed the surface temperature gridded data from IMD and suggested that negative temperature anomalies prevail over the IGP where radiative cooling exerted by fog. Moreover, the negative anomalies in surface temperature can cause further drop in the surface temperature over the IGP during the winter. This study also suggested that the foggy winter is colder than non-foggy winter.

Indian weather is basically governed by two monsoon systems viz., southwest monsoon (summer monsoon) and northeast monsoon (winter monsoon). The former one has a span of four months from June to September whereas the later one has a short span of two months from October to November. These two monsoon systems are the major source of soil moisture over the IGP. In addition, a large moisture content produced by the river Ganga and its tributaries as well as the irrigated wheat field over this region, in the beginning of the winter season, adds moisture to the atmosphere, also develops favourable conditions for the formation of radiation fog over the IGP. Soil moisture in the surface layer plays an important role in the hydrological cycle as well as influencing the feedback between land surface and atmospheric processes. Moreover, the movement of water from the soil into the atmosphere results the cooling of Earth's surface which leads to radiation fog (Chaurasia et al., 2011b). The *in-situ* measurements are insufficient to analyze the spatial and temporal variation of soil moisture in a large scale. In order to characterize the complete spatial and temporal variability of soil moisture, satellite remote sensing provides better opportunity (Wagner et al., 1999; Kerr et al., 2001; Njoku et al., 2003; Thapliyal et al., 2005). Soil moisture retrieval studies over India, using passive microwave remote sensing, have been taken up since many years (Thapliyal et al., 2003; Singh et al., 2005; Said et al., 2008; Srivastava et al., 2009; Singh et al., 2009; Ponnurangam et al., 2011; Chaurasia et al., 2012; Tomer et al., 2015; Chakravorty et al., 2016; Kumar et al., 2019). Soil moisture information has been provided by the passive microwave remote sensing by measuring the dielectric properties of the soil. Accurate estimation of soil moisture and surface temperature are crucial factors of fog detection/monitoring and forecasting system. Sensitivity study using a one dimensional model of the nocturnal boundary layer has been performed for fog forecasting (Bergot and Guedalia, 1994). The necessary information regarding meteorological parameters like surface temperature, soil moisture concentration and wind condition have been given as the input to the model.

In the present study, the effect of soil moisture and surface temperature on fog formation over the IGP has been investigated using SMAP data of 2015 to 2018. The INSAT-3D derived fog products available at www.imd.gov.in and www.mosdac.gov.in have been used for the identification of fog events.

2. Data used

2.1 Soil Moisture Active Passive (SMAP) data

The SMAP satellite, with a sun-synchronous 6 AM/PM orbit, was launched on January 31, 2015 by the National Aeronautics and Space Administration (NASA) for an improved estimation of energy, water and carbon transfer between land and atmosphere. The entire globe has been covered by the SMAP in every 2 to 3 days from an altitude of 685 km. The L-band radiometer (~40 km resolution) has been used for measurements for soil moisture mapping (SMAP Handbook, NASA, 2014). The soil moisture product is reliable and robust (0.04 cm^3 cm^{-3} uncertainty). The SMAP radiometer measurements provide surface temperature measurements with better than 1.3 K uncertainty. The level 3 radiometer global daily soil moisture and surface temperature products having a spatial resolution of 36 km available at www.nsidc.org have been used in the present study.

2.2 INSAT-3D

The INSAT-3D is an advanced geostationary weather satellite operational since 26th July 2013. The Very High Resolution Radiometer (VHRR), 19 channel sounder, Data Relay Transponder (DRT) and Search and Rescue Transponders are onboard INSAT-3D satellite. INSAT-3D is well capable of generating the images of the Earth in six wavelength bands i.e. Visible (VIS), Short Wave Infra-Red (SWIR), Mid Wave Infra-Red (MWIR), Water Vapor (WV), Thermal Infra-Red 1 (TIR1) and Thermal Infra-Red 2(TIR2). The INSAT-3D imager retrieved fog products having a spatial resolution of 4 km and temporal resolution of 30 minutes has been used in this study. This fog products are being generated using the INSAT-3D TIR1 (10.8 μm) and MWIR (3.9 μm) channel data for nighttime fog and TIR1 (10.8 μm) and visible (0.5-0.7 μm) channel for daytime fog (Fog products, INSAT-3D Algorithm Theoretical Basis Development Document (ATBD, 2015, www.mosdac.gov.in). The INSAT-3D fog products available at www.mosdac.gov.in and www.imd.gov.in have been used in the present study.

3. Study region

The study has been carried out for 2015-16, 2016-17 and 2017-18 over six locations namely Amritsar (31.7° N, 74.8° E), Delhi (28.6° N, 77.1° E), Jaipur (26.8° N, 75.8° E), Lucknow (26.8° N, 80.9° E), Varanasi (25.5° N, 82.9° E) and Patna (25.6° N, 85.1° E) in the IGP over which dense fog conditions are observed in every winter. These six locations are shown in Figure 1

4. Methodology

Daily values of soil moisture content and surface temperature have been monitored over six locations in the IGP using SMAP data from 2015 to 2018. Since, the spatial resolution of SMAP is ~40 km, meteorological information from the nearest pixels average to the locations are collected. The entire study has been divided into three parts. The first part contains information regarding the general characteristics of soil moisture and surface temperature during various seasons by using the maximum, minimum and monthly average values of these parameters from SMAP data. In the second part, daily values of soil moisture and surface temperature have been used to study the effect of meteorological parameters on the evolution of fog over the IGP. An increase in moisture content and decrease in surface temperature are favourable conditions for fog development. Therefore, only those samples have been considered for further analysis in which an increase in soil moisture and decrease in surface temperature have been noticed in comparison to its previous day observations. The relative percentage of increase in soil moisture and decrease in surface temperature have been calculated using the formula,

Relative percentage (%) $=\left[\frac{x-y}{y}\right] 100$……..(1)

where,
x = Soil moisture/ surface temperature observations on the current day.
y = Soil moisture/ surface temperature observations on the previous day.
Further, the corresponding fog/no fog events have been identified using the INSAT-3D fog products. The relation between maximum value of soil moisture and number of days having more than 20% soil moisture in monsoon season with the number of fog days in the corresponding winter season have been studied in detail in part 3

5. Results and discussions

5.1 General characteristics of soil moisture and surface temperature over the IGP

The maximum and minimum soil moisture and surface temperature over the six locations in the IGP during the period of study have been analyzed and shown in Table 1 and Table 2 respectively for three years from the month of May to February.

Figure 1. Study regions are indicated in blue colour (1. Amritsar, 2. Delhi, 3. Jaipur, 4. Lucknow, 5. Varanasi and 6. Patna). Picture courtesy: www.earth.google.com.

Table 1. The minimum and maximum soil moisture over six locations in the IGP during 2015-16, 2016-17 and 2017-18.

Location	Maximum soil moisture (cm^3 cm^{-3})			Minimum soil moisture (cm^3 cm^{-3})		
	2015-16	2016-17	2017-18	2015-16	2016-17	2017-18
Amritsar	0.44	0.43	0.45	0.08	0.07	0.11
Delhi	0.32	0.33	0.34	0.11	0.09	0.09
Jaipur	0.32	0.31	0.27	0.06	0.07	0.05
Lucknow	0.46	0.48	0.46	0.09	0.09	0.09
Varanasi	0.47	0.47	0.46	0.07	0.08	0.07
Patna	0.47	0.47	0.47	0.09	0.10	0.09

Table 2. The maximum and minimum surface temperature over six locations in the IGP during 2015-16, 2016-17 and 2017-18.

Location	Maximum surface temperature (K)			Minimum surface temperature (K)		
	2015-16	2016-17	2017-18	2015-16	2016-17	2017-18
Amritsar	311.32	312.03	310.25	285.17	284.65	283.11
Delhi	310.29	309.92	310.41	285.49	284.92	284.18
Jaipur	308.76	309.84	309.14	286.07	285.24	285.66
Lucknow	311.64	311.53	310.29	285.63	284.38	285.19
Varanasi	311.58	311.81	310.45	286.41	284.22	285.46
Patna	311.51	310.59	310.28	286.51	284.99	284.96

From Table 1 it is observed that the maximum soil moisture over Delhi and Jaipur is low (~0.32 (32%)) in comparison to Lucknow, Varanasi and Patna (~0.47 or 47 %). As per different climatic zone of India, Jaipur is under the arid zone, whereas, Delhi is under semi-arid category. These two regions fall under the dry climatic zone where rainfall is less. However, the lowest soil moisture over all the region for all the years shows only a marginal difference (0.05-0.1). For 2017-2018 season, the maximum soil moisture and the minimum soil moisture over Jaipur are observed to be the lowest among all three years under study. Similarly, the maximum surface temperature over Amritsar, Delhi, Lucknow, Varanasi and Patna is ~310 K whereas Jaipur observed to have ~308 K for all three years. However, no remarkable trend has been observed in the minimum surface temperature over different periods of analysis.

The seasons during the study period are classified as pre monsoon (May), southwest monsoon (June-September), northeast monsoon (October-November) and winter season (December-February). Soil moisture concentration over India is mainly governed by the southwest monsoon which brings heavy rainfall. The general characteristics of soil moisture and surface temperature during different seasons have been analyzed and discussed as follows. The monthly average values of soil moisture and surface temperature over six locations in the IGP during 2015-16, 2016-17 and 2017-18 are shown in Figure 2 (a)-(f). Minimum monthly average soil moisture (~0.05 -0.09 cm^3 cm^{-3}) and maximum monthly average surface temperature (~308-310 K) have been observed over all the locations in the IGP during the pre-monsoon period (May)

Similarly, the maximum monthly average soil moisture is recorded during the southwest monsoon period (July-August). From the Figure 2, a gradual increase in soil moisture and decrease in surface temperature have been observed over all the locations in three years during the period from July to August. The southwest monsoon is mainly responsible for the observed feature. The monthly average of soil moisture from May to August over Delhi has shown an increase of ~150% during 2015-16 and 2016-17 in comparison to an increase rate of 100% during 2017-18. Similarly, the monthly average of soil moisture over Amritsar, Patna and Varanasi has shown high values in August (~0.43-0.46 cm^3 cm^{-3}) as compared to May (~0.09-0.12 cm^3 cm^{-3}) in all the three years. Moreover, an increase of ~200-250% in soil moisture has been noticed over Lucknow during the period from July to August for all the years. However, the monthly average of surface temperature has dropped from ~307 K to ~300 K during May-August.

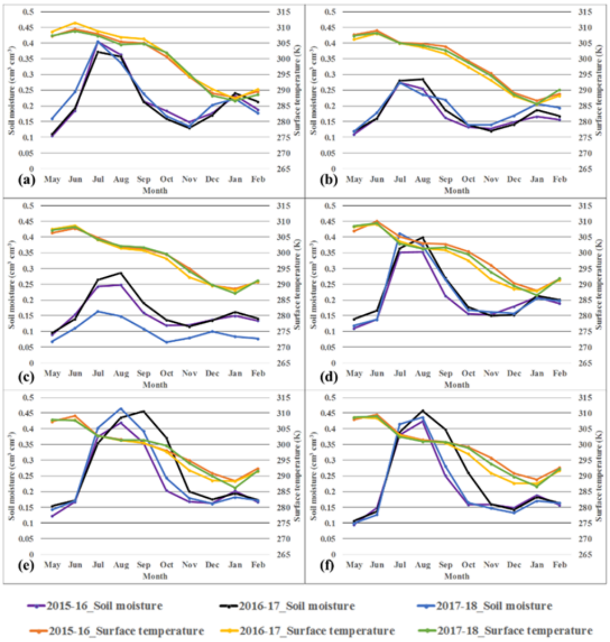

Figure 2. Monthly average of soil moisture and surface temperature during 2015-16, 2016-17 and 2017-18 over (a) Amritsar, (b) Delhi, (c) Jaipur, (d) Lucknow, (e) Patna and (f) Varanasi

In the northeast monsoon period (October-November), both the soil moisture and surface temperature have shown slightly lower values in comparison to southwest monsoon period. This may be due to the short span (i.e. 2 months) and less rainfall in northeast monsoon period as compared to southwest monsoon (i.e. 4 months). For 2016-17 and 2017-18 season, the soil moisture over both Delhi and Jaipur has been decreased to ~0.11 cm^3 cm^{-3} whereas surface temperature dropped to ~290 K. In addition, soil moisture over Jaipur for 2017-18 has been observed to be 0.06 cm^3 cm^{-3} which is the lowest among all locations during the northeast monsoon period. Similarly, the monthly average of soil moisture and surface temperature over the remaining locations have been analyzed. In all the three years, both the soil moisture and surface temperature have shown a decrease of ~0.1-0.15 cm^3 cm^{-3} and ~5 K respectively between southwest monsoon and northeast monsoon over Amritsar, Lucknow, Varanasi and Patna.

The IGP experiences minimum surface temperature and maximum sea level pressure during winter. For all the years, soil moisture has been gradually increased and surface temperature gradually decreased during the period from December to January. An extratropical storm known as Western disturbances that bring sudden winter rain over the IGP could be the most probable reason for the increase in soil moisture and decrease in surface temperature during the winter season. In all the years, a notable increase of 50-100% in soil moisture has been observed in December in comparison to November over all the locations in the IGP. Similarly, the surface temperature also gradually decreased to ~285-287 K in December. Towards the end of February, a gradual decrease in soil moisture followed by an increase in surface temperature has been noticed in all the locations due to the advance of summer season.

5.2 Soil moisture and surface temperature observations before the onset of fog during the winter season

The general characteristics of soil moisture and surface temperature before the onset of fog during winter season (November-February) have been analyzed in detail. Figure 3 (a)-(e) to 5 (a)-(e) represents the temporal variation of soil moisture and surface temperature over the six locations in the IGP during 2015-16, 2016-17 and 2017-18.

From Figure 3 (a)-(e) to 5 (a)-(e), the daily values of those 161 samples in the winter season have been considered for further analysis in which an increase in soil moisture and decrease in surface temperature have been noticed in comparison to its previous day observations. An increase in soil moisture and decrease in surface temperature have been clearly identified in most of the cases before the onset of fog. The fog conditions over the IGP have been monitored using INSAT-3D fog maps which generated at every 30 minutes. Out of the 161 samples in which increase in soil moisture and decrease in surface temperature have been observed, 77.64% cases match with the fog condition indicated by INSAT-3D. The difference in observations in the remaining 22.36% cases could be due to some other factors like difference in geolocation between SMAP and INSAT-3D observations and may also depends upon the time delay between the SMAP observations and fog occurrences. Figure 6 represents the overall statistics between SMAP observations and INSAT-3D fog products during the winter season from 2015-2018. From the Figure 6, it has been observed that the number of samples which shown an increase in soil moisture and decrease in surface temperature is less for Jaipur and Patna as compared to the remaining locations. Jaipur used to have very less rainfall in monsoon period whereas Patna is considered to be a high prone rainfall region. In both the cases, the variation in soil moisture and surface temperature is less which could be the reason for the minimum number of samples. In case of Amritsar, Delhi, Lucknow and Varanasi, the variations in the soil moisture and surface temperature are gradual. The daily SMAP observations are available only at 06:00 UTC whereas the INSAT-3D fog products available at every 30 minutes. A detailed description of some of the events is as follows.

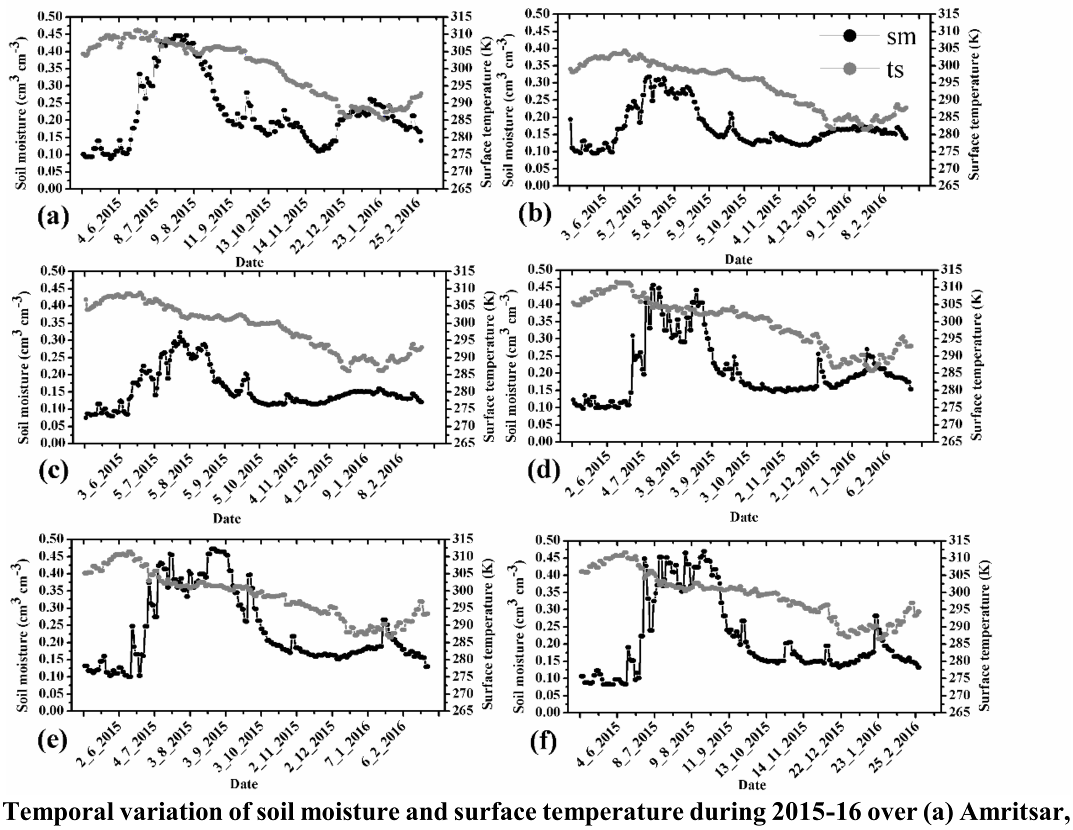

Figure 3. Temporal variation of soil moisture and surface temperature during 2015-16 over (a) Amritsar, (b) Delhi, (c) Jaipur, (d) Lucknow, (e) Patna and (f) Varanasi. Black line represents the soil moisture whereas grey line represents the surface temperature.

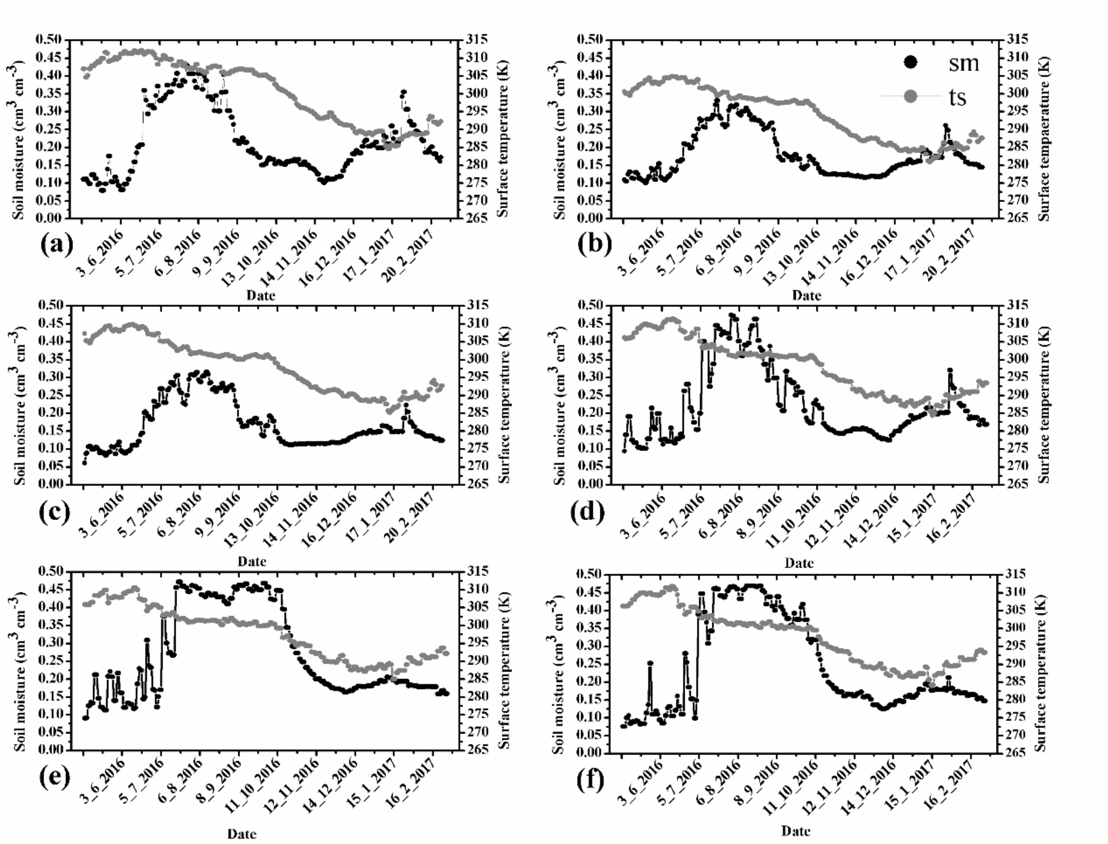

Figure 4. Temporal variation of soil moisture and surface temperature during the winter season of 2016-17 over (a) Amritsar, (b) Delhi, (c) Jaipur, (d) Lucknow, (e) Patna and (f) Varanasi. Black line represents the soil moisture whereas grey line represents the surface temperature.

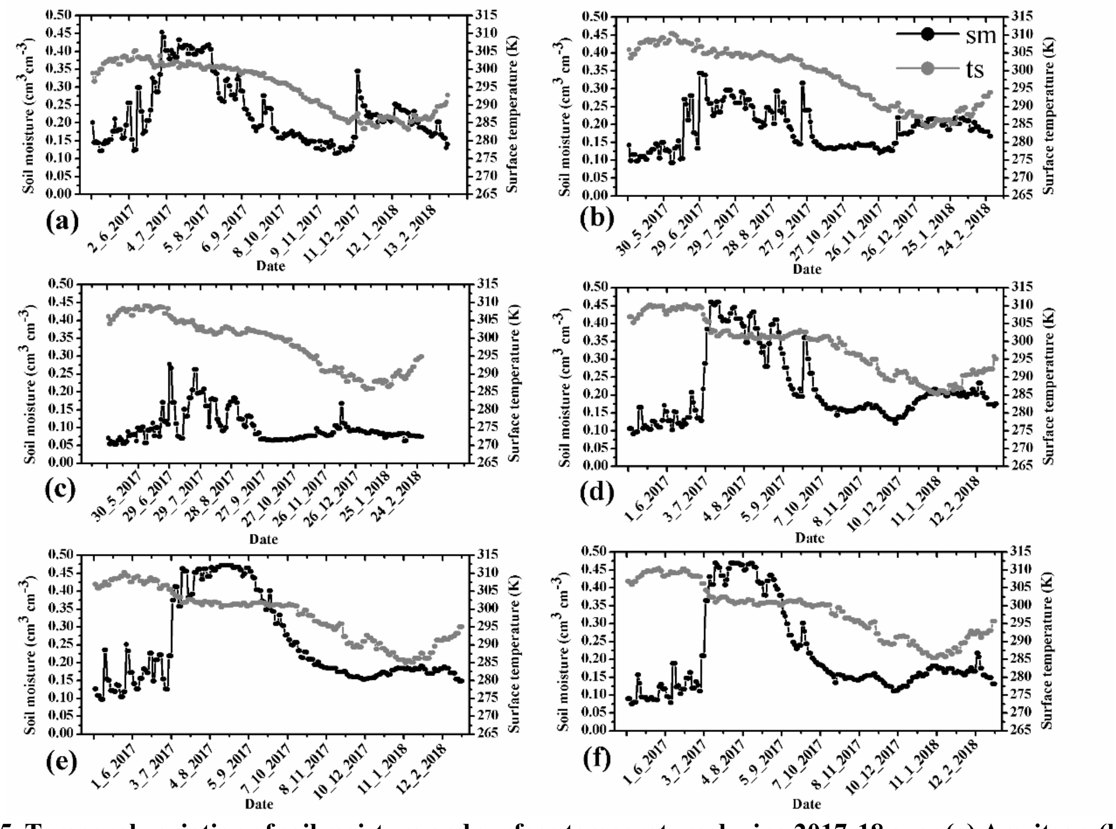

Figure 5. Temporal variation of soil moisture and surface temperature during 2017-18 over (a) Amritsar, (b) Delhi, (c) Jaipur, (d) Lucknow, (e) Patna and (f) Varanasi. Black line represents the soil moisture whereas grey line represents the surface temperature.

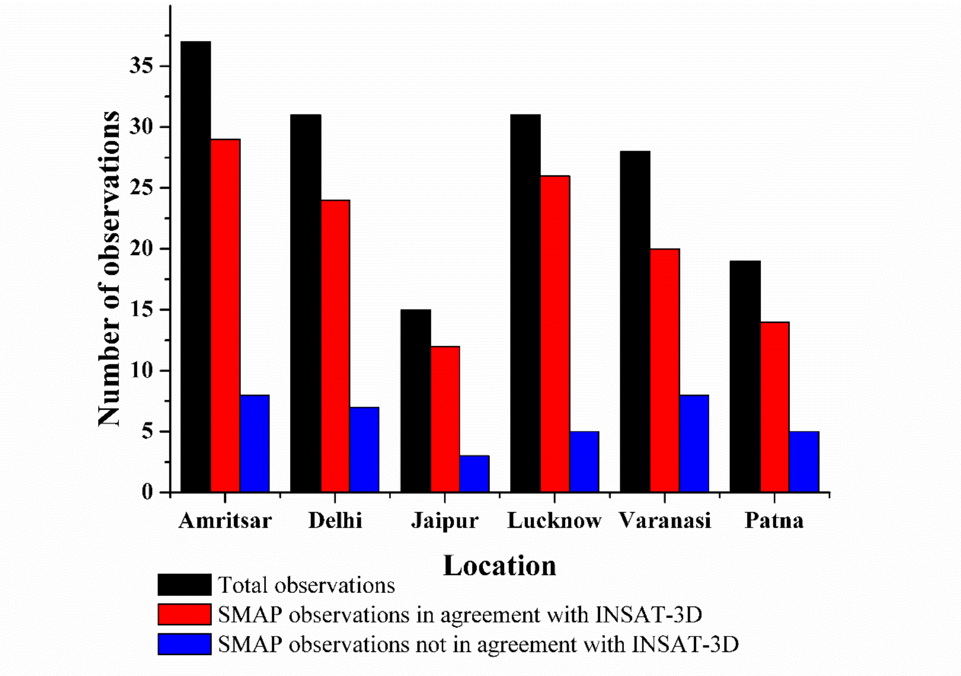

Figure 6. Bar diagram between SMAP observations and INSAT-3D fog products.

Amritsar used to have dense fog condition in every winter. Major parts of the Amritsar soil are of coarse loamy and calcareous in nature made up of roughly equal properties of sand, slit and clay. Generally, these soils support productive forest growth due to their favourable moisture and nutrient capacities (Sehgal and stoops, 1972; Pal et al., 2009). The water holding capacity of these soils is also high. Moreover, the annual rainfall over Amritsar is also high in comparison to Delhi and Jaipur but similar to that of Lucknow and Varanasi. Due to the favourable conditions for fog formation witnessed, Amritsar is one of the severely fog affected regions in the IGP. An increase in soil moisture by 20.2% and decrease in surface temperature by 0.2% have been noticed over Amritsar on 15 January 2016 in comparison to its previous day observations. The INSAT-3D identified fog over Amritsar on the same day at 07:00 UTC. Similarly, an increase in soil moisture by 6.2%, 10.9%, 9.9% and decrease in surface temperature by 0.1%, 0.6% and 0.2% have been observed on 12^{th}, 15^{th} and 23^{rd} of December 2016 respectively over Amritsar before the onset of fog. Fog has been detected over Amritsar at 07:00 UTC, 22:00 UTC and 19:30 UTC respectively. Moreover, fog has been identified over Amritsar on 16 January 2017 at 07:00 UTC where the soil moisture observed to have increased by 12.7% and surface temperature decreased by 0.3% as compared to its previous day observations. For the season 2017-18, a slight increase in soil moisture before the onset of fog has been observed over all the six locations during the third week (11-17) of December 2017. An increase in soil moisture by 116.1% and decrease in surface temperature by 0.5% have been noticed over Amritsar on 12 December 2017. The INSAT-3D identified the fog over Amritsar later at 13:00 UTC [Figure 7(b)] on the same day. In addition, fog has also been detected over the same region on 26 January 2018 at 18:00 UTC [Figure 7(f)] whereas soil moisture shown an increase by 3.5% and surface temperature decrease by 0.2% in comparison to previous day observations.

The national capital region used to have dense fog condition in every winter. Urbanization, industrialization and aerosol loading over Delhi are favourable for fog formation (Gautam et al., 2007). Burning of agricultural waste in nearby regions of Punjab and Haryana also results in severe intensification of fog over Delhi (Sharma et al., 2010). A phenomenon known as urban heat island has been reported over Delhi in recent time (Gautam and Singh, 2018). Urban heat island, refers to the higher temperature seen in Delhi in comparison to adjacent rural areas, is also responsible for fog dissipation. This could be due to intense concrete development, growing population and reduced green cover. The average precipitation days, maximum rainfall and number of fog days are also less for Delhi in comparison to Lucknow, Varanasi and Patna. The majority of soil in Delhi is sandy loam in nature having less water holding capacity which results in low soil moisture on the surface (Pal et al., 2003). This could be another reason for the lesser number of fog days over Delhi. Some of the events over Delhi and Jaipur are discussed as follows.

Soil moisture on 11 December 2017 over Delhi and Jaipur has been observed to be 0.14 and 0.09 $cm^3\ cm^{-3}$ respectively. A notable increase of 48.2% and 70.9% respectively in soil moisture has been observed over both the locations on 12 December 2017. Moreover, the surface temperature over Delhi and Jaipur has also been decreased by 0.7 % and 0.8% respectively during the same period. The INSAT-3D identified the first fog event of the season on 12 December 2017 at 13:00 UTC [Figure 7(b)] and 20:00 UTC [Figure 7(c)] respectively over the locations. Similarly, on 07 January 2017, an increase in soil moisture of 17.3% and decrease in surface temperature by 0.3% have been observed over Delhi before the onset of fog and the INSAT-3D identified fog cover later at 08:00 UTC [Figure 7(d)] over the same location.

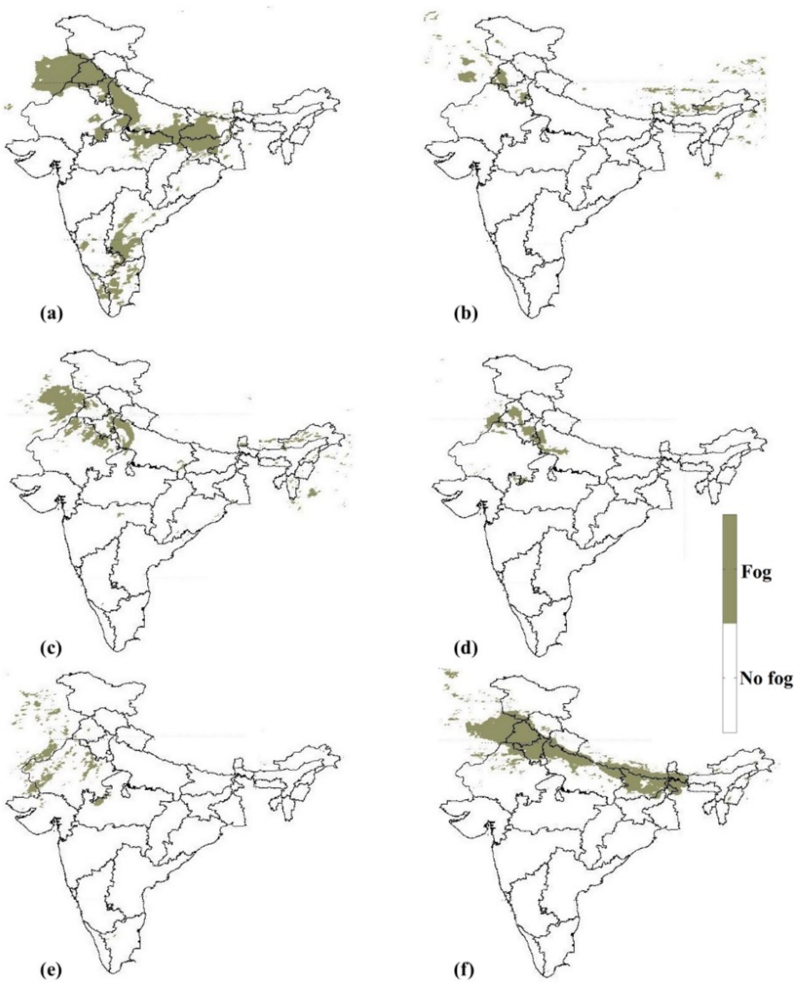

Figure 7. The INSAT-3D fog maps on (a) 20 January 2016 at 07:00 UTC, (b) 12 December 2017 at 13:00 UTC, (c) 12 December 2017 at 20:00 UTC and (d) 07 January 2017 at 08:00 UTC, (e) 26 January 2017 at 18:30 UTC and (f) 26 January 2018 at 18:00 UTC. Fog is indicated by green colour.

Moreover, on 27 January 2017, the soil moisture and surface temperature over Delhi observed to be 0.21 cm^3 cm^{-3} and 286.26 K respectively. An increase in soil moisture of 22.9% and decrease in surface temperature by 0.5% have been identified which are followed by dense fog over the same location at 07:00 UTC. Similarly, fog has been detected over Delhi on 25 December 2017 and on 26 January 2018 at 19:00 UTC and 18:00 UTC [Figure 7(f)] respectively. The soil moisture observations on 25 December 2017 and 26 January 2018 have shown an increase in soil moisture by ~8.0-12.0% as compared to its previous day observations. The corresponding surface temperature on 25 December 2017 and 26 January 2018 has been observed to be 287.35 K and 285.24 K respectively which is ~0.3-0.4% less than that of its previous day observations. An increase of 14.3% in soil moisture and decrease in surface temperature of 0.3% have been noticed over Jaipur on 07 January 2017 and the INSAT-3D identified fog over Jaipur at 17:00 UTC on the same day. Moreover, an increase of 25.4% in soil moisture and decrease in surface temperature of 0.5% over Jaipur have also been observed on 26 January 2017 and the fog has been identified later at 18:30 UTC [Figure 7(e)]. It has also been observed that Jaipur used to have minimum number of fog days as compared to the remaining locations in the IGP. This may be due to the fact that over Jaipur the soil is sandy in nature, which has a very less water holding capacity.

After rainfall or irrigation water percolates deep into the soil very soon. So the soil gets heated up rapidly and cools quickly. The temperature gradient observed over Jaipur is very high. Since, less moisture is available at the surface, the water vapour content over this region is very less. This in turns leads to less number of foggy days over Jaipur. However, in case of Lucknow the variation of surface temperature is gradual. It has also been observed that Lucknow, Varanasi and Patna used to have more number of precipitation days in comparison to Delhi and Jaipur. The annual rainfall over these regions is also notably higher and have abundance moisture sources in the river Ganga and its tributaries. Moreover, the soil type in these regions is alluvial (Bhargava et al., 1981) formed mainly due to slit deposited by the river Ganga and its canal network. These regions are considered to be the most productive agricultural lands in India. The water holding capacity of alluvial soil is relatively higher than that of sandy loam soil in the Delhi-Jaipur region. The alluvial soil can hold the water after the rainfall thus by increasing the moisture content on the soil surface. This leads to a large number of fog days in winter season over these locations in the IGP. Some of the events over Lucknow, Varanasi and Patna are discussed as follows.

In case of Lucknow, an increase of 58.5% in soil moisture and decrease in surface temperature of 0.8% have been observed on 03 December 2015 as compared to the observation on 02 December 2015. Fog has been identified over the same region on 03 December 2015 at 21:00 UTC. Similarly, on 20 January 2016, soil moisture increased to 0.26 cm^3 cm^{-3} from 0.18 cm^3 cm^{-3} and the surface temperature decreased to 286.31 K from 287.43 K and the INSAT-3D detected the fog over the same region later at 07:00 UTC [Figure 7(a)]. In addition, an increase by 12.4% in soil moisture has been observed over the same region on 14 December 2017 followed by fog condition at 22:00 UTC. As the changes in soil moisture and temperature were not remarkable, other parameters such as wind speed, atmospheric pollution level etc. may need to be investigated. Similarly, fog has been identified over Lucknow on 27 December 2016 at 20:30 UTC after an increase in soil moisture (10.4%) and decrease in surface temperature (0.3%). Moreover, on 9th and 28th of January 2017, an increase of 8.3% and 59.7% in soil moisture and decrease in surface temperature of 0.2% and 0.4% have been observed over Lucknow as compared to the soil moisture on 08th and 27th of January 2017 respectively. The INSAT-3D identified fog in both events on 09th and 28th of January 2017 at 07:00 UTC and 21:30 UTC respectively. Similar condition has been observed on 13 February 2018 as well. An increase in soil moisture of 16.1% and decrease in surface temperature of 0.2% have been observed on 13 February 2018 over Lucknow followed by dense fog at 21:30 UTC. It has been observed that over Varanasi, soil moisture increases by 59.8% and surface temperature decreases by 1.3% on 20 January 2016 before the onset of fog. Fog has been detected on 09 January 2017 at 06:30 UTC under similar conditions in the same region. Soil moisture and surface temperature over Varanasi have been observed to be 0.14 cm^3 cm^{-3} and 296.07 K respectively on 02 December 2015 and fog has been detected later at 21:30 UTC. A notable increase of 34.7% in soil moisture and decrease by 1.2% in surface temperature have been observed over Varanasi on 03 December 2015. Moreover, an increase in soil moisture by 5.6% has been noticed over Varanasi on 11 December 2017 before the onset of fog. The INSAT-3D detected fog over Varanasi on 11 December 2017 at 18:30 UTC. Similar conditions have been observed over Patna in which the INSAT-3D detected fog on 18 December 2017 at 18:30 UTC. The soil moisture has shown an increase of 6.2% on 18 December 2017 as compared to its previous day observations. An increase of 59.8% in soil moisture and decrease of 0.5% in surface temperature before the onset of fog have been observed and fog is identified by the INSAT-3D on 20 January 2016 at 07:00 UTC [Figure 7(a)] over Patna. Generally, an increase in soil moisture and decrease in surface temperature have been observed in most of the cases over all the locations in the IGP during the period of study. However, the time scale of difference between increase in soil moisture and decrease in surface temperature with the evolution of fog varies from 02:00 to 14:00 hours depending upon the meteorological conditions over various locations. It has been observed that in all the locations in all three years, the soil moisture concentration is getting increased and surface temperature getting decreased as the fog season progresses.

5.3 Relation between SMAP derived soil moisture in monsoon season and number of fog days in winter season

The maximum soil moisture in monsoon and number of foggy days in winter have been analyzed using SMAP derived soil moisture product and INSAT-3D fog products respectively. From the Figure 8, it has been observed that the maximum soil moisture in monsoon and number of foggy days in winter over the IGP are in agreement in most of the cases. The soil moisture over Jaipur i.e.0.27 cm^3 cm^{-3} during 2017-18 is considered to be the lowest among all the locations during the monsoon season and the corresponding number of foggy days has also been observed to be low i.e. 14. For the season 2017-18, the most number of foggy days have been observed over Patna (47) and the soil moisture also observed to be of maximum (0.47 cm^3 cm^{-3}). Similarly, Delhi have moderate maximum soil moisture and the number of fog days over the Delhi is 24. Similarly, Amritsar, Lucknow and Varanasi have a maximum soil moisture of 0.46 cm^3 cm^{-3} in monsoon and the number of foggy days during winter has observed to be 32, 35 and 30 respectively. In addition, maximum soil moisture over Amritsar, Lucknow, Varanasi and Patna during the season of 2016-17 has been observed to be 0.43, 0.48, 0.47 and 0.47 cm^3 cm^{-3} respectively. The corresponding number of foggy days have also been observed to be high (40, 47, 38 and 45 respectively). However, the number of fog days over Amritsar during 2017-18 season is moderate (33) even though the soil moisture has shown maximum value (0.46 cm^3 cm^{-3}) which needs further analysis. These kind of discrepancies may be due to the effect of other meteorological parameters which play a significant role on the evolution of fog over the IGP. Delhi have moderate number of foggy days (33) with a maximum soil moisture of 0.33 cm^3 cm^{-3} whereas the Jaipur have the least number of foggy days (19). Over all, maximum soil moisture in monsoon and number of foggy days in winter are in agreement in most of the cases, i.e. the number of fog days in the winter season increases with the increase in soil moisture content in the corresponding monsoon season.

Figure 8 also shows the inter year variation in number of fog days. The total number fog days over all the locations have been observed to be the highest in 2016-17 season (222). The minimum number of fog days have been observed in 2015-16 season (111) whereas the number of fog days in 2017-18 season (182) have been observed to be moderate. The winter season of 2017-18 is relatively stronger than 2015-16 but weaker than 2016-17 season. The average of maximum soil moisture value in monsoon over all locations was observed to be 0.42 cm^3 cm^{-3} in 2017 which is the highest in comparison to the remaining seasons (i.e. 0.41 cm^3 cm^{-3} in 2015 and 2016). However, the variations in the average maximum value of soil moisture over the seasons are insignificant, some more general approach is required to provide better estimation of the relation between soil moisture value in monsoon and the corresponding number of fog days in winter which is disused in the following section.

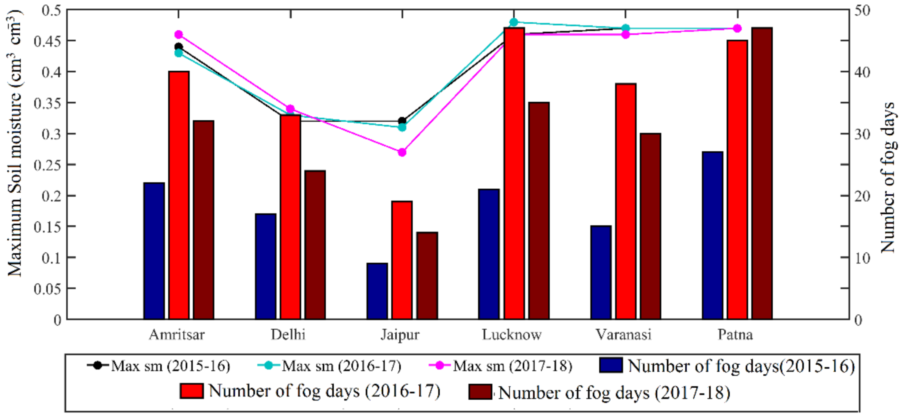

Figure 8. The maximum soil moisture value in monsoon Vs the number of fog days in the winter over the six locations in the IGP during the years 2015-16, 2016-17 and 2017-18.

The effective soil moisture which is available to plant plays a crucial role in the feedback process for atmospheric circulation. In order to analyze the effect of this effective available soil moisture or fog, a minimum soil moisture of 20% is considered to be common threshold for all the regions under study which is shown in Figure 9. The water retention property of soils varies with types of soil, which in turn is characterized by the texture of the soil. The main soil types over the 161 plains are alluvial (Lucknow, Varanasi and Patna), sandy (Jaipur), sandy loam (Delhi) and loamy over Amritsar. All these categories of soils have different water retention capacity and thus the effective soil moisture is different. However, considering the types of all the soils over IGP a minimum threshold of 20% of the available soil moisture has been considered for the present analysis. Relation between the number of days having soil moisture greater than 20% in monsoon season and the corresponding number of fog days in winter season has been analyzed. It has been observed that Patna has the highest number of fog days in all the three years. The number of days having soil moisture greater than 20% in monsoon season is also observed to be the highest for Patna in comparison to the remaining locations. Lucknow and Varanasi observed to have similar number of fog days whereas Jaipur observed to have the lowest number of fog days among all the locations in all the years. For 2017-18, Patna observed to have maximum number of days (100) in which soil moisture value is greater than 20% and the corresponding number of fog days (47) is also observed to be the highest among all the locations during the period of study. Amritsar, Lucknow, Varanasi and Patna observed to have more number of days having soil moisture value greater than 20% as compared to Delhi and Jaipur. This could be due to the fact that the soil moisture concentration is mainly depends upon the monsoon rainfall which is observed to be higher over Amritsar, Lucknow, Varanasi and Patna in comparison to Delhi and Jaipur. The total number of fog days i.e. 222 over all the six locations during 2016-17 is considered to be the highest in comparison to that of 111 and 182 during 2015-16 and 2017-18 respectively. Moreover, the total number of days having soil moisture value greater than 20% over all the locations during the period of study have also been estimated. For 2016-17, the number of days having soil moisture greater than 20% over all the locations have been observed to be 517 which is the highest in comparison to 2015-16 and 2017-18 which are observed to have 468 and 511respectively. The results between the number of days having soil moisture more than 20% in monsoon and the number of fog days in winter season are in agreement, i.e. the number of fog days in the winter season increases with the increase in soil moisture content in the corresponding monsoon season.

The year 2015 is severely affected by the El Nino effect, a climate pattern that describes the unusual warming of surface waters in the eastern tropical Pacific Ocean (Varikoden et al., 2015). Trade winds coming from South America normally blow westward towards Asia during southwest monsoon. Warming of the Pacific Ocean results in weakening of these winds. Therefore, moisture content gets limited which results in reduction and uneven distribution of rainfall across the Indian subcontinent. According to IMD rainfall statistics over India during 2015, deficiency in rainfall during southwest monsoon has been noticed. The annual rainfall over the IGP during the 2015 monsoon season was observed to be ~400 mm. According to IMD rainfall statistics over India, the annual rainfall over the IGP during monsoon of 2016 and 2017 observed to be ~600 mm and ~500 mm respectively. The number of fog days in 2015-16 winter season observed to be the minimum in comparison to the remaining two seasons (i.e. 2016-17 and 2017-18). The reduction in soil moisture due to the minimum rainfall could be the most probable reason for the decrease in the number of fog days during 2015-16. The annual rainfall over the IGP has been observed to be the maximum (i.e. ~600 mm) in 2016 monsoon season and the corresponding number of fog days in winter have also shown maximum value (i.e. 222 days). In addition, for 2017-18 winter season, the number of fog days observed to be moderate (i.e. 182 days) and the annual rainfall during 2017 monsoon has also been observed to be moderate (i.e. ~500 mm). Over all, promising results have been observed between the annual rainfall (which in turn have significant role on the soil moisture content) over the IGP and number of fog days in winter season. Climatological analysis of long term data can further derive more promising relations between meteorological parameters and fog formation.

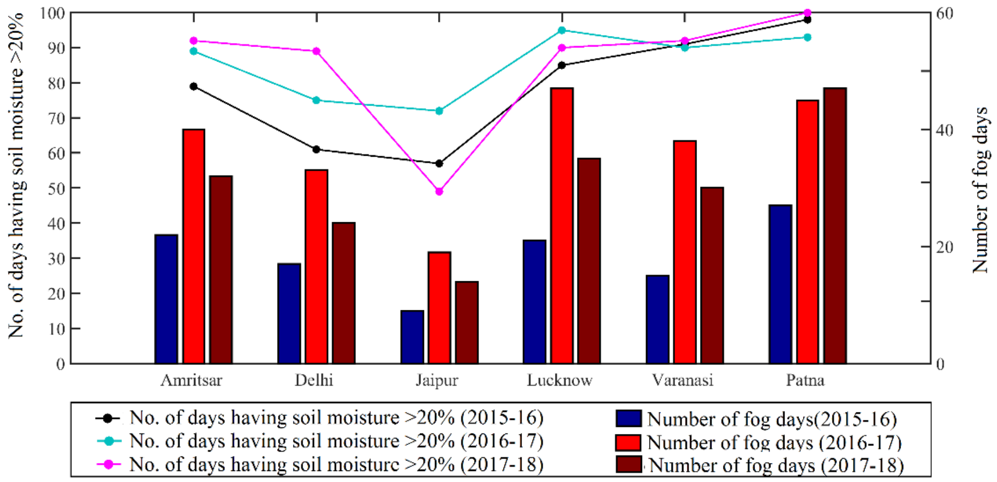

Figure 9. Number of days having soil moisture greater than 20% in monsoon Vs the number of fog days in the winter over the six locations in the IGP during the years 2015-16, 2016-17 and 2017-18.

6. Conclusions

The present work analyzed the effect of meteorological parameters such as soil moisture and surface temperature on the evolution of fog over the IGP covering the period from 2015-2018 using SMAP data. Present study indicated an increase in soil moisture and decrease in surface temperature before the onset of fog over the IGP in a large number of cases. INSAT-3D fog products have been used for the identification of fog events. Promising results have also been obtained between the maximum soil moisture value in monsoon and the corresponding number of fog days in winter. In addition, the relation between the number of days having soil moisture more than 20% in monsoon with the number of fog days in the winter season are also observed to be in agreement. The number of fog days in the winter season increases with the increase in soil moisture content in the corresponding monsoon season. Therefore, the outcomes of these analysis can be used as an input for the fog now casting/forecasting purposes in future applications. However, the operational soil moisture and surface temperature products used in the study are of coarser spatial resolution (~40 km). Thus, it can be suggested that a moderate spatial and better temporal resolution soil moisture and surface temperature information can serve better for fog now-casting/forecasting purposes.

Acknowledgements
Authors are thankful to Shri. D K Das, Former Director and Shri. N M Desai, Director, Space Applications Centre (SAC), ISRO for providing his encouragement and support to carry out the present study. The authors express their sincere gratitude to the Meteorological and Oceanographic Satellite Data Archival Centre (MOSDASC, SAC, ISRO) for providing the INSAT-3D data. The authors also thankful to NASA National Snow and Ice Data Center Distributed Active Achieve Center (NSIDC DAAC) for providing the SMAP data.

References

Anthis A. I., and A.P. Cracknell (1999). Use of satellite images for fog detection (AVHRR) and forecast of fog dissipation (METEOSAT) over lowland Thessalia, Hellas. International Journal of Remote Sensing, 20(6), 1107-1124.

Arun S. H., S.K. Sharma, S. Chaurasia, R. Vaishnav and R. Kumar (2018a). Fog/low clouds detection over the Delhi Earth Station using the Ceilometer and the INSAT-3D/3DR satellite data. International Journal of Remote Sensing, 39(12), 4130-4144.

Arun S. H., S. Chaurasia, A. Misra and R. Kumar (2018b). Fog Stability Index: A novel technique for fog/low clouds detection using multi-satellites data over the Indo-Gangetic plains during winter season. International Journal of Remote Sensing, 39(22), 8200-8218.

Arun S.H., S. Chaurasia, A.K. Varma and R. Kumar (2021). Fog characteristics and it's inter annual variability over the Indo-Gangetic Plains during the winter season using satellite data. Journal of Geomatics, 15(1), 85-94.

Badarinath K.V.S., S.K. Kharol, A.R. Sharma and V.K. Prasad (2009). Analysis of aerosol and carbon monoxide characteristics over Arabian Sea during crop residue burning period in the Indo-Gangetic Plains using multi-satellite remote sensing datasets. Journal of Atmospheric and Solar-Terrestrial Physics, 71(12), 1267-1276.

Bendix J., B. Thies, J. Cermak and T. Nauß (2005). Ground fog detection from space based on MODIS daytime data—A feasibility study. Weather and Forecasting, 20(6), 989-1005.

Bergot T. and D. Guedalia (1994). Numerical forecasting of radiation fog. Part I: Numerical model and sensitivity tests. Monthly Weather Review, 122(6), 1218-1230.

Bhargava G.P., D.K. Pal, B.S. Kapoor and S.C. Goswami (1981). Characteristics and genesis of some sodic soils in the Indo-Gangetic alluvial plains of Haryana and Uttar Pradesh. Journal of the Indian Society of Soil Science, 29(1), 61-70.

Cermak J. and J. Bendix (2011). Detecting ground fog from space–a microphysics-based approach. International Journal of Remote Sensing, 32(12), 3345-3371.

Chakravorty A., B.R. Chahar, O.P. Sharma and C.T. Dhanya (2016). A regional scale performance evaluation of SMOS and ESA-CCI soil moisture products over India with simulated soil moisture from MERRA-Land. Remote Sensing of Environment, 186, 514-527.

Chaurasia S., V. Sathiyamoorthy, B.P. Paul, B. Simon, P.C. Joshi and P.K. Pal (2011a). Night-time fog detection using MODIS data over Northern India. Meteorological Applications, 18(4), 483-494.

Chaurasia S., D.T. Tung, P.K. Thapliyal and P.C. Joshi (2011b). Assessment of the AMSR-E soil moisture product over India. International journal of remote sensing, 32(23), 7955-7970.

Chaurasia S., P.K. Thapliyal and P.K. Pal (2012). Application of a time-series-based methodology for soil moisture estimation from AMSR-E observations over India. IEEE Geoscience and Remote Sensing Letters, 9(5), 818-821.

Chaurasia S. and B.S. Gohil (2015). Detection of daytime fog over India using INSAT-3D data. IEEE Journal of Selected Topics in Applied Earth Observations and Remote Sensing, 8(9), 4524-4530.

Chaurasia S. and R.K. Jenamani (2017). Detection of Fog Using Temporally Consistent Algorithm with INSAT-3D Imager Data Over India. IEEE Journal of Selected Topics in Applied Earth Observations and Remote Sensing, 10(12), 5307-5313.

Dey S. (2018). On the theoretical aspects of improved fog detection and prediction in India. Atmospheric research, 202, 77-80.

Dimri A.P., U.C. Mohanty, M. Azadi and L.S. Rathore (2006). Numerical study of western disturbances over western Himalayas using mesoscale model. Mausam, 57(4), 579.

Ellrod G.P. (1995). Advances in the detection and analysis of fog at night using GOES multispectral infrared imagery. Weather and Forecasting, 10(3), 606-619.

Eyre J.R., J.L. Brownscombe and R.J. Allam (1984). Detection of fog at night using Advanced Very High Resolution Radiometer (AVHRR) imagery. Meteorological Magazine, 113(1346), 266-271.

Gautam R., N.C. Hsu, M. Kafatos and S.C. Tsay (2007). Influences of winter haze on fog/low cloud over the Indo-Gangetic plains. Journal of Geophysical Research: Atmospheres, 112(D5).

Gautam R. (2014). Challenges in early warning of the persistent and widespread winter fog over the Indo-Gangetic Plains: A satellite perspective. In Reducing disaster: Early warning systems for climate change (pp. 51-61). Springer, Dordrecht.

Gautam R. and M.K. Singh (2018). Urban heat island over Delhi punches holes in widespread fog in the Indo-Gangetic Plains. Geophysical Research Letters, 45(2), 1114-1121.

Gultepe I., R. Tardif, S.C. Michaelides, J. Cermak, A. Bott, J. Bendix, M.D. Müller, M. Pagowski, B. Hansen, G. Ellrod and W. Jacobs (2007). Fog research: A review of past achievements and future perspectives. Pure and Applied Geophysics, 164(6-7), 1121-1159.

Jenamani R.K. (2007). Alarming rise in fog and pollution causing a fall in maximum temperature over Delhi. Current Science (00113891), 93(3), 314-322.

Kaskaoutis D.G., S. Kumar, D. Sharma, R.P. Singh, S.K. Kharol, M. Sharma, A.K. Singh, S. Singh, A. Singh and D. Singh (2014). Effects of crop residue burning on aerosol properties, plume characteristics, and long- range transport over northern India. Journal of Geophysical Research: Atmospheres, 119(9), 5424-5444.

Kerr Y.H., P. Waldteufel, J.P. Wigneron, J.A.M.J. Martinuzzi, J. Font and M. Berger (2001). Soil moisture retrieval from space: The Soil Moisture and Ocean Salinity (SMOS) mission. IEEE transactions on Geoscience and remote sensing, 39(8), 1729-1735.

Kudoh J.I. and S. Noguchi (1991). Identification of fog with NOAA AVHRR images. IEEE transactions on geoscience and remote sensing, 29(5), 704-709.

Kumar P., R. Prasad, A. Choudhary, D.K. Gupta, V.N. Mishra, A.K. Vishwakarma, A.K. Singh and P.K. Srivastava (2019). Comprehensive evaluation of soil moisture retrieval models under different crop cover types using C-band synthetic aperture radar data. Geocarto International, 34(9), 1022-1041.

Kutty S. G., A.P. Dimri and I. Gultepe (2020). Climatic trends in fog occurrence over the Indo- Gangetic plains. International Journal of Climatology, 40(4), 2048-2061.

Lee T.F., F.J. Turk and K. Richardson (1997). Stratus and fog products using GOES-8–9 3.9-μ m data. Weather and Forecasting, 12(3), 664-677.

Njoku E.G., T.J. Jackson, V. Lakshmi, T.K. Chan and S.V. Nghiem (2003). Soil moisture retrieval from AMSR-E. IEEE transactions on Geoscience and remote sensing, 41(2), 215-229.

Pal D.K., P. Srivastava and T. Bhattacharyya (2003). Clay illuviation in calcareous soils of the semiarid part of the Indo-Gangetic Plains, India. Geoderma, 115(3-4), 177-192.

Pal D.K., T. Bhattacharyya, P. Srivastava, P. Chandran and S.K. Ray (2009). Soils of the Indo-Gangetic Plains: their historical perspective and management. Current Science, 1193-1202.

Ponnurangam G. G. and Y.S. Rao (2011). Soil moisture mapping using ALOS PALSAR and ENVISAT ASAR data over India. In 2011 3rd International Asia-Pacific Conference on Synthetic Aperture Radar (APSAR) (1-4). IEEE.

Prasad A. K., R.P. Singh and M. Kafatos (2006). Influence of coal based thermal power plants on aerosol optical properties in the Indo- Gangetic basin. Geophysical Research Letters, 33(5).

Said S., U.C. Kothyari and M.K. Arora (2008). ANN-based soil moisture retrieval over bare and vegetated areas using ERS-2 SAR data. Journal of Hydrologic Engineering, 13(6), 461-475.

Sathiyamoorthy V., R. Arya and C.M. Kishtawal (2016). Radiative characteristics of fog over the Indo-Gangetic plains during northern winter. Climate Dynamics, 47(5-6), 1793-1806.

Sehgal J.L. and G. Stoops (1972). Pedogenic calcite accumulation in arid and semi-arid regions of the Indo-Gangetic alluvial plain of erstwhile Punjab (India)—Their morphology and origin. Geoderma, 8(1), 59-72.

Sharma A. R., S.K. Kharol, K.V.S. Badarinath and D. Singh (2010). Impact of agriculture crop residue burning on atmospheric aerosol loading–a study over Punjab State, India. In Annales Geophysicae, 28(2), 367-379.

Singh R. P., S. Dey, S.N. Tripathi, V. Tare and B. Holben (2004). Variability of aerosol parameters over Kanpur, northern India. Journal of Geophysical Research: Atmospheres, 109(D23).

Singh R.P., S.R. Oza, K.N. Chaudhari and V.K. Dadhwal (2005). Spatial and temporal patterns of surface soil moisture over India estimated using surface wetness index from SSM/I microwave radiometer. International Journal of Remote Sensing, 26(6), 1269-1276.

Singh R.P., R. Kumar and V. Tare (2009). Variability of soil wetness and its relation with floods over the Indian subcontinent. Canadian Journal of Remote Sensing, 35(1), 85-97.

Srivastava H.S., P. Patel, Y. Sharma and R.R. Navalgund (2009). Large-area soil moisture estimation using multi-incidence-angle RADARSAT-1 SAR data. IEEE Transactions on Geoscience and Remote Sensing, 47(8), 2528-2535.

Song Y. and S.S. Yum (2013). Development and Verification of the Fog Stability Index for Incheon International Airport Based on the Measured Fog Characteristics. Atmosphere, 23(4), 443-452.

Thapliyal P.K., B.M. Rao, P.K. Pal and H.P. Das (2003). Potential of IRS-P4 microwave radiometer data for soil moisture estimation over India. Mausam, 54(1), 277-286.

Thapliyal P.K., P.K. Pal, M.S. Narayanan and Srinivasan, J. (2005). Development of a time series–based methodology for estimation of large-area soil wetness over India using IRS-P4 microwave radiometer data. Journal of Applied Meteorology, 44(1), 127-143.

Tomer S.K., A. A. Bitar, M. Sekhar, M. Zribi, S. Bandyopadhyay, K. Sreelash, A.K. Sharma, S. Corgne and Y. Kerr (2015). Retrieval and multi-scale validation of soil moisture from multi-temporal SAR data in a semi-arid tropical region. Remote Sensing, 7(6), 8128-8153.

Varikoden H., J.V. Revadekar, Y. Choudhary and B. Preethi (2015). Droughts of Indian summer monsoon associated with El Niño and Non- El Niño years. International Journal of Climatology, 35(8), 1916-1925.

Wagner W., G. Lemoine and H. Rott (1999). A method for estimating soil moisture from ERS scatterometer and soil data. Remote sensing of environment, 70(2), 191-207.

Wantuch F. (2001). Visibility and fog forecasting based on decision tree method. Idojárás, 105, 29-38.

Yi L., B. Thies, S. Zhang, X. Shi and J. Bendix (2015). Optical Thickness and Effective Radius Retrievals of Low Stratus and Fog from MTSAT daytime Data as a Prerequisite for Yellow Sea Fog Detection. Remote Sensing, 8(1).

Displacements at the Riga and Visby IGS Stations in/nearby Baltic Sea Region

Atınç Pırtı
Yildiz Technical University, Department of Surveying Engineering Davutpasa, 34220 Esenler, Istanbul – Turkiye
Email: atinc@yildiz.edu.tr

(Received: Jul 27, 2021; in final form: Oct 15, 2021)

Abstract: The yearly movements of IGS stations-RIGA (Riga, Latvia) and VIS (Visby, Sweden) in the Baltic Sea region have been studied in this paper. The standard data sets were taken from IGS database. For more than two decades, Global Navigation Satellite Systems (GNSS) have played a central role in understanding the movements of the Earth's surface. Continuously operating base stations have recorded GNSS data. The data have been collected and processed to provide precise information on the continuous changes of the GNSS station positions. The aim of this study is to obtain horizontal (yearly) and vertical (seasonal) velocity fields of the RIGA and VIS in Latvia and Baltic Sea region covering a twenty-one year period 2000-2021. According to the results, a motion of about 2-2.5 cm/year (horizontal) was detected at the two IGS stations (VIS and RIGA) located in the nearby Baltic Sea. On the other hand, at the VIS point located in the middle of the Baltic Sea, a total of 5-6 cm height differences were obtained in the spring, summer and autumn seasons between 2000 and 2021, but this value was calculated as 4.2 cm in the winter season. In the RIGA point, located in the capital of Latvia, between 2000 and 2021, a total of 1-1.5 cm height differences were obtained in the spring, summer and autumn seasons, but this value was calculated as 8 mm in the winter season.

Keywords: GNSS, Baltic Sea, Displacements, Climate change, Sea Level, Global warming

1. Introduction

The Baltic Sea is a brackish inland sea located in Northern Europe, from 53°N to 66°N latitude and from 20°E to 26°E longitude. It is bounded by the Scandinavian Peninsula, the mainland of Europe, and the Danish islands. It drains into the Kattegat by way of the Øresund, the Great Belt and the Little Belt. The Kattegat continues through Skagerrak into the North Sea and the Atlantic Ocean. The Baltic Sea is connected by man-made waterways to the White Sea via the White Sea Canal, and to the North Sea via the Kiel Canal. The Baltic Sea might be considered to be bordered on its northern edge by the Gulf of Bothnia, on its north-eastern edge by the Gulf of Finland, and on its eastern edge by the Gulf of Riga. However, these various gulfs can be considered to be simply offshoots of the Baltic Sea, and therefore parts of it. Latvia is located in an area that is exposed to ongoing relaxation of the Earth in response to the past ice mass loss, i.e., Glaci Isostatic Adjustment (GIA). The effect rates up to ~10mm/yr in the vertical direction in northern Scandinavia. The velocities of IGS stations RIGA and VIS have been obtained for a period of twenty-one years: 2000-2021. The Latvian CORS velocities were previously computed by Haritonova (2016) for a period of four years: 2012:2015. The Baltic Sea is located in the transition zone between continental and maritime climates. In the present climate, about half of the Baltic Sea is ice-covered in winter. The Baltic Sea salinity is controlled by river runoff, net precipitation, and water exchange with the North Sea. Regional sea surface temperature varies with season, but is also affected by the ocean circulation. The region is also characterized by land uplift and subsidence, which exert long-term effects on the coastal topography. Climate change will likely affect the regional sea ice and water temperature, as well as sea level and possibly salinity and oxygen conditions in the Baltic Sea deep basins (Ahtiainen and Öhman 2014), (Meier et al. 2017), (Raisanen 2017), (Rispling and Grunfelder 2016), (URL2). Earthquakes are a result of tectonic movements in the Earth's crust. There is a decent amount of tectonic cracks in the Earth's crust below the Baltics. For example, the Liepaja-Riga-Pleskava tectonic zone extends through Latvia's territory from the south-west to the north-east from Liepaja to Valmiera and continues further to the east towards Pleskava. But earthquakes can only appear if cracks are active. At the same time, it should be said that the overall activity of modern tectonic plates is not well-researched. A tectonic earthquake is a sign of an active tectonic crack. To be able to accurately predict earthquakes, it would be best to organize an observation system or create a so-called geodynamic monitoring. This monitoring includes seismological monitoring, water level and temperature measurements in boreholes and measurements of underground movements below the surface of the Earth, explains seismologist of Latvian Environment, Geology and Meteorology Centre Valery Nikulin. There is a network of GPS stations in Latvia – LatPos. It has a total of 25 GPS stations. This network is mainly used for geodetic and cartographic purposes. But there is a possibility this network can be used for research of geodynamic movements. According to historic data, there were three earthquakes near Lake Võrtsjärv in 1987. This information was acquired as a result of macro-seismic research. Earthquake intensity ranged within III-IV based on MSK-64 scale. There was another earthquake in the area even earlier – in 1823. Its intensity was IV-V based on MSK-64 scale. This makes Lake Võrtsjärv a relatively active seismic region. Latvia has only one seismological station – Slitere. It is located in Dundaga. The station was opened in October 2006, it actively cooperates with Latvian State Environment, Geology and Meteorology Centre and Germany's Earth Sciences Research Centre, located in Potsdam. GFZ helps coordinate international, global seismological monitoring network GEOFON. Cooperation with GFZ helps exchange data from other seismological monitoring stations in the Baltic region – Finland, Estonia, Lithuania, Poland, Denmark and Russia. This forms Baltic Virtual Seismic Network (BVSN), (Haritonova, 2016), (Haritonova et al. 2013), (URL1), (Ahtiainen and Öhman 2014), (Haritonova, 2019), (Meier et al. 2017), (Raisanen 2017), (Rispling and Grunfelder 2016). Global warming is expected to vary both geographically and seasonally. Continents are generally expected to warm more rapidly than the oceans, so that nearly all land areas are likely to warm faster than the global average. Particularly strong warming is projected for Northern Hemisphere high-latitude areas in winter, not only over land but even more over the Arctic Ocean, where the warming will be greatly amplified by reduced sea ice. Climate change may affect seashores in several more ways than inland habitats, including effects of rising sea levels, changed wind patterns, and reduced ice cover. Sea level rise has, since the 1960s, been caused by a combination of thermal expansion of the sea and melting ice packs, each accounting for about half of the increase (Church and White 2011). Sea levels are expected to increase at an even higher rate in the future (Church et al. 2013), (Ahtiainen and Öhman 2014), (Meier et al. 2017), (Raisanen 2017), (Rispling and Grunfelder 2016), (URL2).

The goal of this paper, displacements originating from RIGA (Latvia) and VIS (Sweden) IGS points in Baltic Sea region were investigated. For this aim, data (2000-2021) of 2 IGS stations (RIGA, VIS) were used for this study. Receiver Independence Exchange (RINEX) observation data of 2 stations were obtained from IGS server. Analyses were carried out with CSRS-PPP Software and coordinate time series, total displacements were computed by using the coordinate differences.

2. Materials and methods

Global Navigation Satellite Systems (GNSS) technique is widely used for geodetic and geodynamic modelling studies such as monitoring tectonic plate movements, earthquake observation, crustal deformation, etc., as it can produce high precision, low-cost and 3D positioning in a global coordinate system. Determining the amount of displacement generated by earthquakes will play an important role in revealing the earthquake kinematics and consequently understanding the related tectonic movements (Herring, 2003). In this context, the data of two IGS stations nearby of the Baltic Sea region provides great convenience. Two IGS stations located in Latvia and Sweden called as IGS network consists of about 600 IGS stations and was mainly designed to provide static and kinematic applications (Haritonova, 2019), (Meier et al. 2017). However, station data of this network with 30 seconds interval is archived and provides important contributions to reveal crustal deformations and displacements. The displacements of RIGA and VIS points in this study were estimated by examining the time series produced from yearly (2000-2021) solutions. Visby (VIS IGS point) is located on the northwest coast of Gotland, the largest island in the Baltic Sea. About 100 km from the coast of Sweden, the site is terraced and its port, today silted up, is ice-free. Riga, Latvia's capital, is set on the Baltic Sea at the mouth of the River Daugava, see Figure 1.

A total of 372 seismic events have been registered in the Baltic region over the course of 2016. 35 of those seismic events took place in Latvia, on the border between Latvia and Estonia and in the coastal area of the Baltic Sea (Figure 2). It is possible that there may have been more seismic events. Unfortunately, the range of BVSN is small, with an average coverage of 180 km for each station. The background of small seismic noises does not allow specialists identify weak seismic events, the specialist explains. The last registered tectonic earthquake took place in Estonia, Pernava in February 2013. Its magnitude was modest – 1.1. The small magnitudes of earthquakes commonly registered in the Baltic region may suggest that the Baltic region is a peaceful region. Nevertheless, it is important to remind of the most powerful earthquakes that took place in the regions in the past 40 years. For example, an earthquake with a magnitude of 4.7 took place on Osmussaar Island in Estonia. After this earthquake, there had also been three weaker earthquakes or aftershocks. In September 2004, two powerful earthquakes were registered in Kaliningrad with magnitudes of 5.0 and 5.2. Intensity of the earthquake reached 6-6.5 based on EMS-98 scale (modern counterpart of MSK-64 scale) in the epicenter. Kaliningrad earthquake had damaged 2,100 buildings, including schools and kindergartens, 20 people were seriously injured and one person died. Total losses reached USD 5.1 million. Residents of Riga felt an earthquake in November 2010. Based on survey data and eyewitness reports, specialists concluded that tectonic shocks were caused by movement in Olaine-Incukalns and Bergu tectonic zone. Because Slitere seismological observation station is located 140 km away from the epicenter, it was not possible to isolate and identify the underground shock from regular seismic noise. With that, the Baltic region has a relatively small seismic activity. Nevertheless, powerful earthquakes remain a possibility for the region (URL 1), (Haritonova, 2016), (Haritonova et al. 2013), (Haritonova, 2019), (Lidberg et al. 2010), (Meier et al. 2017), (Melgard et al. 2009), (Raisanen 2017), (Rispling and Grunfelder 2016).

Figure 1. Study area and the specifications of two IGS stations nearby/in Baltic Sea

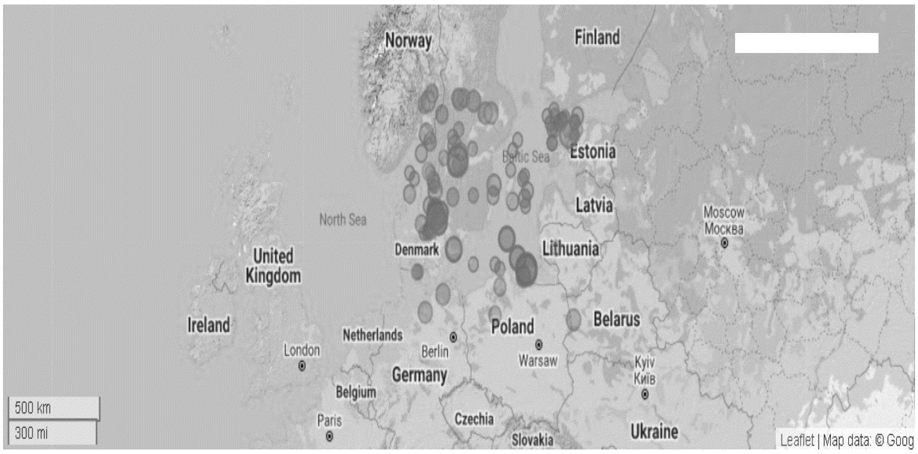

Figure 2. Largest earthquakes in/or near Baltic Sea since 1900

3. Results

24-hour of RINEX observation files (1 January 2000-2021) from two IGS stations were processed by using CSRS-PPP Software (static (24 hours-record interval-30 seconds)). From the solutions, static processing results were obtained by combining the ITRF 2014 epoch 2021.00 coordinates estimated with a precision of 2 mm in the horizontal direction and 7-8 mm in the vertical direction, see Table 1. As can be seen from Figure 3, the average displacement movements of the VIS and RIGA points were computed annually as 2.4 and 2.6 cm as a result of the evaluation of the surveys made during the 21-years measurement period. As mentioned in the previous section, two IGS stations (RIGA and VIS) from IGS network were used in this study time series belonging to RIGA and VIS stations are presented in Figures 4 and 5 for the horizontal and vertical directions (Northing (X) and Easting (Y)I height (h) values). In order to make displacements effect clearly visible in the time series, these data were analysed from January 1 of 2000-2021. The (Receiver Independence Exchange) 24 hours of RINEX observation files with 30 second's interval were obtained from IGS server for these twenty-one years period. As a result of the GNSS observations, it was observed that the horizontal displacement values of RIGA were equal as VIS IGS point. During the period (2020-2021), it was determined that the movement that occurred at the RIGA point was in the north-east direction (Figure 4a). During the same period, it was determined that the movement that occurred at the VIS point was in the north-east direction (Figure 4b). When the results of the two IGS points (static processing by using CSRS-PPP) are compared with each other, the horizontal displacements of the two IGS points separately determined by these tests which differ from a few centimetres up to about 50 cm between 2000 and 2021 (Figure 4). Figures 4 and 5 indicate that the Easting (Y) components shows large values during twenty year periods with changes varying from 2 cm to 42 cm. The time series of coordinate differences of the IGS session confirm that there are displacements of about 49-51 cm in the horizontal components and about 1-6 cm in the height components (Figures 4 and 5). These ΔX and ΔY components for two IGS points change between 2 cm and 28 cm; between 2 cm and 42 cm on 1 January 2020-1 January 2021, respectively. Figure 4 shows the standard deviations and mean values for the two IGS points during the time period. The coordinate differences (Northing (X), Easting (Y)) of two IGS points were in general with standard deviation and mean values less than 21 cm. Where $\Delta X\cos$, $\Delta Y\cos$ and $\Delta h\cos$ are the 3D displacements, Xpost, Ypost, hpost, Xpre, Ypre and hpre indicate the average GNSS based positions estimated from before 2021 and after 2000. The displacement values obtained for 2 IGS stations according to the above procedure are presented in Figure 5. By using the GNSS observations of two IGS point's three dimensional displacement directions are shown in Figure 5. The vertical displacement values for RIGA and VIS IGS points are about 1-6 cm between 2000 and 2021, see Figures 5a and 5b

The mean and standard deviation values of the vertical displacements of the two points were calculated seasonally, see Figure 6. At the VIS point located in the middle of the Baltic Sea, a total of 5-6 cm height changes were obtained in the spring, summer and autumn seasons between 2000 and 2021, but this value was calculated as 4.2 cm in the winter season (Figure 6a). In the RIGA point, located in the capital of Latvia, between 2000 and 2021, a total of 1-1.5 cm height changes were obtained in the spring, summer and autumn seasons, but this value was calculated as 8 mm in the winter season (Figure 6b).

A small and shallow sea such as the Baltic Sea will be affected faster by climate change than the other seas. Although there are increases in sea and ocean levels due to global warming, the low salinity rate in the Baltic Sea and the elimination of the increase in fresh water level as a result of the melting of glaciers by evaporation explain the change in height values. So, the rise in sea level relative to land along most European coasts is projected to be similar to the global average, with the exception of the northern Baltic Sea and the northern Atlantic coast, which are experiencing considerable land rise as a consequence of post-glacial rebound. Another impact of climate change will be the rise in sea level due to melting of land-based glaciers and the expansion of seawater as it warms up. Both factors will cause flooding of existing coastal lowlands (URL1), (URL2).

Table 1. Coordinates and their standard deviations of two IGS points (RIGA and VIS points, ITRF 2014, Epoch 2021.0)

Point	φ_{ITRF}	λ_{ITRF}	h_{ITRF} (m)	Std (φ) [mm]	Std (λ) [mm]	Std (h) [mm]
RIGA	56° 56' 55.03767"	24° 03' 31.60500"	34.727	2	2	8
VIS	57° 39' 13.93912"	18° 22' 02.36000"	79.863	2	2	7

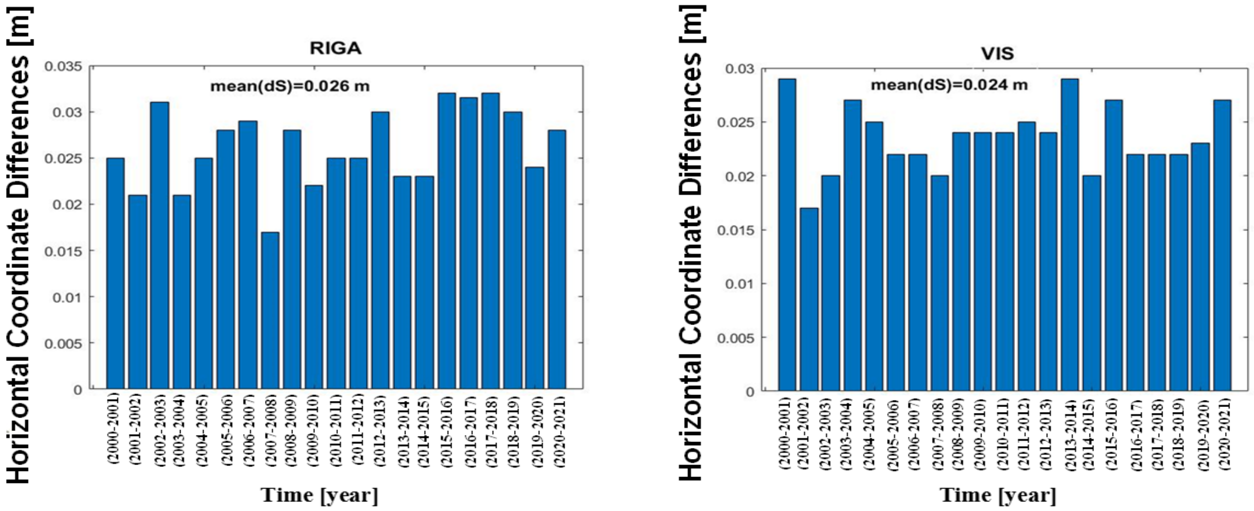

Figure 3. The horizontal displacements graphic of two IGS stations (RIGA and VIS (1 January)) between 2000 and 2021 years

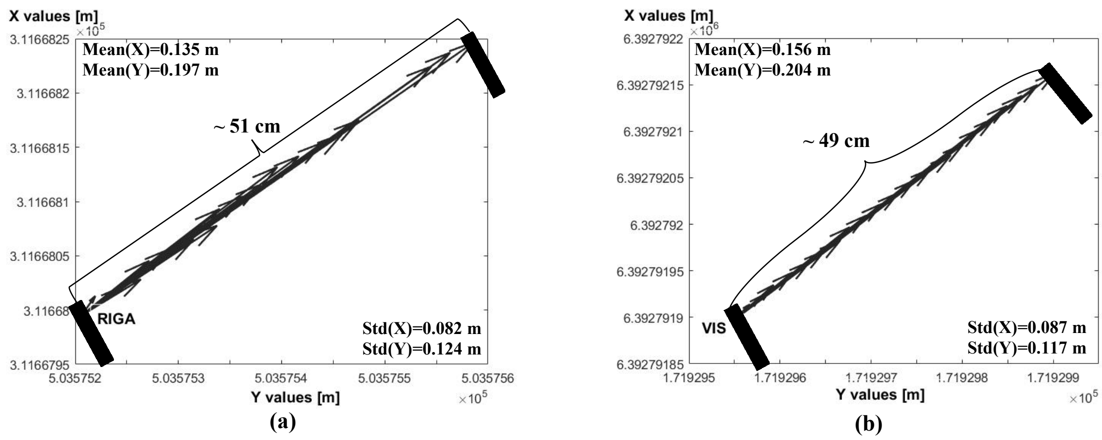

Figure 4. Horizontal Coordinate (Northing (X) and Easting (Y) values on SWEREF99 and Latvia LKS-92) time series obtained from two IGS stations (RIGA (a) and VIS (b)) during monitoring twenty-one (2000-2021) year periods

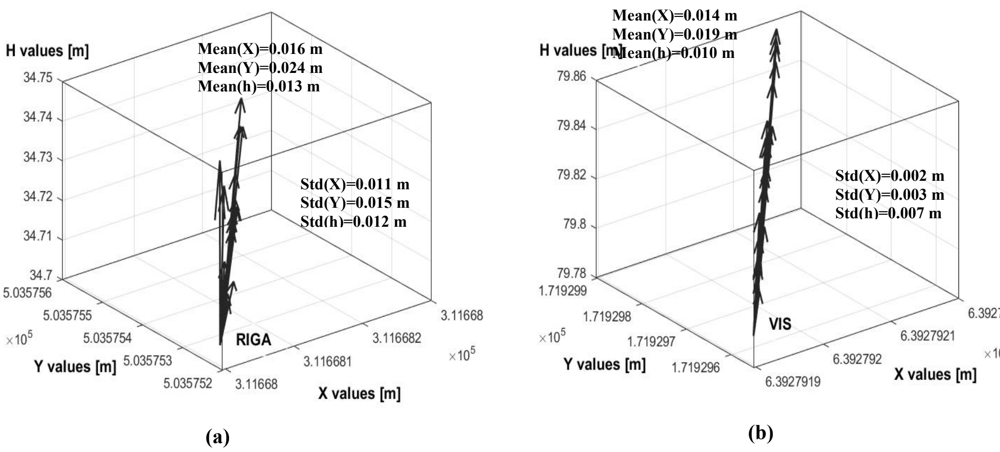

Figure 5. 3D displacement vectors for two IGS points between 2000 and 2021 years, (a) RIGA point, (b) VIS point

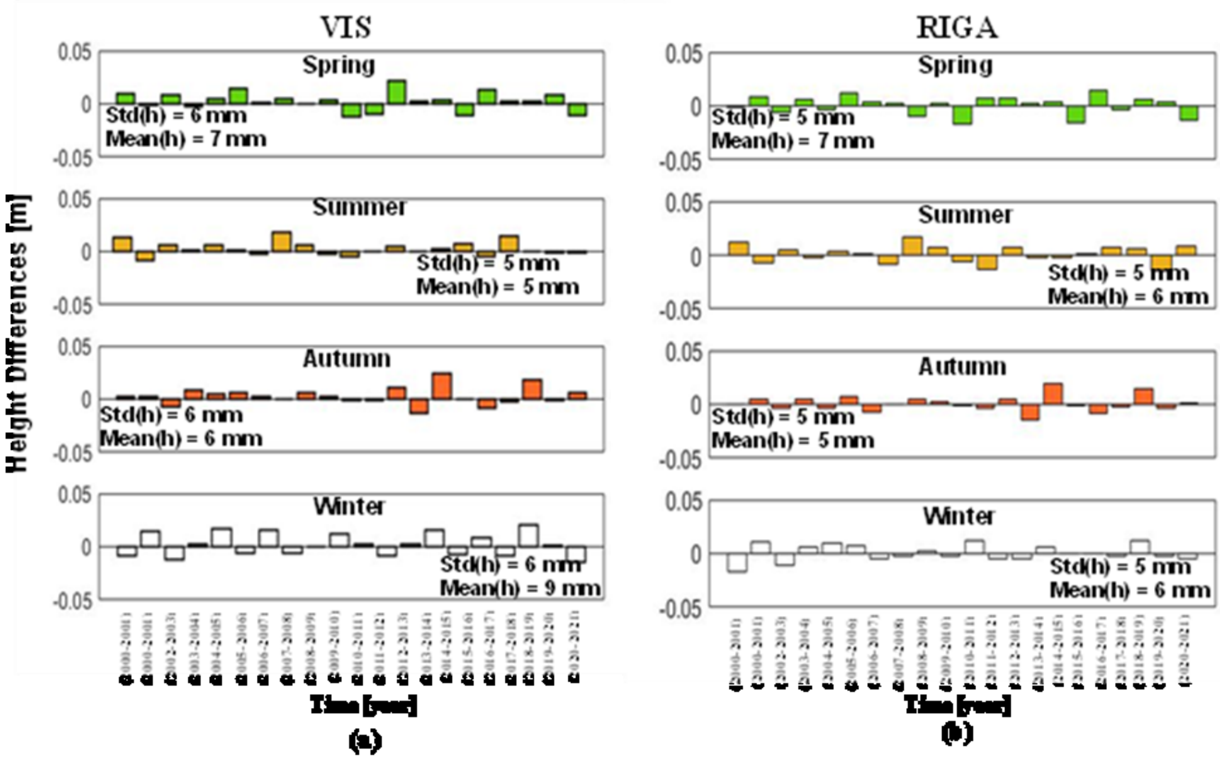

Figure 6. The vertical displacements graphic of two IGS stations (VIS (a) and RIGA (b), (four seasons)) between 2000 and 2021 years

4. Conclusions

Two IGS stations (RIGA and VIS) which belong to IGS data nearby Baltic Sea region are used in this study. Horizontal direction displacements, estimated from the yearly (between 2000 and 2021) coordinate time series, were successfully estimated with precision sub-cm.
The results obtained from 3D displacement estimation are listed below:

- The highest horizontal displacement value with 49-51 cm magnitude in the North-East direction was obtained at the RIGA and VIS stations located in the Baltic Sea Region.
- In the VIS station, which is approximately 352 km away from RIGA and located in the middle of the Baltic Sea, 49 cm directional horizontal motions were detected between 2000 and 2021.
- The horizontal motion obtained at RIGA station is more than VIS station mentioned above
- Vertical movement due to the displacement was obtained approximately 1-6 cm at two IGS stations. VIS point located in the middle of the Baltic Sea, a total of 5-6 cm height differences were obtained in the spring, summer and autumn seasons between 2000 and 2021, but this value was calculated as 4.2 cm in the winter season. In the RIGA point, located in the capital of Latvia, between 2000 and 2021, a total of 1-1.5 cm height differences were obtained in the spring, summer and autumn seasons, but this value was calculated as 8 mm in the winter season.

Medium and large earthquakes occur in the Baltic Sea region. It has been calculated that the displacement movement at the RIGA and VIS points in the Baltic Sea is in the north-east direction and reaches an average value of 2.5 cm annually.

References

Ahtiainen H. and M.C. Öhman (2014). Ecosystem Services in the Baltic Sea: Valuation of Marine and Coastal Ecosystem Services in the Baltic Sea. Nordic Council of Ministers.

Church J.A., P.U. Clark, A. Cazenave, J.M. Gregory, S. Jevrejeva, A. Levermann, M.A. Merrifield, G.A. Milne, et al. (2013). Sea level change. In Climate Change: The physical science basis. Contribution of Working Group I to the Fifth Assessment Report of the Intergovernmental Panel on Climate Change. Cambridge: Cambridge University Press.

Church J.A. and N.J. White (2011). Sea-Level Rise from the Late 19th to the Early 21st Century. Surveys In Geophysics, 32, 585–602. doi: 10.1007/s10712-011-9119-1.

Haritonova, D. (2016). Evaluation of high-precision technique application for observations of Earth's crust movements in Latvia. Doctoral thesis. RTU, Riga: 136

Haritonova, D., Balodis, J., Janpaule, I., Normand, M. (2013). Dısplacements at the GNSS Statıons, 4 th International Conference Cıvıl Engıneerıng`13 Proceedings Part I Land Management and Geodesy,

Haritonova D. (2019). The impact of the Baltic Sea non-tidal loading on GNSS station coordinate time series: the case of Latvia. Baltic Journal of Modern Computing 7(4), 541–549.

Herring T., (2003). MATLAB Tools for viewing GPS velocities and time series. GPS solutions, 7, 194–199

https://llufb.llu.lv/conference/Civil_engineering/2013/partI/Latvia_CivilEngineering2013Vol4PartI_305-309.pdf

Lidberg M., J.M. Johansson, H.G. Scherneck and G.A. Milne (2010). Recent results based on continuous GPS observations of the GIA process in Fennoscandia from BIFROST, J. Geodynam., 50, 8–18, https://doi.org/10.1016/j.jog.2009.11.010.

Meier H., A. Höglund, K. Eilola et al. (2017). Impact of accelerated future global mean sea level rise on hypoxia in the Baltic Sea. Climate Dynamics, 49(1–2), 163–172.

Melgård T., E. Vigen and O. Ørpen (2009). Advantages of combined GPS and GLONASS PPP - experiences based on G2, a new service from Fugro. Proceedings of the 13th IAIN World Congress. Stockholm, Sweden. October 27-30.

Räisänen J (2017). Future Climate Change in the Baltic Sea Region and Environmental Impacts. Climate Science. DOI: 10.1093/acrefore/9780190228620.013.634.

Rispling L and J. Grunfelder (2016). Trends, challenges and potentials in the Baltic Sea Region.pdf.

URL1: http://www.geophysica.fi/pdf/geophysica_2019_54_varna.pdf

URL2: https://helcom.fi/media/publications/BSEP111.pdf

Special Section: Flood Assessment and Modeling

Preface

Flood is perhaps most devastating, wide spread and frequent disaster across the world. The researchers are constantly attempting to reduce the damages through the use of various flood management techniques. In the realms of monsoon, river flooding is a recurrent natural phenomenon. Recent occurrences of extreme precipitation show shift in the flooding pattern and frequencies due to changing climate. Hence, there is need to update the flood prone areas. The conventional means to record hydrological and meteorological parameters of a flood event is often limited to few in situ observations. An accurate monitoring of flood events is increasingly necessary to gain insight about both causes and remedies.

For the last two decades advancement in the field of remote sensing and data science have greatly facilitated the multi-dimensional quantitative approach of flood mapping, modeling and flood risk assessment. The growing availability of multi-temporal satellite data has increased opportunities for monitoring large rivers from space. A variety of passive (AMSR-E/2), and active (SAR, Altimeters, scatterometers etc.), sensors in the visible and microwave range are currently operating, which can delineate food boundaries and estimate inundation area. Radar altimeters show great promise for directly measuring stage variation in large rivers. It is possible to obtain estimates of river discharge from space, using ground measurements and satellite data to construct empirical curves that relate water surface area to discharge. Recently, high temporal resolution scatterometer and passive microwave radiometers are also being used for the mapping of major floods. ISRO/DOS is playing a vital role in supporting the flood management activities, by providing space as well as aerial remote sensing based services and products through VEDAS, MOSDAC, BHUVAN web portals.

The aim of this special section on “Flood Assessment and Modeling” is to enrich our knowledge of application of different satellite technologies independently and also in integrated fashion with mathematical models on a regional and local scales. A wide variety of topics covered including tracking the extreme weather events by studying the atmospheric rivers, high temporal resolution of passive microwave for inundation mapping, Altimetry for river water level estimation, flash flood review, 1D and 2-D coupled models integrated with RS derived hydro-meteorological parameters, WRF-HYDRO etc. for flood inundation and water surface elevation modeling. I am thankful to all the authors who have contributed research article to this special section. Special thank for all the reviewers for timely review and valuable comments. I am grateful to editorial team for editing, formatting and bringing out this special section. This Special section, covering research experiences of flood risk analysis and applications, will undoubtedly provide new tools to flood risk managers to improve risk mitigation, both preventive and remedial.

P. K. Gupta
Guest Editor

Journal of Geomatics Vol. 15, No. 2, October 2021

Spatial Prediction of Flash Floods using Susceptibility Modeling and Geospatial Technology: A Review

Gagandeep Singh* and Ashish Pandey
Indian Institute of Technology Roorkee, Roorkee, India
*Email: gsingh@wr.iitr.ac.in

(Received: Aug 8, 2021; in final form: Oct 6, 2021)

Abstract: Spatial prediction of flash floods is essential for identifying the probable areas, which may be impacted due to the occurrence of an extreme event, and making better decisions and management plans to minimize the damages. Given the dynamic nature of the climate, complexity in the topography, and sparse data monitoring network, it is very challenging to predict flash floods in advance. However, spatial maps presenting the most susceptible flash flood-prone areas can be a valuable resource for planners, decision-makers, and people residing in such areas. Such maps can be obtained through flash flood susceptibility modeling using various remote sensing-based inputs and geospatial technology. Literature suggests that flash flood susceptibility studies are being employed by researchers worldwide for just about a decade now. In this paper, the status, current approaches, and challenges in this domain have been reviewed. The review focuses on using remote sensing and GIS for conducting flash flood susceptibility modeling to generate spatial maps. The study provides a detailed description of the input datasets and conditioning factors required for susceptibility assessment. Various approaches used for flash flood susceptibility assessment and their evolution have also been discussed.

Keywords: Flash flood susceptibility, Remote sensing, GIS, Spatial prediction, Extreme events

1. Introduction

1.1. Flooding and its impact on natural resources/ life

Flooding is a catastrophic global phenomenon that results in voluminous destruction in terms of fatalities and property loss. It is probably the most destructive and recurring natural disaster affecting the ecosystem and its components. In an assessment report titled, "Natural disasters 2018: An opportunity to prepare." published in 2018 by CRED, it has been pointed out very clearly that "Floods have affected more people than any other type of disaster in the 21st century, including in 2018". The data regarding the number of flood events reported worldwide from 1900 to 2018 has been presented in the form of a chart in Figure 1. A disaster event is taken into consideration by the CRED International Disaster Database if at least one criterion is fulfilled: (i) 10 or more people are reported to have been killed, (ii) 100 people are reported to have been affected, (iii) a call for international assistance, (iv) declaration of a state of emergency (Jha et al. 2013). In the last two decades, the number of flood disasters has repeatedly crossed the mark of 100 every year. Floods end up causing mammoth economic loss worldwide. Millions of people get displaced or killed in such events.

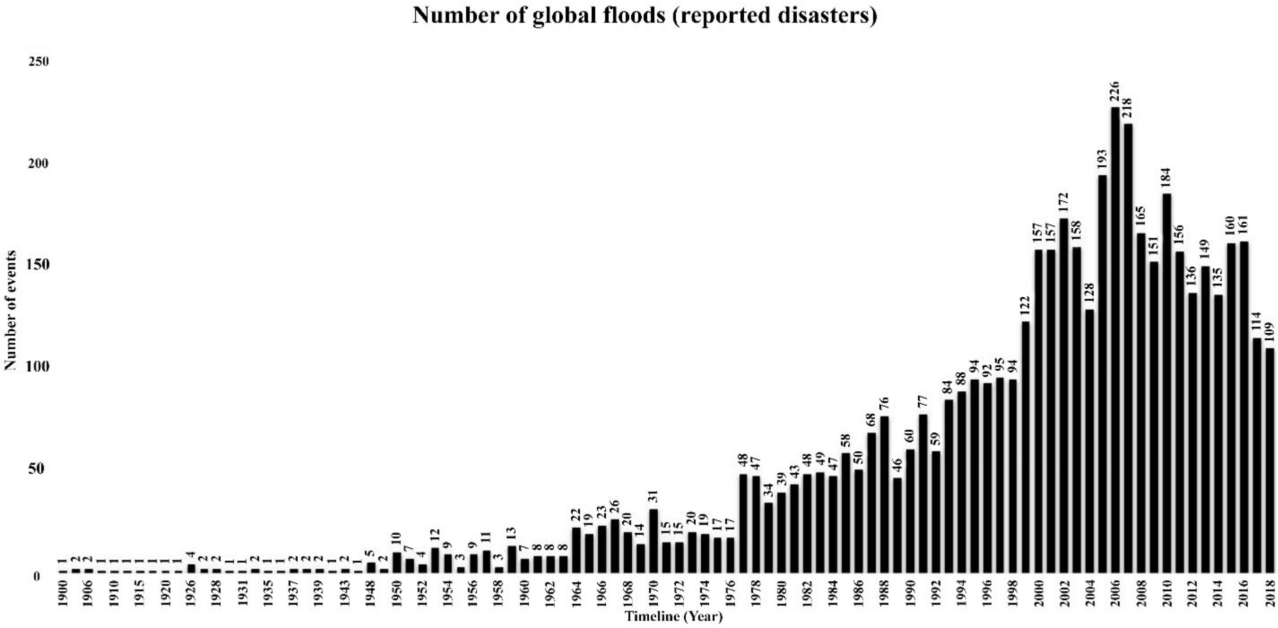

Figure 1. Number of reported flood disasters from 1901 to 2018
Data source: EMDAT (2019): OFDA/CRED International Disaster Database, Université catholique de Louvain – Brussels – Belgium

The receding floodwater consequently causes excessive deposition of mud and silt in the affected areas. In addition, the entire impacted terrain has very high chances of getting contaminated with dangerous materials, viz. chemicals, fuel, untreated sewage, and a massive amount of sharp debris. After the flood event, the standing water in the affected areas is highly vulnerable to outbreaks of life-threatening waterborne diseases like cholera, typhoid, and hepatitis A. There is a total failure of the infrastructure, causing long-term impacts on services like potable drinking water, wastewater treatment, transportation system, electricity, communication, education, and healthcare. Also, flood causes community-based social problems like large-scale crop destruction and loss of cattle. All these consequences bring life to a standstill leaving the communities economically vulnerable.

Floods have consequential impacts on the environment and natural resources in the affected areas. At times floods play a vital role in the sustenance of ecosystem and biodiversity by recharging groundwater systems, filling wetlands, increasing connection between aquatic habitats, and transportation of sediment and nutrients throughout the affected region. On the other hand, the involvement of human intervention in disturbing the river's natural course by either encroaching river banks for residential purposes or exploiting the river bed for mining activities has made the areas highly susceptible to destruction by flooding. Activities like deforestation along the river catchment degrade the hill-slopes and the river flood plains, thereby making the area erosion-prone resulting in excessive sediment and nutrient flow during floods. Consequently, downstream water quality is compromised. Other adverse effects of floods on natural resources include habitat loss, weed species dispersion, water pollution, diminished fish production, loss of wetlands and recreational areas.

Flash floods are highly complex events that depend on specific climate conditions, leading to high-intensity rainfall concentrated over an area for a short period, resulting in excessive surface runoff. These characteristics render the prediction of such events extremely difficult and equally challenging. The prediction models are of great utility in flood hazard assessment and management (Xie et al. 2017).

In this context, susceptibility modeling is critical to identify the most vulnerable areas prone to flash floods and are highly likely to experience damage and destruction. In addition, it also enables engineers, planners, policymakers, and authorities to prepare flash flood management plans to minimize the damage. In view of the available scientific literature, researchers have analyzed flash flood susceptibility. These studies have utilized the potential of geospatial technology to identify areas likely to be affected by flash floods. Furthermore, rapid advancements in remote sensing and GIS have translated into various approaches to model and assess flash flood susceptibility.

The main objective of this study is to present a detailed review of flash flood susceptibility modeling and assessment techniques.

1.2. Relevance of geospatial technology for flash flood susceptibility

Flash floods are highly complex and dangerous phenomena wherein the enormous volume of water precipitates within minutes or a few hours due to extreme rainfall events (Doswell 2015). Such events are usually a consequence of cloudbursts or thunderstorms. Several hydrological factors influence the occurrence of flash floods: antecedent rainfall, land use, land cover, population habitation, soil type, topography, terrain slope, and, most importantly, meteorological conditions (Doswell 2015). Another significant characteristic of a flash flood is the localization of heavy precipitation events. Interestingly flash floods can occur both on or near a river or away. The hydrological and dynamic nature of climatic factors makes predicting flash floods a very challenging affair. Moreover, it becomes more complex in data-scarce areas. Therefore, remote sensing and GIS for susceptibility modeling become a promising approach in identifying the most susceptible areas and can help reduce damages.

Earth observation capabilities have been improving rapidly, with various remote sensing datasets capable of capturing valuable information. Different satellite data products are being employed very effectively to derive input data required to perform susceptibility assessment. Digital elevation model (DEM), being the most innovative satellite product, is used to generate input parameters like slope, curvature, flow direction, aspect, and a few more (Himanshu et al. 2015; Dhami et al. 2018). Additionally, DEMs are also used to derive various indices which play a vital role in analyzing the susceptibility, viz. topographic wetness index, stream power index, topographic position index, etc. Also, input layers like rainfall, land use land cover (LULC), river density, distance from the river, normalized difference vegetation index (NDVI), etc., are derived using satellite data in a GIS environment. These input layers are processed in a GIS environment and then analyzed using various susceptibility modeling techniques and methods.

2. Review approach

A bibliographic search in the "Web of Science Core Collection" database was carried out with "flash flood susceptibility" keywords. The investigation resulted in 156 publications comprising complete research articles in peer-reviewed journals, book chapters, or conference proceedings. Furthermore, to get a sense of flash flood susceptibility (FFS) studies across the globe, the results were analyzed by filtering according to countries/ regions. Figure 2 shows the country-wise distribution of the publications. The analysis revealed that studies based on FFS had been carried out in 57 countries across the globe. Vietnam, China, Romania, Iran, and India are the top 5 countries on the list. The map in Figure 2 has been color-coded based on the number of studies in different countries.

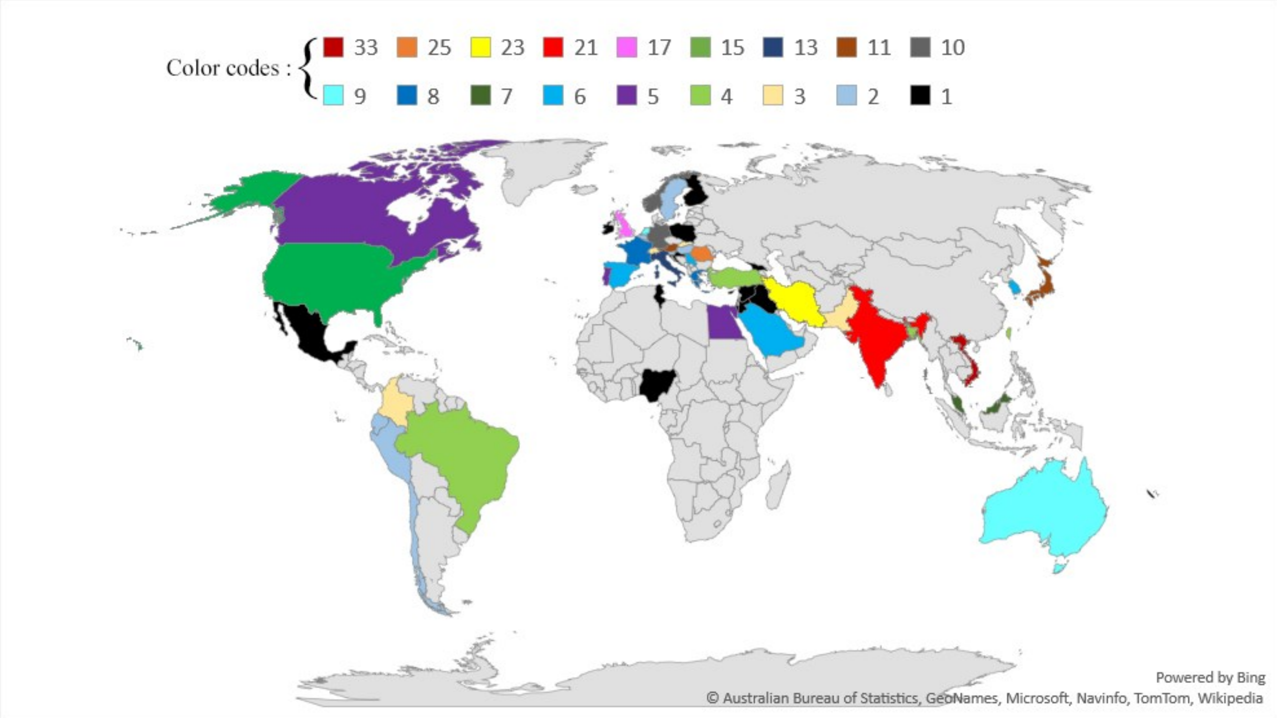

Figure 2. Distribution of the number of articles across the globe

Figure 3 presents the trend in the number of flash flood susceptibility (FFS) studies conducted from 2007 onwards.

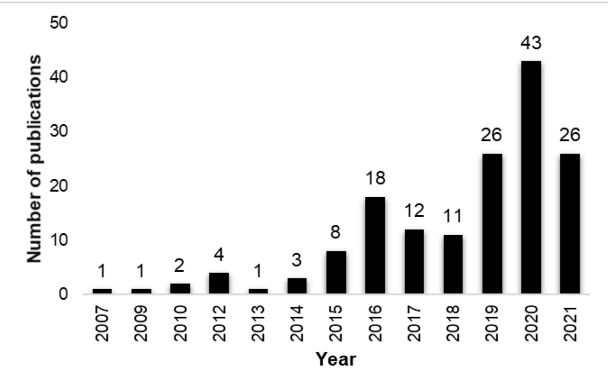

Figure 3. Number of publications on flash flood susceptibility on the Web of Science Database

3. Theoretical background and role of geospatial technology for flash flood susceptibility studies

3.1 Background of FFS

Flash flood susceptibility can be described as assessing the spatial probability of occurrence of flash floods in an area considering the meteorological, morphometric, and hydrological conditions (Santangelo et al. 2011). It is an approach to categorize or prioritize regions based on the degree to which they can be affected by extreme events in the future. In other words, susceptibility is the locational assessment of future events without considering its temporal probability (Tehrany et al. 2014). This approach is efficient in data-scarce areas where there is a deficit of adequate instrumentation to derive information about the recurrence interval of flash floods (Khosravi et al. 2016).

3.2 FF conditioning factors

The magnitude of a flash flood event is influenced by two significant factors: rainfall intensity and duration. Additionally, the catchment characteristics govern flash flood susceptibility through geomorphometric and meteorological factors often referred to as the conditioning factors. For analyzing the flash flood susceptibility, relationship of all the conditioning factors with the distribution of previously occurred flash flood events is assessed (Liu and De Smedt 2005; Tehrany et al. 2015a). Various conditioning factors are selected to comprehend their influence and relationship with flash flooding. Therefore, this section presents the significance of all major flash flood conditioning factors.

The slope for an area is derived from the DEM and is considered one of the most important input parameters that influence the severity of flash floods. The slopes in an area are directly proportional to the magnitude of velocity that could be obtained by the surface runoff (Tehrany et al. 2015b). This plays a crucial role, especially in the mountainous area prone to flash floods primarily due to cloud burst events. Also, areas with low slopes have a higher chance of water accumulation (Popa et al. 2019).

The aspect gives a clear representation of directions in the study area viz. flat, north, northeast, east, southeast, south, southwest, and northwest, which can be related to the direction of water flow. It is a crucial morphometric factor that plays an active role when the soil gets saturated, especially on the shaded slopes responsible for generating more surface runoff than the areas with dry soils on the sunny side (Costache and Bui 2020). It also helps identify flat regions that may be most prone to flood damages (Popa et al. 2019). DEM is employed to derive aspects.

Convergence Index (CI) is a highly significant flash flood conditioning factor (Costache et al. 2020b). CI values may be positive and negative, with negative values indicating high convergence of rivers (Zaharia et al. 2017), leading to a low time of concentration of the runoff and hence higher chances of flash flood occurrence vice-versa. DEM is used to generate a convergence index for an area.

Distance from the rivers and river density are naturally prominent factors in identifying flood-prone areas. Areas near the rivers have more chances to get flooded and vice-versa (Glenn et al. 2012). Buffer analysis in a GIS environment is instrumental in segregating areas close to the river proximity.

The geology of the area defines its hydrological behavior. Soil permeability is one of the critical geologic attributes which governs surface runoff and infiltration. Impermeable geology supports higher depth surface runoff in comparison to permeable soil. Therefore, different rock formations contribute to the runoff as per their nature. Lithology is very closely associated or analogous to geology as it represents the rock and soil types in an area. Hydrological Soil Group (HSG) is another factor that governs water infiltration and contributes to runoff generation. This parameter is used to compute the curve numbers (CN), further employed to calculate surface runoff for catchments (Sharma et al. 2021).

Land use/cover influences the runoff velocity in a catchment. The areas with dense forest cover and high vegetation presence will not allow rainwater to contribute as runoff. Therefore, the higher the vegetation density lower are the chances of flooding (Tehrany et al. 2014). Urban areas are very much prone to increased runoff. Thus, land use/cover plays a prominent role in flash flood susceptibility modeling (Mindje et al. 2019). There are readily available global land use/cover datasets freely available to use. Also, optical satellite imagery from Landsat and Sentinel missions are highly recommended datasets to prepare LULC maps for any area (Chaves et al. 2020; Singh and Pandey 2021).

L-S factor is a morphometric factor that is extensively used to realize the combined effect of length and steepness of the slopes on the behavior of runoff (Zaharia et al. 2017; Costache et al. 2020b). It is calculated using the formula proposed by Moore and Wilson in 1992.

$$LS = (\frac{A_S}{22.13})^m \, (\frac{\sin\theta}{0.0896})^n \qquad (1)$$

Where A_s is the unit contributing area (m^2), Θ is the slope in radians, m and n are exponents ranging between 0.4 to 0.56 and 1.2 to 1.3, respectively. This parameter is derived using a DEM, and QGIS software has a built-in tool in the Terrain Analysis module of SAGA GIS.

Rainfall is the most critical factor responsible for the occurrence of flash floods. Therefore, spatial variability of rain intensity becomes of utmost relevance for susceptibility assessment. A common approach followed is to compute the mean annual rainfall raster from the long-term data collected from a network of well-distributed meteorological and hydrometric stations. Modified Fournier Index (MFI) is widely used to capture the spatial variation of rainfall intensity thus employed (Zaharia et al. 2015; Costache et al. 2020a) by various researchers for susceptibility assessment using the following formula:

$$MFI = \sum_{i=1}^{12} \frac{P_i^2}{P} \qquad (2)$$

Where P_i is the monthly average rainfall for a month i in mm and P is the average annual rainfall.

Normalized Difference Vegetation Index (NDVI) has been explored for flood susceptibility studies in the past (Khosravi et al. 2018; Ali et al. 2020). The importance of vegetation cover in controlling runoff justifies its use for susceptibility analysis. The NDVI values range between -1 and +1. NDVI is conventionally used for monitoring crop health status and agricultural production using remote sensing observations. It is derived using satellite data acquired in near-infrared (NIR) and red band using the following formula:

$$NDVI = \frac{NIR - R}{NIR + R} \qquad (3)$$

Where NIR and R represent the reflectance values in the near infrared and red bands respectively.

Curvature gives an idea about the shape of the ground surface, which governs the accumulation of water or runoff on the slopes. In line with this concept, profile curvature represents the curvature of a vertical plane with respect to the direction of slope (Duman et al. 2006). It represents the direction of the maximum slope. The values may be positive signifying areas less susceptible to surface runoff and negative signifying vice-versa (Zaharia et al. 2017). If the ground surface is convex upwards, the profile curvature is negative (Figure 4a), suggesting accelerated runoff, values nearing zero (Figure 4c) indicate flat surface. In contrast, areas with positive values (Figure 4b) concave upwards and offer decelerated runoff.

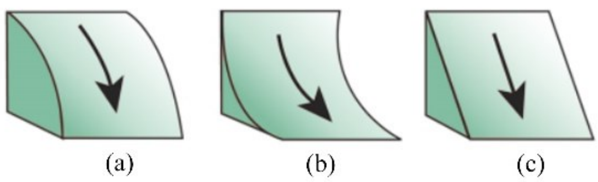

Figure 4. Pictorial representation of profile curvature (a) negative (b) positive and (c) zero value
(Image source: https://desktop.arcgis.com/en/arcmap/10.3/manage-data/raster-and-images/curvature-function.htm*)*

Another exciting concept is the plan curvature represented by the contour created at the horizontal plane and ground surface intersection (Costache, 2019a). Plan curvature plays a vital role in analyzing areas susceptible to flash flooding by differentiating areas with convergent and divergent runoff characteristics. It is perpendicular to the direction of the maximum slope. A laterally convex surface is expressed by positive values (Figure 5a). A laterally concave surface is expressed by negative values (Figure 5b). The linear surface has zero value of plan curvature (Figure 5c). Profile and plan curvature rasters are derived from DEM in GIS software.

Stream Power Index (SPI) indicates the river basin's erosive power and runoff capacity (Moore and Grayson 1991). In other words, it is an indicator of transport and abrasive potential of the flood water (Sharma, 2010).

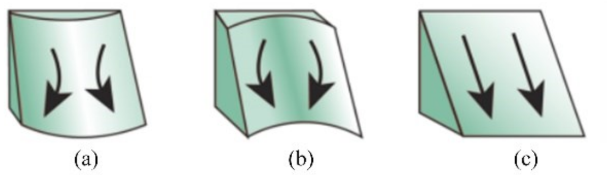

Figure 5. Pictorial representation of plan curvature (a) positive (b) negative and (c) zero value
(Image source: https://desktop.arcgis.com/en/arcmap/10.3/manage-data/raster-and-images/curvature-function.htm*)*

Higher values of SPI signify the faster movement of water, while low values suggest slow motion (Chowdhuri et al. 2020). It is calculated using the following formula:

$$SPI = A_s \tan\beta \qquad (4)$$

Where A_s is the specific catchment area (m^2m^{-1}) and β is the slope expressed in degrees.

Topographic Position Index (TPI) measures the elevation difference between a cell and its neighboring cells (Costache and Bui 2020).

$$TPI = E_c - \left(\frac{1}{n^M}\sum\nolimits_{i\epsilon m} E_i\right) \qquad (5)$$

E_c is the elevation at the central point, E_i is the elevation, and M is the predetermined radius (predetermined matrix length).

Topographic Wetness Index (TWI) underlines the effect of topography on the accumulated water in each pixel (Gokceoglu et al. 2005). It is expressed as the ratio of specific catchment area and the slope angle values. This parameter indicates spatial variation in the wetness (Beven and Kirkby 1979) and is expressed by the following formula:

$$TWI = ln\left(\frac{A_s}{\tan\beta}\right) \qquad (6)$$

Where A_s is the cumulative upslope area contributing at a point (per unit contour length) and $\tan\beta$ is the slope at the point in degrees.

It is worth noting here that not all the above-discussed conditioning factors may influence every study area. Also, there might be the existence of multicollinearity, which may impact the accuracy of the results. Therefore, it is recommended to employ multicollinearity diagnostic rests for determining the most influential factors and ignore the redundant ones in the flash flood susceptibility analysis. The two most popular statistical methods to test multicollinearity are VIF (Variance Inflation Factor) and Tolerance (TOL). VIF greater than 10 or tolerance less than 0.1 confirms the presence of multicollinearity in the conditioning factors (Hair et al. 2009).

3.3 Concept of Flash Flood Potential Index

Flash Flood Potential Index (FFPI) directly addresses the objectives of susceptibility assessment. The concept of FFPI was introduced by Greg Smith in 2003 to determine the hydrological response of the Flash Flood Monitoring and Prediction System to heavy rain by analyzing the physiographic characteristics of the Colorado river basin of the USA. The objective behind introducing this concept was to enhance flash flood forecasts. Only four factors were taken into consideration, namely, slope, vegetation cover, soil type, and land use. Raster layers for each factor were prepared, and relative indexing was assigned to them, ranging from 1 to 10. Each layer was further classified using an equal interval approach, and each layer was given equal weight. Finally, the layers were averaged together to obtain layers representing the flash flood potential.

Gradually, the methodology was evolved, and studies on FFPI were conducted in different parts of the USA and elsewhere considering more variables/ factors (Davis 2002; Kruzdlo 2010; Ceru 2012; Zaharia et al. 2015; Prăvălie and Costache 2013; Minea 2013; Zogg and Deitsch 2013; Tincu et al. 2018). In light of the above-cited literature, it is to be noted that none of these studies considered the locations where flash flood events occurred previously, and the weights to the flash flood conditioning factors were assigned subjectively. Moreover, a GIS was employed to estimate FFPI using a simple overlay technique on the conditioning factors taken into consideration.

Therefore, to address the drawbacks mentioned above, significant modifications were introduced in the approach. All the flash flood susceptibility studies are conducted considering the past flash flood event locations. Furthermore, advanced statistical methods and machine learning techniques are being widely used by researchers worldwide to perform flash flood susceptibility modeling (Tehrany et al. 2015a; Lee et al. 2012; Chapi et al. 2017; Janizadeh et al. 2019; Bui et al. 2019). Therefore, it can be stated that FFPI is a highly effective indexing approach to understand the risk of flash flooding in any area (Zog and Deitsch 2013).

4. FFS modeling approaches

Literature suggests that flash flood susceptibility modeling approaches can be classified under four broad categories: bivariate statistical methods, multi-criteria decision-making approach, machine learning-based approach, and hybrid modeling approach. The following sections provide a detailed overview of each of these approaches.

4.1 Statistical modeling

Frequency Ratio (FR), Weights of Evidence (WoE), and Statistical Index (SI) are among the most popular bivariate statistical models employed for modeling flash flood susceptibility (Tehrany et al. 2014; Khosravi et al. 2016; Rahmati et al. 2016). A few other models like Information Value (IV) and Index of Entropy (IoE) have also been adopted in a few studies to model FFS. These methods are based on the correlation between flash flood locations and the parameters controlling the flash flood occurrences in the area.

However, there is a significant drawback in the bivariate statistical modeling approaches. These methods capture only the spatial relationship between the flash flood event locations and the conditioning factors without considering the relationship between the predictors (Tehrany et al. 2014).

4.2 Multicriteria decision making

This approach is described as a complex decision-making tool that considers quantitative and qualitative factors (Mardani et al. 2015). Analytic hierarchy process (AHP) and technique for order of preference by similarity to ideal solution (TOPSIS) are the two popular MCDM approaches that have been employed for modeling flash flood susceptibility (Khosravi et al. 2019).

MCDM approaches provide a unique capability to determine and assign weights to the conditioning factors and the decision alternatives for analyzing flash flood susceptibility. Methods like AHP are employed to obtain a pair-wise comparison matrix for each conditioning factor and the sub-criteria, and finally, the correct weights are determined.

4.3 Machine learning models

Machine learning (ML) has become one of the most revolutionary multidisciplinary technologies. This is one of the fastest-growing modern-day technologies offering several models to simulate and solve a real-life problem. Some of the most popular machine learning methods being used for flash flood susceptibility modeling include artificial neural networks (Chakrabortty et al. 2021), logistic regression (Nandi et al. 2016), support vector machines (Tehrany et al. 2015b), and decision trees (Khosravi et al. 2018). Researchers have employed several different machine learning algorithms to perform flash flood susceptibility modeling. These algorithms have a typical working framework because the algorithms are trained using a subset of flash flood event locations.

Post-training, the algorithm is tested or validated on the remaining set of flash flood locations. Finally, a comparison is performed to observe the effectiveness of the approach adopted.

4.4 Hybrid models

Hybrid models refer to ensembles of statistical models, multi-criteria decision-making models, and machine learning models. To improve the accuracy of spatial prediction of flash floods, susceptibility assessment is improvised by using combinations or ensembles of two different types of models (Bui et al. 2018; Costache et al. 2019a; Costache 2019b; Costache et al. 2020b; Pham et al. 2020b)

5. Review and synthesis

Table 1 presents studies that demonstrate different approaches adopted by researchers for flash flood modeling studies along with flash flood conditioning factors considered in each research and significant findings. It is to be noted that all the studies presented have employed remote sensing datasets and GIS to prepare the flash flood conditioning factors. Additionally, the overlay tools and ability of a GIS to perform various raster and vector operations make it an integral part of any FFS study. Furthermore, the most crucial part of any FFS modeling study is the validation of the model used. For validation, the use of Receiver Operating Characteristic (ROC) curves is the most sought-after method used in every FFS study. These curves are employed to evaluate the model capability of being able to predict an event correctly. ROC curve represents sensitivity on the Y-axis and (1-Specificity) on the X-axis (Chen et al. 2017). Once the curve is prepared, Area Under Curve (AUC) is determined, indicating the model's effectiveness. AUC values range between 0 and 1. AUC of 1 indicates a perfect model, and 0 refers to a weak model (Costache and Zaharai 2017). AUC values are calculated using the following formula:

$$AUC = \frac{(\sum TP + \sum TN)}{(P + N)} \qquad (8)$$

Where TP represents true positive and TN represents true negative, and their sum indicates the sum of correctly classified pixels. P is the number of pixels representing flash flood event locations, and N represents non-flood locations.

Table 1 presents a compilation of flash flood susceptibility assessment studies in four sections. Section (a) discusses four studies conducted using different statistical methods, section (b) presents a study conducted using MCDM and ML models, section (c) presents three studies conducted using advanced machine learning models, and section (d) presents five studies wherein researchers have employed hybrid models.

The statistical models used for FFS have mathematical representations, which are easily translated into data modeling software like Microsoft EXCEL. All the conditioning factors are analyzed class-wise to obtain the model coefficients for each factor. Finally, these coefficients are used to calculate the FFPI. As far as the machine learning models are concerned, WEKA is the most popular open-source machine learning and data mining software widely employed for FFS studies (Khosravi et al. 2018; Janizadeh et al. 2019; Popa et al. 2019; Costache et al. 2020b). It features a huge number of in-built models and tweaking capabilities that researchers are extensively using worldwide.

Table 1: Existing flash flood susceptibility studies. The list in the table is sorted based on the type of approach adopted (statistical, multi-criteria decision making, machine learning, and hybrid)

#	Reference	Modeling approach	Location/ study area	Data/ conditioning factors	Findings
(a)		**Statistical models**			
1	Costache and Zaharia 2017	Frequency ratio and Weights of Evidence	Bâsca Chiojdului river catchment, Romania	Slope, L-S factor, profile curvature, drainage network density, convergence index, aspect, lithology, LULC, and HSG	FFPI and susceptibility maps were derived on the basis of the torrential inventory, which was split for training and validation purposes. ROC curve was employed to validate the results for both models. However, no comparative assessment was done for the methods. Area percentage distribution under each susceptibility class was presented for both models.
2	Cao et al. 2016	Frequency ratio and Statistical Index	Beijing, China	Elevation, slope, curvature, land use, geology, soil texture, subsidence risk area, SPI, TWI, short-term heavy rain	The authors prepared an inventory of 85 flash flood hazard locations. These were split into 70:30 for training and validation. Validation was done using the area under the curve (AUC) assessment. Results revealed that FR produced higher prediction accuracy in comparison to SI
3	Khosravi et al. 2016	Shannon's entropy, Statistical index, Weighting factor	Haraz, Iran	Slope angle, plan curvature, altitude, TWI, SPI, distance from the river, rainfall, geology, land use, and NDVI	Three different statistical models were applied for flash flood susceptibility mapping. 211 flood locations inventory was split in 70:30 for training and validation purposes. Performance evaluation was done with respect to the FR model. Analysis revealed that the SI model performed the best.
4	Chakrabortty et al. 2021	ANN, DLNN and PSO	Kangsabati River Basin, India	Aspect, elevation, slope, plan curvature, profile curvature, TWI, TRI, SPI, distance from the river, drainage density, distance from the road, rainfall, LULC, and Geology	Three advanced models were employed for performing flash flood susceptibility assessment. The results indicated that the PSO model showed the best results for both training and validation data of the events inventory among the three.
(b)		**Multicriteria Decision Making models**			
5	Khosravi et al. 2019	VIKOR, TOPSIS, SAW, NBT and NB	Jiangxi, China	NDVI, lithology, land use, distance from the river, curvature, altitude, STI, TWI, SPI, soil	Three MCDM models and 2 ML models were employed for flash flood susceptibility mapping. Their validation and comparison were made using the ROC curve method, Kappa, and AUC.

#	Reference	Modeling approach	Location/ study area	Data/ conditioning factors	Findings
				type, slope, and rainfall	
(c)	**Machine learning-based models**				
6	Janizadeh et al. 2019	ADT, MLP, FT, KLR and QDA	Tafresh, Iran	Elevation, slope, slope aspect, distance from rivers, average annual rainfall, land use, soil type, and lithology	Four machine learning-based models were employed. ADT model performed the best among these for both training and validation, followed by MLP, QDA, KLR, and FT. AUC was used for the performance evaluation of the models.
7	Band et al. 2020	BRT, PRF, RRF and ERT	Kalvan, Iran	Altitude, slope, aspect, plan curvature, profile curvature, distance from the river, distance from the road, land use, lithology, soil depth, rainfall, SPI, and TWI	Machine learning approaches sometimes pose a problem of overfitting. To address this shortcoming, four hybrid models with regularized and parallel and boosting techniques were introduced to reduce the errors. ERT model with an AUC of 0.82 outperformed for its predictive capability, followed by RRF, PRF, and BRT.
8	Pham et al. 2020a	KLR, RBFC, NBM, and LMT	Nghe An, Vietnam	Soil, slope, curvature, river density, flow direction, distance from rivers, elevation, aspect, land use, and geology	Four machine learning-based models were applied for flash flood susceptibility assessment and comparison. KLR was the best model using training data, while LMT demonstrated higher predictive ability in the validation. LMT was robust and capable of reducing overfitting.
(d)	**Hybrid models**				
9	Pham et al. 2020b	ABM-CDT, Bag-CDT, Dag-CDT, MBAB-CDT, and single CDT	Tafresh, Iran	Distance from the river, aspect, elevation, slope, rainfall, distance from faults, soil types, land use, and lithology	Five novel machine learning-based hybrid models were employed for susceptibility modeling. An inventory of 320 previous events was prepared for the training and validation of models. ABM-CDT displayed the best predictive capability with an AUC of 0.957, followed by Dag-CDT, MBAB-CDT, Bag-CDT, and CDT.
10	Costache et al. 2019a	LR-FR, LR-WoE, SVM-FR, SVM-WoE	Prahova river catchment (Romania)	Slope angle, land use, lithology, HSG, convergence index, TWI, TPI, aspect, plan	Four hybrid models were proposed for evaluating the flash flood potential. Assessment of model performance revealed that LR-FR and LR-WoE were most effective for success rate and prediction rate. At the same

#	Reference	Modeling approach	Location/ study area	Data/ conditioning factors	Findings
				curvature, and profile curvature	time, SVM-FR and SVM-WoE were the most accurate models for training and validating areas, respectively.
11	Costache et al. 2020a	Integration of AHP with kNN and lazy KS	Prahova river basin in Romania	slope angle, aspect, plan curvature, profile curvature, convergence index, TPI and TWI	FFPI assessment was done using the kNN and lazy KS models stand-alone and their ensembles with AHP. Models were trained and validated using torrential areas inventory. ROC curves and AUC values revealed that all models showed good performance.
12	Costache et al. 2020b	Integration of SI with LR, CART, MLP, RF and SVM	Bâsca Chiojdului Catchment, central south-eastern region of Romania	Slope, L-S Factor, Convergence index, SPI, TWI, profile curvature, TPI, land use, HSG, and lithology	Hybrid integration of bivariate statistical method with five machine learning approaches was employed for obtaining flash flood susceptibility maps. Models were trained and validated based on a torrential area inventory dataset with a split of 70:30. MLP-SI model performed the best with AUC of 0.94 and 0.927 for training and validation, respectively.
13	Costache and Bui 2020	ADT with IoE ADT with AHP	Romania	Slope angle, land use, profile curvature, plan curvature, convergence index, aspect, HSG, and TPI	AHP, IoE, and two hybrid models formed by integration with the ADT algorithm were employed. The models were evaluated using ROC and Kappa. ADT-AHP performed the best with a sensitivity of 100%, specificity of 80.49%, and Kappa statistics of 0.758

ADT: Alternating Decision Tree; IoE: Index of Entropy; AHP: Analytic Hierarchy Process; SI: Statistical index; LR: Logistic Regression; CART: Classification and Regression Trees; kNN: k-Nearest Neigbour; KS: K-Star; MLP: Multilayer Perceptron; RF: Random Forest; SVM: Support Vector Machine; KLR: Kernel Logistic Regression; RBFC: Radial Basis Function Classifier; MNB: Multinomial Naïve Bayes; LMT: Logistic Model Tree; BRT: Boosted Regression Tree; PRF: Parallel Random Forest; RRF: Regularized Random Forest; ERT: Extremely Randomized Trees; ABM-CDT: AdaBoostM1 based Credal Decision Tree; Bag-CDT: Bagging based Credal Decision Tree; Dag-CDT: Dagging based Credal Decision Tree; MBAB-CDT: MultiBoostAB based Credal Decision Tree; CDT: Single Credal Decision Tree; FT: Functional Tree; KLR: Kernel Logistic Regression; QDA: Quadratic Discriminant Analysis; VIKOR: Vlse Kriterijuska Optamizacija I Komoromisno Resenje; TOPSIS: Technique for Order Preference by Similarity to Ideal Solution; SAW: Simple Additive Weighting; Naïve Bayes Trees: NBT; Naïve Bayes: NB; ROC: Receiver Operating Characteristic; AUC: Area Under the Curve

6. Summary and conclusions

The accurate and timely spatial prediction of flash floods is a challenging prospect. In this paper, an attempt has been made to review the progress towards this goal. Various approaches adopted by researchers worldwide have been discussed in detail. A database of 156 articles on flash flood susceptibility was considered for the review.

The main findings of the review are:

(i) A comprehensive review of the studies enabled the identification of sixteen flash flood conditioning factors used in combinations in FFS modeling.

(ii) It is recommended that the following factors viz. slope, aspect, convergence index, distance from the river, geology, lithology, hydrological soil group, land use land cover, L-S factor, rainfall, normalized difference vegetation index, plan curvature, profile curvature, stream power index, topographic position index and topographic wetness index must be considered in all FFS studies.

(iii) Multicollinearity among the above-listed factors can lead to redundancy, which would reduce the accuracy of susceptibility assessment. Therefore, it is recommended to employ tools like VIF and TOL to identify and eliminate redundant factors for the final analysis.
(iv) Table 1 presents the development in FFS modeling approaches. A detailed assessment of case studies has been presented addressing each modeling approach type: statistical methods, multi-criteria decision-making models, machine learning-based models, and hybrid approaches.
(v) A discussion on the gradual evolution of the susceptibility modeling approaches revealed that flash flood locations inventory is an important input to accurately model and predict the spatial occurrence of future events.
(vi) The future scope in flash flood susceptibility lies in improving weights assignment to individual conditioning factors to develop the final FFPI.
(vii) There is a tremendous scope in the development of hybrid models. Numerous model combinations can be developed using machine learning algorithms through open-source data mining software like WEKA.
(viii) Most importantly, this paper highlights the importance and use of geospatial technology in preparing input layers and preparing flash flood susceptibility maps.
(ix) The FFS maps can be very effectively used by the decision-makers and disaster management agencies to plan and reduce the damage caused by flash flood events.

Acknowledgments
We wish to express a deep sense of gratitude and sincere thanks to the Department of Water Resources Development and Management (WRD&M), IIT Roorkee, for providing a conducive environment to conduct this research work. We are grateful to IIT Roorkee for providing the Mahatma Gandhi Central Library (MGCL) remote access portal to access and download the research papers from the Web of Science and other subscription-based journals.

References
Ali S. A., F. Parvin, Q. B. Pham, M. Vojtek, J. Vojteková, R. Costache, N. T. T. Linh, H. Q. Nguyen, A. Ahmad and M. A. Ghorbani (2020). GIS-based comparative assessment of flood susceptibility mapping using hybrid multi-criteria decision-making approach, naïve Bayes tree, bivariate statistics and logistic regression: A case of Topľa basin, Slovakia. Ecological Indicators, 117, 106620.

Band S. S., S. Janizadeh, S. Chandra Pal, A. Saha, R. Chakrabortty, A. M. Melesse, and A. Mosavi (2020). Flash flood susceptibility modeling using new approaches of hybrid and ensemble tree-based machine learning algorithms. Remote Sensing, 12(21), 3568.

Bui D. T., P. T. T. Ngo, T. D. Pham, A. Jaafari, N. Q. Minh, P. V. Hoa, and P. Samui (2019). A novel hybrid approach based on a swarm intelligence optimized extreme learning machine for flash flood susceptibility mapping. Catena, 179, 184-196.

Bui D. T., M. Panahi, H. Shahabi, V. P. Singh, A. Shirzadi, K. Chapi, K. Khosravi, W. Chen, S. Panahi, S. Li and B. B. Ahmad (2018). Novel hybrid evolutionary algorithms for spatial prediction of floods. Scientific reports, 8(1), 1-14.

Cao C., P. Xu, Y. Wang, J. Chen, L. Zheng, and C. Niu (2016). Flash flood hazard susceptibility mapping using frequency ratio and statistical index methods in coalmine subsidence areas. Sustainability, 8(9), 948.

Ceru J. (2012). The flash flood potential index for Pennsylvania. In 2012 ESRI federal GIS conference. http://proceedings.esri.com/library/userconf/feduc12/papers/user/JoeCeru. pdf.

Chakrabortty R., S. Chandra Pal, F. Rezaie, A. Arabameri, S. Lee, P. Roy, A. Saha, I. Chowdhuri and H. Moayedi (2021). Flash-Flood Hazard Susceptibility Mapping in Kangsabati River Basin, India. Geocarto International, 1-21.

Chapi K., V. P. Singh, A. Shirzadi, H. Shahabi, D. T. Bui, B. T. Pham and K. Khosravi (2017). A novel hybrid artificial intelligence approach for flood susceptibility assessment. Environmental modelling and software, 95, 229-245.

Chaves M. E. D., M. C. A. Picoli, and I. D. Sanches (2020). Recent applications of Landsat 8/OLI and Sentinel-2/MSI for land use and land cover mapping: A systematic review. Remote Sensing, 12(18), 3062.

Chen W., H. R. Pourghasemi, and Z. Zhao (2017). A GIS-based comparative study of Dempster-Shafer, logistic regression and artificial neural network models for landslide susceptibility mapping. Geocarto international, 32(4), 367-385.

Chowdhuri I., S. C. Pal, and R. Chakrabortty (2020). Flood susceptibility mapping by ensemble evidential belief function and binomial logistic regression model on river basin of eastern India. Advances in Space Research, 65(5), 1466-1489.

Costache R. (2019a). Flash-Flood Potential assessment in the upper and middle sector of Prahova river catchment (Romania). A comparative approach between four hybrid models. Science of the Total Environment, 659, 1115-1134.

Costache R. (2019b). Flash-flood Potential Index mapping using weights of evidence, decision Trees models and their novel hybrid integration. Stochastic Environmental Research and Risk Assessment, 33(7), 1375-1402.

Costache R., and D. T. Bui (2020). Identification of areas prone to flash-flood phenomena using multiple-criteria decision-making, bivariate statistics, machine learning and their ensembles. Science of The Total Environment, 712, 136492.

Costache R., Q. B. Pham, E. Sharifi, N. T. T. Linh, S. I. Abba, M. Vojtek, J. Vojteková, Pham T. T. N. and D. N. Khoi (2020a). Flash-flood susceptibility assessment using multi-criteria decision making and machine learning supported by remote sensing and GIS techniques. Remote Sensing, 12(1), 106.

Costache R., H. Hong, and Q. B. Pham (2020b). Comparative assessment of the flash-flood potential within small mountain catchments using bivariate statistics and their novel hybrid integration with machine learning models. Science of The Total Environment, 711, 134514.

Costache R., and L. Zaharia (2017). Flash-flood potential assessment and mapping by integrating the weights-of-evidence and frequency ratio statistical methods in GIS environment–case study: Bâsca Chiojdului River catchment (Romania). Journal of Earth System Science, 126(4), 1-19.

CRED/UNISDR (Centre for Research on the Epidemiology of Disaster/United Nations Office for Disaster Risk Reduction). 2015. The Human Cost of Weather-Related Disasters 1995-2015. Geneva/Brussels,CRED/UNISDR. www.unisdr.org/we/inform/publications/46796

Davis R. S. (2002). The flash flood (FF) index: estimating flash flood severity. In Proceedings of the Symposium on Managing the Extremes, Floods and Droughts. Environmental and Water Resources Institute of American Society of Civil Engineers Roanoke, VA.

Dhami B., S. K. Himanshu, A. Pandey, and A. K. Gautam (2018). Evaluation of the SWAT model for water balance study of a mountainous snowfed river basin of Nepal. Environmental Earth Sciences, 77(1), 1-20.

Doswell C. A. (2015). Hydrology, Floods and Droughts | Flooding. Encyclopedia of Atmospheric Sciences, 201–208. doi:10.1016/b978-0-12-382225-3.00151-1

Duman T. Y., T. Can, C. Gokceoglu, H. A. Nefeslioglu, and H. Sonmez (2006). Application of logistic regression for landslide susceptibility zoning of Cekmece Area, Istanbul, Turkey. Environmental Geology, 51(2), 241-256.

Glenn E. P., K. Morino, P. L. Nagler, R. S. Murray, S. Pearlstein, and K. R. Hultine (2012). Roles of saltcedar (Tamarix spp.) and capillary rise in salinizing a non-flooding terrace on a flow-regulated desert river. Journal of Arid Environments, 79, 56-65.

Gokceoglu C., H. Sonmez, H. A. Nefeslioglu, T. Y. Duman, and T. Can (2005). The 17 March 2005 Kuzulu landslide (Sivas, Turkey) and landslide-susceptibility map of its near vicinity. Engineering geology, 81(1), 65-83.

Hair J., W. Black, B. Babin, and R. Anderson, (2009). Multivariate Data Analysis. 7111 Ed. Prentice Hall Publishing, New York

Himanshu S. K., A. Pandey, and S. S. Palmate (2015). Derivation of Nash Model Parameters from Geomorphological Instantaneous Unit Hydrograph for a Himalayan River using ASTER DEM. In Proceedings of International Conference on Structural Architectural and Civil Engineering, Dubai.

Janizadeh S., M. Avand, A. Jaafari, T. V. Phong, M. Bayat, E. Ahmadisharaf, I. Prakash, B. T. Pham and Lee, S. (2019). Prediction success of machine learning methods for flash flood susceptibility mapping in the Tafresh watershed, Iran. Sustainability, 11(19), 5426.

Jha A. K., T. W. Miner, and Z. Stanton-Geddes (2013). Appendix A. Disaster Definitions and Classifications. Emergency Events Database (EM-DAT).

Khosravi K., B. T. Pham, K. Chapi, A. Shirzadi, H. Shahabi, I. Revhaug, I. Prakash and D. T. Bui (2018). A comparative assessment of decision trees algorithms for flash flood susceptibility modeling at Haraz watershed, northern Iran. Science of the Total Environment, 627, 744-755.

KhosraviK., E. Nohani, E. Maroufinia, and H. R. Pourghasemi (2016). A GIS-based flood susceptibility assessment and its mapping in Iran: a comparison between frequency ratio and weights-of-evidence bivariate statistical models with multi-criteria decision-making technique. Natural hazards, 83(2), 947-987.

Khosravi K., H. Shahabi, B. T. Pham, J. Adamowski, A. Shirzadi, B. Pradhan and I. Prakash (2019). A comparative assessment of flood susceptibility modeling using multi-criteria decision-making analysis and machine learning methods. Journal of Hydrology, 573, 311-323.

Kruzdlo R. (2010). Flash Flood Potential Index for the Mount Holly Hydrologic Service Area. A Microsoft PowerPoint presentation available at: http://www. state. nj. us/drbc/library/documents/Flood_Website/flood-warning/user-forums/Krudzlo_NWS. pdf.

Lee M. J., J. E. Kang, and S. Jeon (2012). Application of frequency ratio model and validation for predictive flooded area susceptibility mapping using GIS. In 2012 IEEE international geoscience and remote sensing symposium (pp. 895-898). IEEE.

Lee S., J. C. Kim, H. S. Jung, M. J. Lee, and S. Lee, (2017). Spatial prediction of flood susceptibility using random-forest and boosted-tree models in Seoul metropolitan city, Korea. Geomatics, Natural Hazards and Risk, 8(2), 1185-1203.

Liu Y. B., and F. De Smedt (2005). Flood modeling for complex terrain using GIS and remote sensed information. Water resources management, 19(5), 605-624.

Mardani A., A. Jusoh, K. Nor, Z. Khalifah, N. Zakwan, and A. Valipour (2015). Multiple criteria decision-making techniques and their applications–a review of the literature from 2000 to 2014. Economic research-Ekonomska istraživanja, 28(1), 516-571.

Mindje R., L. Li, A. C. Amanambu, L. Nahayo, J. B. Nsengiyumva, A. Gasirabo, and M. Mindje (2019). Flood susceptibility modeling and hazard perception in Rwanda. International journal of disaster risk reduction, 38, 101211.

Minea G. (2013). Assessment of the flash flood potential of Basca river catchment (Romania) based on physiographic factors. Open Geosciences, 5(3), 344-353.

Moore I. D., and R. B. Grayson (1991). Terrain- based catchment partitioning and runoff prediction using vector elevation data. Water Resources Research, 27(6), 1177-1191.

Moore I. D., and J. P. Wilson (1992). Length-slope factors for the revised universal soil loss equation: simplified method of estimation. Journal of Soil and Water Conservation 47(5):423-428

Nandi A., A. Mandal, M. Wilson, and D. Smith (2016). Flood hazard mapping in Jamaica using principal component analysis and logistic regression. Environmental Earth Sciences, 75(6), 465.

Pham B. T., T. V. Phong, H. D., C. Qi, N. Al-Ansari, A. Amini, and D. Tien Bui (2020a). A comparative study of kernel logistic regression, radial basis function classifier, multinomial naïve bayes, and logistic model tree for flash flood susceptibility mapping. Water, 12(1), 239.

Pham B. T., M. Avand, S. Janizadeh, T. V. Phong, N. Al-Ansari, L. S. Ho, and I. Prakash (2020b). GIS based hybrid computational approaches for flash flood susceptibility assessment. Water, 12(3), 683.

Popa M. C., D. Peptenatu, C. C. Drăghici, and D. C. Diaconu (2019). Flood hazard mapping using the flood and flash-flood potential index in the Buzău River catchment, Romania. Water, 11(10), 2116.

Prăvălie R., and R. Costache (2013). The vulnerability of the territorial-administrative units to the hydrological phenomena of risk (flash-floods). Case study: the subcarpathian sector of Buzău catchment. Analele Universităţii din Oradea–Seria Geografie, 23(1), 91-98.

Rahmati O., H. R. Pourghasemi, and H. Zeinivand (2016). Flood susceptibility mapping using frequency ratio and weights-of-evidence models in the Golastan Province, Iran. Geocarto International, 31(1), 42-70.

Santangelo N., A. Santo, G. D. Crescenzo, G. Foscari, V. Liuzza, S. Sciarrotta, and V. Scorpio (2011). Flood susceptibility assessment in a highly urbanized alluvial fan: the case study of Sala Consilina (southern Italy). Natural Hazards and Earth System Sciences, 11(10), 2765-2780.

Sharma A. (2010). Integrating terrain and vegetation indices for identifying potential soil erosion risk area. Geo-Spatial Information Science, 13(3), 201-209.

Sharma I., S. K. Mishra, and A. Pandey (2021). A simple procedure for design flood estimation incorporating duration and return period of design rainfall. Arabian Journal of Geosciences, 14(13), 1-15.

Singh G., and A. Pandey (2021). Evaluation of classification algorithms for land use land cover mapping in the snow-fed Alaknanda River Basin of the Northwest Himalayan Region. Applied Geomatics, 1-13.

Smith G. (2003). Flash flood potential: Determining the hydro- logic response of FFMP basins to heavy rain by analyzing their physiographic characteristics; http://www.cbrfc. noaa.gov/papers/ffpwpap.pdf, 11p.

Tehrany M. S., B. Pradhan, and M. N. Jebur (2014). Flood susceptibility mapping using a novel ensemble weights-of-evidence and support vector machine models in GIS. Journal of hydrology, 512, 332-343.

Tehrany M. S., B. Pradhan, and M. N. Jebur (2015a). Flood susceptibility analysis and its verification using a novel ensemble support vector machine and frequency ratio method. Stochastic environmental research and risk assessment, 29(4), 1149-1165.

Tehrany M. S., B. Pradhan, S. Mansor, and N. Ahmad (2015b). Flood susceptibility assessment using GIS-based support vector machine model with different kernel types. Catena, 125, 91-101.

Tincu R., G. Lazar, and I. Lazar (2018). Modified flash flood potential index in order to estimate areas with predisposition to water accumulation. Open Geosciences, 10(1), 593-606.

Xie K., K. Ozbay, Y. Zhu, and H. Yang (2017). Evacuation zone modeling under climate change: A data-driven method. Journal of Infrastructure Systems, 23(4), 04017013.

Zaharia L., R. Costache, R. Prăvălie, and G. Ioana-Toroimac (2017). Mapping flood and flooding potential indices: a methodological approach to identifying areas susceptible to flood and flooding risk. Case study: the Prahova catchment (Romania). Frontiers of Earth Science, 11(2), 229-247.

Zaharia L., R. Costache, R. Prăvălie, and G. Minea (2015). Assessment and mapping of flood potential in the Slănic catchment in Romania. Journal of Earth System Science, 124(6), 1311-1324.

Zogg J., and K. Deitsch (2013). The flash flood potential index at WFO Des Moines. National Oceanic and Atmospheric Administration: Silver Spring, MD, USA.

Flood Inundation Mapping and Depth Modelling using Machine Learning algorithms and Microwave data

Gyan Prakash[1*], Praveen Kumar Gupta[2], G Venkata Rao[1] and Deva Pratap[1],
[1]Department of Civil Engineering, National Institute of Technology Warangal, Telangana, 506004, India
[2]Space Applications Centre, ISRO, Ahmedabad, Gujarat, 380015, India
*Email: prakas_191854@student.nitw.ac.in

(Received: Aug 10, 2021; in final form: Oct 6, 2021)

Abstract: Flooding is one of the most devastating natural hazards that significantly impact human life and property. During floods, monitoring and mapping flood extent is crucial in identifying the flood-affected areas and the damage assessment. Space-based monitoring of floods can provide a systematic, spatial, timely, and impartial way to monitor disastrous floods. The study area is a part of the Kosi River in the Bihar state. In this study, using microwave remote sensing data (Sentinel - 1), an independent and open-source tool was developed to monitor the flooding extent and water depth. The tool consists of a hybrid model and a floodwater depth analysis model: The hybrid model is fully automated in which Binarization techniques and Random Forest Classifier (RFC) and K Nearest Neighbor (KNN), supervised Machine Learning(ML) algorithms were used. Using flood inundation maps and Digital Elevation Model (DEM), the floodwater depth analysis model (PyQGIS standalone tool) was developed to calculate the flood water depth. Supervised classification algorithms in the hybrid model were further compared and found that the performance of both the KNN and RFC classifiers was close enough, but the time taken by RFC was less than KNN Classifier. The model results were compared and validated with the August 2017 flood event results over the Darbhanga district. The results of the fully automated model have shown a deviation of 0.9% to 19% compared with the published results over the Darbhanga district. The present study suggests that the RFC ML algorithm can classify the SAR data into flooded and non-flooded areas. The developed tool can be used to monitor floods in near/real-time to issue warnings to the people and rescue operations.

Keywords*:* Flood Inundation, Floodwater Depth, Microwave Remote Sensing, Machine Learning Algorithms, Supervised Classification

1. Introduction

Flood is one of the most devastating natural hazards which is caused due to excessive increase in surface runoff, heavy rainfall, rise in the riverbed, cyclones, and cloud bursts, etc. (Singh, 2015). Among the nations in the world, India is one of the most flood-affected countries due to its unique geo-climatic conditions, precipitation patterns, topographic features, population growth, urbanization, industrialization, etc. (Mohanty et al., 2020). According to National Flood Commission, out of a total geographical area of approximately 329 million hectares, about 40 million hectares are prone to floods (Sharma et al., 2016; Gangwar et al., 2013). Among all the river basins in India, Ganga and Brahmaputra river basins experience the highest number of floods (Mohanty et al. 2020).

It is essential to have information about their intensities and extents to cope with the damage caused by floods. Therefore, the preparation of flood inundation maps is the primary step for damage control and assessing a flood event (Matgen et al., 2007). Compared to in-situ measurement, remote sensing offers practical ways to observe and monitor the surface water dynamics at multiple spatial and temporal scales. There are generally two types of remote sensing datasets are available for the purpose of monitoring the surface water – the optical and microwave remote sensing data. Optical data has been widely used to monitor and map surface water bodies due to the high availability and suitable Spatio-temporal resolutions (Chang Huang et al., 2019). Although the optical data is numerously used for surface water body extraction, the data has several limitations. The most serious one is that the optical data doesn't have the ability to penetrate through the clouds (Shen et al., 2019), which are mainly prevalent during the monsoon season. Microwave sensors are the alternative sources to overcome the drawbacks of optical sensors. Due to the usage of longwave radiation, microwave sensors can penetrate through the clouds and detailed vegetation coverage. Microwave sensors are independent of solar radiation, and they can provide the data in all weather conditions (Chang Huang et al., 2018; Shen et al., 2019).

Several studies have been carried out for flood inundation mapping and damage assessment using microwave data (Anusha and Bharathi 2020; de Groeve 2010; Gouweleeuw et al. 2011; D. C. Mason et al. 2012; Matgen et al. 2007; Schumann and Moller 2015; Shen et al. 2019; Temimi et al. 2005; Tripathi et al. 2020, 2020). (Matgen et al. 2007) extracted the flood extent and depth of floodwater using DEM and SAR data with the help of the HEC-RAS river flow model and reported an RMSE of 41cm for flood water depth. Using image segmentation, (David C. Mason et al. 2012) extracted the flood inundation maps in urban and rural areas with an accuracy of 89% and a false-positive rate of 6%. For urban flood pixels using TerraSAR-X, 75% of pixels were accurately identified as water, with a false positive rate of 24%. Tripathi et al. 2020 used the Binarization method for the classification of MODIS and SAR data by selecting threshold values. They reported that MODIS data had shown an overestimation of 21% in the flood area compared with SAR data. Anusha and Bharathi 2020 used SAR and optical data for flood mapping of the August

2017 flood in Uttar Pradesh with the help of thresholding and Unsupervised classification methods.

ML algorithms such as Support vector machine, random forest, K Nearest Neighbor (KNN), Decision Tree (DT), K-means, and iso-data (ISO) cluster have been used in several studies to minimize the human interference and time taken for flood mapping (Benoudjit and Guida 2019; Campolo et al. 1999; D Amitrano 2018; Elsafi 2014; Feng et al. 2015; Schumann and Moller 2015; Shahabi et al. 2020; R. Sinha et al. 2008; Tehrany et al. 2014, 2015). Benoudjit and Guida 2019 developed an algorithm for flood mapping using Sentinel 1 and Sentinel 2 data with the help of NDWI and a supervised Classifier. They reported an overall accuracy of 77 % for the rural and 74.7% for the urban floods. Shahabi et al. 2020 developed an ensemble model using KNN as meta classifier and Weighted base classifier for flood inundation mapping.
Thus, from the above studies, it can be interpreted that the hybrid/ensemble model results in higher accuracy than individual models. For automation of flood mapping tools with high accuracy results, hybrid models were developed in several studies (Anusha and Bharathi 2020; Matgen et al. 2007; Tehrany et al. 2014; Twele et al. 2016).

The above studies were mostly done for inundation mapping. Thus, there is a need for a coupled model that can also estimate the floodwater depth along with inundation extent. Floodwater Depth Estimation Tool (FwDET) was used to estimate an approximate water depth of the flood plain (Cohen et al., 2018). In this study, a fully automated coupled model approach for flood mapping and depth modeling was made.

2. Study Area

North Bihar faces heavy damages due to floods in the Kosi river (Bhatt et al., 2010). During the last few years, the Kosi River has changed its flow course by 150 Km and caused damage to human lives and properties every year. For more than five decades, flood control management has been working for this basin but continues to bring harm through its devastating floods every year (R. Sinha et al. 2008). The geomorphological properties of the Kosi River have a significant role in these extensive floods. Kosi flows through the slopes of the Himalayas in Tibet and the Southern slopes in Nepal. After that, it enters into Indian region (Kosi River).

In Himalayan region, only it has three tributaries, Arjun, Tamur and Sun-Kosi. Three gauge/discharge stations along the Kosi River, namely, Barahkshetra, Birpur, and Baltara, were used by Central Water Commission (CWC), India. In which Barahkshetra and Birpur show higher peak discharges than Baltara for the same return period. The annual average discharge at Kosi was found 2236 m^3/s, the average monsoon discharge 5156 m3/s being almost five times higher than the non-monsoon discharge 1175 $m^3/$ s huge difference the river vulnerable to extensive flooding (R. Sinha et al. 2008). The average elevation in the study area is 49.81m and 100m max elevation was found in SRTM DEM. Gole and Chitale 1966 reports that the Kosi river is built by large sediment flux, which also plays a vital role in causing westward shifting of Kosi and extensive flooding. Thus, the Kosi river changes its course of flow frequently with a 24 year frequency period and causes a lot of damage in the Northern Bihar region (Bhatt et al. 2010). In August 2008, the Kosi River routed to its old course of flow, followed by the Kosi river 100 years ago, and this flood affected over 2.3 million people in the northern area of Bihar state (Singh et al. 2011). In the present study, taking these damages into account caused by Kosi river flood, a part of Kosi river basin which lies in Bihar of 14,861.535 Km^2 areas and 112 Km long river was selected study area as shown in Figure 1.

3. Data and Methodology

3.1 Data and Pre-Processing

Active microwave remote sensing data in C band, dual polarization with VV and VH polarization from Sentinel-1 satellite was used. The SAR data over the Kosi river basin was acquired for flood events days - from Alaska Satellite Facility (ASF) as Ground Range Detected (GRD) product with a spatial resolution of 10 m and temporal resolution of 10 to 12 days (Table 1).

It is found in various studies that the VH polarization band is more useful in separating Water and Other Land features (Benoudjit and Guida 2019; Matgen et al. 2007; Tavus et al. 2019; Tripathi et al. 2020; Twele et al. 2016) based on their Backscatter value, which can be derived from SNAP tool and all the classification was done on Sigma0_VH_db band of SAR datasets.

SNAP tool was used for pre-processing of SAR data such as radiometric calibration, speckle filtering, orbit file, geometric correction etc. as shown in Figure 2.

Flooded pixels were identified using binarization techniques as used in (Tripathi et al. 2020) by applying threshold values as a trial and error process. These threshold values can be estimated from the histogram shown in Figure 3 (b). There are two peaks can be seen in the histogram in Figure 3(b). Thus, it can be interpreted that the high peak shows other land features, and the low peak shows water. Water mask band was created using the following math in the "band math" in snap tools.

If $\sigma_{o\_VH} < t_h$ then $255*(\sigma_{o\_VH} < t_h)$ else $0*(\sigma_{o\_VH} > t_h$ && σ_{o_VH} !=0) (1)

Similar equation was used for the VV band. Further, the water mask generated using the above equation was checked and found 78% similarity with a published global water mask data of the Kosi River basin. While this published Global water mask (Pekel, J F., et al. 2016) shows a 50 % probability of flood extent, as shown in Figure 4. Pre-processing of DEM data is performed using QGIS software.

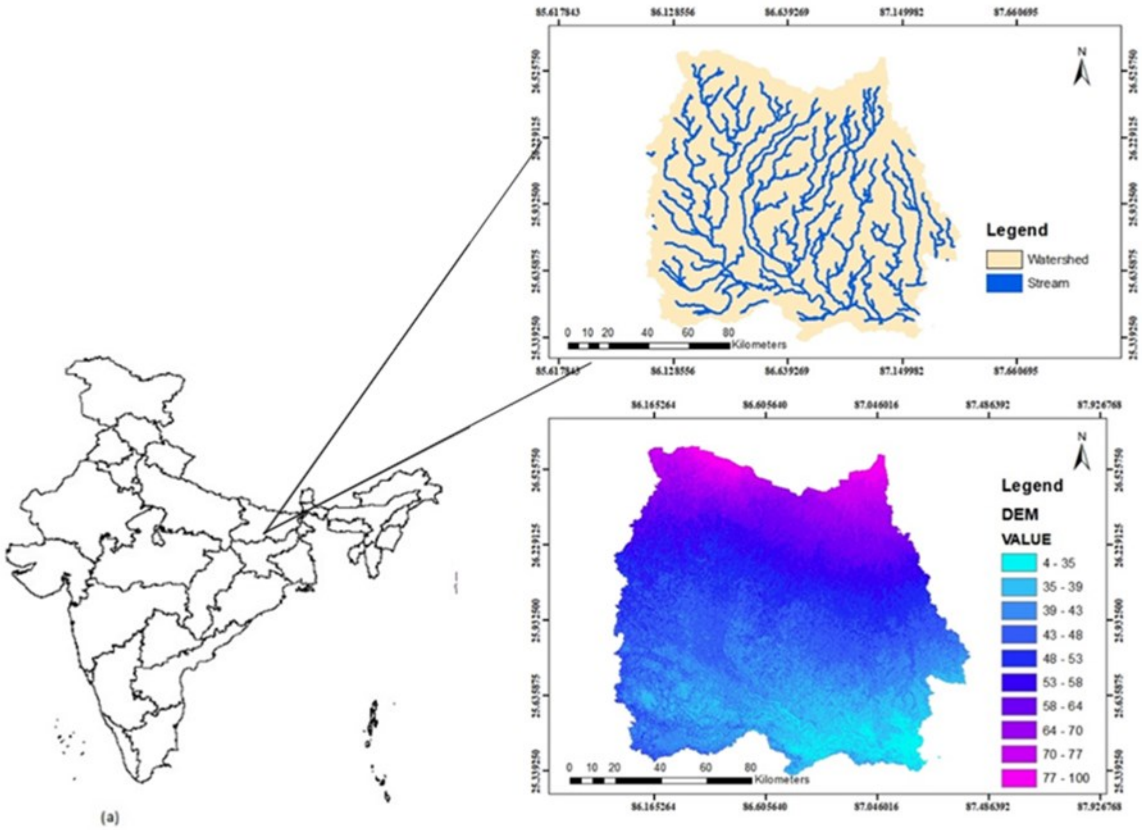

Figure 1. Study area

Table 1. Data used

Data	Type/Format	Source	Acquisition Date	Spatial Resolution	Temporal Resolution	Use	Satellite
SAR	GRD-HD with VH VV Polarization in IW mode	ESA Open Access hub and Alaska Satellite Facility	24/07/2020 11/08/2017, 23/08/2017, 04/09/2017, 16/09/2017	10m 10m	12 days 12 days	Flood Mapping	Sentinel 1 Sentinel 1
DEM	Raster	USGS		30m		Flood water depth estimation	SRTM

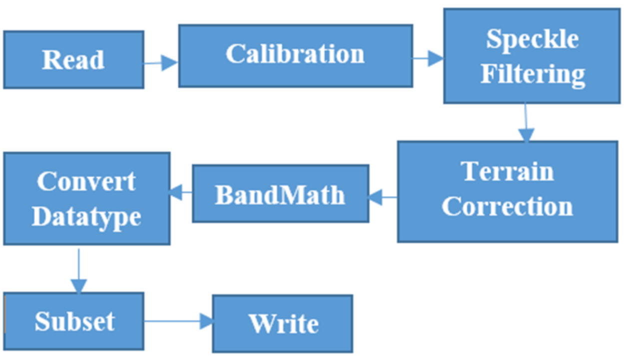

Figure 1. Flowchart of pre-processing

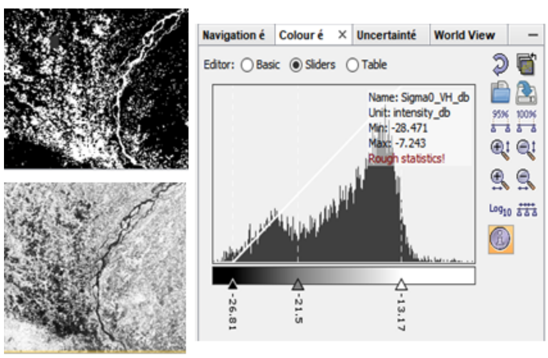

(a) (b)

Figure 3. (a) SNAP tool interface for SAR pre-processing (b) Backscatter value histogram

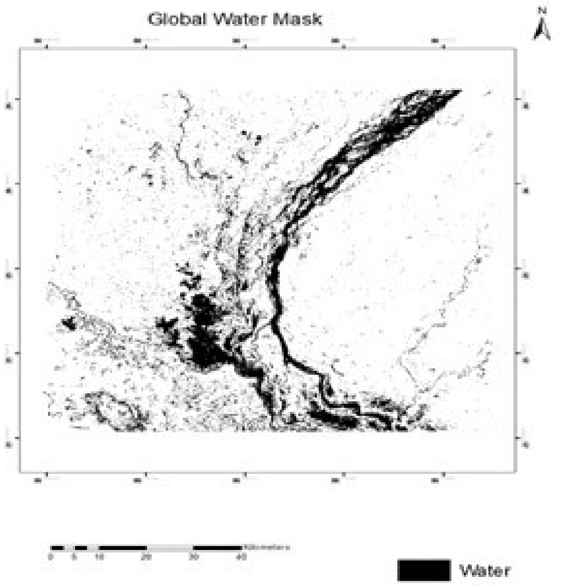

Figure 4. Surface water mask (source: global surface water product)

3.2 Methodology

The main objective of this study is to develop an automated model which will have the potential to provide flood inundation extent and water depth in near real-time. Automated flood mapping and water depth estimation was done in two stages. In the first stage, flood inundation extent was estimated using a hybrid model, which was developed using Machine learning-based supervised classifiers (mainly RFC and KNN). In the second stage, flood extents maps were used along with DEM to estimate floodwater depth maps using the PyQGIS tool based on FwDET (Cohen et al. 2018). The methods used in this study are shown in Figure 5 as a flowchart; further description of the method is discussed below.

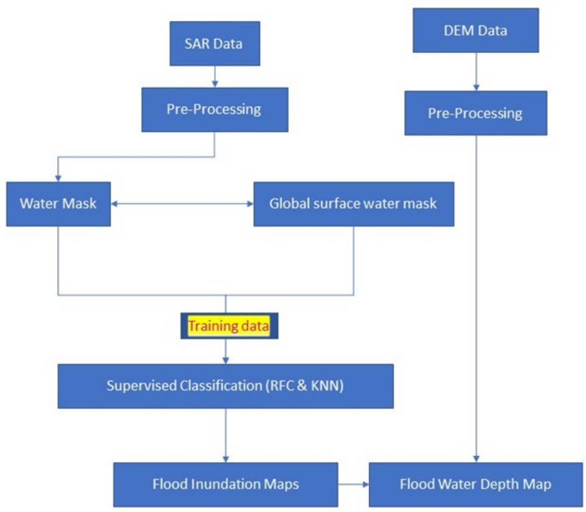

Figure 5. Schematic representation of approach adopted for flood water depth estimation

3.2.1 Hybrid Flood Inundation Model (Classification Using Water Mask and Supervised Machine Learning Algorithm)

This model was developed to get a fully automated approach for flood inundation mapping. The model is based on the concept of the binarization method and supervised ML algorithms. Binarization includes the selection of threshold backscatter values for water bodies and flooded areas using histogram-based thresholds and published global surface water mask data as ground truth. Further, the flooded and the non-flooded area gets separated as shown in Figure 3(a), top panel window is water mask, the lower one is pre-processed data and histogram of the pixel value is seen in Figure 3(b). There are two peaks can be seen in the histogram in Figure 3(b). Thus, it can be interpreted that the taller peak shows other land features, and the smaller peak shows water.

It was found that the pixel value of the water surface was very close to the value same as under the second smaller peak of the histogram. The threshold value for water in this study area varies from -19db to -22db, and using a "band math" tool in SNAP software water mask was created by applying equation (1) in Sigma0_VH_db band image shown in Figure 6(b). This water mask was updated using a published global surface water mask (Pekel, J F., et al. 2016). Further, the water mask band was used as ground truth data for RFC and KNN supervised classification.

Water mask had labeled data of flooded area as 255 and non-flooded area as 0 shown in Figure 6 (b). The labeled information is used as training datasets for the machine learning models. N_estimator (RFC parameter) was set to a value of 100 whereas six neighbors were selected in the KNN algorithm. Models estimated inundations are shown in Figure 8.

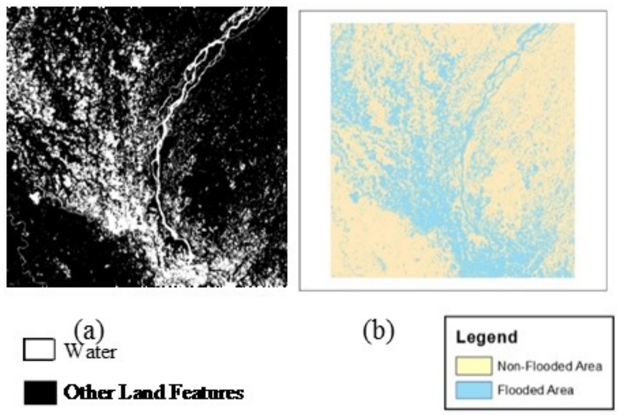

Figure 6. (a) Water Mask (b) Sigma0_VH_db band image

3.2.2 Floodwater Depth Analysis Model

Floodwater depth was estimated with the help of an inundation map and DEM using PyQGIS script and FwDET tool developed by (Cohen et al. 2018). This tool was applied by taking input from the hybrid flood inundation model output. Further, to get the elevation value of pixels in inundation maps was converted into vector form of polygons. These polygons consist of flooded areas and non-flooded areas. Flooded area polygon with grid id of 255 was extracted and merged into a single polygon. So that, these inundated area polygons were further converted into polylines, which can serve as the flood area extent boundary line. The elevation value for these boundary lines was extracted from DEM and a surface interpolated within this boundary line using grow distance tool as in QGIS. The interpolated surface zones. Flood water depth was found after subtracting the surface created within flood extent with DEM in raster format, and each pixel shows the flood water depth at that location in meters. The structure of this depth estimation tool is shown in Figure 7.

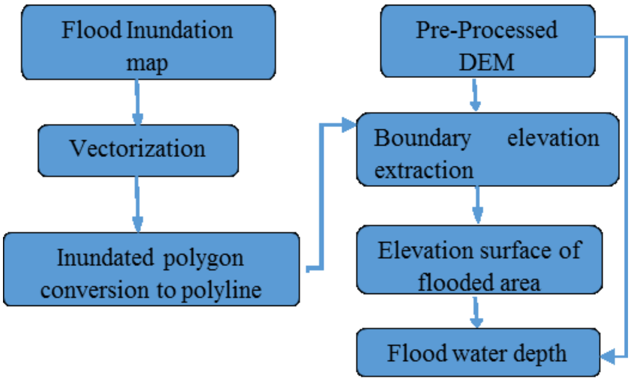

Figure 7. Flow chart of Flood Water Depth Analysis Model

The concept of floodwater depth estimation is constructed from the property of water, i.e., as compared with boundary elevation value, water surface also shows the same elevation value with its boundary of extent. This concept helps in determining the flood water depth of the inundated areas in a river basin. The classified maps show flood extent in the study area, and a floodwater depth map was generated using this tool, as shown in Figure 10.

4. Result and validation

4.1 Hybrid model based inundation

The random forest model results flood inundation map, which shows 5432 Km2 under non-flooded area and 2517 Km2 as flooded area. The KNN model estimated 5892 Km2 as non-flooded area and 2057 Km2 under flooded area. The algorithms, KNN and RFC, show nearly the same flood extent and demonstrated an accuracy of 0.9719 and 0.9726, respectively with ground truth data used in this study. This classification report shows that both Classifiers perform well with a very little difference in performance, but the time taken by KNN classifiers was 28hr, whereas the RFC algorithm takes only 6hr. The confusion matrix, as shown in Figure 10, was generated to asses the classification results.

The confusion matrix shows the performance of KNN and RFC in identifying the flooded and non-flooded area, e.g., in Figure 9 model based on the RFC classifier method identifies 28114541 flooded pixels and 11968 number of pixels confused as a flooded pixel. On the other hand, 57936144 pixels were considered non-flooded pixels and confused in 1990969 pixels as flooded areas. A similar result was found in RFC classifiers.

A floodwater depth map was generated using the algorithm for water depth estimation discussed above, and it is shown in Figure 7. Flood extent from the machine learning approach was used to prepare the Flood depth map shown in Figure 10. A total area of 2515 Km^2 was found inundated in the flood water depth map using an RFC-based flood inundation map. While 145 Km2 area of the inundated part was found overestimated as it shows 0 m flood water depth and further spatial variation of flooded water is shown in table 2.

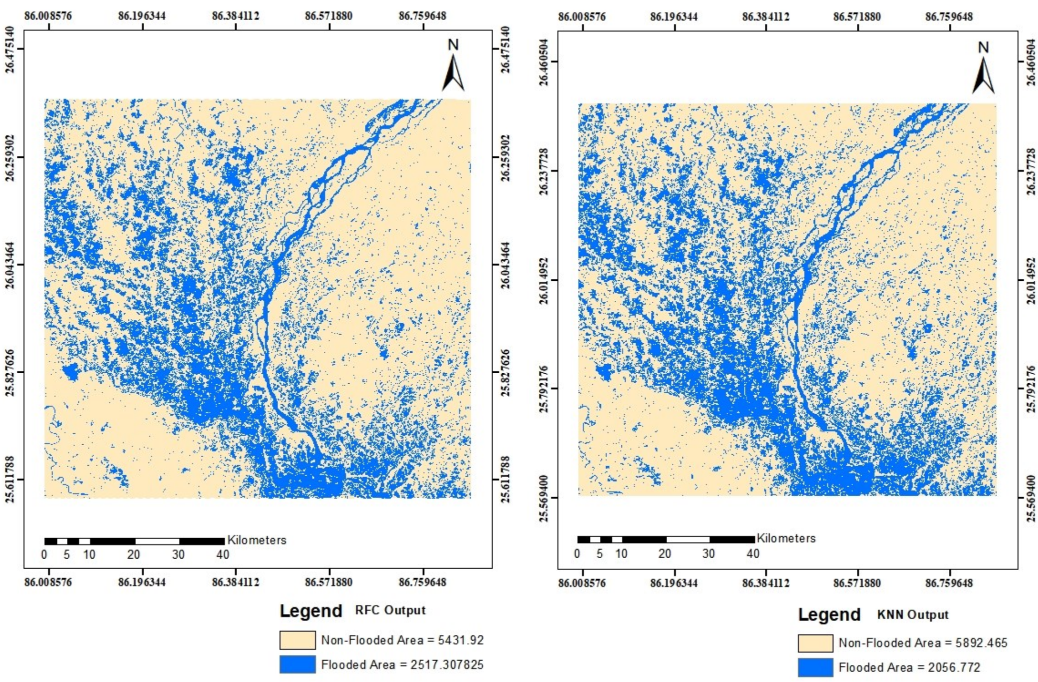

Figure 8. Flood inundation map using RFC (left) and KNN (right) based hybrid model

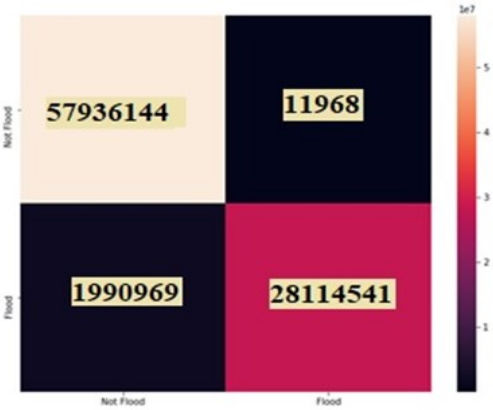

Figure 9. Confusion Matrix of Model

Table 2. Flood water depth Information (26/07/2020)

Depth (m)	Area (Km^2)
0-0.25 m	814.1034
0.25-0.5m	468.1819
0.5-1m	504.8314
1 - 2m	386.8695
2-3m	126.88
3-5m	60.27397
5-10m	9.004411
>10 m	0.098399

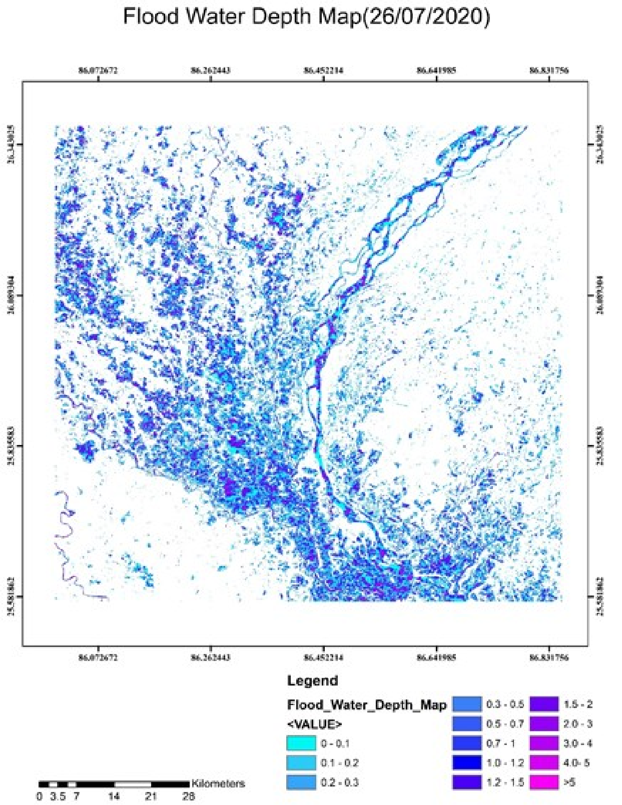

Figure 10. Flood Depth Map using Flood water depth analysis model

4.2 Validation

Further validation of these models results was done with the flood mapping of Darbhanga district 2017 Tripathi et al. 2020. SAR data of 11/08/2017, 23/08/2017, 04/09/2017, and 16/09/2017 dates were used to map inundation using the Binarization technique. The flood inundation map generated by Tripathi et al. 2020 and hybrid model based inundation in the present study were compared for validation. On August 23, 2017, heavy runoff was calculated using TRMM and IMD rainfall products found in (Tripathi et al. 2020).

According to a published study, most inundation area was observed on August 23, 2017. Similarly, model results also show the most flood inundated area on August 23, as shown in Figure 11. Flooded and the non-flooded area were also calculated. Published data shows underestimated whereas model-derived area shows slightly over estimated results. Flood maps estimated using the model can be rectified using a water depth map derived using floodwater depth tool. Floodwater depth maps for different dates are shown in Figure 11.

The automated model shows the flooded area as 104.6, 820, 536 Km^2, and 371.4 Km2 on 11/08/2017, 23/08/2017, 04/09/2017, and 16/09/2017, respectively. When compared with previous studies, these flooded areas found that the flooded area estimated using this model is slightly overestimated, varying from 14.9% to 70% before rectification was done.

To calculate the depth of flooded water, DEM was used to extract the elevation values. Flood water depth information of the study area is shown in the table. Water depth was estimated and found that in the study area during August and September month there was a max water level of 13 meters, as also shown in table 3. There were also some pixels showing a 0-meter depth of water, and these pixels were considered a non-flooded area which was confused by the model as a flooded area. After removing 0 m pixels from the flooded area, it was found that the final Flood Inundation map, along with flood water depth information, was deviating from 0.9% to 19.33 % respective to the published flood map as provided in the table 3.

Thus, depth map accuracy depends on the resolution of DEM. In this study, DEM of 30m spatial resolution was used, and in any case, when a single pixel of 30 meters covers an area where some portion is inundated, and the rest is dry land, then it might happen that the site will be classified as flooded or non-flooded zone thus it could affect the accuracy of the model.

From this study, it can be suggested that coupled model addressing water extent and depth is highly useful to analyze flood events. Figure 11 shows varying flood water depth over Darbhanga district in August and September 2017.

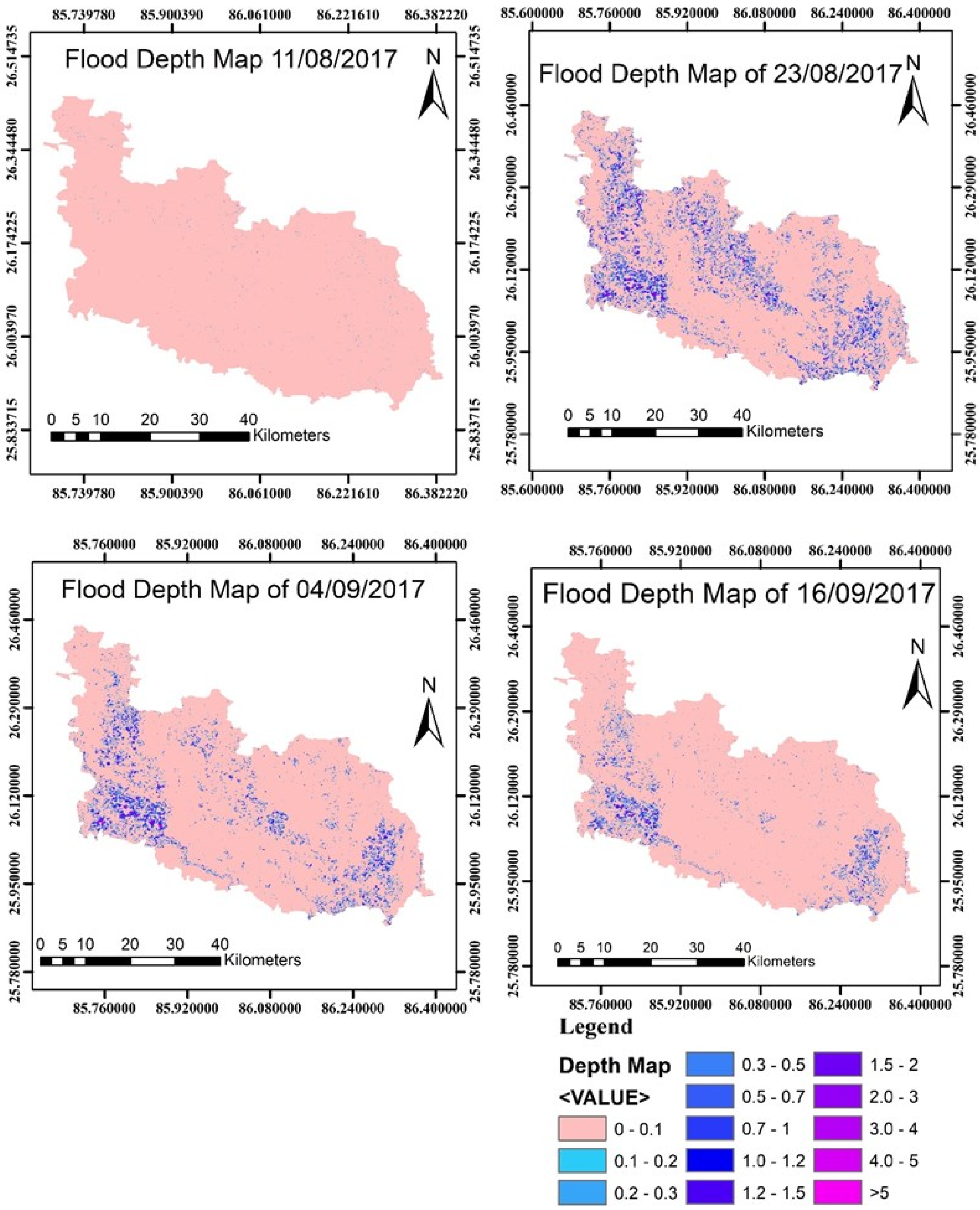

Figure 11. Flood water depth map of Darbhanga 2017 flood

Table 3 Floodwater depth of Darbhanga district 2017 flood

Date	0-1m depth(Km^2)	1-5m depth(Km^2)	5-10m depth(Km^2)	10-13m (Km^2) depth	Total Area (Km^2) (Hybrid Model)	Total Inundated Area in (Tripathi et al. 2020)	Percentage Deviation from previous study(Tripathi et al. 2020)
11/08/2017	20.62	0.051	0	0	21	36	13.88 %
23/08/2017	488.50	70.609	0.626	0.0364	560	554	0.90%
04/09/2017	316.66	41.48	0.388	0.0453	358	330	8.64%
16/09/2017	205.93	18.39	0.023	0	224	188	19.33%

5. Conclusions

In this study, different methods of flood inundation mapping were used using active Microwave C band SAR data. Because the SAR C band having a higher wavelength can penetrate dense clouds and even thin vegetative canopy, thus even in dense cloudy conditions, the SAR image provides precise information. Machin learning classification algorithms, e.g., K- nearest neighbor and Random Forest classifiers, were used, and it was found that the Random Forest classifier gives better results. Inundated surface estimates were also compared with published data over the Darbhanga District and found in good agreement. Subsequently, estimated inundation along with DEM was used to estimate water depth using PyQGIS standalone tool. As mentioned above, all the methods used in the study were packaged to develop an independent and open-source tool to monitor the flooding extent and water depth. This tool consists of a hybrid model for inundation extents and a Flood water depth analysis model. The present study suggests that the RFC ML algorithm can be used to classify the SAR data into flooded and non-flooded areas. The developed tool can be used for monitoring floods in near real-time for rescue operations. The greatest advantage of this tool is that it works independently. ML algorithm for classification and its automation for flood mapping makes this tool usable on any platform. The tool could be most helpful for monitoring flood damages and their effect.

References

Anusha N., and B. Bharathi (2020). Flood detection and flood mapping using multi-temporal synthetic aperture radar and optical data. Egyptian Journal of Remote Sensing and Space Science, 23(2), 207–219.

Benoudjit A., and R. Guida. (2019). A novel fully automated mapping of the flood extent on sar images using a supervised classifier. Remote Sensing, 11(7).

Bhatt C. M., G. Srinivasa Rao, P. Manjushree and V. Bhanumurthy (2010). Space based disaster management of 2008 Kosi floods, North Bihar, India. Journal of the Indian Society of Remote Sensing, 38(1), 99–108.

Campolo M., P. Andreussi and A. Soldati (1999). River flood forecasting with a neural network model, 35(4), 1191–1197.

Cohen S., G. R. Brakenridge, A. Kettner, B. Bates, J. Nelson, R. McDonald, Y. F. Haung, D. Munasinghe and J. Zhang (2018). Estimating Floodwater Depths from Flood Inundation Maps and Topography. Journal of the American Water Resources Association, 54(4), 847–858.

Amitrano D, G. D. Martino, A. Iodice, D. Riccio and G. Ruello (2018). Unsupervised rapid flood mapping using Sentinel-1 GRD SAR images. IEEE Trans Geosci Remote Sens, 56(6), 3290–3299.

de Groeve, T. (2010). Flood monitoring and mapping using passive microwave remote sensing in Namibia. Geomatics, Natural Hazards and Risk, 1(1), 19–35.

Elsafi S. H. (2014). Artificial Neural Networks (ANNs) for flood forecasting at Dongola Station in the River Nile , Alexandria Engineering Journal, 53(3), 655–662. https://doi.org/10.1016/j.aej.2014.06.010

Feng Q., J . Gong, J. Liu and Y. Li (2015). Flood mapping based on multiple endmember spectral mixture analysis and random forest classifier-the case of yuyao, China. Remote Sensing, 7(9), 12539–12562.

Gole C. V., and S. V. Chitale (1966). Inland Delta Building Activity of Kosi River. Journal of the Hydraulics Division, 92(2), 111–126.

Gouweleeuw B., C. Ticehurst, P. Dyce, J. P. Guerschman, A. I. J. M. Van Dijk and P. Thew (2011). An experimental satellite-based flood monitoring system for southern Queensland, Australia. 34th International Symposium on Remote Sensing of Environment - The GEOSS Era: Towards Operational Environmental Monitoring.

Peke, J.F., A. Cottam, N. Gorelick and A. S. Belward (2016) High-resolution mapping of global surface water and its long-term changes. Nature 540, 418–422.

Mason D. C., G. J. P. Schumann, J. C. Neal, J. Garcia-Pintado and P. D. Bates (2012). Automatic near real-time selection of flood water levels from high resolution Synthetic Aperture Radar images for assimilation into hydraulic models: A case study. Remote Sensing of Environment, 124, 705–716.

Mason David C., I. J. Davenport, J. C. Neal, G. J. P. Schumann and P. D. Bates (2012). Near real-time flood detection in urban and rural areas using high-resolution synthetic aperture radar images. IEEE Transactions on Geoscience and Remote Sensing, 50(8), 3041–3052.

Matgen P., G. Schumann, J. B. Henry, L. Hoffmann and L. Pfister (2007). Integration of SAR-derived river inundation areas, high-precision topographic data and a river flow model toward near real-time flood management. International Journal of Applied Earth Observation and Geoinformation, 9(3), 247–263.

Mohanty, M. P., S. Mudgil and S. Karmakar (2020). Flood management in India: A focussed review on the current status and future challenges. International Journal of Disaster Risk Reduction, 49(July 2019), 101660.

Schumann G. J. P., and D. K Moller (2015). Microwave remote sensing of flood inundation. Physics and Chemistry of the Earth, 83–84, 84–95.

Shahabi H., A. Shirzadi, K. Ghaderi, E.Omidvar, N. Al-Ansari, J. J. Clague, M. Geertsema, K. Khosravi, Ata Amini, S. Bahrami, O. Rahmati, K. Habibi, A. Mohammadi, H. Nguyen, A. M. Melesse, B. B. Ahmad and A. Ahmad. (2020). Flood detection and susceptibility mapping using Sentinel-1 remote sensing data and a machine learning approach: Hybrid intelligence of bagging ensemble based on K-Nearest Neighbor classifier. Remote Sensing, 12(2).

Shen X., D. Wang, K. Mao, E. Anagnostou and Y. Hong (2019). Inundation extent mapping by synthetic aperture radar: A review. Remote Sensing, 11(7), 1–17.

Singh S. K., A.C. Pandey and M.S. Nathawat (2011). Rainfall variability and spatio temporal dynamics of flood inundation during the 2008 Kosi flood in Bihar State, India. Asian Journal of Earth Sciences, 4(1), 9–19.

Singh D.A. (2015). Floods in India: Cause and Control

Sinh R., G.V. Bapalu, L. K. Singh and B. Rath, B. (2008). Flood risk analysis in the Kosi river basin, north Bihar using multi-parametric approach of Analytical Hierarchy Process (AHP). Journal of the Indian Society of Remote Sensing, 36(4), 335–349

Sivanpillai R., K. M. Jacobs, C. M. Mattilio and E.V. Piskorski (2020). Rapid flood inundation mapping by differencing water indices from pre- and post-flood Landsat images. Frontiers of Earth Science 2020 15:1, 15(1), 1–11.

Tavus B., S. Kocaman, H. Nefeslioğlu and C. GÖKÇEOĞLU (2019). Flood Mapping Using Sentinel-1 SAR Data: A Case Study of Ordu August 8 2018 Flood. International Journal of Environment and Geoinformatics, 6(3), 333–337.

Tehrany M. S., B. Pradhan and M. N. Jebur (2014). Flood susceptibility mapping using a novel ensemble weights-of-evidence and support vector machine models in GIS. Journal of Hydrology, 512, 332–343.

Tehrany M. S., B. Pradhan, S. Mansor, and N. Ahmad (2015). Flood susceptibility assessment using GIS-based support vector machine model with different kernel types. Catena, 125, 91–101.

Temimi M., R. Leconte, F. Brissette and N. Chaouch (2005). Flood monitoring over the Mackenzie River Basin using passive microwave data. Remote Sensing of Environment, 98(2–3), 344–355.

Tripathi G., A. C. Pandey, B. R. Parida, and A. Kumar (2020). Flood Inundation Mapping and Impact Assessment Using Multi-Temporal Optical and SAR Satellite Data: a Case Study of 2017 Flood in Darbhanga District, Bihar, India. Water Resources Management, 34(6), 1871–1892.

Twele A., W. Cao, S. Plank, and S. Martinis (2016). Sentinel-1-based flood mapping: a fully automated processing chain. International Journal of Remote Sensing, 37(13), 2990–3004.

An integrated approach of flood risk assessment over a severely flood-prone coastal region using geomorphic classifiers, and socio-economic indicators

Mohit Prakash Mohanty[1,2], K.V.H Durga Rao[3] and Subhankar Karmakar[2,4,5*],
[1]Department of Water Resources Development and Management, Indian Institute of Technology Roorkee, Roorkee 247 667, India
[2]Environmental Science and Engineering Department, Indian Institute of Technology Bombay, Mumbai 400 076, India
[3]Disaster Management Support Division, National Remote Sensing Centre, Balanagar, Hyderabad-500625, Telangana, India
[4]Interdisciplinary Program in Climate Studies, Indian Institute of Technology Bombay, Mumbai, 400076, India
[5]Centre for Urban Science and Engineering, Indian Institute of Technology Bombay, Mumbai, 400076, India
*Email: skarmakar@iitb.ac.in

(Received: Aug 10, 2021; in final form: Oct 06, 2021)

Abstract: The present study explores the efficacy of readily available geomorphic classifiers and socio-economic indicators to characterize flood risk over Jagatsinghpur district, a severely flood-prone coastal region in the Mahanadi River Basin. A set of twelve relevant geomorphic classifiers are derived from the high-resolution CartoDEM topographic data through linear binary classification to identify flood hazard zones. On the other side, twenty-one socio-economic indicators are considered through multivariate Data Envelopment Analysis (DEA) to derive socio-economic vulnerability at the village level. Flood risk at the village level is calculated as the combination of geomorphic flood hazard and socio-economic vulnerability. The flood risk zones derived by utilizing geomorphic classifiers are compared to those derived through a comprehensive 1D 2D coupled hydrodynamic modeling. Inundation along the floodplains near the rivers and coastal regions is well captured through both geomorphic analysis and hydrodynamic modeling. A vast majority of villages experience low and very low vulnerability, while only a few face high and very high vulnerability, mainly secluded to Ersama, Jagatsinghpur, Tirtol Nuagaon, and Baligaon talukas. A high degree of similarity in flood risk proves the reliability of the proposed approach for the estimation of flood risk. Given the acute problem of floods, the proposed methodology, characterized by low computational cost, lesser data requirement, and limited flood modeling complexity, may facilitate local authorities and planners deriving effective flood management strategies.

Keywords: flood risk, geomorphic classifiers, hazard, riverine flooding, vulnerability

1. Introduction

It is well known that floods account for the most pervasive mortality and economic damages among all known weather-related natural disasters (Ward et al., 2017; Dottori et al., 2018). Recently, AoN- the leading global professional services firm, reported that global flood events that occurred during March 2019 alone accounted for a mammoth USD 8 billion of economic losses (https://www.preventionweb.net/news/view/64911). The worrying fact is that flood events have been increasing manifold, majorly driven by climate change impacts and changes in socio-economic dynamics, as indicated by several research articles (Blöschl et al., 2017; Thober et al., 2018; Mohanty and Simonovic, 2021b). A recent report by Rentschler and Salhab (2020) prepared for the World Bank highlights that a staggering 1.47 billion people globally live within high flood risk zones. It further apprises that although countries at all levels of development face various degrees of flood risk, the vast majority of the exposed population, i.e., ~ 89% reside in the low- and middle-income countries, most widespread impacts of floods noticed over South-Asia.

One way of comprehending this emerging concern is by quantifying flood risk, which provides a transparent knowledge of the regions and how they are affected by flooding (Trigg et al., 2016; Wing et al., 2019). As per the standard definition, flood risk is the product of flood hazard and vulnerability (Hagenlocher et al., 2018; Mohanty et al., 2020b; Sajjad et al., 2020). Flood hazard is considered the tangible component of flood risk and is quantified based on the degree of depth and velocity of inundated water over the region (Kourgialas and Karatzas, 2011; Costabile et al., 2020). On the other hand, vulnerability is the intangible component and determines the susceptibility of various domains, including humans, physical features, and the environment, to flood damages (Wing et al., 2020; Paprotny et al., 2021). Several approaches quantifying flood hazards and can be categorized into empirical, simple conceptual, and hydrodynamic models (Teng et al., 2017). Empirical models adopt straightforward approaches to retrieve flood information from past observations. In the last two decades, the usability of remotely sensed data and GIS has been widely explored in quantifying flood hazards. The recently launched satellites, such as SWOT, RADARSAT-2, TerraSAR-X, COSMO-SkyMed, and Sentinel-1, contain sophisticated sensors that facilitate in capturing high-resolution images at a faster time (Teng et al., 2017). In particular, satellite images derived from Synthetic aperture radar (SAR) that can overcome cloud cover have been found to help identify flooded regions (Zhan et al., 2021; Clement et al., 2018). The algorithms considered in the process also make it possible to distinguish between permanent water bodies and inundated areas, allowing flooded boundaries to be identified with a high degree of accuracy (Gebremichael et al., 2020). Hydrodynamic models are mathematical models designed to replicate fluid motion by solving St. Venant's equations and are considered the most sophisticated approach (Afshari et al., 2018; Wing et al., 2019). Usually, they consider a wide range of inputs such as topographic (e.g., digital elevation model; DEM, underwater topography, built-up area, and artificial drainage network), hydrologic (e.g., streamflow, lake discharge, point source), and meteorological (e.g., rainfall, snowfall) to derive flood hazard. In most cases, the availability of the datasets is a daunting task, and even more while dealing with data-scarce flood-prone regions existing in several developing and under-developed nations. Based on the representation of flood inundation dynamics, hydrodynamic models can be further grouped into one-dimensional (1D), two-dimensional (2D), and three-dimensional (3D) models.

Although hydrodynamic models are competent in deriving precise flood hazard information, their usage may be limited in some instances due to (i) scarcity of extensive data inputs, (ii) in comprehensive performance over large and complex terrains, (iii) high computational cost and time, and (iv) lack of expertise in handling model simulations by a non-technical user. An alternative computationally less extensive solution is to utilize the river basin's topography to identify flooding patterns (Adnan et al., 2019; Mishra and Sinha, 2020). In particular, hydrological extremes and floods accelerate erosion, transport, and deposition processes, and over extended periods can shape and form geomorphic features. Few studies have recently developed DEM-based floodplain delineation methods to compare the topographic surface and a reference water level. The identification of flood-prone areas is demonstrated through linear binary classification techniques that have proven to be an appealing tool characterized by simple requirements regarding input data, costs, and computational times (Manfreda et al., 2014, 2015). The classifiers include single features (e.g., slope, contributing area, distance to the nearest channel, topographic convergence, etc.) and composite features formulated with the specific aim to represent a metric of flood hazard. **Table 1** enlists recent efforts made to map flood hazards through geomorphic classifiers.

Despite the encouraging usage of geomorphic classifiers in identifying flood-prone regions, their efficacy in flood risk mapping, which requires information on flood hazard and socio-economic vulnerability, has not been explored. Most of the studies have limited their analysis to identifying flood susceptible zones without looking further into the flood hazard component. Moreover, past studies have focussed on geomorphic studies over inland areas affected by riverine flooding; their performance over coastal regions has not been reported so far. It is widely known that coastal environments identified by multiple flood drivers are the most susceptible to flooding (Kron, 2013; Vousdoukas et al., 2018; Tiggeloven et al., 2020). In such regions, the inland areas are inundated from riverine overflow due to extreme rainfall during the monsoon. At the same time, the coastal stretches are affected by storm tide (combination of astronomical tide and storm surge) impacts. The present study explores the efficacy of geomorphic classifiers in flood risk mapping over a severely flood-prone coastal region in India. A set of relevant single and composite classifiers are considered to derive flood hazard zones. The socio-economic vulnerability is quantified at the finest administrative scale of the village level over the study area. The hazard identified by the best performing geomorphic classifier is considered along with the socio-economic vulnerability to derive different levels of flood risk. The flood risk derived by utilizing the geomorphic approach is compared with the other flood risk map developed by using hazard derived from a comprehensive 1D 2D coupled inundation modeling. At last, both the flood risk maps are compared to establish the geomorphic classifier's efficacy in quantifying flood risk.

2. Description of the study area

Jagatsinghpur district is situated between 19° 58' N to 20° 23' N latitude and 86° 3' E to 86° 45' E longitude in the flood-prone delta region of the lower Mahanadi river basin in the state of Odisha, India (Figure 1). It is well-known as a severe flood-prone area in India (Mohapatra, 2015; Sahoo and Bhaskaran, 2018; Mohanty et al., 2021a). The region falls within the deltaic zones of two major rivers, namely, River Mahanadi and Devi. The district receives an annual average rainfall of 1451.60 mm, majorly from the South-west monsoon. It has a coastline spanning up to ~50 km) that faces constant tidal disturbances. The tide is semi-diurnal with the maximum Highest High Water Level (HHWL) of +3.5 m and a minimum Lowest Low Water Level (LLWL) of +0.7 m relative to the chart datum (Gopikrishna and Deo, 2018). Morphologically, more than half of the region is relatively flat (< 4.5 m) (Muralikrishnan et al., 2013), which prolongs the stance of floodwater. Moreover, being predominantly agrarian (~66%), the district is subjected to substantial socio-economic setbacks very frequently in terms of losses in crop production, loss of livestock, and fisheries due to floods almost every year (Mohanty et al., 2020b).

3. Proposed framework and methodology

The proposed framework is illustrated in Figure 2. The flood hazard analysis is carried out using geomorphic classifiers, which are implemented on the DEM. In this study, we considered the CartoDEM of horizontal resolution 10m. CartoDEM is an Indian product synthesized from the Cartosat-1 stereo payload launched in May 2005 by ISRO's Polar Satellite Launch Vehicle (PSLV-C5). Previous studies have reported the high accuracy of CartoDEM while accounting for flood inundation modeling (Mohanty et al., 2020a). Both single and composite classifiers are considered to depict the flood hazard zones. Later, the best performing geomorphic classifier is selected to create the representative geomorphic flood hazard map. Another flood hazard map is derived through a comprehensive 1D 2D coupled hydrodynamic modeling. Village-level socio-economic vulnerability is quantified by considering 21 socio-economic indicators through Data Envelopment Analysis (DEA). The hazard (both geomorphic and hydrodynamic) and socio-economic vulnerability information are aggregated to create two flood risk maps at the village level. A step-by-step disposition of the proposed methodology is described in the following sections.

3.1 Identification of flood hazard zones through geomorphic classifiers

Numerous physical features describe the morphology of a river basin.

Table 1. Recent efforts made to map flood hazard through geomorphic classifiers

Indicators	Case study	DEM	Remarks	References
Modified topographic index (TIm) $TI_m=\log\frac{a_d^n}{\tan(\beta)}$ ad is drained area per unit contour length; and tan(β) is local gradient.	Arno river basin, Italy (8,830 km^2)	DEM obtained from Arno River Basin Authority (20m) SRTM DEM (90 m) ASTER DEM (30 m) National elevation data (30 m)	The index is highly sensitive to DEM resolution; however, a cell size of ~100 m is sufficient for good performance. SRTM DEM showed good performance when compared with the other DEMs.	Manfreda et al. (2011)
Surface curvature (H) Laplacian of the elevation (Δ H) Contributing area (A) Local slope (S)	Tanaro river basin, Italy (8,000 km^2)	SRTM: DEM–VOID (Void filled)and DEM–CON (Hydrologically conditioned) from HydroSHEDS	The classifiers could identify 93% of flood-prone areas while validated with the flood inundation map.	Degiorgis et al. (2012)
Single features Upslope contributing area, As (m2) Surface curvature (∇2H) Local slope, S Distance from the nearest stream, D (m) Elevation to the nearest stream, H (m). Composite indices Modified topographic index (TIm) Downslope index, (DWi) Ratio between the flow distance (D) and elevation (H) ln[hl/H]; where hl is the variable water depth GFI (Geomorphic Flood Index): ln[hr/H]: hr is computed as a the function of the contributing area Ar [hr-H]/tan(αd) and [hr - H]/D.	Tiber River Basin, Italy (17,375 km^2)	-do-	Elevation to the nearest stream (H), downslope index (DWi), and GFi showed better performance.	Manfreda et al. (2014)
	Bradano River Basin, Italy (2765 km^2)	-do-	Among the single features, Distance from the nearest stream (D) and Elevation to the nearest stream (H) performed better, while among composite indices ln[hl/H] and ln[hr/H] performed better. Composite indices were found to be less sensitive to the variations in DEM resolution.	Manfreda et al. (2015)
	Bulbula river sub-catchment, Ethiopia	-do-	Elevation difference (H) and the composite index ln[hr/H] showed the best performance.	Samela et al. (2016)
	Ohio River Basin, US, (29,000 km^2)	-do-	GFI was the most suitable morphologic classifier, as it exhibited a higher accuracy than the other indices.	Samela et al. (2017)

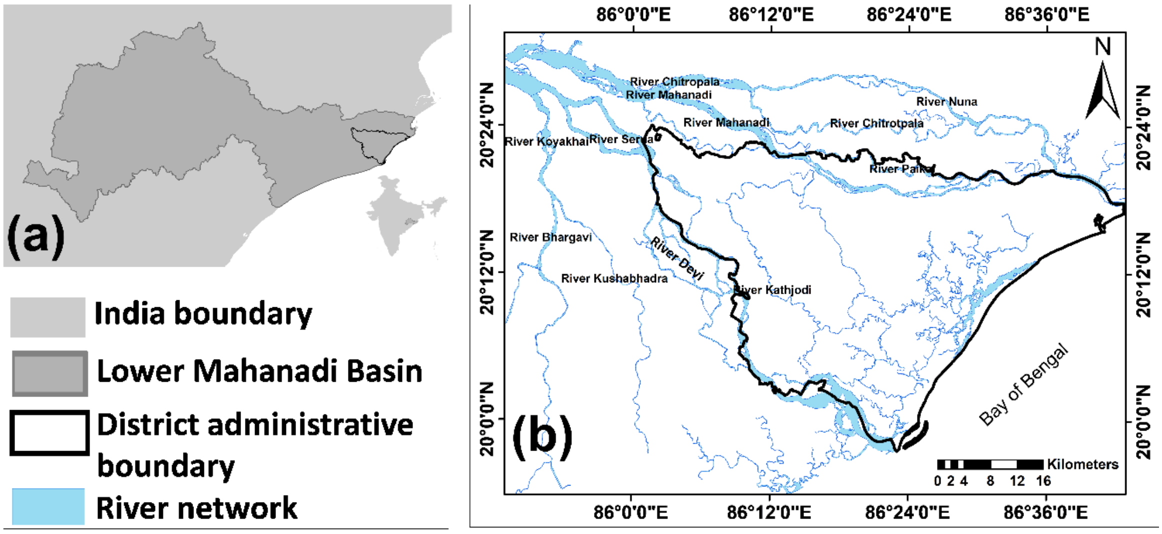

Figure 1. Description of the study area: (a) Location of Jagatsinghpur in the lower Mahanadi river basin; (b) River network in Jagatsinghpur district.

In this study, we considered the relevant indicators that are explicitly capable of capturing flood wave propagation and flood hazards. For example, a few indicators characterize the tendency of the flood water to be accumulated over specific locations over the study area or the tendency of gravitational force to allow the floodwater to move downstream (Samela et al., 2017). Based on this criterion, twelve geomorphic features were finalized. Among them, five were single geomorphic classifiers, while the rest were composite geomorphic classifiers. The composition of single classifiers proposes the latter set of classifiers to estimate the water depth that is calculated as a function of the contributing area. The selected geomorphic classifiers are described below.

Single geomorphic classifiers

1. Upslope contributing area, **A** (m^2): the upslope area of the region that contributes to runoff to the point of focus;
2. Surface curvature, ∇^2 **H**: Laplacian of the elevation;
3. Local slope, **S**: maximum value of slope among the eight possible flow directions;
4. Flow distance to the nearest stream, **D** (m): hydrologic distance from the point under focus to the closest point of the river drainage network;
5. Elevation difference to the nearest stream, **H** (m): the difference between the point's elevation under focus and the final point of the above-identified path.

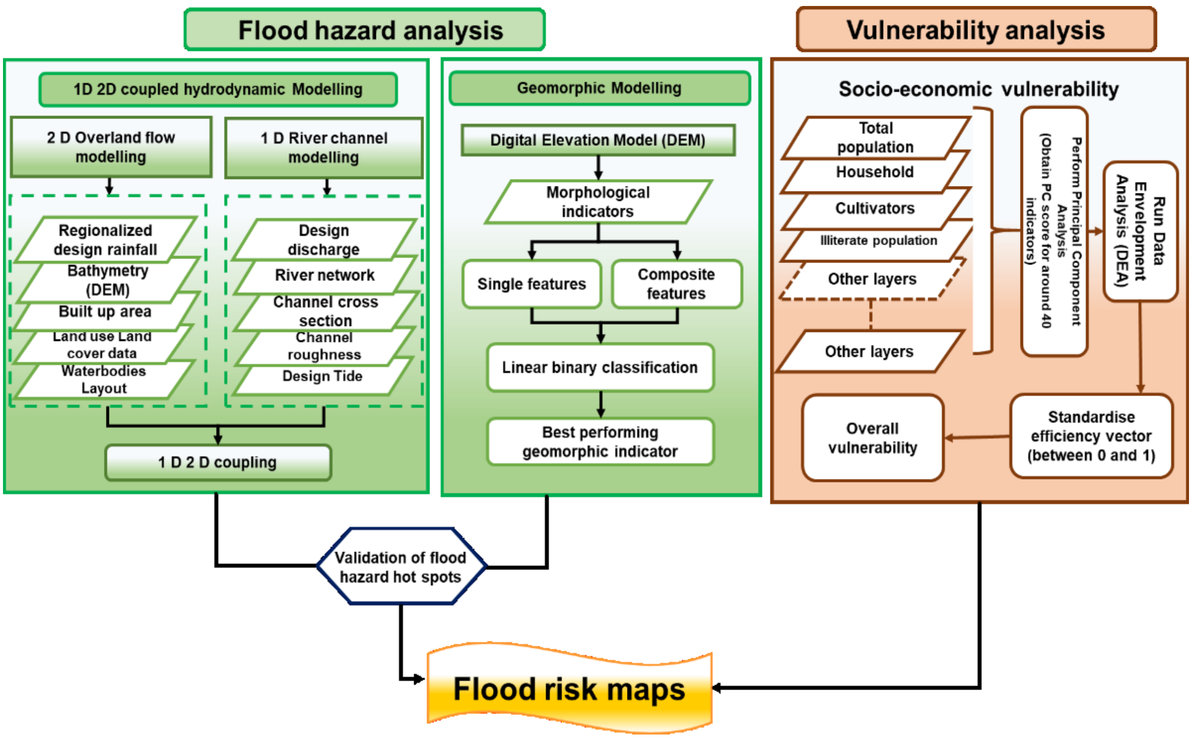

Figure 2. The proposed framework of flood risk mapping considering flood hazards derived through geomorphic analysis and 1D-2D hydrodynamic modeling, and Socio-economic vulnerability analysis.

Composite geomorphic classifiers

1. Modified topographic index(TI_m): it is mathematically represented as,
$TI_m = ln\left[\frac{a_d^n}{\tan(\beta)}\right]$ where a_d (m) is the drained area per unit contour length; $\tan(\beta)$ is the local gradient, and n is an exponent whose value is taken as less than 1.
2. Downslope index: it is mathematically represented as
$\tan(a_d) = \frac{d}{L_d}$
where, L_d (m) is the distance that an amount of water has to travel along its flow path to lose potential energy equal to d (m).
3. H/D: where H is the elevation difference, and D is the flow distance to the nearest stream
4. ln (h_l /H): where, h_l is the water depth , and H is the elevation difference.
5. ln(h_r/H): h_r is determined as a function of the upslope contributing area A in the nearest point of the river drainage network hydrologically connected to the point under focus.
6. (h_r-H)/ tan (α_d): representing the change between water depth h_r and the elevation difference H divided by a surrogate of the hydraulic gradient represented by the downslope index, and
7. (h_r-H)/D: change between water depth h_r and the elevation difference H divided by the distance D.

3.2 1D 2D coupled hydrodynamic modeling

The flood inundation modeling was carried out using the MIKE FLOOD model (DHI, 2019). MIKE FLOOD encompasses the 1D version in MIKE 11 for river channel modeling and the 2D version in MIKE 21 HD for overland or flood plain inundation modeling. The MIKE 11 employs an implicit finite difference scheme developed by Abbott and Ionescu (1967) for solving the Saint-Venant equations, regardless of them being kinematic, diffusive, or dynamic. This robust scheme can support courant numbers as high as 10-20 for subcritical flow (with a Froude number less than 1). The governing equations in the MIKE 11 are continuity and momentum equations, as expressed in equations 1 and 2.

$$\frac{\partial Q}{\partial x}+\frac{\partial A}{\partial t}=q \quad (1)$$

$$\frac{\partial Q}{\partial t}+\frac{\partial(\alpha\frac{Q^2}{A})}{\partial x}+ gA\frac{\partial h}{\partial x}+\frac{gQ|Q|}{C^2AR}=0 \quad (2)$$

where Q is the discharge (m^3/s), A is the cross-sectional area (m^2), q is the lateral inflow (m^3/s/m), h is the stage above datum (m), C is the Chezy's roughness coefficient (m$^{1/2}$/s), R is the hydraulic radius (m), α is the momentum distribution coefficient (s^2/m^3), g is the gravitational acceleration (m/s^2), and x and t are the distance (m) and time (s), respectively.

MIKE 21 HD model employs a non-orthogonal unstructured triangular mesh and is based on the numerical solution of the two-dimensional incompressible Reynolds-averaged Navier-Stokes equations using the assumptions of Boussinesq and hydrostatic pressure. The model functions on a finite element method (FEM) scheme and solves the fully dynamic shallow water equations as expressed in equations (3), (4), and (5)

$$\frac{\partial\zeta}{\partial t}+\frac{\partial p}{\partial x}+\frac{\partial q}{\partial y}=\frac{\partial d}{\partial t} \quad (3)$$

$$\frac{\partial p}{\partial t}+\frac{\partial}{\partial x}\left(\frac{p^2}{h}\right)+\frac{\partial}{\partial y}\left(\frac{pq}{h}\right)+gh\frac{\partial\zeta}{\partial x}\frac{gp\sqrt{p^2+q^2}}{C^2h^2}$$
$$\frac{1}{\varphi_w}\left[\frac{\partial}{\partial x}(h\tau_{xx})+\frac{\partial}{\partial y}(h\tau_{xy})\right]-\Omega_q-fVV_x+\frac{h}{\varphi_w}\frac{\partial}{\partial x}(p_a)=0 \quad (4)$$

$$\frac{\partial q}{\partial t}+\frac{\partial}{\partial y}\left(\frac{q^2}{h}\right)+\frac{\partial}{\partial x}\left(\frac{pq}{h}\right)+gh\frac{\partial\zeta}{\partial y}+\frac{gp\sqrt{p^2+q^2}}{C^2h^2}$$
$$\frac{1}{\varphi_w}\left[\frac{\partial}{\partial y}(h\tau_{yy})+\frac{\partial}{\partial x}(h\tau_{xy})\right]+\Omega_p-fVV_y+\frac{h}{\varphi_w}\frac{\partial}{\partial x}(p_a)=0 \quad (5)$$

The following symbols notations are used in the equations:

$h(x,y,t)$	Water depth (=$\zeta - d, m$)
$d(x,y,t)$	Time-varying water depth (m)
$\zeta(x,y,t)$	Surface elevation (m)
$p,q(x,y,t)$	Flux densities in x-and y-directions (m^3/s/m)= (uh, vh); (u,v)= depth averaged velocities in x- and y-directions
$C(x,y)$	Chezy resistance (m$^{1/2}$/s)
G	Acceleration due to gravity (m/s^2)
f(V)	Wind
V,Vx,Vy (x,y,t)	Wind speed and components in x- and y-direction (m/s)
$\Omega_{x,y}$	Coriolis parameter, latitude dependant (s^{-1})
$p_a(x,y,t)$	Atmospheric pressure (kg/m/s^2)
φ_w	Density of water (kg/m^3)
x,y	Space coordinates (m)
T	Time (s)
$\tau_{xx},\tau_{xy},\tau_{yy}$	Components of effective shear stress

The 1 in 100-yr design storm-tide and design discharge are provided as boundary conditions in MIKE 11, while 1 in 100-yr regionalized design rainfall is provided in MIKE 21 HD. The simulated outputs from MIKE 11 and MIKE 21 HD are coupled in the MIKE FLOOD interface by providing lateral links between river cross-sections and the adjoining floodplains to generate the overland flood inundation. The degree of flood hazard is derived from the flood inundation values and determined as the tuple of depth and velocity (Mohanty et al., 2020b). Extensive details on the validation of flood hazard zones at both 1D and 2D levels is provided in Mohanty et al. (2020a).

3.3 Socio-economic vulnerability

An array of 21 relevant socio-economic for 2011 is selected to determine the village-wise vulnerability values. The details of the indicators are tabulated in Table 2. These indicators are classified into positive (higher the quantity, higher the vulnerability or cost-type) and non-positive (higher the quantity lower the vulnerability or benefit type) categories based on their impacts during flood disasters. The quantitative values of indicators are standardized to reduce the multi-dimensionality, after which Principal Component Analysis (PCA) is performed to decorrelate the indicators further. Data envelopment analysis (DEA) is a widely used nonparametric technique for estimating the relative efficiency of units, referred to as DMUs, when it is difficult to identify absolute measures of efficiency (Mardani et al., 2017; Mohanty et al., 2020).

Table 2. List of positive (*cost-type*), and non-positive (*benefit-type*) indicators

Indicators	Indicators	Justification
Positive (cost-type)	Female Population	A majority of the female population devote their lives to household activities and hence have less scope to participate in educational and social activities.
	Total Population	A larger population leads to increased exposure to floods.
	Main agricultural and cultivators population	They are usually poor and will have a direct adverse effect during a disaster event. The coping ability will also be less, as they need to find some other jobs to fulfill their financial needs
	Population of Children (population < 6 years)	They require special attention during evacuation due to their high care needs and susceptibility to health problems and thereby slowing down the processes during the disaster
	Number of households	A higher number of households increases the vulnerability as the number of economic dependents tends to increase
	Illiterate population	Illiterates tend to have a minor set of employable skills and have reduced access to information with a low level of risk acknowledgment, which increases their vulnerability.
	Illiterate female population	Illiterate females may find it more difficult to follow any evacuation warning and take care of the family during a disaster.
	SC and ST population	The weaker economic sections are categorized as the backward community by the Govt. of India.
	SC and ST population	The weaker economic sections are categorized as the backward community by the Govt. of India.
	SC and ST female population	GoI identifies them as part of the backward community. The women in this community have a greater responsibility in taking care of the family during a disaster.
	Marginal workers (including cultivators, agricultural laborers, household Industry, and others)	This community has temporary jobs and mostly landless laborers.
Non- Positive (benefit-type)	Non-workers	This community are dependent on adult members in their respective family, and they will be more vulnerable during a disaster event, as their coping ability will be meager
	Working population	Unemployed people are vulnerable because of inadequate income and resources to support themselves and recover from disasters. The more unemployed people in a society, the more unstable the society is as more problems may emerge under these adverse circumstances.
	Female working population	The coping capacity will be higher in a family during hazards if the female working population is higher in a community.
	Literate Population	Literacy rate commonly enhances the knowledge about how to cope during the natural hazards and thus reduces the impact
	Female literate population	The higher the ratio of literate people in a community, the higher the capacity to cope with hazards.

Indicators	Indicators	Justification
Non-positive (benefit type)	Amenities (primary education, secondary education, colleges, and medical facilities)	Education can help in creating awareness among the general public in coping with floods. Medical facilities can aid in providing treatment to people during the time of disasters.
	Status of power supplies	The presence of this indicator represents the overall development in the village which positively influences the ability to adapt
	Status of well	It provides a viable source of drinking water during disaster situations
	Status of hand pump	
	Status of river	
	Status of tank	

The model optimizes each observation associated with a DMU to calculate a discrete piecewise frontier determined by the set of Pareto efficient DMUs. The efficiency of each DMU is measured by the distance of its input-output vectors to a piecewise linear frontier. In this study, the slack-based input-oriented BCC method (named after Banker, Charnes, and Cooper) (Banker et al., 1984), which considers variable returns to scale (VRS), is considered. The mathematical expressions for deriving the vulnerability is provided in equations 6 to 9.

$$min\ [\theta_j - \xi(\sum_{x=1}^{X} S_x^- + \sum_{x=1}^{X} S_x^+)] \tag{6}$$

such that $\sum_{j=1}^{J} \lambda_j * PC_{xj} + \sum_{x=1}^{X} S_x^- = \theta_j * PC_{xj}$;

$$\forall x = 1, \ldots, X \tag{7}$$

$$\sum_{j=1}^{J} \lambda_j * QC_{xj} - \sum_{x=1}^{X} S_x^+ = QC_{xj},$$

$$\forall x = 1, \ldots, X \tag{8}$$

$$\sum_{j=1}^{J} \lambda_j = 1; \lambda_j, \xi, S_x^-, S_x^+ \geq 0 \quad \forall x, j \tag{9}$$

The vulnerability for jth village is given by $\mathcal{V}j = 1 - \theta j$ where, θ $(0 < \theta < 1)$ is the technical efficiency of each village, λ_j is the weight assigned to jth village, S_x^- and S_x^+ are the slack and remnant variables. In the last step, the vulnerability indices are discretized into five different classes from very low to very high, based on the values of function f ($i1$, ..., in). This discretization is done by defining the mapping in $\mathcal{V}$ as given in equations 10 and 11:

$$f_d: \mathcal{V} \rightarrow \mathcal{V}_d;\ \mathcal{V}_d = \{v_d \epsilon \mathbb{N}: v_d \leq 5 \tag{10}$$

$$\mathcal{V}_d = \begin{cases} 1, & 0.1 \leq v \leq 0.2 \\ 2, & 0.2 < v \leq 0.3 \\ 3, & 0.3 < v \leq 0.4 \\ 4, & 0.4 < v \leq 0.5 \\ 5, & v > 0.5 \end{cases} \tag{11}$$

where v and v_d represent the value and index of vulnerability for jth village

3.4 Flood risk

The flood risk value for each village is calculated as the product of the corresponding flood hazard and socio-economic vulnerability value. Two sets of flood risk maps are derived by considering the hazards derived from geomorphic analysis and hydrodynamic modeling, with the fixed socio-economic vulnerability values. The gridded hazard values derived through each methodology are converted to village-scale by assigning the median value among the grids falling over the village. In the next step, the hazard is multiplied with the socio-vulnerability value to derive flood risk for the village. Similar to vulnerability, the overall risk values for each village are converted to qualitative scale, namely very-low risk, low-risk, moderate risk, high risk, and very-high risk.

4. Results and discussion

4.1 Geomorphic maps for Jagatsinghpur district

The Single and composite geomorphic maps of the Jagatsinghpur district are illustrated in Figures 3 and 4. In all the figures, we notice a clear and continuous illustration of the geomorphic classifiers, which supports the accurate representation of surface features in the CartoDEM without significant errors. For instance, Figure 3 (d), representing the flow path distance to the nearest stream, captures the river network accurately, appropriately accounting for the geomorphic properties of the study area. The upslope contributing area (Figure 3, a) varied up to 16 km2, with maximum values falling between 8 to 10 km2, while surface curvature values did not exceed 25 over most parts over the region (Figure 3, b). The local slope values were well captured, clearly identifying the high and low values over the entire area (Figure 3, c). We notice that most of the spots far from the river drainage networks contain a slope between 0 to 0.5, while those near the river drainage networks had a higher slope value.

While analyzing the composite set of classifiers, we again discover a continuous distribution of the geomorphic properties over the entire region. The modified topographic index was well represented, with most of the values falling within 15 (Figure 4, a). As expected, the downslope index was found to be maximum over the floodplains of the Mahanadi and Devi rivers (Figure 4, b). H/D values were found to lie between 0 and 1, with maximum values over the main river channels (Figure 4, c). ln (hl/H), and ln (hr/H) classifiers showed similar behavior, with most grid values not exceeding a value of 5 (Figure 4d, and e). More or less similar behavior was also noticed with (hr-H)/ tan (αd) as well (Figure 4, f).

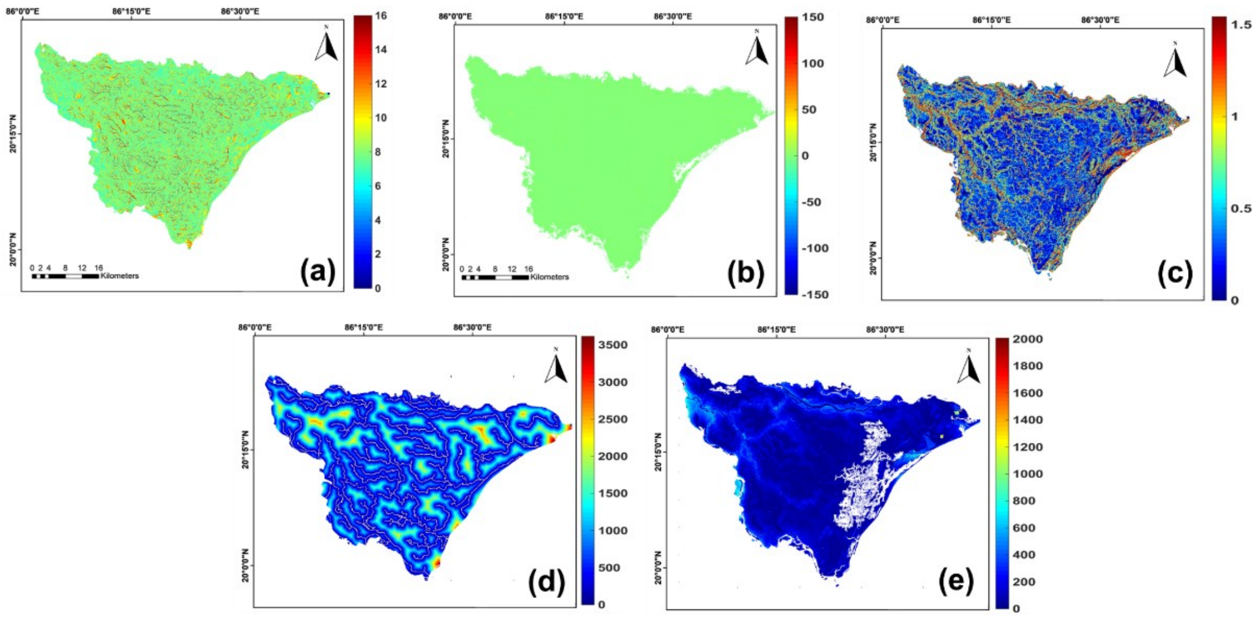

Figure 3. Single geomorphic classifiers-(a) Upslope contributing area, (b) Surface curvature, (c) Local slope , (d) Flow path distance to the nearest stream, and (e) Elevation to the nearest stream- for Jagatsinghpur district derived by using CartoDEM.

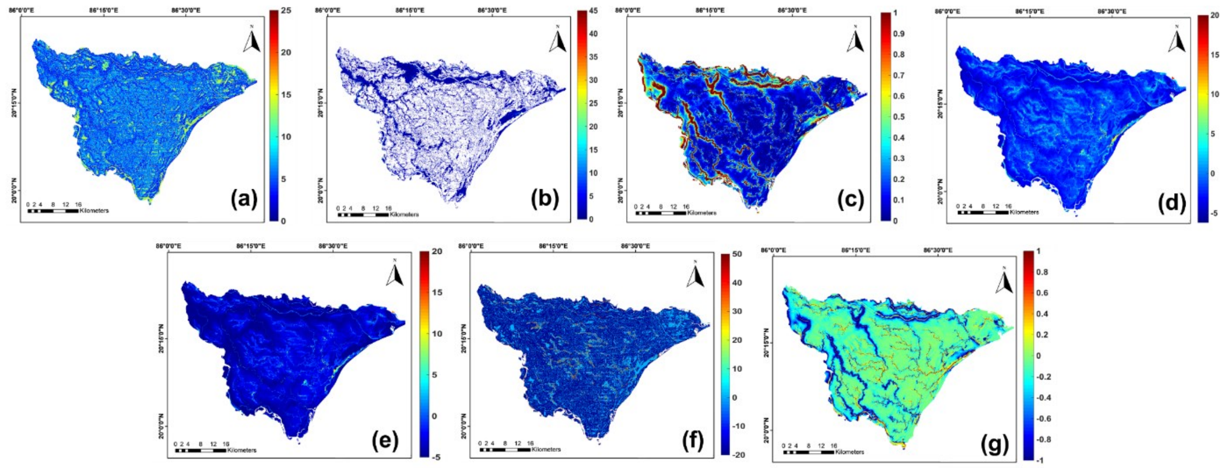

Figure 4. Composite geomorphic classifiers- (a) Modified topographic index, (b) Downslope index, (c) H/D, (d) ln (h_l/H), (e) ln (h_r/H), (f) (h_r–H)/ tan (α_d), (g) (h_r–H)/D - for Jagatsinghpur district derived by using CartoDEM.

(hr-H)/D composite classifier had a mix of high and low values over the region. We noticed lesser values near the floodplains of the river while higher values in the coastal stretches. However, more than 80 percent of the areas were covered between -0.2 to 0.2 (Figure 4, g). The best geomorphic classifier was selected, after which a representative flood hazard map was created (Figure 5, a)

4.2 Flood hazard maps derived using 1D-2D coupled flood modelling

The 1D-2D coupled hydrodynamic flood inundation was carried out using the MIKE FLOOD model as described in section 3.2. The model was initially run over a flexible mesh domain but was later converted into a rectangular grid of 10m × 10m to comply with the grid resolution of the CartoDEM. The 1 in 100-yr flood hazard map derived through hydrodynamic modeling is illustrated in Figure 5,b. This figure shows the riverine inundation in the lower stretches of the major river networks and coastal inundation in the coastal villages. Significantly, the floodplains of Mahanadi falling in Raghunathpur and Tirtol tehsils which are well-known to be severely flood-prone spots, were accurately captured. So also, the coastal stretches experiencing coastal flooding impacts in the Ersama, and Kujang tehsils were also accurately captured. Elaborate details on the validation of flood hazard layer both at 1D river channel and 2D overland level are reported in Mohanty et al. (2020a).

4.3 Socio-economic vulnerability maps

The socio-economic vulnerability map is illustrated in Figure 5, c. We notice that a majority of villages face low and very low vulnerability, while only a few experience high and very high vulnerability in the Jagatsinghpur district. The low-, and very-low vulnerable villages are spread all over the district. In contrast, the high and very-high vulnerable ones are secluded mostly to Ersama, Jagatsinghpur, Tirtol, Nuagaon, and Baligaon talukas. The coastal villages in Ersama and Balikuda talukas contain a significant number of highly vulnerable villages. Unlike the previous flood hazard map, we do not notice a similar distribution of vulnerability.

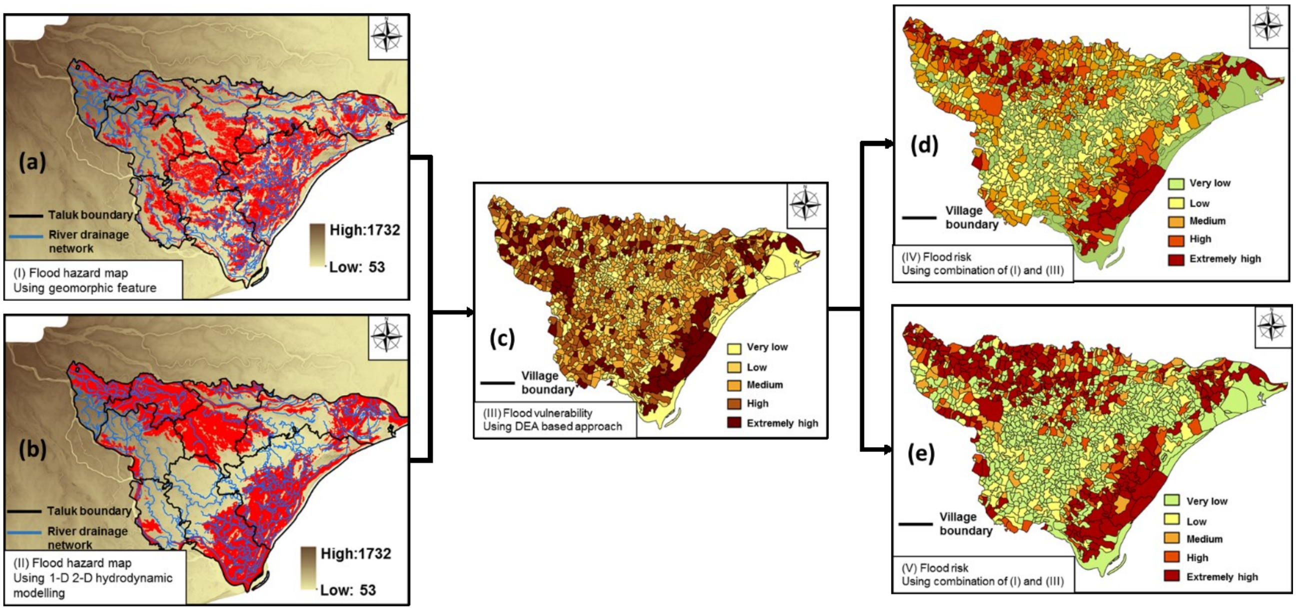

Figure 5. Set of flood-related maps- (a) Representative flood hazard map derived by geomorphic classification; (b) Flood hazard map derived through 1D 2D coupled hydrodynamic modeling, (c) Socio-economic vulnerability map derived through DEA;(d) Flood risk map for the combination of geomorphic flood hazard and socio-economic vulnerability; and (e) Flood risk map for the combination of hydrodynamic flood hazard and socio-economic vulnerability.

For instance, the south-eastern coastal region of Jagatsinghpur contains several villages facing very high vulnerability. At the same time, as we move upwards to the northeastern part, we notice a decline in vulnerability with less vulnerable villages. This is because the socio-economic vulnerability analysis is sensitive due to various influencing socio-economic indicators in the investigation. The North-eastern and western parts contained several high and very high vulnerable villages as well.

4.4 Comparison of flood risk maps

As discussed in Section 3.4, the flood hazard maps from geomorphic analysis and hydrodynamic analysis were considered along with the socio-economic vulnerability map to derive the flood risk map. Figures 5 d and e illustrate the two flood risk maps. We notice a more or less similar pattern in the risk values villages within the Jagatsinghpur district. The risk values over the coastal region through both approaches were well defined.
The impact of coastal inundation was more pronounced in hydrodynamic modeling, resulting in a few more high-risk villages than the other risk map. Similar behavior was also noticed in the floodplains lying near the Mahanadi river and Devi rivers. However, the central part of Jagatsinghpur was very well captured with equal distribution of risk values. In this region, most of the villages experienced very low risk. Overall, we observe that different degrees of risk values are adequately captured through the geomorphic analysis, which promises its application to identify flood risk quickly.

5. Conclusions

The quantification of flood risk is vital for building a comprehensive flood management strategy for any region. A flood risk map containing inherent information on flood hazards and vulnerability serves as an essential tool for the general public, disaster experts, and civic bodies. Based on the flood risk knowledge, appropriate structural and non-structural measures can be planned to improve the resilience for longer terms.

Although the hydrodynamic-based approach is considered the most sophisticated technology for determining flood hazards, they are often limited due to the technicalities involved and lack of expertise by a non-technical user in handling the model. Under such circumstances, geomorphic classifiers that utilize the basin's topography to determine flood susceptible zones can be considered an alternate option. The determination of hazard zones through various classifiers does not yield much computational cost and time. In this study, we considered a set of 12 relevant geomorphic classifiers to characterize the flood hazard zones. The best performing geomorphic classifier was considered to create the most representative flood hazard map. On the other hand, a 1D 2D coupled flood inundation modeling was carried out at a finer scale. A 1 in 100-yr flood hazard map was generated that considered regionalized design rainfall, design discharge, and design storm-tide as input parameters. The socio-economic vulnerability was determined by considering a suite of 21 socio-economic indicators. The combination of flood hazards was considered along with the socio-economic vulnerability map to derive a flood risk map. The two sets of flood risk maps were found to capture various degrees of risk appropriately. Based on this study, we realize that geomorphic classifiers that are computationally less intensive may be considered in place of the hydrodynamic approach to demarcate flood risk zones, mainly when computational cost and time are a restraint. The regions identified as high-risk areas by geomorphic classifiers can be identified, which may be further considered for a detailed flood risk mapping considering the hydrodynamic approach. The geomorphic classification will be suitable for large regions, which are flood-prone and have the limitation of hydrodynamic modeling due to high computational cost and time.

Acknowledgments
The research presented here is supported financially by ISRO-IIT (B)- Space Technology Cell(STC) through sponsored projects (Project No. RD/0114-ISROC00-013, and RD/0119-ISROC00-001), and Department of Science and Technology (SPLICE-Climate Change Programme), Government of India through Project reference number DST/CCP/CoE/140/ 2018, Grant Number: 00000000000010013072 (UC ID: 18192442). The authors are grateful to National Remote Sensing Centre, Hyderabad, for allowing access to the MIKE FLOOD model. IIT Bombay has provided support towards computational resources

References
Abbott M. B., and Ionescu, F. (1967). On the numerical computation of nearly horizontal flows. Journal of Hydraulic Research, 5(2), 97-117.

Adnan M. S. G., Dewan, A., Zannat, K. E., and Abdullah, A. Y. M. (2019). The use of watershed geomorphic data in flash flood susceptibility zoning: a case study of the Karnaphuli and Sangu river basins of Bangladesh. Natural Hazards, 99(1), 425-448.

Afshari S., Tavakoly, A. A., Rajib, M. A., Zheng, X., Follum, M. L., Omranian, E., and Fekete, B. M. (2018). Comparison of new generation low-complexity flood inundation mapping tools with a hydrodynamic model. Journal of Hydrology, 556, 539-556.

Banker R. D., Charnes, A., and Cooper, W. W. (1984). Some models for estimating technical and scale inefficiencies in data envelopment analysis. Management Science, 30(9), 1078-1092.

Blöschl G., Hall, J., Parajka, J., Perdigão, R. A., Merz, B., Arheimer, B., ... and Živković, N. (2017). Changing climate shifts timing of European floods. Science, 357(6351), 588-590.

Clement M. A., Kilsby, C. G., and Moore, P. (2018). Multi- temporal synthetic aperture radar flood mapping using change detection. Journal of Flood Risk Management, 11(2), 152-168.

Costabile P., Costanzo, C., De Lorenzo, G., and Macchione, F. (2020). Is local flood hazard assessment in urban areas significantly influenced by the physical complexity of the hydrodynamic inundation model?. Journal of Hydrology, 580, 124231.

Degiorgis M., Gnecco, G., Gorni, S., Roth, G., Sanguineti, M., and Taramasso, A. C. (2012). Classifiers for the detection of flood-prone areas using remote sensed elevation data. Journal of Hydrology, 470–471, 302-315.

DHI (2019) MIKE FLOOD The integrated water modelling platform https://www.mikepoweredbydhi.com/products/mikeplus accessed on 10 July 2021.

Dottori F., Szewczyk, W., Ciscar, J. C., Zhao, F., Alfieri, L., Hirabayashi, Y., ... and Feyen, L. (2018). Increased human and economic losses from river flooding with anthropogenic warming. Nature Climate Change, 8(9), 781-786.

Gebremichael E., Molthan, A. L., Bell, J. R., Schultz, L. A., and Hain, C. (2020). Flood Hazard and Risk Assessment of Extreme Weather Events Using Synthetic Aperture Radar and Auxiliary Data: A Case Study. Remote Sensing, 12(21), 3588.

Gopikrishna B., and Deo, M. C. (2018). Changes in the shoreline at Paradip Port, India in response to climate change. Geomorphology, 303, 243–255.

Hagenlocher M., Renaud, F. G., Haas, S., and Sebesvari, Z. (2018). Vulnerability and risk of deltaic social-ecological systems exposed to multiple hazards. Science of the total environment, 631, 71-80.

Kourgialas N. N., and Karatzas, G. P. (2011). Flood management and a GIS modelling method to assess flood-hazard areas-a case study. Hydrological Sciences Journal–Journal des Sciences Hydrologiques, 56(2), 212-225.

Kron W. (2005). Flood risk= hazard• values• vulnerability. Water international, 30(1), 58-68.

Kron W. (2013). Coasts: the high-risk areas of the world. Natural hazards, 66(3), 1363-1382.

Manfreda S., Leo, M. Di, and Sole, A. (2011). Detection of Flood-Prone Areas Using Digital Elevation Models. Journal of Hydrologic Engineering, 16(10), 781–790.

Manfreda S., Samela, C., Gioia, A., Gerardo, G., Iacobellis, V., Giuzio, L. (2015). Flood-prone areas assessment using linear binary classifiers based on flood maps obtained from 1D and 2D hydraulic models, Natural Hazards, 79, 735–754.

Manfreda S., Samela, C., Sole, A., and Fiorentino, M. (2014). Flood-Prone Areas Assessment Using Linear Binary Classifiers based on Morphological Indices Salvatore. Vulnerability, Uncertainty, and Risk, 2002–2011.

Mardani A., Zavadskas, E. K., Streimikiene, D., Jusoh, A., and Khoshnoudi, M. (2017). A comprehensive review of data envelopment analysis (DEA) approach in energy efficiency. Renewable and Sustainable Energy Reviews, 70, 1298-1322.

Mishra K., and Sinha, R. (2020). Flood risk assessment in the Kosi megafan using multi-criteria decision analysis: A hydro-geomorphic approach. Geomorphology, 350, 106861.

Mohanty M. P., and Karmakar, S. (2021a). WebFRIS: An efficient web-based decision support tool to disseminate end-to-end risk information for flood management. Journal of environmental management, 288, 112456.

Mohanty M. P., and Simonovic, S. P. (2021b). Changes in floodplain regimes over Canada due to climate change impacts: Observations from CMIP6 models. Science of The Total Environment, 148323.

Mohanty M. P., Nithya, S., Nair, A. S., Indu, J., Ghosh, S., Bhatt, C. M., ... and Karmakar, S. (2020a). Sensitivity of various topographic data in flood management: Implications on inundation mapping over large data-scarce regions. Journal of Hydrology, 590, 125523.

Mohanty M. P., Vittal, H., Yadav, V., Ghosh, S., Rao, G. S., and Karmakar, S. (2020b). A new bivariate risk classifier for flood management considering hazard and socio-economic dimensions. Journal of environmental management, 255, 109733.

Mohapatra M. (2015). Cyclone hazard proneness of districts of India. Journal of Earth System Science, 124(3), 515-526.

Muralikrishnan S., Pillai, A., Narender, B., Reddy, S., Venkataraman, V. R., and Dadhwal, V. K. (2013). Validation of Indian National DEM from Cartosat-1 Data. Journal of the Indian Society of Remote Sensing, 41(1), 1–13.

Paprotny D., Kreibich, H., Morales-Nápoles, O., Castellarin, A., Carisi, F., and Schröter, K. (2020). Exposure and vulnerability estimation for modelling flood losses to commercial assets in Europe. Science of the Total Environment, 737, 140011.

Rentschler J., M. Salhab. 2020. People in Harm's Way: Flood Exposure and Poverty in 189 Countries. Policy Research Working Paper. No. 9447. Washington DC: The World Bank

Sahoo B., and Bhaskaran, P. K. (2016). Assessment on historical cyclone tracks in the Bay of

Sajjad M., Lin, N., and Chan, J. C. (2020). Spatial heterogeneities of current and future hurricane flood risk along the US Atlantic and Gulf coasts. Science of the total environment, 713, 136704.

Samela C., Manfreda, S., Paola, F. De, and Giugni, M. (2016). DEM-Based Approaches for the Delineation of Flood-Prone Areas in an Ungauged Basin in Africa. Journal of Hydrologic Engineering, 21(2), 1–10.

Samela C., Troy, T. J., and Manfreda, S. (2017). Geomorphic classifiers for flood-prone areas delineation for data-scarce environments. Advances in water resources, 102, 13-28.

Samela C., Troy, T. J., and Manfreda, S. (2017). Geomorphic classifiers for flood-prone areas delineation for data-scarce environments. Advances in Water Resources, 102, 13–28.

Teng J., Jakeman, A. J., Vaze, J., Croke, B. F., Dutta, D., and Kim, S. (2017). Flood inundation modelling: A review of methods, recent advances and uncertainty analysis. Environmental modelling and software, 90, 201-216.

Thober S., Kumar, R., Wanders, N., Marx, A., Pan, M., Rakovec, O., ... and Zink, M. (2018). Multi-model ensemble projections of European river floods and high flows at 1.5, 2, and 3 degrees global warming. Environmental Research Letters, 13(1), 014003.

Tiggeloven T., Moel, H. D., Winsemius, H. C., Eilander, D., Erkens, G., Gebremedhin, E., ... and Ward, P. J. (2020). Global-scale benefit–cost analysis of coastal flood adaptation to different flood risk drivers using structural measures. Natural Hazards and Earth System Sciences, 20(4), 1025-1044.

Trigg M. A., Birch, C. E., Neal, J. C., Bates, P. D., Smith, A., Sampson, C. C., ... and Fewtrell, T. J. (2016). The credibility challenge for global fluvial flood risk analysis. Environmental Research Letters, 11(9), 094014.

Vousdoukas M. I., Mentaschi, L., Voukouvalas, E., Verlaan, M., Jevrejeva, S., Jackson, L. P., andFeyen, L. (2018). Global probabilistic projections of extreme sea levels show intensification of coastal flood hazard. Nature communications, 9(1), 1-12.

Ward P. J., Jongman, B., Aerts, J. C., Bates, P. D., Botzen, W. J., Loaiza, A. D., ... and Winsemius, H. C. (2017). A global framework for future costs and benefits of river-flood protection in urban areas. Nature climate change, 7(9), 642-646.

Wing O. E., Pinter, N., Bates, P. D., and Kousky, C. (2020). New insights into US flood vulnerability revealed from flood insurance big data. Nature communications, 11(1), 1-10.

Wing O. E., Sampson, C. C., Bates, P. D., Quinn, N., Smith, A. M., and Neal, J. C. (2019). A flood inundation forecast of Hurricane Harvey using a continental-scale 2D hydrodynamic model. Journal of Hydrology X, 4, 100039.

Zhan P., Zhu, W., and Li, N. (2021). An automated rice mapping method based on flooding signals in synthetic aperture radar time series. Remote Sensing of Environment, 252, 112112.

Atmospheric Rivers and Flood Events in Ganga and Brahmaputra River Basins

Nimisha Singh*, Rohit Pradhan and R. P. Singh
Land Hydrology Division, EPSA, Space Applications Centre (ISRO), Ahmedabad, Gujarat, India
*Email: nimisha@sac.isro.gov.in

(Received: Aug 10, 2021; in final form: Oct 06, 2021)

Abstract: Atmospheric Rivers (ARs) are known to carry huge amount of moisture in a very short interval of time leading to extreme precipitation, which in turn may result in flood like events in some part of the world. They also play an important role in governing the global hydrological cycle by contributing considerable fraction of rainfall. Occurrence of ARs particularly over India and adjoining regions have been studied to some extent but particularly on hydrological extreme event basis. This paper presents novel observations of linking branching of ARs from monsoonal circulation over Indian region leading to flood events in Ganga and Brahmaputra river basins. In this study, identification of ARs was performed by computing Integrated Water Vapour Transport (IVT) from ERA5 ensemble mean dataset that uses specific humidity, zonal and meridional components of wind vectors between 1000 hPa to 300 hPa as initial parameters. The identified AR events were compared with altimeter observed water level over Ganga (25.29° N, 87.12° E; 25.59° N, 81.60° E; 25.51° N, 85.70° E) and Brahmaputra (26.21° N, 91.04° E) virtual gauging sites for the year 2008-2020 depending upon the availability of altimeter time series. Increase in water level was observed within 5-14 days of AR events in Ganga river but had minimal effect over Brahmaputra virtual gauging site. Flux computed for these ARs like phenomenon were correlated with altimeter observed water level which resulted in r=0.47 at Ganga near Prayagraj (25.59° N, 81.60° E). These observations indicate that the rate of recurrence and the amount of the water flux carried by the ARs leads to increased runoff that subsequently increases river flow.

Keywords: Atmospheric Rivers, Integrated Water Vapour Transport (IVT), Altimeter, Water Level, Specific Humidity, Monsoon.

1. Introduction

Atmospheric Rivers (ARs) are described as long and narrow filamentary structures that are responsible for water vapour transport across the mid-latitudes (Shields and Kiehl, 2016). They bear a resemblance with the terrestrial rivers that flow in a channel and are restricted by banks on its either side; ARs are concentrated bands of water vapour carrying huge moisture towards the poles (Mc Gregor, 2019). ARs account for over 90% of moisture transport toward the poles and take up only 10% of Earth's circumference (Zhu and Newell, 1998). At any given point in time, there are 3 to 5 ARs active around any given hemisphere (Zhu and Newell, 1998; Gimeno et al, 2014).

ARs are capable of carrying large amounts of water from one place to another through narrow corridors in the atmosphere and when they deposit their moisture in form of very heavy rainfall, it can lead to floods (Konrad and Dettinger, 2017; Lamjiri et al., 2017; Lavers et al., 2011; Lavers and Villarini, 2013; Paltan et al., 2017; Ralph et al., 2006). ARs over Pacific Ocean that carry moisture all the way from Hawaii and deposit it over California (Guan et al, 2010), commonly known as the Pineapple Express (Lackmann and Gyakum, 1999), have been studied in great detail. In India, ARs have been linked to the extremely heavy precipitation over the West Coast during monsoon (Dhana Lakshmi and Chakraborty, 2021) and the Chennai floods of December 2015 (Dhana Lakshmi and Satyanarayana, 2019).

Different researchers have used different thresholds and variables to identify land falling AR. ARs are usually longer than 2000 km and less than 1000 km wide (Ralph et al., 2004; Guan and Waliser, 2015). Two most common variables used to detect ARs are IWV (Integrated Water Vapour) and IVT (Integrated Vapour Transport). IWV considers the column-integrated water vapour from satellite (Ralph et al., 2004) or atmospheric models (Dettinger et al., 2011) whereas IVT uses specific humidity and wind velocity components to compute vertically integrated horizontal water vapour transport between 1000-300 hPa levels from atmospheric reanalysis data (Zhu and Newell, 1998). IVT is recognized to better capture ARs in the atmosphere (Rutz et al, 2014; Lavers and Villarini, 2013; Nayak et al., 2016). It has been observed that there are more ARs in the winter half of a year due to the association of ARs with extra-tropical cyclones (Gimeno et al., 2014).

In India, some researchers have reported monsoon time AR leading to extreme rainfall in the west coast of India (Dhana Lakshmi and Satyanarayan, 2019, 2020; Dhana Lakshmi et al., 2019. Yang et al. (2018) reported the climatology of AR over Bay of Bengal and showed the linkage to northern Indian extreme rainfall. This shows that although less common, ARs during monsoon are possible and can be crucial in understanding certain extreme events and their association with floods.

Ganga and Brahmaputra river basins in India witness widespread floods during the monsoon season and the frequency of floods in Indian sub-continent have increased in the past decade under a warming climate (Ali et al., 2019). Large-scale global phenomena such as El Nino, Indian Ocean Dipole etc. have been linked to floods and droughts in India. However, effects of ARs in monsoonal extreme events have been studied on a case-to-case basis only (Dhana Lakshmi and Chakraborty, 2021). In this paper, we present new observations linking the branching of ARs from monsoonal circulation to flood events in the Indian Ganga and Brahmaputra River Basin. We show that the frequency and amount of vapour carried by these branches have a direct impact on the river water levels and associated flood events.

2. Study area and data used

Ganga and Brahmaputra are one of the largest river basins of Asia circumscribing countries of the South Asian region including India, China, Nepal and Bangladesh. They are known to support a variety of flora and fauna, also keep up the livelihood of people by supplying fertile agricultural lands, providing drinking water and also in assisting hydropower activities (Rasul, 2015). Dhar and Nandargi, 2000 also tried to summarize the potentialities of both the rivers and concluded that Ganga is known to have greater potential in agricultural irrigation while Brahmaputra is having high hydropower potential. One major characteristic of these two basins is that they particularly lie in the monsoonal strap because of which their water level fluctuates to a large extent. Several regions of these two river basins are also susceptible to flood like conditions due to extreme rainfall taking place during the monsoon period that typically lies between June to September. Chowdhury and Ward, 2004 observed that most extreme floods in Ganga were observed during September month because increase in river water level was found to be maximal. Brahmaputra basin signalizes two spells of flood, one in July and August and other in September (Chowdhury and Sato, 1996). Present study was carried out over Ganga and Brahmaputra river basins along with Bay of Bengal.

The variables used in the study include specific humidity and zonal (U) and meridional (V) component of wind vector at different pressure level between 1000 hPa to 300 hPa for the month of July and August (2001-2020). They were obtained from ERA5 (European Centre for Medium-Range Weather Forecasts Reanalysis 5th Generation) ensemble mean dataset for 1200 UTC having 0.5° × 0.5° spatial resolution (C3S, 2017). ERA5 is the reanalysis climate data produced by ECMWF providing hourly data from 1979 to present at 37 pressure levels. Water level of altimeter gauging sites in Ganga (25.29° N, 87.12° E; 25.59° N, 81.60° E; 25.51° N, 85.70° E) and other in Brahmaputra (26.21° N, 91.04° E) were acquired from THEIA Land Data Centre (Santos da Silva et al., 2010; Normandin et al., 2018; http://hydroweb.theia-land.fr/). This uses Ku-band satellite altimetry (Jason-2/3) to estimate water level. It provides water level at nearly about 250 virtual stations across the globe and has a revisit time of approximately 10 days at our gauging sites.

3. Methodology

In order to detect ARs, one of the most common parameter is to compute Integrated Water Vapour Transport (IVT, Zhu & Newell, 1998). In this study, AR identification was done by calculating IVT for the month of July and August (2001-20) from ERA5 ensemble mean data. IVT is calculated as:

$$IVT = \sqrt{\left(\frac{-1}{g}\int_{1000}^{300} qu\,dp\right)^2 + \left(\frac{-1}{g}\int_{1000}^{300} qv\,dp\right)^2} \quad (1)$$

Here, g is the acceleration of gravity (m s^{-2}), q is specific humidity (kg kg^{-1}), u and v are the zonal and meridional components of wind vector (m s^{-1}) and p is the air pressure (Pa).

IVT intensity threshold was chosen to be 250 kg m^{-1} s^{-1} (Rutz et al., 2014; 2015; Ralph et al., 2017). ARs that passed through India in the month of July and August were identified by applying the threshold criteria of IVT > 250 kg m^{-1} s^{-1} and length to width ratio greater than 2:1. Frequency of ARs in July and August was also recorded for the year 2001-20. Subsequently, altimeter observed water level for Ganga (25.29° N, 87.12° E; 25.59° N, 81.60° E; 25.51° N, 85.70° E) and Brahmaputra (26.21° N, 91.04° E) was analysed within 5-14 days of AR events in Ganga and Brahmaputra river basins for the period 2008-2020 depending upon the availability of altimeter data. Flux was also computed for these AR like phenomena and was related with altimeter observed water level for the above locations. Figure 1 shows flowchart of the algorithm adopted in the study.

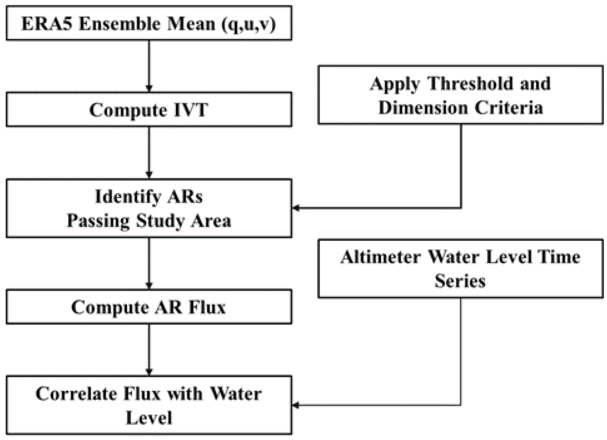

Figure 1. Flowchart of the algorithm adopted in the study.

4. Results and discussion

4.1 Identification and analysis of AR events

ARs satisfying IVT threshold and dimension criteria were identified over the Indian region and adjoining seas for the month of July and August (2001-20) by computing IVT using ERA5 ensemble mean dataset for 1200 UTC. Figure 2 shows IVT and wind vectors during two detected AR events of (a) 13 August 2011 and (c) 16 July 2018 along with zoomed in extent of IVT over India and adjoining regions (b) 13 August 2011 and (d) 16 July 2018. High moisture flux carried by these ARs, that form a part of the monsoon circulation, is clearly distinguished. We observed splitting of these ARs from the monsoonal circulation which extends from Arabian Sea to the western Pacific ocean. After splitting from the monsoonal circulation near northern Bay of Bengal, these ARs turn towards the Ganga and Brahmaputra basins and can extend up to Northwest India (Figure 2b and 2d).

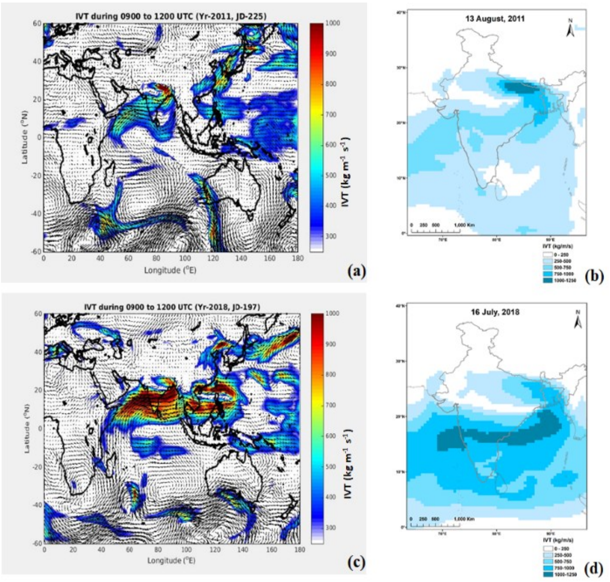

Figure 2. IVT maps with intensity (colour shading) and wind vectors on (a) 13 August 2011 (c) 16 July 2018 for 1200 UTC. Zoomed in spatial extent of IVT over India and adjoining regions on (b) 13 August 2011 (d) 16 July 2018.

AR events, similar to the ones shown in Figure 2, were observed in July and August months of every year between 2001-2020. The centreline of all these ARs, beginning from the point where they split from monsoon circulation, is presented in Figure 3 for every 5-year period (2001-05; 2006-10; 2011-15 and 2016-20). The actual length of these ARs is different, as they originate from the large-scale moisture transport during monsoon, but for the purpose of this study, the origin is taken from the point where they bend and curve towards the Indo-Gangetic plains. It can be clearly seen that the centreline of AR bends towards the Ganga catchment shifting moisture convergence away from the Brahmaputra river basin. On analysing the spatial extent of these centrelines, we observe that all of them are concentrated over the Northern belt of India with a smaller extent over Northeast India.

Figure 4 shows the frequency of ARs observed over the study region for Jul-Aug of 2001-2020, showing highest occurrence of ARs in the year 2003 with 4 events in the two months. Although the occurrence of these ARs varies between 1-4 per year during Jul-Aug, it is interesting to note their timing with respect to flood events in the Ganga and Brahmaputra basins. The influence of these ARs in causing floods can be studied by relating their spatial and temporal occurrence with the flood events in Ganga and Brahmaputra rivers. Instead of analysing the spatial extent of flood in these basins, in this study we use water level along different locations of the rivers as an indicator of flood.

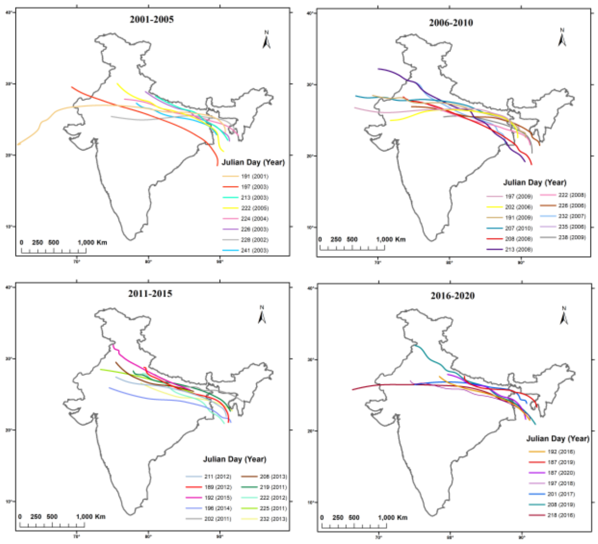

Figure 3. Identification of Atmospheric Rivers (ARs) that passed through India for every five year period (2001-20) of July & August.

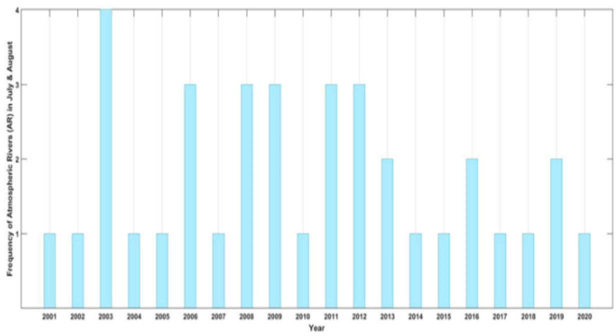

Figure 4. Frequency of ARs in July and August for the year 2001-20.

4.2 Linking AR to flood events

ARs with high IVT have the potential to cause more rainfall and this may lead to increased runoff in the subsequent days. This increased runoff increases the water level in rivers, which can be picked up by altimeters. Figure 5 shows the plot of altimeter observed water level time series for three gauging locations in Ganga (25.29° N, 87.12° E; 25.59° N, 81.60° E; 25.51° N, 85.70° E) and one in Brahmaputra (26.21° N, 91.04° E) along with the days when ARs were observed at their peak lengths. The timing of ARs matches well with high-flow conditions in these gauging locations of Ganga but has minimal effect over Brahmaputra virtual gauging site. During such AR phenomenon, it was observed that the moisture transport tends to shift away from the Brahmaputra basin towards Ganga basin. This results in more precipitation in the Ganga catchment and subsequent increase in river flow. However, the strength of an AR in terms of flux of moisture carried by them usually determines the intensity of rain and subsequent flooding.

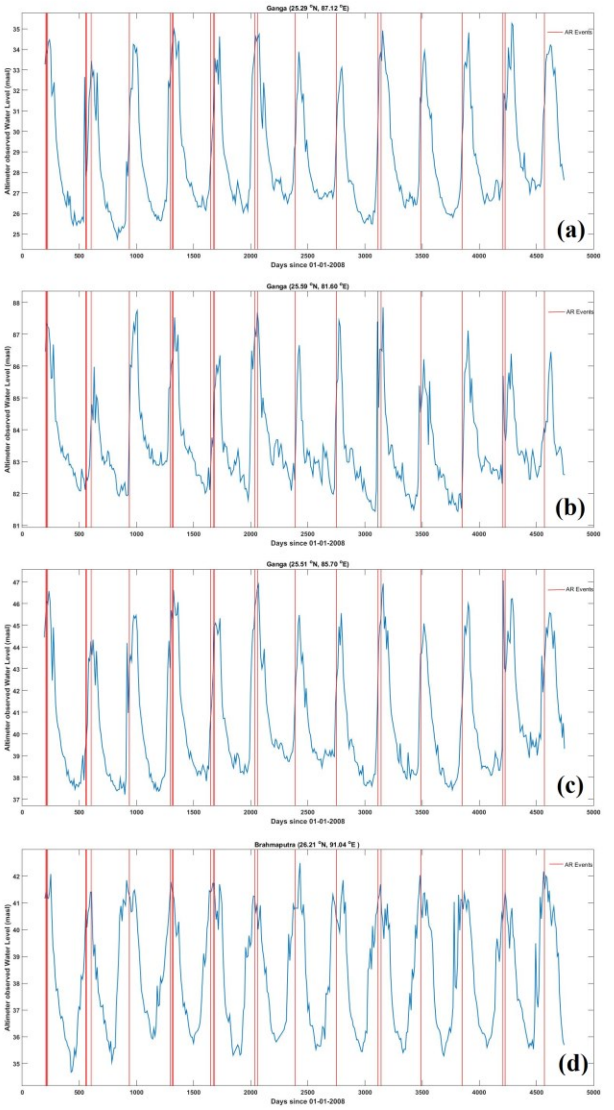

Figure 5. Plots of altimeter observed water level at four gauging locations (a) 25.29° N, 87.12° E; (b) 25.59° N, 81.60° E; (c) 25.51° N, 85.70° E and (d) 26.21° N, 91.04° E with the days of ARs events.

Flux of an AR (represented in kg s^{-1}) is similar to the discharge carried by a river. Flux was computed for each event at the cross-section where maximum IVT value is observed along the length of the AR. This flux was correlated to the river water level observed by altimeter in the subsequent 5-14 days of the event. This gap between AR flux and altimeter observation is taken to account for the lag between ARs moisture being converted to rain and subsequent runoff reaching the river. Figure 6 shows the scatter plot and correlation between AR flux and altimeter observed water level for a gauging site (25.59° N, 81.60° E) in Ganga. Although the correlation coefficient value (r=0.47) is low, we observe a significant direct positive correlation between the two variables. This indicates that the moisture carried by ARs detected in this study has a direct impact on the river water level and thus plays a major role in influencing flood events. This non-periodic splitting of ARs from monsoonal flow and the amount of moisture carried by them during July-August influences the timing of flood events in Ganga river basin. More study is required to quantitatively estimate the impact of these ARs in causing heavy precipitation and flood events in Ganga basin. Identification and prediction of these branching ARs can help improve weather forecasts and flood early warning systems in the region.

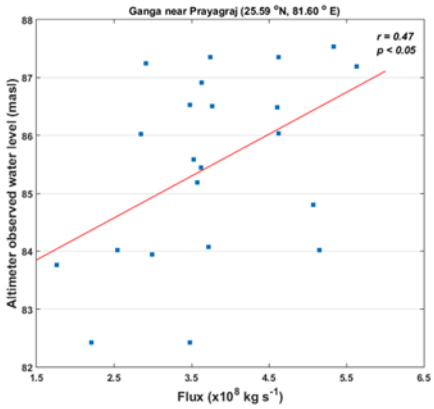

Figure 6. Scatter plot between altimeter observed water level vs Flux for the year 2008-2020.

5. Conclusions

Present study discusses about branching of ARs from the monsoonal wind over Indian Ganga and Brahmaputra river basins. AR identification was performed by computing IVT using ERA5 ensemble mean datasets of July and August for the period 2001-20. These ARs originate from the monsoon circulation near Bay of Bengal and turn towards Ganga and Brahmaputra basins, extending all the way up to Northwest India. Timing of AR events matched well with increasing water level along Ganga River, which was used as an indicator of flood, however, minimal effect was observed over the Brahmaputra river basin. Flux of ARs computed at the cross section with maximum IVT showed correlation 0.47 ($p<0.05$) with altimeter observed water level at one of the gauging location of Ganga (25.59° N, 81.60° E). This study showed that splitting of ARs from the monsoon circulation can have impact on flood events in Ganga river basin.

Acknowledgements
This work was carried out under SARITA program of Land Hydrology Division, EPSA, SAC. The authors are thankful to Shri N M Desai, Director, SAC and Dr. I M Bahuguna, Deputy Director, EPSA. The authors thankfully acknowledge ECMWF for ERA5 Reanalysis data and THEIA Land Data Centre/ CNES for altimeter water level.

References

Ali H., P. Modi and V. Mishra (2019). Increased flood risk in Indian sub-continent under the warming climate, Weather and Climate Extremes, 25, 100212.https://doi.org/10.1016/j.wace.2019.100212.

Chowdhury M. R. and N. Ward (2004). Hydro-Meteorological Variability In The Greater Ganges–Brahmaputra–Meghna Basins, International Journal of Climatology, 24, 1495-1508.

Chowdhury M. R. and Y. Sato (1996). Flood monitoring in Bangladesh: experience from normal and catastrophic floods. Hydrology (Journal of the Japanese Association of Hydrological Sciences), 26, 241–152.

Copernicus Climate Change Service (C3S) (2017): ERA5: Fifth generation of ECMWF atmospheric reanalyses of the global climate. Copernicus Climate Change Service Climate Data Store (CDS), 22 February, 2021. https://cds.climate.copernicus.eu/cdsapp#!/home.

Dettinger M. D., F. M. Ralph, T Das, P. J. Neiman and D. R. Cayan (2011). Atmospheric Rivers, Floods and the Water Resources of California. Water, 3(2):445-478.

Dhana Lakshmi D. and A. N. V. Satyanarayana (2019) Influence of atmospheric rivers in the occurrence of devastating flood associated with extreme precipitation events over Chennai using different reanalysis data sets. Atmospheric Research, 215, 12-36. http://doi.org/10.1016 j.atmosres.2018.08.016.

Dhana Lakshmi D. and A. Chakraborty, (2021). Assessment of WRF-ARW model parameterization schemes for extreme heavy precipitation events associated with atmospheric rivers over West Coast of India, Atmospheric Research, 249, 105330. https://doi.org/10.1016/j.atmosres.2020.105330.

Dhana Laskhmi D. and A. N. V. Satyanarayana (2020). Climatology of landfalling atmospheric Rivers and associated heavy precipitation over the Indian coastal regions. International Journal of Climatology, 1–18.

Dhana Laskhmi D., A. N. V. Satyanarayana and A. Chakraborty (2019). Assessment of heavy precipitation events associated with floods due to strong moisture transport during summer monsoon over India. Journal of Atmospheric and Solar-Terrestrial Physics, 189, 123-140.

Dhar O. and S. Nandargi (2000). A study of floods in the Brahmaputra basin in India. International Journal of Climatology - INT J CLIMATOL. 20. 771-781.

Gimeno L., R. Nieto, M. Vázquez and D. A. Lavers (2014). Atmospheric rivers: A mini-review, Frontiers in Earth Science, 2(1), 1-6, doi:10.339/FEART.2014.00002.

Guan B. and D. E. Waliser (2015). Detection of atmospheric rivers: Evaluation and application of an algorithm for global studies. Journal of Geophysical Research: Atmospheres, 120, 12, 514–12, 535. https://doi.org/10.1002/2015JD024257.

Guan B., N. P. Molotch, D. E. Waliser, E. J. Fetzer and P. J. Neiman (2010), Extreme snowfall events linked to atmospheric rivers and surface air temperature via satellite measurements, Geophysical Research Letters, 37, L20401, doi:10.1029/2010GL044696

Konrad C. P. and M. D. Dettinger (2017). Flood runoff in relation to water vapour transport by atmospheric rivers over the western United States, 1949–2015. Geophysical Research Letters, 44, 11456-11462, https://doi.org/10.1002/2017GL075399.

Lackmann G. M. and J. R. Gyakum (1999). Heavy cold-season precipitation in the northwestern United States: synoptic climatology and an analysis of the flood of 17–18 January 1986. Weather and Forecasting, 14, 687–700.

Lamjiri M. A., M. D. Dettinger, F. M. Ralph, and B. Guan, (2017). Hourly storm characteristics along the U.S. West Coast: Role of atmospheric rivers in extreme precipitation, Geophysical Research Letters, 44, 7020-7028. https://doi.org/10.1002/2017GL074193.

Lavers D. A. and G. Villarini (2013). The nexus between atmospheric rivers and extreme precipitation across Europe. Geophysical Research Letters, 40, 3259–3264. https://doi.org/10.1002/grl.50636.

Lavers D. A., R. P. Allan, E. F. Wood, G. Villarini, D. J. Brayshaw and A. J. Wade (2011). Winter floods in Britain are connected to atmospheric rivers. Geophysical Research Letters, 38: L23803.

McGregor G. R. (2019). Climate and rivers. River Research and Applications, 35, 1119– 1140. https://doi.org/10.1002/rra.3508.

Nayak M. A., G. Villarini and A. A. Bradley (2016). Atmospheric rivers and rainfall during NASA's Iowa Flood Studies (IFloodS) campaign. Journal of Hydrometeorology, 17(1), 257–271. https://doi.org/10.1175/JHM- D- 14- 0185.1.

Normandin C., F. Frappart, A. T. Diepkilé, V. Marieu, E. Mougin, F. Blarel, B. Lubac, N. Braquet, A. Ba (2018). Evolution of the Performances of Radar Altimetry Missions from ERS-2 to Sentinel-3A over the Inner Niger Delta. Remote Sensing, 10(6), 833, doi: 10.3390/rs10060833.

Paltan H., D. Waliser, W. H. Lim, B. Guan, D. Yamazaki, R. Pant and S. Dadson (2017). Global floods and water availability driven by atmospheric rivers. Geophysical Research Letters, 44, 10,387–310,395. https://doi.org/10.1002/2017GL074882.

Ralph F. M., P. J. Neiman and G. A. Wick (2004). Satellite and CALJET aircraft observations of atmospheric rivers over the eastern North-Pacific Ocean during the winter of 1997/98, Monthly Weather Review, 132, 1721 – 1745.

Ralph F. M., P. J. Neiman, G. Wick, S. Gutman, M. Dettinger, D. Cayan and A. B. White (2006). Flooding on California's Russian River: Role of atmospheric rivers. Geophysical Research Letters, 33, L13801.https://doi.org/10.1029/2006GL026689.

Ralph F. M., S. F. Iacobellis, P. J. Neiman, J. M. Cordeira, J. R. Spackman, D. E. Waliser, G. A. Wick, A. B. White and C. Fairall, (2017). Dropsonde observations of total integrated water vapor transport within North Pacific atmospheric rivers. Journal of Hydrometeorology, 18(9), 2577–2596. https://doi.org/10.1175/JHM-D-17-0036.1.

Rasul G. (2015). Water for growth and development in the Ganges, Brahmaputra, and Meghna basins: an economic perspective. International Journal of River Basin Management, 13(3), 387-400. https://doi.org/10.1080/15715124.2015.1012518.

Rutz J. J., W. J. Steenburgh and F. M. Ralph (2014). Climatological characteristics of atmospheric rivers and their inland penetration over the Western United States. Monthly Weather Review, 142(2), 905–921. https://doi.org/10.1175/MWR-D-13-00168.1.

Rutz J. J., W. J. Steenburgh and F. M. Ralph (2015). The inland penetration of atmospheric rivers over western North America: a Lagrangian analysis. Monthly Weather Review, 143(5), 1924–1944. https://doi.org/10.1175/MWR-D-14-00288.1.

Santos da Silva J., S. Calmant, O. Rotuono Filho, F. Seyler, G. Cochonneau, E. Roux and J. W. Mansour (2010). Water Levels in the Amazon basin derived from the ERS-2 and ENVISAT Radar Altimetry Missions. Remote Sensing of the Environment, doi:10.1016/j.rse.2010.04.020.

Shields C. A. and J. T. Kiehl (2016). Atmospheric river landfall-latitude changes in future climate simulations, Geophysical Research Letters, 43, 8775–8782, doi:10.1002/2016GL070470.

Yang Y., Z. Tongtiegang, N. Guangheng and S. Ting (2018). Atmospheric rivers over the Bay of Bengal lead to northern Indian extreme rainfall, International Journal of Climatology, 38, 1010-1021.

Zhu Y. and R. E. Newell (1998). A proposed algorithm for moisture fluxes from atmospheric rivers. Monthly Weather Review, 126(3), 725–735.

An Approach of Satellite and UAS based Mosaicked DEM for Hydrodynamic Modelling – A Case of Flood Assessment of Dhanera City, Gujarat, India.

Kishanlal Darji[1], Dhruvesh P. Patel[1*], Amit Kumar Dubey[2], Praveen K. Gupta[2] and R P Singh[2]
[1] Department of Civil Engineering, School of Technology, PDEU, Gandhinagar, Gujarat, India
[2] Space Applications Centre, ISRO, Ahmedabad
*Correspondence: dhruvesh.patel@sot.pdpu.ac.in

(Received: Aug 15, 2021; in final form: Oct 06, 2021)

Abstract: Digital Elevation Models (DEMs') are an essential source of information, which describe the terrain that allows researchers to estimate various hydrological processes. Flood modelling is an important hydrological process which is applicable to estimate and assess the flood risk in susceptible area, however the accuracy of flood estimation depends on DEM resolution, therefore, the present case describes the generation of mosaicked high-resolution DEM for urban and riverine flood inundation modelling. First stage, satellite based CARTOSAT DEM of 10m x 10m of Rel river catchment is prepared for riverine flooding, whereas in second stage, UAS (Unmanned Aerial System) based 3.6 cm x 3.6 cm high resolution DEM is generated for Dhanera city using UAS (Phantom 4 Pro RTK UAV and Pix4D software). This paper focuses on merging DEM methods where generated high resolution UAS based DEM is mosaicked with CARTOSAT DEM using three methods based on software like Inverse Distance Weighted Interpolation method (IDW method) using Global Mapper software, Nearest Neighbour using ArcGIS software and Stitching method using HEC-RAS software. Out of all the methods, HEC-RAS based merging method is found to be more promising without leading a discontinuity on the edge of DEM. Present flood assessment case of Dhanera and Rel river basin shows the merged DEM can be used as cost-effective approach for accurate flood estimation of flash flooding in an urban and riverine region.

Key Words: DEM, Flood Assessment, UAV, Drone, CARTOSAT, Rel River

1. Introduction

Floods are most frequent and natural disasters worldwide which cause the major economic damage at the global level (Memon et al., 2020; Nagesh Kumar et al., 2020; Popescu et al., 2017). Floods have been recurrent phenomena in India. Almost every year floods of varying magnitude affect some part of the country or the other, which cause huge loss of lives and damage to livelihood systems, property, infrastructure and public utilities (NDMG, 2008; NDMP, 2019). Gujarat 2017, Kerala-2018, and Bihar 2019 are some of recent examples of flooding in India (Gupta, 2020). Floods are not fully preventable, but the associated hazards could be minimized if flood- prone areas are known in advance (Patel et al., 2017; Sahoo and Sreeja, 2017). Therefore, flood assessment has become an important step to reduce the loss of life and properties in floodplains area (Patel et al., 2017). Many hydrologic and hydrodynamic models are widely available for flood assessment and flood prediction; however, modelling techniques are mostly based on the Digital Elevation Model (DEM), and thus the reliability and accuracy of flood simulations results such as inundation, extent, flow velocity, flow depth, flow patterns, are highly dependent on the accuracy and resolution of the DEM data (Agnihotri et al., 2021; Jakovljevic et al., 2019; Saksena and Merwade, 2015). DEMs contain the elevation of a point on a surface above the mean sea level. DEMs are sometimes referred to as Digital Terrain Model (DTM), or Digital Surface Model (DSM) (Ajayi et al., 2017; Poon et al., 2005). Nowadays, many open source satellite based DEM i.e ASTER global, SRTM (30 m x 30 m), GMTED2010 (30 arc-second), GMTED 2010 (15 arc-seconds) GMTED 2010 (7.5 arc-seconds) and (ALOS (12.5 m x 12.5 m), are available for flood assessment studies, however low resolution DEM (generally coarser than 30m) has many vertical inaccuracies and these DEMs are too old to break the accuracy of estimation of flood hazard in urban area (Lakshmi and Yarrakula, 2018). The restricted accessibility to get high-accuracy DEMs states that open-access global DEMs are still used widely in assessment of flood models, mostly in data scarce region (Case presented by (Glas et al., 2020; Pandya et al., 2021; Patel and Pandya, 2021). It has been discovered that high-resolution DEMs like LIDAR, INSAR, UAV based DEM, ground surveying-based DEM, etc. give better flood estimations, and thus can be considered a necessary parameter for any flood modelling (Casado et al., 2018; Pandey et al., 2014; Şerban et al., 2016; Prieto et al., 2020; Pathan et al., 2021). Number of case studies shows that current remote sensing approaches fail to provide sufficient detail to assess the effects of micro-topography and the presence of property flood resistance measures (Casado et al., 2018; Ogunbadewa, 2012; Patel and Srivastava, 2014; Vant-Hull et al., 2007). Under this circumstances, Unmanned Aerial Vehicles (UAVs) or Unmanned Aerial System (UASs) are emerging platform for remote mapping at very high spatial resolution for 3D surveying, archaeological documentation, earth observation and monitoring, 3D city modelling, precision farming, hazard monitoring, environmental monitoring and assessment. Many case presented by (Casado et al., 2018; Govedarica et al., 2018; Kim and Davidson, 2015; Schumann et al., 2019) and suggested that UAV-generated very high-resolution DEM can be used for examining the stream characteristics, stream velocity and floodplain, thereby not only looking and augmenting our scientific understanding of hydrological processes at the (very) small scale, but improve the understanding in particular of flood processes (Ahmad, 2011). Examined the proficiency of UAV in creating digital maps using a light weight fixed wing UAV equipped with a high-resolution digital camera where the conclusion shows a sub-metre accuracy (Leitão et al., 2016 and Tokarczyk et al., 2015). Demonstrated the applicability and the advantages of using UAVs to generate very high resolution DEMs for urban overland flow and flood modelling. Emergency responders have used Unmanned Aircraft Systems (UAS) to acquire core information pre-, during- and post- flood events. High resolution DEM is cost worthy and expensive for flood assessment, especially the area consist with agriculture and forest area. Although it is the important parameter to estimate the sub metric accuracy for flood inundation in river bank inundated urban area. Only a few data can be accessed freely, for example, the DEM data with high resolution may not accessible for everyone and also the data is restricted. On the contrary, the level precise topographic data as an input data for terrain models is a key element of the accuracy of hydraulic flood modelling (Sahid et al., 2018). Consequently, many researchers have developed DEM as an alternative data to obtain reliable flood modelling (Patel et al., 2020). Mosaicking or interpolating DEM is found helpful where the UAV survey is not possible for the entire catchment or where there is scarcity of high-resolution DEM data. Several approaches to ensure smooth transition of DEMs have been proposed (Petrasova et al., 2017; Reuter et al., 2007; Robinson et al., 2014) in the context of global DEM mosaicking and DEM void filling. To ensure seamless transition between DEMs (Robinson et al., 2014), proposed blending DEMs using weighted averaging method where weight is a function of distance to transition line between two DEMs'. Petrasova et al. (2017) presented the case of fusion of LiDAR and UAS based DEMs, and LiDAR and Kinect based DEMs for water flow modelling using GRASS GIS and distance based weighted average method and concluded that the demonstrated technique becomes highly relevant for researchers and practitioners working for high-resolution DEMs mosaicking.

A novel approach has been performed in this paper for Dhanera and Rel River catchment for flood assessment of 2017 to produce the cost efficient UAS based DEM for Dhanera city and obtain a better mosaicked DEM by combining CARTOSAT (10m resolution) and UAS DEM (3.6cm resolution) which can be used for flow simulation in hydrodynamic modelling. CARTOSAT images has been utilized for satellite based DEMs for Rel river catchment, whereas UAS (Phantom 4 Pro RTK UAV and Pix4D software) based 3.6 cm x 3.6 cm high resolution DEM has been considered for Dhanera city. The seamless flow approach has been compared for different mosaicked DEM and identified the best mosaic methods which provide the fast and seamless flow for hydrodynamic modelling. It reduces the requirement of High resolution DEM of entire basin for decision making activities, and provides the cost effective accurate flood assessment approach for riverine urban flooding in developing countries. Paper reports a case study for fusion of DEM using different software techniques and reduce DEM fusion inaccuracy in flood assessment techniques.

2. Study area

The study is demonstrated on Rel river Basin, which is situated in Banaskantha district, Gujarat, India (Figure.1). The Rel-river is originated from the Southern part of the Sundhamata Mountain and meet to the Rann of Kachchh in Gujarat. It has two courses.

The first course flows from the Sundhamata Mountain to Pachala Dam, Jetpura Dam reaching to Bapla and Runi, while the other course mingles in the Kes Pond. Its catchment covers an area of 442 km^2, lies between 240 50'N to 240 75' N latitude and 720 00'E to 720 45' E longitude. The lowest point is near Dhanera taluka and Dhanera city and it is located near the mouth of the Rel River. The Rel-river is an ungauged river with the data-scarce region. The width of the river is about 280 m and 180 m at the location of the Road Bridge and Railway Bridge, respectively. The riverbed slope is about 1 in 500 from U/S of the railway bridge and up to D/S of cause way location. Rel river is having very steep topography in the upper catchment, resulted the flash flood in the D/S region. Catastrophic flood of the maginitue of 273 m^3/s and 3355 m^3/s has been observed in the recent year of 2015 and 2017.

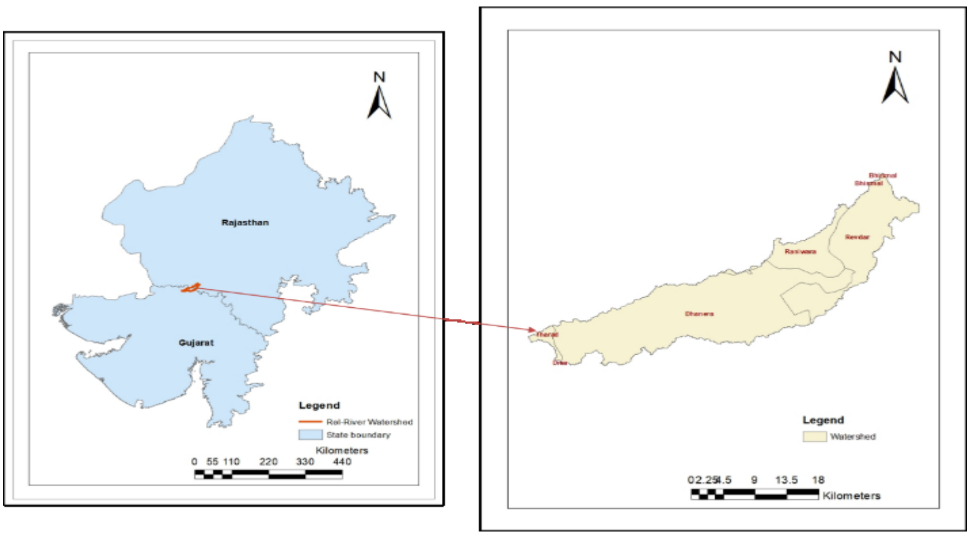

Figure 1. Study area showing Rel river catchment

3. Materials and methods

Method adopted for this research is presented in Figure 2, it has performed in basic 2 different approaches 1) DEM preparation 2) DEM mosaicking. In the first stage, two DEM were prepared. One is high resolution DEM using UAS techniques for Dhanera City, whereas second DEM is for Rel river basin, obtained from satellite based CARTOSAT DEM data. UAS techniques include collecting UAV aerial data and introducing the structure from algorithm to generate point cloud, DSMs and DEMs. Second stage deals with DEM mosaicking techniques for DEM fusion between CARTOSAT DEM and UAS based DEM. In this stage UAV based DEM for Dhanera city is merged with Rel river watershed CARTOSAT DEM using following methods. i) Inverse Distance Method (using Global Mapper) ii) Nearest Neighbour (ArcGIS software) iii) Stitching Method (HEC-RAS software). Flood modelling is performed using the merged DEM as input in HEC-RAS software and comparison is made on the basis of area and depth parameters. The output is generated in form of inundation map, depth profile and maximum depth from HEC-RAS modelling and is compared with the open Source data to check the boundary errors at merging areas. At last, errors corresponding to coarser resolution and vertical accuracy into the resampled DEMs are removed for smooth blending of DEMs.

3.1. Cartosat DEM

The CARTOSAT-1 Digital Elevation Model (CARTODEM) is a National DEM developed by the Indian Space Research Organization (ISRO). The spatial resolution is 10 m in the horizontal plane (Figure 3). Each camera has a pixel size 7 x 7 micron, swath of about 29.42 km, focal length 1945 mm (Rawat et al., 2013).

3.2 UAS DEM

Present study described the use of UAS system for post flood assessment for generating high resolution DEM for Dhanera city. DEM extraction using a UAS is performed in two stage process. Light weight UAV i.e. DJI Phantom 4 Pro RTK with automated flight operation was used for the acquisition of the image data at an altitude of 130 m above the ground level of the image area with 80% overlapping. All images obtained were from a digital, 4K resolution camera (FC300X), affixed to the lower part of the UAV system. The UAV was equipped with 12 mega pixel, focal length of 2.8 mm, and 4K resolution DJI camera. The camera has RGB band and operates in both manual and auto mode (For this study, it was operated manually). After that at second stage, image processing has been performed invoicing initial processing, point cloud &Mesh generation, DSM, orthomosaic and Index. These procedures were performed using the PiX4D mapper software.

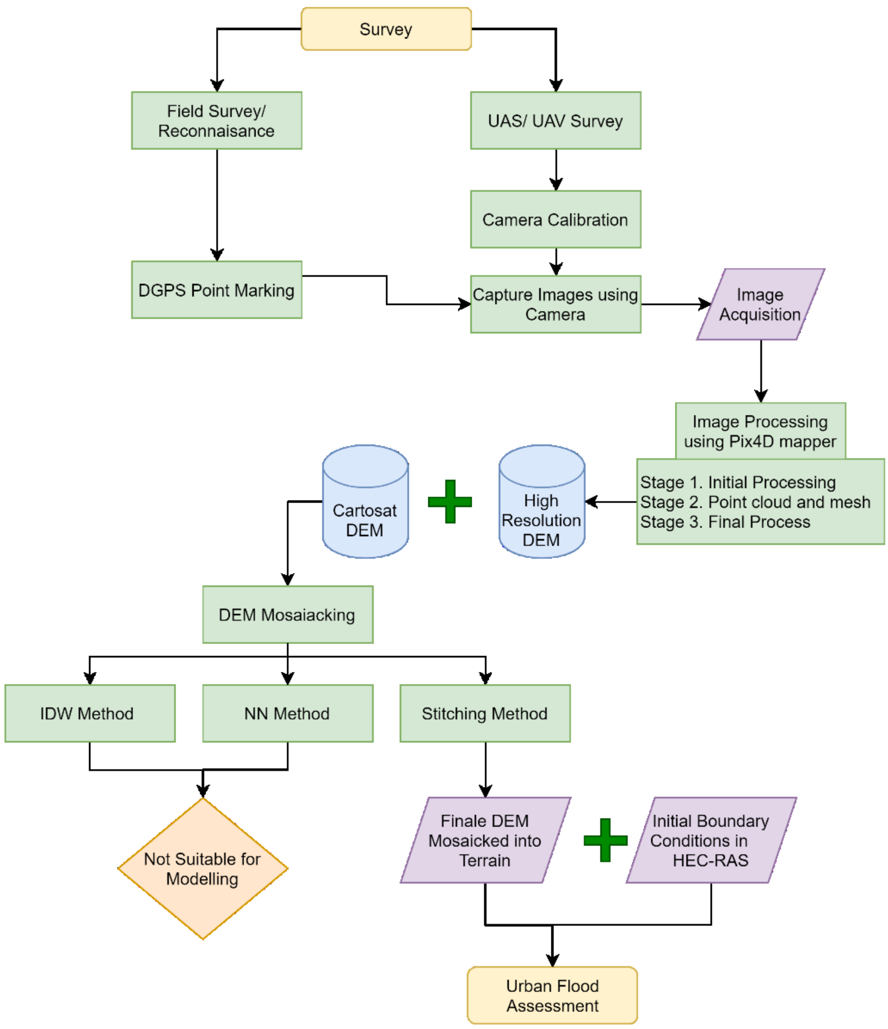

Figure 2. Methodology Chart

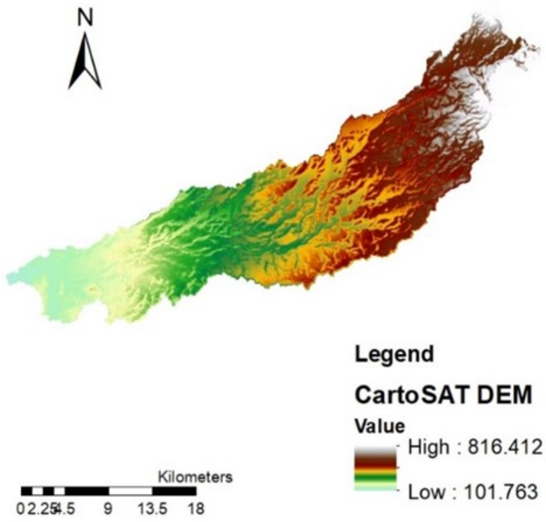

Figure 3. CARTOSAT DEM

3.2.1 Ground Control Point (GCP) Layout

Phantom 4 RTK requires minimal GCP to create accurate map. For the current study area, 7 GCP points were marked. The GCP points are marked with DGPS-RTK. GCP is obtained by continuously operating reference station method of georeferencing the data.

3.2.2 Image Acquisition

Phantom 4 Professional RTK UAV is used for capturing the images over the Dhanera city. The UAV consistent with camera version of and having the image width of 5472px, image height of 3648px, sensor width of 13.2 mm, sensor height of 8 mm, and focal length = 8.8 mm. The KML file for the region is generated (Figure 4). It is divided in to 4 zones and flight plan is decided. The 7 GCP points are marked in the study region (Figure.5). The Aerial images are taken with 80% overlap between consecutive images. The flight height is selected at 130 m so that GSD (ground sampling distance) can be 3.56 cm/px. The area covered during survey is 10 km^2. The RTK module can provide positioning accuracy of 1cm+1ppm (horizontal), 1.5cm+1ppm (vertical). Total 9222 images are collected for the region.

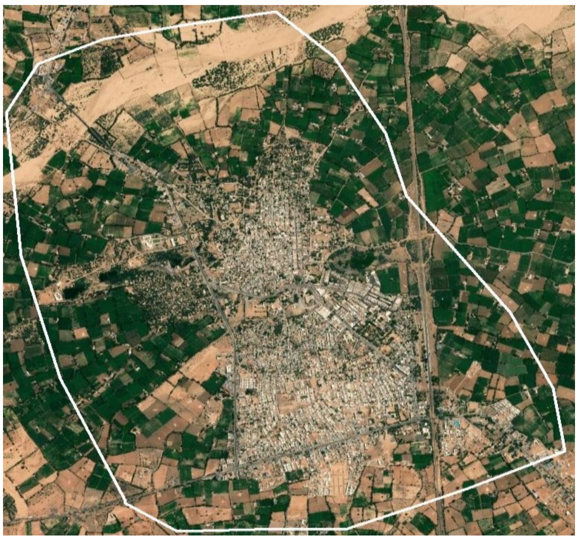

Figure 4. KML file of study area

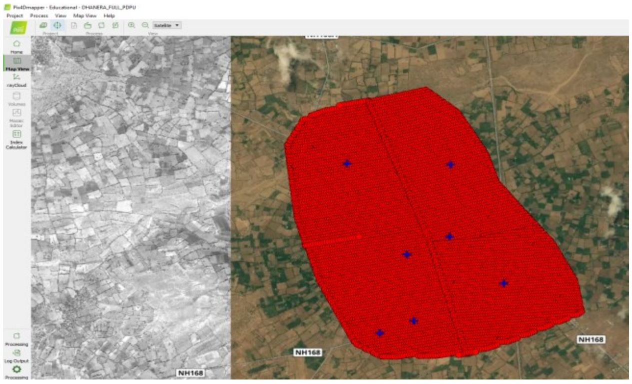

Figure 5. Images with GCP Points at Dhanera city

3.2.3 Image Processing using Pix4D

In this study, 9222 aerial images were captured using UAV for the study area. PIX4Dmapper software was used for analysis, which transforms images into digital spatial models. PIX4Dmapper graphic user performs analysis in three stages namely: Initial Processing, Point Cloud and Mesh, and Final Processing.

i) Initial Processing

In first stage there is key points extraction which identifies specific features as key points in the images. It involves fully automatic iterative proprietary algorithm for bundle block adjustment and sparse cloud point generation shown in (Figures 6-7).

ii) Point Cloud and Mesh

The second stage point cloud and mesh does the point densification where additional tie points are created based on the Automatic Tie points that results in a densified Point Cloud. (Figures 6-7). It also performs 3D textured mesh wherein a 3D textured mesh can be created based on the densified point cloud.

Figure 6. Sample analysis for Pix4D

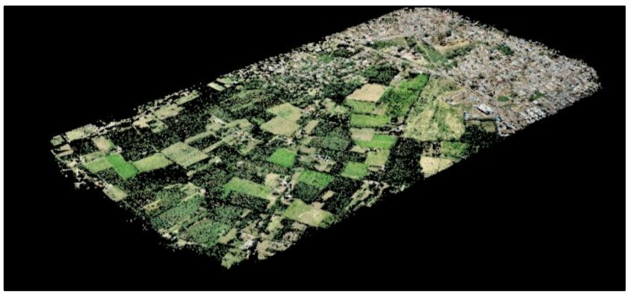

Figure 7. Point cloud of the area

iii) DSM, Orthomosaic and Index
The third stage consists of generating Digital Surface Model (DSM) which will enable the computation of Volumes, Ortho mosaics and Reflectance Maps. This stage uses inverse distance weighting algorithm (IDW) interpolation for DSM generation. Total 9222 images of the project were divided into several portion to match the capability of computer and splited in to 10 parts with around 1000 image in each parts with 20 % overlap. These 10 parts were merged in 3 sections in Pix4D for the final processing. (Figure 7). The MTP (Manual Tie Points) are created on the sub projects with the same location and same name in two adjacent project to merge them in a single project. A minimum three no of MTP are required for merging of the projects. After creation of MTP re-optimization is required to reassess the accuracy of the projects. The three final sections were mosaicked to a single DEM. This Mosaicking also involved Overlapping of some areas. Mosaicking was made using Global Mapper. The process takes about 18 hrs. Final DEM of resolution 3.6cm*3.6cm was obtained at the end for the given area of Dhanera city.

3.3 DEMs Mosaicking

The DEMs are the integral part of Hydrodynamic modelling, however, limited availability of high resolution DEM for entire catchment poses challenge of merging DEMs available from different sources at different scale In this study 3 different mosaicking methods have been applied for mosaicking a CARTOSAT DEM and UAS based DEM. The best way could be the spatial interpolation technology which calculates the DEM grid cell like 1-D hydraulic modelling. There are three methods namely inverse distance weighed interpolation method, nearest neighbour method and terrain stitching method using HEC-RAS as described below.

3.3.1 Inverse Distance Weighted Interpolation method (IDW method) using Global Mapper

This method is adopted using Global Mapper software. This is a comparatively simple way to get merged the different resolution DEM in single one. The mathematical formula of the fusion is based on the weighted average given as below:

$$H_3 = \frac{w1H1+w2H2}{w1+w2} \quad (1)$$

Where, H_1 and H_2 are the height values in first DEM and w_1 and w_2 are the weights of second DEM. The entire process is simulated automatic in computer system.

3.3.2 Nearest Neighbour interpolation using ArcGIS software

This method is adopted using ArcGIS software. Like IDW, this interpolation method is a weighted-average interpolation method. The value of an unknown cell is estimated by inserting and determining the point within a polygon. For each neighbour, the area of the portion of its original polygon that becomes incorporated in the tile of the new point is calculated. This method is most appropriate where sample data points are distributed with uneven density.

3.3.3 Terrain Stitching Method using HEC-RAS

The last method for mosaicking is Terrain Stitching method in HEC-RAS. HEC-RAS is an open and freely available software (URL: https://www.hec.usace.army.mil/software/hec-ras/download.aspx) When multiple terrain data layers with different resolutions are used to make a terrain data set, HEC-RAS uses "Stitching" to merge the edges of the terrain data layers. HEC-RAS can input more than one GeoTIFF files and merges them into a terrain. RAS mapper converts the grids into the GeoTIFF file format. This GeoTIFF format supports pyramided and tiled data. Tiled data uses less area of the terrain by removing the 'No Data Values' and the pyramided data can store multiple terrain layers in varying resolution. Thus it is possible to merge two DEM of different resolutions. Apart from this, HEC-RAS also allows gives output file format which has smaller storage space, faster computational speed and dynamic mapping of results. Once the GeoTIFF files are created RAS Mapper also creates a *.hdf a and a *.vrt file. The *.hdf (Hierarchical Data Format) file contains information on how the multiple GeoTIFF files are stitched together. The *.vrt (Virtual Raster Translator) is an XML file that contains information about all the raster files. The user can drag and drop the *.vrt file on the ArcGIS project and can get information about all the raster files that make up the terrain layer.

3.4 Flood Modeling in HEC-RAS

The HEC-RAS 5.0.1 is utilized the 2D Saint Venant equation (GW Brunner, 2014; HEC-RAS, 2016; Quirogaa et al., 2016):

$$\frac{\partial \zeta}{\partial t} + \frac{\partial p}{\partial x} + \frac{\partial q}{\partial x} = 0 \quad (2)$$

$$\frac{\partial p}{\partial t} + \frac{\partial}{\partial x}\left(\frac{p^2}{h}\right) + \frac{\partial}{\partial y}\left(\frac{pq}{h}\right) = -\frac{n^2 pg\sqrt{p^2+q^2}}{h^2} - gh\frac{\partial \xi}{\partial x} + pf + \frac{\partial}{\rho \partial x}(h\tau_{xx}) + \frac{\partial}{\rho \partial y}(h\tau_{xy}) \quad (3)$$

$$\frac{\partial q}{\partial t} + \frac{\partial}{\partial y}\left(\frac{q^2}{h}\right) + \frac{\partial}{\partial y}\left(\frac{pq}{h}\right) = -\frac{n^2 qg\sqrt{p^2+q^2}}{h^2} - gh\frac{\partial \xi}{\partial y} + qf + \frac{\partial}{\rho \partial y}(h\tau_{yy}) + \frac{\partial}{\rho \partial y}(h\tau_{xy}) \quad (4)$$

where h is the water depth (m), p and q are the specific flow in the x and y direction (m^2 s^{-1}), ξ is the surface elevation (m), g is the acceleration due to gravity (ms-2), n is the Manning resistance, ρ is the water density (kg m-3), τxx, τyy and τxy are the components of the effective shear stress and f is the Corolis (s^{-1}). (Patel et al., 2017; Quirogaa et al., 2016) has presented the case of flood assessment of Bolivian Amazonia and Surat city using HEC-RAS based 2D and 1D/2D coupled hydrodynamic modelling. DEM is a sensitive parameter for 2D modelling in this study. 2D modelling is performed for 4 DEM using HEC-RAS: i) Mosaicked DEM based on IDW method ii) Mosaicked DEM based on NN method iii) Mosaicked DEM based on HEC-RAS iv) CARTOSAT DEM. The results for inundation area and depth are extracted in ARCGIS and maps are produced.

4. Observations and Results

4.1 Point cloud evaluation and high-resolution DEM extraction using UAS

A SfM algorithm is used for restoring camera exposure position and for generation of sparse point cloud and MVS algorithm is used for generation of dense point cloud as per DSM generation method. For this project it took about 384 hours to process DSM, DTM and orthomosaic from the 9222 UAV images at 80 % overlap. As it was not possible to merge all the UAV images in one go, it was divided in 4 parts to perform the processing. Each parts were then mosaicked in global mapper as a single DEM. Accuracy of final DEM obtained was 3.6 cm as shown in Figures 8-9.

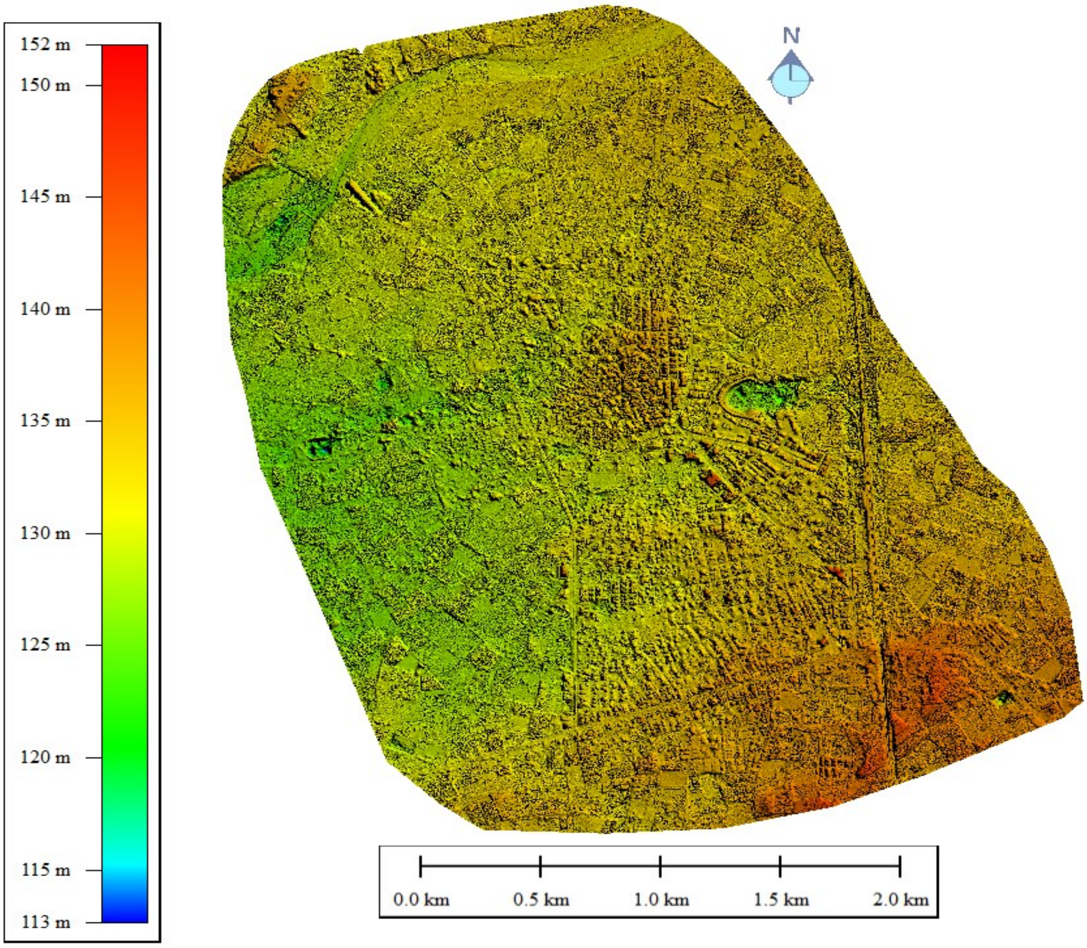

Figure 8. UAS generated DEM

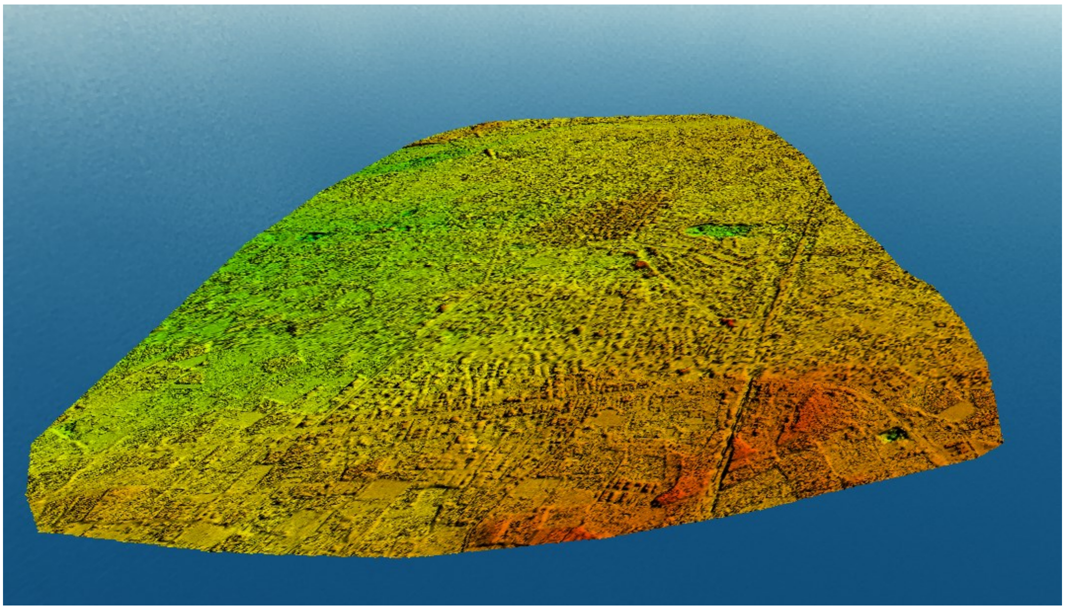

Figure 9. 3D view of high resolution DEM

4.1 DEM mosaicking

4.1.1 IDW method using Global Mapper

The final output obtained by merging the UAV based DEM for Dhanera city and CARTOSAT DEM for entire rel river watershed using IDW method. The basic limitation of this merging method is that the file size of merged DEM is too high (approx. 1TB) and it was unfit to be used as input DEM for flood modelling.

4.1.2 NN method using ArcGIS

The final output of NN merging method for Dhanera city containing UAV DEM and Rel River with CARTODEM. The merging contains less error compared to IDW method but is still unfit for flood modelling due to high file size (approx. 150GB). Thus, flood modelling is done only for a small section to compare the results.

4.1.3 Stitching method using HEC-RAS

The final output obtained can be seen in Figure 10 for merging UAV and CARTOSAT based DEMs in HEC-RAS by stitching method. This method is most suitable as it gives the better modelling results. The section as considered earlier is clipped for this DEM also and 2D unsteady flood modelling is performed (Figure 11).

4.1.4 Cartosat DEM

A section was clipped from all the merged DEM and 2D flood modelling was performed and the depth profile was generated. (Figure 12). The results of all the merged DEM are compared with actual CARTOSAT data DEM. It is observed that the depth -time Series plot of CARTOSAT DEM (Figure 12) validates accurately to the DEM merged by Stitching method.

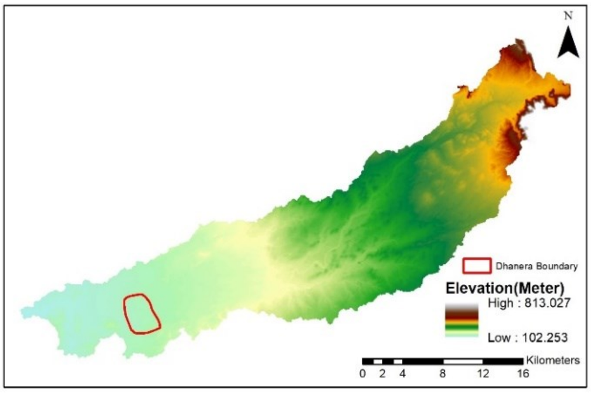

Figure 10. Terrain Stitching Method in HEC-RAS

4.2 Error analysis

R^2 values are obtained based on depth and inundation area values. R^2 is considered as a parameter to check whether which of the merged DEM matches closely with the observed river gauge data. Depth and inundation areas are calculated for all the merged type DEM and CARTOSAT DEM as shown in Table. 1 and Figure 13. It is observed that the area and depth values of stitching method matches closely with the observed, which shows the reliability of merging method.

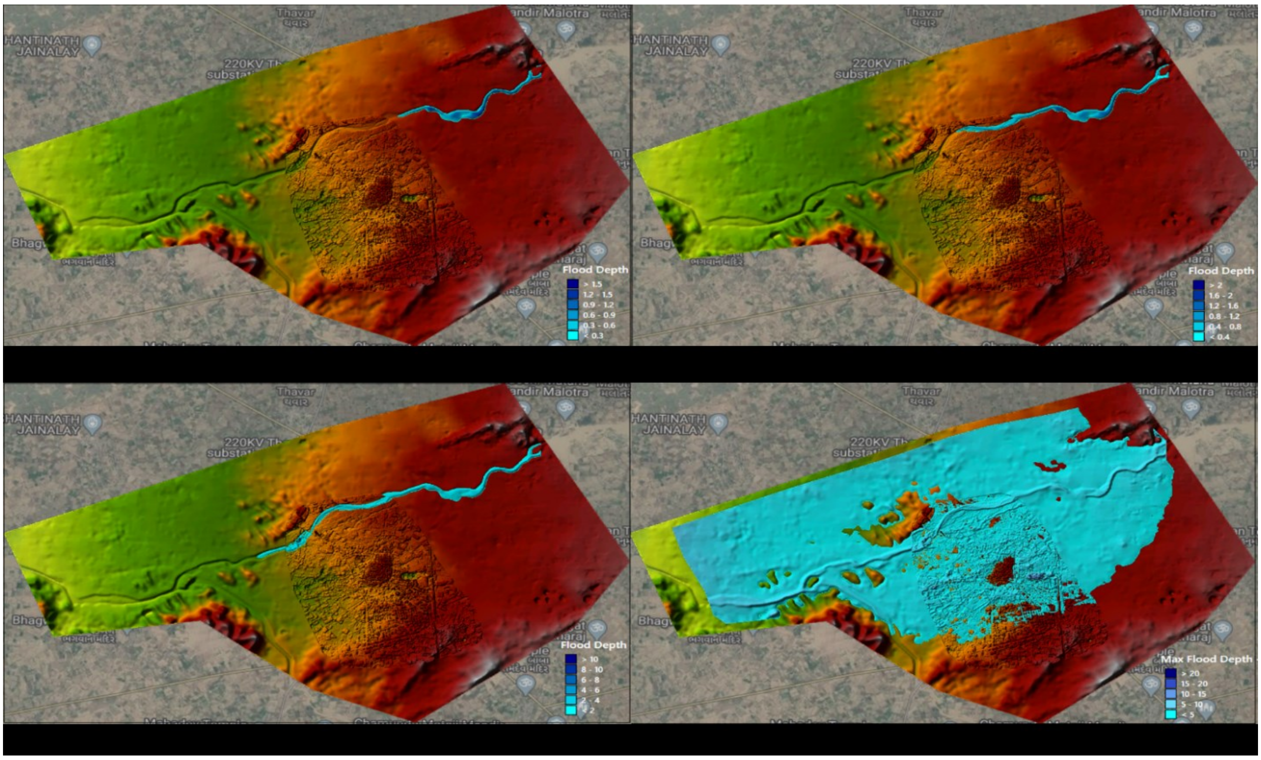

Figure 11. Depth Profile tiles of a) b) c) and d) of the Mosaic DEM (UAV and CARTOSAT)

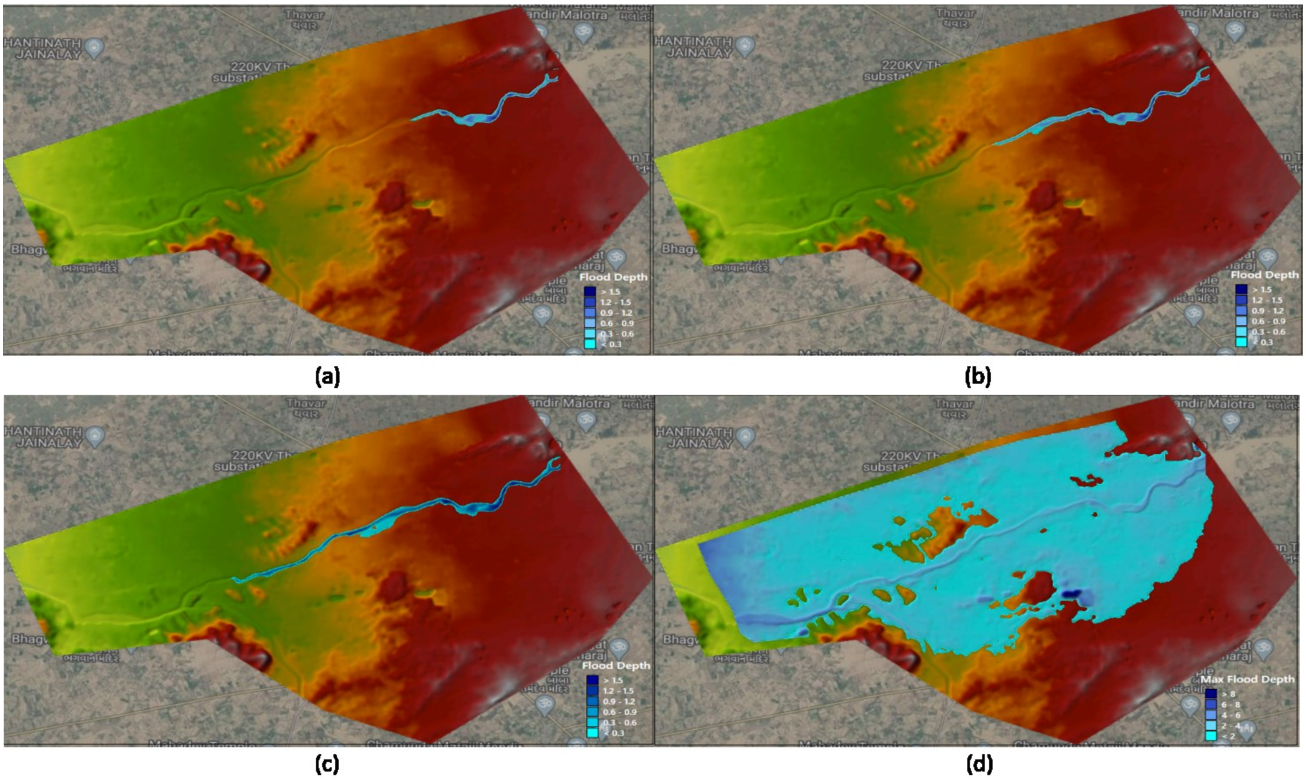

Figure 12. Depth Profile tiles of a) b) c) and d) of CARTOSAT DEM

Table 1. Comparison of Results

Sr.No	List of Parameters	CARTOSAT DEM	Stitching method in HEC-RAS
1	Inundation Area (km^2)	26.03	25.75
2	R^2 Value	0.9014	0.9426

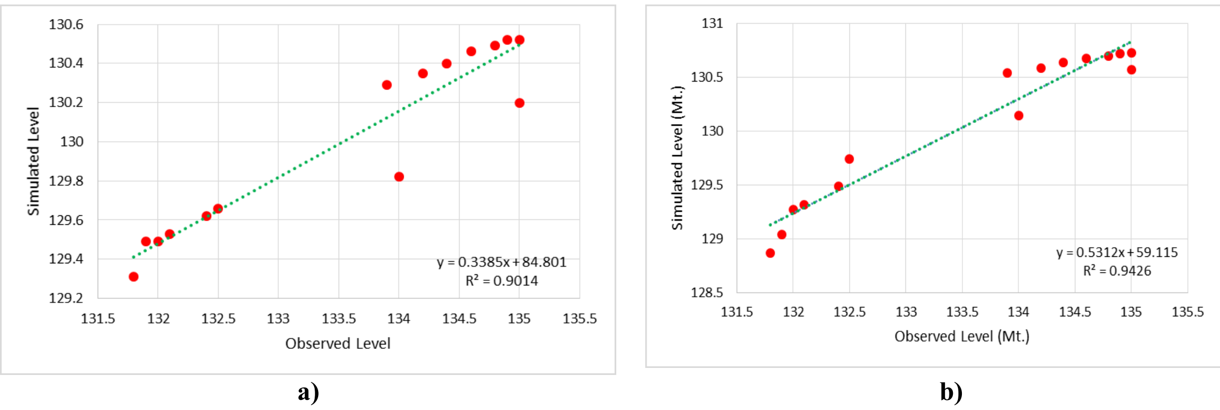

Figure 13. Correction of Observed Gauge level and Simulated Levels a) CARTOSAT DEM b) Mosaic DEM

5. Discussion

1. IDW (Inverse Distance Weighing) method in Global mapper software and Nearest Neighbor method using ArcGIS was used to mosaic both the DEM. The output file size is too high which is not suitable for modelling.
2. Terrain stitching method provides reliable output for flood estimation, hence applicable for cost-effective approach for accurate flood estimation of flash flooding in an urban and riverine region. The file size is 342MB and the processing time is 45 minutes.
3. Value of RMSE for stitching method is lowest out of all as shown in Table 1. Hence Stitching method is considered better out of all the methods.
4. The future stage involves flow simulation using hydrodynamic modelling. Prepared high resolution mosaicked DEM can be used for Flash Flood Hydrodynamic modelling. UAS based DEM can be merged with other open source DEMs like SRTM, ALOS, etc. and also the results can be compared further. Other parameters like arrival time and extreme flooding can be taken into consideration for flood

modelling. Merging methods using GRASS GIS software can also be considered for comparison.

6. Conclusions

Flood are the most vulnerable hazards for developing countries, cause a damage of properties and productivity in large extent, although the appropriate assessment techniques in urban and riverine area would decrease the flood catastrophe and reduce the human risk. Flood inundation and risk maps prepared from hydrodynamic modelling are purely depends on the accuracy of high resolution DEM. Preparation of high resolution DEM for entire catchments are cost associated and not an economic option for flood assessment in developing countries, therefore this study covers the development of high resolution DEM using UAS techniques and mosaics it with satellite based DEM. Merging through stitching method is more accurate from all other methods but also it gives a convenience to researcher to deal with big data in a short time. The terrain generation helps us to deal with DEM of different resolution at a same time which is beneficial in terms of hydrodynamic modelling. The study demonstrated the generation of DEM by UAV system and photogrammetry for Dhanera city which can be used a better data source for urban flood modelling. A very high resolution of DEM of accuracy 3.6cm is generated as an output which can be then merged with open source DEM or other satellite based DEM. Various methods for DEM fusion have been analysed by comparative statements which lastly conclude terrain stitching method provides the reliable output for flood mapping, hence applicable as cost-effective approach for accurate flood mapping in an urban and riverine region. Furthermore when the results of all mosaicked DEM were compared, terrain stitching merged DEM gave the best matched results with CARTOSAT DEM based on parameters like depth and inundation area. Thus a fusion of UAV based DEM and other DEM can be used a good input data source in flood mapping. This study would help to frame the guideline for use of Unmanned Aerial Systems (UAS) in post flood response activity in India.

Acknowledgements
Corresponding author would like to thanks SAC-ISRO for providing the financial support [Grant No: SAC/EPSA/GHCAG/LHD/SARITA/01/19] to execute the work. Also thanks to Mr. Raviraj and Ms. Heena, PDEU for providing initial support to carry out the research work.

References

Agnihotri P. G., S. Eslamian, D. Patel, and A. I. Pathan. (2021). Comparative analysis of 1D hydrodynamic flood model using globally available DEMs a case of the coastal region. International Journal of Hydrology Science and Technology, 1(1), 1. https://doi.org/10.1504/IJHST.2021.10034760

Ahmad A. (2011). Digital mapping using low altitude UAV. Pertanika Journal of Science and Technology, 19(SPEC. ISSUE), 51–58.

Ajayi O. G., A. A. Salubi, A. F. Angbas, and M. G. Odigure. (2017). Generation of accurate digital elevation models from UAV acquired low percentage overlapping images. International Journal of Remote Sensing, 38(8–10), 3113–3134. https://doi.org/10.1080/01431161.2017.1285085

Casado M. R., T. Irvine, S. Johnson, M. Palma, and P. Leinster. (2018). The use of unmanned aerial vehicles to estimate direct tangible losses to residential properties from flood events: A case study of Cockermouth Following the Desmond Storm. Remote Sensing, 10(10), 1–21. https://doi.org/10.3390/rs10101548

Glas H., P. De Maeyer, S. Merisier, and G. Deruyter. (2020). Development of a low-cost methodology for data acquisition and flood risk assessment in the floodplain of the river Moustiques in Haiti. Journal of Flood Risk Management, 13(2), 1–17. https://doi.org/10.1111/jfr3.12608

Govedarica M., G. Jakovljević, and F. Álvarez-Taboada. (2018). Flood risk assessment based on LiDAR and UAV points clouds and DEM. Remote Sensing for Agriculture, Ecosystems, and Hydrology XX, 10783, 66–76. https://doi.org/10.1117/12.2513278

Gupta K. (2020). Challenges in developing urban flood resilience in India. Philosophical Transactions of the Royal Society A: Mathematical, Physical and Engineering Sciences, 378(2168). https://doi.org/10.1098/rsta.2019.0211

GW Brunner. (2014). Combined 1D and 2D Modeling with HEC-RAS. US Army Corps of Engineers.

HEC-RAS. (2016). HEC-RAS user's Manual.

Jakovljevic G., M. Govedarica, F. Alvarez-Taboada, and V. Pajic. (2019). Accuracy assessment of deep learning based classification of LiDAR and UAV points clouds for DTM creation and flood risk mapping. Geosciences (Switzerland), 9(7). https://doi.org/10.3390/geosciences9070323

Kim K. and J. Davidson. (2015). Unmanned aircraft systems used for disaster management. Transportation Research Record, 2532, 83–90. https://doi.org/10.3141/2532-10

Lakshmi S. E. and K. Yarrakula. (2018). Review and critical analysis on digital elevation models. Geofizika, 35(2), 129–157. https://doi.org/10.15233/gfz.2018.35.7

Leitão J. P., M. Moy De Vitry, A. Scheidegger, and J. Rieckermann. (2016). Assessing the quality of digital elevation models obtained from mini unmanned aerial vehicles for overland flow modelling in urban areas. Hydrology and Earth System Sciences, 20(4), 1637–1653. https://doi.org/10.5194/hess-20-1637-2016

Memon N., D. P. Patel, N. Bhatt, and S. B. Patel. (2020). Integrated framework for flood relief package (FRP) allocation in semiarid region: a case of Rel River flood, Gujarat, India. In Natural Hazards (Vol. 100, Issue 1). Springer Netherlands. https://doi.org/10.1007/s11069-

019-03812-z

Nagesh Kumar D., A. R. Shastry, and K. Srinivasa Raju. (2020). Delineation of flood-prone areas using modified topographic index for a river basin. H2Open Journal, 3(1), 58–68. https://doi.org/10.2166/h2oj.2020.021

NDMG. (2008). National Disaster Management Guideline.

NDMP. (2019). National Disaster Management Plan.

Ogunbadewa E. Y. (2012). Investigating availability of cloud free images with cloud masks in relation to satellite revisit frequency in the Northwest of England. Contributions to Geophysics and Geodesy, 42(1), 63–100.

Pandey R. K., J. F. Crétaux, M. Bergé-Nguyen, V. M. Tiwari, V. Drolon, F. Papa, and S. Calmant. (2014). Water level estimation by remote sensing for the 2008 flooding of the Kosi River. International Journal of Remote Sensing, 35(2), 424–440. https://doi.org/10.1080/01431161.2013.870678

Pandya U., D. P. Patel, and S. K. Singh. (2021). A flood assessment of data scarce region using an open-source 2D hydrodynamic modeling and Google Earth Image: a case of Sabarmati flood, India. Arabian Journal of Geosciences, 14(21), 2200. https://doi.org/10.1007/s12517-021-08504-2

Patel D. P. and U. D. Pandya. (2021). Flood stages assessment using open source 1D hydrodynamic modelling in data scarce region. International Journal of Hydrology Science and Technology, 1(1), 1. https://doi.org/10.1504/IJHST.2021.10039735

Patel D. P., J. A. Ramirez, P. K. Srivastava, M. Bray, and D. Han. (2017). Assessment of flood inundation mapping of Surat city by coupled 1D/2D hydrodynamic modeling: a case application of the new HEC-RAS 5. Natural Hazards, 89(1), 93–130. https://doi.org/10.1007/s11069-017-2956-6

Patel D. P. and P. K. Srivastava. (2014). Application of Geo-Spatial Technique for Flood Inundation Mapping of Low Lying Areas. Remote Sensing Applications in Environmental Research. Society of Earth Scientists Series. Springer, Cham, 113–130. https://doi.org/10.1007/978-3-319-05906-8_7

Patel D. P., P. K. Srivastava, S. K. Singh, C. Prieto, and D. Han. (2020). One- Dimensional Hydrodynamic Modeling of the River Tapi. Techniques for Disaster Risk Management and Mitigation, 209–235. https://doi.org/10.1002/9781119359203.ch16

Pathan A. I., P. G. Agnihotri, D. Patel, and C. Prieto. (2021). Identifying the efficacy of tidal waves on flood assessment study — a case of coastal urban flooding. Arabian Journal of Geosciences, 14(20), 2132. https://doi.org/10.1007/s12517-021-08538-6

Petrasova A., H. Mitasova, V. Petras, and J. Jeziorska. (2017). Fusion of high-resolution DEMs for water flow modeling. Open Geospatial Data, Software and Using UAV SfM Supports Classical Theory. Remote Standards, 2(1), 0–7. https://doi.org/10.1186/s40965-017-0019-2

Poon J., C. S. Fraser, Z. Chunsun, L. I. Zhang, and A. Gruen. (2005). Quality assessment of digital surface models generated from ikonos imagery. Photogrammetric Record, 20(110), 162–171. https://doi.org/10.1111/j.1477-9730.2005.00312.x

Popescu D., L. Ichim, and F. Stoican. (2017). Unmanned aerial vehicle systems for remote estimation of flooded areas based on complex image processing. Sensors (Switzerland), 17(3). https://doi.org/10.3390/s17030446

Prieto C., D. Patel, and D. Han. (2020). Preface: Advances in flood risk assessment and management. Natural Hazards and Earth System Sciences, 20(4), 1045–1048. https://doi.org/10.5194/nhess-20-1045-2020

Quirogaa V. M., S. Kurea, K. Udoa, and A. Manoa. (2016). Application of 2D numerical simulation for the analysis of the February 2014 Bolivian Amazonia flood: Application of the new HEC-RAS version 5. Ribagua, 3(1), 25–33. https://doi.org/10.1016/j.riba.2015.12.001

Rawat J. S., V. Biswas, and M. Kumar. (2013). Changes in land use/cover using geospatial techniques: A case study of Ramnagar town area, district Nainital, Uttarakhand, India. Egyptian Journal of Remote Sensing and Space Science, 16(1), 111–117. https://doi.org/10.1016/j.ejrs.2013.04.002

Reuter H. I., A. Nelson, and A. Jarvis. (2007). An evaluation of void-filling interpolation methods for SRTM data. International Journal of Geographical Information Science, 21(9), 983–1008. https://doi.org/10.1080/13658810601169899

Robinson N., J. Regetz, and R. P. Guralnick. (2014). EarthEnv-DEM90: A nearly-global, void-free, multi-scale smoothed, 90m digital elevation model from fused ASTER and SRTM data. ISPRS Journal of Photogrammetry and Remote Sensing, 87, 57–67. https://doi.org/10.1016/j.isprsjprs.2013.11.002

Sahid A. W. Nurrohman, and M. P. Hadi. (2018). An investigation of Digital Elevation Model (DEM) structure influence on flood modelling. IOP Conference Series: Earth and Environmental Science, 148(1). https://doi.org/10.1088/1755-1315/148/1/012001

Sahoo S. N. and P. Sreeja. (2017). Development of Flood Inundation Maps and Quantification of Flood Risk in an Urban Catchment of Brahmaputra River. ASCE-ASME Journal of Risk and Uncertainty in Engineering Systems, Part A: Civil Engineering, 3(1), 1–11. https://doi.org/10.1061/ajrua6.0000822

Saksena S. and V. Merwade. (2015). Incorporating the effect of DEM resolution and accuracy for improved flood inundation mapping. Journal of Hydrology, 530, 180–194. https://doi.org/10.1016/j.jhydrol.2015.09.069

Schumann Muhlhausen, and Andreadis. (2019). Rapid Mapping of Small-Scale River-Floodplain Environments

Sensing, 11(8), 982. https://doi.org/10.3390/rs11080982

Şerban G., I. Rus, D. Vele, P. Breţcan, M. Alexe, and D. Petrea. (2016). Flood-prone area delimitation using UAV technology, in the areas hard-to-reach for classic aircrafts: case study in the north-east of Apuseni Mountains, Transylvania. Natural Hazards, 82(3), 1817–1832. https://doi.org/10.1007/s11069-016-2266-4

Tokarczyk P., J. P. Leitao, J. Rieckermann, K. Schindler, and F. Blumensaat. (2015). High-quality observation of surface imperviousness for urban runoff modelling using UAV imagery. Hydrology and Earth System Sciences, 19(10), 4215–4228. https://doi.org/10.5194/hess-19-4215-2015

Vant-Hull B., A. Marshak, L. A. Remer, and Z. Li. (2007). The effects of scattering angle and cumulus cloud geometry on satellite retrievals of cloud droplet effective radius. IEEE Transactions on Geoscience and Remote Sensing, 45(4), 1039–1044. https://doi.org/10.1109/TGRS.2006.890416

Assessment of surface flooding over India from passive microwave radiometer

Rohit Pradhan*, Nimisha Singh and R P Singh
Land Hydrology Division, EPSA, Space Applications Centre (ISRO), Ahmedabad, India
*Email: rohitp@sac.isro.gov.in

(Received: Aug 19, 2021; in final form: Oct 6, 2021)

Abstract: Orbital measurements of surface flooding have routinely been carried out using Synthetic Aperture Radars and Altimeters. The ability of SAR and Altimeter to provide all-weather, high-resolution and accurate data is diminished by their poor revisit times. In the event of flood, rapid availability of near real-time data for damage assessment and relief applications is of utmost priority. Passive Microwave Radiometers like Advanced Microwave Scanning Radiometer – 2 (AMSR2) provide high repetivity of 1-2 days with coarser resolution, but retain their all-weather capability. In this paper, we present a method for detection and assessment of regional-scale surface flooding using Brightness Temperature at 36.5 GHz from AMSR2. Microwave Polarization Difference Index (MPDI) was used to identify flooded pixels at national scale and the severity of flood was characterised using a normalised flood index. Spatial variability and temporal frequency of surface flooding over India was studied for the period 2013-2020. Near real-time Flood Index product, using this algorithm is available on VEDAS web portal (vedas.sac.gov.in).

Keywords: Flood, inundation, passive radiometer, microwave, AMSR2.

1. Introduction

Flood is one of the most frequent natural disasters affecting millions of people worldwide. Mapping and forecasting these flood events is essential for any flood mitigation plan that can save thousands of lives. Surface hydrological variables like river water level, surface water extent, soil moisture etc. are routinely observed from satellites (Sheffield et al., 2018). Altimeters and Synthetic Aperture Radars (SAR) provide high precision and high-resolution all-weather data, which is key to retrieving these hydrological parameters. However, they suffer from poor revisit time which hampers their use during floods. Altimeters with typical revisit times of 10-35 days may not be able to capture peak water level and flood signal. Similarly, SAR data with 10-day revisit period and limited swath may not always be sufficient to delineate catchment-level flood extent and perform damage assessment.

Microwave radiometers (e.g. AMSRE, AMSR2) record emission from Earth's surface and atmosphere to estimate Brightness Temperature at multiple frequencies and retrieve a variety of geophysical parameters with a revisit time of 1-2 days (Cho et al., 2017). Soil moisture, water vapor, snow cover, sea ice etc. have been retrieved operationally from passive microwave radiometers (Njoku et al., 2003; Kazumori et al., 2012; Dai et al., 2012; Spreen et al., 2008). Emission and reflectivity in microwave region is affected by soil properties such as dielectric constant, soil roughness etc (Ulaby et al., 1981, 1986). Over land surfaces, brightness temperature is related with emissivity and temperature (Fung et al., 1994). When soil surface is completely inundated by water, the emissivity decreases causing reduction in Brightness Temperature (BT) measured in microwave frequencies. The reduction of BT in horizontal polarization is greater compared to that in vertical polarization (Ulaby et al., 1978).

Microwave indices obtained from multi-frequency radiometry have been used for detecting characteristics of land and water surfaces (Paloscia et al., 2018). Brightness Temperature Polarization Ratio (PR), also known as Microwave Polarisation Difference Index (MPDI), at a particular frequency is one such index that is used to study soil moisture, surface inundation and vegetation characteristics (Gupta et al., 2019; Njoku et al., 2003; Zheng et al., 2016) and is given as:

$$\mathrm{MPDI} = \frac{T_{bV}-T_{bH}}{T_{bV}+T_{bH}} = \frac{\varepsilon_V-\varepsilon_h}{\varepsilon_V+\varepsilon_h} \quad (1)$$

Where T_{bH} and T_{bV} are Brightness Temperatures and ε_H and ε_V are emissivity in H and V polarisations, respectively. This index removes the effect of fluctuations in physical temperature of target and considers only the difference in emissivity in the two polarisations. MPDI is governed by the surface water extent and is highest for water-covered regions amongst all the LULC types studied by Li et al. (2013).

Advanced Microwave Scanning Radiometer (AMSR2) is a passive microwave radiometer developed by Japanese Aerospace eXploration Agency (JAXA) that can record BT at seven frequencies in both horizontal (H) and vertical (V) polarisations. Lower frequencies recorded by passive microwave radiometers are less affected by atmosphere but provide poor spatial resolution. On the other hand, clouds and atmospheric water vapor influence higher frequencies (Shi et al., 2015). Passive radiometer data at 36 GHz has been used to retrieve river discharge and delineate flood extent, as it is mainly sensitive to fluctuations in water surface extent (Brakenridge et al., 2007, 2012). This frequency provides an optimum spatial resolution, is less influenced by atmosphere and is sensitive to fluctuations in surface water, making it best suited for detection and monitoring of floods. This paper highlights the utility of passive microwave radiometer to map surface flooding over India. In this paper, we present a novel technique for estimation of surface flooding using AMSR2 derived MPDI at 36.5 GHz over India. MPDI based flood index maps are generated which express the intensity of flooding in a given pixel and long-term analysis of flooding over India is analyzed using this method. Impact of specific extreme events like cyclones are studied in terms of surface flooding caused by the event.

2. Study area and data used

This study was carried out over India and surrounding regions that see high prevalence of flood events. Study area lies between 5° - 40° N and 65° – 100° E excluding the seas and high altitude regions. This region experiences maximum flooding during the monsoon months of June to September with different catchments experiencing peak flooding at different times. Excess precipitation, overflowing rivers and release from man-made structures can contribute to floods in the region. These events can last anywhere from a few days to weeks depending on intensity of flood and its driving factors.

AMSR2 is a passive microwave radiometer that provides BT data in seven frequencies with varying spatial resolutions (Table 1). This data is re-gridded onto global grids at 0.1° and 0.25° resolutions and provided as standard Level 3 products. In this study, we use Level 3 Brightness Temperature (BT) data from AMSR2 at 36.5 GHz in both H and V polarisations for the period 2013-2020 (data available from ftp.gportal.jaxa.jp). At 36.5GHz, the IFOV of AMSR2 is approximately 7x12 km. After re-gridding, this data is available at 0.1°x0.1° spatial resolution over entire globe with 2-day repeat coverage within the study region. As a result, the product is generated as composite of two days. Moderate resolution Imaging Sensor (MODIS) based Land Use Land Cover (LULC) data at 5km grid is used to filter out desert regions and analyse land cover based MPDI.

Table 1. Description of AMSR2 frequencies

SNo.	Central Frequency (GHz)	Polarization	IFOV (km)
1	6.925	H, V	35 × 62
2	7.3	H, V	35 × 62
3	10.65	H, V	24 × 42
4	18.7	H, V	14 × 22
5	23.8	H, V	11 × 19
6	36.5	H, V	7 × 12
7	89.0	H, V	3 × 5

3. Methodology

MPDI (using Equation 1) for study region is computed using 0.1° x0.1° daily gridded AMSR2 BT at 36.5GHz in H and V polarisations. Sea regions are masked out and only land areas are selected for further processing. MPDI computed for the period 2013-2020 is used to generate long-term mean and standard deviation for each grid pixel. These long-term statistics serve as a diagnostic tool for assessing if the MPDI of a particular pixel is anomalously high, which might indicate inundation. These statistics are used to compute the MPDI range for partially to completely inundated pixels, which serves as threshold for identifying flooded pixels and computing a normalised flood index.

For estimating flood extent from daily AMSR2 data, MPDI image is computed from BT in H and V polarisations. Pixels with MPDI>0.1 are marked as completely inundated, whereas, pixels with MPDI between 0.01 and 0.1 are marked as partially inundated. MODIS LULC mask is applied to mask out desert regions as they too have high MPDI values due to large differences in emissivity in H and V polarisation. Pixels with MPDI between 0.01 and 0.1 are further verified to see if their polarisation ratio value exceeds 1.5 times the standard deviation from long-term mean. If these criteria are met, the pixel is confirmed as inundated and further process of converting MPDI to normalised flood index is carried in the next step. Pixels with MPDI<0.01 are marked as non-inundated and not considered for further analysis.

Once flooded pixels are identified based on MPDI, its polarisation ratio is converted to a normalised flood index value ranging from 0 to 1. This flood index is a linear scaling of MPDI values between 0.01 to 0.1 for the identified flooded pixels. For values of MPDI>0.1, flood index is set as 1. Equation 2 describes the linear conversion of MPDI to flood index values used as an indicator of flooding intensity.

$$\text{Flood Index} = \begin{cases} 1 & ;\ \text{MPDI}>0.1 \\ \frac{\text{MPDI}-0.01}{0.1-0.01} & ;0.01\leq\text{MPDI}\leq0.1 \\ 0 & ;\ \text{MPDI}<0.01 \end{cases} \quad (2)$$

Flood index map of each day is composited with the next day to obtain 2-day flood composites. Mean value is taken for pixels where data is available for both dates. Similarly, mean flood index maps for monsoon season and entire year are also generated for analysing extent, intensity and duration of floods throughout the study area. Flood index maps for specific events, like cyclone Tauktae and Yaas during 2021, were generated for understanding the performance of flood detection algorithm during extreme events. Flowchart of methodology used in this study is shown in Figure 1.

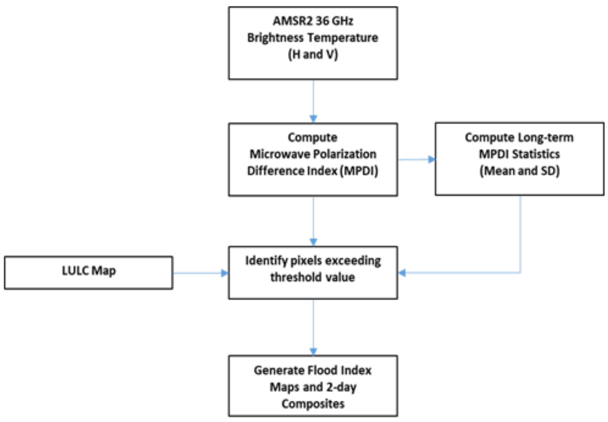

Figure 1. Flowchart of methodology implemented in this study

4. Results and discussion

4.1 MPDI and its statistics

Figure 2 shows the mean and standard deviation of computed MPDI between 2013-2020 for the study region. We can clearly see that MPDI is greater than 0.1 for seas, water bodies and lakes. MPDI for land areas is typically lower than 0.01 represented here in dark blue. Deserts and high altitude regions show high MPDI due to differences in emissivity in H and V polarisations. To overcome this, MODIS LULC was used to mask out the desert regions and barren land areas from the output flood index maps. This does not have any impact on the flood maps for major part of the Indian landmass. Surface vegetation influences MPDI and makes it difficult to detect flood in heavily vegetated areas, which is a major limitation of this work.

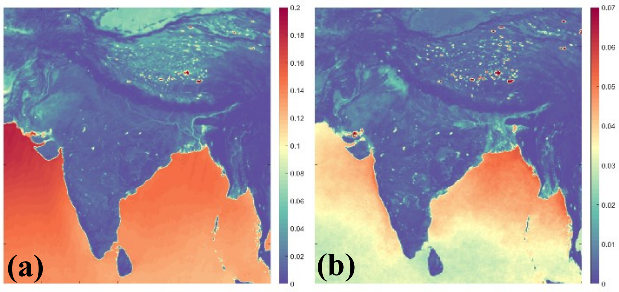

Figure 2. (a) Mean and (b) standard deviation of MPDI for the study region during 2013-2020.

4.2 Flood Index

Daily flood index maps were generated for the study period and averaged to get the mean flood index map. For dissemination purpose, 2-day composite flood index maps were generated to cover the gaps in daily BT gridded data. Figure 3 shows the mean flood index averaged over the study period for all pixels within the study region. It is clear that flood index picks up water bodies like rivers, lakes, reservoirs with good accuracy. Tributaries of rivers and frequently flooded regions are also picked up by the flood index.

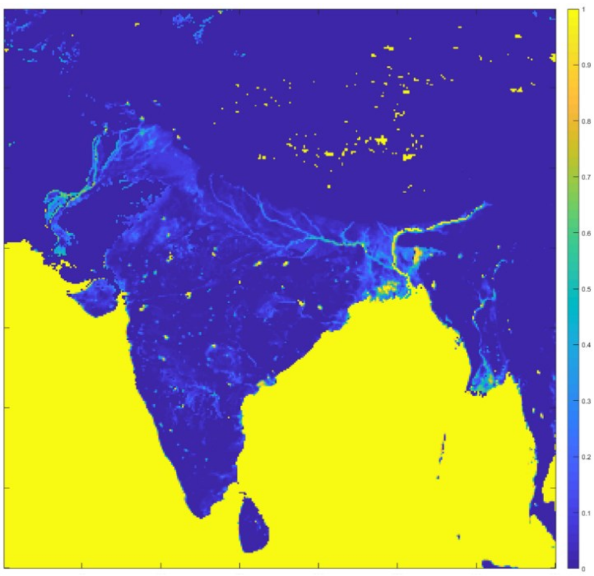

Figure 3. Mean flood index map for the study period 2013-2020

However, regions under dense vegetation cover, like forests of Northeast India and Western Ghats, hardly show any inundated areas due to influence of vegetation on MPDI values. Due to coarse resolution of AMSR2 data, coastal regions show up as partially flooded as both sea water and coastal land is present within the same pixel. One feature of this flood index product is that it can also pick up inundated agricultural fields, which are typically associated with rice cultivation. This is prominent in Punjab and Haryana regions during May-June (Singh et al., 2017) and appear as inundated pixels in flood maps.

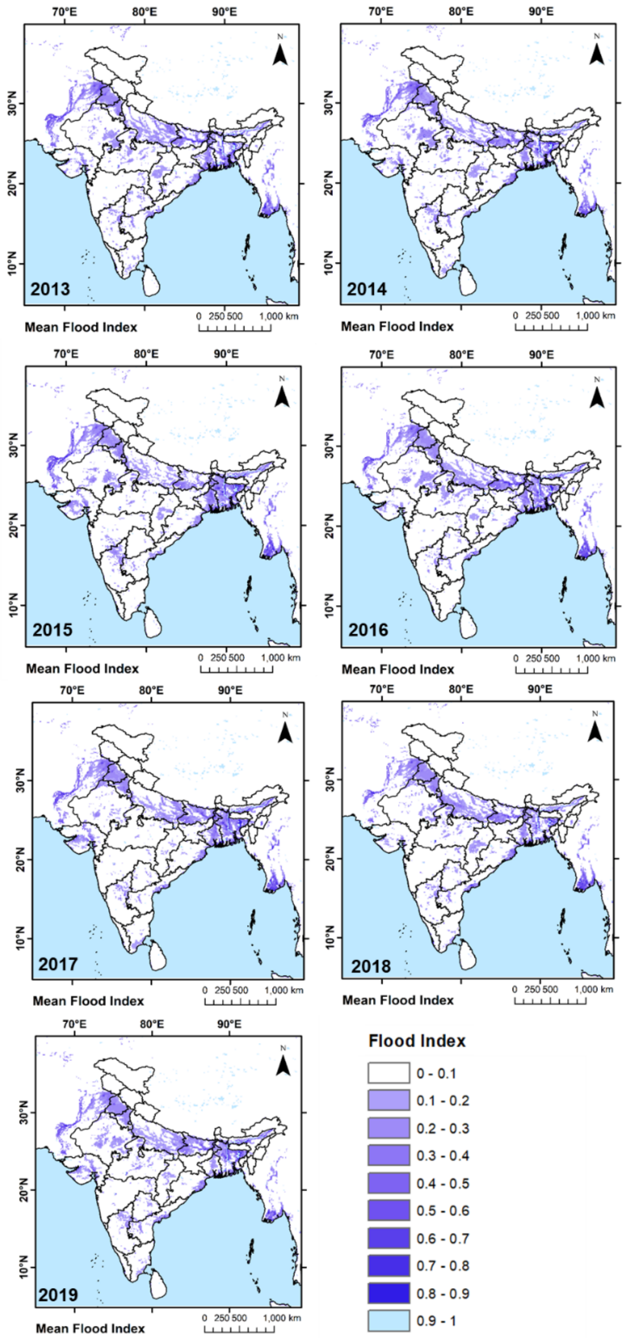

Figure 4. Mean flood index maps for monsoon (JJAS) season during 2013-2019.

Figure 4 shows the mean monsoonal flood index for each season between 2013-2019. Frequently inundated regions of Ganga and Brahmaputra basins are clearly seen along with the agricultural inundation for rice cultivation in

Punjab, Haryana, West Bengal and Chhattisgarh. Regions of Myanmar and Bangladesh that show frequent flooding, including river delta, are represented as flooded in these maps. From Figures 3 and 4 mean flood index maps, it is clear that the flood index described in this study represents frequently flooded regions during monsoon periods. To understand the performance of this technique during localised flood events, we look at the 2-day composite flood index maps for certain extreme events like cyclones. Figure 5 shows the prevalence of flood across the study area for the year 2020. Pixels where flood index is greater than 0.5 are only considered and the total number of days for which index was above this value is shown as prevalence map. This map clearly shows the frequently flooded regions of India and the persistence of flood in that region.

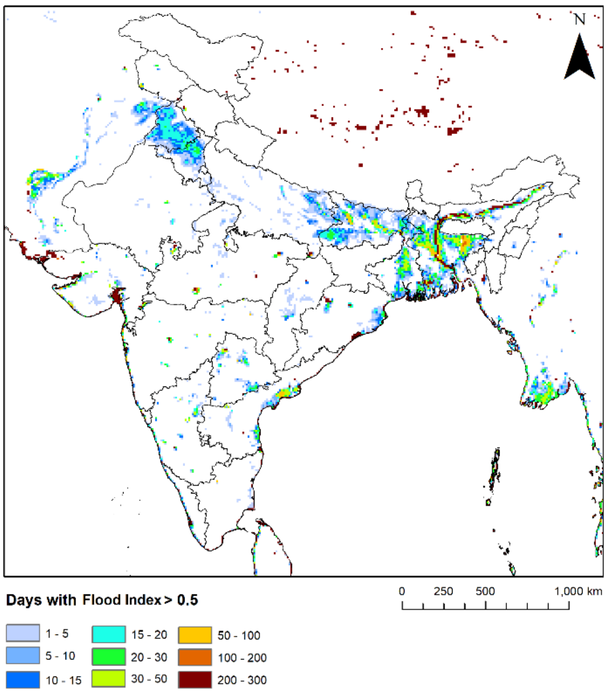

Figure 5. Number of flooding days during 2020 where pixels with flood index greater than 0.5 are considered as flooded.

4.3 Performance of Flood Index during extreme events

Tauktae, an extremely severe cyclonic storm, developed over Arabian Sea and made landfall over Gujarat near Diu on May 17, 2021. Figure 6 shows the 2-day composite flood index map for 18-19 May 2021 which clearly picks up the inundated areas. Heavy rain due to Cyclone Tauktae created flood like situation in many parts of Gujarat including the coastal districts of Amreli and Bhavnagar along with Rajkot, Botad, Ahmedabad and Surat. Effects of Cyclone Tauktae were felt inland, including Northern regions of Madhya Pradesh and parts of Uttar Pradesh as well.

Within a few days after Cyclone Tauktae, a very severe cyclonic storm named Yaas developed over Bay of Bengal and hit the Odisha coast on May 26, 2021. Figure 7 shows the 2-day composite flood index map for 27-28 May 2021 which clearly picks up the inundated areas.

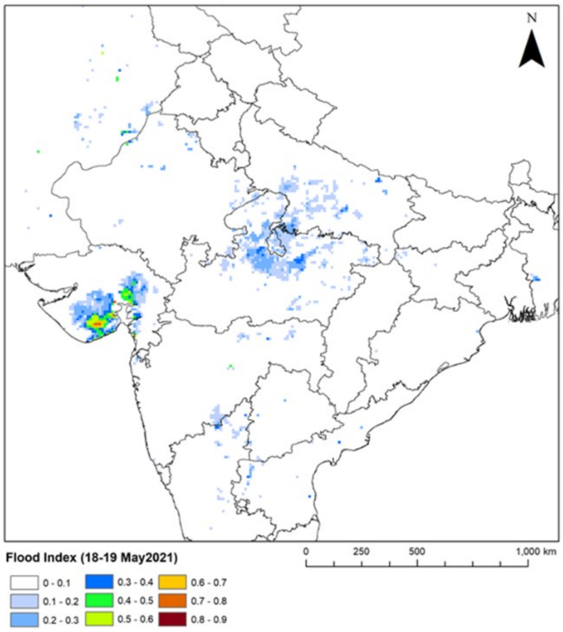

Figure 6. Flood index map for 18-19 May 2021 showing flooded regions due to impact of Cyclone Tauktae over Gujarat and central India.

Heavy rain from Cyclone Yaas created flood like situation in the coastal districts of Orissa and West Bengal. Effect of Cyclone Yaas was observed all the way upto Jharkhand, Bihar and Eastern parts of Uttar Pradesh. Coastal districts of Orissa including Bhadrak, Kendrapara and Balasore saw heavy flooding due to Cyclone Yaas. Patna and its adjoining districts in Bihar also saw flooding due to heavy rains from Cyclone Yaas which continued to batter the region on 26-27 May 2021. Surface flooding map using AMSR2 36 GHz MPDI clearly shows the affected regions of Orissa, Bihar, Jharkhand and West Bengal.

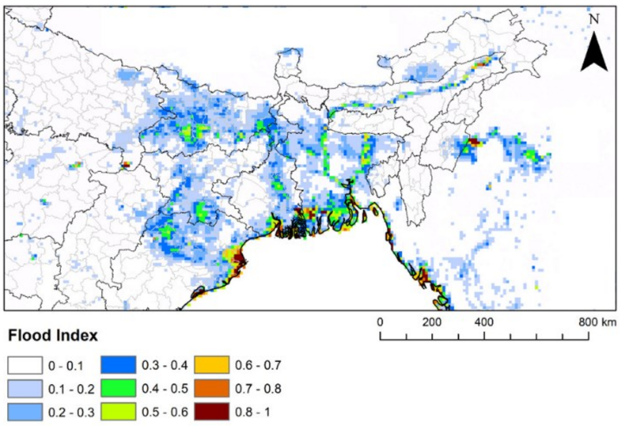

Figure 7. Flood index map for 27-28 May 2021 showing flooded regions due to impact of Cyclone Yaas over Odisha and Eastern India.

Figures 5 and 6 clearly show the capability of 36.5 GHz BT data in capturing signal of surface flooding and the corresponding flood index product in representing the severity of flooding at a regional scale. Multiple observations with 2-day repetivity can help us better understand the progression of flood wave across any catchment and help in preparedness and mitigation efforts during severe flood events.

5. Conclusions

In this paper, we present a novel technique for detecting surface flooding using AMSR2 Brightness Temperature at 36.5GHz. MPDI based flood index described in this study was able to detect inundated areas across India with two-day repetivity. Desert and barren land regions were masked out due to their high polarisation ratios. Agricultural fields of Punjab and Haryana that are inundated for rice cultivation were also picked up by this method. Performance of flood index was evaluated during flood events caused by Cyclone Tauktae and Yaas and showed good match with SAR based flood maps, although at a coarser resolution. Higher spatial coverage and two-day repetivity are two major strengths of this method for flood detection over conventional techniques.

Acknowledgements
This work was carried out under SARITA program of Land Hydrology Division, EPSA, SAC. The authors wish to thank Shri N M Desai, Director, SAC and Dr I M Bahuguna, Deputy Director, EPSA for their guidance and support. AMSR2 Brightness Temperature data from JAXA and MODIS LULC data from NASA are thankfully acknowledged.

References

Brakenridge G.R., S. Cohen, A. J. Kettner, T. de Groeve, S. V. Nghiem, J. P. M. Syvitski and B. M. Fekete (2012). Calibration of Satellite Measurements of River Discharge Using a Global Hydrology Model, 475, 123-136.

Brakenridge G.R., S. V. Nghiem, E. Anderson and R. Mic (2007). Orbital microwave measurement of river discharge and ice status. Water Resources Research, 43, W04405, doi:10.1029/2006WR005238.

Cho E., C. H. Su, D. Ryu, H. Kim and M. Choi (2017). Does AMSR2 produce better soil moisture retrievals than AMSR-E over Australia? Remote Sensing of Environment, 188, 95-105.

Dai L., T. Che, J. Wang and P. Zhang (2012). Snow depth and snow water equivalent estimation from AMSR-E data based on a priori snow characteristics in Xinjiang, China. Remote Sensing of Environment, 127, 14-29.

Fung A. K. (1994). Microwave scattering and emission models and their applications. Norward M. A: Artec House.

Gupta P.K., R. Pradhan, R. P. Singh and A. Misra (2019). Scatterometry for land hydrology science and its applications. Current Science, 117(6), 1014-1021.

Kazumori M., T. Egawa and K. Yoshimoto (2012). A retrieval algorithm of atmospheric water vapor and cloud liquid water for AMSR-E, European Journal of Remote Sensing, 45(1), 63-74.

Li Y., K. Zhao, X. Zheng and J. Ren (2013). Analysis of microwave polarization difference index characteristics about different vegetation types in northeast of China. International Conference on Remote Sensing, Environment and Transportation Engineering, RSETE 2013. 10.2991/rsete.2013.9.

Njoku E. G., T. J. Jackson, V. Lakshmi, T. K. Chan and S. V. Nghiem (2003). Soil moisture retrieval from AMSR-E, IEEE transactions on Geoscience and remote sensing, 41(2), 215-229.

Paloscia S., P. Pampaloni and E. Santi (2018). Radiometric microwave indices for remote sensing of land surfaces. Remote Sensing, 10(12), 1859.

Shi L., Y. Qiu, J. Shi and S. Zhao (2015). Atmospheric influences analysis in passive microwave remote sensing. 2015 IEEE International Geoscience and Remote Sensing Symposium (IGARSS), 2334-2337, IEEE.

Sheffield J., E. F. Wood, M. Pan, H. Beck, G. Coccia, A. Serrat- Capdevila and K. Verbist (2018). Satellite remote sensing for water resources management: Potential for supporting sustainable development in data- poor regions, Water Resources Research, 54(12), 9724-9758.

Singh D., P. K. Gupta, R. Pradhan, R., A. K. Dubey and R. P. Singh (2017). Discerning shifting irrigation practices from passive microwave radiometry over Punjab and Haryana, Journal of Water and Climate Change, 8(2), 303-319.

Spreen G., L. Kaleschke and G. Heygster (2008). Sea ice remote sensing using AMSR- E 89- GHz channels, Journal of Geophysical Research: Oceans, 113(C2).

Ulaby F.T., P. P. Batlivala and M. C. Dobson (1978). Microwave backscatter dependence on surface roughness, soil moisture and soil texture, Part-I: Bare soil, IEEE Transactions on. Geoscience Electronics, GE-16, 286-295.

Ulaby F. T., R. K. Moore and A. K. Fung (1986). Microwave Remote Sensing, from Theory to Applications. Vol. 3, Deedham M. A.: Artech House.

Ulaby F. T., R. K. Moore, R. K. and A. K. Fung (1981). Microwave Remote Sensing, Fundamanetals and Radiometery. Vol. 1, Deedham M. A.: Artech House.

Zheng W., D. Sun and S. Li (2016). Coastal flood monitoring based on AMSR-E data. 2016 IEEE International Geoscience and Remote Sensing Symposium (IGARSS), 4399-4401, IEEE.

Flood assessment in the Brahmaputra River using microwave remote sensing and hydrological modelling

Amit Kumar Dubey* and R. P. Singh
Space Applications Centre, Ahmedabad, India
*Email: a_dubey@sac.isro.gov.in

(Received: Aug 28, 2021; in final form: Oct 06, 2021)

Abstract: Floods in the Brahmaputra River are very frequent and inundate large area of flood-plains. To assess the real time flood inundation, Synthetic Aperture Radar (SAR) observations are very crucial during the monsoon season. To understand and assess the flood conditions in the Brahmaputra River, a flood event in the year 2020 is selected for this study. To estimate the flood discharge hydrograph, WRF-Hydro model simulation is used. In this study, in synchronous Sentinel-1 SAR images are used to extract the flood inundation at middle reach of the Brahmaputra River. Flood inundation due to high flood discharge was delineated using logarithm of cross polarization (VH) ratio. The flood discharge during the flood event with high discharge (~50,000 m^3/sec) simulated through WRF-Hydro model and in-synchronous SAR images are found to be an effective combination for real-time flood assessment and modelling.

Keywords: Flood assessment, Hydrological modelling, WRF-Hydro

1. Introduction

Floods are widely occurring natural disaster worldwide, which affect the all aspects of human life (Subyani et al. (2017) and Serinaldi et al. (2018)). Rapidly warming climate and urbanization are one of the major factors behind large scale floods. (Apurv et al. (2015), Su et al. (2016), and Miller and Hutchins (2017)). Understanding of flood characteristics is import to mitigate the flood disaster effects in the flood-plain regions. Annual flooding in the Brahmaputra River is major concern for Assam, India and Bangladesh. Each year North eastern region receives very high intensity of rainfall starting with pre-monsoon rain spells. Different tributaries of the Brahmaputra also carry large amount of river discharge, therefore congestion of flow between rivers also inundate large region during high flow conditions. The Brahmaputra River originates from Tibet and flows through India and Bangladesh. It finally drains in to Bay of Bengal. Floods in the Brahmaputra not only affect large population it also submerges huge area of agriculture land and seriously affect the livelihood of millions of people. More intense rain and frequent flood events are predicted in the Brahmaputra River using climate change projections (Apurv et al. 2015 and Ghosh and Dutta 2012). The future projections

The Brahmaputra is large transboundary river with dynamic complex morphology. Each year it reshapes the river patterns due to high influx of sediment from upstream catchment (Karmaker et al. (2017) and Chembolu and Dutta (2018)). During the monsoon season the basin remains covered from clouds, therefore there is limitation in use of optical remote sensing. However, microwave SAR images provide better alternative for flood inundation mapping during monsoon season, due to its capability to see through clouds. Sentinel-1 satellite generate multi-temporal images for a region with 12-day repeat cycle with 1 satellite and 6-day repeat cycle with 2 satellites. It provides continuous coverage during the monsoon season, which makes it suitable candidate to monitor long duration floods in the Brahmaputra River.

Kaziranga National Park is one of the highest flood prone zone in the Brahmaputra river valley. It inundates each year as flood waves pass through the river. The floods in the year 2020 also inundates large region of Kaziranga National Park, which is diverse ecosystem and vulnerable to each year floods.

2. Study Area and Data

The Brahmaputra River originates from Tibet and travel through India and Bangladesh drains into the Bay of Bengal. It is one the major river system in the world. Its total length is 2900 km in which 918 km is in the India and 337 km in the Bangladesh. The rainfall pattern in the North Eastern part of India is very dynamic with average annual rainfall of 2300 mm over Assam (Singh et al. (2004)). The Brahmaputra is one of the highest flowing river of India with multiple flood waves within the monsoon season. The hydrograph varies from average lean flow of 4420 m^3s^{-1} and average flood flow of 51156 m^3s^{-1} with an average of 6 flood waves passing annually (Singh et al., 2004; Karmaker and Dutta (2010)). The Brahmaputra River basin is very large (Figure 1) and has varying river bed slope and river flow width from upstream to downstream of the river. The average bed slope is found in the range of 10^{-4} with braided belt width ranging between 2 km to 18 km (Goswami (1985)). The river has very fine bed material with highly morphologically dynamic features such as active bank erosion, river bed migration and sand bar deposition/erosion (Khan and Islam (2003), Sarma (2005), Sarker et al. (2014), and Chembolu and Dutta (2018)).

In this study, we have used Global Satellite Mapping of Precipitation (GSMaP) precipitation data for WRF-Hydro model simulations. GSMaP-gauge product version-7 which is calibrated with in-situ data is used for flood discharge simulations. Meteorological forcing for the WRF-Hydro was taken from 24 hr operational WRF forecast provided by Meteorological & Oceanographic Satellite Data Archival Centre (MOSDAC) at Space Applications Centre, Ahmedabad. Meteorological forcing consists air temperature (T2D), near-surface wind speed component u (U2D) and v (V2D), specific humidity (Q2D) and shortwave radiation (SWDOWN), longwave radiation (LDOWN). Microwave images was used from Sentinel-1 satellite, which provide dual-polarization data primarily in VV and VH mode.

3. Methodology

In this study, we have used SAR images from Sentinel-1 satellite and an uncoupled WRF-Hydro model to study a flood event in the Brahmaputra River. The model is equipped with different terrestrial physics options such as overland flow, subsurface, and channel flow for discharge estimation. To generate daily discharge hydrograph WRF daily weather forecast was used as a WRF-Hydro model forcing. The model was simulated for the period of year 2013-2020 with calibration and validation on year 2018 and 2019, respectively. The details of model set-up, calibration and validation is documented in Dubey et al., 2021. The model performance was statistically satisfactory. Sentinel-1 satellite microwave images were used to extract flood inundation region for the region near Kaziranga National Park. Microwave satellite images of cross-polarization were used in identification of flood inundation after the flood event (Figure 2). In this study we have used VH polarization instead of VV polarization for flood extraction. VV polarization is very sensitive to surface roughness characteristics, Hence, we have used amplitude ratio of VH polarization and its logarithm to identify the region of changes. The ratio of cross polarization (VH) for post and pre flood event highlighted the changes due to flood event.

4. Results and Discussion

The extreme flood event (Figure 4 to Figure 7) occurred in the month of July 2020 was simulated using WRF-Hydro model and it was found that it inundated large flood-plains. The simulated discharge revealed that the peak discharge was about 50,000 m^3/sec at Guwahati for the Brahmaputra River. In synchronous satellite images of Sentinel-1 satellite were also analysed for the same period.

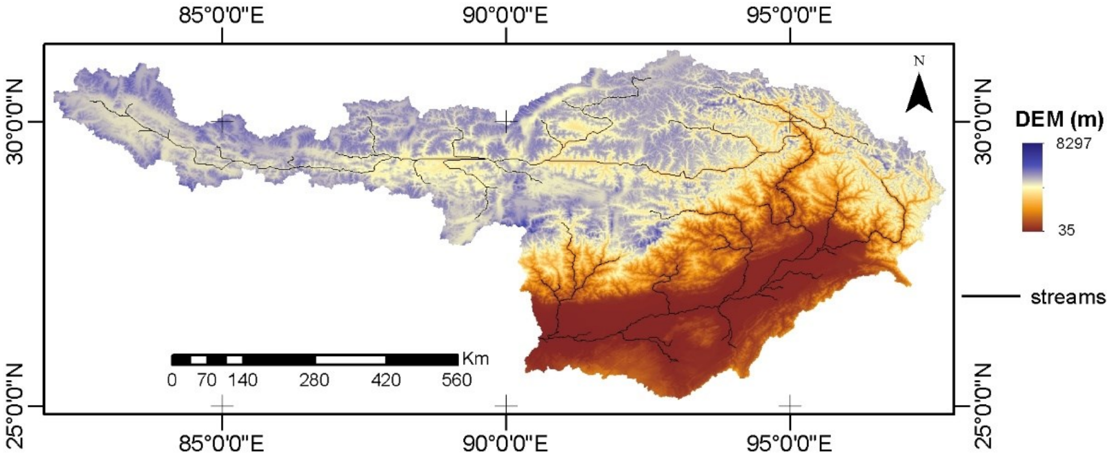

Figure 1. Study area showing drainage network, topography of the Brahmaputra River.

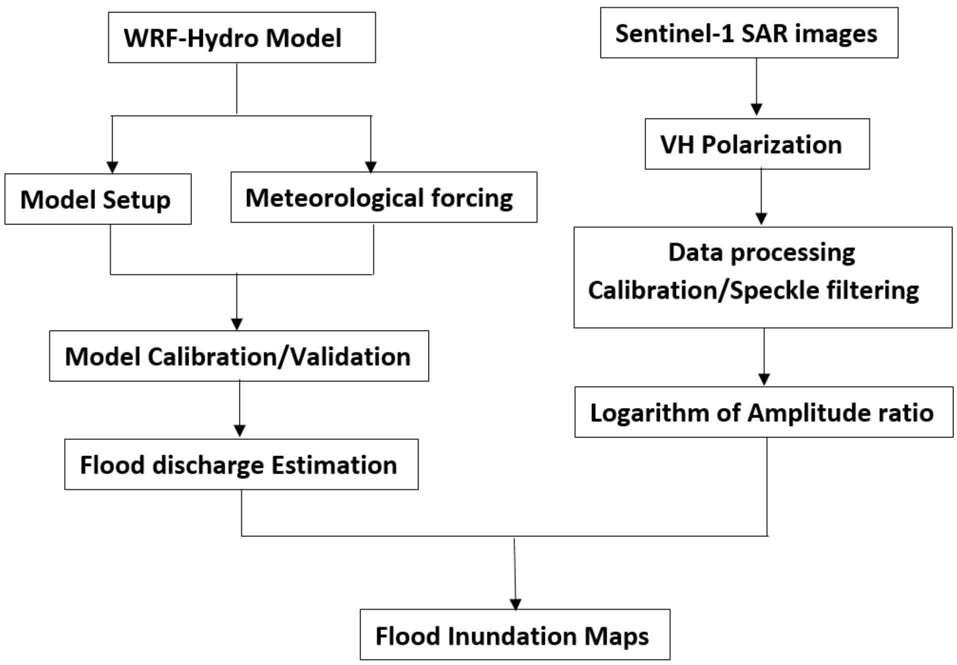

Figure 2. Flow chart showing the methodology adopted in this study.

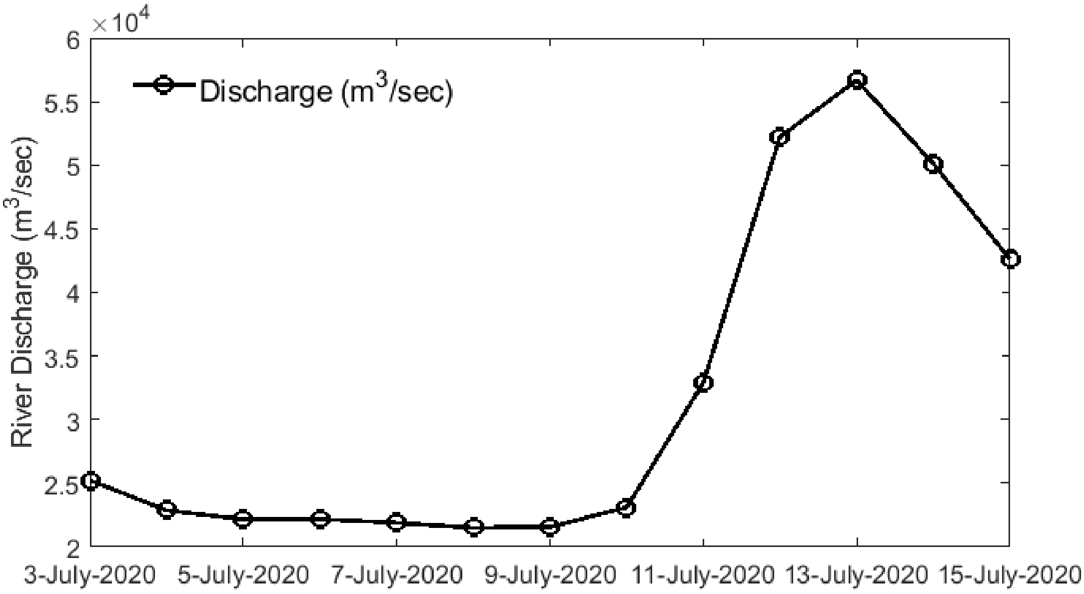

Figure 3. WRF-Hydro simulated discharge hydrograph for the flood event from 03-15 July 2020 in the Brahmaputra River.

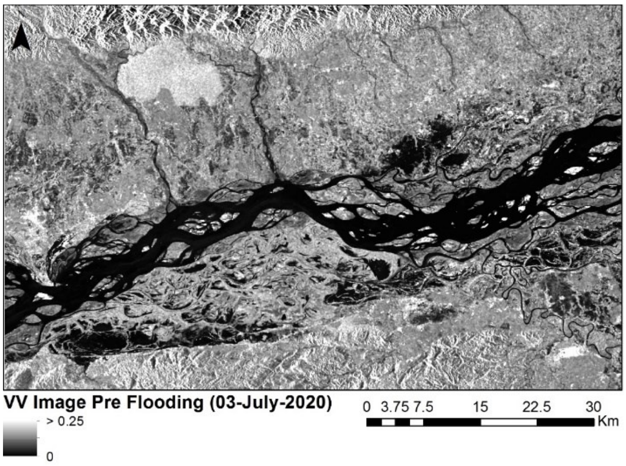

Figure 4. Sentinel-1 microwave satellite image of VV polarization prior to flood event (03-July-2020).

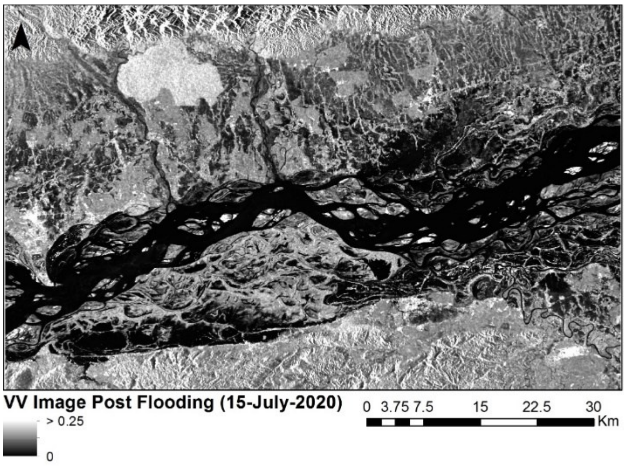

Figure 5. Sentinel-1 microwave satellite image of VV polarization after the flood event (15-July-2020).

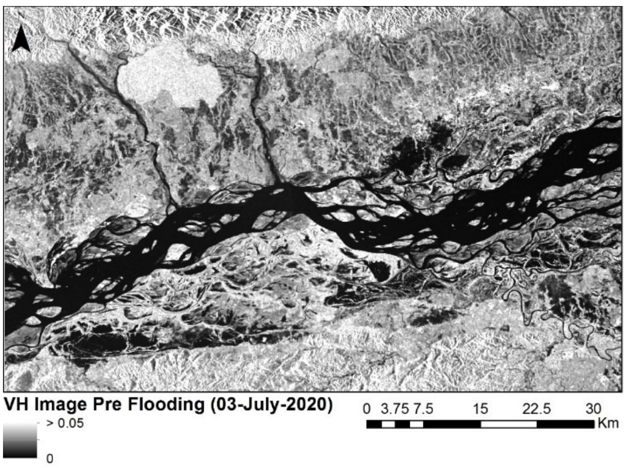

Figure 6. Sentinel-1 microwave satellite image of VH polarization prior to flood event (03-July-2020).

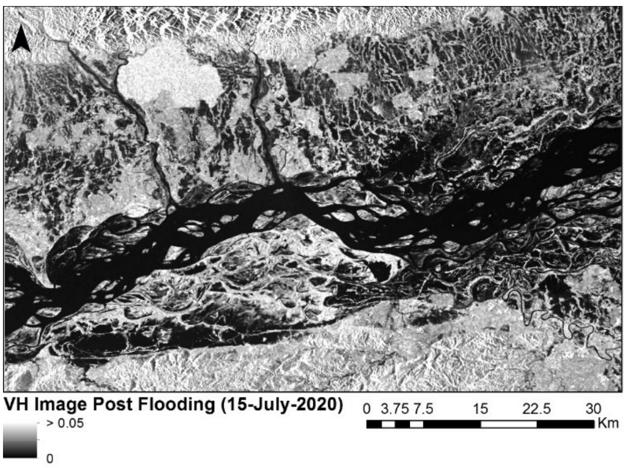

Figure 7. Sentinel-1 microwave satellite image of VH polarization after the flood event (15-July-2020).

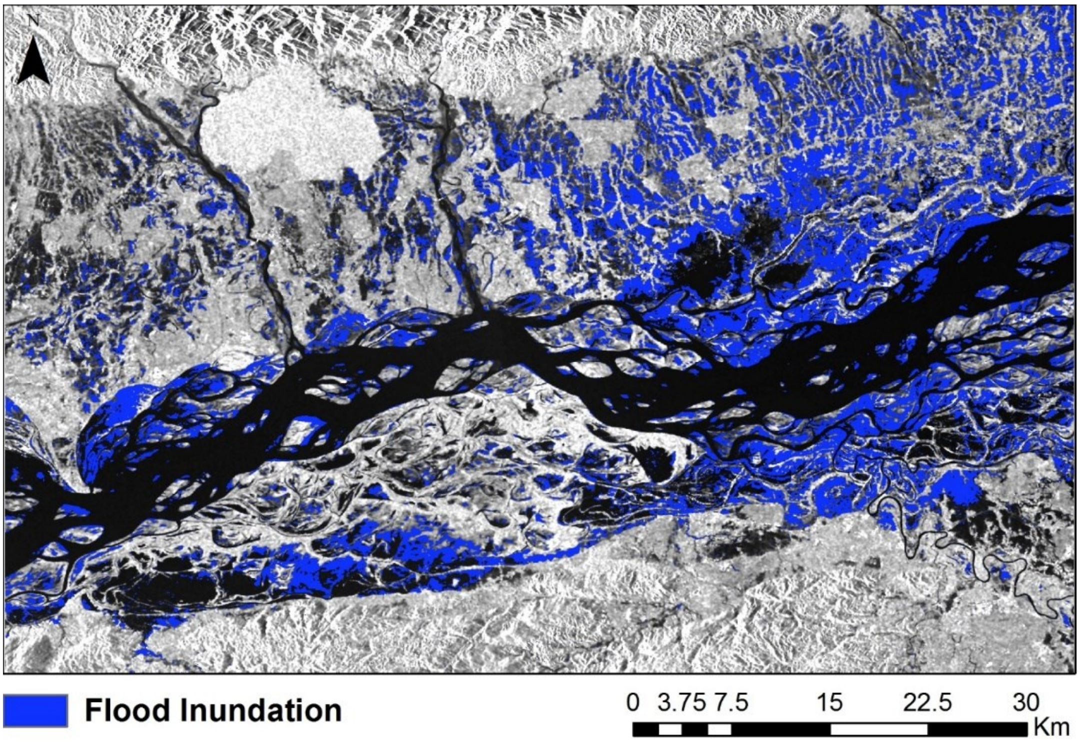

Figure 8. Flood inundation extraction on 15-July-2020 after the flood event in the Brahmaputra River

The cross polarisation (VH) image was found useful in identifying the flood prone region near Kaziranga National Park, Assam, India. The amplitude image of VV polarization was more sensitive towards the surface roughness results in higher return signal. Whereas the VH polarization was found to be better in identifying the water pixels due to lesser return signal form water body. The polarization ratio of VH for pre and post flood event was found to be very effective for identifying the flood inundation due to high flood discharge (Figure 8).

5. Conclusions

Flood discharge estimation using WRF-Hydro model was found to capture the extreme flood event occurred in the month of July 2020. The peak flood discharge during this event was about 50,000 m^3/sec and risen rapidly within the span of few days. The rapid rise in flood discharge created widespread floods in the Brahmaputra River and inundated large region of Kaziranga National Park, Assam. Cross polarization microwave SAR images of Sentinel-1 satellite were used in flood inundation mapping. The logarithm of cross polarization amplitude ratio of VH found to be effective technique in extraction of flood inundation region. The flood discharge during the flood event with high discharge (~50,000 m^3/sec) simulated through WRF-Hydro model and in-synchronous SAR images were found to be an effective combination for real-time flood assessment and modelling.

Acknowledgements
Authors express their gratitude towards Director Space Applications Centre (ISRO), Ahmedabad. We also extend our thanks to the Deputy Director (EPSA) for encouragement and motivation for this study.

References

Apurv T., R. Mehrotra, A. Sharma, M. K. Goyal, and S. Dutta (2015). Impact of climate change on floods in the Brahmaputra basin using CMIP5 decadal predictions. Journal of Hydrology, 527, 281–291.

Chembolu V., and S. Dutta (2018). An entropy based morphological variability assessment of a large braided river. Earth Surface Processes and Landforms, 43, 2889–2896.

Dubey A. K., P. Kumar, V. Chembolu, S. Dutta, R. P. Singh, and A. S. Rajawat, (2021). Flood modelling of a large transboundary river using WRF-Hydro and microwave remote sensing. Journal of Hydrology, 598, 126391.

Ghosh S., and S. Dutta (2012). Impact of climate change on flood characteristics in Brahmaputra basin using a macro-scale distributed hydrological model. Journal of Earth System Science, 121, 637–657.

Goswami D.C. (1985). Brahmaputra River, Assam, India: Physiography, basin denudation, and channel aggradation. Water Resources Research, 21, 959–978.

Karmaker T., and S. Dutta (2010). Generation of synthetic seasonal hydrographs for a large river basin. Journal of Hydrology, 381, 287–296.

Karmaker T. and S. Dutta (2011). Erodibility of fine soil from the composite river bank of Brahmaputra in India. Hydrological Processes, 25, 104–111.

Karmaker T., H. Medhi, and S. Dutta (2017). Study of channel instability in the braided Brahmaputra River using satellite imagery. Current Science (00113891) 112.

Khan N.I. and A. Islam (2003). Quantification of erosion patterns in the Brahmaputra–Jamuna River using geographical information system and remote sensing techniques. Hydrological Processes, 17, 959–966.

Miller J.D. and M. Hutchins (2017). The impacts of urbanization and climate change on urban flooding and urban water quality: A review of the evidence concerning the United Kingdom. Journal of Hydrology: Regional Studies, 12, 345–362.

Singh V., N. Sharma and C.S.P. Ojha (2004). The Brahmaputra basin water resources. 47. Springer Science & Business Media.

Sarker M.H., C.R. Thorne, M.N. Aktar, M.R. Ferdous (2014). Morphodynamics of the Brahmaputra–Jamuna River, Bangladesh, Geomorphology, 215, 45–59.

Sarma J. (2005). Fluvial process and morphology of the Brahmaputra River in Assam, India. Geomorphology, 70, 226–256.

Serinaldi F., F. Loecker, C.G. Kilsby and H. Bast (2018). Flood propagation and duration in large river basins: a data-driven analysis for reinsurance purposes. Natural Hazards, 94, 71–92.

Subyani D., A. Daniels, S. Murray, T. Kirsch (2017). The human impact of floods: a historical review of events 1980–2009 and systematic literature review. PLoS Curr 5, 1–19.

Su F., L. Zhang, T. Ou, D. Chen, T. Yao, K. Tong and Y. Qi (2016). Hydrological response to future climate changes for the major upstream river basins in the Tibetan plateau. Global and Planetary Change, 136, 82–95.

Journal of Geomatics Vol. 15, No. 2, October 2021

Rainfall-Runoff relationship for the Lower Tapi Basin

Aditi Rathod[1*], Amit Kumar Dubey[2], Sanskriti Mujumdar[1] and Nirav Agrawal[1]
[1] Faculty of Technology and Engineering, The Maharaja Sayajirao University of Baroda, Baroda, India
[2]Land Hydrology Division (GHCAG/EPSA), Space Applications Centre, (ISRO) Ahmedabad, India
*Email: aditirathod.a@gmail.com

(Received: Sept 14, 2021; in final form: Oct 06, 2021)

Abstract: Floods are key contributors to the massive loss of lives, property, infrastructure, and public services. Due to climate change and accompanying variability, floods have occurred in places that were previously variability, floods have occurred in places that were previously not considered flood-prone. The purpose of the study is to use SWAT to model rainfall-runoff in the lower Tapi basin from Ukai Dam to Surat City. Surat is the city one of most populated which is located at the mouth of the Tapi River. In the years 1998 and 2006, one of the worst floods occurred. The Rainfall-Runoff relationship for the Lower Tapi Basin was established using the Soil and Water Assessment Tool (SWAT). SWAT a physically based distributed parameter can be used to predict runoff, soil effect, and the impact of land management methods on water. The SWAT model was created for the 1998-2017 baseline scenarios. The SWAT model is calibrated and validated using the SWAT-cup. On a daily time scale, the model was calibrated at the Mandvi gauging site. For auto-calibration and validation, the SWAT-CUP SUFI-2 software was employed. The major objective function was the coefficient of determination (R^2), during Calibration and Validation. Model performance was good in daily calibration and validation, with R2 values of 0.87 and 0.83 respectively. SWAT model was shown to be capable of replicating hydrologic components in the Lower Tapi basin in this study.

Keywords: SWAT Model, SWAT-CUP SUFI-2, Calibration and Validation,

1. Introduction

Floods are by far the most common natural calamity. Flooding is an overflowing of water onto land that is normally dry. Floods affect more than a third of the world's area, affecting around 82 percent of the world's inhabitants (Maxx Dilley et al., 2005). The study region is in the Tapi lower basin, which is downstream of the Ukai dam and leads to Surat city, Surat, where flooding is a natural threat. Surat city had experienced flood in 1998 and 2006. The main reason of flood was a heavy discharge from Ukai dam.

The most important hydrological variable used in water resource studies is runoff. In river basin where there is no gauged station, direct runoff is complicated and tedious. Traditional runoff prediction models necessitate a large amount of meteorological and hydrological data. Many watersheds hydrology models have been developed, but the paucity of spatial data and temporal has hampered their deployment, mostly in poor nations. For estimating high discharge, direct runoff and hydrographs in combination with proper rainfall runoff model Geographical information system (GIS) and remote sensing is an ideal tool. The widespread use of these models has been affected and enhanced by the development of remote sensing techniques and Geographic Information System capabilities.

India is the most diverse country in the world. From culture and tradition, to topography and climate, environment and geography, all has different varieties. Rainfall in different parts of the world varies greatly in strength and distribution. The area's Rainfall-Runoff behavior must be investigated immediately in order to better understand the hydrological phenomena as they change over time and how to affect those changes. Catchment modelling is also essential for estimating various hydrological variables in order to develop effective and safe water structures. For Research hydrologist and Practicing engineers involved in the development and implementation for integrated water resource system Hydrological modelling is an essential and successful mechanism (Schultz, G.A.,, 2001).

1.1. SWAT model

a) Introduction to SWAT

The USDA Agricultural Research Service (USDA-ARS) and Texas a&MAgriLite Research collaborated to create SWAT a public domain model. The model allows the user to study long term consequences and is physically based with easy computational efficiency and employs easily available inputs. This model has been developed in early 1990. SWAT model is continuous in its development process with the passage of time to address the various emerging issues in hydrological modelling. During the course of the development of the model, various tools such as, multiple hydrological response units, auto irrigation and fertilization options, nutrition cycling routine, Bacteria transport routine etc. have been added to the model. With the use of this model, water as well as sediment circulation and can be tested and forecasted. Runoff in urban catchments can be estimated using this model. The entire catchment region has been separated into sub-catchments in order to use the model in a real-world setting. Based on the land use, land cover similarities and soil management techniques the sub catchments are separated into minor Hydrological Response Units (HRU). SWAT's hydrologic component is based on land use, land cover and soil management techniques. The following water balance equation is used to calculate the hydrologic component of SWAT:

$$SW_t = SW_o + \sum_{i=1}^{n}\left(R_{day} - Q_{surf} - E_a - W_{seep} - Q_{gw}\right) \quad (1)$$

Where SW_t is the final soil water content (mmH_2O),SW_o is the initial soil water content (mm H_2O), t is time in days,

R_{day} is amount of precipitation on day i (mm H_2O),Q_{surf} is the amount of surface runoff on day i (mm H_2O), E_a is the amount of evapotranspiration on day i (mm H_2O), W_{seep} is the amount of percolation and by pass exiting the soil profile bottom on day i (mm H_2O), Q_{gw} the amount of return flow on day i (mmH_2O) (Jain et al., 2017)

There are two phases to the hydrology of the basin: land phase and routing phase. The land phase describes the entry of water, sediment, pesticides, and other materials into the channel, whereas the routing phase describes the transport of water, sediments, and other materials from the basin through the drainage network of the basin. Daily humidity, solar radiation, temperature, rainfall, wind speed, and other variables are inputs to the SWAT model. To estimate evapotranspiration, various methods such as Priestly-Taylor, Penman Monteith and Hargreaves are used in the models. For obtaining the better estimation and forecasting of water, sediment circulation etc. from the basin, simulation of hydrological cycle integrating overall water circulation the basin is essential.

b) Evaluation of SWAT Model`

Model performance evaluation can be done to fulfil the following objectives. i) Quantitative aspect, determining the model ability in representing the historical as well future watershed behaviour ii) To suggest the improvement in modelling approach with the consideration of various factors such as adjustment of model parameters, use of additional information, model structure modification, consideration of important spatial and temporal characteristics of watershed etc.iii) Comparison with the past modelling practices/approaches with the current approach(Jaehak Jeong, 2010).The performance of the model has been assessed using a variety of methods.The model parameters are improved after a simulation run of the SWAT model to match the observed and simulated hydrographs at the outlet(Subhadip Kangsabanik et al., 2017).Optimization is done to minimize a scalar quantity known as objective function. The objective function can be defined by the different methods. Most two approach of performance evaluation used are as

(1) Nash-Sutcliffe efficiency (NSE):

To estimate the efficiency of evaluating the performances of hydrological models, Nash and Sutcliffe developed the following equation:

$$NSE = 1.0 - \frac{\sum_{i=1}^{n}\left(\mathrm{o}i^{obs} - \mathrm{P}i^{sim}\right)^2}{\sum_{i=1}^{n}\left(\mathrm{O}i^{obs} - \mathrm{O}i^{mean}\right)^2} \quad (2)$$

The efficiency NSE proposed by the above equation varies from 1 to -∞. The observed time series data mean value would be a better predictor than the model if the efficiency rating was negative. The above method has a key problem in that it calculates discrepancies between observed and anticipated values on a square basis, which causes larger values to be inflated and smaller values to be ignored. As a result of this impact, model performance is overestimated during peak flow and underestimated during lean flow. This model efficiency is not more sensitive for systematic model over or under predictions during lean periods.

(2) Coefficient of Determination(R^2):

R2 is a coefficient that runs from 0 to 1, and it explains the observed dispersion from the values that were simulated. There is no correlation if the value is 0, whereas a value of 1 denotes that the observed and expected values are perfectly correlated (Nina Omani et al., 2007).Major drawback of this method for defining model efficiency is that it only quantifies the dispersion. A model with that systematically over or under predicts all the time may have good correlation even the predictions are wrong.

1.2. Objectives

The study's major goal is to use the Soil and Water Assessment Tool model to investigate the Rainfall-Runoff behaviour of the Lower Tapi basin. To model the discharge using SWAT-CUPs (SWAT-Calibration uncertainty programmes), which employ the sequential uncertainty fitting (SUFI-2) algorithm.

2. Study Area

The Tapi River is the Peninsula's second-largest westward-flowing interstate waterway. It starts in the Multai forest reserve in Madhya Pradesh's Betul district, at an elevation of 752 meters. The river's overall length from source to outfall into the Arabian Sea stretches over 724 kilometers, with the first 282 kilometers flowing through Madhya Pradesh and 54 km forming the state's common border with Maharashtra. It flows across Maharashtra for 228 kilometers before entering Gujarat. The Tapi River flows across Gujarat for 214 kilometers before joining the Arabian Sea at the Gulf of Cambay after passing through Surat.

The Tapi basin is divided into three sub-basins: the Upper Basin (29,430 sq. km) up to the Hatnur confluence of the Purna with the main Tapi, the Middle Tapi Basin (25,320 sq. km) from Hatnur to the Gidhade gauging site, and the Lower Tapi Basin (25,320 sq. km) from the Gidhade gauging site up to the sea (10,395 sq. km). The Lower Tapi basin had maximum rainfall is 1427.45mm while minimum annual rainfall is recorded in year of 1991 is 578.94mm (CWC, March, 2014). The Lower Tapi Basin spans a large region of 4108.90 Sq. km (CWC, March, 2014).

Surat is located in the Lower Tapi Basin, (Figure 1) which runs between the Ukai Dam and the Arabian Sea. One of the worst floods in Surat's history occurred in the years 1998 and 2006. The flood of 2006 is remembered as a huge occurrence that caused a calamity, resulting in the mass demolition of properties worth INR 20 billion.

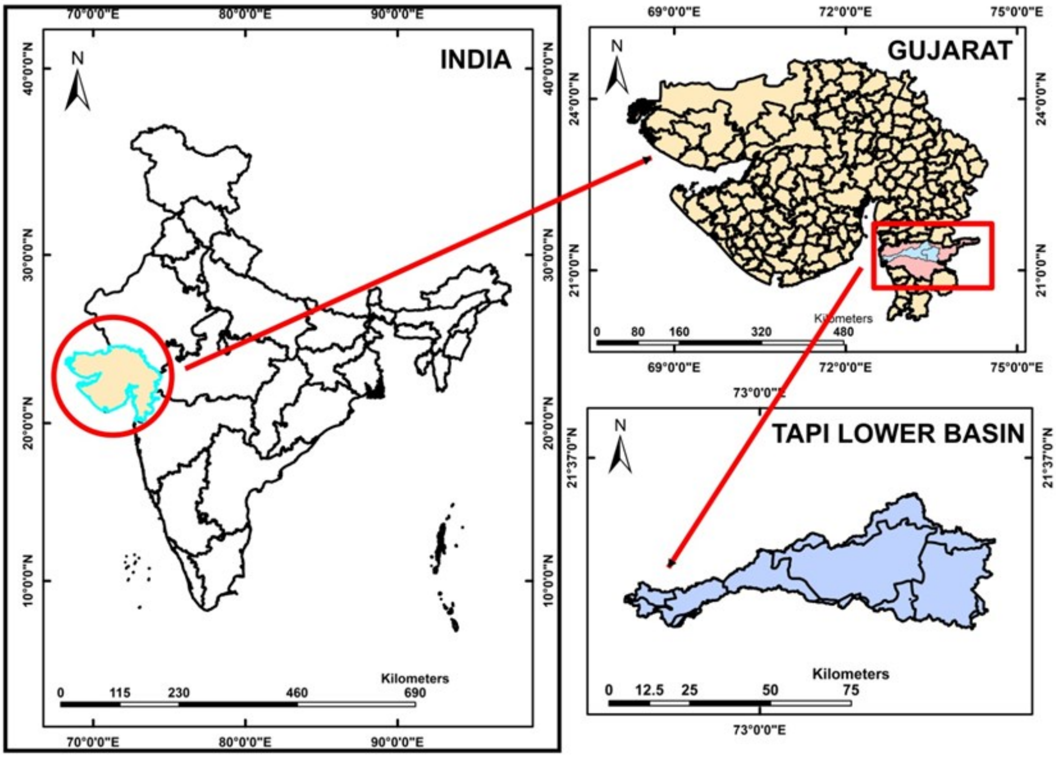

Figure 1. Location Map of Lower Tapi basin

3. Methodology

A high number of geographical and temporal inputs are required by the SWAT. SWAT, as a model that is spread in a semi-distributed manner, must use GIS technologies to process, aggregate, and evaluate this data spatially. As a result, the model was integrated with ArcSWAT for ArcGIS is a free supplement plugin that makes ArcGIS easier to use. The flow chart Figure 2 depicts the SWAT at the basin's outlet; a methodology for runoff modelling has been developed.

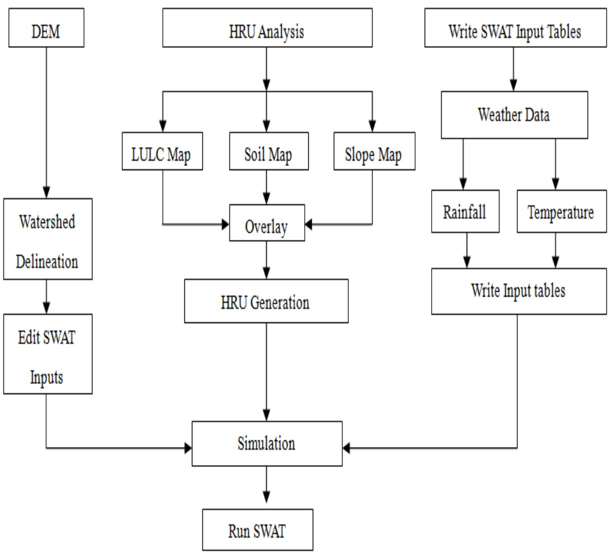

Figure 2. Rainfall-Runoff Modelling Methodology

3.1. Digital Elevation Model (DEM)

A digital elevation model (DEM) is a three-dimensional depiction surface of a terrain derived from elevation data. A digital elevation model (DEM) is a digital depiction of the elevation of the land surface in relation to any reference datum. DEM was taken from the Bhuvan ISRO website. The DEM image has a resolution of 30x30 metres. The DEM is used to define the stream network, longest reaches, and drainage surfaces of the watershed and sub-basins. The DEM was also used to derive channel slope, terrain slope, and reach length are all topographic factors. Figure 3 shows the Digital Elevation Model for Lower Tapi basin.

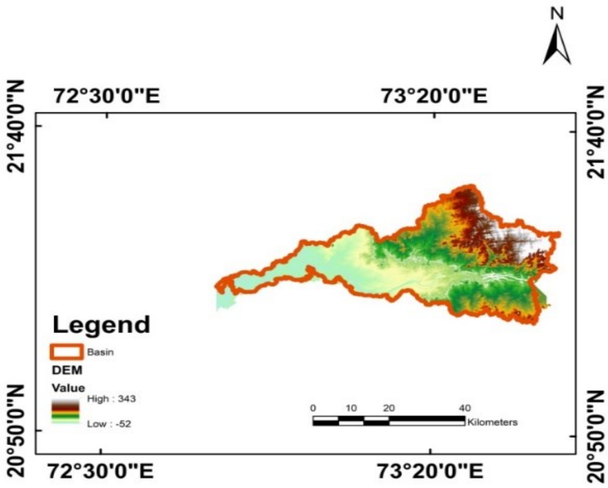

Figure 3. Digital Elevation Model

3.2. Landuse/Landcover classification

The LANDSAT 8 Image was used to create the Landuse data (acquired on December 2020). The data was obtained from the USGS Archive. There are seven bands in the downloaded file. Then, this picture is projected into correct projection using ArcGIS, same as the DEM with the same datum. For image classification the supervised classification technique is use by recognising distinct signatures found in the Tapi lower basin and then to make it compatible with ArcSWAT the image was converted to grid format in ArcGIS. Water, pasture, Agricultural Land-Generic, Mixed Forest, and Residential are among the major classifications. Figure 4 depicts the land use map of the Tapi lower basin, while Table 1 shows the area covered by various land use types.

Table 1. LULC classes in Tapi Basin

SWAT Code	Land use description	Area (ha)	Watershed Area (%)
WATR	Water	3747.4348	2.31
PAST	Pasture	52743.0246	32.52
AGRL	Agricultural Land-Generic	64231.9705	39.60
FRST	Mixed Forest	38126.2247	23.50
URBN	Residential	3347.6122	2.06
	Total	162196.2668	100

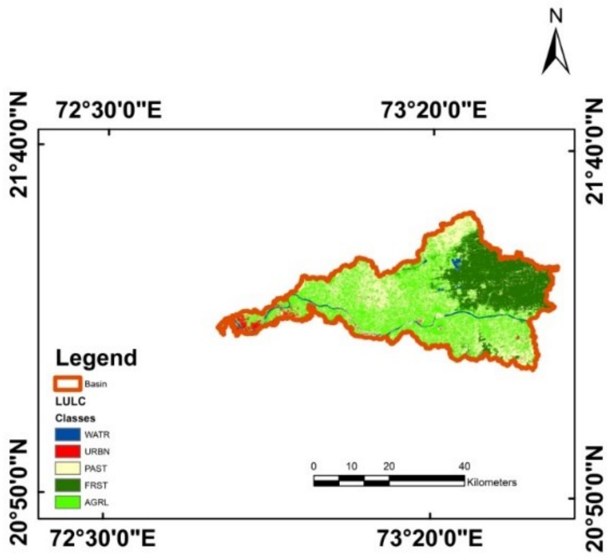

Figure 4. Land Use Map

3.3. Map of the soil

The Food and Agriculture Organization of the United Nations (FAO/UNESCO) provided a soil map with a geographical resolution of1:50,000, 000.00. The soil data from the Tapi Lower Basin has been separated into three groups. Clay loam, loam, and clay are the textures of the soils. Figure 5 depicts a soil map of the Tapi lower basin.

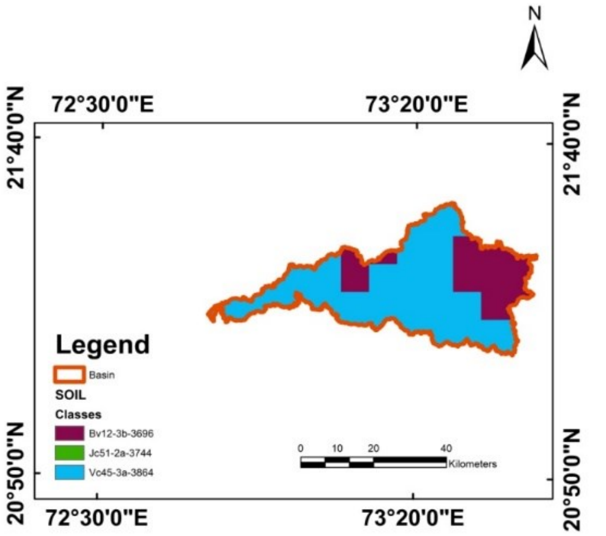

Figure 5. Soil Map

3.4 Hydro meteorological data

For the modelling of numerous physical processes, SWAT requires daily values for solar radiation, relative humidity, precipitation, wind speed, and maximum and minimum temperature. The daily Maximum Temperature, Minimum Temperature and Rainfall data for Lower Tapi basin were provided by State Water Data Centre (SWDC). From 1998 to 2017, 20 years of daily rainfall data and 20 years of daily maximum and minimum temperature data were used in this study area. Figure 6 shows the delineation of sub-basin of Lower Tapi basin.

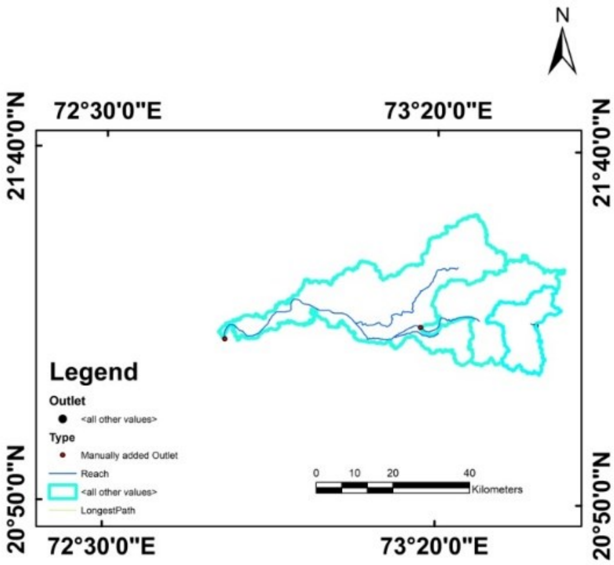

Figure 6. Delineation of sub-basin of Lower Tapi basin

4. Model setup

The SWAT model's whole database has been produced, and the model has been set up for the research area. Using a DEM-based automatic technique, ArcSWAT2012 enables us to define sub-watersheds. The model includes a DEM file. The catchment area's outlet was identified, for the purposes of this investigation, the watershed was defined (Figure 5), and all of the parameters for each subbasin, and calculations were made. The catchment's total size is estimated to be 1621.9627 km2. The research area's minimum and greatest elevations are -50 and 342 metres, respectively. There are three sub-basins in the watershed.

We may import a land use and soil map, assess slope characteristics, and calculate land HRUs for each sub-watershed using SWAT. The land use category identifies the land use layer foe each category, and the soil look up table specifies the type of soil to be represented.

The database was classed into three hydrological soil groups (HSGs): Clay Loam, Clay and Loam, and Clay and Loam. The LULC map has been reorganised into five categories. The slope map has been categorised into three categories: 0 – 10%, 10% – 20%, and 20% – 99%. The land use, soil, and slope data layers were then superimposed. Hydrologic response units (HRUs) have been distributed throughout the basin. A total of 29 HRUs were develops in the Lower Tapi basin. To exclude minor land use, soil, and slope, a 10% threshold has been developed for all land use, soil, and slope classes.

Daily precipitation and temperature data are required by the model. Weather station locations can be loaded into the current project and weather data can be assigned to sub-watersheds using SWAT. Daily precipitation data as well as daily maximum and minimum temperature data from 8 raingauge sites was used from the same years.

The ArcSWAT toolbar's 'Write Input Tables' menu is used to load weather data. This tool enables the users to add weather station sites to their current project and allocate weather data to sub-watersheds. For every kind of meteorological data loaded, one gauge is linked by each sub-watershed. The initial watershed input parameters must be defined before SWAT can be executed. These numbers are derived from defaults or automatically determined depending on the watershed demarcation and land use/soil/slope characteristics. The model was then used to simulate surface runoff.

To achieve the study's goal, the SWAT2012/Arc 2012.10.24 interface was used. SWAT-CUP is a free computer application that can be used for sensitivity analysis, calibration, and validation.

An interface's primary purpose is to connect the input or output of a calibration software and model. Using trial-and-error method Auto calibration and validation were carried out, which required fewer model runs to get the best possible simulation that was closer to the actual values (Davy Sao et al., 2020).

5. Analysis and discussion of results

For the calibration, validation and estimation of the uncertainty of the SWAT model, SWAT-CUP a free software tool is used. The software prefers MCMC SUFI2, GLUE, ParaSol, and PSO procedures. The data was loaded from a SWAT Model text input file, and the SWAT CUP software's SUFI2 algorithm was used to do auto calibration and validation. SWAT-CUP SUFI2 is a calibration and validation software used in hydrological studies and investigation,(Kh. Gorgij, A. Dehvari and M. R. Dahmardeh , 2020). For multi-site and multivariable analysis SUFI2 can be used. The present study and analysis have been done on daily time steps.

The first three years of observed data (1998-2000) were used to warm up the model, and then data from 2001 to 2010 were used to calibrate the model's parameters, with the performance of the calibrated model being evaluated using data from 2011 to 2017. The SUFI-2 iterative procedure will narrow the parameters value after each iteration phase. The simulation in the iteration process was set to 500. The number of iterations can be determined once the statistical coefficient is calculated; the best simulation with the best statistical coefficient result can be displayed. Uncertainties in factors such as the driving variable, the conceptual model, the parameters, and the observed data(Abbaspour et al.,, 2007).In addition to the Coefficient of correlation (R2), Nash-Sutcliff Efficiency (NSE), and RMSE standard deviation ratio, the P-factor and r-factor are employed to know the strength of calibration and uncertainty measurements (RSR)(Abbaspour et al., 2007). The p-factor must be close to 1 and the r-factor should be close to 0 in ideal conditions. When the values of p-factor and r-factor approach acceptable levels, the parameter uncertainties are within the required parameter ranges. The most common error index metric is the root mean square error (RMSE). Equation (3) can be used to determine RSR.

$$RSR = \frac{\sqrt{\sum_{i=1}^{n}(O_i^{obs} - P_i^{sim})^2}}{\sqrt{\sum_{i=1}^{n}(O_i^{obs} - P_i^{mean})^2}} \qquad (3)$$

The coefficient of determination was used as the second assessment criterion (R2). The main objective function was R2. The equation number (4) is used to calculate R2.

$$R^2 = \frac{[\sum_{i=1}^{n}\left(Q_i^{sim} - \overline{Q}_i^{sim}\right)\left(Q_i^{obs} - \overline{Q}_i^{obs}\right)]^2}{\sum_{i=1}^{n}\left(Q_i^{sim} - \overline{Q}_i^{sim}\right)^2 \sum_{i=1}^{n}\left(Q_i^{obs} - \overline{Q}_i^{obs}\right)^2} \qquad (4)$$

Where Q_i^{sim} and Q_i^{obs} represent simulated and observed values and $\overline{Q}_i^{sim}$ and $\overline{Q}_i^{obs}$ show mean simulated and mean observed values.

The Nash-Sutcliffe efficiency criterion was used as the third evaluation criterion (NSE). NSE could be computed using the equation (5)

$$NSE = 1.0 - \frac{\sum_{i=1}^{n}\left(o_i^{obs} - P_i^{sim}\right)^2}{\sum_{i=1}^{n}\left(o_i^{obs} - o_i^{mean}\right)^2} \qquad (5)$$

Table 2. Performance Ratings for Statistical Parameters

Indices	R^2	NSE	RSR
Range	0 to 1	-∞ to 1	0 to ∞
Optimal Value	1	1	0
Satisfactory Value	>0.5	>0.5	≤0.7

SWAT model calibration and validation

In SWAT model, to reduce the discrepancy between the observed and simulated daily, monthly and yearly stream flow, as well as to correspond anticipated values with an acceptable degree of fit, model calibration was performed(A. van Griensven et al., 2005).

The model's parameters were calibrated using observed data from 2001 to 2010, with the most sensitive parameters, such as the SCS runoff curve number (CN2.mgt), base flow alpha factor (ALPHA BF), groundwater delay factor (GW DELAY.gw), and threshold water depth in shallow aquifer required for return to occur, being adjusted (GWQMN.gw).
The ability of a model to mimic hydrological activity in the study area is determined by comparing model simulated values to observed values (Haan et al., 1982). To simulate daily flow data, the SUFI-2 algorithm's SWAT-CUP software was utilized for auto calibration and validation. The SWAT CUP software's SUFI2 algorithm produces visual comparisons as well as statistical criteria such as coefficient of determination (R2), Nash-Sutcliffe Efficiency (NSE) and RMSE- observations standard deviation ratio (RSR).

The overall qualitative visual match, like peak matching, overall agreement in hydrograph characteristics and recession tendencies are shown by Visual comparison.

Figures 7 and 8 exhibit graphs of observed and model computed runoff for the daily calibration and validation periods, respectively. Few high peaks are underestimated, as seen in the images, and in many cases, there is a distinct difference between observed and simulated flow. The model anticipates high runoff, which is progressively retreating when there is persistent heavy rainfall, indicated by brown circle in Figure 8. This indicates that basin characteristics such as slope play an important role in achieving a hydrological response (82.15 percent area coverage for slopes ranging from 0 to 10%). The red circle indicated the computation of high runoff with high rainfall.

Figure 9 and 10 exhibits correlation graphs between observed and simulated data. For the calibration and validation periods, the R2 values were 0.87 and 0.83, respectively, revealing a very excellent correlation between observed and simulated streamflow data.

Table 3 shows the results of statistical evaluation criteria used to check model performance for daily periods. Based on the performance ratings listed in Table 2, the model's performance can be rated as very good, as shown in these tables.

Table 3. Daily calibration and validation statistical model results

Statistical Parameter	R^2	NSE	RSR
Calibration (year 2001-2010)	0.87	0.86	0.37
Validation (year 2011-2017)	0.83	0.82	0.43

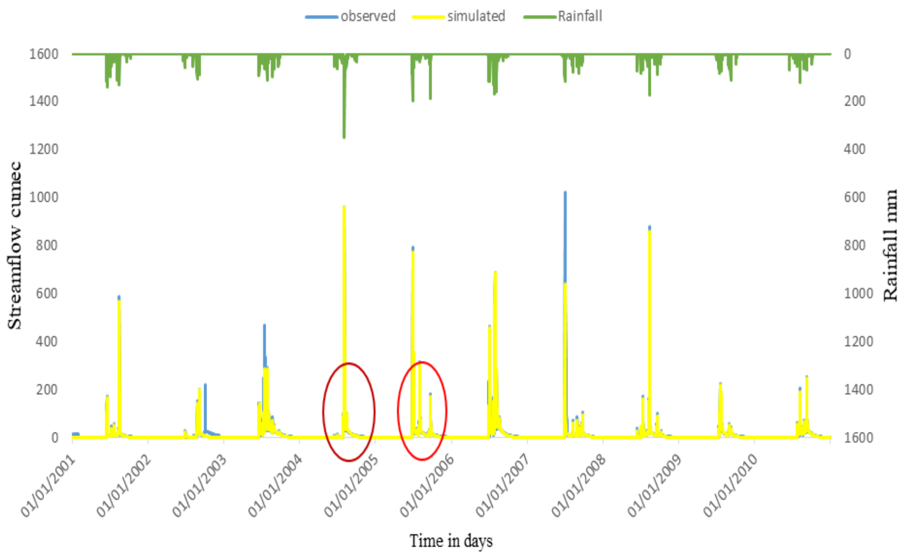

Figure 7. Daily Calibration from 2001 to 2010

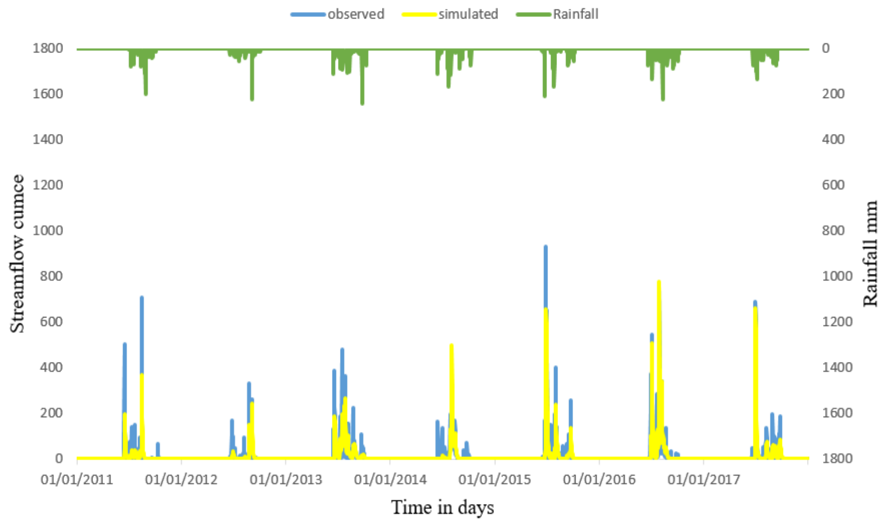

Figure 8. Daily Validation from 2011 to 2017

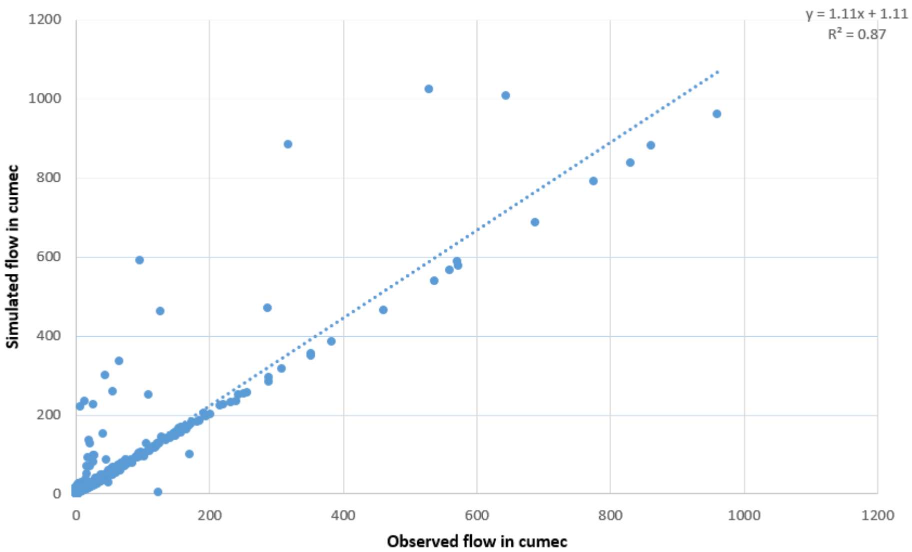

Figure 9. Correlation performance of calibration

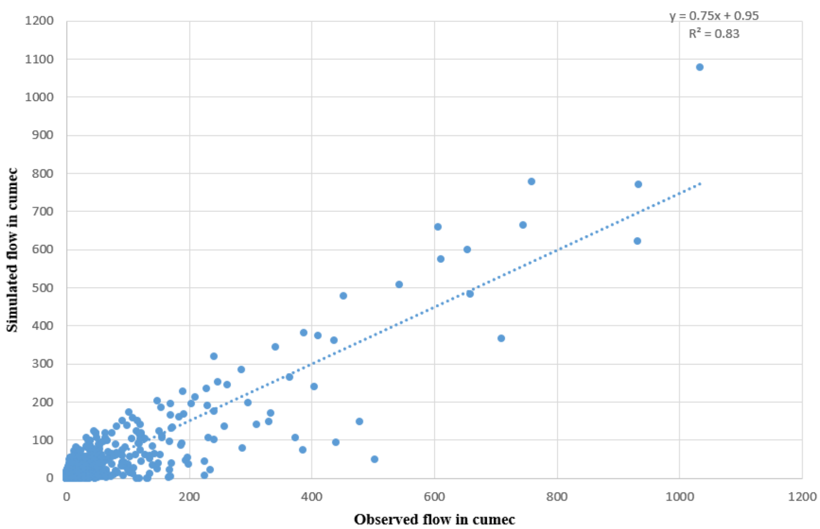

Figure 10. Correlation performance of validation

6. Conclusions

Observed stream flow data were used to calibrate and validate the SWAT model. During the Lower Tapi basin's calibration and validation periods, the SWAT model worked admirably. For calibration and validation, twenty-year discharge data is separated into two equal halves. From 1998 to 2010, the flow was auto-calibrated using daily observed and simulated flows. Validation of flows from 2011 to 2017 is carried out. The calibration result revealed that the calibrated and observed daily flows are in good agreement (R2=0.87, NSE=0.86, RSR=0.37). For validation, the R2 is 0.83, the NSE is 0.82, and the RSR is 0.43.

References

Harka A. E., N. T. Roba and A. K. Kassa (2020). Modelling rainfall runoff for identification of suitable water harvesting sites in Dawe River watershed, Wabe Shebelle River basin Ethiopia, Journal of Water and Land Development, 187-195.

Griensven A. V., T. Mexiner, S.Grunwald, T.Bishop, M.Diluzio and R.Srinivasan (2005). A global sensitivity analysis tool for the parameters of multi-variable catchment models, Journal of Hydrology, 10-23.

Yaduvanshi A., R. K. Sharma, S. C. Kar and A. K. Sinha (2017). Rainfall–runoff simulations of extreme monsoon rainfall events in a tropical river basin of India, Nat Hazards, 90, 844-861.

CWC (2014). Annual report of central water commission.

Kuhn C. (2014). Modeling rainfall-runoff using SWAT in a small urban wetland, FES 724 Watershed Cycles and Processes | spring 2014, 1-19.

Schultz G. A. (2001). Integrated Hydrologic Modeling and GIS in Water Resources Management, Journal of Computing in Civil Engineering, 217-223.

Jeong J., N. Kannan, J. Arnold, R. Glick, L. Gosselink and R. Srinivasan (2010). Development and Integration of Sub-hourly Rainfall–Runoff Modeling Capability within a Watershed Model, Water Resource Manage 24, 4506-4527.

Abbaspour K. C., J. Yang, I. Maximov, R. Siber, K. Bogner, J. Mieleitner, J. Zobrist, R. Srinivasan (2007). Modelling hydrology and water quality in the pre-alpine/alpine Thur watershed using SWAT, Journal of Hydrology, 333, 413– 430.

Gorgij K., A. Dehvari and M. R. Dahmardeh (2020). Uncertainty Analysis of Hydrological Parameters in the Sarbaz Watershed Using the SWAT Model and the SUFI-2 Algorithm, Journal of Hydrosciences and Environment, ISSN: 2345-5608, 43-56.

Sao D., Tasuku K., L. H. Tu, P. Thouk, A. Fitriyah and C. Oeurng (2020). Evaluation of Different Objective Functions Used in the SUFI-2 Calibration Process of SWAT-CUP on Water Balance Analysis: A Case Study of the Pursat River Basin, Cambodia, Water, 1-22.

Dilley M. (2005). Natural Disaster Hotspots a Global Risk Analysis, The World BankHazard Management Unit, 1-132.

Omani N., M. Tajrishy and A. Abrishamchi (2007). Modeling of a River Basin Using SWAT Model and GIS, Riverside Kuching, Sarawak, Malaysia, 510-517.

Shanbor K. and M. Jain, (2017). Rainfall-Runoff Modeling of a River Basin using SWAT Model, International Journal of Engineering Research & Technology (IJERT), ISSN: 2278-0181, 6(12), 293-302.

Kangsabanik S. and S. Murmu (2017). Rainfall-runoff modelling of Ajay River catchment using SWAT model, IOP Conference Series: Earth and Environmental Science, 67, 7th International Conference on Environment and Industrial Innovation, Malaysia, 24-26 April 2017.

Shivhare V., M. K. Goel and C. K. Singh (2014). Simulation of Surface Runoff for Upper Tapi Sub catchment area (burhanpur watershed) using SWATS, The International Archives of the Photogrammetry, Remote Sensing and Spatial Information Sciences, Volume XL-8, 391-397.

Tejaswini V. and K.K. Sathian (2017). Calibration and Validation of Swat Model for Kunthipuzha Basin Using SUFI-2 Algorithm, International Journal of Current Microbiology and Applied Sciences ISSN: 2319-7706 7, 2162-2172.

Coupled Model for Flood Prone Lower Tapi River Basin Integrating Satellite Inputs

Swati S. Patel[1]* and Praveen.K. Gupta[2]
[1]Kalol Institute of Technology and Research Centre, Kalol, 382721, India
[2]Space Applications Centre (ISRO), Ahmedabad, 380015, India
*Email: swatipatel191993@yahoo.com

(Received: Sept 16, 2021; in final form: Oct 6, 2021)

Abstract: Coupled hydrological-hydraulic model is very important and needs to be considered for water resources planning and management. Most of the work has been done on either hydrological aspect or hydraulic behaviour separately using mathematical models. This research work aims to develop and test an integrated modelling system coupling hydrological and hydraulic processes in the lower Tapi basin that incorporates mainstream from Ukai reservoir to the Gulf of Cambay while the length of the Lower Tapi River Basin in Tapi River is estimated as 127 km. The MIKE SHE model is a deterministic fully distributed and physically based hydrological modelling tool has been integrated with MIKE 11, which is a 1D river simulation model. The model also uses a network of regular grids to discretize the horizontal plane of a watershed, and represent the spatial variability of the hydrological process. Coupled MIKE SHE and MIKE 11 model has been parameterized integrating the remote sensing derived hydro-meteorological and biophysical variables to simulate the hydrological water balance and river flows. Model has been calibrated using the satellite altimeter derived and simulated river water levels. Model calibration was satisfactory with coefficient of determination (R^2) 0.97. Tested integrated model simulations were carried out to simulate the evapotranspiration, surface runoff, soil moisture, and stream flows. Major water balance components such as actual evapotranspiration and Surface Runoff were obtained 50.2% and 39.7%, respectively. Further, ET was partitioned into evaporation and transpiration, which were of 37.2% and 62.8%, respectively. Calibrated integrated model would be useful for long-term hydrological simulations for planning and management of water resources in the region.

Keywords: coupled model, MIKESHE, MIKE11, hydrological water balance, river flow simulation

1. Introduction

In order to utilize available water resources efficiently, we need to develop strategies that are based on the thorough study of hydrological balance and its complex nature along with river flows. Therefore, an integrated model needs to be developed to study the 2-D overland flow in the basin as well as river flow simulations. Certain constraints in this model must be accentuated, as well as simulated results should be validated for the given period in terms of observed hydrological parameters. This calibration will allow us to understand the hydrological-hydraulic interactions more efficiently and thoroughly (Zhiqiang et al. 2008). Coupling of hydrological and hydraulic processes enable the simulation of river flow along with hydrological water balance (Clilverd et al., 2016).

Most of the research work carried out independently either on hydrological aspect or hydraulic behaviour using mathematical models. The present research work aims to develop and test an integrated modelling system (coupling hydrological and hydraulic processes) in the lower Tapi basin with satellite data integration. Coupling of both MIKE SHE and MIKE 11 have been used to simulate the hydrological water balance and river flows (Mirela-Alina and Ana, 2015; Clilverd et al., 2016). Integrated model simulations were carried out to quantify water fluxes such as AET, overland flow, soil moisture, stream flows etc. in the Lower Tapi river Basin chosen as study area (Saidislomkhon et al. 2016).

2. Study area and data

Study area for the purpose of this research work is the lower Tapi river basin that incorporates mainstream from Ukai Reservoir to the Gulf of Cambay (Figure 1). The length of the Lower Tapi River is calculated as 127km. Ghala gauging site is considered taking into account availability of satellite altimeter data. Climatic aspects of Ghala are considered to represent the entire lower Tapi Zone. There exists a forest area of 2428 square km in the basin. The coastal plains in Gujarat are composed of alluvial soil with a layer of black soil on the surface. There are few satellite altimeter (SARAL-Altika) tracks for water level estimations and shown in Figure 2.

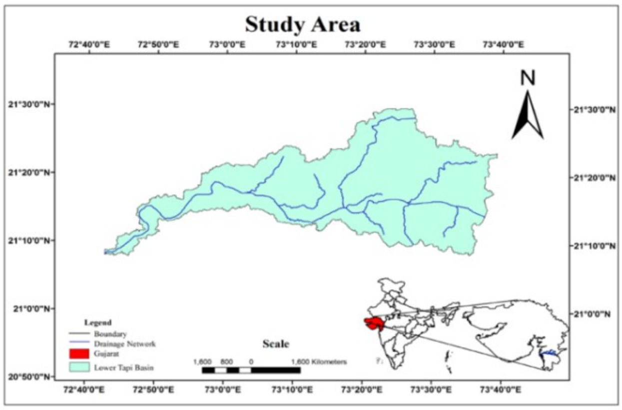

Figure 1. Location of lower Tapi river basin

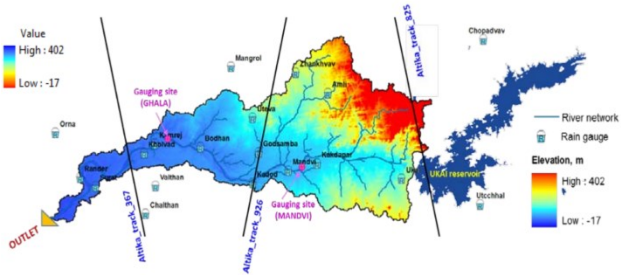

Figure 2. Lower Tapi basin along with altimeter passes and drainage network

List of datasets used for the parametrization of coupled hydrological-hydraulic model, hereafter "coupled model" is presented in Table 1 along with their sources.

Table 1. List of datasets used in the study

Sr. No.	Data	Source
1	DEM	Satellite: SRTM (30 m)
2	LULC	Satellite: AWiFS (Resouresat-2)
3	Soil	NSBSS_LUP
4	Rainfall	NOAA CPC
5	PET (Potential Evapotranspiration)	MODIS PET
6	LAI (Leaf Area Index)	MODIS 4-day composite
7	River cross sections	CWC Tapi division Surat
8	Strickler's roughness (M)	From literature and using LULC (Subramanya,
9	Study area boundary	Delineated using DEM
10	Drainage network	Delineated using DEM
11	Ukai releases	Ukai Division No.1, Ukai
12	Water level for nearby Ghala	SARAL-ALTIKA

3. Methodology

Present study aims for the simulation of water balance and river flows using coupled model in integrated fashion using remote sensing derived hydrological and bio-physical parameters. Coupled model with MIKESHE (DHI, 2007a and 2007b) and MIKE 11 (DHI, 2007) for water balance and river flow simulations has been used. Approach used in this study is presented in Figure 3. All the hydrological inputs (remote sensing, in situ, ancillary data) have been prepared in the GIS environment and transformed into the model pre-defined formats using the GIS-model interfaces. These model inputs have been used for the parameterization of integrated model. Model calibration and validation (DHI, 2007c) have been carried out by comparing the observed/measured water levels with the simulated results through the adjustment of model control parameters such as Strickler's roughness and soil hydraulic conductivities. Simulated results have been analysed to estimate the various water balance components in the lower Tapi basin.

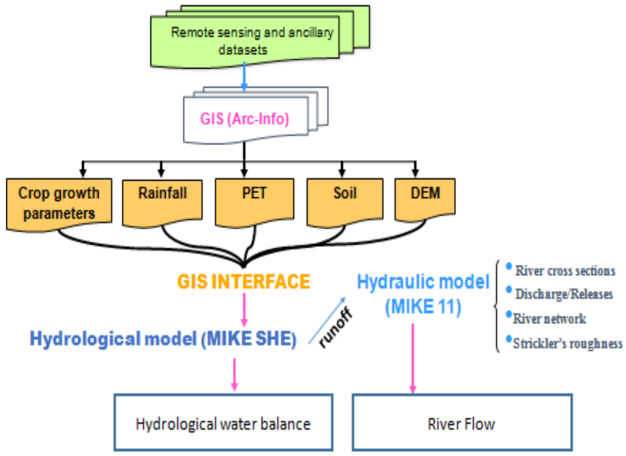

Figure 3. Schematic outline of the coupled model

3.1. MIKE SHE/ MIKE 11 Parameterization

Remote sensing based hydro-meteorological parameters and other ancillary data used in the coupled modelling are presented in the subsequent section.

a) Digital Elevation Model (DEM) (Topography)

Topography is defined by a DEM that describes the elevation of any point in a given area at a specific spatial resolution. In this study, 30m resolution SRTM (Shuttle Radar Topography Mission) DEM of 30m resolution is considered. Maximum elevation in the basin goes upto 386 m whereas minimum value observed to -20 m. Average topography in the basin is 78.1 m with standard deviation of 69.2 m. Figure 4 presents topographical variations in the study area.

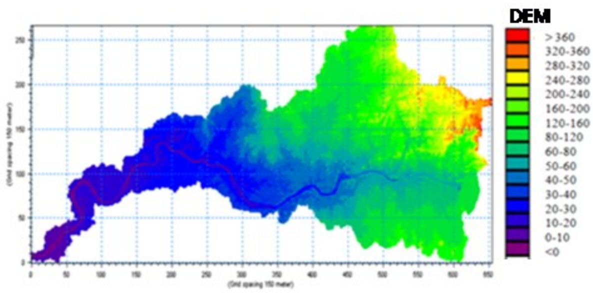

Figure 4. DEM of the study srea

b) Potential Evapotranspiration (PET)

Global potential evapotranspiration product (MOD16) from MODIS is downloaded from Goddard Spcae Flight Centre of NASA. PET is available with 8 day composite and spatial resolution of 1 km. Potential evapotranspiration for a particular day is shown in Figure 5.

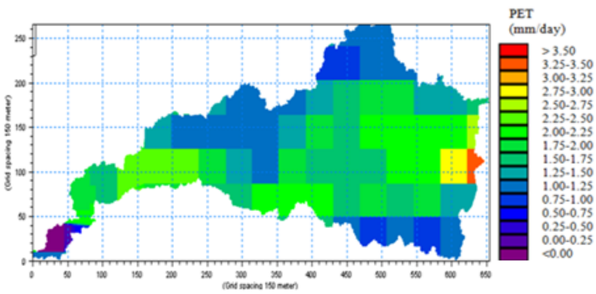

Figure 5. PET for a particular day

c) Precipitation (Rain)

Multi-sensors along with model based rainfall product of climate prediction centre of NOAA is used in the present study. Data is available with daily temporal and 10 km spatial resolutions. Rainfall variations for a particular day is presented in Figure 6.

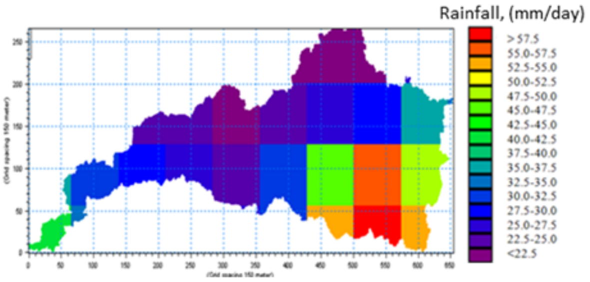

Figure 6. Precipitation for a particular day

3.1.2 Other data used in the study are as follows;

a) Soil

Soil data from National Bureau of Soil Survey and Land Use Planning (NBSS&LUP) is used in the study. There four major soil types in the study area which includes sandy loam (23.7%), loam (16.4%), silty (34.3%) and clayey soils (25.6%). Spatial variability of soil types is present in Figure 7.

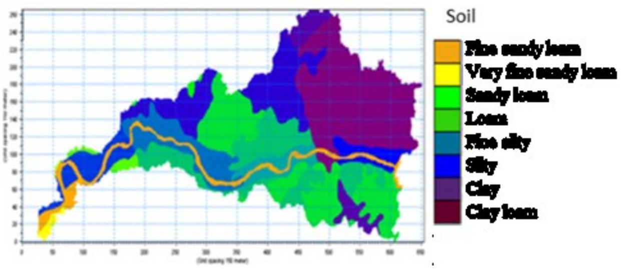

Figure 7. Soil type Map in the study area

b) Land Use Land Cover (LULC)

Advanced Wide Field Sensor (AWiFS) data of Resourcesat-2 is used to classify land cover classes in the study basin. unsupervised classifier ISO data is used for the land cover classifications. Total 6 major land cover classes obtained in the basin and these are water bodies (17.7%), forest (14.8%), agriculture (43.7%), built-up (2.5%) and scrub lands (21.3%). These land cover classes have been used to estimate Strickler's coefficient, which is reciprocal of Mannings, roughness coefficients.

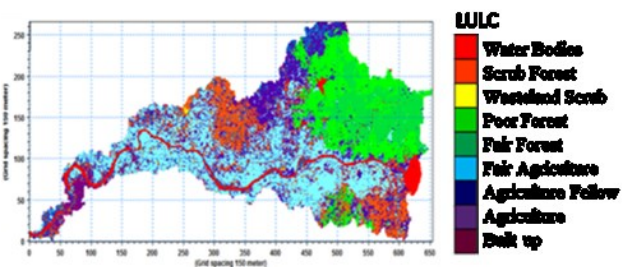

Figure 8. LULC class map in the study area

c) Strickler's coefficient (M)

Initial values of the Strickler's coefficient (M) are assigned based on the land cover classes which are estimated using remote sensing data. Value of M varies from 18-45 in the basin. Mean value of the M in the study area is 30.1 with standard deviation of 7.5. Strickler's coefficient is a model control parameter for the model calibration. Strickler's coefficient variation in the study area is presented in Figure 9.

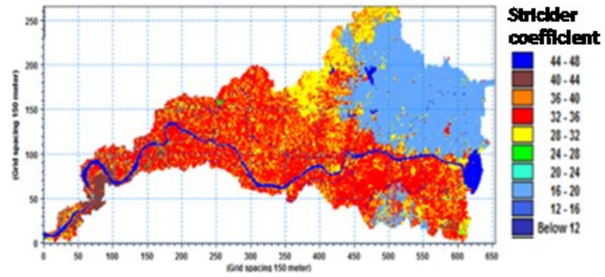

Figure 9. Strickler's coefficient variation in the study area

3.2. River data

3.2.1. River Network

Pre-processing of the DEM is one of the important steps needed to be carried out as a first step in automatic extraction of drainage networks and delineation of basin. Therefore, a hydrologically corrected DEM was prepared and after that based on flow direction matrix and flow accumulations an ordered drainage network was delineated. Subsequently, drainage network was imported to the MIKE-11 model environment. Driange network used in the MIKE-11 model is presented in Figure 10. Red dots are representing locations where cross sections have been defined in the model along the river.

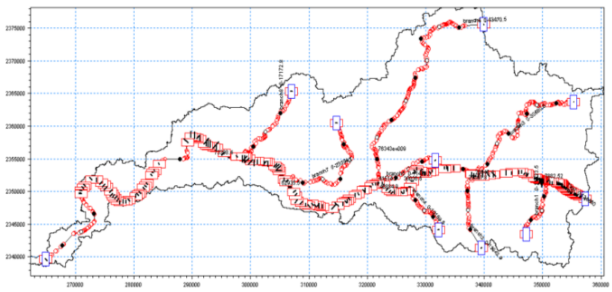

Figure 10. Longitudinal profile of river network as input of MIKE11

3.2.2. Cross Sections

Cross sections data of lower Tapi river basin are collected from the Central Water Commission (CWC) office, Tapi division Surat. A total of 250 plus cross sections data covering major variations along the entire river are collected. Figure 11 illustrate the cross sectional variation of the river from upstream to downstream locations. Depth of river bed varies approximately from 4 m to 30 m along the river from upstream to downstream.

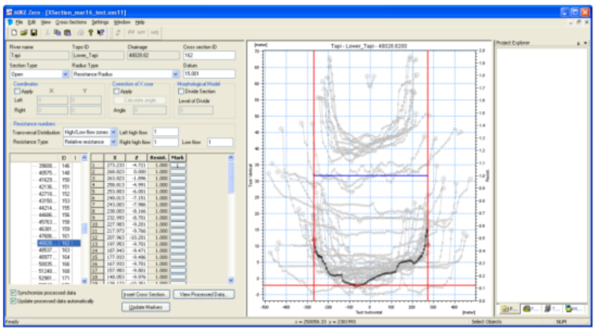

Figure 11. Major cross sections from Upstream to Downstream of the Lower Tapi River Section.

4. Results and discussion

Coupled model, integrated with remote sensing derived hydro-meteorological products, simulations have been carried out for the monsoon season of the year 2013. model simulated results during the study period have been analysed in the spatial and time domain. Analysis of results is presented in the following section.

MIKE SHE Simulated Results

Major water balance components such as Actual Evapotranspiration (AET) and surface runoff are found to be 50.2% and 39.7% of total rainfall, respectively. Fraction of evaporation and transpiration obtained are 37.2% and 62.8% respectively of total evapotranspiration. The following overall water balance estimates are obtained for lower Tapi river basin and shown in Table 2.

Table 2. Total water Balance of lower Tapi basin

Parameters	Values(mm)
Precipitation	1905.0
Evapotranspiration	957.0
-Evaporation	356.0
-Transpiration	601.0
Soil moisture change	185.0
Runoff	756.0

Spatial Domain Results: Different components of the water balance are extracted from MIKE SHE in spatial domain and presented in Figures 12-18.

1. *Average water content (monsoon season average) in the root zone (soil Moisture)*

An average soil moisture map of the basin was prepared by aggregating the daily maps during the monsoon season of 2013. It may be observed that along the river network and in the downstream regions soil moisture is high as compared to regions or flood plains which are away from the river/stream sections. This is because of accumulation of surface runoff in the streams and subsequently in the main river system. In the upstream area especially in the southern region, average soil moisture found to be slightly low. Result of average water content in the root zone is presented in Figure 12.

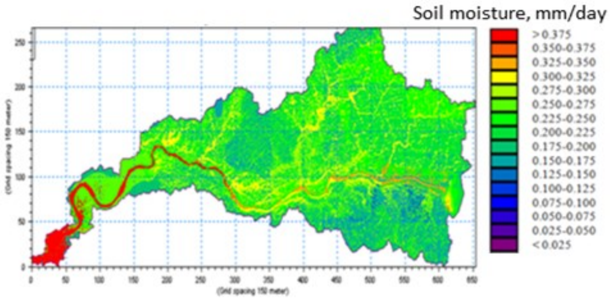

Figure 12. Result of average water content in the root zone

2. *Actual Evapotranspiration (AET)*

Actual evapotranspiration (AET) is summation of evaporation and transpiration losses in a particular location. Mean AET in the basin is 4.1 mm with standard deviation of 0.73 mm. Results of AET is presented in Figure 13.

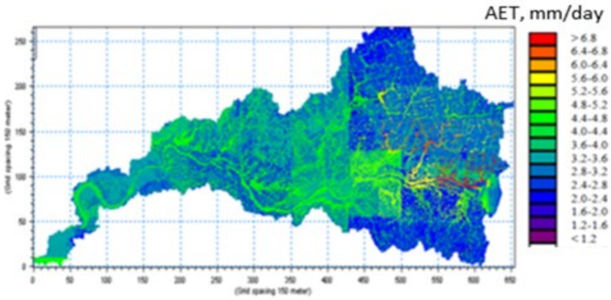

Figure 13. Result of actual evapotranspiration

3. *Actual Transpiration*

Actual transpiration is mainly contributed by the vegetation and similar trend is observed in the basin. Agriculture and forest regions are showing high transpiration losses and it is very low in the river/streams and other water bodies. Small amount of transpiration from water bodies is due to presence of aquatic vegetation. Mean value of transpiration is 2.1 mm with standard deviation (SD) of 1.2 mm in the basin. Results of actual transpiration is presented in Figure 14.

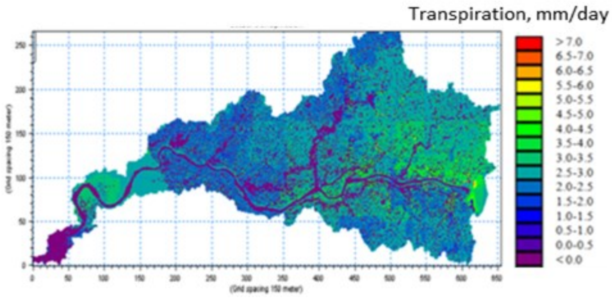

Figure 14. Result of actual transpiration

4. *Actual Evaporation from Ponded Water*

Evaporation is mainly occurring in open water bodies and from the fields which are having soil moisture but very less vegetation. It can be remarked that all the river/stream network along with other water bodies are showing high evaporation whereas it is quite low in other land cover classes. Result of actual evaporation from ponded water and other land cover classes is presented in Figure 15. Mean of evaporation is 1 mm with SD of 1.7 mm in the basin, although maximum value goes up to 7 mm per day.

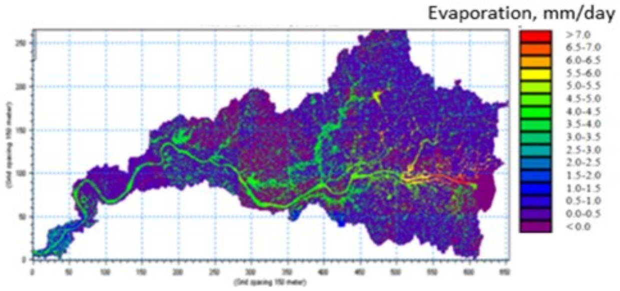

Figure 15. Result of actual evaporation in the basin

5. *Canopy Interception Storage*

Interception losses from canopy of the vegetation is presented in Figure 16. Mainly forested regions which are in the upstream of the lower Tapi basin show high interception losses. Mean interception loss is 0.11 mm with SD of 0.16 mm.

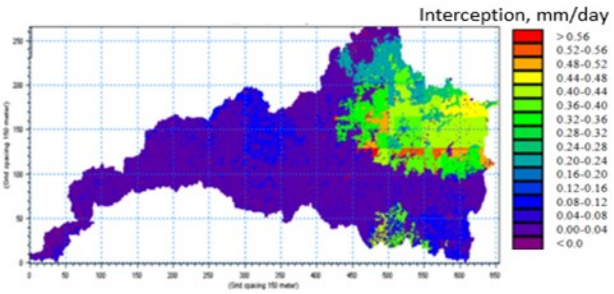

Figure 16. Result of canopy interception storage

6. *Depth of Overland Water*

Water depth over the ground surface is estimated and aggregated for the season to show accumulated water depth in the basin (Figure 17). Main river and its tributaries streams show high water depth. it may be observed that in the flood plain depressions also water depth is high. Mean accumulated water depth, representing the monsoon season, in the basin found to be 0.064 m with SD of 0.39 m.

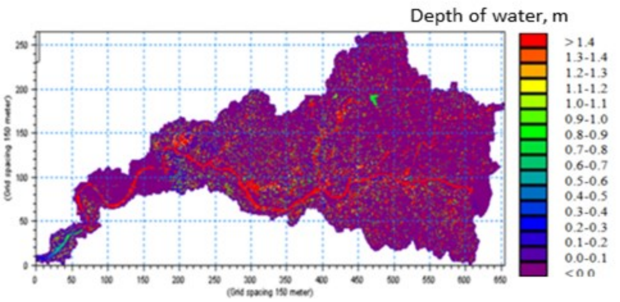

Figure 17. Result of depth of accumulated overland water during the season

7. *Infiltration to UZ (negative)*

Infiltration to the ground surface is estimated and presented in Figure 18. Mean infiltration is 1.1 mm with standard deviation of 0.45 mm per day.

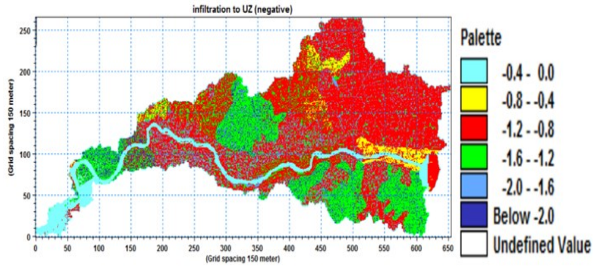

Figure 18. Result of infiltration to unsaturated zone (negative)

Time series plots:
Time series plot for different water balance components such as AET, overland water (runoff), soil moisture etc. for a particular cell for the monsoon season has been extracted and sample results have been shown in the section below., in all-time series plots.

1. *Average water content in the root zone*
Variation of average water content in a particular cell in time domain is shown in Figure 19. By observing the time series plot, it is found that obtained results for soil moisture gradually increase as the monsoon starts then remains more or less stable during monsoon period and decreases as the monsoon terminates.

Figure 19. Time series of average water content in the root zone

2. *Actual Evapotranspiration*
AET profile in a particular cell in time domain is shown in Figure 20. Variation of AET is depend on the transpiration losses as well as evaporation from water bodies and these two are govern by variability of rainfall as well as land cover types.

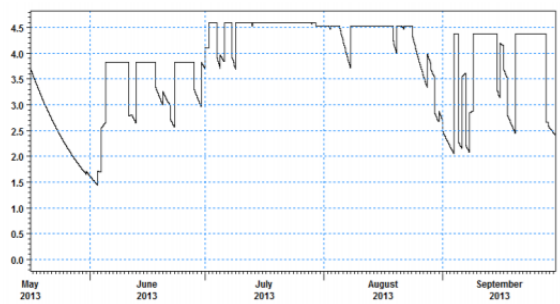

Figure 20. Time series of Actual Evapotranspiration

3. Depth of Overland Water

Water depth on the ground surface fluctuates throughout the monsoon period and mainly govern by the rainfall pattern. Time series of depth of overland water depth in a particular cell is presented in Figure 21.

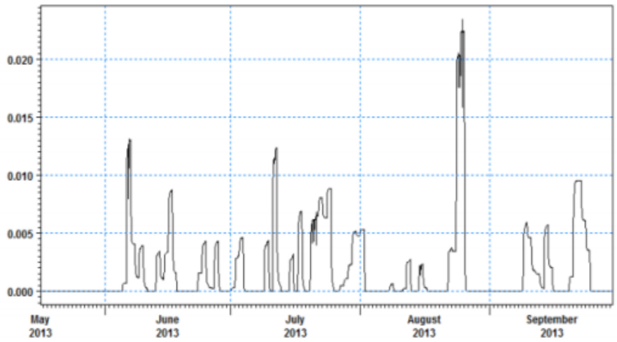

Figure 21. Time series of depth of overland water

MIKE 11 Simulated Results

Hydro-dynamic model MIKE-11 was coupled dynamically with the hydrological model MIKE SHE. Runoff from hydrological model is integrated with the hydro-dynamic model on daily time steps. Therefore, river flow simulations have been performed and water surface elevation along with discharge are estimated. Water Surface Elevation at different cross sections of Lowet Tapi river along the longitudinal profile of the river is shown in Figure 22. The spikes in the profiles are indicative of the tributaries junctions.

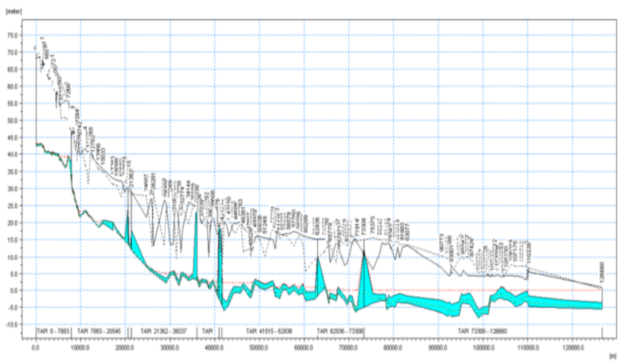

Figure 22. Water surface elevation along the longitudinal profile of the river

Model Calibration

The coupled model was tested using the satellite altimeter (SARAL-Altika) retrieved water levels in absence of in situ measurements with simulated river water levels. Approach for the retrieval of river water level from altimeter is adopted from Gupta et al., 2015. Model calibration was done at Ghala river gauging site (Figure 2). A very good match between the model simulated and altimeter retrieved water levels is obtained. The accuracy in terms of coefficient of determination was obtained with a value of 0.97. Coupled model calibration results is presented in Figure 23.

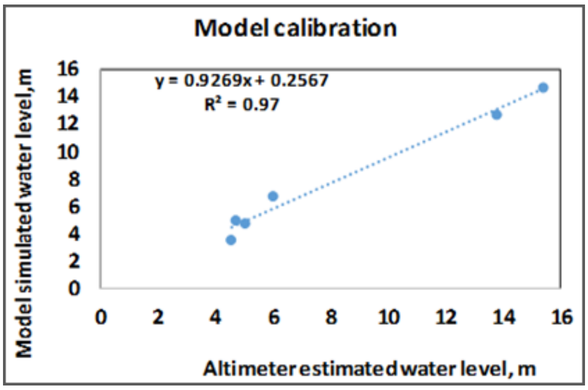

Figure 23. Model calibration results

5. Conclusions

Coupled MIKE SHE and MIKE 11 model has been parameterized integrating the remote sensing derived hydro-meteorological and biophysical variables to simulate the hydrological water balance and river flow over the Lower Tapi river basin. Model was calibrated using the satellite altimeter derived and simulated river water levels. Tested integrated model simulations were carried out to simulate the evapotranspiration, surface runoff, soil moisture, and stream flows. The following conclusions are derived from the present study:

- An integrated modelling system is developed and tested for Lower Tapi basin. The modelling of hydrological water balance is done using MIKESHE and simulation of river flow is done using MIKE11.
- Remote Sensing Provides hydro-meteorological and biophysical variables and plays vital role for the parameterization of data intensive physically base models.
- Major water balance components such as Actual Evapotranspiration and Surface Runoff were obtained 50.2% and 39.7%, respectively for the monsoon season of2013.
- ET was further partitioned into evaporation and Transpiration and were of 37.2% and 62.8%, respectively.
- Model calibration using altimeter based river water levels was satisfactory with coefficient of determination (R^2)0.97.
- Calibrated integrated model would be useful for long-term hydrological simulations for planning and management of water resources in the region.

Acknowledgements

We thank Human Resource Department, Space Applications Centre (SAC), ISRO Ahmedabad to provide an opportunity for conducting research work at SAC. Thanks to Dr. R.P. Singh, Head of Land Hydrology Division, for his guidance and support.

References

DHI, MIKE SHE User Manual, Volume 1 (2007a) Reference Guide. Danish Hydraulic Institute – Water and Environment: Hørsholm, Denmark.

DHI, MIKE SHE User Manual. Volume 2 (2007b) Reference Guide. Danish Hydraulic Institute – Water and Environment: Hørsholm, Denmark.

DHI, MIKE ZERO Auto Calibration and Parameter Optimisation Tool (2007c) User Guide Danish Hydraulic Institute–Water and Environment: Hørsholm, Denmark.

Clilverd H. M., J. R. Thompson, C. M. Heppell, C. D. Sayer and J. C. Axmacher (2016). Coupled Hydrological/Hydraulic Modelling of River Restoration Impacts and Flood plain Hydrodynamics. River Research and Applications. https://doi.org/10.1002/rra.3036

Gupta P. K., A. K. Dubey, N. Goswami, R. P. Singh and P. Chauhan (2015). Use of SARAL-Altika Observations for Modeling River Flow. Marine Geodesy, 48, 614-625.

Mirela-Alina S. and V. Ana (2015). Applicability of MIKE SHE to Simulate Hydrology in Argesel River Catchment. Agriculture and Agricultural Science Procedia 6, 517-524.

Saidislomkhon U., Y. Mitani and T. Kusuda (2016). An Integrated Hydrological Model for Water Balance Estimation in the Chirchik River Basin, Northern Uzbekistan, Computational water, Energy, and Environmental Engineering, 5, 87-97. http://dx.doi.org/10.4236/cweee.2016.53009

Zhiqiang Z., W. Shengping, G. Sun, G. M. Steven, H. Zhang, J. Li, M. Zhang, E. Klaghofer and P. Strauss (2008). Evaluation of the MIKE SHE Model for Application in the Loess Plateau, China, Journal of American water resources association, 44 (5), 1108-1120. Available: https://doi.org/10.1111/j.1752-1688.2008.00244.x.

Subramanya K. (1997). Flow in open channel hydraulics (Second edition), Tata McGraw-Hill Publishing, New Delhi.

Reviewers for Journal of Geomatics, Volume 15 No. 1 and 2

Editorial Board places on record its sincere gratitude to the following peers for sparing their valuable time to review papers of the Journal of Geomatics, Volume 15. We express special thanks to Dr. P.K. Gupta, Guest editor for bringing out the special section on “Flood Assessment and Modelling”

Mr. Vibhuti Bhushan Jha	Dr. Bhaskar Nikam	Dr. Sudhakar Sharma
Dr. Amit Kumar Dubey	Dr. Dhruvesh Patel	Dr Markand P. Oza
Dr. Raj Setia	Dr. G.D. Bairagi	Dr. C.P. Singh
Dr. Harish Chandra Karnatak	Dr. Ragunath K.P	Dr. Saravanavel J
Dr. Suresh Babu D.S	Shri. R.J. Bhanderi	Shri. J.G. Patel
Shri. T.V.R. Murthy	Dr. V.N. Sridhar	Dr. J.S. Parihar
Dr. S. Chander	Dr. Nitant Dube	Shri. Nimisha Singh
Dr. Anand S.S	Dr. V.V Rao	Dr. Praveen Thakur
Dr. K.R. Manjunath	Dr. Suraj Kumar Singh	Dr. Reet Kamal Tiwari
Dr. Kriti Avishek	Dr. Sudhkar Reddy	Dr. Hitendra Padalia
Dr. M.G. Thakkar	Mr. Prasun Kumar Gupta	Dr. Hariom Singh
Mr. Ravi Bhandari	Dr. Stutee Gupta	Dr. Eric Stemn
Prof. V.S. Hegde	Dr. Gireesh Gopinath	Dr. Prashant Kumar
Dr. Govindan Kutti	Dr. Kaushik Gopalan	Prof. Will E. Featherstone
Prof. Ashraf El-Kutb Mousa	Dr. Mehul Pandya	Dr. Rahul Nigam
Dr. Cynthia Borkai Boye	Dr. Nandita Goswami	Dr. Ashish Pandey
Dr. Kamlesh Patel	Dr. Chinni Kumar	

Author index (Vol. 15)

INDIAN SOCIETY OF GEOMATICS: AWARDS

National Geomatics Award for Excellence

This award has been instituted to recognize outstanding and conspicuously important contribution in promoting geomatics technology and applications at the country level. The contributions should have made major impact on the use of this technology for national development.
Areas of contribution considered for the award are:

1. Geographical Information System
2. Global Positioning System
3. Photogrammetry
4. Digital Cartography
5. Applications of Geomatics

The award shall consist of Rs. 50,000/- in cash, a medal and citation.

Eligibility

Any citizen of India, engaged in activities related to geomatics technology and its applications is eligible for this award. The prize is awarded on the basis of work primarily done in India.

The age limit for awardees is 45 years or above as on June 30 of the year of award.

Selection

A duly constituted Award Committee will evaluate all nominations received. The committee shall consist of eminent experts in the field of geo-spatial technology, to be identified by the Executive Council, ISG. The committee shall forward selected name/s to ISG – EC for approval and announcement. Apart from those persons, whose nominations have been received, the Committee may consider any person or persons who, in their opinion, have made outstanding contributions to development of geo-spatial technology and applications.

The award can be withheld in any year if, in the opinion of the committee, no candidate is found suitable in that particular year.

Presentation of the Award

The award shall be presented during the Annual Convention of ISG. Local Hospitality shall be taken care by ISG & Air fare (low cost) may be reimbursed if awardees request for it.

How to make Nomination

The nominations can be proposed by Head of a major research institute/ centre; Vice-Chancellor of a university; Secretary of Government Scientific Departments; President of a National Academy, President, Indian Society of Geomatics / Indian Society of Remote Sensing / Indian National Cartographic Association / ISG fellow or two life members of the society with more than 10 year old membership.

A candidate once nominated would be considered for a total period of two years. Nomination should be sent in the prescribed format to Secretary, ISG.

The last date for receiving nominations shall be September 30 or otherwise extended.

Format for nomination of Geomatics Award for Excellence

1. Name of the Nominee
2. Postal Address
3. Academic Background (Bachelor degree onwards)
4. Field of Specialisation
5. Important positions held (in chronological order)
6. Professional Experience including foreign assignments.
7. Important Awards / Honours
8. Important Publications/Patents: (A set of ten most important publications to be enclosed with this form)
9. Contributions of Nominee based on which the nomination is sent (in 1000 words, also provide a statement in 50 words which may be used for citation.):
10. Other Relevant Information:

Proposer:

Signature
Name
Address
Phone/ Fax
E-mail
Life Membership No. (in case of ISG Member):

Place & Date

Endorsed by (in case nomination is by 2 ISG Life members)

Signature
Name
Address
Phone/ Fax
E-mail
Life Membership No. (in case of ISG Member):

Place & Date
(The proposer should give a brief citation of the nominee's work)

National Geomatics Award

National Geomatics Award to be given each year: a) for original and significant contribution in Geomatics technology, b) for innovative applications in the field of Geomatics. Each award comprises a medal, a citation and a sum of Rs 25,000/- The guidelines for these awards are available on ISG website.

ISG Chapter Award for Best Performance

The best chapter award will be given to an active chapter of Indian Society of Geomatics, which has made significant contribution to further the mandate and goal of the society. The award consists of a citation and medal

President's Appreciation Medal for Contribution to the ISG

This award will be given to a member of the society, who has made noteworthy contribution to the growth of the ISG (its main body or any chapter). The Award consists of a Medal and a Citation.

Prof. Kakani Nageswara Rao Endowment Young Achiever Award

Indian Society of Geomatics instituted a new award from year 2013 named "Prof. Kakani Nageswara Rao Endowment Young Achiever Award", to encourage young researchers/scientists/academicians pursuing research in the field of geospatial technology/applications. The award carries a cash prize of Rs. 10,000/- along with a citation.

NATIONAL GEOMATICS AWARD

Indian Society of Geomatics has instituted two National Geomatics Awards to be given each year for (a) Original and significant contribution in Geomatics technology, (b) Innovative application(s) in the field of Geomatics. Each award comprises a medal, a citation and a sum of Rs. 25,000/-.

The guidelines for the award are as under

Areas of contribution considered for the award (both technology and applications)

1. Geographical Information System
2. Global Positioning System
3. Photogrammetry
4. Digital Cartography
5. Remote Sensing

Eligibility

Any citizen of India engaged in scientific work in any of the above-mentioned areas of research is eligible for the award.

The awards are to be given for the work largely carried out in India.

- First award will be given for original contribution in the field of Geomatics technology supported by publications in a refereed journal of repute.
- Second award will be given for carrying out innovative application(s). Supported by publications in rear reviewed Journals of repute.
- The contribution for the first award should have been accepted by peers through citation of the work.
- Work based on the applications of existing technologies will not be considered for the first award.
- The work should have made impact on the overall development of Geomatics.

How to Send Nomination

Nominations should be sent in the prescribed format, completed in all aspects to the Secretary, Indian Society of Geomatics, Space Applications Centre Campus, Ahmedabad 380 015 by August 31 of the year of award.

Selection Process

An expert committee, consisting of at least three members, constituted by the Executive Council of the Indian Society of Geomatics, will scrutinize the nominations and recommend the awardees' names to the Executive Council. The Council will decide on the award based on the recommendations.

FORMAT FOR AWARD NOMINATION

1. Name of the Candidate:
2. Present Position:
3. Positions held earlier (chronological order):
4. Academic qualifications (Bachelor's degree onwards):
5. Names of at least three Indian Scientists/Technologist in the area as possible referees *:
6. Brief write up on the work (500 words) for which award is claimed:
7. Publication(s) on the above work (reprint(s) to be enclosed):
8. List of other publications of the candidate:
9. Citation of the work for which award is claimed:
10. Impact of the work (for which award is claimed) on the development in the field of Geomatics (500 words):
11. Whether the work has already won any award? If so, give details:

The Applications in the above format (five copies) should be submitted (by Registered Post or Speed Post) to

The Secretary, Indian Society of Geomatics,
Space Applications Centre Campus,
Ahmedabad-380015

so as to reach by September 30 of the year of award

*ISG is, however, not bound to accept these names and can refer the nomination to other experts/peers

INDIAN SOCIETY OF GEOMATICS: FELLOWS

Shri Pramod P. Kale, Pune
Dr George Joseph, Ahmedabad
Dr A.K.S. Gopalan, Hyderabad
Dr Prithvish Nag, Varanasi
Dr Baldev Sahai, Ahmedabad
Shri A.R. Dasgupta, Ahmedabad
Dr R.R. Navalgund, Bengaluru
Shri Rajesh Mathur, New Delhi
Dr Ajai, Ahmedabad
Prof P. Venkatachalam, Mumbai
Dr Shailesh Nayak
Prof I.V. Murli Krishna
Prof SM Ramasamy, Tiruchirapalli
Dr Ashok Kaushal, Pune
Shri A.S. Kiran Kumar, Bengaluru
Prof. P.K. Verma, Bhopal
Maj. Gen. Siva Kumar, Hyderabad
Dr A S Rajawat, Ahmedabad
Dr Shakil Romshoo, Srinagar

INDIAN SOCIETY OF GEOMATICS: PATRON MEMBERS

P-1 Director, Space Applications Centre (ISRO), Jodhpur Tekra Satellite Road, Ahmedabad - 380 015
P-2 Settlement Commissioner, The Settlement Commissioner & Director of Land Records-Gujarat, Block No. 13, Floor 2, Old Sachivalay, Sector-10, Gandhinagar – 382 010
P-3 Commissioner, Mumbai Metropolitan Region Development Authority, Bandra-Kurla Complex, Bandra East, Mumbai - 400 051
P-4 Commissioner, land Records & Settlements Office, MP, Gwalior - 474 007
P-5 Director General, Centre for Development of Advanced Computing (C-DAC), Pune University Campus, Ganesh Khind, Pune - 411 007
P-6 Chairman, Indian Space Research Organization (ISRO), ISRO H.Q., Antariksha Bhavan, New BEL Road,Bengaluru 560 231
P-7 Director General, Forest Survey of India, Kaulagarh Road, P.O. I.P.E., Dehra Dun – 248 195
P-8 Commissioner, Vadodara Municipal Corporation, M.S. University, Vadodara - 390 002
P-9 Director, Centre for Environmental Planning and Technology (CEPT), Navarangpura, Ahmedabad - 380 009
P-10 Managing Director, ESRI INDIA, NIIT GIS Ltd., 8, Balaji Estate, Sudarshan Munjal Marg, Kalkaji, New Delhi - 110 019
P-11 Director, Gujarat Water Supply and Sewerage Board (GWSSB), Jalseva Bhavan, Sector – 10A, Gandhinagar - 382 010
P-12 Director, National Atlas & Thematic Mapping Organization (NATMO), Salt Lake, Kolkata - 700 064
P-13 Director of Operations, GIS Services, Genesys International Corporation Ltd., 73-A, SDF-III, SEEPZ, Andheri (E), Mumbai - 400 096
P-14 Managing Director, Speck Systems Limited, B-49, Electronics Complex, Kushiaguda, Hyderabad - 500 062
P-15 Director, Institute of Remote Sensing (IRS), Anna University, Sardar Patel Road, Chennai - 600 025
P-16 Managing Director, Tri-Geo Image Systems Ltd., 813 Nagarjuna Hills, PunjaGutta, Hyderabad - 500 082
P-17 Managing Director, Scanpoint Graphics Ltd., B/h Town Hall, Ashram Road, Ahmedabad - 380 006
P-18 Secretary General, Institute for Sustainable Development Research Studies (ISDRS), 7, Manav Ashram Colony, Goplapura Mod, Tonk Road, Jaipur - 302 018
P-19 Commandant, Defense institute for GeoSpatial Information & Training (DIGIT), Nr. Army HQs Camp, Rao Tula Ram Marg, Cantt., New Delhi - 110 010
P-20 Vice President, New Rolta India Ltd., Rolta Bhavan, 22nd Street, MIDC-Marol, Andheri East, Mumbai - 400 093
P-21 Director, National Remote Sensing Centre (NRSC), Deptt. of Space, Govt. of India, Balanagar, Hyderabad - 500 037
P-22 Managing Director, ERDAS India Ltd., Plot No. 7, Type-I, IE Kukatpalli, Hyderabad - 500 072
P-23 Senior Manager, Larsen & Toubro Limited, Library and Documentation Centre ECC Constr. Gp., P.B. No. 979, Mount Poonamallee Road, Manapakkam, Chennai - 600 089.
P-24 Director, North Eastern Space Applications Centre (NE-SAC), Department of Space, Umiam, Meghalaya 793 103
P-25 Progamme Coordinator, GSDG, Centre for Development of Advanced Computing (C-DAC), Pune University Campus, Pune – 411 007
P-26 Chief Executive, Jishnu Ocean Technologies, PL-6A, Bldg. No. 6/15, Sector – 1, Khanda Colony, New Panvel (W), Navi Mumbai – 410 206
P-27 Director General, A.P. State Remote Sensing Applications Centre (APSRAC), 8th Floor, "B" Block, Swarnajayanthi Complex, Ameerpet, Hyderabad- 500 038
P-28 Director, Advanced Data Processing Res. Institute (ADRIN), 203, Akbar Road, Tarbund, Manovikas Nagar P.O., Secunderabad –500 009
P-29 Managing Director, LEICA Geosystems Geospatial Imaging Pvt. (I) Ltd., 3, Enkay Square, 448a Udyog Vihar, Phase-5, Gurgoan- 122 016
P-30 Director, Defense Terrain Research Limited (DTRL), Ministry of Defense, Govt. of India, Defense Research & Development Organisation, Metacafe House, New Delhi – 110 054
P-31 Chairman, OGC India Forum, E/701, Gokul Residency, Thakur Village, Kandivali (E), Mumbai – 400 101
P-32 Managing Director, ML Infomap Pvt. Ltd., 124-A, Katwaria Sarai, New Delhi – 110 016
P-33 Director, Rolta India Limited, Rolta Tower, "A", Rolta Technology Park, MIDC, Andheri (E), Mumbai – 400 093
P-34 Director, State Remote Sensing Applications Centre, Aizawl – 796 012, Mizoram

Instructions for Authors

The journal covers all aspects of Geomatics – geodata acquisition, pre-processing, processing, analysis and publishing. Broadly this implies inclusion of areas like GIS, GPS, Photogrammetry, Cartography, Remote Sensing, Surveying, Spatial Data Infrastructure and Technology including hardware, software, algorithm, model and applications. It endeavors to provide an international forum for rapid publication of developments in the field – both in technology and applications.

A manuscript for publication must be based on original research work done by the author(s). It should not have been published in part or full in any type of publication nor should it be under consideration for publication in any periodical. Unsolicited review papers will not be published.

The Editorial Board or the Indian Society of Geomatics is not responsible for the opinions expressed by the authors.

Language

The language of the Journal will be English (Indian). However, manuscripts in English (US) and English (British) are also acceptable from authors from countries located outside India.

Manuscript Format

Each paper should have a title, name(s) of author(s), and affiliation of each of the authors with complete mailing address, e-mail address, an abstract, four to six keywords, and the text. The text should include introduction/background, research method, results, discussion, followed by acknowledgements and references. The main text should be divided in sections. Section headings should be concise and numbered in sequence, using a decimal system for subsections. Figures, images and their captions should be inserted at appropriate points of the text. Figures, images and tables should fit in two column format of the journal. If absolutely necessary, figures, images and tables can spread across the two columns. Figures and images, however, should not exceed half a page in height. A title should be provided for each Table, Image and Figure. All figures and images should be in 600 dpi resolution and sized as per column/margin width. Authors must ensure that diagrams/figures should not lose easy readability upon reduction to column size. The SI (metric) units and international quantities should be used throughout the paper. In case measurements are given in any other system, equivalent measurements in SI (metric) units should be indicated in brackets.

Use MS Word with English (UK/US) or English (Indian) dictionary. The page size should be A4 paper, with 2 cm margin on all sides. Title, authors and affiliation should be centred. Abstract should be justified across margins. The manuscript text should be in two columns of 8.2 cm each with a gutter of 6mm between them. Use only Times New Roman fonts. Title should be 12 points bold. Authors and affiliation should be 9 points. All other text including headings should be 10 points. Heading numbering scheme should be decimal e.g. 1, 1.1, 1.2.3, etc. Headings should be in bold.

Normally length of a published paper should be about 6-10 pages in A4 size including figures. Use of illustrations in colour should be restricted and resorted to only where it is absolutely necessary and not for enhancing the look of the paper. If the number of colour illustrations exceeds five, authors' institution may be asked to reimburse the extra cost involved, which at current rates is about Rs. 2500 per coloured figure/diagram/plate/illustration.

Submission of Manuscript

Submissions should be in electronic form via email. The manuscript may be sent by email to editorjogisg@gmail.com. In exceptional cases hard copy submission in camera ready form may be allowed with the prior permission of the Chief Editor. Submission in any other form will be returned to the author. To speed up the review process, authors are advised to provide a list of three probable reviewers with their institutional address and e-mail IDs.

Guidelines for Citing References

Names of all cited publications should be given in full. No abbreviations should be used. Following procedure is to be adopted.

Journal Publications

Bahuguna, I.M. and A.V. Kulkarni (2005). Application of digital elevation model and orthoimages derived from IRS-1C Pan stereo data in monitoring variations in glacial dimensions, Journal of the Indian Society of Remote Sensing, 33(1), 107- 112. (to be referred to in the text as Bahuguna and Kulkarni (2005) or if more than two sets of authors are to be referred to, as (Bahuguna and Kulkarni, 2005; Jain et al., 1994)) When more than two authors are to be referred to, use Jain et al. (1994). However, in References, all authors are to be mentioned.

Publication in a Book

Misra, V.N. (1984). Climate, a factor in the rise and fall of the Indus Civilization – Evidence from Rajasthan and Beyond in Frontiers of the Indus Civilization (B.B. Lal and S.P. Gupta: Chief Editors) Books and Books, New Delhi, pp. 461-489

Papers Published in Seminar/ Symposium Proceedings

Jain, A., A.R. Shirish, M. Das, K. Das, M.C. Porwal, and P.S. Roy (1994). Remote Sensing and Geographic Information System – An approach for the assessment of biotic interference in the forest ecosystem. Proceedings. 15th Asian Conference on Remote Sensing, Bangalore, November 17-23, 1994, pp. 65-72.

Books

Possehl, Gregory L. (1999). Indus Age: The beginnings. Oxford and IBH Publishing Corporation, New Delhi.

Reviewing

Each paper will be reviewed by three peers. Papers forwarded by members of the Editorial or Advisory Boards along with their comments would get processed faster and may be reviewed by two referees only.

Sample format for Authors is available in downloadable form at ISG website: www.isgindia.org/JOG/Sample_format.doc

Copyright

The copyright of the paper selected for publication will rest with the Indian Society of Geomatics. Corresponding author shall be required to sign a copyright assignment form, on behalf of all authors, once the paper is selected for publication. Authors are, however, at liberty to use this material elsewhere after obtaining permission from the Indian Society of Geomatics.

If the authors have used any copyright material in their manuscript, it is understood that they have obtained permission from the owner of the copyright material and they should convey the same along with the manuscript to the Chief Editor.

Certificate of Original Work

The authors will also provide a certificate that the paper is an original work, not published or being considered for publication elsewhere.

In the event the certificate turns out to be false, the Journal shall ban the author(s) from publishing in the Journal for a period of five years and inform the same to all other related publications.

Reprints

Authors will be allowed to download the (PDF) of their paper from ISG Website www.isgindia.org, No hard copy reprints will be provided.

ISG

To,
The Secretary, Indian Society of Geomatics
6202, Space Applications Centre (ISRO)
AHMEDABAD – 380 015. INDIA

Sir,

I want to become a Member/ Life Member/ Sustaining Member/ Patron Member/ Foreign Member/ Student Member of the Indian Society of Geomatics, Ahmedabad for the year _____. Membership fee of Rs. _____ /- is being sent to you by Cash/ DD/ Cheque. (In case of DD/ Cheque No.__________dated_________drawn on Bank

______________________________ . **I agree to abide by the Constitution of the Society.**

Date:

Place: **Signature**

- Name: Mr/Ms/Mrs/Dr____
- Address: ____

____PIN: _____________

Phone: ______________ Fax: ________________Email:

______________________________________ • Date of Birth

____

•Qualifications____

- Specialisation: ____
- Designation: _________________________ Organisation. ____________________________
- Membership in other Societies: ____
- Mailing Address: ____

____PIN: ___________________

Proposed by:
(Member's Name and No)
Signature of Proposer

For Office Use: A/P/L Member No.		Receipt No.		Date:	

Indian Society of Geomatics (ISG), Room No. 6202 Space Applications Centre (ISRO), Ahmedabad-380015, Gujarat. Url: www.isgindia.org Phone: +91-79 26916202
Email: secretary@isgindia.org or sasharma@sac.isro.gov.in Fax +91-79-26916287

MEMBERSHIP FEES

Sr. No.	Membership Category	Life/Patron Membership fees ₹ Indian	US $ Foreign	Annual Subscription ₹ Indian
1.	Annual Member	10	---	300
2.	Life Member a) Admitted below 45 years of age	2500	250	
	b) Admitted after 45 years of age	2000	200	
3.	Sustaining Member	---	---	2000
4.	Patron Member	50000	3000	---
5.	Student Member	10	---	100

MEMBERSHIP GUIDELINES

- Subscription for Life Membership is also accepted in two equal instalments payable within duration of three months, if so desired by the applicant. In such a case, please specify that payment will be in instalments and also the probable date for the second instalment (within three months of the first instalment).
- A Member of the Society should countersign application of membership as proposer.
- Subscription in DD or Cheque should be made out in the name of **'Indian Society of Geomatics'** and payable at Ahmedabad.
- Direct deposit in ISG A/Cs must include bank fee RS. 25/- for cash payment.
- Financial year of the Society is from April 1 to March 31.
- For further details, contact Secretary, Indian Society of Geomatics at the address given above.
- ISG has chapters already established at the following places. Ahmedabad, Ajmer, Bhagalpur, Bhopal, Chennai, Dehradun, Delhi, Hissar, Hyderabad, Jaipur, Ludhiana, Mangalore, Mumbai, Mysore, Pune, Shillong, Trichi, Srinagar, Vadodara, Vallabh Vidya Nagar, Visakhapatnam and Trivandrum. Applicants for membership have the option to contact Secretary/Chairman of the local chapter for enrolment. Details can be found at the website of the Society: www.isgindia.org.
- Journal of the Society will be sent to Life Members by softcopy only.

Indian Society of Geomatics (ISG), Room No. 6202 Space Applications Centre (ISRO), Ahmedabad-380015, Gujarat. Url: www.isgindia.org Phone: +91-79 26916202
Email: secretary@isgindia.org or sasharma@sac.isro.gov.in Fax +91-79-26916287

Geomatics Revealed

IGiS

Integrated GIS & IP Software

VERSION 2.0

MAKE IN INDIA

National Awards on Technology
By The Former President of India,
Dr. A. P. J. Abdul Kalam

Launch of IGiS Version 2.0
By Padam Shri AS Kiran Kumar, Chairman, ISRO and
Shri Tapan Mishra, DIRECTOR, SAC, ISRO.

What's new in IGiS

IGiS Version 2.0 is full of enhancements which you'll appreciate every day. New advanced GIS/IP and SAR modules are vital now a days. New COM Based Architecture makes you even more productive. The more you do with IGiS Version 2.0, the more you'll wonder how you ever did without it.

Enhancements in IGiS Version 2.0

- Advanced GIS / Image Processing
- Microwave SAR Analysis
- Meteorological Analysis
- COM Based Scalable Architecture
- New Ribbon Bar GUI
- Python Customization
- OGC Standards

Product Development Partner

इसरो isro
Government of India | Department of Space
Indian Space Research Organisation - (ISRO)

SGL Scanpoint Geomatics Ltd.
www.scanpointgeomatics.com

Scanpoint Geomatics Ltd.
Corporate Office : 12, Abhishree Corporate Park, Iskcon - Ambli Road, Ahmedabad - 380 058. Gujrat (India)
[P] +91 2717 297096-98 [F] +91 2717 297039 [E] info@scanpointgeomatics.com [W] www.scanpointgeomatics.com

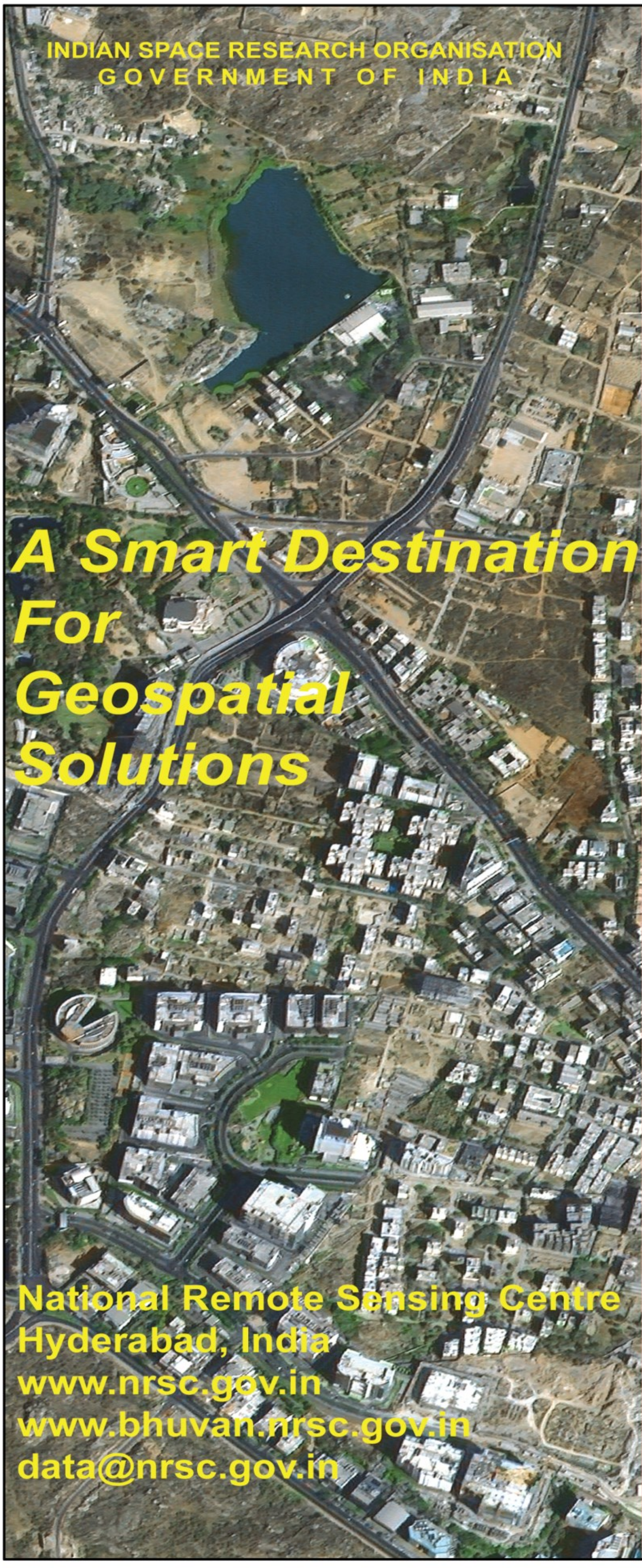

INDIAN SPACE RESEARCH ORGANISATION
GOVERNMENT OF INDIA

A Smart Destination For Geospatial Solutions

National Remote Sensing Centre
Hyderabad, India
www.nrsc.gov.in
www.bhuvan.nrsc.gov.in
data@nrsc.gov.in

nrsc

इसरो isro

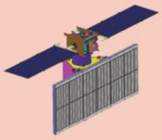

Only Organization in the Country to Acquire & Supply Satellite Data to Users

Aerial Acquisition for Specific User Demands & Disaster Management Support

Open Data & Value Added Products Dissemination Through Bhuvan

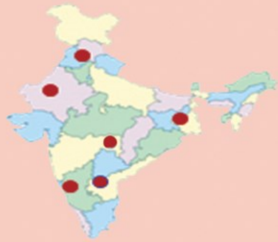

Region Specific Solutions

Capacity Building in Remote Sensing Applications